Fu-Gen Wu *Editor*

Fluorescent Materials for Cell Imaging

Springer

Fluorescent Materials for Cell Imaging

Fu-Gen Wu
Editor

Fluorescent Materials for Cell Imaging

Springer

Editor
Fu-Gen Wu
State Key Laboratory of Bioelectronics
School of Biological Science and Medical Engineering
Southeast University
Nanjing, Jiangsu, China

ISBN 978-981-15-5061-4 ISBN 978-981-15-5062-1 (eBook)
https://doi.org/10.1007/978-981-15-5062-1

This Springer imprint is published by the registered company Springer Nature Singapore Pte Ltd.
The registered company address is: 152 Beach Road, #21-01/04 Gateway East, Singapore 189721, Singapore

Contents

Introduction: Fluorescent Materials for Cell Imaging

Hao-Ran Jia, Ya-Xuan Zhu, and Fu-Gen Wu

Cell, the basic structural and functional unit of almost all living organisms (except viruses), has been recognized as one of the most important foundations of contemporary biology. Composed by a variety of biomolecules such as proteins, DNA, lipids, and sugars, a single cell is also a small but complete living organism with sophisticated biological structures [1]. Generally, cells can be classified into two types according to their structural differences, namely prokaryotes and eukaryotes. Although all cells contain an outer physical barrier called plasma membrane that isolates the intracellular components from the surrounding environment, the prokaryotic cells are fundamentally distinct from the eukaryotic ones in their internal organization. Prokaryotes lack a nucleus and other membrane-bound organelles with all their cellular components located together in the cytoplasm; in contrast, eukaryotes possess a complex endomembrane system composed of various membranous organelles, e.g., endoplasmic reticulum (ER), Golgi apparatus, mitochondrion, and lysosome. These organelles work in coordination with other subcellular structures and participate in many essential biological activities such as apoptosis, autophagy, mitosis, migration, cell signaling, and material transport, to maintain the regular metabolism and functions of organisms.

Cell imaging refers to the visualization of cell morphology, structure, and dynamics with the assistance of imaging systems. The development of modern cell biology heavily relies on the use of various imaging techniques that serve as the "eyes" of biologists. Over 300 years ago, Antoni van Leeuwenhoek with the aid of his manually made simple microscope first saw and described spermatozoa, red corpuscles, and bacteria [2]. These discoveries marked a new era in our pursuit of the nature of life, because nobody knew how conception worked, what composed blood, or what caused diseases in that time. In 1838, German scientist Matthias Schleiden established the cell theory for plants that all plant organisms consist of cells or cell derivatives, on the basis of his large amounts of microscopic observations, which marked the beginning of the plant cytology [3]. He also emphasized the importance of the cell nucleus and its relationship with cell division. One year later, Theodor Schwann extended Schleiden's theory to the animal world, forming a general cell theory. After entering the twentieth century, the advent of fluorescence microscopy brought a revolution in all fields of cell and molecular biology. Compared with traditional transmitted light microscopy, fluorescence microscopy utilizes fluorescent probes to illuminate the target molecules, structures, or compartments in cells with high sensitivity. However, the spatial resolution of these optical

H.-R. Jia · Y.-X. Zhu · F.-G. Wu (✉)
State Key Laboratory of Bioelectronics, School of Biological Science and Medical Engineering, Southeast University, Nanjing, Jiangsu, China
e-mail: wufg@seu.edu.cn

F.-G. Wu (ed.), *Fluorescent Materials for Cell Imaging*, https://doi.org/10.1007/978-981-15-5062-1_1

imaging techniques is still insufficient to clearly unravel some nanoscale cellular structures owing to the diffraction limitation of light. In the 1930s, Ernst Ruska and Max Knoll designed and built the first transmission electron microscope (TEM) that used electrons, not light, to observe the specimens, which marked another important milestone in the progress of imaging technology [4]. Considering that the spatial resolution of a modern TEM is 0.1 nm, approximately 2000 times higher than that of a light microscope, cell biologists can acquire ultrahigh-quality cell images to uncover many sophisticated cellular structures and subtle changes of cellular states. To date, with the help of diverse cell imaging techniques, we have gained a comprehensive understanding of how a cell works to govern the generation, maintenance, and function of cellular organizations, and have acquired numerous incredibly detailed images of cellular organelles, domains, and even biomacromolecules [5]. Although the framework of cell biology has now been completed, many essential issues still remain to be answered, e.g., what is the mechanism of cell aging. We believe that the progress in imaging technologies can promote the future development of cell biology. In this chapter, we first briefly introduce the existing imaging techniques for cell observations. Then, the principles and benefits of fluorescence imaging are discussed. Finally, we focus on the recent advances of various fluorescent materials and their applications in cell imaging.

1 Optical Imaging Techniques

Optical microscopes use the light source to illuminate specimens. Since the first invention of the simple light microscope, optical imaging has served as a fundamental tool of biological discovery for more than three centuries. Until now, a variety of optical microscopes have been designed with the aim of improving the imaging resolution and providing more detailed cellular information. Generally, most cellular structures are different from their surroundings in optical properties, but conventional light microscopy is unable to discriminate them. To solve this problem, optical contrasting techniques have been developed for observing transparent and unstained samples, which include darkfield microscopy, phase contrast microscopy, polarization microscopy, differential interference contrast (DIC) microscopy, and Hoffman modulation contrast microscopy [6]. These techniques utilize the differences in the refractive index between specimens and their surroundings, and can convert the refractive index differences to detectable brightness changes in the images. For example, the DIC microscopy, also known as Nomarski microscopy, uses polarized light and splits the light into two beams through a two-layered modified Wollaston prism, wherein one beam is directed through the specimen and the other only passes through the background. Due to the refractive index gradients in different areas, the two rays will generate a path difference, which can be finally visualized as a difference in brightness. In particular, DIC microscopy is extremely suitable to study cellular events such as apoptosis where cells experience tremendous shape changes [7]. Another common strategy for enhancing the imaging contrast is using dyes or counterstains to amplify the optical signals of samples. In particular, the emergence of diverse fluorescent probes like organic fluorescent molecules, fluorescent proteins, quantum dots (QDs), and conjugated polymers, as imaging contrast agents has substantially boosted the advancement of fluorescence microscopy. The principles of fluorescence and detailed introduction of fluorescent materials will be discussed later. Currently available fluorescence imaging techniques include epi-illumination fluorescence microscopy, confocal microscopy, two-/multiphoton fluorescence microscopy, fluorescence correlation microscopy (FCM), fluorescence-lifetime imaging microscopy (FLIM), etc [5, 8]. Fig. 1 schematically displays the working mechanisms of epi-illumination microscopy, confocal microscopy, and nonlinear laser scanning microscopy. To be noted, one of the biggest improvements of modern fluorescence imaging is the adoption of laser as the light source. Lasers produce coherent light beams that are extremely intense, highly

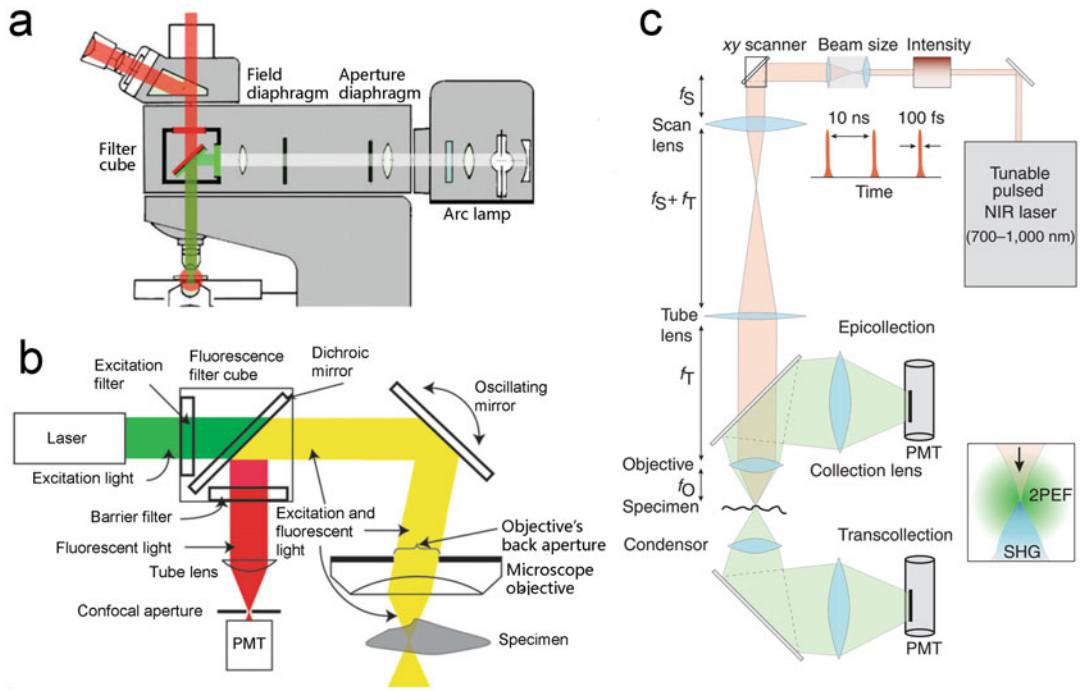

Fig. 1 (**a**) Schematic diagram illustrating the working mechanism of the epi-illumination fluorescence microscopy. Reprinted with permission from Ref. [10]. Copyright 2005, Nature Publishing Group. (**b**) Layout of the confocal microscopy. Reprinted with permission from Ref. [11]. Copyright 2005, Nature Publishing Group. (**c**) Principle of the generic nonlinear laser scanning microscopy. Reprinted with permission from Ref. [12]. Copyright 2005, Nature Publishing Group

directional, and very pure in frequency, through a process of optical amplification based on the stimulated emission of electromagnetic radiation. In doing so, the fluorescent probes can be excited more efficiently and emit stronger fluorescence signals. The employment of these advanced imaging techniques has helped biologists to observe many once invisible structures in cells. For instance, Gaus et al. successfully visualized the membrane lipid structure and raft domains of living cells by using two-photon microscopy [9]. It was found that in macrophages, the liquid-ordered domains are frequently observed in membrane protrusions (filopodia), adhesion points, and cell–cell contacts.

Many cellular behaviors specifically appear in some restricted areas of cells, such as the plasma membrane. Recently, total internal reflection fluorescence (TIRF) microscopy has attracted broad interest in the observation of membrane-associated processes, e.g., endocytosis, exocytosis, and cell adhesion [13]. As a class of evanescent wave microscopy, TIRF microscopy excites fluorophores not by direct light illumination, but by using an evanescent wave that occurs when the incident light is totally reflected at the interface of two transparent media with different refractive indices. In this case, only the fluorophores in very close proximity (within 100 nm) to the coverslip can be excited, ensuring the elimination of background fluorescence outside the focal plane and extremely high signal-to-noise contrast (Fig. 2). Besides, TIRF microscopy provides a convenient tool for the real-time monitoring of nanoparticle–membrane interactions, which can instruct the rational design and surface modification of drug-loaded nanoparticles (NPs) for enhanced therapeutic efficiency [14].

In 1873, Ernst Abbe discovered that two neighboring objects with a distance closer than ~200 nm cannot be resolved by lens-based light microscopy [15]. Due to the existence of this

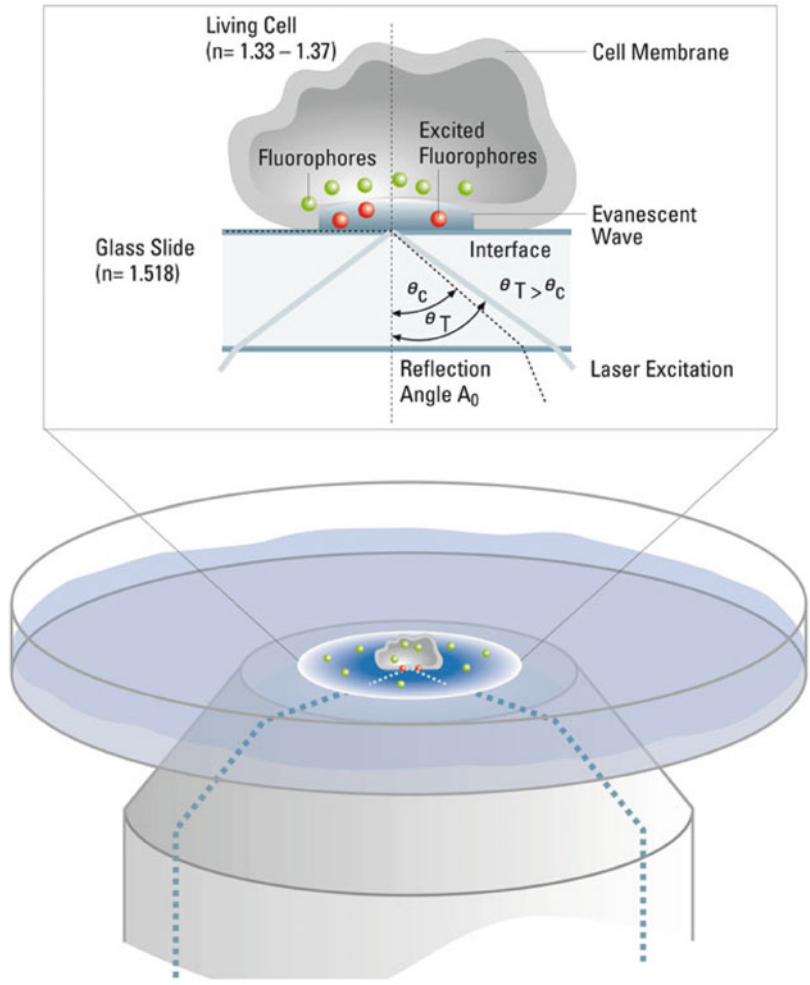

Fig. 2 Schematic illustrating the principle of TIRF microscopy. Reprinted with permission from Ref. [14]. Copyright 2012, Springer

diffraction limit, the imaging resolution of most traditional optical microscopes is severely restricted, which prevents researchers to gain more insights into the molecular structures and organizations of living cells. Recent advances in "super-resolution" imaging techniques, including stimulated emission depletion (STED) microscopy, structured illumination microscopy (SIM), stochastic optical reconstruction microscopy (STORM), ground state depletion microscopy followed by individual molecular return (GSDIM), and photoactivated localization microscopy (PALM), provide feasible strategies to surpass the diffraction limit and acquire high-quality cell images [16]. The development of these methods allows us to visualize the morphology and dynamics of nanometer-sized cellular structures. As an example, STED microscopy relies on the saturated depletion of excited molecules at the periphery of a scanning focal spot, which is capable of realizing a lateral resolution less than 20 nm. In 2008, Hein and co-workers successfully utilized STED microscopy to visualize the ER with subdiffraction resolution in the interior of a living mammalian cell using yellow fluorescent protein (YFP) tags [17]. The STED image clearly shows the ring structures formed by the tubular network of the ER, whereas confocal imaging failed to visualize these details (Fig. 3).

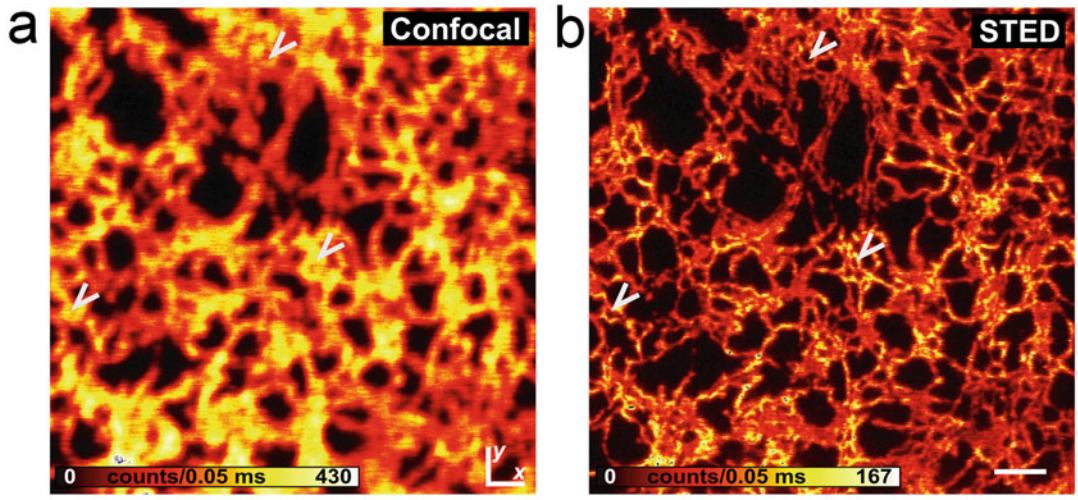

Fig. 3 Confocal (**a**) and STED (**b**) images showing the ER structures in mammalian cells labeled by the fluorescent protein Citrine. Reprinted with permission from Ref. [17]. Copyright 2008, The National Academy of Sciences of the USA

In living cells, not all biological molecules can be easily labeled with fluorescent probes for fluorescence imaging, which poses a great challenge to the molecular-level detection within cells. Currently, Raman microscopy represents an emerging class of tools for imaging and analyzing living biological samples, especially cells, at a molecular level. Raman microscopy is based on the Raman scattering, a technique capable of detecting molecular vibrations that can reflect molecular species, structures, and environmental conditions. It is worth noting that Raman microscopy senses the biological samples directly by light without requiring an additional fluorescence labeling procedure. Beyond the selective detection of the target molecules, Raman microscopy can realize time-resolved mapping of the dynamic distributions of many essential biomolecules such as proteins (e.g., cytochrome c) and lipids in living cells [18]. However, it is technically difficult to precisely extract useful information from the complicated Raman spectra, and the autofluorescence of intracellular molecules may obscure Raman signals. More recently, nonlinear optical imaging methods such as second harmonic generation (SHG) microscopy, thrid harmonic generation microscopy, sum frequency generation vibrational spectroscopy, coherent anti-Stokes Raman scattering (CARS) microscopy, and stimulated Raman scattering (SRS) microscopy have emerged as promising strategies that can achieve single-cell analysis with highly improved sensitivity [19]. These nonlinear imaging techniques exploit basic light–matter interactions originated from the intrinsic optical characteristics of chemical structures to perform biological imaging. Benefiting from their quantitative and label-free imaging as well as exceptional chemical specificity, SHG, CARS, and SRS microscopy begin to serve as an important class of tools complementary to fluorescence imaging techniques.

2 Non-Optical Imaging Techniques

Apart from the above optical imaging approaches, there are also some non-optical imaging methods that are irreplaceable for us to have comprehensive knowledge of cells. Over the past decades, an increasing number of human diseases have been demonstrated to be closely related to the disorder of intracellular protein trafficking, which highlights the importance of understanding the

membrane-associated protein trafficking pathways. Electron microscopy (EM) is the only technique capable of providing sufficient resolution for the observation of intracellular proteins and small membrane subdomains, serving as a powerful biological tool [20]. Different from optical microscopy that involves the above-mentioned diffraction barrier, EM utilizes the electron beam as the source of illuminating radiation and thus can provide magnified images with ultra-high spatial resolutions (typically within 1 nm). There are different types of electron microscopes, including reflection electron microscope (REM), scanning electron microscope (SEM), TEM, low voltage electron microscope (LVEM), and scanning transmission electron microscope (STEM). To be noted, biological samples must receive a fixation treatment (cryofixation or chemical fixation) before the EM observation to preserve the cellular architecture. For cells and tissues, cryofixation is so far the best available method of immobilization, because chemical fixation may cause structural artifacts and the redistribution of some soluble proteins. Observing cryofixed cells via EM is called cryogenic electron microscopy (CryoEM), an imaging technique that ensures researchers to view the cells in their most natural state. In a lately reported study, Sartori-Rupp et al. adopted CryoEM to reveal the structure of tunneling nanotubes (TNTs) that are long, actin-rich membranous protrusions responsible for the intercellular transport of various cargoes in neuronal cells, and proved that neuronal TNTs have distinct structural features compared to other cell protrusions [21].

Another nonnegligible imaging technique capable of measuring physical and chemical properties in nanoscale dimensions is scanning probe microscopy (SPM), which is a big imaging family with more than 20 members including scanning tunneling microscopy, atomic force microscopy (AFM), scanning thermal microscopy, scanning electrochemical microscopy (SECM), scanning ion conductance microscopy, near-field acoustic microscopy, and so on [22]. Consisting of a cantilever with a sharp tip at its end, a scanning probe microscope detects the surface of samples without physical contact and can provide true topographic imaging of the cell surfaces. Nowadays, using SPM to solve certain biological and biomedical questions is gaining wider acceptance. For example, Takahashi et al. applied voltage-switching mode SECM to acquire high-quality topographical and electrochemical images of living cells, which allowed the mapping of the sites of neurotransmitter release from a differentiated rat adrenal pheochromocytoma (PC12) cells [23]. In another study, Carvalho et al. confirmed the specific molecular recognition between fibrinogen and an unknown receptor on the erythrocyte membrane with the help of AFM [24]. The fibrinogen−erythrocyte interaction showed a binding force of 79 pN that is lower than but comparable to that of fibrinogen−platelet binding (97 pN). This work exemplified the application of AFM-based force spectroscopy as a sensitive and high-fidelity imaging tool for the diagnosis of genetic mutation-induced hematological diseases.

3 Principles and Advantages of Fluorescence Imaging

Among the existing cell imaging strategies, fluorescence spectroscopy is still considered to be the primary research tool in cell biology and many other disciplines. Since George Gabriel Stokes first illustrated the phenomenon of fluorescence in 1852, [25] this basic physical event has revolutionized the way how biologists observe the cells. Fluorescence is the light emitted from a fluorescent molecule/material after absorbing light, which is a three-stage process as depicted in the Jablonski diagram (Fig. 4) [26]. To be specific, when absorbing photon energy supplied by an external source such as an incandescent lamp or a laser, fluorescent molecules are excited from the ground state S_0 to the higher singlet electronic state S_1 (Stage 1: excitation). This process is different from chemiluminescence where the excited state is created by chemical reactions. The energy at this stage is partially dissipated through internal conversion and the molecules relax to a lower vibrational level S_2 (Stage 2: internal conversion). The internal conversion

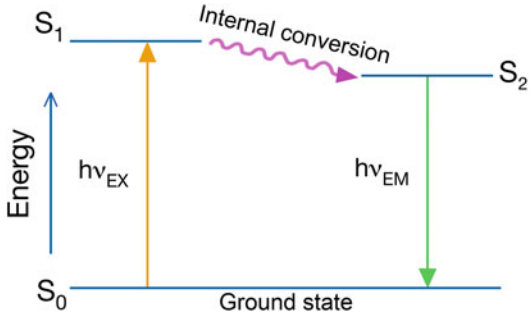

Fig. 4 Jablonski diagram illustrating the processes of light excitation, internal conversion, and emission of fluorescence

process is extremely rapid, generally within 10^{-12} s, and occurs prior to fluorescence emission. Then, the fluorophore returns to its ground state S_0 by emitting fluorescence. To be noted, not all the molecules return to the ground state via fluorescence emission. Other ways of depopulating the S_2 state involve nonradiative relaxation and intersystem crossing to a triplet state, etc. The triplet state is distinguished from the singlet one by the opposite orientation of an electron spin. Molecules in this state can relax via photon emission, which is called phosphorescence, or nonradiative relaxation. According to the Jablonski diagram, the energy of the fluorescence emission is generally less than that of excitation due to the energy dissipation via internal conversion, leading to a longer wavelength of the emitted fluorescence. The difference between the excitation and emission wavelengths, i.e., the Stokes shift, is fundamental to the sensitivity of the fluorescence imaging measurements. The Stokes shift makes it possible to filter out the excitation light without blocking the emissive signals and to exclusively visualize the objects of interest with low background signals. In contrast, traditional bright field imaging methods require the detection of transmitted/reflected signals against the incident light at the same wavelength. Thus, fluorescence imaging greatly enhances the signal-to-background contrast as well as the imaging resolution.

Another important merit of the fluorescence imaging is the non-invasive observation of specimens, which is appealing to researchers when observing living cells. Although some approaches such as transmission electron microscopy can provide high-quality visualization of cell structures with nanometer-scale spatial resolution, they involve harsh sample preparations (e.g., chemical fixation, dehydration, and metal coating) and only present a static, snapshot view of the cells. In contrast, fluorescence imaging allows the nondestructive and real-time observations of living cells for tracking the dynamics of diverse cellular behaviors with high spatial and temporal resolutions [5]. Unlike many imaging approaches that directly illuminate cells by light or electron sources, fluorescence imaging depends on the light emission from fluorescent probes upon excitation by a light source, and utilizes the fluorescence signals of these probes to indirectly reflect the locations or structures of cellular components. More importantly, fluorescent probes can also serve as highly sensitive indicators to detect the intrinsically non-fluorescent species and parameters of cells, such as metal ions, [27, 28] glutathione, [29, 30] reactive oxygen species (ROS), [31] adenosine triphosphate (ATP), [32] pH value, [33] and oxygen level [34]. Therefore, compared with other imaging techniques, fluorescence imaging has found much broader applications in biological areas, dominantly benefiting from the development of various fluorescent materials with desirable properties.

4 Fluorescent Materials for Cell Imaging

Generally, the fluorescent materials for cell imaging can be classified as endogenous cellular molecules and synthesized probes. It has been found that some intracellular coenzymes such as nicotinamide adenine dinucleotide (NADH) and flavin adenine dinucleotide (FAD) possess inherent fluorescence under light excitation [35]. These coenzymes play essential roles in a variety of cellular oxidation–reduction reactions, and thus can serve as specific biomarkers to reflect the metabolic states or mitochondrial activities in cells/tissues [36, 37]. For example, Piston et al.

employed the two-photon excitation microscopy as a non-invasive tool to image the subcellular glucose metabolism within intact pancreatic islets by detecting the autofluorescence arising from NADH [36]. Furthermore, Shi and co-workers developed an optical method for detecting early-stage Alzheimer's disease (AD) based on the different autofluorescence spectral profiles of tryptophan, NADH, and FAD in healthy and AD brains [37]. However, inherent biomolecules suitable for cell fluorescence imaging are extremely limited. In 1962, the discovery of green fluorescent protein (GFP), an intrinsically fluorescent gene product from the bioluminescent jellyfish *Aequorea victoria*, has ushered the cell fluorescence imaging into a new era [38, 39]. GFP is a considerably stable protein with 238 amino acids and contains a highly fluorescent chromophore constrained in a barrel of β-sheet structure, which forms spontaneously during the assembly of the polypeptides without the involvement of enzymatic synthesis. This remarkable feature means that molecular biologists can create genetic fusions of GFP to any protein of interest in living cells or entire organisms by introducing the GFP-encoding gene sequences. However, wild-type GFP gradually failed to meet the increasingly high standard of fluorescence imaging due to its low extinction coefficient and expression level, which motivates the advent of diverse optimized GFP variants, e.g., enhanced GFP (EGFP, Fig. 5a), SuperGlow (sg) GFP, and blue EGFP [38]. Apart from green fluorescence, the emission color of fluorescent proteins can be genetically manipulated to yield blue fluorescent proteins (BFPs), cyan fluorescent proteins (CFPs), YFPs, orange fluorescent proteins (OFPs), and red fluorescent proteins (RFPs), all of which share a similar structural framework (Fig. 5b), by either changing the local environment around the chromophore (e.g., the location of charged amino acid residues, hydrogen bonding networks, and hydrophobic interactions within the protein matrix) or directly introducing different chromophores (Fig. 5c) [38–40]. This super family of fluorescent proteins has provided researchers an unprecedented variety of high-performance choices for multicolor cell imaging. Therefore, fluorescent proteins are an ideal tool for uncovering a wide range of cell-related processes such as the dynamics of gene expression, intermolecular interactions, the behaviors of cellular organelles, cell mitosis, membrane dynamics, and calcium signaling. Whereas, fluorescent proteins are large biomolecules and, in some cases, can inevitably affect the function of the attached cellular proteins [26]. Besides, the fluorescence intensity of fluorescent proteins depends not only on their structures but also on the cellular environment in which the marker protein is expressed.

Over the past decades, the explosion in the diversity of artificially synthesized fluorescent probes has greatly promoted the development of cell biology. Compared with endogenous fluorescent molecules, synthesized fluorescent materials are mostly used by researchers to realize the fluorescence imaging of cells, mainly ascribed to their simple staining procedures, high fluorescence quantum yields, and good photostability, etc. Typically, these cell probes can be divided into small-molecule dyes (e.g., cyanines, rhodamines, diarylethenes, Alexa Fluor® dye series, BODIPY® dye series, fluorescein-based dyes, coumarins, and pyrenes), fluorescent antibodies, and fluorescent nanomaterials (e.g., inorganic QDs, carbon dots (CDs), fluorescent metal nanoclusters, and fluorescent dye-loaded NPs). Until now, organic chemists have designed and synthesized many thousands of fluorescent molecules that hold the potential to cover almost all aspects of cell imaging. More importantly, many of these molecular probes are commercially available, which provides great convenience for biological researchers, especially those without the experience of chemical synthesis, to select suitable fluorescence tools according to their investigations. For imaging different cellular structures, there are molecular probes designed to target cytoskeletal proteins, mitochondrion, lysosome, peroxisome, yeast vacuole, ER, Golgi apparatus, cell nucleus, lipid droplet, and plasma membrane, to name a few [41, 42]. Furthermore, many fluorescent molecules can also serve as the tracers of cellular functions like viability, proliferation, endocytosis, and signal transduction, or as the

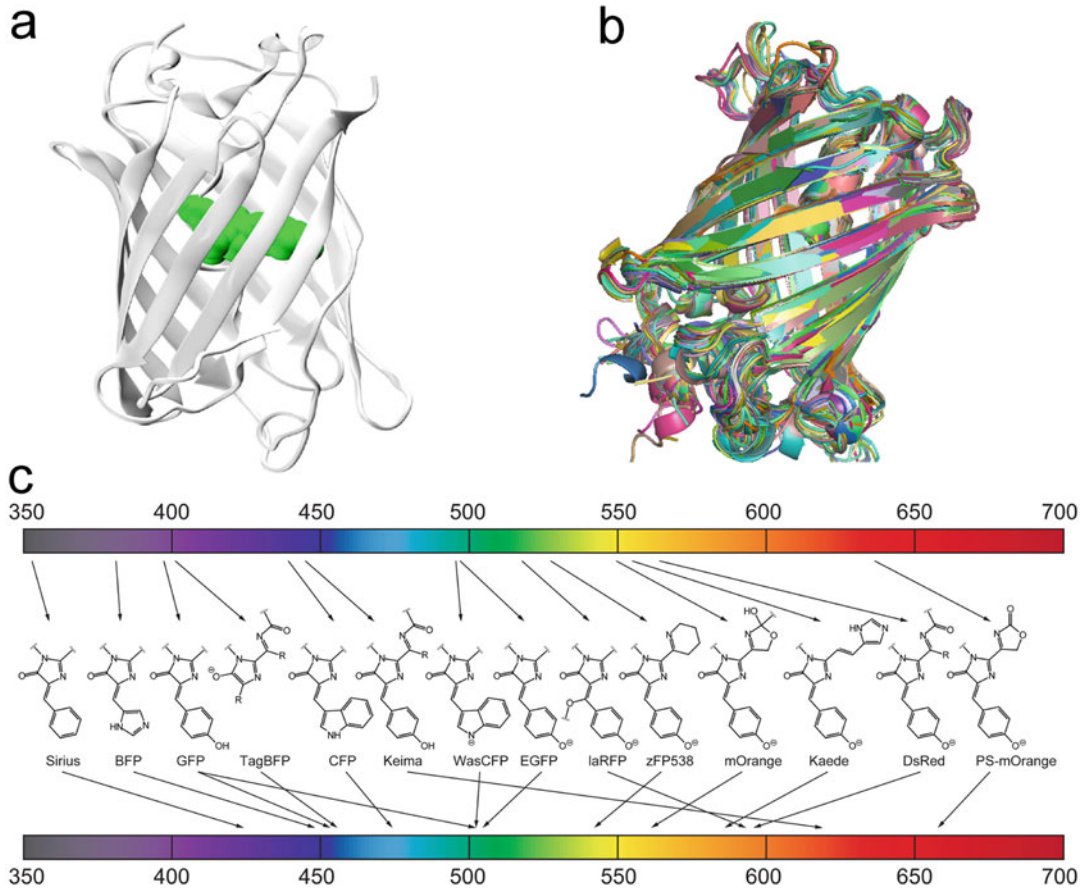

Fig. 5 (**a**) Crystal structure of an EGFP. Reprinted with permission from Ref. [38]. Copyright 2017, American Chemical Society. (**b**) Alignment of 202 crystal structures of different fluorescent proteins extracted from the protein data bank. Reprinted with permission from Ref. [39]. Copyright 2013, American Chemical Society. (**c**) Chemical structures of the chromophores in fluorescent proteins with different emission wavelengths. Reprinted with permission from Ref. [38]. Copyright 2017, American Chemical Society

sensitive indicators of intracellular ROS, glutathione, ions, pH values, membrane potentials, and so on [42]. Recently, the luminogens with aggregation-induced emission (AIE) characteristics, termed AIEgens, have become a class of "star molecules" in the applications of cell imaging. In contrast to the aggregation-caused quenching effect confronted by most conventional luminogens, AIE effect refers to the phenomenon that some molecules emit weak fluorescence in their solutions, but generate intense fluorescence upon forming aggregates. Since the discovery and description of AIE effect by Tang et al. in 2001, [43] the AIEgen family has experienced an exponential growth over the past two decades [44]. Compared with traditional fluorescent molecules, AIEgens possess excellent photostability, good biocompatibility, and low background emission, and are thus extremely suitable for bioimaging applications. For instance, Zheng and co-workers reported a naphthalimide-based fluorescent probe that enables the simultaneous labeling of lipid droplets and lysosomes with high specificity [45]. Interestingly, the as-designed AIEgen emitted yellow fluorescence in lipid droplets but red fluorescence in lysosomes, due to the different environments inside these subcellular entities. Using this unique AIE probe, the authors dynamically tracked the movement of lipid droplets and lysosomes in living cells.

Immunofluorescence techniques refer to the use of fluorescent molecule-conjugated antibodies for the specific fluorescence labeling of target antigens. As a fundamental tool in cell biology studies, immunofluorescence allows the rapid, sensitive, and quantitative analysis of cells, which facilitates researchers to gain a better understanding of phenotype mutation, cellular signaling pathways, and subcellular structures, etc. [46] Compared to the fluorescent protein-based imaging strategies, immunofluorescence imaging can minimize the risk of altering the intrinsic structures or functions of the target proteins. Generally, immunofluorescence staining employs either fluorophore-conjugated primary antibodies for the direct labeling of the target sites or primary antibodies along with fluorophore-conjugated secondary antibodies (immunoglobulins that bind to primary antibodies). The former strategy is simpler and more efficient to achieve immunofluorescence imaging; however, in some cases, the target markers expressed in cells/tissues are too rare to confer sufficient immunofluorescence signals. In comparison, the two-step labeling strategy can use fluorescent secondary antibodies to amplify the signals of primary antibodies, and thus significantly improves the detection sensitivity. Recently, many advanced conjugation techniques have been developed in a bid to simplify operation and increase the efficiency of targeting and amplifying the marker signals. For example, enzyme-amplification techniques, particularly the tyramide signal amplification, are commonly used strategies, which dramatically increase the immunofluorescence sensitivity over traditional detection procedures [47]. This class of methods typically utilizes the highly specific recognition between biotin and avidin to introduce enzymes to the antigenic sites for signal amplification. In 2010, Haun et al. developed a modular and broadly applicable targeting platform on the basis of the covalent, bioorthogonal reaction between 1,2,4,5-tetrazine and *trans*-cyclooctene [48]. The cycloaddition is chemoselective, catalyst-free, serum-tolerant, and adaptable to metal nanomaterials, making it superior to the classic biotin–avidin binding strategy. Apart from developing new signal amplification techniques, researchers are also dedicated to seeking alternative fluorescent tags because traditional organic fluorophores usually suffer from severe photobleaching. As a class of novel fluorescent materials, QDs with tunable narrow-band emission, intense fluorescence signals, and enhanced photostability, have been demonstrated as promising fluorescent tags for labeling antibodies [49, 50].

With the vast development of nanotechnology, fluorescent nanomaterials have emerged as a major class of probes for cell imaging applications [51]. Despite the prosperous advancement of molecular fluorescent dyes, most of these dyes are hydrophobic and lack of good dispersity in aqueous solutions, which drastically impairs their final imaging performance in biological systems. Besides, organic dyes often suffer from optical instability and evident cytotoxicity. To overcome these challenges, diverse fluorescent molecules have been combined with nanomaterials such as nanomicelles, [52–56] liposomes, [57, 58] and polymeric NPs, [59, 60] to form fluorescent nanoprobes with favorable optical properties and robust cell imaging capabilities. For example, Hu et al. loaded TPA-BTTDO, a hydrophobic AIE probe capable of labeling lysosomes and lipid droplets with different fluorescence, into polymeric nanomicelles that were formed by 1,2-distearoyl-*sn*-glycero-3-phosphoethanolamine-*N*-[methoxy (polyethylene glycol)-2000] (DSPE-PEG2000), and employed this fluorescent nanoprobe to visualize the lipid droplet−lysosome interplay in living cells [55]. In another study, our group physically incorporated a hydrophobic heptamethine cyanine dye me-IR825 into the inner core of Pluronic F127-formed micelles [56]. The as-prepared nanomicelles exhibited preferential accumulation in cancer cells and achieved selective fluorescence imaging of mitochondria. Besides their improved cell imaging performance, fluorescent nanomaterials can be modified by diverse targeting/binding ligands/groups to increase the selectivity of fluorescent sensors to specific cells or subcellular organelles. For instance, Yang et al. designed mitochondria-targeting mesoporous silica NPs

(MSNs) for the real-time detection of hydrogen peroxide (H_2O_2) and pH fluctuations in living cells [61]. The MSNs were loaded with two fluorescent probes, Cy-O-SeH (for H_2O_2 detection) and fluorescein (for pH sensing), and functionalized with triphenylphosphonium to endow the nanosensors with mitochondria-targeting ability. For lysosomal imaging, Wu and co-workers conjugated morpholine, a targeting unit for lysosomes, onto the surface of CDs and achieved the highly selective fluorescence imaging of lysosomes in living cells [62]. In another study, Ghosh et al. reported a lipid nanoagent containing an ER-targeting moiety (*p*-toluenesulfonyl group), a fluorescent tag with DNA-damaging capability (1,8-naphthalimide), and an ER stress inducer (17AAG, an Hsp90 inhibitor) [63]. This nanoagent could realize ER-specific fluorescence imaging and induce ER stress in HeLa cervical cancer cells. Recently, the fluorescence imaging of plasma membranes has attracted broad attention; however, plasma membrane is a highly active and complex biointerface that controls the movement of substances into and out of the cells, which poses enormous challenges to the stable and long-lasting plasma membrane imaging because of the rapid internalization of the stains by the cells or the easy detachment of the stains from the cells. In 2015, our group rationally designed a plasma membrane nanoprobe by covalently conjugating a glycol chitosan (GC) polymer with PEG-cholesterol chains and fluorescein isothiocyanate (FITC) dyes [64]. Benefiting from the multisite membrane anchoring effect of cholesterol moieties, this probe (denoted as GC-PEG cholesterol-FITC) realized stable fluorescence imaging of mammalian plasma membranes for 6 h (Fig. 6a), which surpassed the imaging performance of DiD (Fig. 6b), a commercial fluorescent dye for membrane staining. Our subsequent study further demonstrated that this nanoprobe is also applicable to bacterial as well as fungal cells for universal cell surface imaging (Fig. 6c) [65]. Apart from in vitro cell imaging applications, we also developed a red fluorescent dye cyanine 5 (Cy5)-conjugated polymeric probe named Chol-PEG-Cy5 that realized the non-invasive plasma membrane labeling of the epidermal cells of live zebrafish embryos (Fig. 6d) [66]. Further, besides those nanomaterials that serve as the carriers of fluorescent dyes, there is also a class of nanomaterials that possess intrinsic fluorescence properties, including semiconductor QDs, metal nanoclusters (metal: Au, Ag, Cu, or Pt), silicon NPs, carbon nanomaterials (e.g., CDs and graphene QDs), upconversion NPs, and conjugated polymer-based NPs/dots. In comparison with small-molecule dyes, these fluorescent nanomaterials typically possess excellent photostability, high quantum yields, and tunable emission spectra, which guarantees their broad applications in cell imaging.

Currently, the development of novel fluorescent materials for use as cell imaging probes is still ongoing. In spite of the impressive progress we have already made, many challenging issues remain unsolved in the field of cell fluorescence imaging. For example, some organelles and intracellular structures still lack the corresponding fluorescent probes, especially those with high selectivity. Moreover, many commercially available cell imaging agents are only applicable to fixed and permeabilized cells because these probes cannot cross intact plasma membranes, which makes it extremely difficult to observe the dynamic behaviors of subcellular structures such as cytoskeletons and nucleoli in living cells. Furthermore, live cell fluorescence imaging requires that the applied probes have negligible toxicity to the tested cells and cause little disturbance to the cellular activities. Therefore, more efforts are needed in the future to design cell-permeable and more biocompatible fluorescent probes capable of realizing the real-time observation of living cells. Another major challenge faced by many cell imaging probes is that their fluorescence signals inside cells are too weak to realize high-quality imaging. To address this issue, developing more efficient signal amplification strategies or new fluorescent probes with higher quantum yields is in urgent need.

In this book, we mainly introduce the cell imaging applications of various newly emerged molecular and nanoscale fluorescent probes, which will be discussed in the following chapters in detail. To be specific, Chapter “Semiconductor

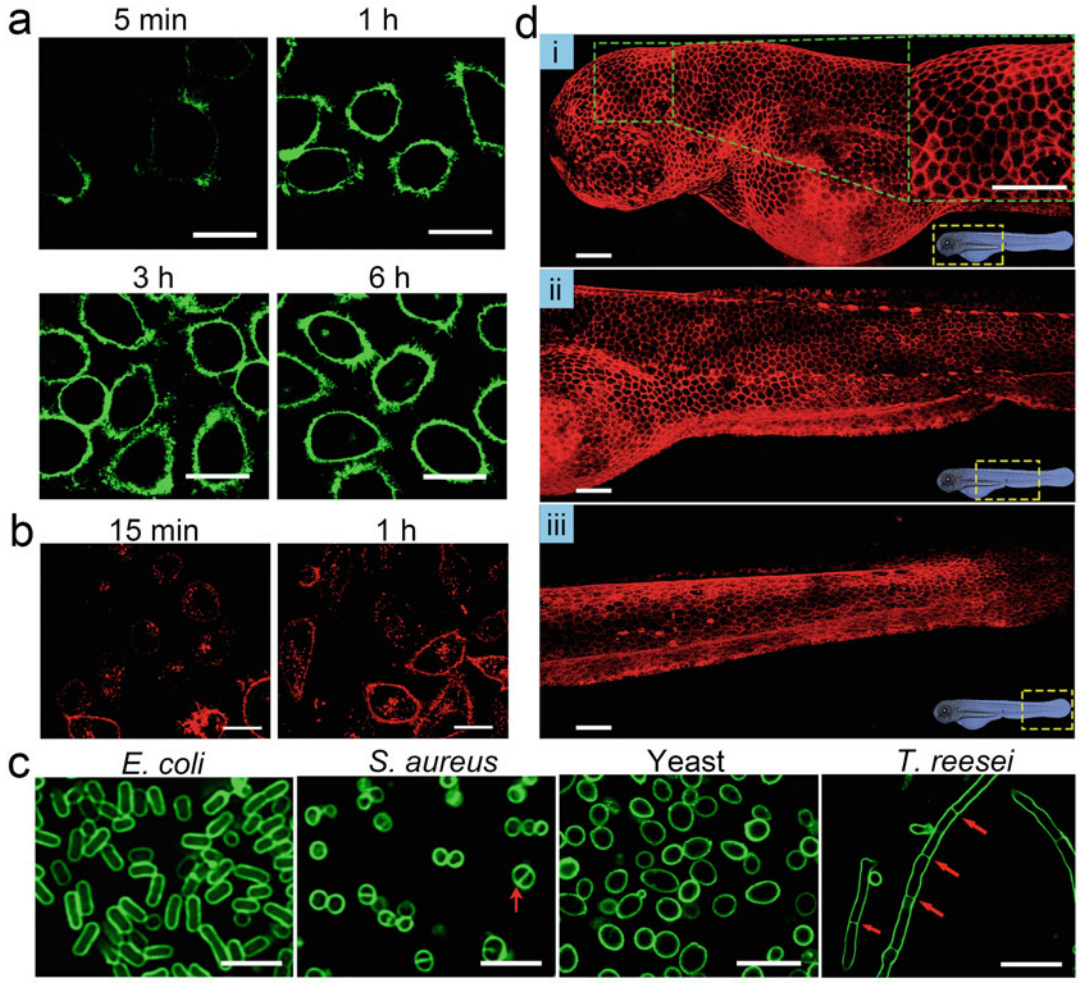

Fig. 6 (**a**) Confocal fluorescence images of human alveolar type II (AT II) cells after being stained by GC-PEG cholesterol-FITC for 5 min, 1 h, 3 h, and 6 h, respectively. Scale bars = 20 μm. (**b**) Confocal fluorescence images of AT II cells after being stained by DiD for 15 min and 1 h, respectively. Scale bars = 20 μm. (**a** and **b**): Reprinted with permission from Ref. [64]. Copyright 2015, The Royal Society of Chemistry. (**c**) Confocal fluorescence images of GC-PEG cholesterol-FITC-stained *Escherichia coli* (*E. coli*), *Staphylococcus aureus* (*S. aureus*), yeast, and *Trichoderma reesei* (*T. reesei*). Scale bars = 4 μm. Reprinted with permission from Ref. [65]. Copyright 2016, American Chemical Society. (**d**) Reconstructed three-dimensional confocal fluorescence images of the zebrafish embryonic epidermis labeled by Chol–PEG–Cy5. From top to bottom: head (i), trunk (ii), and tail (iii). Scale bars = 100 μm. Reprinted with permission from Ref. [66]. Copyright 2019, The Royal Society of Chemistry

Quantum Dots for Cell Imaging" will focus on how the most commonly used QDs, the semiconductor QDs, are used in cell imaging; Chapters "Carbon Nanodots for Cell Imaging" and "Silicon Nanoparticles for Cell Imaging" will summarize the recent advances of carbon nanodots and metal-free silicon NPs, respectively, in the fluorescence imaging of cells; Chapter "Fluorescent Metal Nanoclusters for Bioimaging" will discuss the applications of metal nanoclusters and hybrid metal nanoclusters in fluorescence cell imaging; Chapter "Lanthanide-Based Upconversion Nanoparticles for Bioimaging Applications" will introduce the illumination mechanism of upconversion NPs (especially the lanthanide-based upconversion NPs) and their broad uses for cell imaging; Chapter "Conjugated Polymers and Polymer Dots for Cell Imaging" will

summarize the progress of cellular imaging applications of various fluorescent conjugated polymers and polymer dots; Chapters "Aggregation-Induced Emission (AIE) Probes for Cell Imaging" and "Luminescent Coordination Compounds for Cell Imaging" will focus on two types of molecular probes, i.e., AIE molecules and fluorescent coordination compounds, and their promising advantages in the field of cell imaging.

References

1. Alberts B, Bray D, Hopkin K, Johnson A, Lewis J, Raff M, Roberts K, Walter P (2009) Essential cell biology. Garland Science, New York
2. Gest H (2004) The discovery of microorganisms by Robert Hooke and Antoni van Leeuwenhoek, Fellows of the Royal Society. Notes Rec R Soc Lond 58:187–201
3. Sekeres J, Zarsky V (2018) 180 years of the cell: from Matthias Jakob Schleiden to the cell biology of the twenty-first century. Concepts in cell biology-history and evolution. Springer, Heidelberg
4. Knoll M, Ruska E (1932) Das elektronenmikroskop. Z Physik 78:318–339
5. Stephens DJ, Allan VJ (2003) Light microscopy techniques for live cell imaging. Science 300:82–86
6. Cox G (2012) Optical imaging techniques in cell biology. Taylor and Francis, Boca Raton
7. Gumienny TL, Lambie E, Hartwieg E, Horvitz HR, Hengartner MO (1999) Genetic control of programmed cell death in the *Caenorhabditis elegans* hermaphrodite germline. Development 126:1011–1022
8. Periasamy A (ed) (2001) Methods in cellular imaging. Oxford University Press, Oxford
9. Gaus K, Gratton E, Kable EPW, Jones AS, Gelissen I, Kritharides L, Jessup W (2003) Visualizing lipid structure and raft domains in living cells with two-photon microscopy. Proc Natl Acad Sci U S A 100:15554–15559
10. Lichtman JW, Conchello JA (2005) Fluorescence microscopy. Nat Methods 2:910–919
11. Conchello JA, Lichtman JW (2005) Optical sectioning microscopy. Nat Methods 2:920–931
12. Helmchen F, Denk W (2005) Deep tissue two-photon microscopy. Nat Methods 2:932–940
13. Poulter NS, Pitkeathly WT, Smith PJ, Rappoport JZ (2015) The physical basis of total internal reflection fluorescence (TIRF) microscopy and its cellular applications. Methods Mol Biol 1251:1–23
14. Parhamifar L, Moghimi SM (2012) Total internal reflection fluorescence (TIRF) microscopy for real-time imaging of nanoparticle-cell plasma membrane interaction. Methods Mol Biol 906:473–482
15. Abbe E (1873) Beitrage zur Theorie des Mikroskops und der mikroskopischen Wahrmehmung. Arc F Mikr Anat 9:413–468
16. Godin AG, Lounis B, Cognet L (2014) Super-resolution microscopy approaches for live cell imaging. Biophys J 107:1777–1784
17. Hein B, Willig KI, Hell SW (2008) Stimulated emission depletion (STED) nanoscopy of a fluorescent protein-labeled organelle inside a living cell. Proc Natl Acad Sci U S A 105:14271–14276
18. Hamada K, Fujita K, Smith NI, Kobayashi M, Inouye Y, Kawata S (2008) Raman microscopy for dynamic molecular imaging of living cells. J Biomed Opt 13:044027
19. Streets AM, Li A, Chen T, Huang Y (2014) Imaging without fluorescence: nonlinear optical microscopy for quantitative cellular imaging. Anal. Chem. 86:8506−8513
20. Koster AJ, Klumperman J (2003) Electron microscopy in cell biology: integrating structure and function. Nat Rev Mol Cell Biol 4:SS6–SS10
21. Sartori-Rupp A, Cervantes DC, Pepe A, Gousset K, Delage E, Corroyer-Dulmont S, Schmitt C, Krijnse-Locker J, Zurzolo C (2019) Correlative cryo-electron microscopy reveals the structure of TNTs in neuronal cells. Nat Commun 10:342
22. Wickramasinghe HK (2000) Progress in scanning probe microscopy. Acta Mater 48:347–358
23. Takahashi Y, Shevchuk AI, Novak P, Babakinejad B, Macpherson J, Unwin PR, Shiku H, Gorelik J, Klenerman D, Korchev YE, Matsue T (2012) Topographical and electrochemical nanoscale imaging of living cells using voltage-switching mode scanning electrochemical microscopy. Proc Natl Acad Sci U S A 109:11540–11545
24. Carvalho FA, Connell S, Miltenberger-Miltenyi G, Pereira SV, Tavares A, Ariëns RA, Santos NC (2010) Atomic force microscopy-based molecular recognition of a fibrinogen receptor on human erythrocytes. ACS Nano 4:4609–4620
25. Stokes GG (1852) On the change of refrangibility of light. Phil Trans R Soc Lond 142:463–562
26. Lakowicz JR (ed) (2013) Principles of fluorescence spectroscopy. Kluwer Academic, New York
27. Guo Y, Zhang L, Zhang S, Yang Y, Chen X, Zhang M (2015) Fluorescent carbon nanoparticles for the fluorescent detection of metal ions. Biosens Bioelectron 63:61–71
28. Gao G, Jiang YW, Jia HR, Yang J, Wu FG (2018) On-off-on fluorescent nanosensor for Fe^{3+} detection and cancer/normal cell differentiation via silicon-doped carbon quantum dots. Carbon 134:232–243
29. Guo Y, Zhang X, Wu FG (2018) A graphene oxide-based switch-on fluorescent probe for glutathione detection and cancer diagnosis. J Colloid Interface Sci 530:511–520
30. Yin J, Kwon Y, Kim D, Lee D, Kim G, Hu Y, Ryu JH, Yoon J (2014) Cyanine-based fluorescent probe for highly selective detection of glutathione in cell

cultures and live mouse tissues. J Am Chem Soc 136:5351–5358
31. Gomes A, Fernandes E, Lima JLFC (2005) Fluorescence probes used for detection of reactive oxygen species. J Biochem Biophys Methods 65:45–80
32. Li C, Numata M, Takeuchi M, Shinkai S (2005) A sensitive colorimetric and fluorescent probe based on a polythiophene derivative for the detection of ATP. Angew Chem Int Ed 44:6371–6374
33. Peng HS, Stolwijk JA, Sun LN, Wegener J, Wolfbeis OS (2010) A nanogel for ratiometric fluorescent sensing of intracellular pH values. Angew Chem Int Ed 49:4246–4249
34. Piao W, Tsuda S, Tanaka Y, Maeda S, Liu F, Takahashi S, Kushida Y, Komatsu T, Ueno T, Terai T, Nakazawa T, Uchiyama M, Morokuma K, Nagano T, Hanaoka K (2013) Development of azo-based fluorescent probes to detect different levels of hypoxia. Angew Chem Int Ed 52:13028–13032
35. Andersson H, Baechi T, Hoechl M, Richter C (1998) Autofluorescence of living cells. J Microsc 191:1–7
36. Piston DW, Knobel SM (1999) Real-time analysis of glucose metabolism by microscopy. Trends Endocrinol Metab 10:413–417
37. Shi L, Lu L, Harvey G, Harvey T, Rodríguez-Contreras A, Alfano RR (2017) Label-free fluorescence spectroscopy for detecting key biomolecules in brain tissue from a mouse model of Alzheimer's disease. Sci Rep 7:2599
38. Acharya A, Bogdanov AM, Grigorenko BL, Bravaya KB, Nemukhin AV, Lukyanov KA, Krylov AI (2017) Photoinduced chemistry in fluorescent proteins: curse or blessing? Chem Rev 117:758–795
39. Dedecker P, De Schryver FC, Hofkens J (2013) Fluorescent proteins: Shine on, you crazy diamond. J Am Chem Soc 135:2387–2402
40. Shaner NC, Patterson GH, Davidson MW (2007) Advances in fluorescent protein technology. J Cell Sci 120:4247–4260
41. Zhu H, Fan J, Du J, Peng X (2016) Fluorescent probes for sensing and imaging within specific cellular organelles. Acc Chem Res 49:2115–2126
42. Johnson I, Spence M (eds) (2010) Molecular probes handbook: a guide to fluorescent probes and labeling technologies. Life Technologies Corporation, Carlsbad
43. Luo J, Xie Z, Lam JWY, Cheng L, Chen H, Qiu C, Kwok HS, Zhan X, Liu Y, Zhu D, Tang BZ (2001) Aggregation-induced emission of 1-methyl-1,2,3,4,5-pentaphenylsilole. Chem Commun 1740–1741
44. Cai X, Liu B (2020) Aggregation-induced emission: recent advances in materials and biomedical applications. Angew Chem Int Ed 59:9868–9886
45. Zheng X, Zhu W, Ni F, Ai H, Gong S, Zhou X, Sessler JL, Yang C (2019) Simultaneous dual-colour tracking lipid droplets and lysosomes dynamics using a fluorescent probe. Chem Sci 10:2342–2348
46. Miller DM, Shakes DC (1995) Immunofluorescence microscopy. Method Cell Biol 48:365–394
47. Toda Y, Kono K, Abiru H, Kokuryo K, Endo M, Yaegashi H, Fukumoto M (1999) Application of tyramide signal amplification system to immunohistochemistry: a potent method to localize antigens that are not detectable by ordinary method. Pathol Int 49:479–483
48. Haun JB, Devaraj NK, Hilderbrand SA, Lee H, Weissleder R (2010) Bioorthogonal chemistry amplifies nanoparticle binding and enhances the sensitivity of cell detection. Nat Nanotechnol 5:660–665
49. Wu X, Liu H, Liu J, Haley KN, Treadway JA, Larson JP, Ge N, Peale F, Bruchez MP (2003) Immunofluorescent labeling of cancer marker Her2 and other cellular targets with semiconductor quantum dots. Nat Biotechnol 21:41–46
50. Kaul Z, Yaguchi T, Kaul SC, Hirano T, Wadhwa R, Taira K (2003) Mortalin imaging in normal and cancer cells with quantum dot immuno-conjugates. Cell Res 13:503–507
51. Li Q, Liu L, Liu JW, Jiang JH, Yu RQ, Chu X (2014) Nanomaterial-based fluorescent probes for live-cell imaging. TrAC Trends Anal Chem 58:130–144
52. Savić R, Eisenberg A, Maysinger D (2006) Block copolymer micelles as delivery vehicles of hydrophobic drugs: micelle–cell interactions. J Drug Target 14:343–355
53. Chen H, Kim S, Li L, Wang S, Park K, Cheng JX (2008) Release of hydrophobic molecules from polymer micelles into cell membranes revealed by Förster resonance energy transfer imaging. Proc Natl Acad Sci U S A 105:6596–6601
54. Pan GY, Jia HR, Zhu YX, Wu FG (2018) Turning double hydrophilic into amphiphilic: IR825-conjugated polymeric nanomicelles for near-infrared fluorescence imaging-guided photothermal cancer therapy. Nanoscale 10:2115–2127
55. Hu R, Chen B, Wang Z, Qin A, Zhao Z, Lou X, Tang BZ (2019) Intriguing "chameleon" fluorescent bioprobes for the visualization of lipid droplet-lysosome interplay. Biomaterials 203:43–51
56. Pan GY, Jia HR, Zhu YX, Sun W, Cheng XT, Wu FG (2018) Cyanine-containing polymeric nanoparticles with imaging/therapy-switchable capability for mitochondria-targeted cancer theranostics. ACS Appl Nano Mater 1:2885–2897
57. McNamara KP, Rosenzweig Z (1998) Dye-encapsulating liposomes as fluorescence-based oxygen nanosensors. Anal Chem 70:4853–4859
58. Zope HR, Versluis F, Ordas A, Voskuhl J, Spaink HP, Kros A (2013) In vitro and in vivo supramolecular modification of biomembranes using a lipidated coiled-coil motif. Angew Chem Int Ed 52:14247–14251
59. Reisch A, Klymchenko AS (2016) Fluorescent polymer nanoparticles based on dyes: seeking brighter tools for bioimaging. Small 12:1968–1992
60. Wan Q, Jiang R, Guo L, Yu S, Liu M, Tian J, Liu G, Deng F, Zhang X, Wei Y (2017) Novel strategy toward AIE-active fluorescent polymeric nanoparticles from polysaccharides: preparation and cell imaging. ACS Sustain Chem Eng 5:9955–9964
61. Yang L, Li N, Pan W, Yu Z, Tang B (2015) Real-time imaging of mitochondrial hydrogen peroxide and pH

fluctuations in living cells using a fluorescent nanosensor. Anal Chem 87:3678–3684
62. Wu L, Li X, Ling Y, Huang C, Jia N (2017) Morpholine derivative-functionalized carbon dots-based fluorescent probe for highly selective lysosomal imaging in living cells. ACS Appl Mater Interfaces 9:28222–28232
63. Ghosh C, Nandi A, Basu S (2019) Lipid nanoparticle-mediated induction of endoplasmic reticulum stress in cancer cells. ACS Appl Bio Mater 2:3992–4001
64. Wang HY, Jia HR, Lu X, Chen B, Zhou G, He N, Chen Z, Wu FG (2015) Imaging plasma membranes without cellular internalization: multisite membrane anchoring reagents based on glycol chitosan derivatives. J Mater Chem B 3:6165–6173
65. Wang HY, Hua XW, Jia HR, Li C, Lin F, Chen Z, Wu FG (2016) Universal cell surface imaging for mammalian, fungal, and bacterial cells. ACS Biomater Sci Eng 2:987–997
66. Jia HR, Zhu YX, Xu KF, Pan GY, Liu X, Qiao Y, Wu FG (2019) Efficient cell surface labelling of live zebrafish embryos: wash-free fluorescence imaging for cellular dynamics tracking and nanotoxicity evaluation. Chem Sci 10:4062–4068

Semiconductor Quantum Dots for Cell Imaging

Yuxuan Hu, Yuqi Wang, and Deju Ye

1 Introduction

It is one of the fundamental goals to visualize and elucidate the interplay of biomolecules in biology with spatial and temporal pattern, which generally requires a fast, sensitive, and reliable detection method. Fluorescence imaging techniques, which have high sensitivity and facile operation, have become as prominent approaches for biological studies [1]. In the past few decades, a number of organic fluorophores capable of offering different fluorescence emission have been developed for visualizing and tracking biomolecules in living systems. However, most of the reported organic fluorophores generally have broad absorption and emission profiles, which may limit their ability for multiplex imaging [2]. In addition, their applications for long-term imaging of biomolecules in live cells are also subject to photobleaching. Alternately, luminescent inorganic semiconductor nanocrystals, such as quantum dots (QDs), which show improved optical and physicochemical properties over traditional organic fluorophores, have emerged as a novel class of fluorophores for cell imaging [3, 4].

Y. Hu · Y. Wang · D. Ye (✉)
State Key Laboratory of Analytical Chemistry for Life Science, School of Chemistry and Chemical Engineering, Nanjing University, Nanjing, Jiangsu, People's Republic of China
e-mail: dejuye@nju.edu.cn

QDs are a class of inorganic semiconductor nanoparticles made of groups II and VI elements or groups III and V elements (Fig. 1a). As the size of nanoparticle is smaller than or close to the bulk exciton Bohr diameter of a given semiconductor material, the band gap decreases with the size and becomes discrete (Fig. 1b) [5]. Owing to this quantum size effect, the photoluminescence (PL) wavelength of QDs can be readily adjusted by changing their diameter [6]. Such a size-dependent fluorescence could allow to design QDs with emission ranging from visible to near-infrared (NIR) region for biological applications (Fig. 2a) [7]. Besides, QDs have many other prominent optical properties such as (1) broad absorption along with narrow and symmetric PL spectra (full-width at half-maximum of ~25–40 nm, Fig. 2b) [7, 8]; (2) high fluorescence quantum yields (QY) and large molar extinction coefficients (up to ~10–100× that of traditional organic dyes) [9, 10]; (3) large stokes shifts; (4) high resistance to photobleaching; and (5) good chemical stability [11–16]. Taking the advantages of these optical properties, QDs have emerged as one of the most attractive fluorescent probes for reliable cell imaging [17–26].

During the past two decades, many QDs consisting of different materials have been explored to offer various fluorescence emission. Some of the commonly used QDs along with their PL emission ranges are shown in Fig. 2c. Among them, cadmium chalcogenide QDs like CdS QDs, CdSe QDs, and CdTe QDs are the most widely

F.-G. Wu (ed.), *Fluorescent Materials for Cell Imaging*, https://doi.org/10.1007/978-981-15-5062-1_2

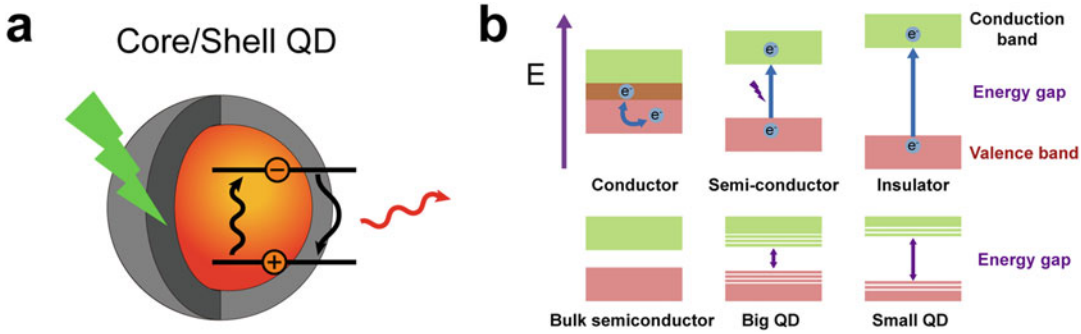

Fig. 1 (**a**) Cartoon illustration of a Core/Shell QD. (**b**) Electronic structure shows the energy gap of a conductor, semiconductor, insulator (top panel), and QD with different size (bottom panel). As shown in QDs, the continuous energy bands separate into discrete energy levels, and the bandgap energy decreases with size. (Reprinted with permission from Ref. [5]. Copyright © 2010 Royal Society of Chemistry)

used QDs due to their narrow PL spectra and high QYs in visible to NIR regions; however, the potential toxicity of Cd^{2+} toward living biology has received many concerns. Alternately, InP QDs without using of Cd^{2+} have been developed to minimize the intrinsic toxicity. Similar to CdSe QDs, the PL of InP QDs can also be engineered to cover the spectral range from the visible and NIR regions [27–30]. However, InP QDs are very susceptible to oxidative degradation, thus extra care should be taken during the synthesis. To achieve PL emission in NIR-I and NIR-II windows, PbS, PbSe/Te QDs have been developed for in vivo imaging applications, but similar to Cd^{2+}, the intrinsic toxicity of Pb^{2+} remains a concern [31, 32]. In addition, silver chalcogenide QDs such as Ag_2S and Ag_2Se QDs with a strong NIR PL have also been developed for bioimaging [33].

Though QDs like CdS QDs and CdSe QDs have a narrow and strong PL, they have a relatively high surface area to volume ratio, thus presenting a lot of atoms on their surfaces. Because surface atoms possess unoccupied electron orbitals, they generally exhibit enhanced chemical reactivity capable of either preventing or delaying the photon emission. This will decrease both the chemical stability and photostability, resulting in the downfall of PL intensity [34, 35]. This problem can be solved by formation of a core-shell structure via coating these QDs with a semiconductor quantum shell that possesses a wider bandgap than that of CdS QDs or CdSe QDs [19, 36]. ZnS is one of the most commonly used shell due to its large bandgap and high biocompatibility. Other materials including ZnSe, CdS, and alloyed materials (e.g., CdZnS) have also been used as the shell to improve both QYs and photostability of cadmium-based QDs [37–41].

2 Surface Modification and Functionalization of QDs

Because the majority of high quality QDs are normally synthesized in nonpolar organic solvent in the presence of surfactants, such as tri-n-octylphosphine (TOP), tri-n-octylphosphine oxide (TOPO) [42], and octadecyl-amine [43], the as-prepared QDs are coated with hydrophobic ligands, which make them generally water-insoluble and unsuitable for direct applications in biological systems. To apply them for cell imaging, surface functionalization is required. Through efficient surface functionalization, hydrophilic groups can be introduced on the surface of the QDs, making them water-soluble and

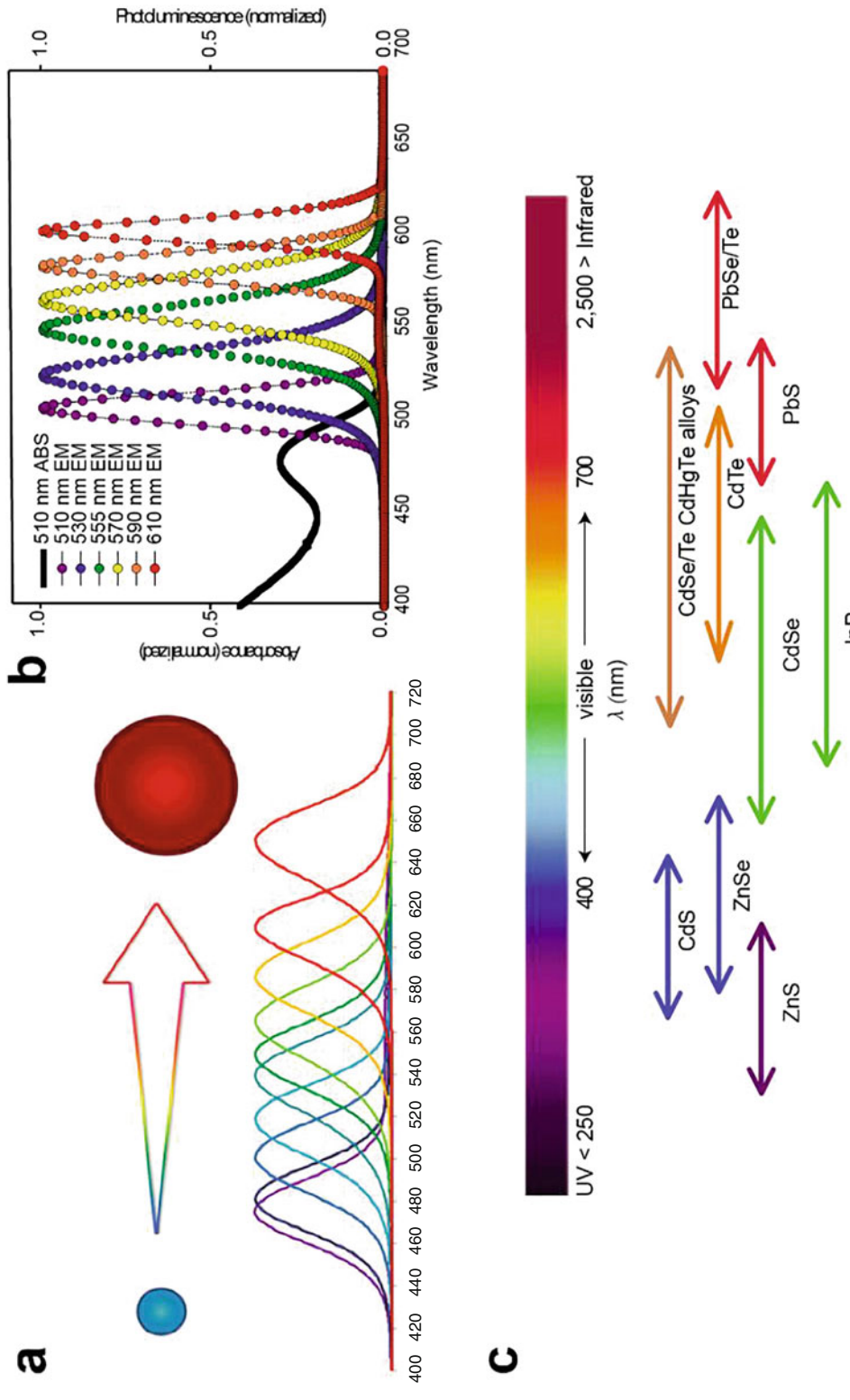

Fig. 2 (**a**) The emission profile of QDs can be precisely tuned into different color via changing the nanoparticle size. (**b**) Representative fluorescence emission of QDs at six different wavelength shows narrow and symmetric PL spectra. The black line is the absorption spectrum of a 510-nm-emitting QDs. (**c**) Commonly used QDs with different composites and their PL emission range. (Reprinted with permission from Ref. [7]. Copyright © 2005, Springer Nature)

stable in aqueous solutions. Moreover, different targeting ligands and biomolecules can be further linked to the surface of hydrophilic QDs to facilitate the specific interaction with a molecular target of interest in biological environment. Generally, there are two approaches employed to modify the surface of QDs: one is through noncovalent binding and the other is through covalent conjugation. Noncovalent binding relies on the hydrophobic interactions, electrostatic absorption, or specific affinity interactions between biomolecules and QDs. Covalent conjugation relies on the formation of chemical bonds via chemical reaction between biomolecules and chemical groups on the surface of QDs. Figure 3 summarizes the commonly used groups on the surface amenable for surface functionalization of QDs.

2.1 Encapsulation of QDs

Encapsulation of hydrophobic QDs with amphiphilic compounds involves the use of hydrophobic interactions to introduce hydrophilic groups on the surface of QDs that are coated with hydrophobic ligands (e.g., TOP and TOPO). Amphiphilic phospholipids (Fig. 3i) and many synthesized amphiphilic polymers (Fig. 3ii) are widely used to encapsulate QDs. For example, alkyl chain-appended poly(acrylic acid) (PAA) is one of the most efficient amphiphilic polymers for QDs encapsulation because of its low cost, high efficacy, and easy modification [44–46]. In addition, hydrophilic and neutral poly(ethylene glycol) (PEG) chains are normally conjugated to the phospholipids and amphiphilic polymers, which can greatly reduce the non-specific absorption of biomolecules (e.g., proteins) and improve the biocompatibility essential for cell imaging applications [47]. After encapsulation, the original hydrophobic ligands on the surface of QDs are kept, which can protect QDs from interacting with surrounding water molecules, thus allowing to preserve the PL quantum yield for fluorescence imaging.

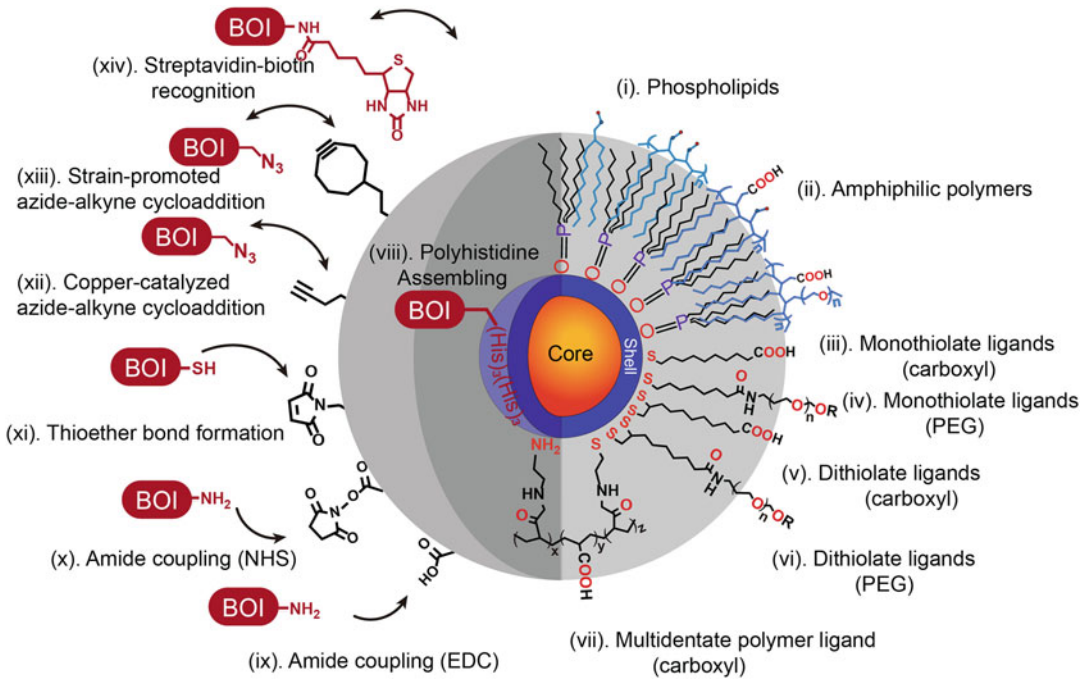

Fig. 3 Overview of representative approaches for the surface modification and functionalization of QDs. (Partially adapted from ref. [10]. Copyright © 2013, © SAGE Publications)

2.2 Ligand Exchange

Ligand exchange is a strategy of using hydrophilic ligands to replace the original hydrophobic ligands on the surface of QDs. Free thiol-containing hydrophilic molecules are one of the most widely used exchanging ligands due to the strong binding between the thiol group and the metal ions (e.g., Cd^{2+}, Zn^{2+}) in the QDs. For example, small molecule monothiolate ligands, such as mercaptoacetic acid (MAA) [48–50], mercaptopropionic acid (MPA) [51, 52], and mercaptoundecanoic acid (MUA) [53, 54] (Fig. 3iii) with a carboxylic group on the end can easily replace the hydrophobic ligands (e.g., TOP, TOPO) on QDs and improve their solubility after deprotonation in aqueous solution. The use of small size of these monothiolate ligands can help QDs maintain their small hydrodynamic size. Moreover, the introduction of carboxylic groups can also be allowed for further conjugation with biomolecules. Different to the use of carboxylic groups, monothiolate ligands attached with a PEG chain have also been used to maintain the colloidal stability of QDs at different pH value (Fig. 3iv) [55, 56]. In addition, a variety of dithiolate ligands (Fig. 3v and vi) and multidentate thiol ligands (Fig. 3vii) appending with carboxylic groups or PEG chains have also been applied to improve the colloidal stability and photostability of the QDs for long-term fluorescence imaging in living systems.

2.3 Electrostatic Absorption

As QDs can be synthesized or engineered to have numerous charges on the surface, it is allowed to absorb oppositely charged biomolecules (e.g., nucleotides, proteins) via electrostatic interactions. A widely used method for electrostatic absorption of proteins to QDs is self-assembly of proteins that contain positive surface or domains (e.g., the leucine zipper at the C-terminal) on the surface of negatively charged QDs [57–59]. Another efficient approach is through metal-affinity coordination of recombinant proteins that contain His-tag motifs with zinc ions (Zn^{2+}) on the surface of CdSe/ZnS core/shell QDs (Fig. 3viii) [60, 61].

2.4 Covalent Conjugation

Although noncovalent binding through hydrophobic interactions or electrostatic adherence is simple and efficient to modify QDs with biomolecules, the process is uncontrollable and the attached biomolecules can easily dissociate from QDs before interaction with a target. Alternately, the link of biomolecules to QDs via covalent bonds has emerged as a more stable and controllable method to modify QDs. One of the most common covalent conjugation methods is based on coupling agent (e.g., 1-(3-dimethylaminopropyl)-3-ethylcarbodiimide (EDC))-assisted formation of amide bonds between the primary amines in biomolecules and carboxylic acid groups on QDs' surface (Fig. 3ix). In some case, the carboxylic groups are converted to *N*-hydroxysuccinimide (NHS) esters to facilitate the coupling with primary amines (Fig. 3x) [62]. As proteins usually contain primary amine groups, it is easy to directly conjugate proteins with QDs using the amide bonds without the need of additional chemical modifications. However, proteins usually have more than one primary amine or carboxylic acid, which can produce undesirable cross-linking and aggregation. Another popular method is the use of coupling reaction between free thiol in biomolecules and maleimide-modified QDs (Fig. 3xi) [63]. This method can prevent undesired cross-linking and aggregation, which can provide a higher specificity than the EDC-mediated coupling reaction. In addition, "click reaction" between alkyne and azide has also been applied for covalent modification of QDs. For example, copper-catalyzed click reaction between azide and terminal alkyne (Fig. 3xii) and strain-promoted azide-alkyne cycloaddition (Fig. 3xiii) are orthogonal to other biomolecules abundant in cells, which have shown a high accuracy to introduce biomolecules to the surface of QDs. In addition, the specific and strong binding between biotin and streptavidin

has also been demonstrated for surface functionalization of QDs (Fig. 3xiv).

3 QDs for Cell Imaging

Beneficial from established surface modification and functionalization methods, QDs have shown promise for the detection of biomolecules and biological processes in complex biological environment. There are two general approaches to facilitate QDs for fluorescence imaging in cells according to the action mechanism. The first approach is to introduce biomarkers on QDs' surface to facilitate the specific recognition by the cells. In this approach, the fluorescence of QDs is "always on," which can be applied to track the delivery and location of QDs in cells. The other approach is relied on the change of the fluorescence of QDs upon interaction of a biomolecule of interest in the cells. In this approach, the fluorescence of QDs is "activatable," which is useful for the real-time cell imaging. To date, different QDs have been used for a variety of cell imaging studies, which are discussed in the following sections.

3.1 Fluorescence "Always on" QDs for Cell Imaging

In 1998, two seminal papers demonstrated the applications of water-soluble QDs as "Always on" fluorescence imaging probes by two independent groups nearly at the same time. In paper one, Bruchez et al. used two different size of CdSe/CdS QDs to label 3T3 mouse fibroblast cells [3]. They functionalized the "green" QDs (smaller size QDs with green fluorescence) with trimethoxysilylpropyl urea and acetate groups, allowing to specifically label the cell nucleus. On the other hand, they functionalized the "red" QDs (larger size QDs with red fluorescence) with biotin, which could label F-actin filaments after pre-treatment with phalloidin-biotin and streptavidin. Upon co-incubation with these two kinds of QDs, they found that 3T3 cells could be simultaneously stained by "green" and "red" QDs. As shown in Fig. 4(a), the actin filaments were specifically stained by the "red" QDs that exhibited bright red fluorescence, while the nucleus was labeled by the "green" QDs and appeared green fluorescence.

In the other paper, Chan et al. used mercaptoacetic acid as a hydrophilic ligand to modify the surface of CdSe/ZnS QDs through the ligand-exchange approach, affording water-soluble mercapto-QDs [4]. The mercapto-QDs were further modified with transferrin capable of binding to the transferrin receptors expressed on the cell surface. They demonstrated that the QD-transferrin conjugates could be efficiently transported into HeLa cells, resulting in strong punctuate intracellular fluorescence (Fig, 4b, right). By comparison, HeLa cells incubated with transferrin-free QDs showed much weaker intracellular fluorescence (Fig, 4b, left). These

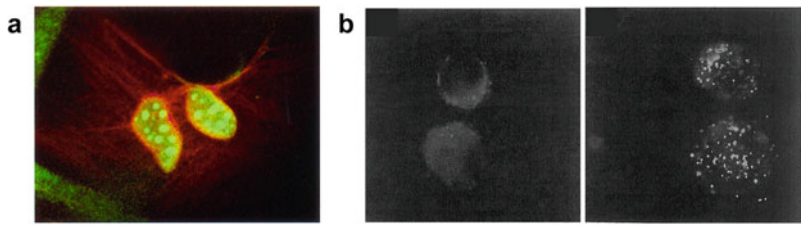

Fig. 4 (**a**) Fluorescence imaging of 3T3 cells with a combination of "green" and "red" QDs. Red fluorescence shows the location of actin filaments stained by the "red" QDs, and green fluorescence shows the nucleus stained by the "green" QDs. Reprinted with permission from Ref. [3]. (Copyright © 1998 The American Association for the Advancement of Science.) (**b**) Fluorescence imaging of HeLa cells with transferrin-free QDs (left) and QD-transferrin conjugates (right). Reprinted with permission from Ref. [4]. (Copyright © 1998 The American Association for the Advancement of Science)

two papers indicated that with proper functionalization, QDs have largely improved biocompatibility, which were capable of reliable fluorescence imaging of cells.

Inspired by these two works, in 2002, Wu et al. covalently linked QDs with streptavidin and immunoglobulin G (IgG) for immunofluorescent labeling of cell receptors, cytoskeletons, and nuclear antigens at subcellular level (Fig. 5) [16]. They demonstrated that the human SK-BR-3 breast cancer marker Her2 was successfully labeled after incubation with monoclonal anti-Her2 antibody and QD 535-IgG conjugates. Bright green fluorescence was observed on the cell membranes (Fig. 5a). Using QD 630-streptavidin conjugates, the nuclei of fixed epithelial cells were efficiently labeled to display strong red fluorescence after incubation with biotinylated anti-human IgG and human anti-nuclear antigen (ANA) antibodies (Fig. 5b). They also demonstrated that both the microtubules and nucleus within the same cells could be simultaneously labeled by a combination of QD 535-streptavidin and QD 630-streptavidin conjugates (Fig. 5c, green for microtubules and red for nucleus). When using a combination of

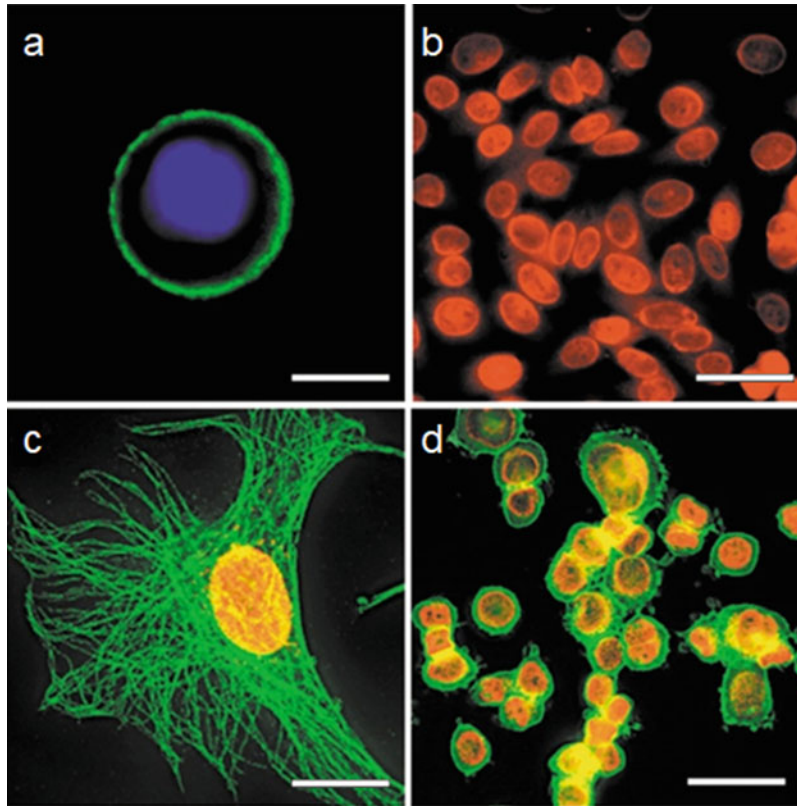

Fig. 5 Labeling of membranes and intracellular targets with QDs. (**a**) Fluorescence staining of Her2 receptors on human SK-BR-3 breast cancer cells with monoclonal anti-Her2 antibody and QD 535-IgG conjugates (green). (**b**) Fluorescence staining of nucleus of fixed human epithelial cells with QD 630-streptavidin conjugates. The fixed cells were stained with human anti-nuclear antigen (ANA) antibodies and biotinylated anti-human IgG, followed by incubation with the QD 630-streptavidin conjugates. (**c**) Simultaneous fluorescence labeling of microtubules (green) and nucleus (yellow-red) in a cell with QD 535-streptavidin and QD 630-streptavidin conjugates. (**d**) Simultaneous fluorescence labeling of Her2 receptors (green) and nucleus (yellow-red) in a cell with QD 535-IgG (green) and QD 630-streptavidin (yellow-red) conjugates. Scale bar: 10 μm for (**a**), and 50 μm for (**b**), (**c**) and (**d**). (Reprinted with permission from Ref. [16]. Copyright © 2003 Springer Nature Limited)

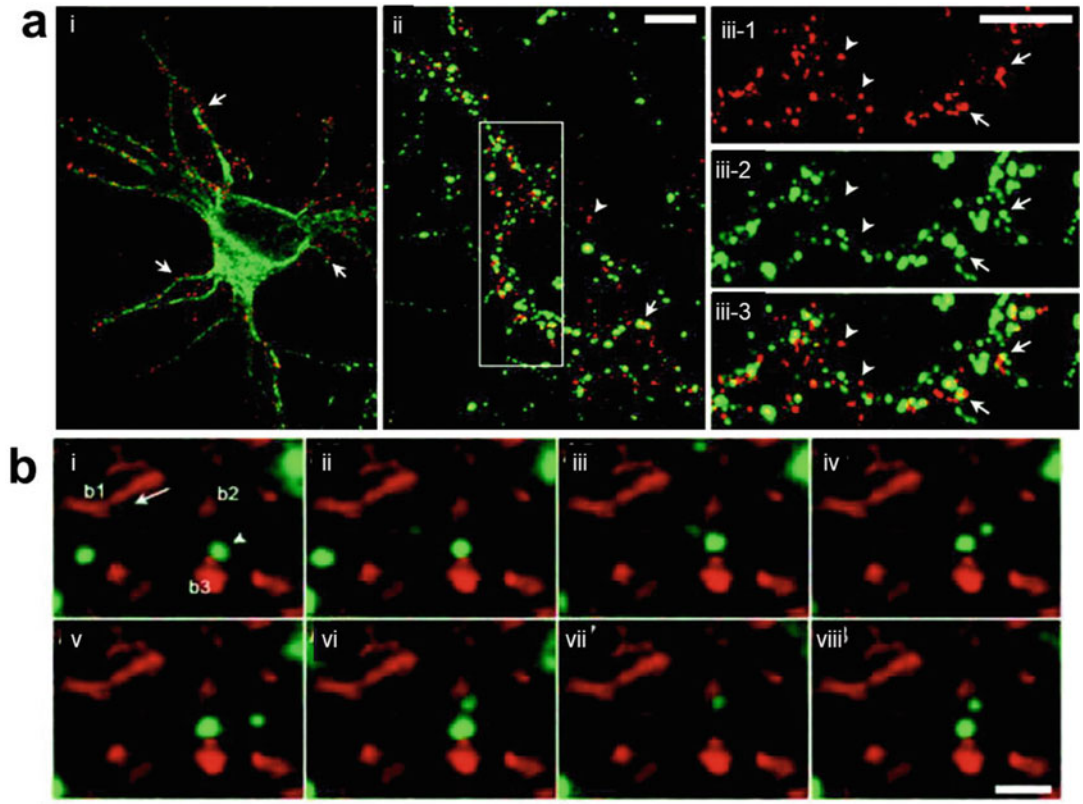

Fig. 6 (**a**) Fluorescence imaging of GlyR in neurons using QD-streptavidin nanoparticles. Red fluorescence shows the location of GlyRs stained by the formation of QD-GlyRs clusters in the somatodendritic domains, and green fluorescence shows the location of microtubules. Arrows indicate the clusters of QD-GlyRs located on the dendrites. (**b**) Dynamic fluorescence imaging of neurons showed that GlyR alternated between free and confined diffusion states in extrasynaptic and synaptic domains. Images are extracted from a sequence of 850 frames (acquisition time: 75 ms). Green fluorescence shows the QD-GlyRs and red fluorescence shows the synaptic boutons. Scale bars: 10 μm for (**a**) and 2 μm for (**b**). (Reprinted with permission from Ref. [64]. Copyright © 2003, American Association for the Advancement of Science)

QD 525-IgG and QD 630-streptavidin conjugates, both the Her2 (green) and nucleus (red) could also be efficiently labeled at the same cells. These results demonstrated that QDs were useful for multicolor imaging of different biomolecules in cells.

In addition to the use of QDs to stain biomolecules and organelles in cells, QDs were also successfully applied for long-term tracking of biomolecules due to the high resistance to photobleaching, thus facilitating to visualize the biological process in live cells in real time. For example, Dahan et al. used QDs to track endogenous glycine receptors (GlyR) in cultured neurons [64]. In their study, streptavidin-coated QDs were synthesized. When the neurons were incubated with a primary antibody (mAb2b), biotinylated anti-mouse Fab fragments and the QD-streptavidin nanoparticles, the GlyRs within the synaptic and extrasynaptic domains were detected by the fluorescence from the formation QD-GlyR clusters in the neurons (Fig. 6a). Thanks to the high photostability of QDs, the lateral movement of GlyRs in living cultured neurons was successfully tracked in real time. They demonstrated that the movement of single QD-GlyRs could be tracked in the membrane for over 20 min, much longer than that using Cy3 as a

fluorescent tag (~5 s). Through continuous acquirement of fluorescence images (75-ms per image) for 60 s, it was revealed that a GlyR alternated between free and confined diffusion states in extrasynaptic and synaptic domains (Fig. 6b). Moreover, long-term fluorescence imaging for 20 min and 40 min duration was also performed to allow visualization of the lateral dynamics of GlyRs in the neuronal membrane. This study demonstrated that QDs were favorable for tracking the mobility of individual GlyRs in neurons via fluorescence imaging, which have been further applied as single-molecule fluorescent probes to track the dynamics of other membrane receptors, such as EGF [65], GABA [66], Kv2.1 [67], and AMPA glutamate receptors (AMPARs) [68].

Though the QD-streptavidin conjugates have shown promising results for cell imaging, the relatively big size of streptavidin proteins might increase the coating thickness, thus leading to large nanoparticle sizes (>~15 nm). In addition, because each streptavidin (or avidin) can bind to four biotin molecules, it is difficult to monovalently label biomolecules using the streptavidin-coated QDs. To overcome these limitations, in 2008, Murcia et al. prepared two types of hydrophilic ligands, 2-(2-aminoethoxy) ethanol (AEE)- and phospholipid/lipopolymer (LIPO)-coated CdSe/ZnS core/shell QDs that enabled monovalent conjugation to sulfhydryl phospholipids for the first time. The subsequent labeling of individual cell membrane lipids with these QDs of 10 nm size showed that the lipid diffusion was not affected. Importantly, the highly photostable and photoluminescent QDs have much improved brightness and resolution over small organic dyes, which could enable single molecule tracking of the lateral mobility on NRK fibroblasts membrane, with an imaging speed of 1000 frames per second and a spatial resolution of less than 100 nm [69]. This study highlighted the efficacy of smaller size of QDs for high-speed tracking of lipids on cell membranes, which could be engineered as single-molecule fluorescent probes for multicolor imaging and tracking of individual proteins in cells.

In 2012, Sukhanova employed a single-domain antibody (sdAbs) from llama IgG (Fig. 7a) as a surface functionalization group to develop ultra-small sdAbs-QDs for tumor cell analysis [70]. The monomeric sdAbs have a size of 13 kDa, which are 12 times smaller than that of mAbs, ensuring high capacity to refold. The as-prepared sdAbs-QDs have much smaller size compared to IgG-coated QDs, which show strong specificity toward carcinoembryonic antigen (CEA) capable of quantitative discrimination of CEA-negative from CEA-positive tumor cells through fast flow cytometric analysis. Based on this work, in 2014, Rakovich et al. also prepared ultra-small and bright sdAbs-QDs to detect Her2 receptor on the cell membrane of breast and lung cancer cell lines [71]. Due to the small size of sdAbs, the four sdAbs on the surface of QDs were covalently linked with all the antigen recognizing sites that face outward. In their study, the performance of sdAbs-QD was compared with mAbs labeled with conventional organic dyes (Alexa Fluor (AF) 568 and AF 488). As shown in Fig. 7b, bright fluorescence was observed in A549 cells and NCI-H596 cells with high expression of Her2 receptors when incubated with sdAbs-QDs, while these cells incubated with mAbs-AF488 and mAbs-AF568 showed much weaker fluorescence. These results suggested that, despite QDs have much bigger sized compared with AF488 and AF568 molecules, the outward orientation of the small size of sdAbs makes the sdAbs-QDs perform much better than mAbs-AF488 and mAbs-AF568 when applied for the detection of Her2 positive lung cells.

The researches mentioned above mainly focused on the "always on" QD-based probes for fluorescence imaging of receptors or lipids on the cell membrane; however, imaging of intracellular biomolecules in living cells is much more difficult for them. As the intracellular environment is crowd and most biomolecules are generally distributed heterogeneity within the cells, the "always on" QDs are hard to accurately locate

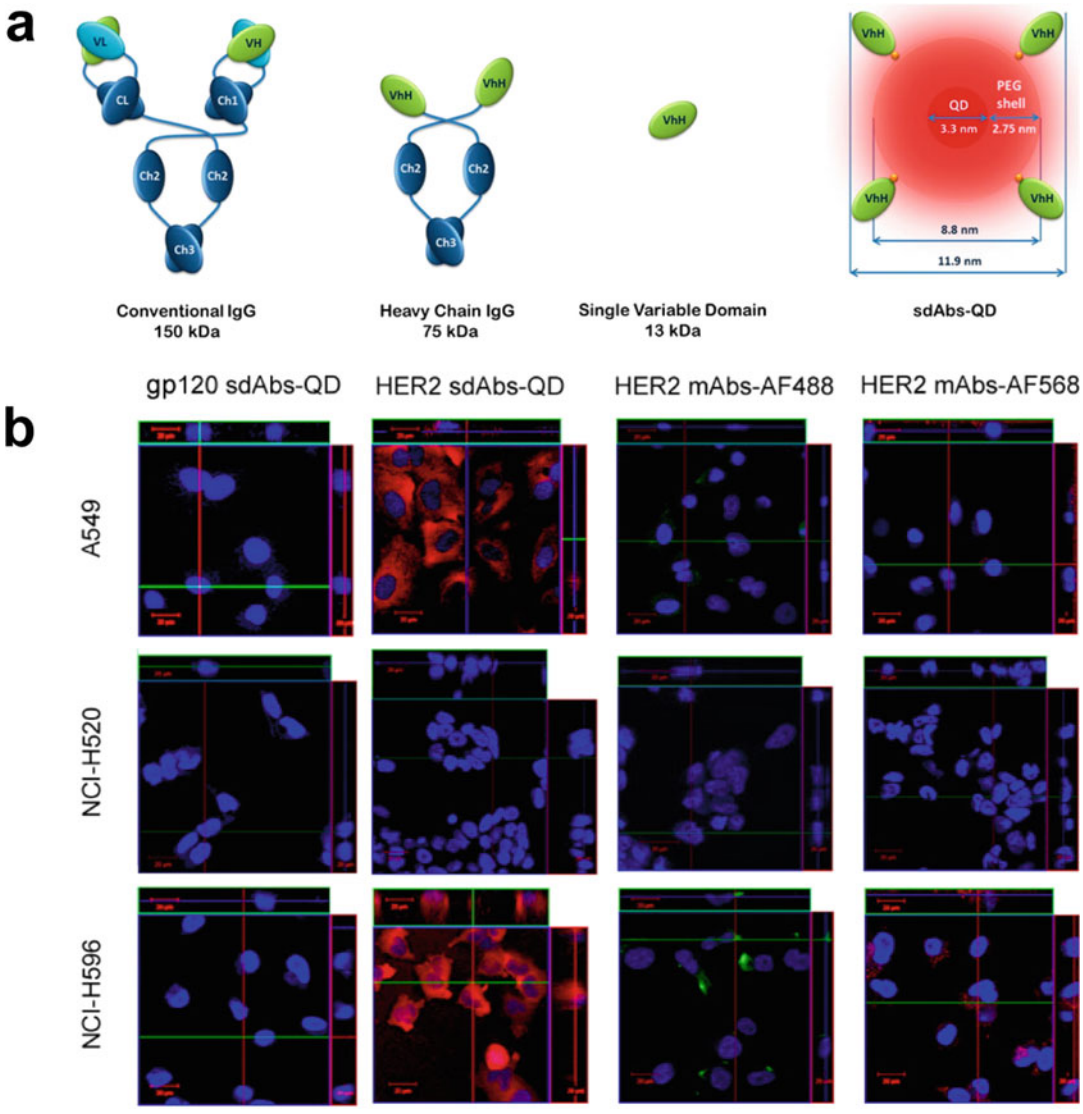

Fig. 7 (**a**) Cartoon structures of conventional IgG, heavy chain IgG, sdAbs and sdAbs-QD conjugates. (**b**) Fluorescence imaging of Her2-positive (NCI-H596, A549) and -negative (NCI-H520) lung cancer cells following incubation with mAbs-AF488, mAbs-AF568, Her2 sdAbs-QD, and gp120 sdAbs-QD conjugates. (Reprinted with permission from Ref. [71]. Copyright © 2014, American Chemical Society)

and concentrate near the site of biomolecule of interest. The fluorescence may be distributed throughout the cells and results in low signal-to-noise to detect the biomolecules. In order to overcome these limitations, people have developed a number of fluorescence "turn-on" QDs as efficient fluorescent probes for the imaging of biomolecules in living cells over the past few years.

3.2 Fluorescence "Turn-on" QDs for Cell Imaging

Fluorescence "turn on" probes are a type of probes that can switch on their fluorescence upon interaction with a biomolecule of interest. As the initial fluorescence of the probes is off, the background is low, which is allowed to overcome the limitation of high background resulting from

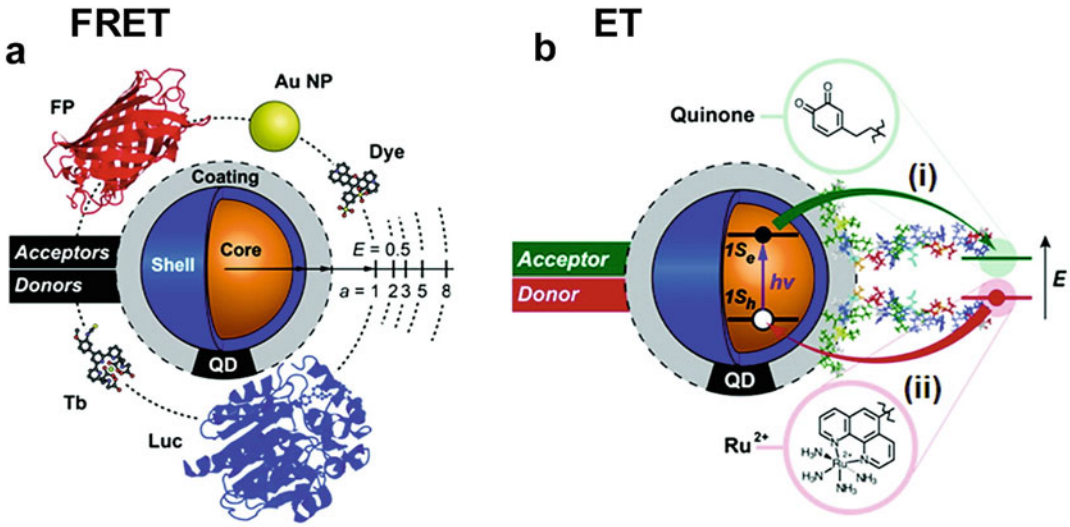

Fig. 8 The two general mechanisms employed to engineer QDs as fluorescence "turn on" probes. (**a**) QD-based fluorescence "turn-on" probes can be designed via FRET process. QDs are good FRET donors for fluorescent proteins, organic dyes, and gold nanoparticles. (**b**) QD-based fluorescence "turn-on" probes can be designed via (ET) process. QDs can serve as either an electron donor (i) or acceptor (ii) toward molecules on the surface (Reprinted with permission from Ref. [72]. Copyright © 2011, American Chemical Society)

"always on" fluorescence. There are two major mechanisms applied to engineer QDs as "turn on" probes. The first one is based on Förster (Fluorescence) Resonance Energy Transfer process (FRET, Fig. 8a) and the other relies on photo-induced electron transfer process (PET, Fig. 8b) [72].

In the FRET process, light energy absorbed by an energy donor (e.g., QDs) is transferred to a nearby energy acceptor instead of emitting fluorescence through radiative transition process. Therefore, the fluorescence of QDs is reduced [73]. Upon reaction with biomolecules, the energy acceptors are destroyed or departed away from QDs, the FRET process is eliminated and the fluorescence of QDs was recovered, resulting in enhanced fluorescence to report the corresponding biomolecules [74]. Due to the broad absorption, narrow PL emission, and size-tunable fluorescence emission, QDs show high capacity to serve as efficient energy donors, which is promising to design FRET-based "turn on" probes [75, 76]. In the PET process, electronic carriers are generated upon irradiation and can be transferred to the LUMO of a quencher, leading to the quenched fluorescence. Due to their inherent electronic properties, QDs can be present as effective PET donors or acceptors towards the combining electroactive species [77]. Upon breaking of the PET process by a target molecule, the fluorescence of QDs is recovered, which can be employed for real-time detection of the target. Based on these two mechanisms, a variety of "turn on" (or activatable) QD-based fluorescent probes have been designed with a high potential to detect various biomolecules and biological processes in living cells.

3.2.1 Imaging of Small Molecules in Cells

There are a variety of endogenous small molecule compounds participated in many essential physiological processes. Accurate detection of these small biomolecules is of great significance to the diagnosis of diseases and study of physiological processes. In 2003, Medintz et al. have employed QDs as the FRET donor to construct self-assembled nanoscale biosensors for the detection of maltose in vitro [78]. In their study, multiple copies of engineered *Escherichia coli* maltose-

binding protein (MBP) were assembled on CdSe/ZnS core-shell QDs' surface via an efficient Zn-histidine coordination (Fig. 9a). The MBP-QDs were further mixed with a dark quencher QSY9-labeled β-cyclodextrin to form QDs-MBP-β-cyclodextrin-QSY9 nanoassemblies via the binding between β-cyclodextrin and MBP. The proximity between QDs and the quencher QSY 9 (within a few nm) and the excellent spectral overlap between QDs emission (maximum emission ~560 nm) and QSY9 absorption (maximum absorption ~565 nm) could produce efficient FRET process from QDs to QSY9, allowing to quench the PL of QDs (Fig. 9b). Addition of maltose could effectively compete and displace the β-cyclodextrin-QSY9 bound on MBP, and the fluorescence of QDs was recovered in a maltose concentration-dependent manner (Fig. 9c). This FRET-based competitive binding assay has become an important strategy to engineer QDs as activatable fluorescent probes for the detection of many other biomolecules [101].

Different to the recovery of fluorescence through a competitive binding process, cleavage of linkers that bridge the QDs and quencher molecules by a molecule of interest has been proposed as a general approach to eliminate the FRET process, thereby recovering the QDs fluorescence. For example, Shmirian et al. used a disulfide linker to bridge QDs and a rhodamine dye, and developed a QD-based probe (QD-rhodamine) for ratiometric fluorescence sensing of H_2S based on FRET process (Fig. 10a) [79]. Upon excitation of the QD-rhodamine conjugates, the energy of QD could transfer to rhodamine dye via the FRET process. The fluorescence of QDs was reduced while the fluorescence of rhodamine was enhanced. When the disulfide bonds were cleaved by H_2S, the conjugated rhodamine molecules were liberated and departed from the surface of QDs, leading to the elimination of FRET process. This leads to the recovery of QDs fluorescence along with decrease in rhodamine fluorescence. As such, a ratiometric response between rhodamine and QDs fluorescence intensity could be correlated quantitatively to the concentration of H_2S. The limit of detection (LOD) toward H_2S was found to be 1.36 ± 0.03 μM. They also applied the QD-rhodamine conjugates to detect H_2S in HeLa cells. After being incubated with the QD-rhodamine conjugates, the QD/rhodamine fluorescence intensity ratio was small due to the low level of endogenous H_2S in HeLa cells. After addition of sodium sulfide to elevate the H_2S levels, the intracellular fluorescence of QDs increased while the fluorescence of rhodamine decreased. An increase of QD/rhodamine fluorescence intensity ratio was observed, which could report on the H_2S levels in live HeLa cells (Fig. 10b).

In 2008, Freeman et al. reported QD-based fluorescence "turn on" probes for the detection of NAD(P)H (reduced form) and $NAD(P)^+$ (oxidized form), which are essential enzymatic cofactors in cells (Fig. 11a) [51]. In their study, CdSe/ZnS core/shell QDs that display maximum fluorescence emission at 635 nm were functionalized with bovine serum albumin (BSA), which were then further modified by covalent conjugation with organic dye Nile blue (maximum absorbance ~630 nm) via the EDC-mediated formation of amide bonds. Due to the close attachment to the QDs' surface, Nile blue could act as an efficient FRET donor to quench the fluorescence of QDs. When NAD(P)H cofactors were present, Nile blue was reduced into its reduced form, and the absorption at 630 nm was disappeared. As such, the FRET process from QDs to the Nile blue (reduced form) was terminated, resulting in the recovery of QDs fluorescence. It is interesting that the use of BSA layers to spatially separate Nile blue from the QDs was crucial to detect NAD(P)H. They found that the direct conjugation of Nile blue to the surface of QDs without BSA layers did not show fluorescence enhancement upon reduction of Nile blue by NAD(P)H, which was presumably due to the fluorescence quenching of QDs by both oxidized and reduced Nile blue through electron-transfer mechanisms. As a variety of redox enzymes share the same $NAD(P)^+$ cofactor, the reported QD-probe capable of measuring NAD(P)H/ $NAD(P)^+$ is useful to analyze the activity of $NAD(P)^+$-dependent redox enzymes and quantify their substrates. They demonstrated the

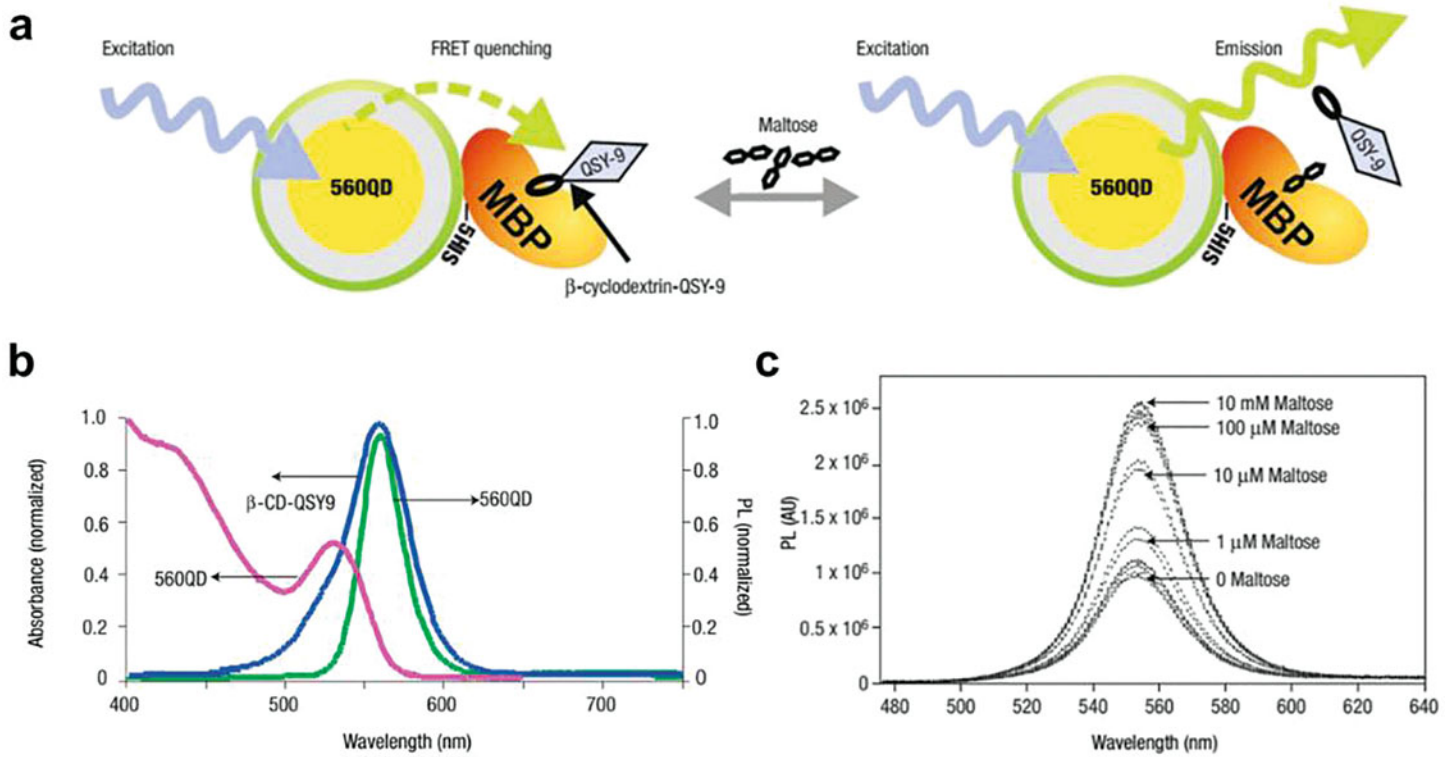

Fig. 9 (**a**) Schematic diagram of MBP-QD nanosensor. Maltose-binding proteins (MBP) were assembled on the surface of CdSe/ZnS core-shell QDs, following by adsorption of QSY9-labeled β-cyclodextrin via host–guest interactions. The adsorption of QSY9 on the surface of 560QDs induced FRET process to quench the QD fluorescence, while the addition of maltose will displace QSY9-labeled β-cyclodextrin, resulting in the elimination of FRET process and recovery of 560QD fluorescence. (**b**) Absorption (pink) and emission spectra (green) of 560QD. Blue line shows the absorption spectra of β-cyclodextrin-QSY9, which has good spectral overlap with the emission of 560QD. (**c**) Fluorescence spectra of 560QD-10MBP upon titration with varying concentration of maltose. (Reprinted with permission from Ref. [78]. Copyright © 2003, Springer Nature)

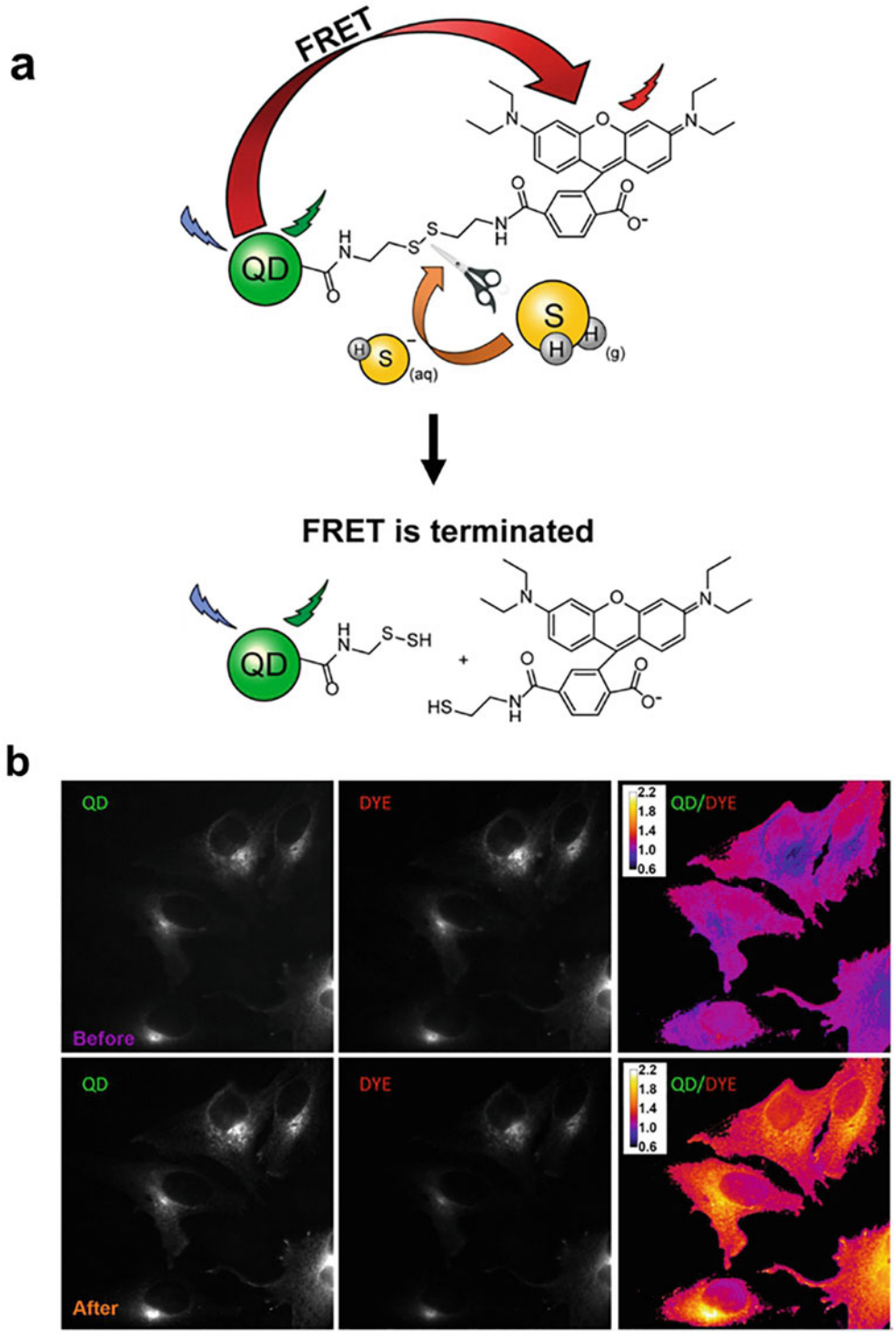

Fig. 10 (**a**) Illustration of QD-rhodamine conjugate for ratiometric fluorescence imaging of H_2S based on the FRET process. (**b**) Fluorescence and ratiometric images of H_2S levels in HeLa cells before and after addition of sodium sulfide. The fluorescence of QDs and rhodamine in HeLa cells are both acquired. (Reprinted with permission

designed QD-BSA-Nile blue constructs were capable of detecting the NAD^+-dependent alcohol dehydrogenase based on the enhanced fluorescence, which was allowed to quantify ethanol. Moreover, the QD-BSA-Nile blue constructs were further applied to image the levels of NAD(P)H intracellularly during the glycolysis and the Kreb's cycle. An obviously increasing fluorescence of QDs was observed in HeLa cells after incubation with 50 mM $_D$-glucose (Fig. 11c). When the intracellular metabolism of HeLa cells was inhibited by an anticancer drug (e.g., taxol), the increased intracellular fluorescence upon $_D$-glucose stimulation was abolished, suggesting that the NADH-activatable QDs may be applied to rapidly evaluate the cellular efficacy of anticancer drugs.

In addition to detect small reducing agents (e.g., H_2S, NADH), the applications of QDs to detect reactive oxygen species (ROS) have also been demonstrated. One of the interesting studies was focused on the development of CdSe/ZnS QD-Cytochrome c (Cyt c) conjugates for the detection of intracellular superoxide radical ($O_2^{\bullet-}$), which is one of the major ROS participating in many physiological and pathological processes. In their study, the QD-Cyt c nanosystems were prepared by electronic absorption of oxidized Cyt c on the surface of negatively capped CdSe/ZnS QDs (Fig. 12a) [80]. The oxidized Cyt c assembled on the surface of QDs could accept the electrons from QDs and quench QDs PL through the PET process. After reaction with $O_2^{\bullet-}$, the oxidized Cyt c was converted into its reduced state, and the PET process was interrupted. The QDs PL was recovered, which was applicable for the detection of $O_2^{\bullet-}$. The authors demonstrated that the QD-Cyt c (oxidized) nanosystems were capable of imaging the $O_2^{\bullet-}$ in cells generated from phorbol myristate acetate (PMA) stimulation. Upon incubation with the nanosystems, bright fluorescence was observed in HeLa cells after addition of PMA (Fig. 12b, left), which was not observed in control HeLa cells (no PMA treatment) or PMA-stimulated normal human liver HL-7702 cells (Fig. 12b, middle).

3.2.2 Imaging of Enzyme Activity in Cells

Owing to the important roles of enzymes in biological systems, tremendous efforts have been devoted to detect enzyme activity. Fluorescence "turn on" probes are of particular interest as continuous activation of fluorescence could be triggered by enzymatic catalysis, enabling signal amplification to generate sufficient target-to-background ratio (SBR) for real-time imaging of enzyme activity in living systems [81]. Taking the advantages of good photophysical properties of QDs, the development of fluorescence "turn on" QDs for the imaging of enzyme activity in living cells has attracted much attention. In 2005, Chang et al. reported protease-activated QDs with signal amplification for cancer imaging [82]. They conjugated gold nanoparticles (AuNPs) to QDs via a collagenase type XI-recognitive peptide linker. The fluorescence of QDs was quenched by the tethered AuNPs via the FRET process. After incubation with collagenase, the peptide linker was cleaved, and the AuNPs were released. The FRET process on longer occurred, resulting in a 52% rise in QDs luminescence, which could be applied to detect the collagenase activity.

In 2010, Choi et al. prepared a QD-peptide complex (QD-Pep1) as a fluorogenic assay for cellular imaging of human immunodeficiency virus protease (HIV-1 PR) activity [83]. In their work, a modular peptide (6E-GLAib-SQNYPIVQ-K(dabcyl), Pep1) containing six negatively charged glutamic acid residues was synthesized, which could attach on the surface of positively charged QDs through electrostatic interaction. Due to the presence of quencher dabcyl in the peptide substrate, the fluorescence of QDs at 495 nm was quenched by dabcyl via the

Fig. 10 (continued) from Ref. [79]. Copyright © 2016, American Chemical Society)

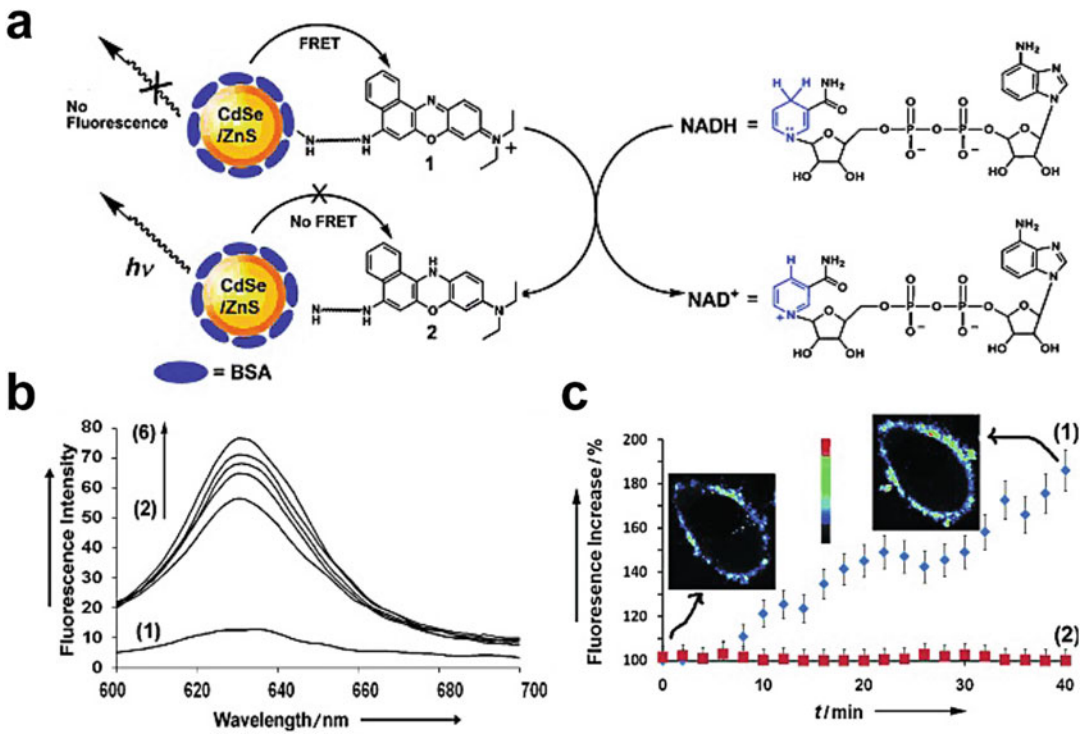

Fig. 11 (**a**) Illustration of the mechanism of a Nile blue-functionalized QD for the detection of conversion between NAD(P)H (reduced form) and $NAD(P)^+$ (oxidized form). (**b**) Time-dependent fluorescence changes of the Nile blue-functionalized QDs upon incubation with 0.5 mM NADH. (**c**) Time-dependent changes of fluorescence in Nile blue-functionalized QD-labeled HeLa cells upon stimulation with 50 mM $_D$-glucose. (Reprinted with permission from Ref. [51]. Copyright © 2009 WILEY-VCH Verlag GmbH & Co. KGaA, Weinheim)

FRET process. Upon reaction with HIV-1 PR, the peptide (SQNYPIVQ) could be recognized and cut by HIV-1 PR, leading to the release of dabcyl from QDs (Fig. 13a). Fluorescence recovery at 495 nm was observed, allowing for the detection of HIV-1 PR activity and screening of its inhibitors in vitro. The QD-Pep1 was then used to monitor protease activity in HIV-1 transfected HeLa cells via fluorescence imaging. As shown in Fig. 13b, HIV-1 plasmid transfect HeLa cells showed bright punctate fluorescence in the cytosol after incubation with QD-Pep1, which could be applied for cell-based visual screening of inhibitors again HIV-1.

In addition to integration of QDs with quenchers to prepare pre-quenched fluorescent probes, QDs can also be conjugated with organic dyes to enable ratiometric fluorescence imaging of enzyme activity through the FRET process. For example, Li et al. have devised QDs-based molecular beacons through conjugation of QDs with organic dye Rhodamine B (RB) to detect matrix metalloproteinases-2 (MMP-2), an enzyme involved in tumor invasion and metastasis [84]. Specifically, an N-acetyl-$_L$-cysteine (NAC)-stabilized CdTe QD with a 540 nm emission was covalently linked to RB via a MMP-2-specific peptide substrate (GPLGVRGKGG) (Fig.14a). Within the molecular beacons, the QDs are energy donors and the RB molecules are chosen as the acceptors due to the good spectral overlap between QDs fluorescence and RB absorption. Under excitation at 365 nm, the fluorescence of QDs was low while the fluorescence of RB was high owing to the FRET from QDs to RB. The peptide was selectively cleaved when treated with MMP-2, resulting in the QDs fluorescence recovery at 540 nm, while the RB

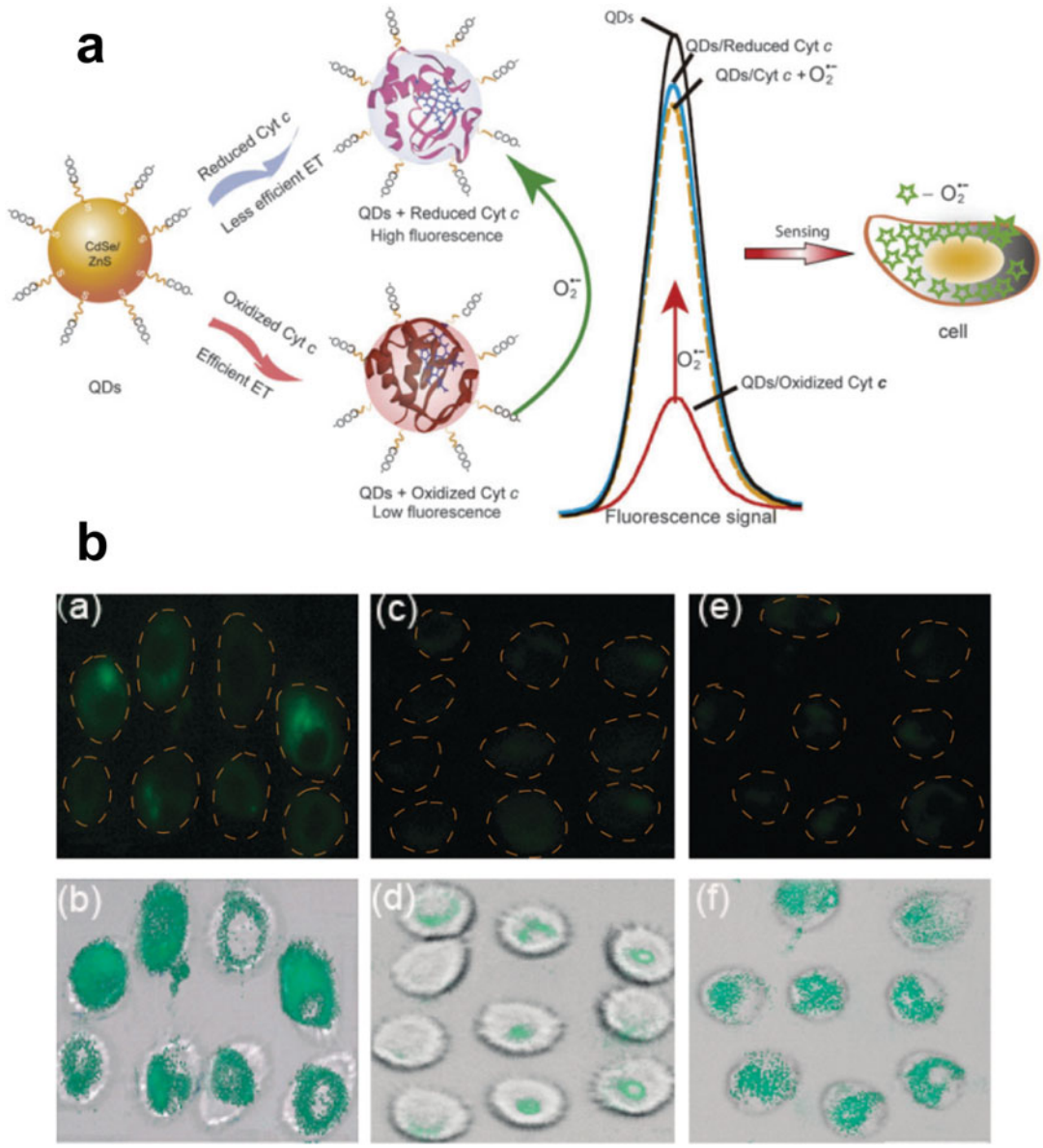

Fig. 12 (**a**) Schematic diagram of QD-Cyt c (oxidized) nanosystems for the detection of $O_2^{\bullet-}$. Oxidized Cyt c assembled on the surface of QDs could accept the electrons from QDs and quench the QDs fluorescence through the PET process. After reacted with $O_2^{\bullet-}$, the oxidized Cyt c was converted into its reduced state, and the PET process was interrupted, resulting in recovery of QDs fluorescence. (**b**) Fluorescence imaging of $O_2^{\bullet-}$ in PMA-stimulated HeLa (left), and PMA-stimulated HL-7702 cells (middle), and untreated HeLa cells with QD-Cyt c nanosystems. (Reprinted with permission from Ref. [80]. Copyright © 2011, Royal Society of Chemistry)

fluorescence decreases concomitantly. By using the probe, the authors successfully detected MMP-2 activity in MDA-MB-231 cells through ratiometric fluorescence imaging (Fig.14b). With replacing the QD 540 and RB with QD 720 nm and a NIR dye ICG-Der-02 (MPA), they further

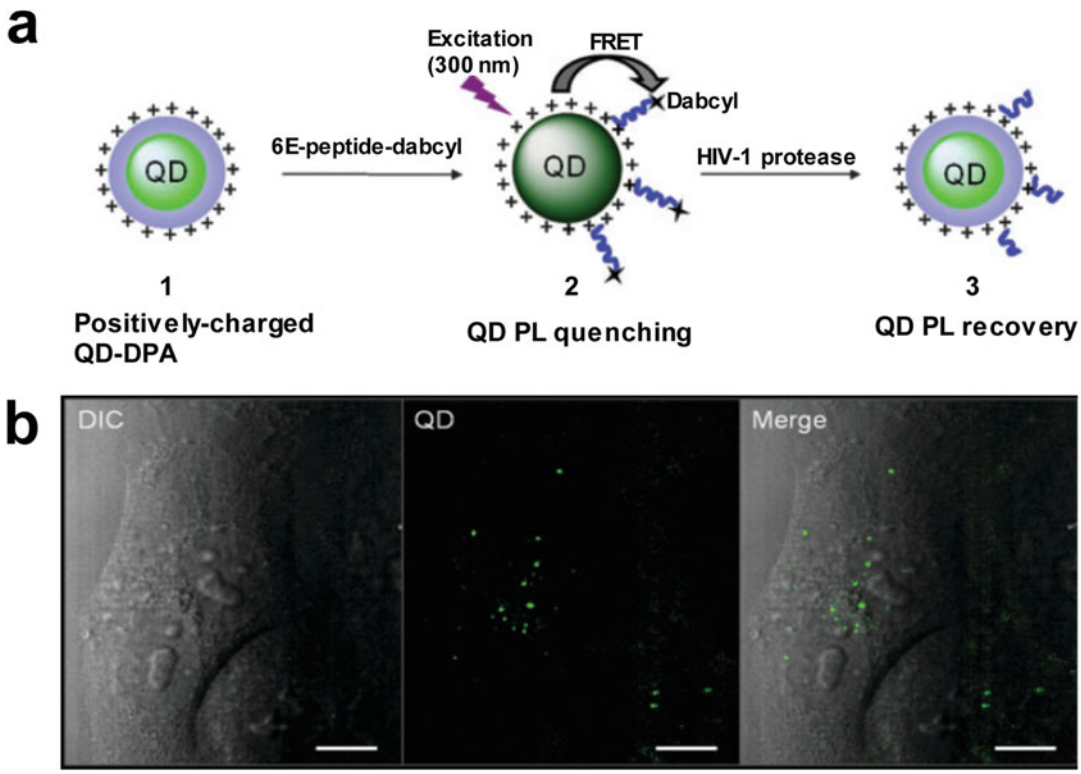

Fig. 13 (**a**) Schematic of the QD-Pep1 nanocomplexes for fluorescence sensing of HIV-1 PR activity. The Pep1 complexed on the surface of QDs can be recognized and cut by HIV-1 PR, leading to the release of dabcyl from QDs and recovery of QDs fluorescence. (**b**) Confocal fluorescence imaging of HIV-1 plasmid transfected HeLa cells with the QD-Pep1 probe. Green fluorescence indicates the activated QDs fluorescence by HIV-1 PR inside HeLa cells. Scale bar: 10 μm. (Reprinted with permission from Ref. [83]. Copyright © 2010, Royal Society of Chemistry)

demonstrated that the QDs-based molecular beacons were useful for imaging of MMP-2 activity in vivo.

In 2010, Boeneman reported another approach to engineer QDs for the imaging of intracellular enzyme dynamics in living cells. In their study, the imaging mechanism was based on the enzyme recognition-induced generation of FRET process rather than termination of FRET process (Fig. 15a). They demonstrated that mCherry-His_6 fluorescent protein could bind to the surface of Ni^{2+}-supplemented Invitrogen Qdot 565 nm ITK carboxyl QDs via metal-affinity coordination between the His_6 residues and the Ni^{2+}-COOH QD surface, resulting in the FRET from QDs to the mCherry (Fig. 15b) [85]. After microinjection of the Qdot 565 nm ITK carboxyl QDs into COS-1 cells pretreated with 250 μM Ni^{2+}, it was found that only cells expressing mCherry-His_6 showed an evident FRET signal, with fluorescence emission overlapping between the sensitized mCherry from QDs and direct excitation of mCherry (Fig. 15c). Cells expressing His_6 tag free mCherry showed no FRET signal after injection with the same QDs. These results indicated that the microinjection of QDs was able to specifically bind with cytoplasmic mCherry-His_6, allowing to intracellularly generate FRET signal capable of locating the expression site of mCherry-His_6. Interestingly, they also found that the formation of QD-mCherry-His_6 complexes could improve the photostability of mCherry, which was helpful for long-term imaging of mCherry dynamics in cells.

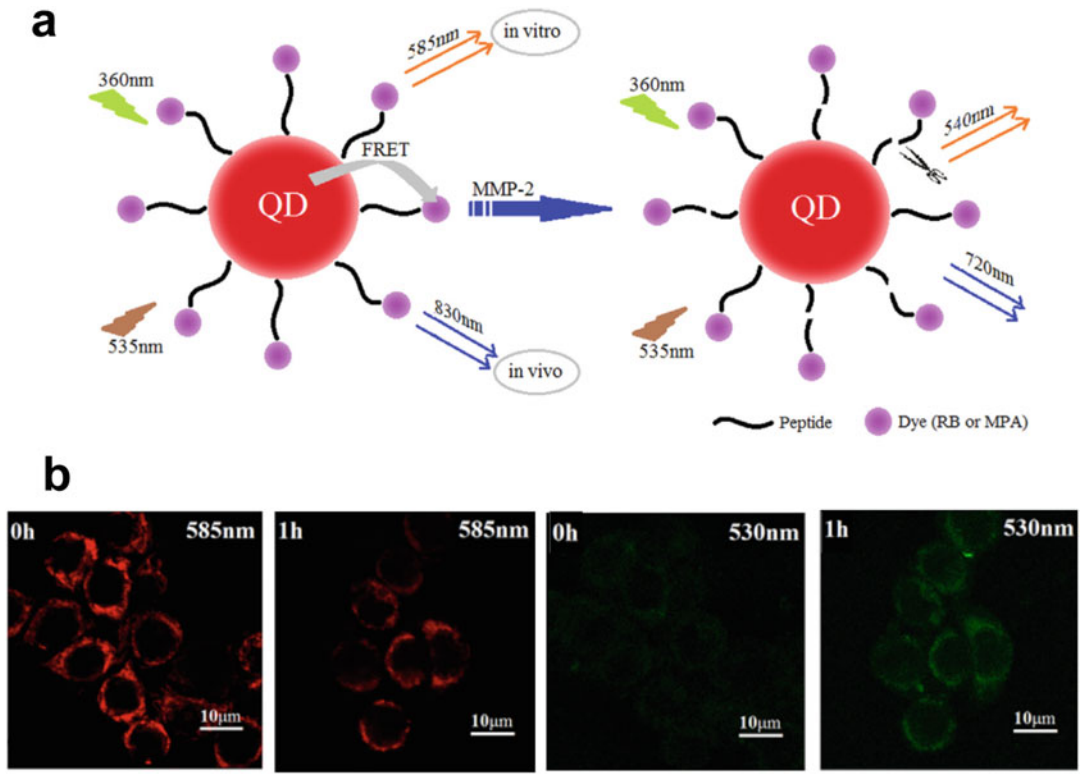

Fig. 14 (**a**) The schematic of FRET-based QD probes for the detection of MMP-2 activity in vitro and in vivo. (**b**) Fluorescence images of MDA-MB-231 cells at 585 nm and 530 nm channels following incubation with the 540QD-peptide-RB probes at 0 and 1 h. (Reprinted with permission from Ref. [84]. Copyright © 2014 Elsevier B.V. All rights reserved)

3.2.3 Imaging of Nucleic Acids in Cells

Nucleic acids are a class of molecular targets essential for life. In the past few decades, much attention has been paid to detect nucleic acids or engineer nucleic acids as versatile biomaterials for biological applications. Generally, the application of luminescent QDs for nucleic acids detection is through conjugation of oligonucleotides to the surface of QDs. The oligonucleotides on the QDs can specifically recognize and hybridize with complementary DNA or RNA molecules, thereby changing the QDs fluorescence. In 2004, Kim et al. employed QDs to construct molecular beacons (MB) for the detection of target DNA [86]. They covalently conjugated MAA-coated CdSe/ZnS core-shell QDs with quencher dabcyl-labeled hairpin oligonucleotides (5′ (C_6NH_2) GCGACTTTGGG TTTGGGTTTCTCGC (DABCYL)-3′) via EDC-assisted coupling reaction. The fluorescence of QDs was quenched by the dabcyl via the FRET process. When adding the target DNA sequence, the hairpin oligonucleotides opened and the distance between QDs and dabcyl increased, resulting in a decrease in FRET efficiency and recovery of QD fluorescence. Using the enhanced fluorescence, the concentration of target DNA could be measured. The applications of QDs to develop QD-MBs have many advantages, such as higher photobleaching resistance than traditional organic dye-based MBs and improved signal-to-noise ratios over “always on” nucleic acid staining agents. According to the different fluorescence emission wavelength of QDs, many dark quenchers such as dabcyl, black hole quenchers (BHQ), Iowa black (IaB) quenchers, and AuNPs

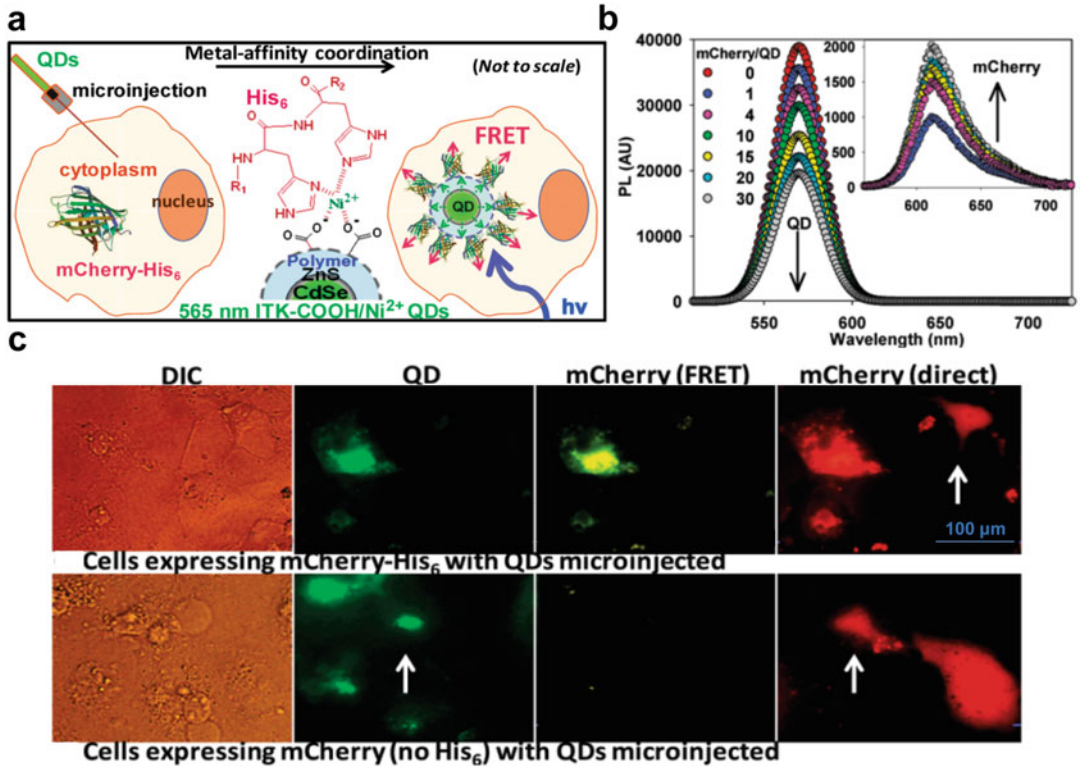

Fig. 15 (**a**) Illustration of intracellular assembly of 565 nm ITK/Ni^{2+} QDs and mCherry-His_6. (**b**) The fluorescence spectra of QD upon complexing with increasing amount of mCherry-His_6. Inset, the corresponding fluorescence spectra of mCherry-His_6 binding to the surface of QDs. The fluorescence of QDs at 565 nm decreases as the amount of mCherry-His_6 increases, while the fluorescence of mCherry-His_6 increases concomitantly. (**c**) Fluorescence imaging of cells expressing mCherry-His_6 (up) and mCherry without His_6 tags (down) following microinjection with the 565 nm ITK/Ni^{2+} QDs. Green fluorescence and red fluorescence show the location of QDs and mCherry inside the cells, and the yellow fluorescence indicates the existence of FRET process due to the assembly of 565 nm ITK/Ni^{2+} QDs and mCherry-His_6 in the cells. (Reprinted with permission from Ref. [85]. Copyright © 2010, American Chemical Society)

have been employed to quench the fluorescence of QDs, allowing to construct QD-MBs with different fluorescence emission for multicolor imaging [87–89]. In addition, organic fluorophores such as TAMRA, Cy5, and ROX have also been used as energy acceptors to build QD-MBs for ratiometric fluorescence detection [61, 90].

In 2010, Yeh et al. employed CdSe/ZnS core-shell QDs as energy donors and AuNPs as quencher to construct a QD-MB-AuNP probe for fluorescence imaging of viral RNA in cells (Fig. 16a) [89]. They added a His_6 tag to the 5′ end of a Coxsackie virus B6 (CVB6) genome targeted hairpin oligonucleotide, which can provide strong metal-affinity coordination to facilitate its binding to the surface of CdSe/ZnS QDs. On the 3′ end of the hairpin oligonucleotide, a free amino group was introduced to allow the conjugation with the AuNPs that contained monosulfo-NHS esters. In addition, a 12 bp sequence was inserted at the 3′ end as a spacer to improve hybridization efficacy. They demonstrated that the as-prepared QD-MB-AuNP probe exhibited low fluorescence via the efficient FRET process from the QDs to the AuNPs. After addition of CVB6 genome, QD fluorescence increased 7.3-fold within 50 min. To enable intracellular delivery for the detection of CVB6 infection in cells, cell penetration peptides (Tat) were further applied to modify the

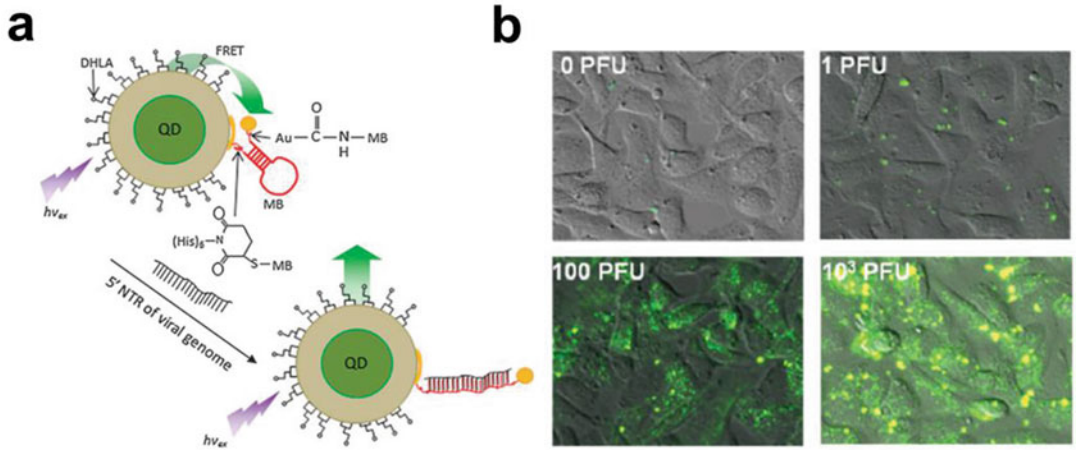

Fig. 16 (**a**) Illustration of the QD-MB-AuNP probes for the detection of viral genome based on the FRET mechanism. QD-MB-AuNP was synthesized by assembly of CdSe/ZnS core-shell QDs with AuNP via hairpin oligonucleotides. (**b**) Fluorescence imaging of BGMK cells infected with varying dosage of CVB6, followed by incubation with QD-MB-AuNP probes. (Reprinted with permission from Ref. [89]. Copyright © 2010, Royal Society of Chemistry)

QD–MB–AuNP into Tat-QD-MB-AuNP probe. As shown in Fig. 16b, Buffalo green monkey kidney (BGMK) cells incubated with the probe showed bright intracellular fluorescence upon infection with CVB6, and the number of fluorescent cells increased with the dosage of CVB6 added. Moreover, by tracking the intracellular fluorescence in the infected BGMK cells, it was feasible for the detection of newly transcribed RNA, thus allowing for the dynamic monitoring of viral infection among host cells.

The above-mentioned two QD-MBs were designed via the increase of the distance between QDs and the energy acceptors through opening of the hairpin oligonucleotides upon hybridization with target nucleotides (e.g., DNA, RNA). Alternately, complimentary hybridization with target oligonucleotides to decrease the distance between QDs and the energy acceptors, thereby changing the QD fluorescence to detect nucleic acids, has also been reported. For example, Bakalova et al. developed a QD-conjugated hybridization probe amenable for the screening of small-interfering RNA (siRNA) sequences towards mRNA targets, which were useful for RNA interference (RNAi) in cells [91]. They linked different single-stranded siRNA sequences on the surface of CdSe/ZnS QDs to build the hybridization probes. The target mRNA was labeled with organic fluorophore Cy5. When the target Cy5-mRNA hybridized with the QD-siRNA probes, the fluorescence of Cy5 increased due to the FRET process from QDs to Cy5. The increase of Cy5 fluorescence could act as an indicator to evaluate the hybridization ability of siRNA, which might be further used for the down-regulation of target gene. This hybridization-enhanced FRET process was also demonstrated by the formation of "sandwich" type of QD-hybridization probes for the detection of nucleic acids, such as hemagglutinin H5 DNA fragments of avian influenza viruses [92], echinoderm microtubule-related protein-like 4 (EML4)-anaplastic lymphoma kinase gene [93], and many other target DNA fragments [94, 95].

In 2014, Wei et al. reported a DNA-templated heterobivalent QD nanoprobe that was allowed to target cancer cells and detect intracellular mRNA via fluorescence imaging [96]. They designed a hybrid DNA sequence that contains a phosphorothioate domain in the middle (purple, Fig. 17a) and two phosphate domains (blue and orange) at each end. The phosphorothioate domain is used for the growth of CdTe QDs as well as for

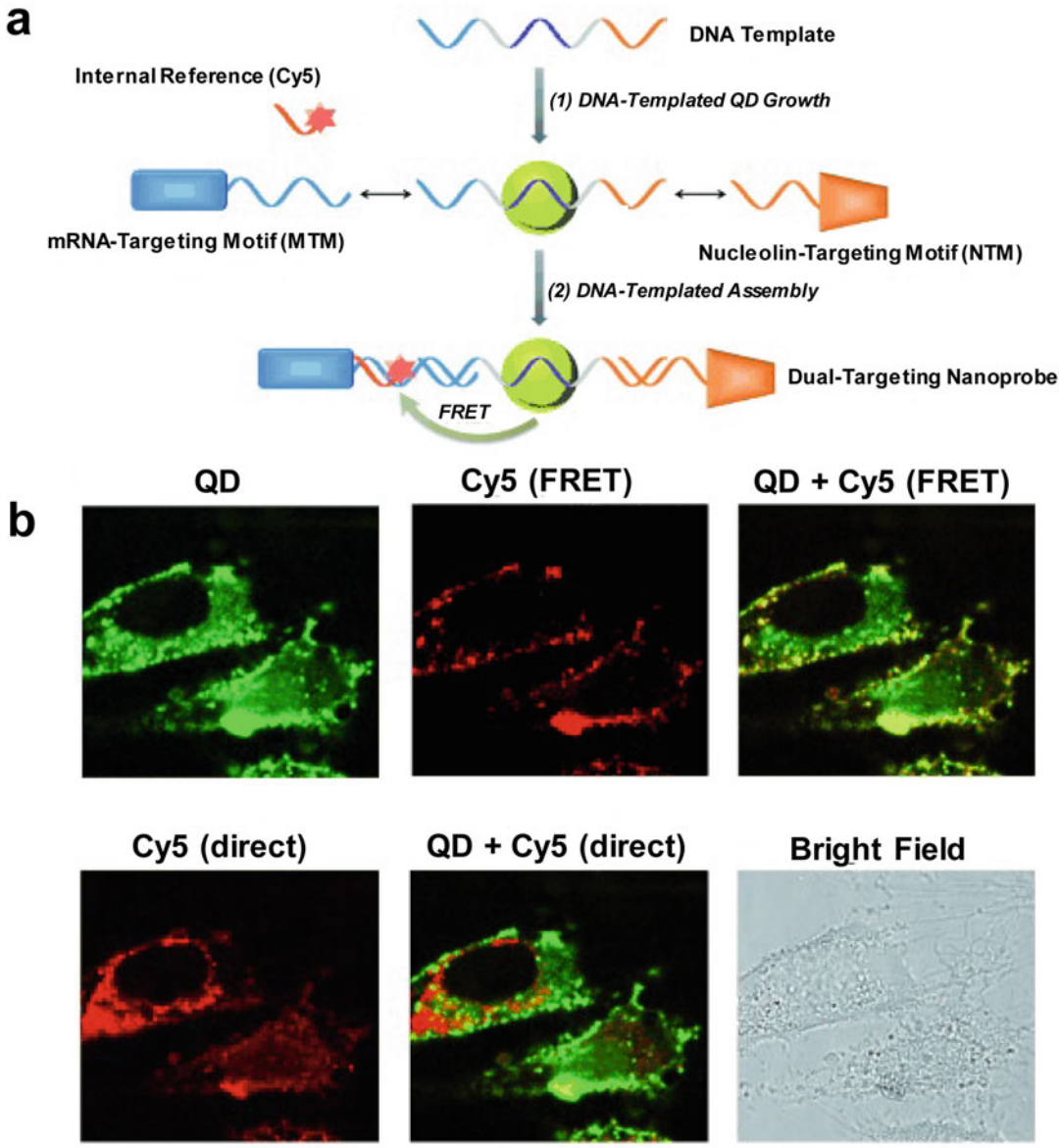

Fig. 17 (**a**) Schematic illustration of the construction of DNA-templated heterobivalent QD nanoprobe, and their applications for the detection of mRNA in tumor cells. (**a**) Schematic illustration of the construction, the dual-targeting strategy, and intracellular delivery route of the heterobivalent QD nanoprobe. (**b**) Fluorescence imaging of HeLa cells after incubation with the heterobivalent QD nanoprobe for 4 h. By comparing the fluorescence locations of QDs and Cy5 resulting from direct excitation and FRET process, the intracellular expression of survivin mRNA could be easily detected. (Reprinted with permission from Ref. [96]. © 2014 WILEY-VCH Verlag GmbH & Co. KGaA, Weinheim)

efficient binding of the DNA sequence to QDs through strong coordination between Cd^{2+} and sulfur. The two phosphate domains are consisted of an extracellular nucleolin-binding aptamer AS1411 and an intracellular survivin mRNA-targeting motif (MTM). After complexing with

QDs, a Cy5-labeled short oligonucleotide was assembled with MTM to enable FRET process from QDs to Cy5. As such, the initial fluorescence of QDs decreases while the Cy5 fluorescence increases upon excitation of QDs. When applied for cell imaging, the nanoprobe could enter the HeLa cells via AS1411 aptamer-mediated micropinocytosis, following by cytosolic delivery due to the leaky macropinosomes. The survivin mRNA that was upregulated in the cytosol could subsequently bind to the MTM in the nanoprobe, liberate the Cy5-labeled oligomer, and recover QD fluorescence. By comparing the fluorescence locations of QDs and Cy5 resulting from direct excitation and FRET process, the intracellular expression of survivin mRNA could be easily detected (Fig. 17b). This approach of integrating two different oligonucleotides to design QD-based nanoprobes was also extended to develop a QD-based photosensitizer, which can target to tumor cells and be activated by adenosine triphosphate (ATP), thereby allowing for the measuring of intracellular ATP and selective photodynamic therapy of tumors [97].

In addition to design QD-based probes to detect nucleic acids based on the complimentary hybridization process, there are also some examples of using antibiotics or proteins functionalized QDs to detect DNA. For example, Shen et al. devised an activatable QD-based NIR probe for sensitive fluorescence imaging of DNA in living tumor cells (Fig. 18a) [98]. In this study, negative NAC-coated CdTe QDs with NIR fluorescence were directly labeled with cationic Al (III)-gatifloxacin (Al-GFLX) complexes to form QD-Al-GFLX conjugates through strong electrostatic interactions. Owing to an efficient PET process between QDs and Al-GFLX, the NIR fluorescence of QDs was quenched. Upon interaction with double-stranded DNA (dsDNA), the QD-Al-GFLX nanocomplexes were dissociated due to the high binding affinity between dsDNA and the Al-GFLX complex, thus eliminating the PET process. The NIR fluorescence of QDs was recovered, which was sensitive to detect dsDNA in aqueous solution. Moreover, QD-Al-GFLX could be further applied for the detection of endogenous dsDNA in live cancer cells. As shown in Fig. 18b, bright fluorescence of QDs that overlapped well with the blue fluorescence from the nucleus staining appeared in the HeLa cells after being incubated with QD-Al-GFLX. In contrast, the incubation with QDs or Al-GFLX alone showed little NIR fluorescence in the nucleus, confirming that QD-Al-GFLX were useful for the detection of endogenous dsDNA in live cells.

3.2.4 Imaging of Cellular Microenvironment

The non-invasive imaging of different cellular microenvironment such as pH and temperature is of great significance in elucidating biological processes. The applications of QDs to design fluorescent probes for the measurement of cellular microenvironment have shown promising results. For example, many "turn-on" QD-based fluorescent probes have been developed for the measurement of intracellular pH essential for many cellular processes. One of the general approaches to design pH-sensitive fluorescent probes is the direct use of QDs because their PL can be affected by the environmental parameters (e.g., pH, temperature, and electric field). Liu et al. have synthesized a MAA-capped CdSe/ZnSe/ZnS QD that could be directly used as an intracellular pH sensor [99]. They demonstrated that the fluorescence of the MAA-capped QDs increased as pH increased from 4 to 10 in both aqueous solution (Fig. 19a) and fixed cells. The MAA-capped QDs were also feasible to detect the intracellular pH in SKOV-3 ovarian cancer cells. When the cellular pH became more basic upon stimulation with chloroquine for 30 min, a stronger fluorescence of QDs within cells was observed (Fig. 19b).

Another approach to engineer QDs as pH sensors is the use of pH-sensitive chromophores to tune the fluorescence of QDs under different pH. Because QDs are normally sensitive to charge transfer, their PL can be altered when the charge transfer between QDs and incorporated chromophores is changed by different pH. According to this mechanism, Medintz et al. developed QD-dopamine-peptide bioconjugates as charge-transfer coupled intracellular pH sensors by exploring pH-dependent oxidation of

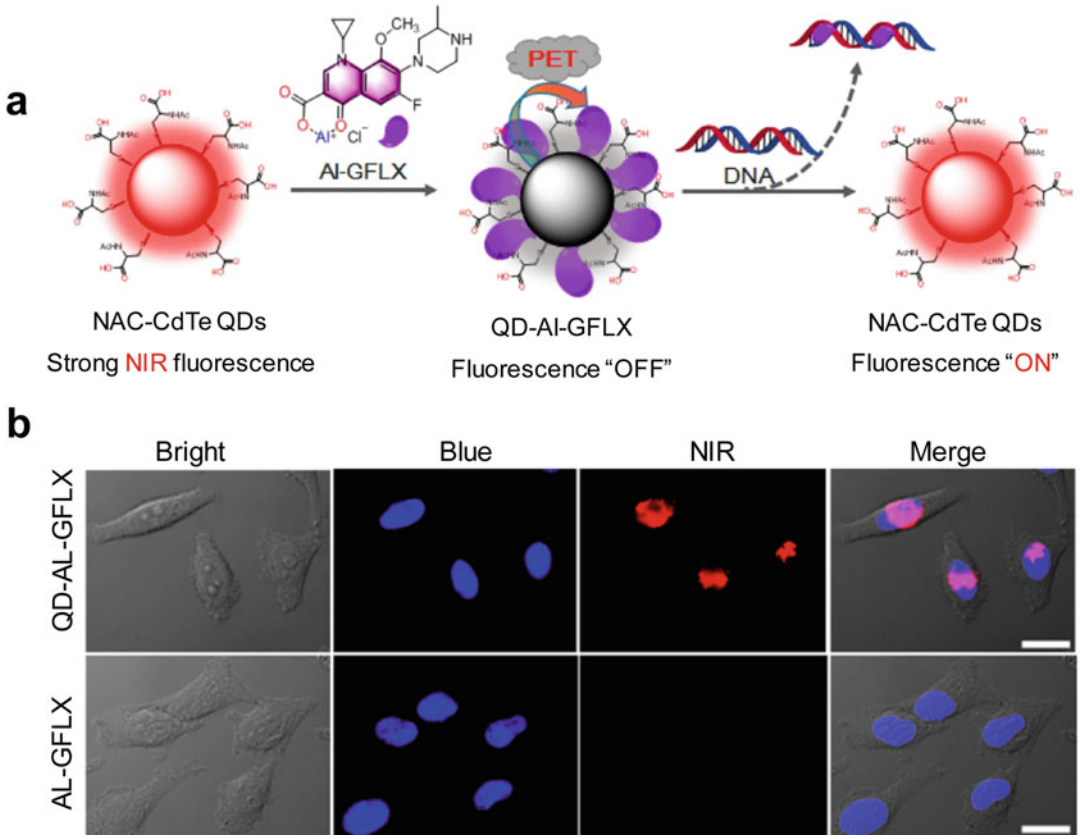

Fig. 18 (**a**) General design of "turn-on" NIR fluorescent QD-Al-GFLX nanoprobe for DNA detection. The NIR fluorescence of QDs was quenched owing to an efficient PET process between QDs and Al-GFLX, while the fluorescence recovers upon interaction with dsDNA. (**b**) Fluorescence imaging of dsDNA in live HeLa cells after incubation with QD-Al-GFLX and Al-GFLX, respectively. Red color indicates the NIR fluorescence from QDs, and blue color indicates the nucleus stained by DAPI. Scale bars: 20 μm. (Reprinted with permission from Ref. [98]. Copyright © 2017, American Chemical Society)

dopamine to quinone (Fig.20a) [100]. In their work, a dopamine-labeled peptide was assembled to QDs via the His_6 sequence. The assembly of peptide on the surface of QDs via the strong metal-coordination affinity could offer the proximity for efficient electron transfer process to manipulate the QD PL. At low pH, the dopamine on the surface of QDs is present as hydroquinone predominantly, which is a poor electron acceptor, and the QD PL is little quenching. As pH increases to basic values, the dopamine is easily oxidized into quinone by ambient O_2, thus becoming as an efficient electron acceptor to quench the QD PL. When the QD-dopamine-peptide conjugates were dispersed in aqueous solution, the QD PL decreased linearly as the pH increased from 6.5 to 11.5, suggesting the potential to measure the pH values (Fig. 20b). After microinjection into COS-1 cells, they demonstrated that the intracellular fluorescence of QDs dropped steadily when the cells were treated with nystatin, a polyene antifungal drug that can induce intracellular alkalosis. In contrast, the red fluorescence of the internal standard of Fluorophorex 20 nm nanosphere (FLX) was little changed. It was notable that the intracellular pH values could be accurately derived from the PL data upon imaging for over 60 min, suggesting that the QD-dopamine-peptide assemblies could

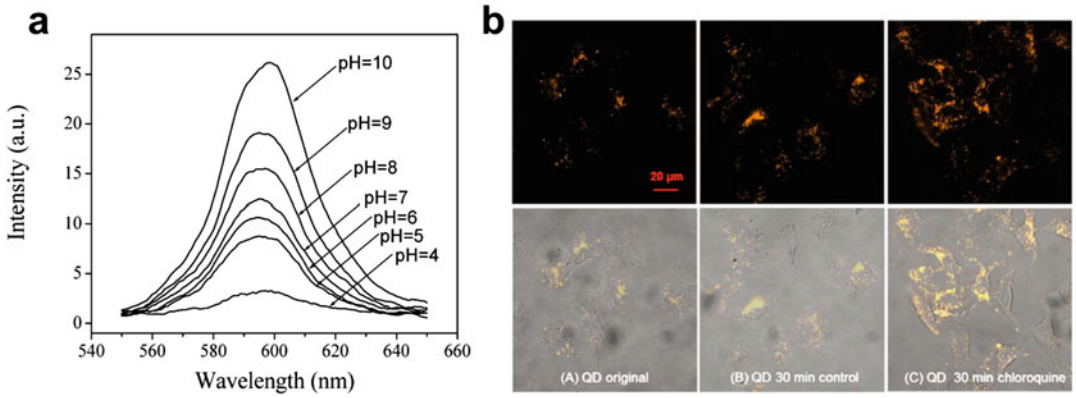

Fig. 19 (**a**) Fluorescence spectra of QD-probe under different pH. (**b**) Fluorescence imaging of pH change in living SKOV-3 ovarian cancer cells with the MAA-capped CdSe/ZnSe/ZnS quantum dots. As the cellular pH becomes more basic upon stimulation with chloroquine, a stronger fluorescence of QDs within cells was observed. (Reprinted with permission from Ref. [99]. Copyright © 2007, American Chemical Society)

efficiently monitor the intracellular changes (Fig. 20c).

In 2012, Dennis et al. incorporated pH-sensitive fluorescent proteins (FPs) into photostable QDs and developed a QD-based radiometric pH sensor (Fig. 21a) [101]. They conjugated FPs of mOrange (p*K*a = 6.9) and mOrgange M163K (p*K*a = 7.9) to QDs to allow FRET process between QDs and FPs, respectively. Because the absorbance and emission intensities of mOrange and mOrgange M163K were pH dependent, their absorbance and emission intensities decreased with pH. The FRET process between QD and conjugated FPs in proximity varied under different pH, thus tuning the FP/QD emission ratio upon photoexcitation of QDs. It was found that the fluorescence ratio between FPs and QDs (F_A/F_D) increased by >12-fold when the pH in the solution increases from 6 to 8 (Fig. 21b). A p*K*a of 7.0 was derived from the sigmoidal fit, which was appropriate for the detection of the physiological pH in cells. As shown in Fig. 21c, both the mOrgane fluorescence and the FRET signal were obviously reduced when HeLa cells were loaded with the C-terminal polyarginine-modified QD-Orange probe for additional 2 h, attributed to the low pH values in endosomes (pH ~4.5–5.5). When the endosomal acidification in HeLa cells was inhibited, the FRET signal in HeLa cells was not changed between time 0 and 2 h after probe delivery into cells.

Besides pH, the applications of QDs for to measure temperature in cells have also been demonstrated. For example, Zhang el al reported $CuInS_2$/ZnS QDs, whose fluorescence is dependent on the temperature (Fig. 22a) [102]. They encapsulated the synthesized $CuInS_2$/ZnS QDs with amphiphilic polymers to form QD-micelles, which showed improved water solubility and biocompatibility for biological applications. They demonstrated that the red fluorescence of the QD-micelles in PBS buffer increased as the temperature decreased (Fig. 22b). The fluorescence intensity at 645 nm at 0 °C PBS buffer was found to be 3.88 times that at 60 °C. After being incubated with the QD-micelles under different temperature, the intracellular fluorescence became weaker when the temperature increased from 25 to 40 °C (Fig. 22c), with a good linear relationship between the fluorescence intensity and temperature. Such temperature-sensitive QD-micelles could also be useful for the measurement of temperature in living mice through non-invasive fluorescence imaging (Fig. 22d).

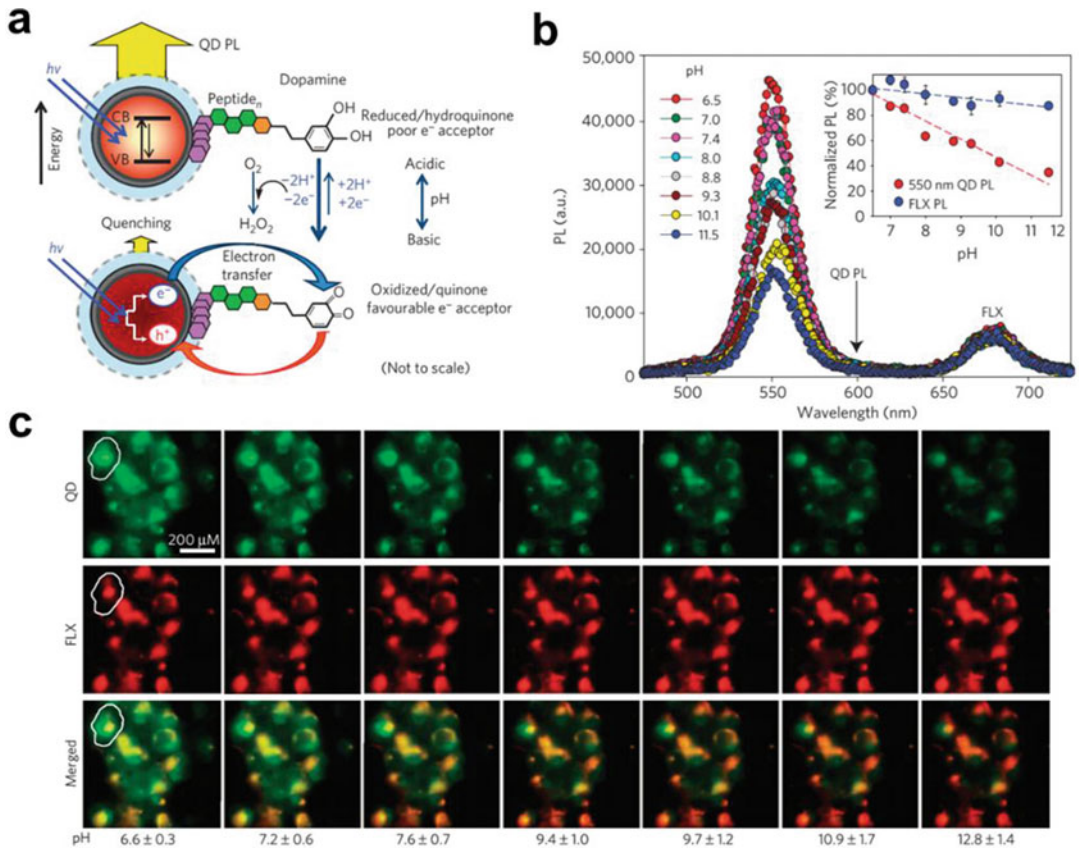

Fig. 20 (**a**) Schematic illustration of QD-dopamine-peptide bioconjugates for the detection of pH. (**b**) Fluorescence spectra of QD-dopamine conjugates at increasing pH values in solution. Inset: linear plots of the normalized PL intensity of QDs and FLX versus pH values from 6.5 to 11.5. (**c**) Fluorescence imaging of COS-1 cells at different pH. The green fluorescence is from QDs and the red fluorescence is from the internal standard of FLX. (Reprinted with permission from Ref. [100]. Copyright © 2010 Springer Nature Limited)

4 Conclusion and Future Outlook

QDs, with their extraordinary electronic and optical properties, have shown promising results for fluorescence imaging in cells. The high photostability of QDs could allow for long-term tracking and monitoring of dynamic biological processes in cells. The broad and strong absorption of QDs could make them serve as efficient energy donors to design various FRET-based fluorescent probes for real-time cellular imaging. Moreover, the size-dependent fluorescence wavelength together with symmetric and narrow emission could enable to design different color QDs for multiplex imaging of biomolecules in cells.

Although many encouraging results have been demonstrated from cell imaging with QDs, there are still some challenges related to the QDs remaining to be overcome. One of the major challenges is the potential issue of toxicity of QDs toward living biology due to the use of toxic heavy metal ions (e.g., Cd^{2+}, Pb^{2+}). Initially, it was assumed that the release of toxic metal ions and excitation-induced generation of free radical in the body would cause damage to normal tissue cells and organs. The overwhelming majority of evidence disclosed to date, however, indicated that well designed QDs with core-shell structure, proper hydrophilic coating, and the optimization of dosage, the potential toxicity

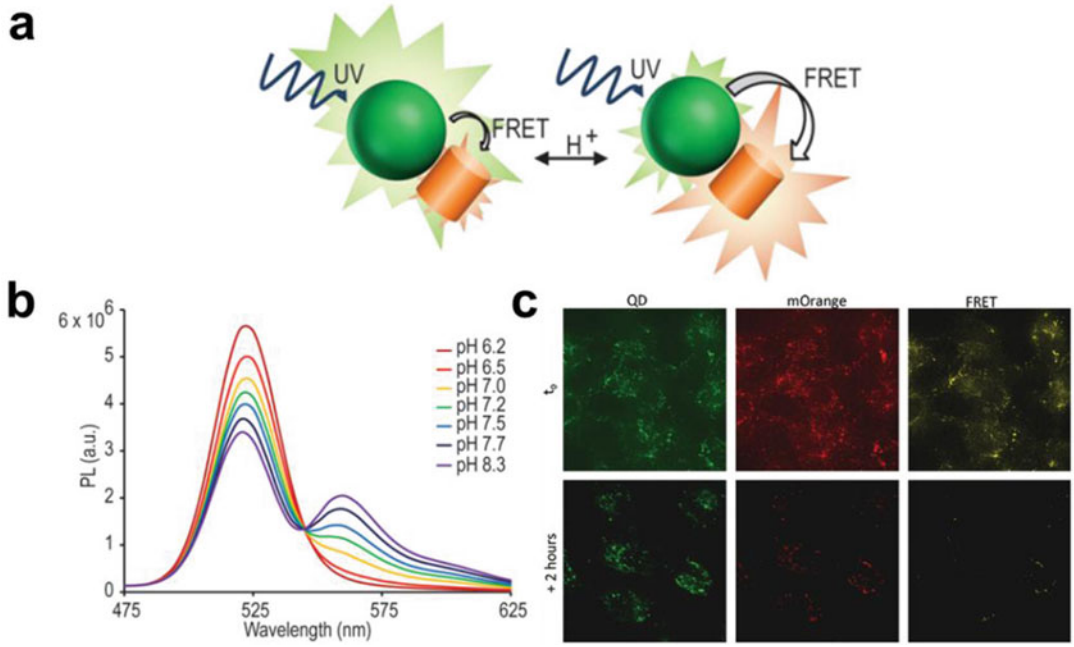

Fig. 21 (**a**) Schematic illustration of the pH-sensitive fluorescent proteins/QDs conjugates for the detection of pH. The FRET process between the quantum dot and fluorescent protein changes with the alternation of pH value. (**b**) Fluorescence spectra of QDs and fluorescent protein under different pH. (**c**) Fluorescence images of HeLa cells immediately and 2 h after delivery of the QD-Orange probes. Both the mOrgane fluorescence and the FRET signal were obviously reduced after incubation for 2 h, suggesting the maturation of the endosome. (Reprinted with permission from Ref. [101]. Copyright © 2012, American Chemical Society)

QDs toward cells and body could be dramatically mitigated. For example, Cho and co-workers investigated the Cd^{2+} release and cell toxicity of core-shell QDs and core-only QDs [103]. It was showed that the ZnS shell could significantly prevent Cd^{2+} from releasing and cause nearly non-toxic to MCF-7 cells, while the core-only CdTe QDs could cause cell death via mechanisms involving both Cd^{2+} release and ROS generation. In addition, the direct biosynthesis of QDs in living biological systems has been emerging as a sustainable and environment benign approach to synthesize biocompatible QDs. For example, Stürzenbaum et al. have realized the biosynthesis of luminescent CdTe QDs in a live earthworm via an intrinsic metal detoxification pathway [104]. The isolated QDs from worm's body were capable of applications in cell imaging, with negligible toxicity observed. Shao et al. have explored the applications of selenium metabolism for the biosynthesis of CdSe QDs in living yeast. They demonstrated that the overexpression of the *MET6* gene in the engineered cells could significantly enhance the yield of QDs [105]. It is anticipated that the biosynthesis of QDs directly in the living biology, without using harsh conditions and organic solvent, could be highly biocompatible for biological applications. However, it is mentioned that most of these biosynthesized QDs have lower PL quantum yields compared to that synthesized via chemical approaches. In addition, the size and fluorescence emission wavelength of QDs are difficult to control during biosynthesis. In the future, the efficient approach to control the biosynthesis of QDs with improved quantum yield and manipulated fluorescence emission wavelength for fluorescence imaging is highly demanded.

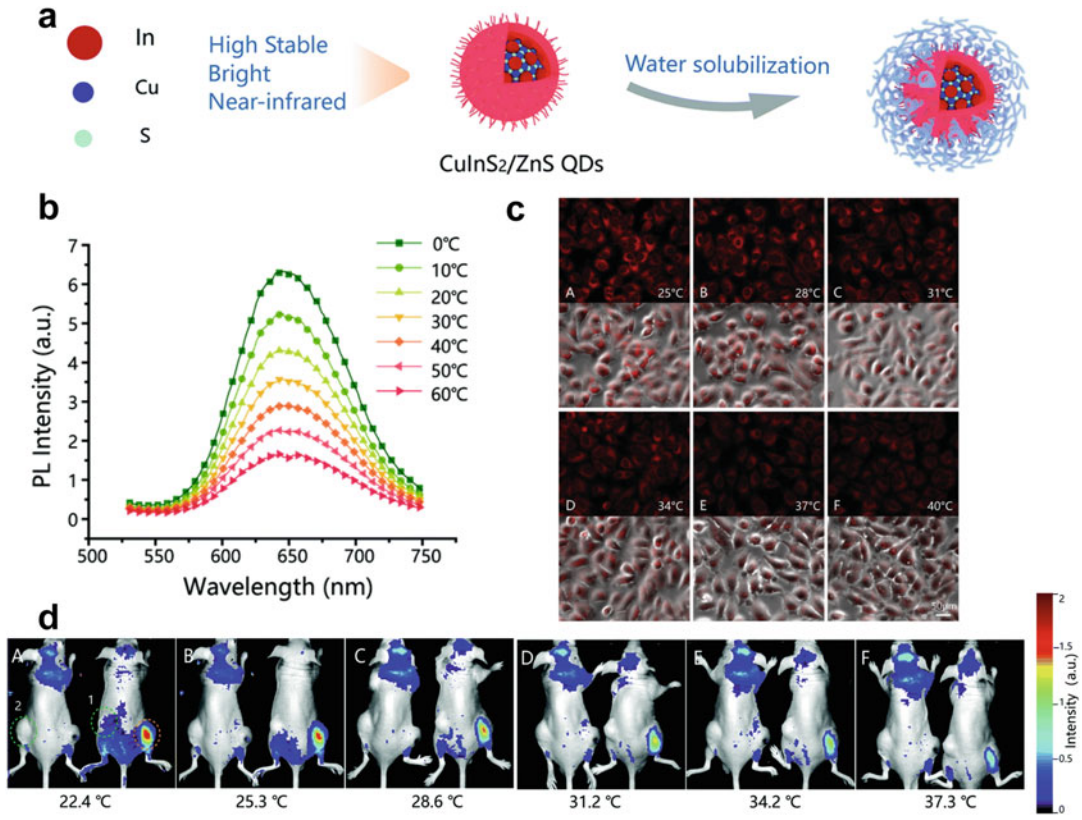

Fig. 22 (**a**) Schematic illustration of the preparation of the QD-micelles. (**b**) Fluorescence spectra of $CuInS_2/ZnS$ QD-micelles in PBS at different temperature. (**c**) Fluorescence imaging of HeLa cells incubated with the QD-micelles at indicated temperature. (**d**) In vivo fluorescence images of tumor-bearing nude mice injected with QD-micelles at different temperature. (Reprinted with permission from Ref. [102]. Copyright © 2019, Royal Society of Chemistry)

In addition to the side toxicity, the efficient delivery of QDs into a specific organelle of a living cell in a non-invasive manner is another challenge for cell imaging. It is recognized that QDs with the nanoscale size can generally enter living cells via an energy-dependent endocytosis pathway, which will trap these QDs within lysosomes. When applied to detect biomolecules and biological processes in the cytosol or other organelles (e.g., mitochondria, nucleus), the QDs are required to escaped from the lysosomes and then translocated into the desired organelles. Current approaches such as microinjection are suffered from the low throughput and invasiveness to the cells. The use of lysosomal rupture agents to help QDs escape from the lysosomes have also been demonstrated, while these agents may also cause toxicity to the cells and potentially disturb many biological processes in cells. Therefore, the development of efficient methods to modify QDs that have good ability to bypass the lysosomal trapping is crucial for achieving efficient fluorescence imaging of a cellular molecular target.

References

1. Miyawaki A (2003) Visualization of the spatial and temporal dynamics of intracellular signaling. Dev Cell 4:295–305
2. Schröck E, du Manoir S, Veldman T, Schoell B, Wienberg J, Ferguson-Smith MA, Ning Y, Ledbetter DH, Bar-Am I, Soenksen D, Garini Y, Ried T (1996)

Multicolor spectral karyotyping of human chromosomes. Science 273:494–497
3. Bruchez M, Moronne M, Gin P, Weiss S, Alivisatos AP (1998) Semiconductor nanocrystals as fluorescent biological labels. Science 281:2013–2016
4. Chan WCW, Nie S (1998) Quantum dot bioconjugates for ultrasensitive nonisotopic detection. Science 281:2016–2018
5. Zrazhevskiy P, Sena M, Gao X (2010) Designing multifunctional quantum dots for bioimaging, detection, and drug delivery. Chem Soc Rev 39:4326–4354
6. Alivisatos AP (1996) Semiconductor clusters, nanocrystals, and quantum dots. Science 271:933–937
7. Medintz IL, Uyeda HT, Goldman ER, Mattoussi H (2005) Quantum dot bioconjugates for imaging, labelling and sensing. Nat Mater 4:435–446
8. Zeng R, Zhang T, Liu J, Hu S, Wan Q, Liu X, Peng Z, Zou B (2009) Aqueous synthesis of type-II CdTe/CdSe core–shell quantum dots for fluorescent probe labeling tumor cells. Nanotechnology 20:095102
9. Dabbousi BO, Rodriguez-Viejo J, Mikulec FV, Heine JR, Mattoussi H, Ober R, Jensen KF, Bawendi MG (1997) (CdSe)ZnS core−shell quantum dots: synthesis and characterization of a size series of highly luminescent nanocrystallites. J Phys Chem B 101:9463–9475
10. Leatherdale CA, Woo WK, Mikulec FV, Bawendi MG (2002) On the absorption cross section of CdSe nanocrystal quantum dots. J Phys Chem B 106:7619–7622
11. Sukhanova A, Devy J, Venteo L, Kaplan H, Artemyev M, Oleinikov V, Klinov D, Pluot M, Cohen JHM, Nabiev I (2004) Biocompatible fluorescent nanocrystals for immunolabeling of membrane proteins and cells. Anal Biochem 324:60–67
12. Murphy CJ (2002) Peer reviewed: optical sensing with quantum dots. Anal Chem 74:520A–526A
13. Parak WJ, Gerion D, Pellegrino T, Zanchet D, Micheel C, Williams SC, Boudreau R, Le Gros MA, Larabell CA, Alivisatos AP (2003) Biological applications of colloidal nanocrystals. Nanotechnology 14:R15–R27
14. Niemeyer CM (2001) Nanoparticles, proteins, and nucleic acids: biotechnology meets materials science. Angew Chem Int Ed 40:4128–4158
15. Alivisatos P (2004) The use of nanocrystals in biological detection. Nat Biotechnol 22:47–52
16. Wu X, Liu H, Liu J, Haley KN, Treadway JA, Larson JP, Ge N, Peale F, Bruchez MP (2003) Immunofluorescent labeling of cancer marker Her2 and other cellular targets with semiconductor quantum dots. Nat Biotechnol 21:41–46
17. Freeman R, Bahshi L, Finder T, Gill R, Willner I (2009) Competitive analysis of saccharides or dopamine by boronic acid-functionalized CdSe-ZnS quantum dots. Chem Commun 764–766
18. Ruan G, Agrawal A, Marcus AI, Nie S (2007) Imaging and tracking of tat peptide-conjugated quantum dots in living cells: new insights into nanoparticle uptake, intracellular transport, and vesicle shedding. J Am Chem Soc 129:14759–14766
19. Bhatia D, Arumugam S, Nasilowski M, Joshi H, Wunder C, Chambon V, Prakash V, Grazon C, Nadal B, Maiti PK, Johannes L, Dubertret B, Krishnan Y (2016) Quantum dot-loaded monofunctionalized DNA icosahedra for single-particle tracking of endocytic pathways. Nat Nanotechnol 11:1112–1119
20. Petryayeva E, Algar WR, Medintz IL (2013) Quantum dots in bioanalysis: a review of applications across various platforms for fluorescence spectroscopy and imaging. Appl Spectrosc 67:215–252
21. Choi Y, Cho Y, Kim M, Grailhe R, Song R (2012) Fluorogenic quantum dot-gold nanoparticle assembly for beta secretase inhibitor screening in live cell. Anal Chem 84:8595–8601
22. So MK, Xu C, Loening AM, Gambhir SS, Rao J (2006) Self-illuminating quantum dot conjugates for in vivo imaging. Nat Biotechnol 24:339–343
23. Snee PT, Somers RC, Nair G, Zimmer JP, Bawendi MG, Nocera DG (2006) A ratiometric CdSe/ZnS nanocrystal pH sensor. J Am Chem Soc 128:13320–13321
24. Nag OK, Stewart MH, Deschamps JR, Susumu K, Oh E, Tsytsarev V, Tang Q, Efros AL, Vaxenburg R, Black BJ, Chen Y, O'Shaughnessy TJ, North SH, Field LD, Dawson PE, Pancrazio JJ, Medintz IL, Chen Y, Erzurumlu RS, Huston AL, Delehanty JB (2017) Quantum dot-peptide-fullerene bioconjugates for visualization of in vitro and in vivo cellular membrane potential. ACS Nano 11:5598–5613
25. Freeman R, Finder T, Bahshi L, Willner I (2009) β-Cyclodextrin-modified CdSe/ZnS quantum dots for sensing and chiroselective analysis. Nano Lett 9:2073–2076
26. Peng H, Zhang L, Kjällman THM, Soeller C, Travas-Sejdic J (2007) DNA hybridization detection with blue luminescent quantum dots and dye-labeled single-stranded DNA. J Am Chem Soc 129:3048–3049
27. Xie R, Battaglia D, Peng X (2007) Colloidal InP nanocrystals as efficient emitters covering blue to near-infrared. J Am Chem Soc 129:15432–15433
28. Xu S, Ziegler J, Nann T (2008) Rapid synthesis of highly luminescent InP and InP/ZnS nanocrystals. J Mater Chem 18:2653–2656
29. Yong KT, Ding H, Roy I, Law WC, Bergey EJ, Maitra A, Prasad PN (2009) Imaging pancreatic cancer using bioconjugated InP quantum dots. ACS Nano 3:502–510
30. Tamang S, Lincheneau C, Hermans Y, Jeong S, Reiss P (2016) Chemistry of InP nanocrystal syntheses. Chem Mater 28:2491–2506
31. Hyun BR, Chen H, Rey DA, Wise FW, Batt CA (2007) Near-infrared fluorescence imaging with water-soluble lead salt quantum dots. J Phys Chem B 111:5726–5730

32. Hu R, Law WC, Lin G, Ye L, Liu J, Liu J, Reynolds JL, Yong KT (2012) PEGylated phospholipid micelle-encapsulated near-infrared PbS quantum dots for in vitro and in vivo bioimaging. Theranostics 2:723–733
33. Gui R, Jin H, Wang Z, Tan L (2015) Recent advances in synthetic methods and applications of colloidal silver chalcogenide quantum dots. Coordin Chem Rev 296:91–124
34. Bryant GW, Jaskolski W (2005) Surface effects on capped and uncapped nanocrystals. J Phys Chem B 109:19650–19656
35. Gómez DE, Califano M, Mulvaney P (2006) Optical properties of single semiconductor nanocrystals. Phys Chem Chem Phys 8:4989–5011
36. Hines MA, Guyot-Sionnest P (1996) Synthesis and characterization of strongly luminescing ZnS-capped CdSe nanocrystals. J Phys Chem 100:468–471
37. Peng X, Schlamp MC, Kadavanich AV, Alivisatos AP (1997) Epitaxial growth of highly luminescent CdSe/CdS core/shell nanocrystals with photostability and electronic accessibility. J Am Chem Soc 119:7019–7029
38. Reiss P, Bleuse J, Pron A (2002) Highly luminescent CdSe/ZnSe core/shell nanocrystals of low size dispersion. Nano Lett 2:781–784
39. Xie R, Kolb U, Li J, Basché T, Mews A (2005) Synthesis and characterization of highly luminescent CdSe−core $CdS/Zn_{0.5}Cd_{0.5}S/ZnS$ multishell nanocrystals. J Am Chem Soc 127:7480–7488
40. Kershaw SV, Susha AS, Rogach AL (2013) Narrow bandgap colloidal metal chalcogenide quantum dots: synthetic methods, heterostructures, assemblies, electronic and infrared optical properties. Chem Soc Rev 42:3033–3087
41. Reiss P, Protière M, Li L (2009) Core/shell semiconductor nanocrystals. Small 5:154–168
42. Samokhvalov P, Artemyev M, Nabiev I (2013) Basic principles and current trends in colloidal synthesis of highly luminescent semiconductor nanocrystals. Chem Eur J 19:1534–1546
43. Zhang P, Han H (2012) Compact PEGylated polymer-caged quantum dots with improved stability. Colloid Surface A 402:72–79
44. Dubertret B, Skourides P, Norris DJ, Noireaux V, Brivanlou AH, Libchaber A (2002) In vivo imaging of quantum dots encapsulated in phospholipid micelles. Science 298:1759–1762
45. Luccardini C, Tribet C, Vial F, Marchi-Artzner V, Dahan M (2006) Size, charge, and interactions with giant lipid vesicles of quantum dots coated with an amphiphilic macromolecule. Langmuir 22:2304–2310
46. Ballou B, Lagerholm BC, Ernst LA, Bruchez MP, Waggoner AS (2004) Noninvasive imaging of quantum dots in mice. Bioconjug Chem 15:79–86
47. Papagiannaros A, Levchenko T, Hartner W, Mongayt D, Torchilin V (2009) Quantum dots encapsulated in phospholipid micelles for imaging and quantification of tumors in the near-infrared region. Nanomed Nanotechnol 5:216–224
48. Kim Y, Kim W, Yoon HJ, Shin SK (2010) Bioconjugation of hydroxylated semiconductor nanocrystals and background-free biomolecule detection. Bioconjug Chem 21:1305–1311
49. Algar WR, Krull UJ (2006) Adsorption and hybridization of oligonucleotides on mercaptoacetic acid-capped CdSe/ZnS quantum dots and quantum dot-oligo-nucleotide conjugates. Langmuir 22:11346–11352
50. Wilson R, Spiller DG, Beckett A, Prior IA, Sée V (2010) Highly stable dextran-coated quantum dots for biomolecular detection and cellular imaging. Chem Mater 22:6361–6369
51. Freeman R, Gill R, Shweky I, Kotler M, Banin U, Willner I (2009) Biosensing and probing of intracellular metabolic pathways by NADH-sensitive quantum dots. Angew Chem Int Ed 48:309–313
52. Mitchell GP, Mirkin CA, Letsinger RL (1999) Programmed assembly of DNA functionalized quantum dots. J Am Chem Soc 121:8122–8123
53. Hering VR, Gibson G, Schumacher RI, Faljoni-Alario A, Politi MJ (2007) Energy transfer between CdSe/ZnS core/shell quantum dots and fluorescent proteins. Bioconjug Chem 18:1705–1708
54. Hoshino A, Fujioka K, Oku T, Suga M, Sasaki YF, Ohta T, Yasuhara M, Suzuki K, Yamamoto K (2004) Physicochemical properties and cellular toxicity of nanocrystal quantum dots depend on their surface modification. Nano Lett 4:2163–2169
55. Lees EE, Nguyen TL, Clayton AHA, Mulvaney P (2009) The preparation of colloidally stable, water-soluble, biocompatible, semiconductor nanocrystals with a small hydrodynamic diameter. ACS Nano 3:1121–1128
56. Åkerman ME, Chan WCW, Laakkonen P, Bhatia SN, Ruoslahti E (2002) Nanocrystal targeting in vivo. Proc Natl Acad Sci U S A 99:12617–12621
57. Ji X, Zheng J, Xu J, Rastogi VK, Cheng TC, DeFrank JJ, Leblanc RM (2005) (CdSe)ZnS quantum dots and organophosphorus hydrolase bioconjugate as biosensors for detection of paraoxon. J Phys Chem B 109:3793–3799
58. Goldman ER, Balighian ED, Mattoussi H, Kuno MK, Mauro JM, Tran PT, Anderson GP (2002) Avidin: a natural bridge for quantum dot-antibody conjugates. J Am Chem Soc 124:6378–6382
59. Goldman ER, Medintz IL, Whitley JL, Hayhurst A, Clapp AR, Uyeda HT, Deschamps JR, Lassman ME, Mattoussi H (2005) A hybrid quantum dot−antibody fragment fluorescence resonance energy transfer-based TNT sensor. J Am Chem Soc 127:6744–6751
60. Lao UL, Mulchandani A, Chen W (2006) Simple conjugation and purification of quantum dot−antibody complexes using a thermally responsive elastin-protein L scaffold as immunofluorescent agents. J Am Chem Soc 128:14756–14757

61. Medintz IL, Berti L, Pons T, Grimes AF, English DS, Alessandrini A, Facci P, Mattoussi H (2007) A reactive peptidic linker for self-assembling hybrid quantum dot−DNA bioconjugates. Nano Lett 7:1741–1748
62. Hermanson GT (2008) Bioconjugate techniques, 2nd edn. Elsevier, Heidelberg
63. Oh E, Susumu K, Blanco-Canosa JB, Medintz IL, Dawson PE, Mattoussi H (2010) Preparation of stable maleimide-functionalized Au nanoparticles and their use in counting surface ligands. Small 6:1273–1278
64. Dahan M, Lévi S, Luccardini C, Rostaing P, Riveau B, Triller A (2003) Diffusion dynamics of glycine receptors revealed by single-quantum dot tracking. Science 302:442–445
65. Lidke DS, Nagy P, Heintzmann R, Arndt-Jovin DJ, Post JN, Grecco HE, Jares-Erijman EA, Jovin TM (2004) Quantum dot ligands provide new insights into erbB/HER receptor–mediated signal transduction. Nat Biotechnol 22:198–203
66. Bouzigues C, Morel M, Triller A, Dahan M (2007) Asymmetric redistribution of GABA receptors during GABA gradient sensing by nerve growth cones analyzed by single quantum dot imaging. Proc Natl Acad Sci U S A 104:11251–11256
67. Tamkun MM, O'Connell KMS, Rolig AS (2007) A cytoskeletal-based perimeter fence selectively corrals a sub-population of cell surface Kv2.1 channels. J Cell Sci 120:2413–2423
68. Heine M, Groc L, Frischknecht R, Béïque JC, Lounis B, Rumbaugh G, Huganir RL, Cognet L, Choquet D (2008) Surface mobility of postsynaptic AMPARs tunes synaptic transmission. Science 320:201–205
69. Murcia MJ, Minner DE, Mustata GM, Ritchie K, Naumann CA (2008) Design of quantum dot-conjugated lipids for long-term, high-speed tracking experiments on cell surfaces. J Am Chem Soc 130:15054–15062
70. Sukhanova A, Even-Desrumeaux K, Kisserli A, Tabary T, Reveil B, Millot JM, Chames P, Baty D, Artemyev M, Oleinikov V, Pluot M, Cohen JHM, Nabiev I (2012) Oriented conjugates of single domain antibodies and quantum dots: toward a new generation of ultrasmall diagnostic nanoprobes. Nanomedicine NBM 8:516–525
71. Rakovich TY, Mahfoud OK, Mohamed BM, Prina-Mello A, Crosbie-Staunton K, Van Den Broeck T, De Kimpe L, Sukhanova A, Baty D, Rakovich A, Maier SA, Alves F, Nauwelaers F, Nabiev I, Chames P, Volkov Y (2014) Highly sensitive single domain antibody–quantum dot conjugates for detection of HER2 biomarker in lung and breast cancer cells. ACS Nano 8:5682–5695
72. Algar WR, Susumu K, Delehanty JB, Medintz IL (2011) Semiconductor quantum dots in bioanalysis: crossing the valley of death. Anal Chem 83:8826–8837
73. Clapp AR, Medintz IL, Mattoussi H (2006) Förster resonance energy transfer investigations using quantum-dot fluorophores. ChemPhysChem 7:47–57
74. Willard DM, Mutschler T, Yu M, Jung J, Van Orden A (2006) Directing energy flow through quantum dots: towards nanoscale sensing. Anal Bioanal Chem 384:564–571
75. Clapp AR, Medintz IL, Fisher BR, Anderson GP, Mattoussi H (2005) Can luminescent quantum dots be efficient energy acceptors with organic dye donors? J Am Chem Soc 127:1242–1250
76. Willard DM, Carillo LL, Jung J, Van Orden A (2001) CdSe-ZnS quantum dots as resonance energy transfer donors in a model protein−protein binding assay. Nano Lett 1:469–474
77. Algar WR, Stewart MH, Scott AM, Moon WJ, Medintz IL (2014) Quantum dots as platforms for charge transfer-based biosensing: challenges and opportunities. J Mater Chem B 2:7816–7827
78. Medintz IL, Clapp AR, Mattoussi H, Goldman ER, Fisher B, Mauro JM (2003) Self-assembled nanoscale biosensors based on quantum dot FRET donors. Nat Mater 2:630–638
79. Shamirian A, Samareh Afsari H, Wu D, Miller LW, Snee PT (2016) Ratiometric QD-FRET sensing of aqueous H_2S in vitro. Anal Chem 88:6050–6056
80. Li DW, Qin LX, Li Y, Nia RP, Long YT, Chen HY (2011) CdSe/ZnS quantum dot–cytochrome c bioconjugates for selective intracellular $O_2^{\bullet -}$ sensing. Chem Commun 47:8539–8541
81. Yan R, Ye D (2016) Molecular imaging of enzyme activity in vivo using activatable probes. Sci Bull 61:1672–1679
82. Chang E, Miller JS, Sun J, Yu WW, Colvin VL, Drezek R, West JL (2005) Protease-activated quantum dot probes. Biochem Bioph Res Co 334:1317–1321
83. Choi Y, Lee J, Kim K, Kim H, Sommer P, Song R (2010) Fluorogenic assay and live cell imaging of HIV-1 protease activity using acid-stable quantum dot-peptide complex. Chem Commun 46:9146–9148
84. Li X, Deng D, Xue J, Qu L, Achilefu S, Gu Y (2014) Quantum dots based molecular beacons for in vitro and in vivo detection of MMP-2 on tumor. Biosens Bioelectron 61:512–518
85. Boeneman K, Delehanty JB, Susumu K, Stewart MH, Medintz IL (2010) Intracellular bioconjugation of targeted proteins with semiconductor quantum dots. J Am Chem Soc 132:5975–5977
86. Kim JH, Morikis D, Ozkan M (2004) Adaptation of inorganic quantum dots for stable molecular beacons. Sens Actuators B Chem 102:315–319
87. Cady NC, Strickland AD, Batt CA (2007) Optimized linkage and quenching strategies for quantum dot molecular beacons. Mol Cell Probes 21:116–124

88. Wu CS, Oo MKK, Cupps JM, Fan X (2011) Robust silica-coated quantum dot–molecular beacon for highly sensitive DNA detection. Biosens Bioelectron 26:3870–3875
89. Yeh HY, Yates MV, Mulchandani A, Chen W (2010) Molecular beacon-quantum dot-Au nanoparticle hybrid nanoprobes for visualizing virus replication in living cells. Chem Commun 46:3914–3916
90. Liu L, Li H, Qiu T, Zhou G, Wong KY, He Z, Liu Z (2011) Construction of a molecular beacon based on two-photon excited fluorescence resonance energy transfer with quantum dot as donor. Chem Commun 47:2622–2624
91. Bakalova R, Zhelev Z, Ohba H, Baba Y (2005) Quantum dot-conjugated hybridization probes for preliminary screening of siRNA sequences. J Am Chem Soc 127:11328–11335
92. Chou CC, Huang YH (2012) Nucleic acid sandwich hybridization assay with quantum dot-induced fluorescence resonance energy transfer for pathogen detection. Sensors 12:16660–16672
93. Kang T, Kim HC, Joo SW, Lee SY, Ahn IS, Yoon KA, Lee K (2013) Optimization of energy transfer between quantum dots and gold nanoparticles in head-to-head configuration for detection of fusion gene. Sens Actuators B Chem 188:729–734
94. Su S, Fan J, Xue B, Yuwen L, Liu X, Pan D, Fan C, Wang L (2014) DNA-conjugated quantum dot nanoprobe for high-sensitivity fluorescent detection of DNA and micro-RNA. ACS Appl Mater Interfaces 6:1152–1157
95. Peng Y, Qiu C, Jockusch S, Scott AM, Li Z, Turro NJ, Ju J (2012) CdSe/ZnS core shell quantum dot-based FRET binary oligonucleotide probes for detection of nucleic acids. Photochem Photobio Sci 11:881–884
96. Wei W, He X, Ma N (2014) DNA-templated assembly of a heterobivalent quantum dot nanoprobe for extra- and intracellular dual-targeting and imaging of live cancer cells. Angew Chem Int Ed 53:5573–5577
97. Shen Y, Tian Q, Sun Y, Xu JJ, Ye D, Chen HY (2017) ATP-activatable photosensitizer enables dual fluorescence imaging and targeted photodynamic therapy of tumor. Anal Chem 89:13610–13617
98. Shen Y, Zhang N, Sun Y, Zhao WW, Ye D, Xu JJ, Chen HY (2017) Activatable QD-based near-infrared fluorescence probe for sensitive detection and imaging of DNA. ACS Appl Mater Interfaces 9:25107–25113
99. Liu YS, Sun Y, Vernier PT, Liang CH, Chong SYC, Gundersen MA (2007) pH-sensitive photoluminescence of CdSe/ZnSe/ZnS quantum dots in human ovarian Cancer cells. J Phys Chem C 111:2872–2878
100. Medintz IL, Stewart MH, Trammell SA, Susumu K, Delehanty JB, Mei BC, Melinger JS, Blanco-Canosa JB, Dawson PE, Mattoussi H (2010) Quantum-dot/dopamine bioconjugates function as redox coupled assemblies for in vitro and intracellular pH sensing. Nat Mater 9:676–684
101. Dennis AM, Rhee WJ, Sotto D, Dublin SN, Bao G (2012) Quantum dot–fluorescent protein FRET probes for sensing intracellular pH. ACS Nano 6:2917–2924
102. Zhang H, Wu Y, Gan Z, Yang Y, Liu Y, Tang P, Wu D (2019) Accurate intracellular and in vivo temperature sensing based on $CuInS_2$/ZnS QD micelles. J Mater Chem B 7:2835–2844
103. Cho SJ, Maysinger D, Jain M, Röder B, Hackbarth S, Winnik FM (2007) Long-term exposure to CdTe quantum dots causes functional impairments in live cells. Langmuir 23:1974–1980
104. Stürzenbaum SR, Höckner M, Panneerselvam A, Levitt J, Bouillard JS, Taniguchi S, Dailey LA, Khanbeigi RA, Rosca EV, Thanou M, Suhling K, Zayats AV, Green M (2012) Biosynthesis of luminescent quantum dots in an earthworm. Nat Nanotech 8:57–60
105. Cui R, Liu HH, Xie HY, Zhang ZL, Yang YR, Pang DW, Xie ZX, Chen BB, Hu B, Shen P (2009) Living yeast cells as a controllable biosynthesizer for fluorescent quantum dots. Adv Funct Mater 19:2359–2364

Carbon Nanodots for Cell Imaging

Xiaodong Zhang, Xiaokai Chen, and Fu-Gen Wu

1 Introduction

Carbon nanodots (CNDs), also known as carbon dots (CDs), graphene quantum dots (GQDs), carbon quantum dots (CQDs), carbonized polymer dots, or C-dots, are zero-dimensional fluorescent carbonaceous nanomaterials with a typical size of <10 nm [1–3]. CNDs were first discovered from the purification of single-walled carbon nanotube fragments in 2004 [4], and they have been widely investigated since pure CNDs with multicolor emission were prepared by Sun et al. [5].

Generally, CNDs have an internal core composed of sp^2-hybridized carbon atoms, and an external surface with various functional groups such as amino, carboxyl, hydroxyl, epoxy, ether, and carbonyl groups [6–8]. Both the conjugated carbon core and surface defects can affect the optical properties, conductivity, and catalytic activity of the CNDs [9]. Many CNDs possess interesting excitation-dependent emission properties [10–13], which means that the emission wavelengths have redshifts with the increasing excitation wavelengths. It is believed that the distinct optical properties of CNDs are highly related to their carbon core and surface defects [9].

Compared to other fluorescent materials, CNDs have several advantages that are beneficial for biomedical applications. First, most CNDs have good water-dispersity due to the abundant hydrophilic groups on their surfaces, which makes further hydrophilic modification unnecessary [14–16]. Second, their surface groups such as amino and carboxyl groups endow CNDs with the convenience of conjugating with functional molecules such as targeting ligands and drugs [17–19]. Third, CNDs have a strong anti-photobleaching property [20–22]. For example, it was reported that the fluorescence intensity of CNDs prepared by glycerol and (3-aminopropyl) triethoxysilane (APTES) only decreased to ~60% after 200 min ultraviolet (UV) light irradiation [23]. In contrast, other fluorescent probes including CdTe quantum dots, gold nanoclusters (Au NCs), and fluorescein isothiocyanate (FITC) were almost completely quenched under the same condition. Fourth, CNDs can be facilely prepared at a low cost. They have been synthesized from various precursors such as small organic molecules [24, 25], polymers [26, 27], bulk carbon [28], cells [29, 30], and biomass resources [3] through different approaches. Acidic oxidation, hydrothermal/solvothermal route, microwave-assisted synthesis, and electrochemical preparation are the commonly used inexpensive approaches for the preparation of CNDs [9, 31]. Fifth, the optical properties of CNDs can be tuned through changing the precursors and reaction conditions such as temperature and time

X. Zhang · X. Chen · F.-G. Wu (✉)
State Key Laboratory of Bioelectronics, School of Biological Science and Medical Engineering, Southeast University, Nanjing, Jiangsu, China
e-mail: wufg@seu.edu.cn

F.-G. Wu (ed.), *Fluorescent Materials for Cell Imaging*, https://doi.org/10.1007/978-981-15-5062-1_3

[32]. For example, Jiang et al. used three isomers of phenylenediamines (including *m*-phenylenediamine, *o*-phenylenediamine, and *p*-phenylenediamine) as the carbon sources to obtain blue-, green-, and red-emitting CNDs, respectively [33]. Zhang et al. reported that the fluorescence color of the CNDs prepared by *L*-valine (as the carbon sources) and H_3PO_4 (as the oxidant) could be changed from green to yellow through prolonging the reaction time [34].

Owing to their superior properties, CNDs have broad applications in catalysis [35], electronics [36], sensing [37], drug delivery [38], and bioimaging [39, 40]. In this chapter, we will summarize the use of CNDs in imaging a variety of cells, including mammalian cells, microbial cells, and plant cells.

2 Preparation of CNDs

"Bottom-up" and "top-down" approaches are the two commonly used methods to prepare nanoparticles. CNDs as fluorescent nanomaterials can also be synthesized via the two strategies. The "bottom-up" approach to synthesize CNDs is realized through the carbonization of small organic molecules or the stepwise chemical fusion of small aromatic molecules, while the "top-down" approach is achieved by breaking down carbonaceous materials. To realize the "bottom-up" or "top-down" synthesis of CNDs, hydrothermal/solvothermal, microwave-assisted, electrochemical, and acidic oxidation methods have been proposed.

2.1 Hydrothermal/Solvothermal Method

Hydrothermal/solvothermal method, as the most popular "bottom-up" approach for synthesizing CNDs, only requires an inexpensive heating system and a hydrothermal reactor, and can realize the high-quality synthesis of CNDs with simple procedures [41–43]. The hydrothermal/solvothermal temperature used for the preparation of CNDs is usually in the range of 120–300 °C [9], and the reaction temperature and reaction time can largely affect the size and optical properties of the as-prepared CNDs [44, 45].

Zhang et al. prepared nitrogen-doped and fluorescence-tunable CNDs by a one-pot solvothermal reaction using CCl_4 and $NaNH_2$ [44]. They found that the size of the CNDs increased with increasing reaction time, and their excitation and emission wavelengths had a redshift when the reaction duration prolonged from 1 to 8 h. Li et al. demonstrated that the CNDs with different surface densities of amino groups and the excitation-dependent/excitation-independent fluorescence property could be prepared through controlling hydrothermal reaction temperature [45]. They found that the CNDs prepared at lower temperatures (e.g., 160 °C) had a higher surface density of amino groups with the excitation-independent fluorescence property. By comparison, the CNDs synthesized at higher temperatures (e.g., 240 °C) had a lower surface density of amino groups with the excitation-dependent fluorescence property.

Besides, the reaction solvent also plays an important role in the preparation of CNDs. For example, the CNDs obtained from *o*-phenylenediamine using the hydrothermal method had the maximum emission wavelength located at 567 nm under 420 nm excitation with a low photoluminescence quantum yield (PLQY) of 2% [46]. In contrast, the *o*-phenylenediamine-derived CNDs using ethanol as the reaction solvent had a much higher PLQY of 17.6% under 420 nm excitation [33].

2.2 Microwave-Assisted Method

Compared with the hydrothermal/solvothermal method, the microwave-assisted method is a much faster approach for the synthesis of nanomaterials with a reaction duration from minutes to tens of minutes [47–50]. The CNDs prepared via the microwave-assisted method usually have a narrow size distribution, which is mainly because microwave has a deep penetration depth and uniform heating performance. If the raw materials can form CNDs under

hydrothermal/solvothermal conditions, they may also be used to synthesize CNDs through the microwave-assisted method. However, the CNDs prepared by the two different approaches may have some differences.

Huang et al. prepared the CNDs using the mixture containing glycerol and (3-aminopropyl)triethoxysilane (APTES) under microwave irradiation within a short reaction period of 30 min [23]. After the incubation of these CNDs with HeLa cells, some dot-like fluorescence signals were observed in the cytoplasms. By contrast, the CNDs prepared using similar raw materials by the solvothermal method targeted the mitochondria after incubation with the HeLa cells, as demonstrated by our group [51].

2.3 Electrochemical Method

Compared with the above-mentioned "bottom-up" methods, the electrochemical method for the preparation of CNDs has some distinct advantages, such as low cost, low energy consumption, the capability of real-time monitoring of the CND formation, and large-scale production [52, 53]. Moreover, both thermally stable and unstable raw materials can be used to synthesize CNDs using the electrochemical method. Besides, the size and properties of the as-prepared CNDs can be tuned through changing the reaction conditions, such as electrode potential, electrolyte type, electrolyte concentration, and reaction time. For example, Deng et al. developed a simple method to prepare CNDs through the electrochemical carbonization of low-molecular-weight alcohols [54]. The size of the CNDs could be tuned by changing the electrode potential, and the fluorescence emission of the resultant CNDs was excitation- and size-dependent.

Besides its use for the "bottom-up" synthesis of CNDs, the electrochemical method can also serve as a "top-down" way to produce CNDs [55, 56]. It is proposed that OH• and O• radicals formed from the anodic oxidation of water can oxidize bulk carbon sources, leading to the formation of small hydroxylated carbon particles [57]. To introduce functional groups or heteroatoms into the CNDs, choosing different electrolyte solutions is considered as an available way [58, 59]. For instance, to prepare nitrogen (N)-doped CNDs, Li et al. used N-containing tetrabutylammonium perchlorate in acetonitrile as the electrolyte to introduce N atoms into the resultant CNDs [58].

2.4 Acidic Oxidation Method

Besides the electrochemical exfoliation, the acidic oxidation method is also a common "top-down" way to produce CNDs. The acidic oxidation method has been successfully used to exfoliate CNDs from various carbon sources, such as carbon fibers [60], carbon nanotubes [61], nanodiamonds [62], graphite oxide [63], plant soot [64], coal [65], carbon black [66], and activated carbon [67]. Large-quantity synthesis of CNDs from bulk carbon sources can be realized by this method. Furthermore, acidic treatment usually endows CNDs with negatively charged groups on their surfaces, making them hydrophilic and easy to be further modified. For example, Zhang et al. synthesized water-dispersible CNDs with tunable photoluminescence via the one-pot acidic oxidation of nanodiamonds using H_2SO_4, HNO_3, and $KMnO_4$ [62]. During the oxidation process, many functional groups such as carboxyl and hydroxyl groups were introduced on the surface of the CNDs. In addition, the CNDs were successfully used in cytoplasm imaging due to its excellent water dispersibility and biocompatibility.

3 CNDs for Mammalian Cell Imaging

Owing to their superior fluorescence properties and excellent biocompatibility, CNDs show great potential in biomedical applications. Imaging cells especially mammalian cells using CNDs is a hot research topic [68–70]. CNDs have been used to light up the whole cells or some parts of

the cells, and monitor the locations and concentrations of the molecules/ions in the cells. Besides, thanks to the presence of many reactive groups on their surfaces, CNDs can be modified with targeting moieties and realize selective imaging of the cells especially the cancer cells.

3.1 CNDs for Subcellular Imaging

In mammalian cells, various subcellular structures such as the nucleus, mitochondrion, lysosome, Golgi apparatus, endoplasmic reticulum, ribosome, and plasma membrane are essential components of the cells. Each subcellular structure performs its specialized role to support the fundamental cellular functions. Thus, visualization and monitoring of subcellular components are of great importance. Compared with other fluorescent probes, CNDs have many functional groups on their surfaces, enabling subcellular structure-targeting moieties to be easily conjugated with the CNDs. On the other hand, because a variety of carbon sources can be used for the preparation of CNDs, the as-prepared CNDs have different surface properties, and even have intrinsic subcellular structure-targeting ability without further modifications. Besides, CNDs have excellent photostability, making them suitable for the long-term monitoring of subcellular components. Additionally, CNDs can be facilely prepared with low cost, making them much cheaper than the commercial subcellular imaging probes.

3.1.1 CNDs for Nucleus/Nucleolus Imaging

Cell nucleus which contains the majority of cellular genetic materials acts as the brain of the cell. Thus, many efforts have been devoted to visualizing cell nuclei [71, 72]. However, the probes with large sizes are hard to enter the nuclei because of the presence of the small nuclear pores [73]. Thanks to their ultrasmall size and excellent fluorescence properties, CNDs show great potential in imaging cell nuclei.

As shown in Fig. 1, Yang et al. synthesized the amine group-containing CNDs, and functionalized the CNDs with nuclear localization signal (NLS) peptide through carboxyl–amine reaction for realizing cell nucleus imaging [74]. Besides, it has been reported that zwitterionic CNDs may have the intrinsic nucleus-targeting ability [75, 76]. For example, Jung et al. prepared zwitterionic CNDs using citric acid and β-alanine as raw materials [75]. The CNDs had excitation-dependent photoluminescence, which could monitor the cell nuclei in blue, green, and red fluorescence channels. Similarly, ascorbic acid and polyethyleneimine were used as raw materials to fabricate nitrogen-doped zwitterionic CNDs [76]. The as-prepared CNDs could also enter the cell nucleus without further modification.

As the largest structure in a nucleus, the nucleolus is the site of ribosome biogenesis, and plays an important role in the formation of signal recognition particles and the cellular response to stress [77, 78]. Several studies have reported that CNDs can enter the cell nuclei and even target the nucleoli [79–82].

Barbosa et al. found that the surface modification of the CNDs with ethylenediamine could endow the CNDs with the nucleolus-targeting ability [79]. Besides, CNDs with intrinsic nucleolus-imaging ability were also reported. For example, Kong et al. synthesized highly bright fluorescent CNDs by refluxing polyethylene glycol in the presence of sodium hydroxide, which were used to selectively stain cell nucleoli [80]. The nucleolus-targeting ability of the CNDs may be attributed to the large number of oxygen-containing functional groups on their surfaces, which make the CNDs easy to interact with the weakly alkaline chromatin of the nuclei rather than other subcellular structures. Our group reported the one-pot hydrothermal synthesis of nucleolus-targeting CNDs using *m*-phenylenediamine and *L*-cysteine [81]. Different from the commercial nucleolus-imaging probe SYTO RNASelect which can only be used to stain the nucleoli of the fixed cells, the as-prepared CNDs could realize nucleolus imaging in both fixed and living cells (Fig. 2), making it possible for the in situ monitoring of nucleolus-related biological behaviors. For the nucleolus-targeting mechanism of the CNDs, we found

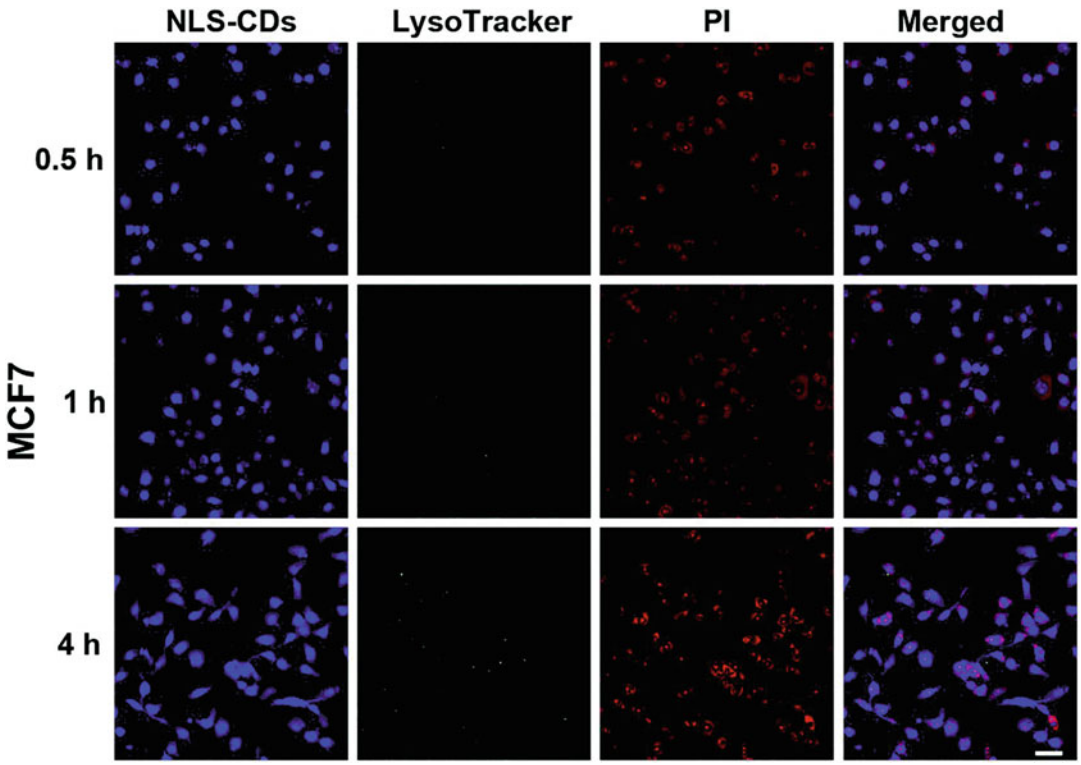

Fig. 1 Confocal microscopic images showing the nuclear imaging performance of NLS-conjugated CDs (NLS-CDs). Reprinted with permission from Ref. [74]. Copyright © 2015 Royal Society of Chemistry

that the CNDs could selectively bind to RNA instead of DNA after entering the nucleus. Furthermore, the fluorescence intensity of the CNDs was markedly increased after interaction with RNA, which makes the RNA-bound CNDs much brighter than free CNDs. Recently, we also found that the mixture of metal ions and *p*-phenylenediamine could form red-emitting CNDs after hydrothermal treatment, and the as-prepared CNDs could be used for the real-time and high-resolution fluorescence imaging of the nucleoli of living cells [82].

3.1.2 CNDs for Mitochondrial Imaging

Besides the cell nucleus, the mitochondrion is also an important organelle for the cell, because it is the "powerhouse" of the cell and is related to various cellular functions such as energy conversion, storage of calcium ions, and regulation of cellular metabolism [83]. Owing to the large membrane potential gradient of the mitochondrion, mitochondrion-targeting probes are usually positively charged, which enable the interaction of these probes with mitochondria.

Triphenylphosphonium (TPP), a commonly used mitochondrion-targeting ligand, was successfully conjugated with the CNDs derived from citric acid and urea [84]. The TPP-functionalized CNDs were used for both one- and two-photon mitochondrial imaging in living cells. Our group synthesized fluorescent CNDs through the hydrothermal treatment of chitosan, ethylenediamine, and mercaptosuccinic acid [85]. The as-prepared CNDs were endocytosed by the cells through the caveolae-mediated pathway and then specifically targeted mitochondria without further modification. We presumed that the raw materials mercaptosuccinic acid and chitosan/ethylenediamine could form delocalization structures and positively charged surfaces, respectively, which endowed the CNDs with excellent mitochondrion-targeting

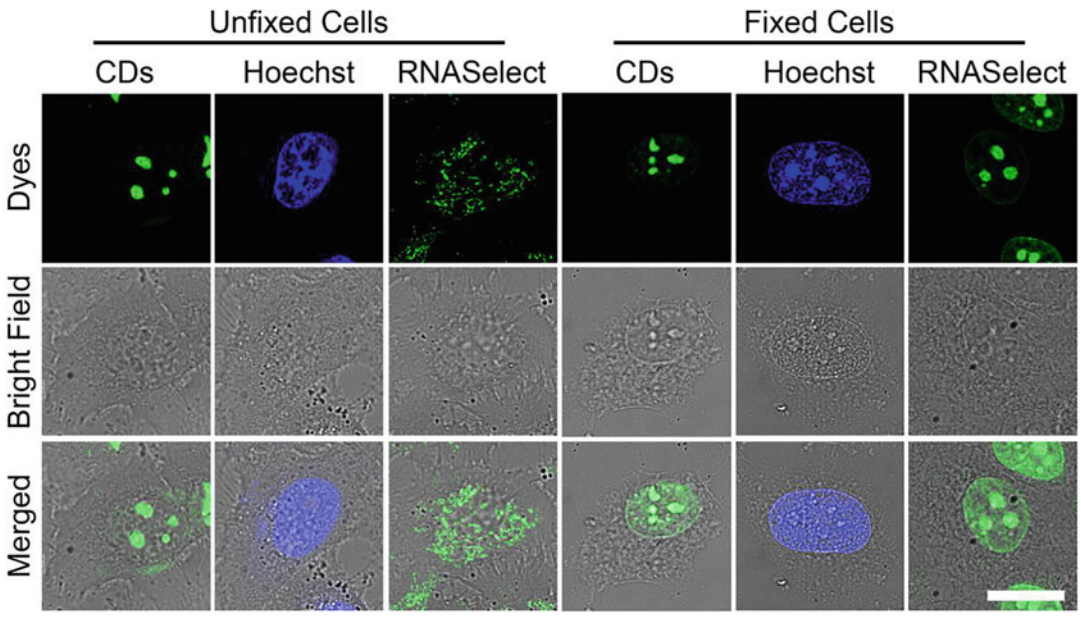

Fig. 2 Confocal microscopic images showing the nucleolus-imaging performance of CDs and SYTO RNASelect in unfixed and fixed cells. Reprinted with permission from Ref. [81]. Copyright © 2018 American Chemical Society

ability. Different from the commercial mitochondrial imaging dye Mito-Tracker which cannot be used to image mitochondria for a long time, the CNDs could firmly attach to mitochondria and realize long-term mitochondrial tracking for more than 24 h. Besides, our group prepared a series of CNDs with inherent mitochondrial targeting/imaging capability using the solvothermal treatment of glycerol and silane molecules (Fig. 3) [51]. The cationic (3-aminopropyl)trimethoxysilane (APTMS) CDs were easy to accumulate in mitochondria rather than in other organelles due to the large membrane potential of the mitochondria. Interestingly, the CNDs could effectively distinguish cancerous cells from normal ones due to the differences in the mitochondrial membrane potentials and uptake efficiencies of the two types of cells.

3.1.3 CNDs for Lysosomal Imaging

Lysosomes are the waste disposal system of cells and essential in various physiological processes (e.g., autophagy and protein degradation) [86–88]. Generally, acidotropic dyes and some large molecules are the two types of lysosome-targeting reagents. The former type usually includes weakly basic amines, such as morpholine and commercial lysosomal imaging agents Lyso-Tracker/Lyso-Sensor probes. They can target the lysosomes due to their acidic environment. The latter one (i.e., Alexa Fluor 594-conjugated dextran and BODIPY-conjugated bovine serum albumin) can be internalized by cells and enter the lysosomes through the endo-lysosomal pathway.

Taking advantage of the lysosome-targeting ability of morpholine derivatives, Wu et al. modified the CNDs (prepared by citric acid and polyethylenimine) with morpholine groups for long-term lysosomal imaging [89]. Similar to the morpholine derivatives, the ruthenium (II) complex (Ru1) is also a ligand that can target lysosomes. Based on this, Zhang et al. constructed the nanohybrids composed of CNDs and Ru1 for one- and two-photon imaging of lysosomes [90]. Besides, it was reported that some amine-containing CNDs have the intrinsic lysosome-targeting ability. For example, E et al. found that amine group-functionalized CNDs prepared from citric acid and urea could image the lysosomes [91]. Zhang et al. used *p*-benzoquinone and ethanediamine to prepare highly

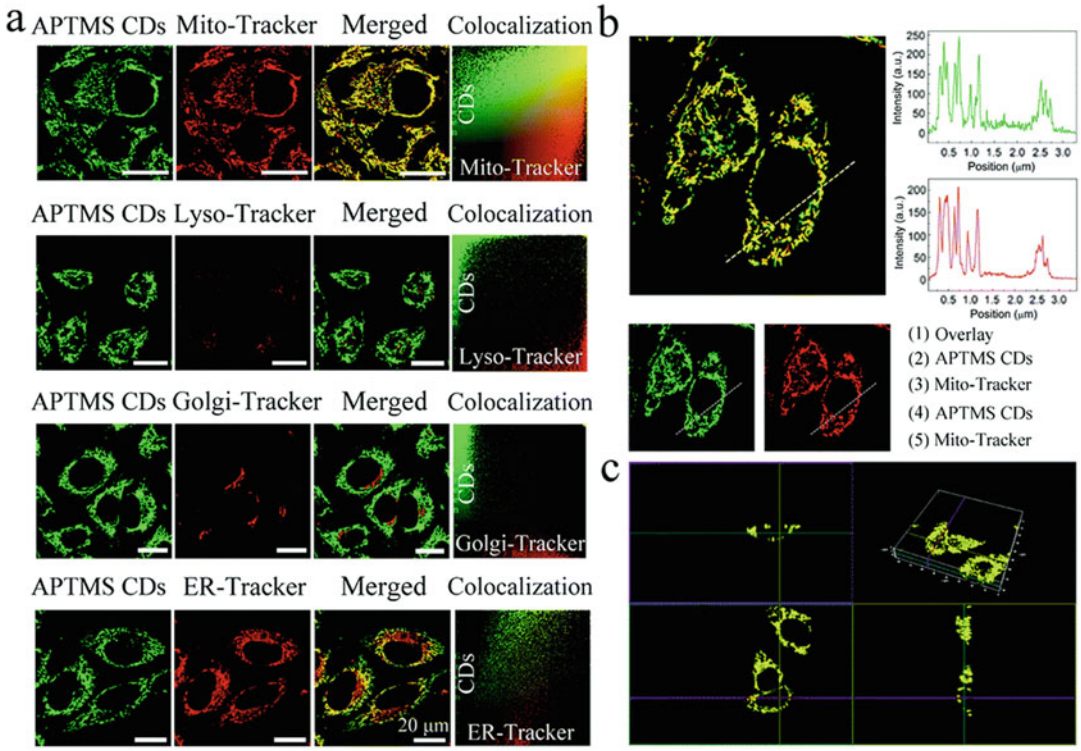

Fig. 3 (**a**) Confocal microscopic images showing the colocalization of APTMS CDs with Mito-Tracker, Lyso-Tracker, Golgi-Tracker, or ER-Tracker. (**b**) Fluorescence distribution of APTMS CDs and Mito-Tracker. (**c**) Three dimensional merged confocal microscopic images of Mito-Tracker- and APTMS CD-costained HeLa cells viewed via multiple cross sections. Reprinted with permission from Ref. [51]. Copyright © 2017 Royal Society of Chemistry

photoluminescent lysosome-targeting CNDs [92]. They believed that the lysosome-targeting ability of the CNDs was attributed to their abundant hydrophilic groups, especially the amine groups. Liu et al. reported the synthesis of lysosome-targeting CNDs using dexamethasone and 1,2,4,5-tetraaminobenzene as the raw materials [93]. The authors attributed the lysosomal targeting performance of the CNDs to the acidotropic effect of the amine groups on the surface of the CNDs. Chen et al. found that the surface amine groups could improve the lysosome-targeting specificity of the CNDs that were prepared from methionine and citric acid and further modified by a naphthalimide derivative [94]. Zhao et al. synthesized lysosome-targetable CNDs using 1,3,6-trinitropyrene and NaOH without further modification [95]. They also believed that the amine groups endowed the CNDs with lysosome-targeting ability. Recently, Qin et al. developed a novel fluorescent probe based on CNDs prepared from *N*-methyl-1,2-phenylenediamine hydrochloride [96]. The CNDs were non-fluorescent in water, but emitted strong yellow fluorescence in cells. Besides, the CNDs had good lysosome-targeting ability due to the presence of amine groups, making them suitable for fast imaging lysosomes without washing steps. Singh et al. reported a simple and facile hydrothermal method to synthesize the CNDs using neem root extracts as the raw materials [97]. The as-prepared CNDs with strong lysosomal specificity were suitable for structured illumination microscopy and two-photon microscopy (Fig. 4). The authors presumed that the presence of the ether, carboxyl, and amino groups on the surface of the CNDs might ensure the appropriate lipophilicity for lysosomal targeting. Similarly, Guo et al. used a facile microwave-assisted method to prepare green-emitting CNDs with

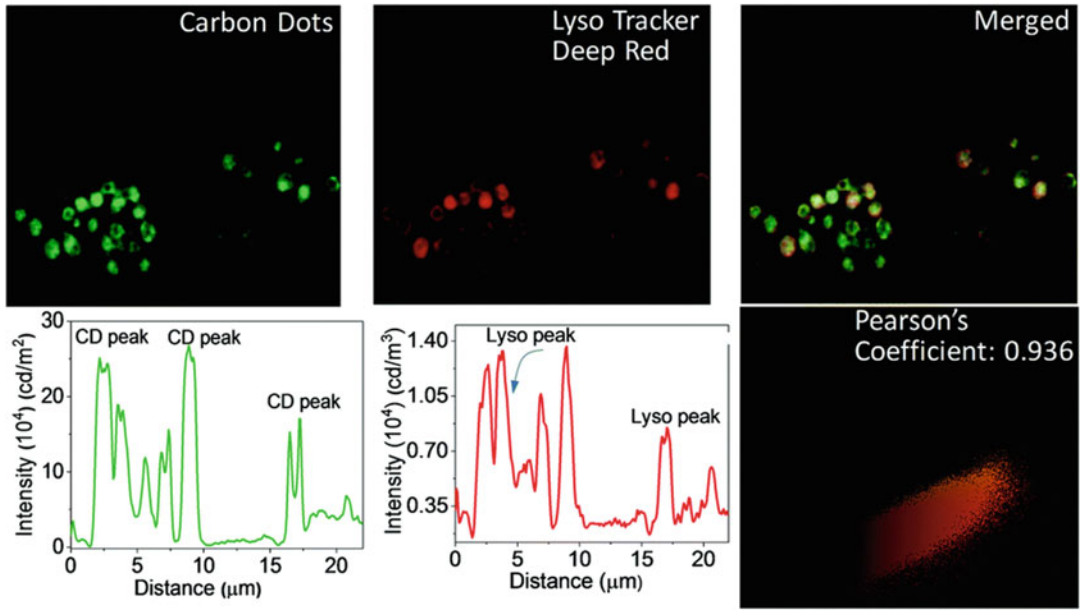

Fig. 4 Evaluation of the colocalization of the CNDs (carbon dots) with Lyso-Tracker Deep Red probes in RAW cells. Reprinted with permission from Ref. [97]. Copyright © 2019 Royal Society of Chemistry

intrinsic lysosome-targeting ability using citric acid and *N*,*N*-dimethylaniline as the raw materials [98]. The CNDs could specifically monitor the lysosomes in various cell lines for more than 48 h, and even stain the lysosomes in apoptotic cells and fixed cells.

3.1.4 CNDs for Golgi Apparatus Imaging

The Golgi apparatus is a crucial eukaryotic organelle for biogenesis, secretion, and intracellular distribution of a wide range of macromolecules [99]. The morphological change of the Golgi apparatus is related to external stimuli, which can thus effectively reflect the physiological state of cells. As a result, it is urgently needed to develop new fluorescent probes capable of real-time monitoring the morphology of the Golgi apparatus.

Li et al. developed a pyrolysis method to prepare chiral CNDs using citric acid and *L*-cysteine as the carbon sources [100]. The chiral CNDs (termed LC-CQDs) had a high PLQY of 68% and showed excellent photostability. Moreover, as shown in Fig. 5, long-time Golgi apparatus targeting and monitoring was realized using the CNDs. The authors believed that the Golgi apparatus-targeting ability of the CNDs was attributed to the presence of the cysteine residues on their surfaces. In another work, Wang et al. reported a simple molecular fusion route for industrial production of sulfonated CNDs from 1,3,6-trinitropyrene [101]. The 1,3,6-trinitropyrene molecules were completely converted into the CNDs without byproducts after a green sulfonation reaction at a low hydrothermal temperature of 130 °C. Then, the CNDs were used to target and visualize the Golgi apparatuses in living cells.

3.2 CNDs for Monitoring the pH and Ions/Molecules in the Cells

3.2.1 CNDs for Intracellular pH Sensing

Intracellular pH modulates the functions of many organelles and plays a pivotal role in biological systems, such as cell proliferation and apoptosis, ion transport, and muscle contraction [102]. As a result, it is essential to monitor the pH distribution and change in living cells. CNDs with good

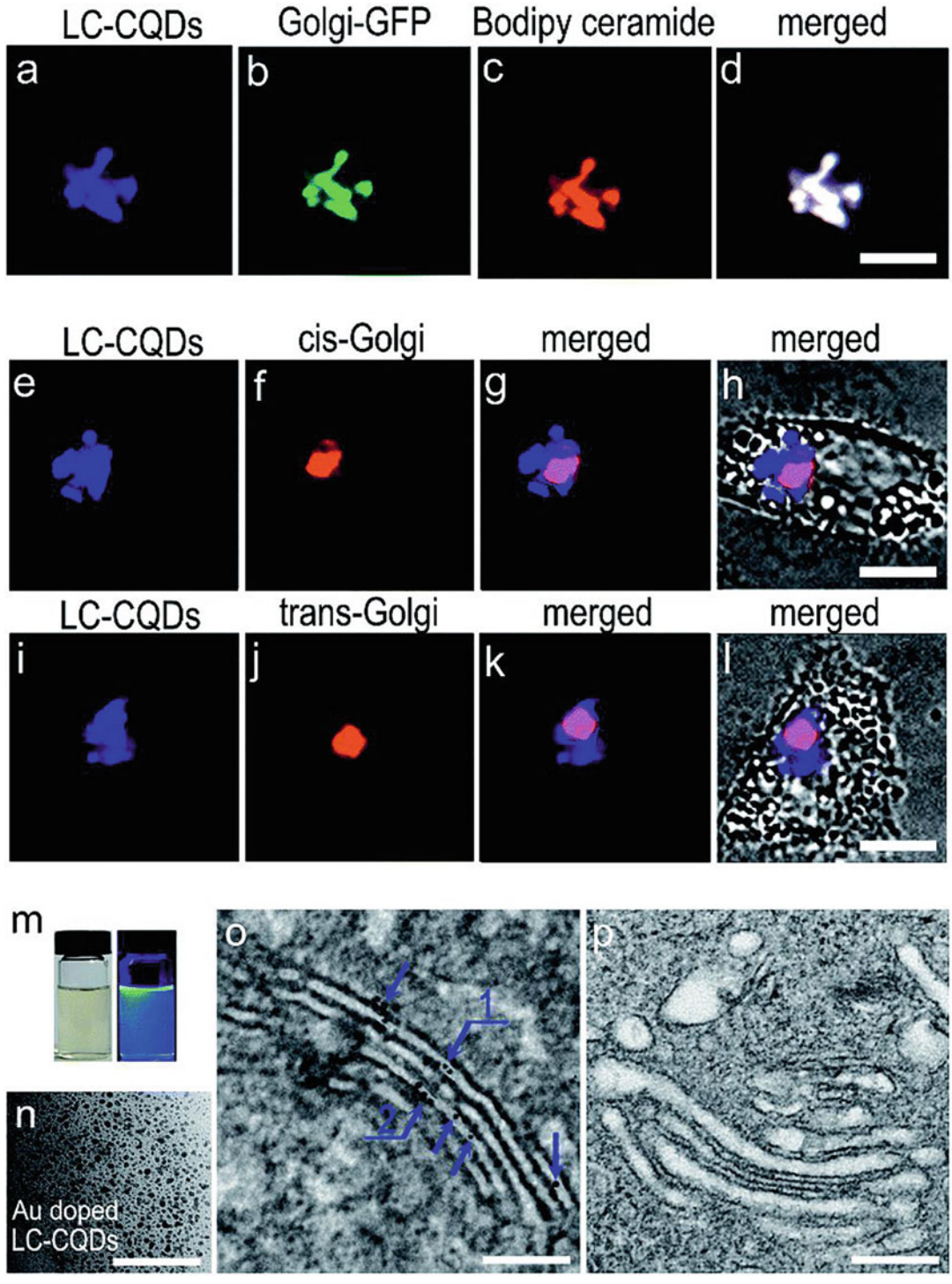

Fig. 5 Evaluation of the Golgi apparatus-targeting ability of the LC-CQDs. (**a**–**d**) Fluorescence images of the LC-CQDs (blue), Golgi-GFP (green, Golgi apparatus-specific green fluorescent protein), and Bodipy ceramide (red, a commercial dye for Golgi apparatus) in a HEp-2 cell. (**e**–**h**) Fluorescence images showing the colocalization of the LC-CQDs and the cis-Golgi. (**i**–**l**) Fluorescence images showing the colocalization of the LC-CQDs and the trans-Golgi. (**m**) Photographs of the Au-doped LC-CQDs under illumination by white light (left) and UV (365 nm) light (right). (**n**) TEM image of the Au-doped LC-CQDs. (**o**, **p**) TEM images of the Golgi apparatus of the cells incubated with (**o**) and without (**p**) Au-doped LC-CQDs. Reprinted with permission from Ref. [100]. Copyright © 2017 Royal Society of Chemistry

water-dispersity usually have numerous pH-sensitive groups such as amino groups and carboxyl groups on their surfaces, endowing the fluorescence of CNDs with pH responsiveness [10, 14, 92, 103–106].

Zhang et al. developed a simple method to prepare highly photoluminescent CNDs by mixing *p*-benzoquinone and ethanediamine under ambient conditions [92]. The as-synthesized CNDs had massive amino groups (came from ethanediamine) and lysosomal targeting ability, and their fluorescence emission could sensitively respond to the pH in the lysosomes. Moreover, the CNDs were successfully used to monitor the lysosomal pH dynamics during the apoptosis of living cells. Ye et al. fabricated red-emitting CNDs with two-photon fluorescence excitation ability by one-pot hydrothermal method using *p*-phenylenediamine, *o*-phenylenediamine, and dopamine [106]. The CNDs exhibited a broad pH-sensitive range from 1.0 to 9.0 due to the aggregation and disaggregation of the CNDs. Owing to the excellent fluorescence properties and pH-responsive ability, the CNDs could be used as a fluorescent agent to sense and visualize pH fluctuation in cells, tissue, and zebrafish.

Besides, ratiometric probes with more accurate sensing results have also been designed based on CNDs. Nie et al. prepared a ratiometric probe based on CNDs and pH-sensitive fluorescein isothiocyanate (FITC) [10]. Similarly, CNDs with dual emissions located at 475 and 545 nm under single-wavelength excitation were prepared by the one-pot hydrothermal treatment of citric acid and basic fuchsin (Fig. 6) [105]. Taking advantage of the pH sensitivity of the as-obtained CNDs at the two emissions, ratiometric detection of intracellular pH was successfully realized using the CNDs.

3.2.2 CNDs for Intracellular Metal Ion Sensing

Various metal ions are present in the cells. Some of the metal ions are essential for living cells, while others are toxic to the cells [107]. Therefore, the in situ detection of these metal ions is important for the diagnosis of metal ion-related diseases. Up till now, CNDs have been used to detect many kinds of metal ions (such as Zn^{2+}, Al^{3+}, Fe^{3+}, Cu^{2+}, Ag^{+}, and Hg^{2+}) in living cells.

Zinc (Zn), an essential element in the human body, is an indispensable component of many enzymes. Thus, sensitive detection of Zn^{2+} is important to understand these enzyme-related physiological processes. Yang et al. designed Zn^{2+}-passivated CNDs whose fluorescence could be effectively quenched by ethylenediaminetetraacetic acid disodium salt (EDTA) [108]. Moreover, taking advantage of the complexation between Zn^{2+} and EDTA, the fluorescence of the Zn^{2+}-passivated CND/EDTA complex could be recovered by the addition of external Zn^{2+} with a detection of limit (LOD) of 5.1×10^{-7} M, making the system suitable for monitoring the intracellular Zn^{2+} concentration.

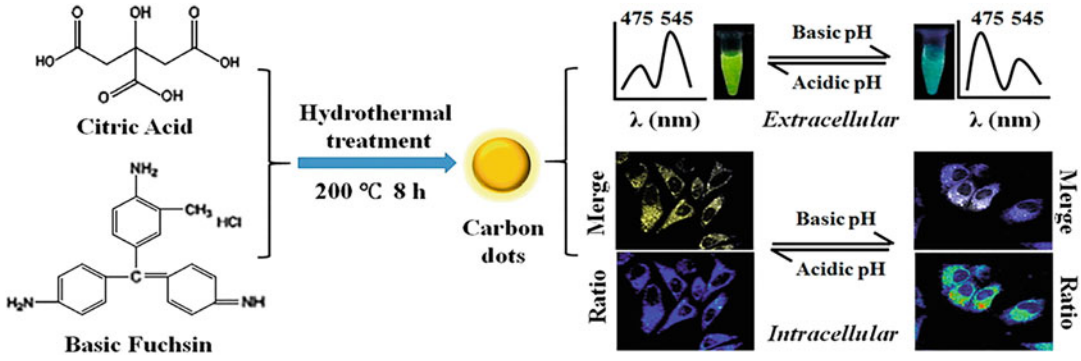

Fig. 6 Schematic illustrating the synthesis of the CNDs (carbon dots) and their application for extracellular and intracellular pH sensing. Reprinted with permission from Ref. [105]. Copyright © 2016 American Chemical Society

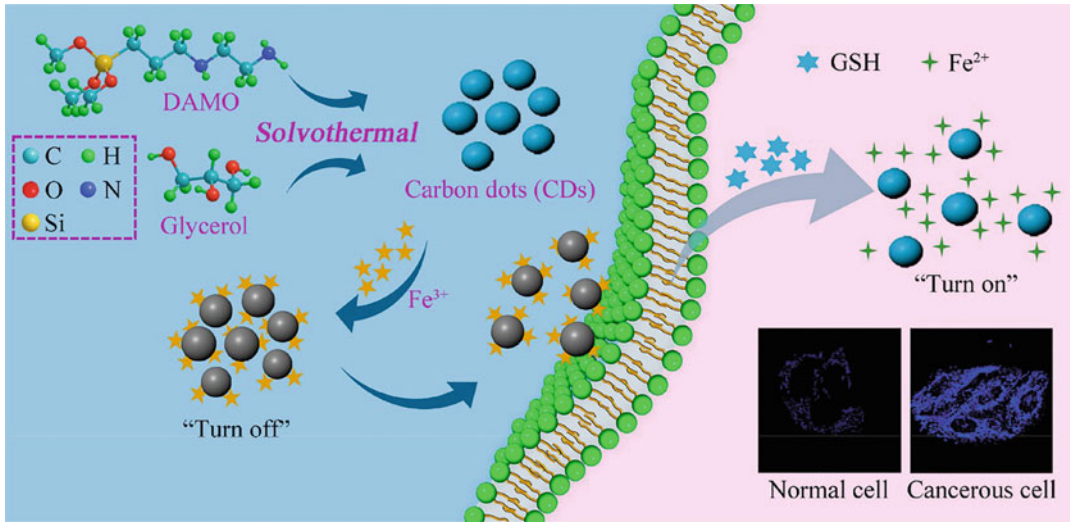

Fig. 7 Schematic illustrating the preparation of the CNDs and their applications for Fe^{3+} detection and cancer/normal cell differentiation. Reprinted with permission from Ref. [115]. Copyright © 2018 Elsevier Ltd. All rights reserved

Al^{3+} ion has been widely investigated in the etiology of neurological disorders, such as Parkinson's disease, Alzheimer's disease, and dialysis encephalopathy [109]. Hence, the accurate detection of Al^{3+} is crucial for understanding the progression of neurological diseases. Kong et al. synthesized amphiphilic blue-emitting CNDs from citric acid and methionine, which could be quenched by morin (MR) through electrostatic interaction [109]. After the addition of Al^{3+}, the system could emit strong green emission due to the Förster resonance energy transfer (FRET) process between the CNDs and the MR-Al^{3+} complex. Besides, the designed system could be used to visualize the Al^{3+} distribution in human umbilical vein endothelial cells.

Ferric ion (Fe^{3+}) can regulate cellular metabolism and oxygen transport in hemoglobin in the human body. The fluorescence of many CNDs shows excellent responsiveness to Fe^{3+} [110–115]. For example, it was reported that the N-doped CNDs derived from a popular antibiotic aminosalicylic acid showed excellent sensitivity to Fe^{3+} in living cells [113]. Similarly, a CND-based fluorescent probe with the "on-off-on" property was fabricated by our group via a one-pot solvothermal method using glycerol and *N*-[3-(trimethoxysilyl)propyl]ethylenediamine (DAMO) as the raw materials (Fig. 7) [115]. The fluorescence of CNDs could be selectively and sensitively quenched by Fe^{3+} with a low LOD of 16 nM. The potential Fe^{3+} detection mechanism of the CNDs was attributed to the presence of the amino groups on the surface of the CNDs. The amino groups may have strong interaction with Fe^{3+}, making the electrons in the excited state transfer to Fe^{3+} and quenching the fluorescence of CNDs.

Besides Fe^{3+} ions, Cu^{2+} ions also play essential structural roles in many proteins and enzymes and are involved in many physiological behaviors. However, high concentrations of intracellular Cu^{2+} are toxic to organisms. To detect the Cu^{2+} concentration in the cells, Salinas-Castillo et al. developed a microwave-assisted strategy to prepare the CNDs with both down- and up-conversion fluorescence properties using citric acid and polyethylenimine as the precursors [116]. The CNDs showed low cytotoxicity and were successfully used for imaging intracellular Cu^{2+} with high selectivity and sensitivity.

Silver has a long and intriguing history as an antibiotic for fighting against bacterial infections, but high concentrations of Ag^{+} can elicit high toxicity [117]. Therefore, sensitive detection of Ag^{+} is highly required. Zuo et al. prepared

fluorine (F)-doped CNDs using 4,5-difluoro-1,2-benzenediamine and tartaric acid as the raw materials, and found that the F-doped CNDs could selectively bind to Ag^+, making the F-doped CNDs suitable for the detection of Ag^+ in various biological systems including mammalian cells [118].

Hg^{2+} as one of the most hazardous and toxic ions to the environment and human health is responsible for many fatal diseases such as nervous system damage and nephritic syndrome even at a low concentration of 2 mg/kg per day [119]. To detect the intracellular Hg^{2+}, two kinds of CNDs were prepared using "citric acid + 1,2-ethylenediamine" and "citric acid + *N*-(*β*-aminoethyl)-*γ*-aminopropyl methyldimethoxysilane (AEAPMS)" as the starting materials [120]. Both of the two types of the CNDs could be effectively quenched by Hg^{2+}, and even trace the Hg^{2+} in living cells. The excellent Hg^{2+} detection selectivity of the CNDs was possibly due to the fact that Hg^{2+} ions have a stronger affinity for the electron-rich surface (due to the presence of amino and carboxyl groups) of the CNDs than other metal ions.

Besides the above-mentioned metal ions, CNDs have also been used to detect other ions, such as Fe^{2+} [121], Sn^{2+} [122], Sn^{4+} [123], Mo^{6+} [123], Pb^{2+} [124], Cr^{6+} [125], and even anions, including I^- [126] and phosphate [127]. However, only a few studies have reported that the CNDs can be used for detecting these ions in the presence of cells or in physiological conditions. In the future, the feasibility of using CNDs for in vitro and in vivo ion detection should be extensively investigated.

3.2.3 CNDs for Intracellular Molecule Sensing

Besides pH and metal ions, CNDs are also a powerful tool for the detection of intracellular molecules. As fluorescent probes, CNDs can detect and image molecules through "turn-off", "on-off-on", and ratiometric ways.

Hydrogen peroxide (H_2O_2) is a prominent member of the reactive oxygen species (ROS) family and necessary in biological systems, and hence the detection of H_2O_2 and the elucidation of its biological functions have become an important research topic in the biological and medical fields. Du et al. designed a CND-based nanoprobe for detecting mitochondrial H_2O_2 by conjugating the CNDs with TPP and 3-oxo-3′,6′-bis(4,4,5,5-tetra-methyl-1,3,2-dioxaborolan-2-yl)-3*H*-spiro [isobenzofuran-1,9′-xanthene]-6-carboxylic acid (PFl) for mitochondrial targeting and H_2O_2 recognition, respectively, in which the CNDs served as the carrier and the FRET donor [128].

Hydrogen sulfide (H_2S) is an endogenous gaseous signaling compound generated in cells via the enzymatic or non-enzymatic pathway, which can regulate cardiovascular, neuronal, and immune systems [129]. Yu et al. designed a CND-based ratiometric fluorescent probe for intracellular H_2S detection [130]. The blue-emitting CNDs ($em = 425$ nm) were conjugated with green-emitting naphthalimide-azide ($em = 526$ nm). No FRET process occurred between the CNDs and naphthalimide-azide without H_2S. After the addition of H_2S, the naphthalimide-azide could be reduced to an energy acceptor naphthalimide-amine by H_2S. As a result, the fluorescence ratio (I_{526}/I_{425}) increased with increasing H_2S concentrations.

Formaldehyde (FA) is an important intermediate in cellular metabolism in mammals, and is related to Alzheimer's disease, cancer, and other diseases. Thus, to develop approaches for detecting FA with high sensitivity and selectivity in living cells is highly required. To this end, as reported by Liu et al., dexamethasone and 1,2,4,5-tetraaminobenzene (TAB) were used to synthesize the lysosome-targeted CNDs for the ratiometric fluorescence detection of FA (Fig. 8) [93]. The residual *o*-diamino groups in the synthesized CNDs could react quickly and selectively with FA, leading to the ratiometric fluorescence response to FA through altering the intramolecular charge transfer (ICT) process from the amino groups (electron donors) to the carbonyl groups (electron acceptors) of the CNDs. Chen et al. synthesized naphthalimide derivative (ND)-conjugated CNDs for monitoring lysosomal FA, in which the fluorescence intensity of green fluorescent ND ($em = 535$ nm) and blue-

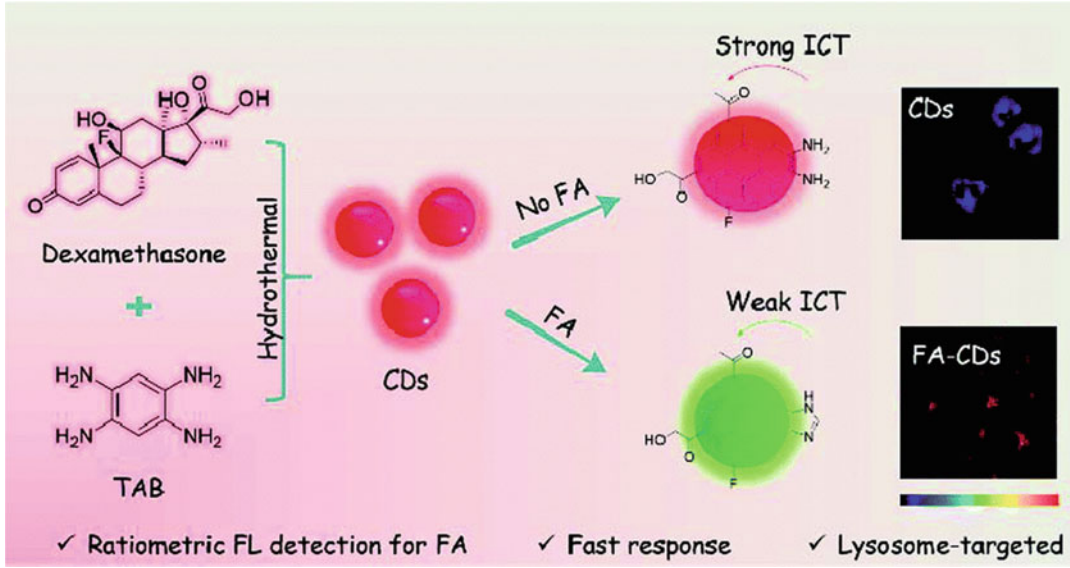

Fig. 8 Schematic illustrating the synthesis of the CNDs (CDs) and their possible mechanism for FA detection. Reprinted with permission from Ref. [93]. Copyright © 2019 Royal Society of Chemistry

fluorescent CNDs ($em = 414$ nm) served as the response signal and the reference signal, respectively [94]. The fluorescence intensity ratio (F_{535}/F_{414}) of the probe was linearly dependent on the FA concentration with a LOD of 3.4×10^{-7} M. Combined with its lysosome-targeting ability, the probe was suitable for the ratiometric fluorescence imaging of FA in lysosomes.

Glutathione (GSH) is an important antioxidant that prevents the cells from being damaged by ROS and heavy metals. Besides, it also participates in many physiological processes such as cell metabolism. As we stated above, our group reported that Fe^{3+} could quench the fluorescence of the CNDs made from glycerol and DAMO [115]. More interestingly, we found that GSH could recover the fluorescence of the CNDs quenched by Fe^{3+}. Based on the different GSH contents in normal cells and cancerous cells [131], we successfully distinguished cancerous cells from normal ones using the mixture of CNDs and Fe^{3+}. Sun et al. also designed an "on-off-on" probe based on the CNDs prepared from citric acid and diethylenetriamine [132]. The fluorescence of the CNDs could be significantly quenched by Hg^{2+}, and could be recovered after the addition of GSH. Then the CND-based fluorescent agent was successfully applied in monitoring the Hg^{2+} and GSH in living cells.

Ascorbic acid (AA), as an essential nutrient for humans, functions as a cofactor in many enzymatic reactions, and is related to many diseases. As a result, to develop a sensitive method for detecting the intracellular AA level is of great importance [133]. Feng et al. prepared near-infrared-emitting CNDs which could be quenched by cobalt oxyhydroxide (CoOOH) nanoflakes by energy transfer [134]. After the addition of AA, CoOOH was reduced to Co^{2+}, resulting in the "turn-on" of the CND fluorescence. The as-prepared nanosystem had high AA detection selectivity and sensitivity with an LOD of 270 nM. Furthermore, the nanosystem was successfully employed for two-photon imaging of endogenous AA in living cells and deep tissues.

Sensitive and selective glucose sensing is highly needed because glucose detection is incredibly important to the patients suffering from diabetes. Kiran et al. found that the boronic acid-functionalized CNDs could enter the cells and form aggregates due to the presence of

glucose in the cells, leading to the fluorescence quenching of the CNDs [135]. As a result, intracellular glucose detection could be realized using the CNDs.

Besides small molecule imaging, CNDs can be used for macromolecule sensing, such as DNA [136] and RNA [137]. Han et al. synthesized carboxyl- and hydroxyl-containing CNDs through acidic oxidation of conductive carbon nanoparticles, and modified the CNDs with *p*-phenylenediamine and 4-carboxybutyl triphenylphosphonium to endow the CNDs with positive charges [138]. Interestingly, the fluorescence intensity of the as-prepared green-emitting CNDs could be enhanced by double-stranded DNA (dsDNA) and single-stranded RNA (ssRNA), and both the absorption and emission profiles of the CNDs had a bathochromic shift after the addition of ssRNA but not dsDNA. Besides, the CNDs could penetrate through various biological barriers, and could emit spectrally distinguishable fluorescence when they bound to dsDNA and ssRNA in living cells, thus realizing real-time visualization of dsDNA and ssRNA in situ.

In addition, CNDs have been successfully used for detecting other molecules such as dopamine [139], tetracycline [140], amino acids [141, 142], and even proteins [143]. Similar to ions, most of these molecules are detected by CNDs without cells. As a result, novel CNDs that are suitable for in vitro and in vivo molecule detection are urgently needed.

3.3 CNDs for Selective Cell Imaging

Owing to their flexibility of surface functionalization, CNDs can be conjugated with targeting motifs for targeted cell imaging. Based on this, Li et al. designed a type of transferrin-modified CNDs for imaging transferrin receptor-overexpressed cancer cells [144]. Wang et al. connected the CNDs with DNA aptamers by carboxyl–amine reaction, and the resultant aptamer-modified CNDs maintained both the bright fluorescence of the CNDs and the recognition ability of the DNA aptamer [18]. The authors also demonstrated that the aptamer-conjugated CNDs could sensitively and selectively image human breast cancer cells (MCF-7 cells).

Besides, it has been reported that some CNDs can selectively image the cells without further modifications. Zheng et al. developed a pyrolysis strategy to synthesize the tumor-targeting CNDs (termed CD-Asp) without the modification of any extra targeting ligands using *D*-glucose and *L*-aspartic acid as the raw materials (the tumor-targeting performance of the CNDs was shown in Fig. 9) [145]. The self-targeting ability of the CNDs was attributed to the presence of *D*-glucose and *L*-aspartic acid residues, which helped the CNDs to cross the blood–brain barrier through the GLUT-1 and ACT2 transporters. Bhunia et al. used tumor-targeting folate molecules as the carbon source to prepare CNDs [146]. The as-prepared CNDs could target folate receptor-overexpressed cancer cells as they expected.

4 CNDs for Microbial Cell Imaging

Microbial infection induced by bacteria, fungi, and viruses is one of the major public health problems worldwide [147]. To fight against microbial infections, early, sensitive, and accurate detection of microorganisms is of great importance. The fluorescence-based methods are considered as a powerful tool for microbial detection. Owing to the outstanding optical properties of CNDs, recent decades have witnessed considerable research progress in their applications in microbial imaging and sensing [148].

Mehta et al. reported the synthesis of *Saccharum officinarum* juice-derived CNDs [149]. The CNDs were proven to be suitable for bacterial and fungal imaging. Nandi et al. synthesized hydrocarbon chain-functionalized amphiphilic CNDs for bacterial detection and imaging [150]. The fluorescence intensity and spectral position of the CNDs were dependent

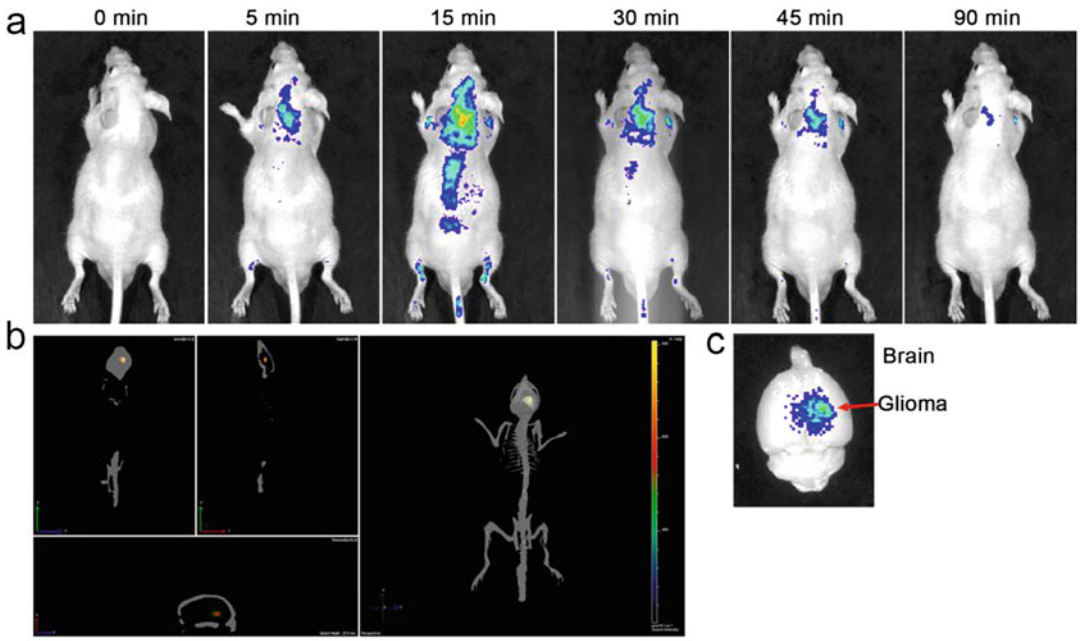

Fig. 9 (**a**) In vivo fluorescence images of C6 glioma-bearing mice after the injection of CD-Asp. (**b**) Three-dimensional reconstruction of CD-Asp distribution in the brain 20 min after injection. (**c**) Ex vivo fluorescence image of the brain 90 min after the injection of CD-Asp. Reprinted with permission from Ref. [145]. Copyright © 2015 American Chemical Society

on the bacterial species, and could be used for distinguishing bacteria.

4.1 CNDs for Gram-Positive and Gram-Negative Bacterial Distinguishment

The Gram staining method is a standard diagnostic method to classify bacteria into Gram-positive and Gram-negative ones. Gram-negative bacteria but not Gram-positive ones are sensitive to some antibiotics such as streptomycin and gentamicin, while Gram-positive bacteria but not Gram-negative ones are sensitive to other antibiotics such as penicillin. Thus, differentiating Gram-positive and Gram-negative bacteria is very important.

Our group prepared quaternized CNDs using the reaction between carboxyl group-containing lauryl betaine and amine group-containing CNDs [151]. The as-synthesized quaternized CNDs (termed CDs-C_{12}) had polarity-sensitive fluorescence emission property, leading to the significantly enhanced fluorescence when the CNDs interacted with the Gram-positive bacteria. Moreover, owing to the presence of both hydrophobic hydrocarbon chains and positively charged quaternary ammonium groups on their surfaces, the CNDs could selectively attach to Gram-positive bacteria (Fig. 10), realizing the bacterial differentiation. Recently, we developed a simpler method for the one-step synthesis of quaternized CNDs via the solvothermal treatment of glycerol and dimethyloctadecyl [3-(trimethoxysilyl)propy]ammonium chloride (termed Si-QAC) [152]. Similarly, the as-obtained CNDs had the bacterial contact-enhanced fluorescence emission property and could be used for fast Gram-type identification.

Besides Gram-positive bacterial imaging, the CNDs have been also used for selective Gram-negative bacterial imaging. Colistin, a well-known antibiotic against Gram-negative bacteria, was reacted with diammonium hydrogen citrate to prepare CNDs [153]. Owing to the excellent specificity of colistin to Gram-negative bacteria, selective imaging of Gram-negative bacteria over

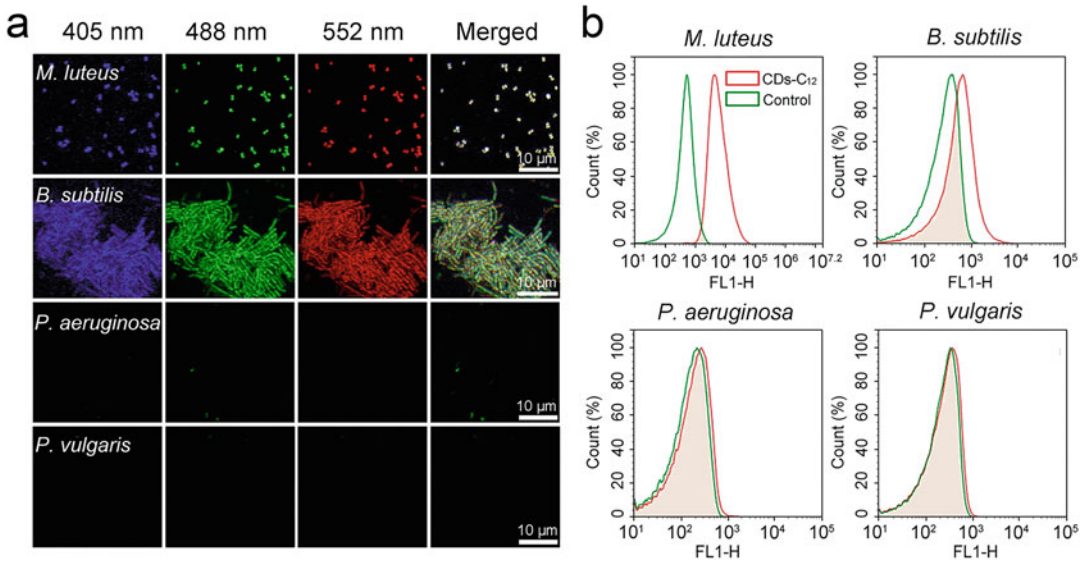

Fig. 10 (**a**) Confocal microscopic images of Gram-positive bacteria (*Micrococcus luteus* (*M. Luteus*) and *Bacillus subtilis* (*B. subtilis*)) and Gram-negative bacteria (*Pseudomonas aeruginosa* (*P. aeruginosa*) and *Proteus vulgaris* (*P. vulgaris*)) after incubation with the quaternized CNDs (CDs-C_{12}) for 1 h under 405, 488, and 552 nm laser excitations. (**b**) Corresponding flow cytometric data. Reprinted with permission from Ref. [151]. Copyright © 2016 American Chemical Society

Gram-positive ones was realized using the CNDs. Similarly, amikacin, an antibiotic with strong bactericidal activity against most Gram-negative bacteria, and diammonium hydrogen citrate were used to prepare CNDs [154]. The amikacin-functionalized CNDs were successfully used for the selective detection of Gram-negative bacteria with an LOD of 552 colony forming units (CFU)/mL.

4.2 CNDs for Microbial Live/Dead Differentiation

To assess the microbial inactivation performance of antimicrobial agents, the distinguishment between live and dead microbial cells is of great importance. Thus, various methods and techniques have been developed for microbial live/dead differentiation, such as the plate counting method, atomic force microscopy, and fluorescence-based methods. Among them, the fluorescence labeling method is one of the most commonly used approaches for rapidly and sensitively distinguishing live/dead microbial cells [155].

Our group prepared bacteria-derived CNDs with a highly negative zeta potential of −42 mV [29]. The CNDs were hard to be internalized by live bacterial cells due to the strong electrostatic repulsion between the CNDs and the bacterial surfaces, but could enter the dead cells with damaged cell surfaces. As a result, the CNDs could selectively image the dead microbial cells (Fig. 11). Compared to propidium iodide (PI) which is a commercial dye for dead cell imaging, the as-synthesized CNDs showed low toxicity to microbial cells and excellent photostability. Nitrogen- and phosphorus-doped CNDs with tunable surface potentials were prepared using a facile hydrothermal method [156]. Similarly, the obtained CNDs selectively stained dead bacterial cells but not live ones due to the electrostatic repulsion between the negatively charged CNDs and the negatively charged bacterial walls.

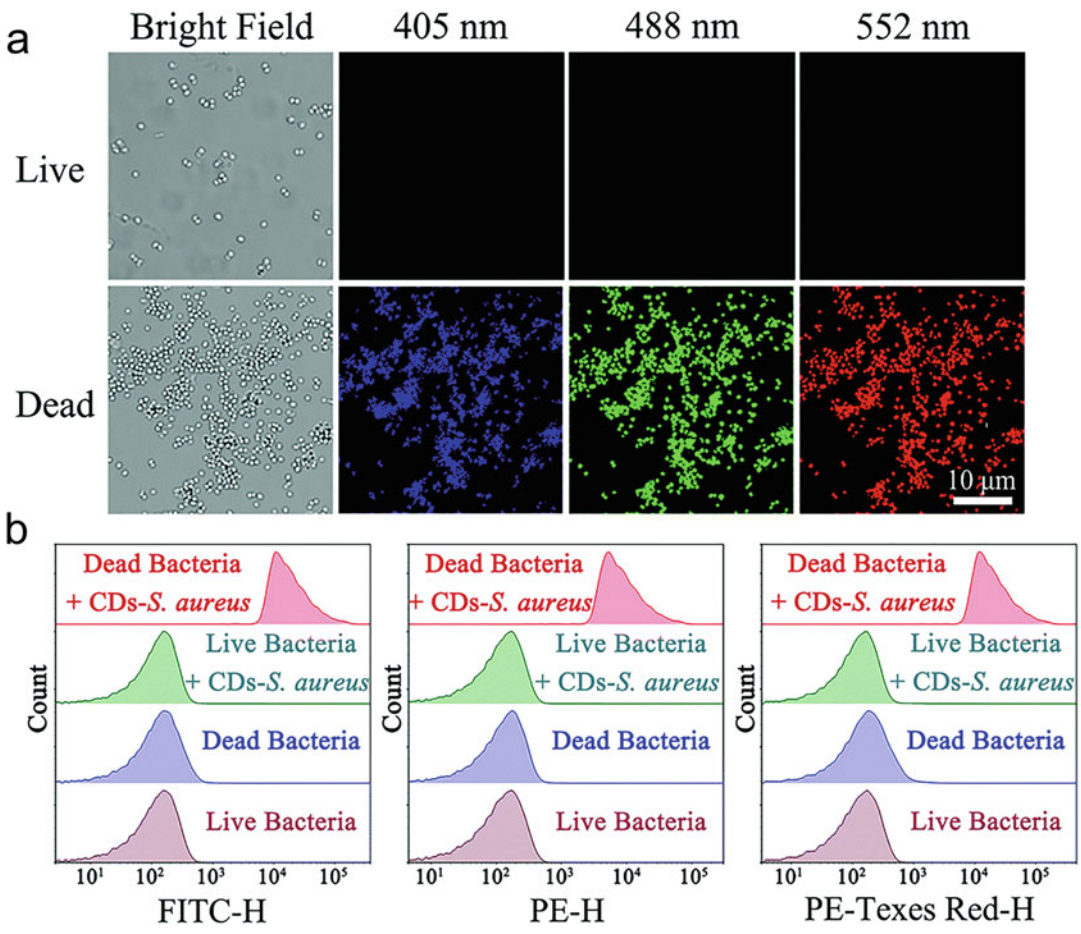

Fig. 11 Confocal microscopic images (**a**) and flow cytometric results (**b**) of live and dead *S. aureus* stained with the CNDs (CDs-*S. aureus*) for 1 h. Reprinted with permission from Ref. [29]. Copyright © 2017 Royal Society of Chemistry

4.3 CNDs for Microbial Biofilm Imaging

Microbial biofilms are surface-attached communities of microbes encased in an extracellular matrix of biomolecules and display high levels of antibiotic tolerance, because most antibiotics cannot penetrate the biofilms effectively [157]. Similar to antibacterial agents, fluorescent materials could also be blocked by the sticky extracellular polymeric substance (EPS) matrix, which hinders their successful biofilm imaging.

Ritenberg et al. showed that the amphiphilic CNDs could readily bind to the EPS scaffold of the bacteria *P. aeruginosa*, making them suitable for the fluorescence microscopic visualization of the EPS structural features [158]. Lin et al. developed a one-step hydrothermal carbonization method to synthesize the CNDs from the bacteria *Lactobacillus plantarum* (*L. plantarum*) [30]. The as-prepared CNDs were found to be capable of imaging the microorganisms within the biofilms. Our group prepared Si-QAC/glycerol-derived CNDs by a solvothermal method [152] and used the obtained CNDs with ultrasmall size (~3.3 nm) and strong positively charged surfaces (zeta

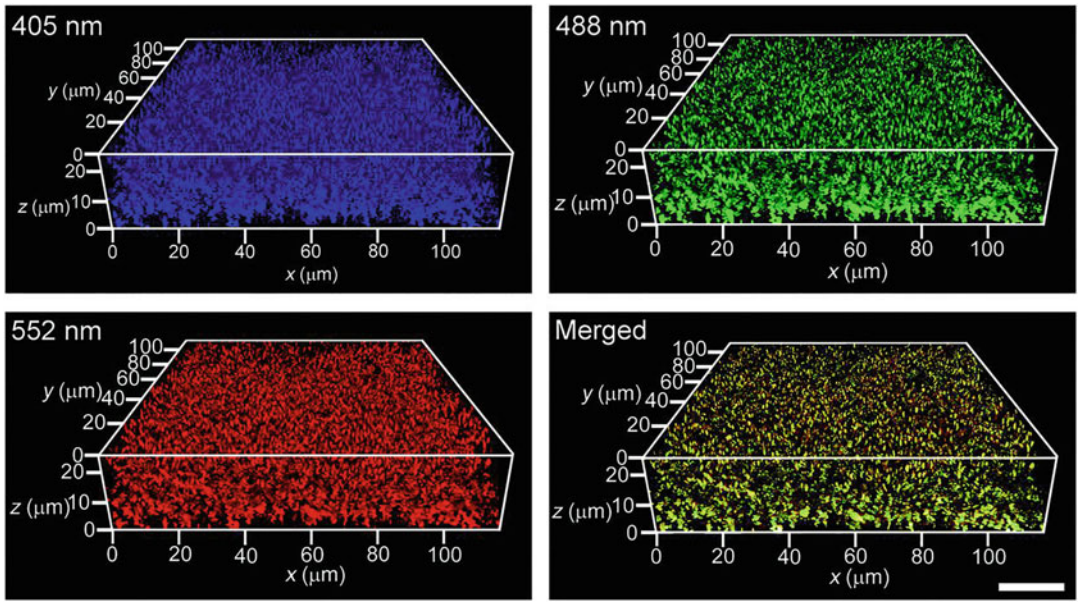

Fig. 12 Three-dimensional confocal microscopic images of an *S. aureus* biofilm stained with the CNDs (Si-QAC CDs). These images include the ones taken under different excitation wavelengths and the merged one. Reprinted with permission from Ref. [159]. Copyright © 2019 Royal Society of Chemistry

potential: ~33 mV) for excellent fluorescence imaging of the *S. aureus* biofilms [159] (Fig. 12).

As stated above, CNDs have become a powerful tool for microbial imaging, including Gram-positive and Gram-negative bacterial distinguishment, microbial live/dead differentiation, and biofilm imaging. Although many studies have demonstrated that CNDs can image bacteria and fungi, few studies have reported virus imaging using CNDs. Besides, taking advantage of the excellent optical properties of CNDs and super-resolution fluorescence imaging techniques [151, 160], the imaging of subcellular structures in microbial cells may also be realized; however, relevant studies are still lacking.

5 CNDs for Plant Cell Imaging

Besides mammalian and microbial cells, CNDs also show potential in imaging plant cells. CNDs usually have ultrasmall sizes, enabling their penetration into the walls and membranes of the plant cells.

Zhang et al. found that the chiral CNDs fabricated from *D*-cysteine and citric acid could be absorbed by mung beans during the period of seed germination, and were detected in the vascular system of the root, stem, and leaf after 5-day incubation [161]. Wang et al. synthesized bright CNDs using *L*-glutamic acid with nitric acid as a carbonization agent and ethylene glycol as a passivation agent [162]. The CNDs with negligible cytotoxicity could be endocytosed by intact plant cells with 10 min and even directly stain the nuclei of these cells (Fig. 13). Li et al. found that the CNDs prepared from *p*-phenylenediamine have a strong affinity for cellulose through hydrogen bonding, and the PLQY of the CNDs dramatically increased from 8% to 44% when the CNDs were dispersed in cellulose matrices [163]. The authors demonstrated that the affinity of the CNDs for binding cellulose endowed them with the capability of imaging the cellulosic plant cell walls.

Recent studies have reported that some CNDs are able to enhance the production of cereal crops [164] and promote carbohydrate accumulation in

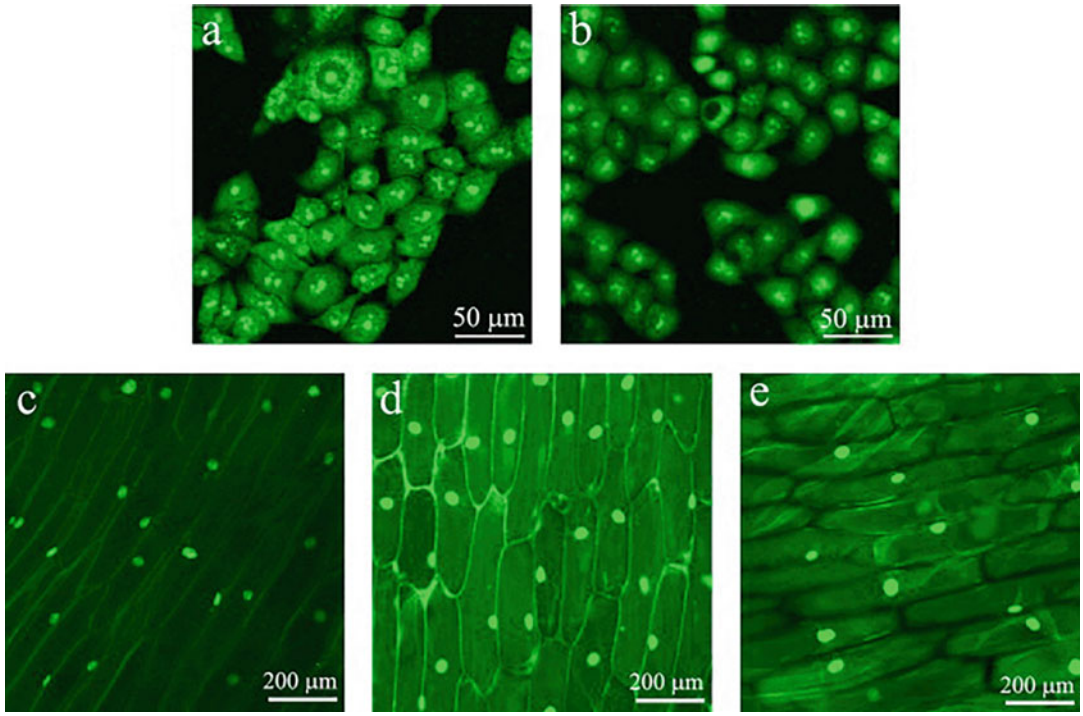

Fig. 13 Confocal microscopic images of HeLa cells incubated with CNDs (**a**) and acridine orange (AO) (**b**), and onion epidermal cells incubated with CNDs for 10 and 60 min (**c**, **d**) and AO (**e**). Reprinted with permission from Ref. [162]. Copyright © 2014 Elsevier Ltd. All rights reserved

mung bean plants [161]. However, the detailed interaction mechanisms between CNDs and plants remain largely unknown. Using CNDs for plant cell imaging will help the researchers to investigate the interactions between CNDs and plants, and study the biodistribution of the CNDs in the plants. Besides, whether the various CNDs synthesized by the researchers can be used for plant cell imaging should be tested to enrich the applications of the CNDs and foster the advancement of the CND-related plant research. Further, to get a deep understanding of the interaction between CNDs and plant cells, the evaluation of the CNDs for organelle-specific imaging in plant cells is highly desirable.

6 Conclusion and Future Perspective

With their ultrasmall size, ease of preparation and modification, good anti-photoblinking and anti-photobleaching properties, and excellent biocompatibility, CNDs have become popular probes for bioimaging. Up to now, CNDs have been successfully used in imaging various cells, including mammalian cells, microbial cells, and plant cells. Subcellular distributions and selective/sensitive detection of ions/molecules using CNDs can be achieved by controlling their size, charge, and surface chemistry.

Although many efforts have been devoted to the preparation of CNDs and cell imaging using CNDs, there are still several issues that need to be addressed in the future. First, most CNDs have broad and excitation-dependent emissions, limiting their imaging applications when they are used in combination with other fluorescent probes. Hence, novel CNDs with bright and narrow emissions are highly desired. Second, a large number of CNDs with novel optical properties such as two-photon excitation [165–167], long-wavelength emission [168–170], room-temperature phosphorescence [50, 171–173],

photo-activation [174], piezochromic luminescence [174–176], up-conversion properties [177–179], and electrochemiluminescence [143], have been synthesized, and their applications in bioimaging also need to be investigated. Third, many CNDs have poor water-dispersity and low cellular uptake efficiency. Thus, developing suitable surface modification strategies for these CNDs is in urgent need for improving their cell imaging performance. Fourth, the structures of most CNDs are not clear, and the mechanisms of the interactions between CNDs and cells, organelles, or intracellular ions/molecules need to be further investigated. It is challenging to rationally design CNDs with suitable compositions, sizes, and surface chemistries for monitoring the cells, organelles, ions, and molecules with high selectivity and sensitivity. Fifth, although CNDs have been used for imaging many organelles (including nuclei, mitochondria, lysosomes, and Golgi apparatus), ions, and molecules, new kinds of CNDs need to be synthesized to image other subcellular structures (such as plasma membrane, cell wall, endoplasmic reticulum, ribosome, centrosome, lipid droplet, and peroxisome) and intracellular ions/molecules. Sixth, owing to their surface modifiability, the diverse CNDs can be conjugated with specific targeting ligands to be ideal probes for imaging various cells (such as cancer cells, inflammation-related cells, stem cells, and immune cells), subcellular structures, and intracellular ions/molecules. Hence, more efforts should be devoted to the modification of the CNDs for realizing the selective imaging of these cells and cellular structures/compositions. Seventh, most of the CNDs can be quenched by the ions/molecules, thus realizing molecule/ion detection. However, the design of CND-based "turn-on" probes for intracellular ion/molecule imaging is still lacking. Eighth, recent studies regarding the use of CNDs for bioimaging mainly focus on mammalian cell imaging, but the applications of CNDs in microbial cells and plant cells are still insufficient. The imaging performance of the developed CNDs for microbial and plant cell imaging should be extensively evaluated. Last, due to their excellent optical properties and good biocompatibility, CNDs may have potential in the selective imaging of cellular biomacromolecules such as the protein antigens on the cell surfaces. The feasibility of using CNDs for monitoring the biomacromolecules should be tested.

References

1. Li XM, Rui MC, Song JZ, Shen ZH, Zeng HB (2015) Carbon and graphene quantum dots for optoelectronic and energy devices: a review. Adv Funct Mater 25:4929–4947
2. Zhu SJ, Song YB, Zhao XH, Shao JR, Zhang JH, Yang B (2015). The photoluminescence mechanism in carbon dots (graphene quantum dots, carbon nanodots, and polymer dots): current state and future perspective. Nano Res 8:355–381
3. Meng WX, Bai X, Wang BY, Liu ZY, Lu SY, Yang B (2019) Biomass-derived carbon dots and their applications. Energy Environ Mater 2:172–192
4. Xu XY, Ray R, Gu YL, Ploehn HJ, Gearheart L, Raker K, Scrivens WA (2004) Electrophoretic analysis and purification of fluorescent single-walled carbon nanotube fragments. J Am Chem Soc 126:12736–12737
5. Sun YP, Zhou B, Lin Y, Wang W, Fernando KAS, Pathak P, Meziani MJ, Harruff BA, Wang X, Wang HF, Luo PJG, Yang H, Kose ME, Chen BL, Veca LM, Xie SY (2006) Quantum-sized carbon dots for bright and colorful photoluminescence. J Am Chem Soc 128:7756–7757
6. Bao L, Zhang ZL, Tian ZQ, Zhang L, Liu C, Lin Y, Qi BP, Pang DW (2011) Electrochemical tuning of luminescent carbon nanodots: from preparation to luminescence mechanism. Adv Mater 23:5801–5806
7. Zheng HZ, Wang QL, Long YJ, Zhang HJ, Huang XX, Zhu R (2011) Enhancing the luminescence of carbon dots with a reduction pathway. Chem Commun 47:10650–10652
8. Yang JJ, Gao G, Zhang XD, Ma YH, Jia HR, Jiang YW, Wang ZF, Wu FG (2017) Ultrasmall and photostable nanotheranostic agents based on carbon quantum dots passivated with polyamine-containing organosilane molecules. Nanoscale 9:15441–15452
9. Xu D, Lin Q, Chang HT (2020) Recent advances and sensing applications of carbon dots. Small Methods 4 (4):1900387
10. Nie H, Li MJ, Li QS, Liang SJ, Tan YY, Sheng L, Shi W, Zhang SXA (2014) Carbon dots with continuously tunable full-color emission and their application in ratiometric pH sensing. Chem Mater 26:3104–3112
11. Pan LL, Sun S, Zhang AD, Jiang K, Zhang L, Dong CQ, Huang Q, Wu AG, Lin HW (2015) Truly fluorescent excitation-dependent carbon dots and their

applications in multicolor cellular imaging and multidimensional sensing. Adv Mater 27:7782–7787
12. Sharma A, Gadly T, Gupta A, Ballal A, Ghosh SK, Kumbhakar M (2016) Origin of excitation dependent fluorescence in carbon nanodots. J Phys Chem Lett 7:3695–3702
13. van Dam B, Nie H, Ju B, Marino E, Paulusse JMJ, Schall P, Li MJ, Dohnalova K (2017) Excitation-dependent photoluminescence from single-carbon dots. Small 13:1702098
14. Wang CX, Xu ZZ, Cheng H, Lin HH, Humphrey MG, Zhang C (2015) A hydrothermal route to water-stable luminescent carbon dots as nanosensors for pH and temperature. Carbon 82:87–95
15. Wang N, Wang YT, Guo TT, Yang T, Chen ML, Wang JH (2016) Green preparation of carbon dots with papaya as carbon source for effective fluorescent sensing of Iron (III) and Escherichia coli. Biosens Bioelectron 85:68–75
16. Fan YZ, Zhang Y, Li N, Liu SG, Liu T, Li NB, Luo HQ (2017) A facile synthesis of water-soluble carbon dots as a label-free fluorescent probe for rapid, selective and sensitive detection of picric acid. Sens Actuators B Chem 240:949–955
17. Li SH, Amat D, Peng ZL, Vanni S, Raskin S, De Angulo G, Othman AM, Grahamb RM, Leblanc RM (2016) Transferrin conjugated nontoxic carbon dots for doxorubicin delivery to target pediatric brain tumor cells. Nanoscale 8:16662–16669
18. Wang ZG, Fu BS, Zou SW, Duan B, Chang CY, Yang B, Zhou X, Zhang LN (2016) Facile construction of carbon dots via acid catalytic hydrothermal method and their application for target imaging of cancer cells. Nano Res 9:214–223
19. Feng T, Ai XZ, An GH, Yang PP, Zhao YL (2016) Charge-convertible carbon dots for imaging-guided drug delivery with enhanced in vivo cancer therapeutic efficiency. ACS Nano 10:4410–4420
20. Liu Q, Guo BD, Rao ZY, Zhang BH, Gong JR (2013) Strong two-photon-induced fluorescence from photostable, biocompatible nitrogen-doped graphene quantum dots for cellular and deep-tissue imaging. Nano Lett 13:2436–2441
21. Liu YB, Zhou L, Li YN, Deng RP, Zhang HJ (2017) Highly fluorescent nitrogen-doped carbon dots with excellent thermal and photo stability applied as invisible ink for loading important information and anti-counterfeiting. Nanoscale 9:491–496
22. Sun MH, Liang C, Tian Z, Ushakova EV, Li D, Xing GC, Qu SN, Rogach AL (2019) Realization of the photostable intrinsic core emission from carbon dots through surface deoxidation by ultraviolet irradiation. J Phys Chem Lett 10:3094–3100
23. Huang YF, Zhou X, Zhou R, Zhang H, Kang KB, Zhao M, Peng Y, Wang Q, Zhang HL, Qiu WY (2014) One-pot synthesis of highly luminescent carbon quantum dots and their nontoxic ingestion by zebrafish for in vivo imaging. Chem Eur J 20:5640–5648
24. Zhu SJ, Meng QN, Wang L, Zhang JH, Song YB, Jin H, Zhang K, Sun HC, Wang HY, Yang B (2013) Highly photoluminescent carbon dots for multicolor patterning, sensors, and bioimaging. Angew Chem Int Ed 52:3953–3957
25. Xu Q, Pu P, Zhao JG, Dong CB, Gao C, Chen YS, Chen JR, Liu Y, Zhou HJ (2015) Preparation of highly photoluminescent sulfur-doped carbon dots for Fe(III) detection. J Mater Chem A 3:542–546
26. Zhang Z, Hao JH, Zhang J, Zhang BL, Tang JL (2012) Protein as the source for synthesizing fluorescent carbon dots by a one-pot hydrothermal route. RSC Adv 2:8599–8601
27. Ge JC, Jia QY, Liu WM, Guo L, Liu QY, Lan MH, Zhang HY, Meng XM, Wang PF (2015) Red-emissive carbon dots for fluorescent, photoacoustic, and thermal theranostics in living mice. Adv Mater 27:4169–4177
28. Hu SL, Wei ZJ, Chang Q, Trinchi A, Yang JL (2016) A facile and green method towards coal-based fluorescent carbon dots with photocatalytic activity. Appl Surf Sci 378:402–407
29. Hua XW, Bao YW, Wang HY, Chen Z, Wu FG (2017) Bacteria-derived fluorescent carbon dots for microbial live/dead differentiation. Nanoscale 9:2150–2161
30. Lin FM, Li CC, Dong L, Fu DG, Chen Z (2017) Imaging biofilm-encased microorganisms using carbon dots derived from L. plantarum. Nanoscale 9:9056–9064
31. Zheng XT, Ananthanarayanan A, Luo KQ, Chen P (2015) Glowing graphene quantum dots and carbon dots: properties, syntheses, and biological applications. Small 11:1620–1636
32. Peng H, Li Y, Jiang CL, Luo CH, Qi RJ, Huang R, Duan CG, Travas-Sejdic J (2016) Tuning the properties of luminescent nitrogen-doped carbon dots by reaction precursors. Carbon 100:386–394
33. Jiang K, Sun S, Zhang L, Lu Y, Wu AG, Cai CZ, Lin HW (2015) Red, green, and blue luminescence by carbon dots: full-color emission tuning and multicolor cellular imaging. Angew Chem Int Ed 54:5360–5363
34. Zhang CF, Hu ZB, Song L, Cui YY, Liu XF (2015) Valine-derived carbon dots with colour-tunable fluorescence for the detection of Hg^{2+} with high sensitivity and selectivity. New J Chem 39:6201–6206
35. Hutton GAM, Martindale BCM, Reisner E (2017) Carbon dots as photosensitisers for solar-driven catalysis. Chem Soc Rev 46:6111–6123
36. Semeniuk M, Yi ZH, Poursorkhabi V, Tjong J, Jaffer S, Lu ZH, Sain M (2019) Future perspectives and review on organic carbon dots in electronic applications. ACS Nano 13:6224–6255
37. Li MX, Chen T, Gooding JJ, Liu JQ (2019) Review of carbon and graphene quantum dots for sensing. ACS Sens 4:1732–1748

38. Mishra V, Patil A, Thakur S, Kesharwani P (2018) Carbon dots: emerging theranostic nanoarchitectures. Drug Discov Today 23:1219–1232
39. Sharma V, Tiwari P, Mobin SM (2017) Sustainable carbon-dots: recent advances in green carbon dots for sensing and bioimaging. J Mater Chem B 5:8904–8924
40. Li HX, Yan X, Kong DS, Jin R, Sun CY, Du D, Lin YH, Lu GY (2020) Recent advances in carbon dots for bioimaging applications. Nanoscale Horiz 5:218–234
41. Wang W, Cheng L, Liu WG (2014) Biological applications of carbon dots. Sci China Chem 57:522–539
42. Song YB, Zhu SJ, Yang B (2014) Bioimaging based on fluorescent carbon dots. RSC Adv 4:27184–27200
43. Liu X, Pang JH, Xu F, Zhang XM (2016) Simple approach to synthesize amino-functionalized carbon dots by carbonization of chitosan. Sci Rep 6:31100
44. Zhang YQ, Ma DK, Zhuang Y, Zhang X, Chen W, Hong LL, Yan QX, Yu K, Huang SM (2012) One-pot synthesis of N-doped carbon dots with tunable luminescence properties. J Mater Chem 22:16714–16718
45. Li XM, Zhang SL, Kulinich SA, Liu YL, Zeng HB (2014) Engineering surface states of carbon dots to achieve controllable luminescence for solid-luminescent composites and sensitive Be^{2+} detection. Sci Rep 4:4976
46. Vedamalai M, Periasamy AP, Wang CW, Tseng YT, Ho LC, Shih CC, Chang HT (2014) Carbon nanodots prepared from o-phenylenediamine for sensing of Cu^{2+} ions in cells. Nanoscale 6:13119–13125
47. Zhang XD, Chen XK, Kai SQ, Wang HY, Yang JJ, Wu FG, Chen Z (2015) Highly sensitive and selective detection of dopamine using one-pot synthesized highly photoluminescent silicon nanoparticles. Anal Chem 87:3360–3365
48. Wu FG, Zhang XD, Kai SQ, Zhang MY, Wang HY, Myers JN, Weng YX, Liu PD, Gu N, Chen Z (2015) One-step synthesis of superbright water-soluble silicon nanoparticles with photoluminescence quantum yield exceeding 80%. Adv Mater Interfaces 2:1500360
49. Zhang YQ, Liu XY, Fan Y, Guo XY, Zhou L, Lv Y, Lin J (2016) One-step microwave synthesis of N-doped hydroxyl-functionalized carbon dots with ultra-high fluorescence quantum yields. Nanoscale 8:15281–15287
50. Jiang K, Wang YH, Gao XL, Cai CZ, Lin HW (2018) Facile, quick, and gram-scale synthesis of ultralong-lifetime room-temperature-phosphorescent carbon dots by microwave irradiation. Angew Chem Int Ed 57:6216–6220
51. Gao G, Jiang YW, Yang JJ, Wu FG (2017) Mitochondria-targetable carbon quantum dots for differentiating cancerous cells from normal cells. Nanoscale 9:18368–18378
52. Li HT, Ming H, Liu Y, Yu H, He XD, Huang H, Pan KM, Kang ZH, Lee ST (2011) Fluorescent carbon nanoparticles: electrochemical synthesis and their pH sensitive photoluminescence properties. New J Chem 35:2666–2670
53. Hou YX, Lu QJ, Deng JH, Li HT, Zhang YY (2015) One-pot electrochemical synthesis of functionalized fluorescent carbon dots and their selective sensing for mercury ion. Anal Chim Acta 866:69–74
54. Deng JH, Lu QJ, Mi NX, Li HT, Liu ML, Xu MC, Tan L, Xie QJ, Zhang YY, Yao SZ (2014) Electrochemical synthesis of carbon nanodots directly from alcohols. Chem Eur J 20:4993–4999
55. Li HT, He XD, Kang ZH, Huang H, Liu Y, Liu JL, Lian SY, Tsang CHA, Yang XB, Lee ST (2010) Water-soluble fluorescent carbon quantum dots and photocatalyst design. Angew Chem Int Ed 49:4430–4434
56. Li Y, Hu Y, Zhao Y, Shi GQ, Deng LE, Hou YB, Qu LT (2011) An electrochemical avenue to green-luminescent graphene quantum dots as potential electron-acceptors for photovoltaics. Adv Mater 23:776–780
57. Lu J, Yang JX, Wang JZ, Lim AL, Wang S, Loh KP (2009) One-pot synthesis of fluorescent carbon nanoribbons, nanoparticles, and graphene by the exfoliation of graphite in ionic liquids. ACS Nano 3:2367–2375
58. Li Y, Zhao Y, Cheng HH, Hu Y, Shi GQ, Dai LM, Qu LT (2012) Nitrogen-doped graphene quantum dots with oxygen-rich functional groups. J Am Chem Soc 134:15–18
59. Ananthanarayanan A, Wang XW, Routh P, Sana B, Lim S, Kim DH, Lim KH, Li J, Chen P (2014) Facile synthesis of graphene quantum dots from 3D graphene and their application for Fe^{3+} sensing. Adv Funct Mater 24:3021–3026
60. Peng J, Gao W, Gupta BK, Liu Z, Romero-Aburto R, Ge LH, Song L, Alemany LB, Zhan XB, Gao GH (2012) Graphene quantum dots derived from carbon fibers. Nano Lett 12:844–849
61. Shinde DB, Pillai VK (2012) Electrochemical preparation of luminescent graphene quantum dots from multiwalled carbon nanotubes. Chem Eur J 18:12522–12528
62. Zhang XY, Wang SQ, Zhu CY, Liu MY, Ji Y, Feng L, Tao L, Wei Y (2013) Carbon-dots derived from nanodiamond: photoluminescence tunable nanoparticles for cell imaging. J Colloid Interface Sci 397:39–44
63. Wang QL, Zheng HZ, Long YJ, Zhang LY, Gao M, Bai WJ (2011) Microwave–hydrothermal synthesis of fluorescent carbon dots from graphite oxide. Carbon 49:3134–3140
64. Tan MQ, Zhang LX, Tang R, Song XJ, Li YM, Wu H, Wang YF, Lv GJ, Liu WF, Ma XJ (2013) Enhanced photoluminescence and characterization of multicolor carbon dots using plant soot as a carbon source. Talanta 115:950–956
65. Hu C, Yu C, Li MY, Wang XN, Yang JY, Zhao ZB, Eychmüller A, Sun YP, Qiu JS (2014) Chemically

tailoring coal to fluorescent carbon dots with tuned size and their capacity for Cu (II) detection. Small 10:4926–4933
66. Dong YQ, Chen CQ, Zheng XT, Gao LL, Cui ZM, Yang HB, Guo CX, Chi YW, Li CM (2012) One-step and high yield simultaneous preparation of single- and multi-layer graphene quantum dots from CX-72 carbon black. J Mater Chem 22:8764–8766
67. Qiao ZA, Wang YF, Gao Y, Li HW, Dai TY, Liu YL, Huo QS (2010) Commercially activated carbon as the source for producing multicolor photoluminescent carbon dots by chemical oxidation. Chem Commun 46:8812–8814
68. Lai CW, Hsiao YH, Peng YK, Chou PT (2012) Facile synthesis of highly emissive carbon dots from pyrolysis of glycerol; gram scale production of carbon dots/mSiO$_2$ for cell imaging and drug release. J Mater Chem 22:14403–14409
69. Mehta VN, Jha S, Singhal RK, Kailasa SK (2014) Preparation of multicolor emitting carbon dots for HeLa cell imaging. New J Chem 38:6152–6160
70. Feng J, Wang WJ, Hai X, Yu YL, Wang JH (2016) Green preparation of nitrogen-doped carbon dots derived from silkworm chrysalis for cell imaging. J Mater Chem B 4:387–393
71. Ding P, Wang HY, Song B, Ji XY, Su YY, He Y (2017) In situ live-cell nucleus fluorescence labeling with bioinspired fluorescent probes. Anal Chem 89:7861–7868
72. Li D, Qiao ZZ, Yu YR, Tang JL, He XX, Shi H, Ye XS, Lei YL, Wang KM (2018) In situ fluorescence activation of DNA–silver nanoclusters as a label-free and general strategy for cell nucleus imaging. Chem Commun 54:1089–1092
73. Chen XK, Zhang XD, Guo YX, Zhu YX, Liu XY, Chen Z, Wu FG (2019) Smart supramolecular "Trojan horse"-inspired nanogels for realizing light-triggered nuclear drug influx in drug-resistant cancer cells. Adv Funct Mater 29:1807772
74. Yang L, Jiang WH, Qiu LP, Jiang XW, Zuo DY, Wang DK, Yang L (2015) One pot synthesis of highly luminescent polyethylene glycol anchored carbon dots functionalized with a nuclear localization signal peptide for cell nucleus imaging. Nanoscale 7:6104–6113
75. Jung YK, Shin E, Kim BS (2015) Cell nucleus-targeting zwitterionic carbon dots. Sci Rep 5:18807
76. Ci JL, Tian Y, Kuga S, Niu ZW, Wu M, Huang Y (2017) One-pot green synthesis of nitrogen-doped carbon quantum dots for cell nucleus labeling and copper (II) detection. Chem Asian J 12:2916–2921
77. Boisvert FM, van Koningsbruggen S, Navascués J, Lamond AI (2007) The multifunctional nucleolus. Nat Rev Mol Cell Biol 8:574–585
78. Frottin F, Schueder F, Tiwary S, Gupta R, Körner R, Schlichthaerle T, Cox J, Jungmann R, Hartl F, Hipp M (2019) The nucleolus functions as a phase-separated protein quality control compartment. Science 365:342–347
79. Barbosa CDES, Corrêa JR, Medeiros GA, Barreto G, Magalhães KG, de Oliveira AL, Spencer J, Rodrigues MO, Neto BAD (2015) Carbon dots (C-dots) from cow manure with impressive subcellular selectivity tuned by simple chemical modification. Chem Eur J 21:5055–5060
80. Kong WQ, Liu RH, Li H, Liu J, Huang H, Liu Y, Kang ZH (2014) High-bright fluorescent carbon dots and their application in selective nucleoli staining. J Mater Chem B 2:5077–5082
81. Hua XW, Bao YW, Wu FG (2018) Fluorescent carbon quantum dots with intrinsic nucleolus-targeting capability for nucleolus imaging and enhanced cytosolic and nuclear drug delivery. ACS Appl Mater Interfaces 10:10664–10677
82. Hua XW, Bao YW, Zeng J, Wu FG (2019) Nucleolus-targeted red emissive carbon dots with polarity-sensitive and excitation-independent fluorescence emission: high-resolution cell imaging and in vivo tracking. ACS Appl Mater Interfaces 11:32647–32658
83. McBride HM, Neuspiel M, Wasiak S (2006) Mitochondria: more than just a powerhouse. Curr Biol 16:R551–R560
84. Wang BB, Wang YF, Wu H, Song XJ, Guo X, Zhang DM, Ma XJ, Tan MQ (2014) A mitochondria-targeted fluorescent probe based on TPP-conjugated carbon dots for both one-and two-photon fluorescence cell imaging. RSC Adv 4:49960–49963
85. Hua XW, Bao YW, Chen Z, Wu FG (2017) Carbon quantum dots with intrinsic mitochondrial targeting ability for mitochondria-based theranostics. Nanoscale 9:10948–10960
86. De Duve C, Wattiaux R (1966) Functions of lysosomes. Annu Rev Physiol 28:435–492
87. Chen XK, Zhang XD, Xia LY, Wang HY, Chen Z, Wu FG (2018) One-step synthesis of ultrasmall and ultrabright organosilica nanodots with 100% photoluminescence quantum yield: long-term lysosome imaging in living, fixed, and permeabilized cells. Nano Lett 18:1159–1167
88. Zhang XD, Chen XK, Guo YX, Jia HR, Jiang YW, Wu FG (2020) Endosome/lysosome-detained supramolecular nanogels as an efflux retarder and autophagy inhibitor for repeated photodynamic therapy of multidrug-resistant cancer. Nanoscale Horiz 5:481–487
89. Wu LL, Li XL, Ling YF, Huang CS, Jia NQ (2017) Morpholine derivative-functionalized carbon dots-based fluorescent probe for highly selective lysosomal imaging in living cells. ACS Appl Mater Interfaces 9:28222–28232
90. Zhang DY, Zheng Y, Zhang H, He L, Tan CP, Sun JH, Zhang W, Peng XY, Zhan QQ, Ji LN, Mao ZW (2017) Ruthenium complex-modified carbon nanodots for lysosome-targeted one- and two-photon imaging and photodynamic therapy. Nanoscale 9:18966–18976

91. E S, Mao QX, Yuan XL, Kong XL, Chen XW, Wang JH (2018) Targeted imaging of the lysosome and endoplasmic reticulum and their pH monitoring with surface regulated carbon dots. Nanoscale 10:12788–12796
92. Zhang QQ, Yang T, Li RS, Zou HY, Li YF, Guo J, Liu XD, Huang CZ (2018) A functional preservation strategy for the production of highly photoluminescent emerald carbon dots for lysosome targeting and lysosomal pH imaging. Nanoscale 10:14705–14711
93. Liu HF, Sun YQ, Li ZH, Yang J, Aryee AA, Qu LB, Du D, Lin YH (2019) Lysosome-targeted carbon dots for ratiometric imaging of formaldehyde in living cells. Nanoscale 11:8458–8463
94. Chen S, Jia Y, Zou GY, Yu YL, Wang JH (2019) A ratiometric fluorescent nanoprobe based on naphthalimide derivative-functionalized carbon dots for imaging lysosomal formaldehyde in HeLa cells. Nanoscale 11:6377–6383
95. Zhao SJ, Wu SL, Jia QY, Huang L, Lan MH, Wang PF, Zhang WJ (2020) Lysosome-targetable carbon dots for highly efficient photothermal/photodynamic synergistic cancer therapy and photoacoustic/two-photon excited fluorescence imaging. Chem Eng J 388:124212
96. Qin HY, Sun YQ, Geng X, Zhao KR, Meng HM, Yang R, Qu LB, Li ZH (2020) A wash-free lysosome targeting carbon dots for ultrafast imaging and monitoring cell apoptosis status. Anal Chim Acta 1106:207–215
97. Singh H, Sreedharan S, Tiwari K, Green NH, Smythe C, Pramanik SK, Thomas JA, Das A (2019) Two photon excitable graphene quantum dots for structured illumination microscopy and imaging applications: lysosome specificity and tissue-dependent imaging. Chem Commun 55:521–524
98. Guo S, Sun YQ, Geng X, Yang R, Xiao LH, Qu LB, Li ZH (2020) Intrinsic lysosomal targeting fluorescent carbon dots with ultrastability for long-term lysosome imaging. J Mater Chem B 8:736–742
99. Beams HW, Kessel RG (1968) The Golgi apparatus: structure and function. Int Rev Cytol 23:209–276
100. Li RS, Gao PF, Zhang HZ, Zheng LL, Li CM, Wang J, Li YF, Liu F, Li N, Huang CZ (2017) Chiral nanoprobes for targeting and long-term imaging of the Golgi apparatus. Chem Sci 8:6829–6835
101. Wang L, Wu B, Li WT, Li Z, Zhan J, Geng BJ, Wang SL, Pan DY, Wu MH (2017) Industrial production of ultra-stable sulfonated graphene quantum dots for Golgi apparatus imaging. J Mater Chem B 5:5355–5361
102. Han JY, Burgess K (2010) Fluorescent indicators for intracellular pH. Chem Rev 110:2709–2728
103. Jia XF, Li J, Wang EK (2012) One-pot green synthesis of optically pH-sensitive carbon dots with upconversion luminescence. Nanoscale 4:5572–5575
104. Hu YP, Yang J, Tian JW, Jia L, Yu JS (2014) Waste frying oil as a precursor for one-step synthesis of sulfur-doped carbon dots with pH-sensitive photoluminescence. Carbon 77:775–782
105. Shangguan JF, He DG, He XX, Wang KM, Xu FZ, Liu JQ, Tang JL, Yang X, Huang J (2016) Label-free carbon-dots-based ratiometric fluorescence pH nanoprobes for intracellular pH sensing. Anal Chem 88:7837–7843
106. Ye XX, Xiang YH, Wang QR, Li Z, Liu ZH (2019) A red emissive two-photon fluorescence probe based on carbon dots for intracellular pH detection. Small 15:1901673
107. Stohs SJ, Bagchi D (1995) Oxidative mechanisms in the toxicity of metal ions. Free Radic Biol Med 18:321–336
108. Yang MX, Tang QL, Meng Y, Liu JJ, Feng TL, Zhao XH, Zhu SJ, Yu WX, Yang B (2018) Reversible "off-on" fluorescence of Zn^{2+}-passivated carbon dots: mechanism and potential for the detection of EDTA and Zn^{2+}. Langmuir 34:7767–7775
109. Kong DP, Yan FY, Luo YM, Ye QH, Zhou S, Chen L (2017) Amphiphilic carbon dots for sensitive detection, intracellular imaging of Al^{3+}. Anal Chim Acta 953:63–70
110. Zhang HJ, Chen YL, Liang MJ, Xu LF, Qi SD, Chen HL, Chen XG (2014) Solid-phase synthesis of highly fluorescent nitrogen-doped carbon dots for sensitive and selective probing ferric ions in living cells. Anal Chem 86:9846–9852
111. Gong XJ, Lu WJ, Paau MC, Hu Q, Wu X, Shuang SM, Dong C, Choi MMF (2015) Facile synthesis of nitrogen-doped carbon dots for Fe^{3+} sensing and cellular imaging. Anal Chim Acta 861:74–84
112. Shangguan JF, Huang J, He DG, He XX, Wang KM, Ye RZ, Yang X, Qing TP, Tang JL (2017) Highly Fe^{3+}-selective fluorescent nanoprobe based on ultra-bright N/P codoped carbon dots and its application in biological samples. Anal Chem 89:7477–7484
113. Song Y, Zhu CZ, Song JH, Li H, Du D, Lin YH (2017) Drug-derived bright and color-tunable N-doped carbon dots for cell imaging and sensitive detection of Fe^{3+} in living cells. ACS Appl Mater Interfaces 9:7399–7405
114. Atchudan R, Edison TNJI, Aseer KR, Perumal S, Karthik N, Lee YR (2018) Highly fluorescent nitrogen-doped carbon dots derived from Phyllanthus acidus utilized as a fluorescent probe for label-free selective detection of Fe^{3+} ions, live cell imaging and fluorescent ink. Biosens Bioelectron 99:303–311
115. Gao G, Jiang YW, Jia HR, Yang JJ, Wu FG (2018) On-off-on fluorescent nanosensor for Fe^{3+} detection and cancer/normal cell differentiation via silicon-doped carbon quantum dots. Carbon 134:232–243
116. Salinas-Castillo A, Ariza-Avidad M, Pritz C, Camprubí-Robles M, Fernández B, Ruedas-Rama MJ, Megia-Fernández A, Lapresta-Fernández A, Santoyo-Gonzalez F, Schrott-Fischer A, Capitan-Vallvey LF (2013) Carbon dots for copper detection with down and upconversion fluorescent properties as excitation sources. Chem Commun 49:1103–1105

117. Sotiriou GA, Pratsinis SE (2011) Engineering nanosilver as an antibacterial, biosensor and bioimaging material. Curr Opin Chem Eng 1: 3–10
118. Zuo GC, Xie AM, Li JJ, Su T, Pan XH, Dong W (2017) Large emission red-shift of carbon dots by fluorine doping and their applications for red cell imaging and sensitive intracellular Ag^{+} detection. J Phys Chem C 121:26558–26565
119. Makam P, Shilpa R, Kandjani AE, Periasamy SR, Sabri YM, Madhu C, Bhargava SK, Govindaraju T (2018) SERS and fluorescence-based ultrasensitive detection of mercury in water. Biosens Bioelectron 100:556–564
120. Yan FY, Zou Y, Wang M, Mu XL, Yang N, Chen L (2014) Highly photoluminescent carbon dots-based fluorescent chemosensors for sensitive and selective detection of mercury ions and application of imaging in living cells. Sens Actuators B Chem 192:488–495
121. Prathumsuwan T, Jamnongsong S, Sampattavanich S, Paoprasert P (2018) Preparation of carbon dots from succinic acid and glycerol as ferrous ion and hydrogen peroxide dual-mode sensors and for cell imaging. Opt Mater 86:517–529
122. Yazid SNAM, Chin SF, Pang SC, Ng SM (2013) Detection of Sn(II) ions via quenching of the fluorescence of carbon nanodots. Microchim Acta 180:137–143
123. Tabaraki R, Abdi O, Yousefipour S (2017) Green and selective fluorescent sensor for detection of Sn (IV) and Mo (VI) based on boron and nitrogen-co-doped carbon dots. J Fluoresc 27:651–657
124. Kumar A, Chowdhuri AR, Laha D, Mahto TK, Karmakar P, Sahu SK (2017) Green synthesis of carbon dots from Ocimum sanctum for effective fluorescent sensing of Pb^{2+} ions and live cell imaging. Sens Actuators B Chem 242:679–686
125. Zhang HY, Wang Y, Xiao S, Wang H, Wang JH, Feng L (2017) Rapid detection of Cr(VI) ions based on cobalt(II)-doped carbon dots. Biosens Bioelectron 87:46–52
126. Du FK, Zeng F, Ming YH, Wu SZ (2013) Carbon dots-based fluorescent probes for sensitive and selective detection of iodide. Microchim Acta 180:453–460
127. Sun S, Jiang K, Qian SH, Wang YH, Lin HW (2017) Applying carbon dots-metal ions ensembles as a multichannel fluorescent sensor array: detection and discrimination of phosphate anions. Anal Chem 89:5542–5548
128. Du FK, Min YH, Zeng F, Yu CM, Wu SZ (2014) A targeted and FRET-based ratiometric fluorescent nanoprobe for imaging mitochondrial hydrogen peroxide in living cells. Small 10:964–972
129. Li L, Rose P, Moore PK (2011) Hydrogen sulfide and cell signaling. Annu Rev Pharmacol Toxicol 51:169–187
130. Yu CM, Li XZ, Zeng F, Zheng FY, Wu SZ (2013) Carbon-dot-based ratiometric fluorescent sensor for detecting hydrogen sulfide in aqueous media and inside live cells. Chem Commun 49:403–405
131. Zhang XD, Wu FG, Liu PD, Gu N, Chen Z (2014) Enhanced fluorescence of gold nanoclusters composed of $HAuCl_4$ and histidine by glutathione: glutathione detection and selective cancer cell imaging. Small 10:5170–5177
132. Sun XH, Yang SH, Guo MZ, Ma S, Zheng MD, He J (2017) Reversible fluorescence probe based on N-doped carbon dots for the determination of mercury ion and glutathione in waters and living cells. Anal Sci 33:761–767
133. Kim DO, Lee KW, Lee HJ, Lee CY (2002) Vitamin C equivalent antioxidant capacity (VCEAC) of phenolic phytochemicals. J Agric Food Chem 50:3713–3717
134. Feng LL, Wu YX, Zhang DL, Hu XX, Zhang J, Wang P, Song ZL, Zhang XB, Tan WH (2017) Near infrared graphene quantum dots-based two-photon nanoprobe for direct bioimaging of endogenous ascorbic acid in living cells. Anal Chem 89:4077–4084
135. Kiran S, Misra RDK (2015) Mechanism of intracellular detection of glucose through nonenzymatic and boronic acid functionalized carbon dots. J Biomed Mater Res A 103:2888–2897
136. Loo AH, Sofer Z, Bousa D, Ulbrich P, Bonanni A, Pumera M (2016) Carboxylic carbon quantum dots as a fluorescent sensing platform for DNA detection. ACS Appl Mater Interfaces 8:1951–1957
137. Mahani M, Mousapour Z, Divsar F, Nomani A, Ju HX (2019) A carbon dot and molecular beacon based fluorometric sensor for the cancer marker microRNA-21. Microchim Acta 186:132
138. Han GM, Zhao J, Zhang RL, Tian XH, Liu ZJ, Wang AD, Liu RY, Liu BH, Han MY, Gao XH, Zhang ZP (2019) Membrane-penetrating carbon quantum dots for imaging nucleic acid structures in live organisms. Angew Chem Int Ed 58:7087–7091
139. Mao Y, Bao Y, Han DX, Li FH, Niu L (2012) Efficient one-pot synthesis of molecularly imprinted silica nanospheres embedded carbon dots for fluorescent dopamine optosensing. Biosens Bioelectron 38:55–60
140. Liu XQ, Wang T, Wang WJ, Zhou ZP, Yan YS (2019) A tailored molecular imprinting ratiometric fluorescent sensor based on red/blue carbon dots for ultrasensitive tetracycline detection. J Ind Eng Chem 72:100–106
141. Deng JH, Lu QJ, Hou YX, Liu ML, Li HT, Zhang YY, Yao SZ (2015) Nanosensor composed of nitrogen-doped carbon dots and gold nanoparticles for highly selective detection of cysteine with multiple signals. Anal Chem 87:2195–2203
142. Copur F, Bekar N, Zor E, Alpaydin S, Bingol H (2019) Nanopaper-based photoluminescent enantioselective sensing of L-lysine by L-cysteine modified carbon quantum dots. Sens Actuators B Chem 279:305–312

143. Han TQ, Yan T, Li YY, Cao W, Pang XH, Huang QJ, Wei Q (2015) Eco-friendly synthesis of electrochemiluminescent nitrogen-doped carbon quantum dots from diethylene triamine pentacetate and their application for protein detection. Carbon 91:144–152
144. Li Q, Ohulchanskyy TY, Liu RL, Koynov K, Wu DQ, Best A, Kumar R, Bonoiu A, Prasad PN (2010) Photoluminescent carbon dots as biocompatible nanoprobes for targeting cancer cells in vitro. J Phys Chem C 114:12062–12068
145. Zheng M, Ruan SB, Liu S, Sun TT, Qu D, Zhao HF, Xie ZG, Gao HL, Jing XB, Sun ZC (2015) Self-targeting fluorescent carbon dots for diagnosis of brain cancer cells. ACS Nano 9:11455–11461
146. Bhunia SK, Maity AR, Nandi S, Stepensky D, Jelinek R (2016) Imaging cancer cells expressing the folate receptor with carbon dots produced from folic acid. ChemBioChem 17:614–619
147. Zhang XD, Chen XK, Yang JJ, Jia HR, Li YH, Chen Z, Wu FG (2016) Quaternized silicon nanoparticles with polarity-sensitive fluorescence for selectively imaging and killing Gram-positive bacteria. Adv Funct Mater 26:5958–5970
148. Lin FM, Bao YW, Wu FG (2019) Carbon dots for sensing and killing microorganisms. C 5:33
149. Mehta VN, Jha S, Kailasa SK (2014) One-pot green synthesis of carbon dots by using Saccharum officinarum juice for fluorescent imaging of bacteria (Escherichia coli) and yeast (Saccharomyces cerevisiae) cells. Mater Sci Eng C 38:20–27
150. Nandi S, Ritenberg M, Jelinek R (2015) Bacterial detection with amphiphilic carbon dots. Analyst 140:4232–4237
151. Yang JJ, Zhang XD, Ma YH, Gao G, Chen XK, Jia HR, Li YH, Chen Z, Wu FG (2016) Carbon dot-based platform for simultaneous bacterial distinguishment and antibacterial applications. ACS Appl Mater Interfaces 8:32170–32181
152. Yang JJ, Gao G, Zhang XD, Ma YH, Chen XK, Wu FG (2019) One-step synthesized carbon dots with bacterial contact-enhanced fluorescence emission property: fast Gram-type identification and selective Gram-positive bacterial inactivation. Carbon 146:827–839
153. Chandra S, Mahto TK, Chowdhuri AR, Das B, Sahu SK (2017) One step synthesis of functionalized carbon dots for the ultrasensitive detection of Escherichia coli and iron (III). Sens Actuators B Chem 245:835–844
154. Chandra S, Chowdhuri AR, Mahto TK, Samui A, Sahu SK (2016) One-step synthesis of amikacin modified fluorescent carbon dots for the detection of Gram-negative bacteria like *Escherichia coli*. RSC Adv 6:72471–72478
155. Chen XK, Zhang XD, Li CC, Sayed SM, Sun W, Lin FM, Wu FG (2019) Superbright organosilica nanodots as a universal sensor for fast discrimination and accurate quantification of live/dead cells. Sens Actuators B Chem 295:49–55
156. Lu F, Song YX, Huang H, Liu Y, Fu YJ, Huang J, Li H, Qu HH, Kang ZH (2017) Fluorescent carbon dots with tunable negative charges for bio-imaging in bacterial viability assessment. Carbon 120:95–102
157. Chen XK, Zhang XD, Lin FM, Guo YX, Wu FG (2019) One-step synthesis of epoxy group-terminated organosilica nanodots: a versatile nanoplatform for imaging and eliminating multidrug-resistant bacteria and their biofilms. Small 15:1901647
158. Ritenberg M, Nandi S, Kolusheva S, Dandela R, Meijler MM, Jelinek R (2016) Imaging Pseudomonas aeruginosa biofilm extracellular polymer scaffolds with amphiphilic carbon dots. ACS Chem Biol 11:1265–1270
159. Ran HH, Cheng XT, Bao YW, Hua XW, Gao G, Zhang XD, Jiang YW, Zhu YX, Wu FG (2019) Multifunctional quaternized carbon dots with enhanced biofilm penetration and eradication efficiencies. J Mater Chem B 7:5104–5114
160. Belkahla H, Boudjemaa R, Caorsi V, Pineau D, Curcio A, Lomas JS, Decorse P, Chevillot-Biraud A, Azaïs T, Wilhelm C, Randriamahazaka H, Hémadi M (2019) Carbon dots, a powerful non-toxic support for bioimaging by fluorescence nanoscopy and eradication of bacteria by photothermia. Nanoscale Adv 1:2571–2579
161. Zhang ML, Hu LL, Wang HB, Song YX, Liu Y, Li H, Shao MW, Huang H, Kang ZH (2018) One-step hydrothermal synthesis of chiral carbon dots and their effects on mung bean plant growth. Nanoscale 10:12734–12742
162. Wang ZY, Qu YN, Gao XT, Mu CJ, Bai JP, Pu QS (2014) Facile preparation of oligo(ethylene glycol)-capped fluorescent carbon dots from glutamic acid for plant cell imaging. Mater Lett 129:122–125
163. Li W, Zhang HR, Zheng YJ, Chen S, Liu YL, Zhuang JL, Liu WR, Lei BF (2017) Multifunctional carbon dots for highly luminescent orange-emissive cellulose based composite phosphor construction and plant tissue imaging. Nanoscale 9:12976–12983
164. Tripathi S, Sarkar S (2014) Influence of water soluble carbon dots on the growth of wheat plant. Appl Nanosci 5:609–616
165. Pan LL, Sun S, Zhang L, Jiang K, Lin HW (2016) Near-infrared emissive carbon dots for two-photon fluorescence bioimaging. Nanoscale 8:17350–17356
166. Lan MH, Zhao SJ, Zhang ZY, Yan L, Guo L, Niu GL, Zhang JF, Zhao JF, Zhang HY, Wang PF, Zhu GY, Lee CS, Zhang WJ (2017) Two-photon-excited near-infrared emissive carbon dots as multifunctional agents for fluorescence imaging and photothermal therapy. Nano Res 10:3113–3123
167. Lu SY, Sui LZ, Liu JJ, Zhu SJ, Chen AM, Jin MX, Yang B (2017) Near-infrared photoluminescent polymer–carbon nanodots with two-photon fluorescence. Adv Mater 29:1603443
168. Yang CH, Zhu SJ, Li ZL, Li Z, Chen C, Sun L, Tang W, Liu R, Sun Y, Yu M (2016) Nitrogen-doped carbon dots with excitation-independent

long-wavelength emission produced by a room-temperature reaction. Chem Commun 52:11912–11914
169. Wu ZL, Liu ZX, Yuan YH (2017) Carbon dots: materials, synthesis, properties and approaches to long-wavelength and multicolor emission. J Mater Chem B 5:3794–3809
170. Shamsipur M, Barati A, Karami S (2017) Long-wavelength, multicolor, and white-light emitting carbon-based dots: achievements made, challenges remaining, and applications. Carbon 124:429–472
171. Li QJ, Zhou M, Yang QF, Wu Q, Shi J, Gong AH, Yang MY (2016) Efficient room-temperature phosphorescence from nitrogen-doped carbon dots in composite matrices. Chem Mater 28:8221–8227
172. Jiang K, Wang YH, Cai CZ, Lin HW (2018) Conversion of carbon dots from fluorescence to ultralong room-temperature phosphorescence by heating for security applications. Adv Mater 30:1800783
173. Jiang K, Gao XL, Feng XY, Wang YH, Li ZJ, Lin HW (2020) Carbon dots with dual-emissive, robust, and aggregation-induced room-temperature phosphorescence characteristics. Angew Chem Int Ed 59:1263–1269
174. Jiang L, Ding HZ, Lu SY, Geng T, Xiao GJ, Zou B, Bi H (2020) Photoactivated fluorescence enhancement in F,N-doped carbon dots with piezochromic behavior. Angew Chem Int Ed 59:9986–9991
175. Lu SY, Xiao GY, Sui LZ, Feng TL, Yong X, Zhu SJ, Li BJ, Liu ZY, Zou B, Jin MX, Tse JS, Yan H, Yang B (2017) Piezochromic carbon dots with two-photon fluorescence. Angew Chem Int Ed 56:6187–6191
176. Zhan Y, Geng T, Liu YL, Hu CF, Zhang XJ, Lei BF, Zhuang JL, Wu X, Huang D, Xiao GJ, Zou B (2018) Near-ultraviolet to near-infrared fluorescent nitrogen-doped carbon dots with two-photon and piezochromic luminescence. ACS Appl Mater Interfaces 10:27920–27927
177. Zhu SJ, Zhang JH, Tang SJ, Qiao CY, Wang L, Wang HY, Liu X, Li B, Li YF, Yu WL, Wang XF, Sun HC, Yang B (2012) Surface chemistry routes to modulate the photoluminescence of graphene quantum dots: from fluorescence mechanism to up-conversion bioimaging applications. Adv Funct Mater 22:4732–4740
178. Alam AM, Park BY, Ghouri ZK, Park M, Kim HY (2015) Synthesis of carbon quantum dots from cabbage with down-and up-conversion photoluminescence properties: excellent imaging agent for biomedical applications. Green Chem 17:3791–3797
179. Li JY, Liu Y, Shu QW, Liang JM, Zhang F, Chen XP, Deng XY, Swihart MT, Tan KJ (2017) One-pot hydrothermal synthesis of carbon dots with efficient up- and down-converted photoluminescence for the sensitive detection of morin in a dual-readout assay. Langmuir 33:1043–1050

Silicon Nanoparticles for Cell Imaging

Xiaokai Chen, Xiaodong Zhang, and Fu-Gen Wu

1 Silicon Nanoparticles

Silicon nanoparticles (SiNPs) are metal-free and photoluminescent nanomaterials containing silicon, a nontoxic and naturally abundant element in the Earth's crust [1–3]. There are mainly two types of SiNPs: one contains a Si(0)-dominated core and the other contains a Si(4)-dominated core [4]. As an emerging and attractive kind of fluorescent materials, SiNPs present many attractive features: (1) ultrasmall size endowing their excretion from a living body via renal clearance, (2) intrinsic photoluminescence which can be tuned by controlling their size and surface composition, (3) metal-free composition eliminating the heavy metal-caused toxicity of conventional semiconductor quantum dots and ensuring biocompatibility, (4) the presence of various surface functional groups providing the chances of further surface modifications, and (5) enough silicon-containing raw materials from the Earth's crust that may ensure their low-cost fabrication [4–32]. Up to date, the versatile SiNPs have been used as biomedical imaging agents, anticancer nanodrugs/nanocarriers, antimicrobial agents, light-emitting diodes, biological/chemical sensors, photovoltaic materials, catalysts, battery electrodes, and solar concentrators [1, 2, 33–47].

X. Chen · X. Zhang · F.-G. Wu (✉)
State Key Laboratory of Bioelectronics, School of Biological Science and Medical Engineering, Southeast University, Nanjing, Jiangsu, China
e-mail: wufg@seu.edu.cn

1.1 Synthesis

The preparation methods of colloidal SiNPs can be divided into three classes [3]. The methods in class I adopting the "top-down" approach include the etching of bulk silicon and breaking down silicon-rich oxides. The methods in class II via the "bottom-up" approach depend on the self-assembly of small-molecule silicon precursors, including the reduction of silicon precursors and the reaction between silicon halides and silicon Zintl salts. The preparation methods in class III need both the "top-down" and "bottom-up" processes, involving the decomposition of silicon-containing precursors and the re-assembly processes to form the final SiNPs. Specific examples include the preparation of SiNPs in supercritical fluids, the generation of SiNPs using laser pyrolysis, and the synthesis of SiNPs adopting plasma.

However, many of the SiNPs prepared via the above-mentioned methods contain hydrophobic surfaces, which greatly limits the applications of these SiNPs in the biomedical field. Thus, numerous researchers have made their efforts to obtain water-dispersible SiNPs. In 2004, Li et al. successfully turned hydrophobic SiNPs into water-dispersible ones by grafting a water-soluble polymer poly(acrylic acid) on the surface of the SiNPs [24]. Then, using the precursors including silicon nanowires and glutaric acid, water-dispersible SiNPs with good pH stability and strong fluorescence emission were synthesized via a simple one-pot microwave-assisted method by He et al.

F.-G. Wu (ed.), *Fluorescent Materials for Cell Imaging*, https://doi.org/10.1007/978-981-15-5062-1_4

in 2011 [18], which provides a new approach for the facile preparation of SiNPs with good water-dispersity. After that, another one-step synthetic method based on the hydrothermal treatment of (3-aminopropyl)trimethoxysilane (APTMS) and sodium citrate was reported by Zhang et al. in 2014 for the rapid and large-scale preparation of highly photoluminescent SiNPs with excellent aqueous stability [27].

1.2 Photoluminescence Properties

According to the origin of photoluminescence, the fluorescent SiNPs can be classified into two classes. The fluorescence of the SiNPs in class I comes from Si and the average size of these SiNPs is usually below 10 nm. The SiNPs in class I show size-dependent fluorescence and usually have long fluorescence lifetimes (usually in microseconds). These optical properties are similar to those of semiconductor quantum dots. The photoluminescence mechanism of the SiNPs in class I can be attributed to the quantum confinement effect. Specifically, the ultrasmall size of the SiNPs ($<$10 nm) results in the squeezed electrons and holes, followed by the dramatically increased bandgaps, which causes the formation of the discrete energy levels of SiNPs. Under light irradiation, the electrons absorb energy and are excited from the ground state to an unstable level (excited state). Owing to their instability, the energized electrons then return to the ground state, during which excess energy is released in the form of fluorescence. In addition to the size effect, the surface effect can also affect the optical properties of the SiNPs in class I. For example, different surface molecules may induce distinct defects, thus tuning the fluorescence emission [42, 48].

The SiNPs in class II possess shorter fluorescence lifetimes (usually in nanoseconds) and commonly have blue or green emissions. For this kind of SiNPs, the silicon-formed nanostructure provides a basic framework and is not responsible for the fluorescence, and the photoluminescence is attributed to the introduced molecular fluorophores [49, 50]. Therefore, the changes of size and surface groups have negligible influence on the emission tunability of the SiNPs.

SiNPs possess outstanding photoluminescence properties, which are represented by their high photoluminescence quantum yields (PLQYs), size and surface tailorable emissions, and photostability [28, 51–59]. For better biomedical applications, many researchers have realized the improvement of the photoluminescence properties of SiNPs recently. In 2006, Jurbergs et al. adopted a plasma technique to synthesize SiNPs with an average diameter of 3 nm under an anaerobic environment [60]. By passivating the surface of the SiNPs with an organic ligand, a high PLQY exceeding 60% was achieved at the wavelength of ~789 nm. After that, through the surface modification with diphenylamine and carbazole, both of which are aromatic electron-rich and have high nucleophilicity, the PLQY of the SiNPs was successfully improved to ~75% by Li et al. [61]. In 2015, a series of superbright water-dispersible SiNPs were synthesized by our group via a microwave-assisted method using three similar amine-containing silane molecules APTMS, *N*-[3-(trimethoxysilyl)propyl]ethylenediamine (DAMO), and 3-[2-(2-aminoethylamino) ethylamino]propyl-trimethoxysilane (AEEA) [4]. All the SiNPs emitted blue fluorescence under ultraviolet (UV) light irradiation and the DAMO SiNPs showed the brightest fluorescence with a PLQY value of 82.4% (Fig. 1a). Then, another advance was made by Li et al. in 2016 [62]. By adopting the strategy that changed the surface of SiNPs with nitrogen, they successfully improved the photoluminescence properties of the SiNPs with an ultrahigh PLQY up to 90% and narrow photoluminescence bandwidth (full width at half maximum (FWHM) $\approx$ 40 nm, Fig. 1b). Two years later, our group realized the preparation of SiNPs with a PLQY of 100% via a one-step hydrothermal treatment of a silane molecule (DAMO or AEEA) and rose bengal (RB) for 4 h [50]. The SiNPs with a PLQY of 74% can be prepared through the hydrothermal

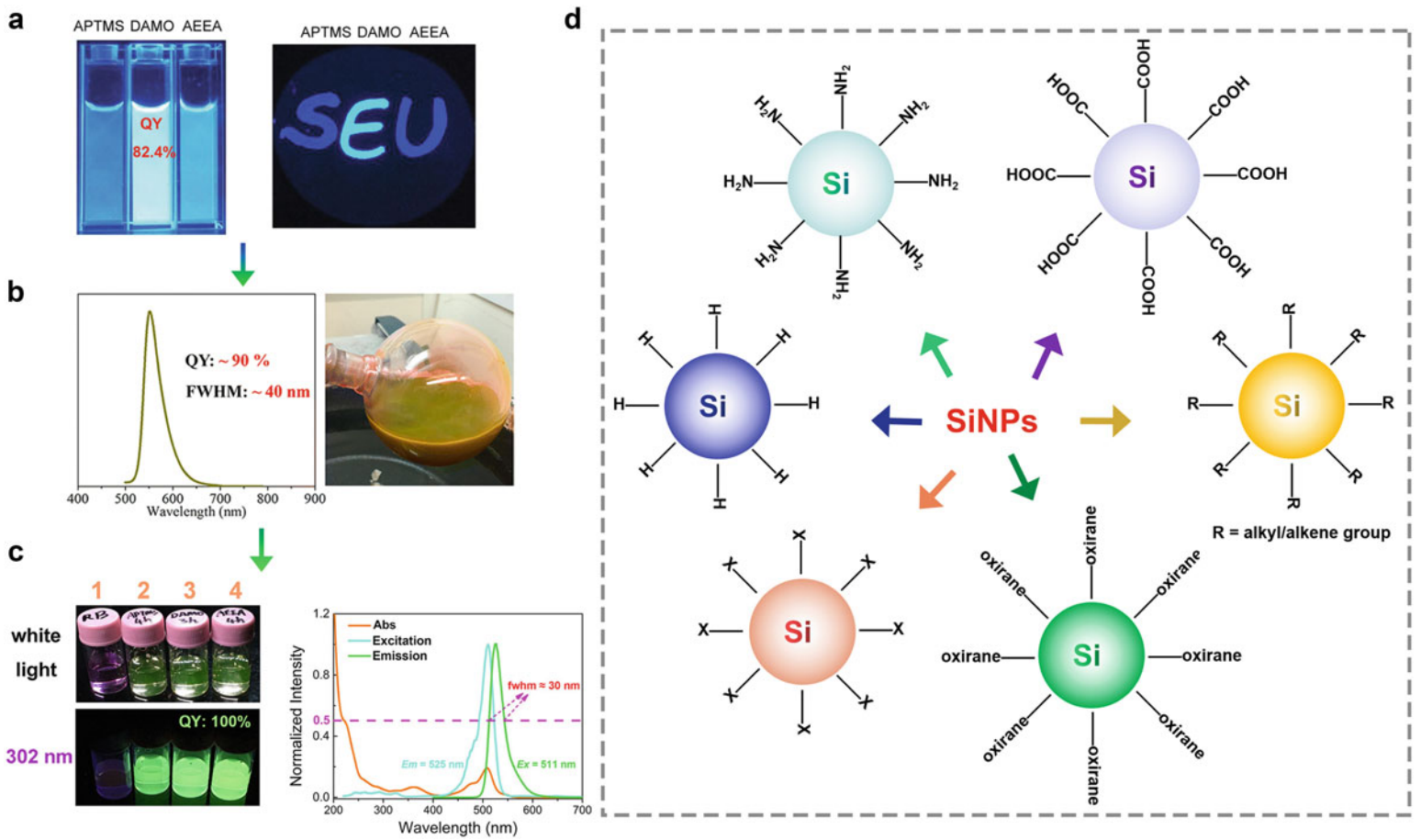

Fig. 1 (**a**) Photographs of the three SiNP suspensions and a filter paper with three fluorescent letters "S," "E," and "U" (written by using the corresponding SiNP suspensions as fluorescent inks) taken under 365 nm UV light irradiation. Reprinted with permission from Ref. [4]. Copyright © 2015 Wiley. (**b**) Photoluminescence emission spectrum of SiNPs (the surface of the SiNPs was capped with nitrogen) and photograph of the SiNPs suspended in glyme taken under ambient light. Reprinted with permission from Ref. [62]. Copyright © 2016 American Chemical Society. (**c**) Photographs of (1) RB solution and the suspensions of (2) APTMS SiNPs, (3) DAMO SiNPs, and (4) AEEA SiNPs taken under white and 302 nm UV light irradiation (left), and the ultraviolet–visible (UV–vis) absorption, fluorescence excitation, and fluorescence emission spectra of the AEEA SiNP suspension (right). Reprinted with permission from Ref. [50]. Copyright © 2018 American Chemical Society. (**d**) Schematic illustration of various classes of SiNPs with different surface terminations. The termination "X" means "halogen"

reaction between APTMS and RB. The FWHM of the as-synthesized SiNPs was further decreased to ~30 nm (Fig. 1c). The superior fluorescence properties of the as-prepared SiNPs were attributed to the "heavy atom effect" which means the halide loss of RB during the hydrothermal process promoted the enhancement of their photoluminescence efficiency.

1.3 Surface Chemistry

According to their different surface terminations, as indicated in Fig. 1d, SiNPs can be divided into the following several classes: amino-, carboxyl-, alkyl/alkene-, oxirane-, halogen-, or hydrogen-terminated SiNPs [4, 47, 50, 63–66]. SiNPs with hydrogen and halogen surfaces are hydrophobic which are not readily dispersed in common solvents, and hence the hydrogen- and halogen-terminated SiNPs require further modifications to passivate their surfaces for improving their dispersity in previously incompatible solvents. SiNPs with alkyl/alkene group termination are hydrophobic and hard to be further functionalized. SiNPs terminated with amino, carboxyl, or oxirane groups are usually water-dispersible and easily modifiable, and therefore their biomedical applications can be broadened with appropriate surface functionalizations.

On the other hand, proper surface engineering can alter the optical performance of SiNPs [9, 22, 63, 67]. As reported by Dohnalová et al., the fluorescence emission of SiNPs could be effectively adjusted by changing the surface termination [22]. Specifically, the carbon (C)-terminated SiNPs emit blue-green fluorescence with short decaying time (ns) due to an excitonic recombination process in the SiNP core. When the C-modified surface of SiNPs is replaced by the oxygen (O)-terminated one, the excited carriers on the surface states can be ultrafast trapped, resulting in the disabled recombination of excitons from the core-related states. Thus, the emission of the SiNPs with O termination is changed to red luminescence with long decaying time (μs).

2 SiNPs for In Vitro Cellular Imaging

The use of fluorescent SiNPs for in vitro cell imaging has gained intense interest due to their strong photoluminescence, broad excitation spectra, and good photostability [6, 68–71]. The favorable photoluminescence features provide the nanoparticles with advantages exceeding conventional molecular fluorophores for cell imaging [72]. As a class of biocompatible and low-cost fluorescent nanoprobes, surface-modifiable SiNPs are an attractive candidate to replace other kinds of nanoparticles whose applications are limited by the shortcomings such as high toxicities, complicated synthetic procedures, fluorescence overlaps caused by multi-color photoluminescence emission, poor water dispersibility, difficulty of functionalization, or high cost [4, 50, 73, 74]. In this section, we emphasize the use of SiNPs for in vitro cellular imaging, including mammalian cell imaging, microbial cell imaging, and plant cell imaging.

2.1 SiNPs for Mammalian Cell Imaging

In the past decade, SiNPs have been extensively investigated as a tracker for mammalian cell (including normal and cancer cell) imaging [5, 34, 75]. Herein, we will focus on the development of functional SiNP-based nanoprobes for various cell imaging purposes, such as macrophage imaging, immunofluorescence imaging, visualization of intracellular distributions of SiNPs, intracellular biomolecule/ion monitoring, tumor cell-specific imaging, and organelle imaging [10, 76–80].

2.1.1 Macrophage Imaging

It is widely known that macrophages are related to the inflammatory processes activated by the stimulation of exogenous agents including particles [81, 82]. The interactions between nanoparticles and phagocytic cells are important for the monitoring and modulation of the

behaviors and fates of the cells via these fluorescent nanoparticles. For example, Choi et al. investigated the inflammatory responses and cytotoxicity of photoluminescent SiNPs in RAW 264.7 macrophages [81]. They revealed that the ultrasmall SiNPs (<4 nm) could interact with the macrophages by attaching to the cell membranes or entering the cells through the pores in the cell membranes. Interestingly, these SiNPs induced negligible inflammatory responses and cytotoxicity, showing the excellent biocompatibility of the SiNPs.

In another work, paramagnetic and manganese-doped SiNPs were synthesized by Tu et al. in 2010 [83]. To actively target macrophages and image the macrophage density, the SiNPs were coated with dextran sulfate, a ligand for macrophage scavenger receptor class A (SR-A). The SR-A is a cell surface receptor and is primarily expressed by mature macrophages. Then, direct two-photon imaging at 780 nm excitation was performed. As shown in Fig. 2a, the uptake of the functionalized SiNPs was successfully visualized. The results indicated that the probes specifically accumulated in the macrophages by a receptor-mediated process. The authors have also verified that the prepared SiNPs could be used as a promising diagnostic agent for the detection of some diseases such as atherosclerosis, as a high macrophage density is associated with atherosclerotic plaques vulnerable to rupture.

2.1.2 Immunofluorescence Imaging

Immunofluorescence is a microscopy-based technique to detect specific antigens utilizing fluorescence-labeled antigen-targeting antibodies. Furthermore, immunofluorescence can also be used for the diagnosis of certain diseases through the detection of the fluorescent antibody–antigen complexes, which is widely used in both laboratory researches and clinical surgeries [86]. Taking advantage of their strong fluorescence, high photostability, and favorable biocompatibility, SiNPs have been recently employed as highly efficient fluorescent probes for immunofluorescence imaging [7, 17, 77, 87, 88]. As shown in Fig. 2b, the carboxyl group-containing antibody goat-antimouse immunoglobulin G (IgG) was conjugated to the amine-terminated SiNPs by Zhong et al. via the amine–carboxyl reaction [7]. The resultant SiNPs-IgG conjugates could serve as probes for cellular immunofluorescence labeling, which was verified by the green-fluorescent cellular microtubules that were stained with the green-emitting SiNPs-IgG conjugates (the nuclei were labeled by a blue-fluorescent cell-nucleus dye Hoechst).

In addition, Tu et al. demonstrated that antibody-conjugated SiNPs could achieve time-gated immunofluorescence imaging of live cancer cells using the drastic photoluminescence lifetime differentiation between SiNPs and organic dyes [87]. After separately staining the cell membrane and nucleus with the antibody-conjugated SiNPs and the organic dye (Hoechst 33342), the authors successfully distinguished the cell membrane and nucleus of a single cell from each other by the time-gated fluorescence imaging of the long-lived antibody-conjugated SiNPs (with lifetime in microseconds) and the short-lived organic dyes (with lifetime in nanoseconds), respectively. The distinguishment between different types of cells could also be achieved using a similar time-correlated imaging technique, which overcomes the limitations caused by fluorescence overlap when adopting the conventional multiplexing strategy.

2.1.3 Intracellular Distributions of SiNPs

With the rapid development of nanoscience and nanotechnology, nanocarriers have emerged as multifunctional platforms for cancer diagnosis and therapy with a variety of useful properties, such as: (1) long blood circulation time for increasing the uptake of drugs in target area, which will be further enhanced after modifying the surface of nanocarriers with targeting ligands; (2) improved intracellular uptake assisted with the cell-penetrating molecules; (3) ability to protect the loaded drugs from being prematurely degraded; (4) contrast/fluorescence properties for direct visualization after loading with various contrast/fluorescent materials; (5) capability to respond to various stimuli (e.g., pH, redox, and heat) for controllable release of drugs

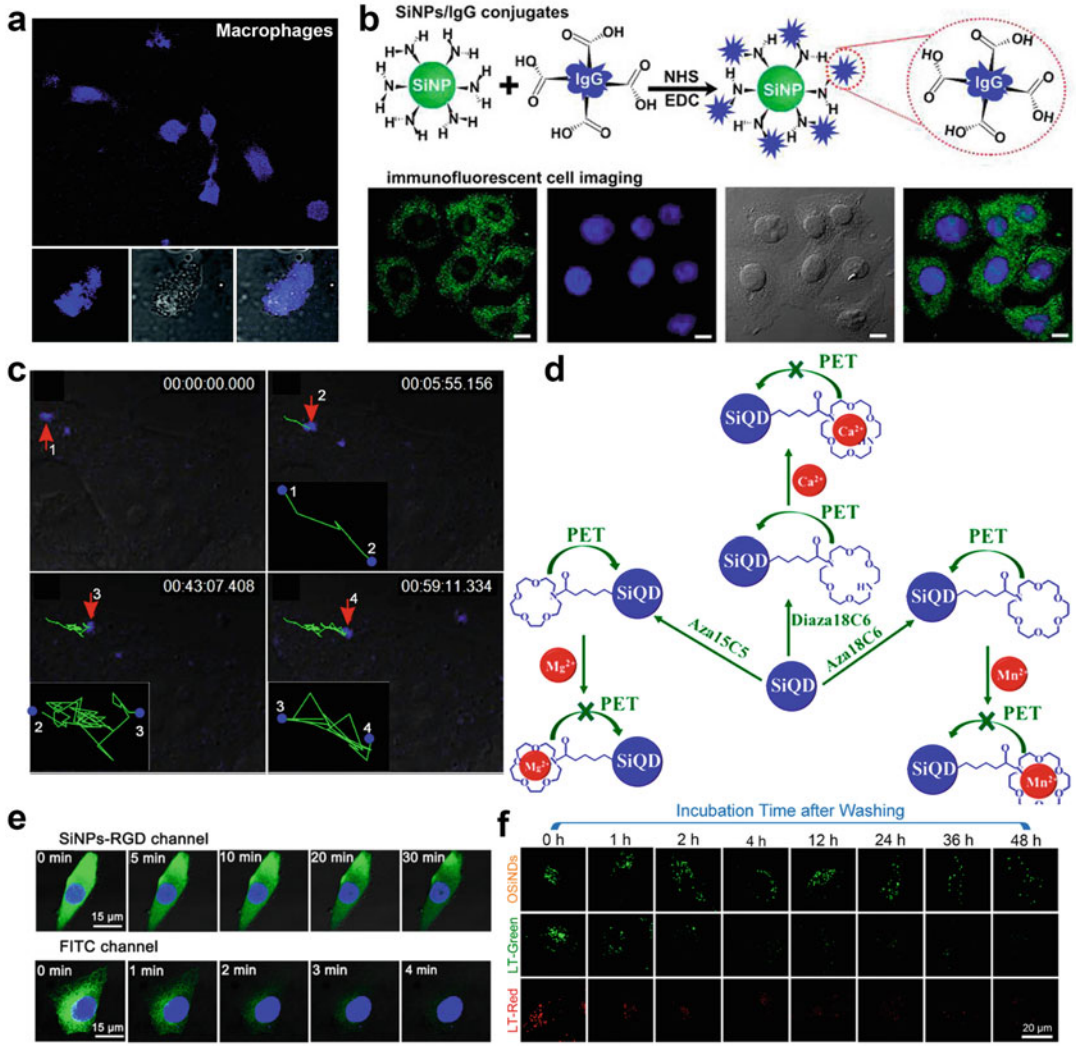

Fig. 2 (**a**) Two-photon microscopic images of macrophages treated with fluorescent SiNPs with excitation at 780 nm. Reprinted with permission from Ref. [83]. Copyright © 2010 American Chemical Society. (**b**) Schematic illustration of the antibody-conjugated SiNPs and their application in immunofluorescence imaging. Reprinted with permission from Ref. [7]. Copyright © 2015 American Chemical Society. (**c**) Real-time and long-term tracking of the movement of the SiNP-based complexes in one live HeLa cell (a human cervical carcinoma cell line). Reprinted with permission from Ref. [84]. Copyright © 2016 Springer Nature. (**d**) Schematic illustrating the design of fluorescent SiNP-based sensor system for the detection of metal ions in live cells. Reprinted with permission from Ref. [78]. Copyright © 2016 American Chemical Society. (**e**) Photostability comparison of the fluorescence signals of U87MG cells (human glioblastoma cells) incubated with arginine–glycine–aspartic acid sequence-conjugated SiNPs (SiNPs-RGD) and FITC. Reprinted with permission from Ref. [85]. Copyright © 2015 American Chemical Society. (**f**) Confocal fluorescence images illustrating the lysosomal imaging performance of OSiNDs, Lyso-Tracker Green (LT-Green), and Lyso-Tracker Red (LT-Red) in A549 cells (human lung cancer cells). Reprinted with permission from Ref. [50]. Copyright © 2018 American Chemical Society

[89, 90]. Understanding the intracellular distributions of nanocarriers will provide invaluable knowledge for revealing the subcellular fates of the nanocarriers and thus further facilitate their use in drug delivery. For instance, Pang et al. introduced photoluminescent SiNPs as a new

type of gene carrier [84]. The SiNP-based carriers feature bright and stable fluorescence, high deoxyribonucleic acid (DNA) loading/transfection efficiency, and favorable biocompatibility. Utilizing the fluorescence of the gene carriers (SiNPs), they successfully observed the long-term dynamic movements of the SiNPs in live cells in real time (Fig. 2c). The results provided important information on the intracellular behaviors of the gene carriers, such as the cellular uptake, intracellular distribution, and endosomal escape process. Moreover, the work presented the prospect of the fluorescent SiNP-based gene vectors as powerful tools for gene therapy.

2.1.4 Biomolecule or Ion Monitoring

Chemosensors play an important role in biological and medical fields. Biocompatible SiNPs with unique photoluminescence properties are of great interest and have been developed as a type of new materials to function as chemosensors for the detection of biomolecules or intracellular ions [13, 78, 91, 92]. For example, based on the fluorescence "turn-on" of silicon quantum dots (SiQDs) made from silicon tetrachloride, Dhenadhayalan et al. designed a multiple sensor system based on the aza-crown ether-functionalized SiQDs including SiQDs/aza15C5, SiQDs/aza18C6, and SiQDs/diaza18C6 for detecting individual Mg^{2+}, Mn^{2+}, and Ca^{2+} ions, respectively (Fig. 2d) [78]. The corresponding detection limits of the above three metal ions were 1.81, 0.47, and 3.15 μM. The practical application of the SiQD-based sensor system for intracellular metal ion detection was proven in the live HeLa cells. The authors explained the detection mechanism as a photoinduced electron transfer (PET)-based process: (1) After the SiQDs were coordinated with aza-crown ethers, the PET took place from the aza-crown ether moiety to the valence band of the SiQD core when the aza-crown ether-capped SiQDs were under photo-excitation, followed by the reduced probability of electron–hole recombination, resulting in the decreased fluorescence of the SiQDs. (2) When the specific metal ions were added, the PET effect was inhibited due to the presence of the charge–electron binding force between the metal ions and the aza-crown ethers, thus restoring the fluorescence of the SiNPs.

In another work, Zhao et al. constructed a ratiometric fluorescent probe using chlorin e6 (Ce6)-modified SiNPs [91]. The red-fluorescent Ce6 molecules (negatively charged) were attached to the surface of the blue-fluorescent amine-terminated SiNPs (positively charged) through electrostatic interaction. The designed probe Si–Ce6 nanocomplex emitted dual fluorescence with two emission peaks at 490 and 660 nm when using 410 nm as an excitation wavelength. When reactive oxygen species (ROS) were present, the fluorescence of SiNPs decreased while that of Ce6 remained constant, and the fluorescence intensity ratio of Ce6 (I_{660}) to SiNPs (I_{490}) increased linearly with the concentration of ROS. Thus, the dually emitting probe (the Si–Ce6 nanocomplex) could be used for the efficient detection and imaging of the ROS. Specifically, the constructed probe could be applied to sensitively and selectively detect the hydroxyl radical (•OH) with a low detection limit of ~0.97 μM. Furthermore, this study presented a successful example of monitoring the endogenous release of •OH in living cells using the SiNP-based nanoprobe.

2.1.5 Specific Tumor Cell Imaging

Fast and effective diagnosis of cancer cells has great significance in cancer treatments. Among various imaging technologies, the fluorescence imaging technology has been developed as a commonly used method due to the advantages of simplicity, high sensitivity, and rapidity [93–95]. SiNPs can be ideal candidates as cancer cell-specific probes by modifying their surfaces with specific targeting molecules [79, 85, 96]. In 2011, Erogbogbo et al. reported that amine-containing biomolecules including lysine, folate, anti-mesothelin, and transferrin could be covalently attached to biocompatible SiNPs terminated with carboxyl groups via the amine–carboxyl reaction [96]. Particularly, the folate- and anti-mesothelin-conjugated SiNPs showed selective uptake by Panc-1 cells (a human pancreatic adenocarcinoma cell line which has receptors for all the four biomolecules mentioned above (lysine, folate,

anti-mesothelin, and transferrin)). Additionally, as presented in Fig. 2e, Song et al. introduced a kind of peptide-conjugated SiNPs as probes for real-time labeling of cancer cells [85]. A cyclic peptide containing arginine–glycine–aspartic acid sequence (c(RGDyC)) was chosen as a representative peptide and conjugated to blue-fluorescent SiNPs (the resultant complexes were termed SiNPs-RGD). Taking advantage of the strong fluorescence (PLQY: ~28%) and robust photostability of the SiNPs and the tumor-targeting ability of the RGD, the SiNPs-RGD realized the long-term fluorescence labeling of cancer cells. The above examples illustrate that SiNPs can be a valuable optical probe for cancer diagnosis.

2.1.6 Organelle Imaging

Organelle is a specialized intracellular unit that performs a specific function in cellular behaviors. For example, the nucleus controls gene expression, the mitochondrion is responsible for cellular aerobic metabolism, and the lysosome regulates cell recycling [80]. Therefore, monitoring the states and changes of specific cellular organelles via fluorescent materials is crucial to understand and control the behaviors and fate of the whole cell. In 2018, our group reported for the first time the long-term imaging of lysosomes in living, fixed, and permeabilized cells using green-fluorescent organosilica nanodots (OSiNDs) [50]. The OSiNDs exhibited intrinsic lysosomal tracking ability without the introduction of lysosome-targeting ligands like morpholine and had exceptional lysosomal targeting performance with a very high Pearson's coefficient of 0.98. More importantly, the lysosomal monitoring time of these OSiNDs was up to 48 h, and the probes did not disturb the pH environment of lysosomes during the monitoring process (Fig. 2f). Overall, the presented lysosomal imaging performance of OSiNDs outperformed that of the current commercial lysosomal trackers (e.g., Lyso-Tracker Green and Lyso-Tracker Red) [50]. Furthermore, the work indicated that the excellent long-term lysosomal imaging capability of OSiNDs was attributed to their acidic environment-induced precipitation/aggregation of the OSiNDs within the acidic lysosomes.

Unfortunately, to the best of our knowledge, there have been no reports regarding the applications of photoluminescent SiNPs for imaging mitochondria, nucleus, or other organelles. New SiNPs capable of visualizing various subcellular structures are therefore highly desired.

2.2 SiNPs for Microbial Cell Imaging

Microbial infections cause millions of deaths annually. Rapid, effective, and economically friendly diagnosis of microorganisms such as bacteria, bacterial biofilms, and fungi is essential for the treatment of infectious diseases [97, 98]. As stated above, SiNPs feature ultrasmall size (<10 nm), bright photoluminescence, strong photostability, and good biocompatibility, and show great potential as fluorescent probes for microbial detection. In recent years, extensive efforts have been devoted to developing photoluminescent SiNP-based diagnostic agents. In this section, we focus on the recent advances in the use of SiNPs for imaging bacterial cells, bacterial biofilms, and fungal cells.

2.2.1 SiNPs for Imaging Bacterial Cells

To efficiently treat bacterial infections, sensitive and accurate identification of bacterial cell types is highly desirable. Currently, fluorescent SiNPs have been successfully adopted to identify bacterial cell types [93, 97, 99, 100]. As shown in Fig. 3a, blue-emitting quaternized SiNPs with polarity-sensitive fluorescence were prepared by our group for selective imaging of Gram-positive bacterial cells [99]. We demonstrated that the fluorescence emission property of the as-prepared quaternized SiNPs was influenced by the polarity of the solvent used to disperse these SiNPs, and the SiNPs generated the strongest emission intensity when they were dispersed in ethanol. The above results could explain the significantly enhanced fluorescence emission of the SiNPs when they accumulated inside the hydrophobic bacterial cells. Especially, we revealed that the quaternized SiNPs could realize

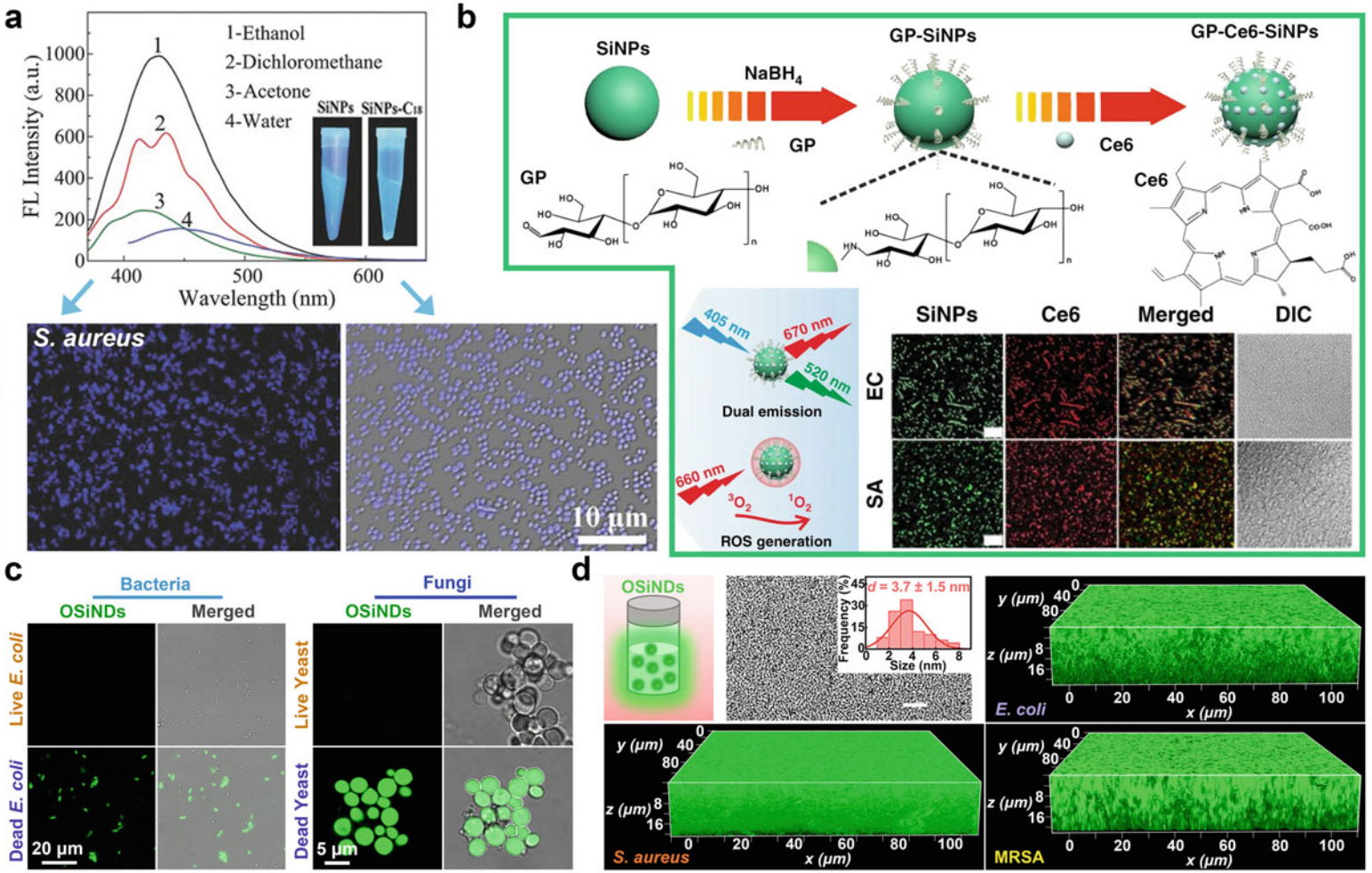

Fig. 3 (**a**) Fluorescence spectra of *N*-alkyl betaine-conjugated SiNPs (termed SiNPs-C_{18}) dispersed in different solvents (the insets are the photographs of SiNP aqueous suspension and SiNP-C_{18} aqueous suspension under 365 nm UV light irradiation), and the application of SiNPs-C_{18} in the imaging of Gram-positive bacteria (*S. aureus* cells). Reprinted with permission from Ref. [99]. Copyright © 2016 Wiley. (**b**) Synthetic route of the green-emitting SiNP-based agents with dual fluorescence emission and their application in the imaging of Gram-positive and Gram-negative bacterial cells. Scale bar: 10 μm. Reprinted with permission from Ref. [101]. Copyright © 2019 Nature Publishing Group. (**c**) Confocal microscopic images of bacterial and fungal cells stained with green-emitting OSiNDs. Reprinted with permission from Ref. [93]. Copyright © 2019 Elsevier Ltd. (**d**) Schematic illustrating the green fluorescence of OSiNDs, TEM image and corresponding size distribution histogram of OSiNDs, and three dimension-reconstructed confocal microscopic images of different bacterial biofilms stained with OSiNDs. Reprinted with permission from Ref. [47]. Copyright © 2019 Wiley. GP: glucose polymer. *E. coli*: *Escherichia coli*. MRSA: methicillin-resistant *Staphylococcus aureus*

sensitive and selective labeling of Gram-positive bacteria (taking *Staphylococcus aureus* (*S. aureus*) as a representative), which was possibly due to the strong interactions between the quaternized SiNPs and the cell walls/membranes of Gram-positive bacteria. Specifically, the Gram-positive bacteria with the negatively charged teichoic acids and thick peptidoglycan layers have a stronger affinity for the quaternary ammonium compounds than the Gram-negative bacteria with lipopolysaccharide-linked outer membranes.

In another work, Tang et al. prepared multifunctional SiNPs that could be used for simultaneously imaging Gram-positive and Gram-negative bacterial cells [101]. As indicated in Fig. 3b, the SiNPs prepared via a photochemical synthetic method using APTMS and 1,8-naphthalimide as the precursor and the reducing agent, respectively, were functionalized with glucose polymer (GP) and loaded with Ce6. The obtained GP-Ce6-SiNPs with dual emission (the red fluorescence from Ce6 molecules and the green fluorescence from SiNPs) could be rapidly internalized by Gram-positive and Gram-negative bacterial cells via an adenosine triphosphate (ATP)-binding cassette (ABC) transporter pathway. By tracking the green fluorescence of SiNPs and the red fluorescence of Ce6, diverse bacteria could be labeled with high sensitivity.

On the other hand, the wide use of antibiotics has led to the generation of multidrug-resistant bacteria (MRB) with high levels of drug tolerance, resulting in the decreased efficacies of antibacterial drugs and leading to a serious threat to the worldwide health [102, 103]. Very recently, our group successfully employed OSiNDs with green fluorescence emission as an imaging reagent for visualizing MRB [47]. We explained the efficient uptake of OSiNDs by MRB via the following three reasons: First, the OSiNDs had ultrasmall size (<5 nm), so they could enter bacterial cells. In addition, the surface of the OSiNDs contained epoxy groups, which might facilitate the bacterial uptake of the OSiNDs. Besides, the OSiNDs were negatively charged, which could protect the NPs from being recognized by the efflux proteins and intracellular enzymes of MRB, thus preventing the OSiNDs from being pumped out of the bacterial cells and degraded. This work reported the first successful example that applied SiNPs for the imaging of MRB, which may give an impetus to the development of new nanomaterials for the circumvention of bacterial multidrug resistance.

2.2.2 SiNPs for Imaging Fungal Cells

In addition to the threat of pathogenic bacterial infections, public health is also imperiled by invasive fungal infections. The threat to human health is continuously expanded due to the emergence of drug-resistant fungi, resulting in significant morbidity and mortality in infected patients [104]. The severe situation caused by drug-resistant fungal infections highlights the urgent need for new diagnostic and therapeutic agents. Metal-free SiNPs may be promising candidates for the theranostics of fungal infections. Unfortunately, few reports have employed the ultrasmall and photoluminescent SiNPs as fluorescent probes for imaging living fungal cells, let alone for tracking drug-resistant fungi. Up to date, only our group has reported the use of green-fluorescent SiNPs (termed OSiNDs) to label dead fungal cells [93]. We found that very few OSiNDs could be internalized by live bacterial/fungal cells (taking *E. coli* and Yeast as representatives, respectively), in sharp contrast to the rapid penetration of the probes into the dead bacterial/fungal cells with damaged surfaces, leading to the bright fluorescence of the dead bacterial/fungal cells (Fig. 3c).

2.2.3 SiNPs for Imaging Biofilms

Biofilm is a three-dimensional microbial community where microbes reside in an extracellular polymeric substance (EPS) matrix and are highly protected by the EPS [105, 106]. Biofilms have stubborn drug resistance and can cause persistent bacterial infections, since most antibacterial agents are not capable of penetrating into the full depth of the biofilms, thus reducing their therapeutic efficacies [107–109]. For a better treatment of biofilm-associated infections, the need for effective imaging tools should be stressed. However, few reports have employed SiNPs as fluorescent probes for imaging biofilms.

Our group has synthesized bright epoxy group-terminated OSiNDs with a size of ~3.7 nm, a slightly negative zeta potential of −3.2 mV, and a high PLQY of ~31% [47]. The ultrasmall size of the OSiNDs endowed the NPs with the ability to penetrate bacterial biofilms, because it was reported that 10 nm is a critical size for homogeneous biofilm staining [110]. The negative zeta potential of OSiNDs prevented the probes from being detained by the EPS matrix of the bacterial biofilms. We have also confirmed that the green-fluorescent OSiNDs could rapidly and deeply penetrate various types of bacterial biofilms including the biofilms formed by Gram-positive *S. aureus*, Gram-negative *E. coli*, and MRSA (Fig. 3d), achieving the universal and favorable imaging of biofilms for the first time. Through the reaction between the amine group and the epoxy group, the amine-containing antibiotic vancomycin (Van) was conjugated to the epoxy group-terminated OSiNDs. The resultant OSiNDs-Van could successfully inhibit the growth of MRSA and even eliminate the biofilms formed by MRSA. This work illustrates the possibility of using metal-free SiNPs for the theranostics of biofilm-caused infections.

2.3 SiNPs for Plant Cell Imaging

Currently, nanotechnology plays a critical role in the development of agriculture considering that more and more functional nanoparticles have found applications in plants [111]. Especially, photoluminescent nanoparticles with favorable optical properties, low cytotoxicity, surface modifiability, as well as physiological stability can be ideal materials for the plant research, such as plant cell imaging. The high-quality plant cell imaging may help to reveal the detailed structure of plant cells, illustrate the signal transduction process in plant cells, and investigate the nutrition transport process within plant cells. Fluorescent SiNPs with ultrasmall sizes (<5 nm) could be excellent probes for plant cell imaging, due to the small pore sizes (3.2–5.2 nm) of plant cells [111, 112]. However, only a few studies on plant cell imaging have been reported.

In 2019, Li et al. proposed a biomimetic approach for the facile synthesis of red-emissive SiNPs using unicellular algae of diatoms as a reaction precursor [113]. The resultant ultrasmall SiNPs with an average size of 2.0 nm had the ability to enter plant cells via the pathway of free diffusion (Fig. 4a). Additionally, the SiNPs possessed a high quantum yield of ~15% and a narrow FWHM of ~35 nm. As shown in Fig. 4b, the confocal images of the cucumber seedling root, the stem longitudinal section, and the leaf transverse section indicated that the SiNPs could be internalized by cucumber seedlings and transmitted from the root to the leaf section, showing the phytophysiology effect of the SiNPs on the growth of cucumber seedlings.

3 SiNPs for In Vivo Cellular Imaging

In vivo imaging is crucial for revealing target morphology/distribution and improving the therapeutic efficiencies of site-specific operations. As biocompatible and photoluminescence-tunable nanomaterials, SiNPs have high clinical potential for use as diagnostic probes with well-defined morphology, favorable photoluminescence, and modifiable surfaces yielding desirable properties and functions [114]. Recent progress in the development of fluorescent SiNP-based multimodal imaging nanoprobes has advanced their applications in imaging-guided drug delivery and theranostics of malignant tumors or infections [115, 116]. The aim of this section is to describe the recent advances in the development of in vivo imaging technologies based on SiNPs.

Briefly, various in vivo models have been adopted for testing the feasibility of using SiNPs for in vivo imaging applications, such as zebrafish including embryos and adults, *Caenorhabditis elegans* (*C. elegans*), and mice [19, 76, 114, 116–120]. First, for the application of fluorescent SiNPs in live/dead discrimination of zebrafish, green-fluorescent OSiNDs which could only light up dead zebrafish with strong green fluorescence were used by our group to differentiate

between live and dead zebrafish (including embryos and adults) [93]. Furthermore, due to their high sensitivity to cell viability, the OSiNDs could be applied to monitor the real-time change of the cellular viability in zebrafish upon the treatment of the commonly used anticancer drug doxorubicin, showing the great potential of the OSiNDs in evaluating the drug toxicity/efficacy in vivo. Regarding the use of SiNPs for imaging living zebrafish embryos, Ye et al. synthesized amino group-terminated SiNPs (~4.2 nm) with excellent water dispersibility via a one-pot microwave-assisted method [120]. The SiNPs featured bright blue-green fluorescence with a high PLQY of 47% and a long lifetime of 12.8 ns. As shown in Fig. 5a, evident green fluorescence signals of the as-prepared SiNPs successfully appeared in the zebrafish embryos. Additionally, the authors demonstrated that the internalized SiNPs did not affect the natural development of the zebrafish embryos to the zebrafish larvae, proving the good in vivo safety of the SiNPs.

On the other hand, Srivastava et al. observed the phototoxicity of SiNPs in vivo using zebrafish as an animal model [117]. The used SiNPs (~5 nm) had a long photoluminescence lifetime of ~13.56 μs and could function as photosensitizers that could transfer the absorbed energy from optical light to oxygen molecules in proximity, generating the cytotoxic singlet oxygen. Zebrafish were microinjected with the SiNPs at the dorsal trunk regions, and then irradiated by the blue light or kept in the dark. Figure 5b revealed that the SiNP-treated zebrafish with light irradiation showed remarkable green fluorescence signals near the microinjection sites, while the one without light treatment showed no fluorescence signals. The subsequent acridine orange (a dye for the detection of cell apoptosis) staining results revealed the presence of cell apoptosis near the microinjection site of the zebrafish, whereas no apoptosis was found for the SiNP-treated zebrafish without light irradiation, confirming the phototoxic effect of the used SiNPs under light irradiation.

In another example, Wu et al. produced two kinds of SiNPs with separate blue and red fluorescence using a biomimetic preparation approach [19]. The resultant SiNPs had PLQYs of 15–20%, narrow FWHM values of ~30 nm, and nontoxicity. By simultaneously employing the blue- and red-fluorescent SiNPs, dual-color fluorescence imaging in vivo was realized by selecting *C. elegans* as an animal model. The blue- and red-emitting SiNPs were microinjected to the digestive (intestine) and reproductive (gonad) systems of *C. elegans*, respectively. As displayed in Fig. 5c, the blue and red fluorescence signals of the blue-emitting SiNPs and the red-emitting SiNPs were detected in the gut lumen/intestinal cells and gonad of *C. elegans*, respectively, proving the feasibility of using SiNPs for dual-color imaging in vivo.

Regarding the mouse model, Erogbogbo et al. prepared near-infrared (NIR)-emitting SiNPs using a method of laser pyrolysis followed with acid etching [121]. Then the synthesized SiNPs were encapsulated by the PEGylated micelles with various surface terminations including the amine, folate, methoxy, and carboxyl groups. Through the amine–carboxyl reaction, the RGD peptide was linked to the surface of the carboxyl group-terminated micelle encapsulating SiNPs. The obtained micelle-encapsulated SiNPs were successfully applied in multiple cancer-related imaging in vivo, including tumor vasculature imaging, sentinel lymph node tracking, and multiplex NIR imaging in living mice (Fig. 5d). Notably, the micelle-encapsulated SiNPs had long tumor accumulation time (>40 h) in vivo, exhibiting the stable photoluminescence and strong tumor-targeting ability of the micelle-functionalized SiNPs.

Besides, for achieving multimodal imaging in vivo, a new macrocyclic ligand–$^{64}Cu^{2+}$ complex was synthesized by Tu et al. and used to label dextran-coated SiNPs which had an average hydrodynamic diameter of 15.1 ± 7.6 nm [115]. By employing the in vivo positron emission tomography (PET) imaging technology, the authors revealed the in vivo biodistribution of the SiNP-based complex, in which the urinary bladder and the liver were the main sites for drug accumulation after 5 min and 1 h post tail-vein injection. At 4 h and 24 h post injection, the complex mainly accumulated in the liver

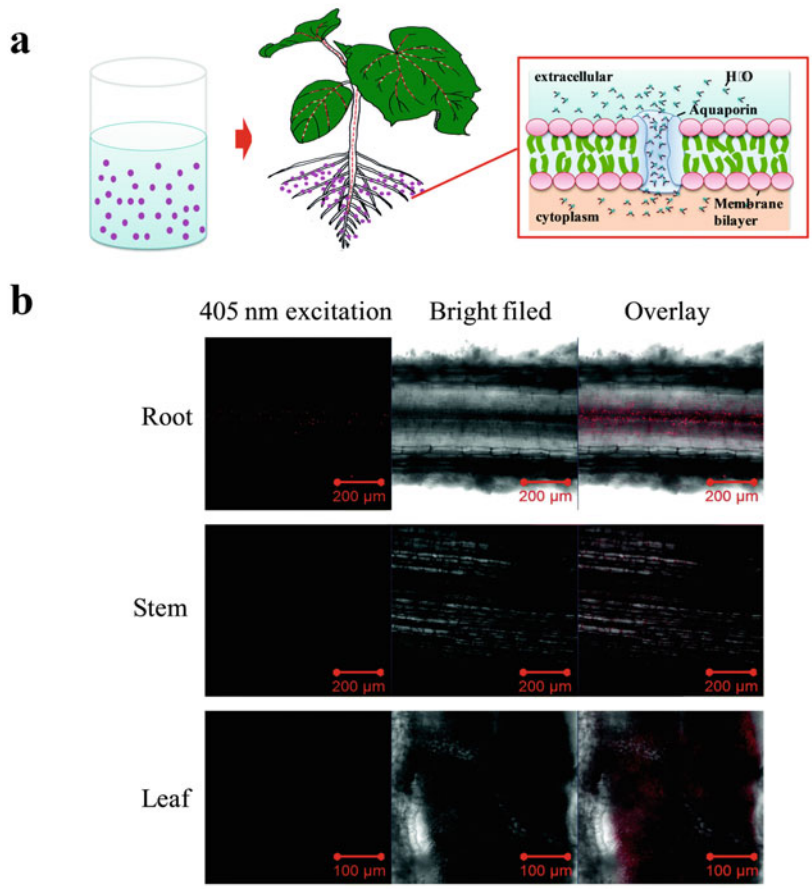

Fig. 4 (**a**) Schematic illustration of the uptake and transport of SiNPs (obtained using unicellular algae of diatoms as a reaction precursor) by cucumber seedlings. (**b**) Confocal microscopic images of the cucumber seedling root, the stem longitudinal section, and the leaf transverse section after 10 days of cultivation in the presence of SiNP suspension (0.3 mg/mL). Reprinted with permission from Ref. [113]. Copyright © 2015 Royal Society of Chemistry

(Fig. 5e). The real-time biodistribution results of the SiNP-based agents may provide useful information for designing new SiNP-based nanomaterials for in vivo theranostics.

4 Conclusion and Future Perspective

Over the past decades, SiNPs have achieved remarkable progress in the improvement of their physicochemical properties (e.g., core composition, size, surface chemistry, and photoluminescence) and cell imaging applications both in vitro and in vivo. Especially, the cell imaging applications of SiNPs have been significantly expanded from mammalian cell lines to microbial cells, and even to plant cells. Furthermore, satisfactory results about the utilization of SiNPs as probes for in vivo imaging have been obtained using various animal models.

Despite the great progress achieved up till now, many efforts are still required in the future: (1) Developing a gentle synthetic method to achieve the efficient, low-cost, and large-scale preparation of fluorescent SiNPs is of great importance, since many adopted methods of preparing silicon nanomaterials require harsh preparation conditions, such as high temperature, oxygen-free atmosphere, vacuum, electric field, or ion sputtering. (2) Simple methods for the preparation of water-dispersible SiNPs with bright red/NIR photoluminescence still remain highly desirable, as most reported SiNPs are blue- or green-fluorescent and their cell imaging applications are largely limited by the

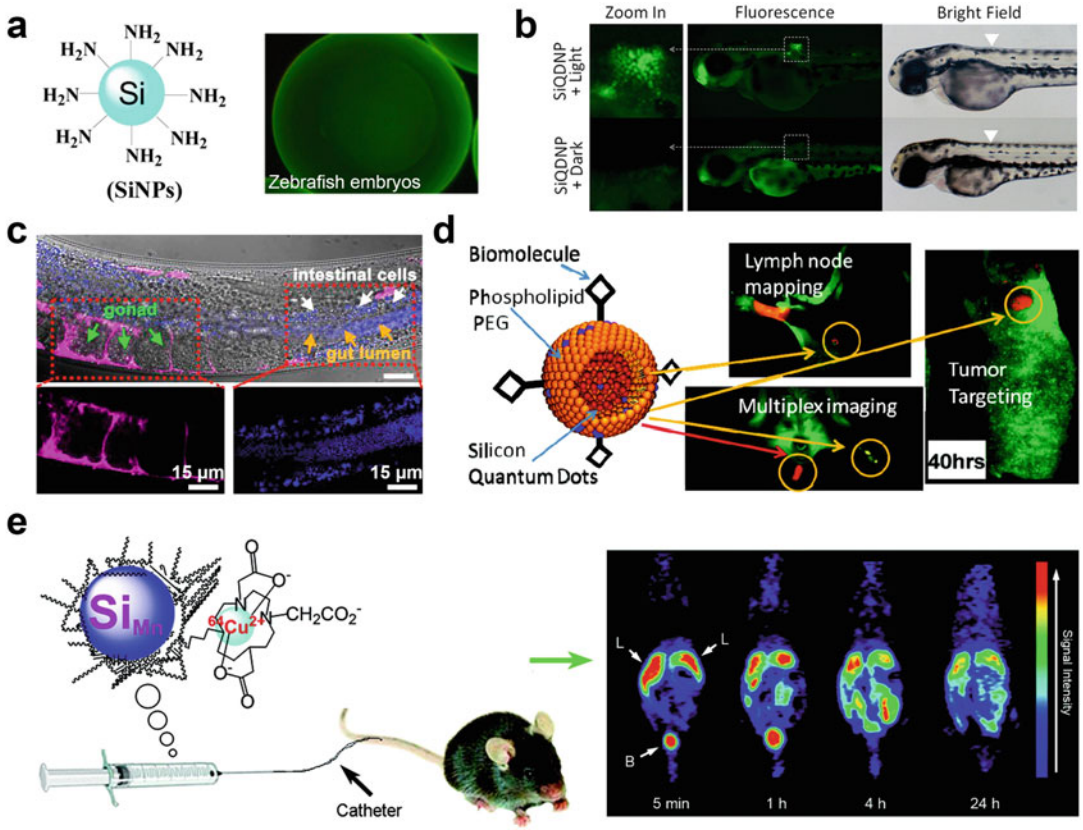

Fig. 5 (**a**) Schematic illustration of SiNPs and their imaging application in zebrafish embryos. Reprinted with permission from Ref. [120]. Copyright © 2016 American Chemical Society. (**b**) Fluorescence and bright field microscopic images of zebrafish microinjected with the SiNP suspension at the dorsal trunk regions, followed by illumination under 450 nm blue light-emitting diode light or keeping in the dark for 6 h. The white triangles in the bright field panels indicate the microinjection sites. Reprinted with permission from Ref. [117]. Copyright © 2019 American Chemical Society. (**c**) Representative confocal microscopic images of the as-prepared SiNPs in *C. elegans* by microinjection. The gonad and gut lumen are stained by red- and blue-emitting SiNPs, respectively (top). The two bottom panels are the enlarged images corresponding to the boxed areas in the top panel. The scale bar in the top panel is 20 μm and the ones in the bottom panels are 15 μm. Reprinted with permission from Ref. [19]. Copyright © 2015 American Chemical Society. (**d**) Schematic illustrating the structure of the functionalized SiNPs used for in vivo targeted cancer imaging, sentinel lymph node mapping, and multiplex NIR imaging. Reprinted with permission from Ref. [121]. Copyright © 2011 American Chemical Society. (**e**) Schematic illustrating the synthesis of ^{64}Cu-DO3A-conjugated dextran Si_{Mn} NPs and their application in PET imaging in vivo. Reprinted with permission from Ref. [115]. Copyright © 2011 American Chemical Society

autofluorescence of cells and the low tissue penetration depths of their fluorescence. (3) The SiNP-based probes with superior optical properties for targeting specific subcellular structures (such as plasma membranes/cell walls, centrosomes, endoplasmic reticulum, mitochondria, peroxisomes, and cell nuclei) are still lacking and need to be developed for the better monitoring of the states and changes of these subcellular components and even the whole cells. In addition, the subcellular structure-targeting mechanisms of these SiNPs are largely unknown and require to be elucidated, which will enable the rational design of desired SiNPs with satisfactory targeting capabilities. (4) The SiNP-based nanomaterials that can realize the accurate

discrimination of cell types also need to be developed. (5) Fluorescent SiNPs capable of imaging fungal cells are still lacking. (6) The research on the use of fluorescent SiNPs in plant cell imaging is still in its infancy. For example, more SiNP-based fluorescent probes that can light up the cell wall, cell membrane, and specific organelles of the plant cells, or the plant issues, need to be prepared. In addition, efforts should be made in using SiNPs to visualize and detect the biomolecules and ions in plant cells. We believe that the development of these functional SiNPs will significantly expand the applications of SiNPs in the related fields.

References

1. Dasog M, Kehrle J, Rieger B, Veinot JGC (2016) Silicon nanocrystals and silicon-polymer hybrids: synthesis, surface engineering, and applications. Angew Chem Int Ed 55:2322–2339
2. Thiessen AN, Ha M, Hooper RW, Yu HY, Oliynyk AO, Veinot JGC, Michaelis VK (2019) Silicon nanoparticles: are they crystalline from the core to the surface? Chem Mater 31:678–688
3. Cheng XY, Lowe SB, Reece PJ, Gooding JJ (2014) Colloidal silicon quantum dots: from preparation to the modification of self-assembled monolayers (SAMs) for bio-applications. Chem Soc Rev 43:2680–2700
4. Wu FG, Zhang XD, Kai SQ, Zhang MY, Wang HY, Myers JN, Weng YX, Liu PD, Gu N, Chen Z (2015) One-step synthesis of superbright water-soluble silicon nanoparticles with photoluminescence quantum yield exceeding 80%. Adv Mater Interfaces 2:1500360
5. Peng F, Su YY, Zhong YL, Fan CH, Lee ST, He Y (2014) Silicon nanomaterials platform for bioimaging, biosensing, and cancer therapy. Acc Chem Res 47:612–623
6. Atkins TM, Cassidy MC, Lee M, Ganguly S, Marcus CM, Kauzlarich SM (2013) Synthesis of long T_1 silicon nanoparticles for hyperpolarized ^{29}Si magnetic resonance imaging. ACS Nano 7:1609–1617
7. Zhong YL, Sun XT, Wang SY, Peng F, Bao F, Su YY, Li YY, Lee ST, He Y (2015) Facile, large-quantity synthesis of stable, tunable-color silicon nanoparticles and their application for long-term cellular imaging. ACS Nano 9:5958–5967
8. Chen X, Soeriyadi AH, Lu X, Sagnella SM, Kavallaris M, Gooding JJ (2014) Dual bioresponsive mesoporous silica nanocarrier as an "AND" logic gate for targeted drug delivery cancer cells. Adv Funct Mater 24:6999–7006
9. Cheng XY, Hinde E, Owen DM, Lowe SB, Reece PJ, Gaus K, Gooding JJ (2015) Enhancing quantum dots for bioimaging using advanced surface chemistry and advanced optical microscopy: application to silicon quantum dots (SiQDs). Adv Mater 27:6144–6150
10. Ji XY, Peng F, Zhong YL, Su YY, Jiang XX, Song CX, Yang L, Chu BB, Lee ST, He Y (2015) Highly fluorescent, photostable, and ultrasmall silicon drug nanocarriers for long-term tumor cell tracking and in-vivo cancer therapy. Adv Mater 27:1029–1034
11. Han YX, Chen YL, Feng J, Liu JJ, Ma SD, Chen XG (2017) One-pot synthesis of fluorescent silicon nanoparticles for sensitive and selective determination of 2,4,6-trinitrophenol in aqueous solution. Anal Chem 89:3001–3008
12. Ma SD, Chen YL, Feng J, Liu JJ, Zuo XW, Chen XG (2016) One-step synthesis of water-dispersible and biocompatible silicon nanoparticles for selective heparin sensing and cell imaging. Anal Chem 88:10474–10481
13. Zhang XD, Chen XK, Kai SQ, Wang HY, Yang JJ, Wu FG, Chen Z (2015) Highly sensitive and selective detection of dopamine using one-pot synthesized highly photoluminescent silicon nanoparticles. Anal Chem 87:3360–3365
14. Zhong YL, Peng F, Wei XP, Zhou YF, Wang J, Jiang XX, Su YY, Su S, Lee ST, He Y (2012) Microwave-assisted synthesis of biofunctional and fluorescent silicon nanoparticles using proteins as hydrophilic ligands. Angew Chem Int Ed 51:8485–8489
15. He Y, Kang ZH, Li QS, Tsang CHA, Fan CH, Lee ST (2009) Ultrastable, highly fluorescent, and water-dispersed silicon-based nanospheres as cellular probes. Angew Chem Int Ed 48:128–132
16. Warner JH, Hoshino A, Yamamoto K, Tilley RD (2005) Water-soluble photoluminescent silicon quantum dots. Angew Chem Int Ed 44:4550–4554
17. He Y, Su YY, Kang ZH, Xu TT, Zhang RQ, Fan CH, Lee ST (2009) Photo and pH stable, highly-luminescent silicon nanospheres and their bioconjugates for immunofluorescent cell imaging. J Am Chem Soc 131:4434–4438
18. He Y, Zhong YL, Peng F, Wei XP, Su YY, Lu YM, Su S, Gu W, Liao LS, Lee ST (2011) One-pot microwave synthesis of water-dispersible, ultraphoto- and pH-stable, and highly fluorescent silicon quantum dots. J Am Chem Soc 133:14192–14195
19. Wu SC, Zhong YL, Zhou YF, Song B, Chu BB, Ji XY, Wu YY, Su YY, He Y (2015) Biomimetic preparation and dual-color bioimaging of fluorescent silicon nanoparticles. J Am Chem Soc 137:14726–14732
20. Cheng XY, McVey BFP, Robinson AB, Longatte G, O'Mara PB, Tan VTG, Thordarson P, Tilley RD, Gaus K, Gooding JJ (2017) Protease sensing using

nontoxic silicon quantum dots. J Biomed Opt 22:087002
21. Woods M, Carlsson S, Hong Q, Patole SN, Lie LH, Houlton A, Horrocks BR (2005) A kinetic model of the formation of organic monolayers on hydrogen-terminated silicon by hydrosilation of alkenes. J Phys Chem B 109:24035–24045
22. Dohnalová K, Poddubny AN, Prokofiev AA, de Boer WDAM, Umesh CP, Paulusse JMJ, Zuilhof H, Gregorkiewicz T (2013) Surface brightens up Si quantum dots: direct bandgap-like size-tunable emission. Light: Sci Appl 2:e47
23. Choi JK, Dung MX, Jeong H-D (2014) Novel synthesis of covalently linked silicon quantum dot–polystyrene hybrid materials: silicon quantum dot–polystyrene polymers of tunable refractive index. Mater Chem Phys 148:463–472
24. Li ZF, Ruckenstein E (2004) Water-soluble poly (acrylic acid) grafted luminescent silicon nanoparticles and their use as fluorescent biological staining labels. Nano Lett 4:1463–1467
25. Wolf O, Dasog M, Yang Z, Balberg I, Veinot JGC, Millo O (2013) Doping and quantum confinement effects in single Si nanocrystals observed by scanning tunneling spectroscopy. Nano Lett 13:2516–2521
26. Gonzalez CM, Iqbal M, Dasog M, Piercey DG, Lockwood R, Klapotke TM, Veinot JGC (2014) Detection of high-energy compounds using photoluminescent silicon nanocrystal paper based sensors. Nanoscale 6:2608–2612
27. Zhang J, Yu SH (2014) Highly photoluminescent silicon nanocrystals for rapid, label-free and recyclable detection of mercuric ions. Nanoscale 6:4096–4101
28. Takeoka S (2000) Size-dependent photoluminescence from surface-oxidized Si nanocrystals in a weak confinement regime. Phys Rev B 62:16820–16825
29. Liu JW, Erogbogbo F, Yong KT, Ye L, Liu J, Hu R, Chen HY, Hu YZ, Yang Y, Yang JH, Roy I, Karker NA, Swihart MT, Prasad PN (2013) Assessing clinical prospects of silicon quantum dots: studies in mice and monkeys. ACS Nano 7:7303–7310
30. Croissant JG, Fatieiev Y, Khashab NM (2017) Degradability and clearance of silicon, organosilica, silsesquioxane, silica mixed oxide, and mesoporous silica nanoparticles. Adv Mater 29:1604634
31. Cao ZH, Peng F, Hu ZL, Chu BB, Zhong YL, Su YY, He SD, He Y (2017) In vitro cellular behaviors and toxicity assays of small-sized fluorescent silicon nanoparticles. Nanoscale 9:7602–7611
32. Licciardello N, Hunoldt S, Bergmann R, Singh G, Mamat C, Faramus A, Ddungu JLZ, Silvestrini S, Maggini M, De Cola L, Stephan H (2018) Biodistribution studies of ultrasmall silicon nanoparticles and carbon dots in experimental rats and tumor mice. Nanoscale 10:9880–9891
33. Zhang XD, Chen XK, Wang HY, Jia HR, Wu FG (2019) Supramolecular nanogel-based universal drug carriers formed by "soft–hard" co-assembly: accurate cancer diagnosis and hypoxia-activated cancer therapy. Adv Therap 2:1800140
34. Chinnathambi S, Chen S, Ganesan S, Hanagata N (2014) Silicon quantum dots for biological applications. Adv Healthc Mater 3:10–29
35. Singh MP, Atkins TM, Muthuswamy E, Kamali S, Tu CQ, Louie AY, Kauzlarich SM (2012) Development of iron-doped silicon nanoparticles as bimodal imaging agents. ACS Nano 6:5596–5604
36. Bose S, Ganayee MA, Mondal B, Baidya A, Chennu S, Mohanty JS, Pradeep T (2018) Synthesis of silicon nanoparticles from rice husk and their use as sustainable fluorophores for white light emission. ACS Sustain Chem Eng 6:6203–6210
37. Wu CY, Peng X, Lu QJ, Li HT, Zhang YY, Yao SZ (2018) Ultrasensitive silicon nanoparticle ratiometric fluorescence determination of mercury(II). Anal Lett 51:1013–1028
38. Ban R, Zheng FF, Zhang JR (2015) A highly sensitive fluorescence assay for 2,4,6-trinitrotoluene using amine-capped silicon quantum dots as a probe. Anal Methods 7:1732–1737
39. Guo YM, Zhang LF, Cao FP, Mang LH, Lei XL, Cheng SJ, Song JT (2016) Hydrothermal synthesis of blue-emitting silicon quantum dots for fluorescent detection of hypochlorite in tap water. Anal Methods 8:2723–2728
40. Jose AR, Sivasankaran U, Menon S, Kumar KG (2016) A silicon nanoparticle based turn off fluorescent sensor for Sudan I. Anal Methods 8:5701–5706
41. Chen HY, Wu L, Wan YQ, Huang LL, Li NX, Chen JY, Lai GS (2019) One-step rapid synthesis of fluorescent silicon nanodots for a hydrogen peroxide-related sensitive and versatile assay based on the inner filter effect. Analyst 144:4006–4012
42. McVey BFP, Prabakar S, Gooding JJ, Tilley RD (2017) Solution synthesis, surface passivation, optical properties, biomedical applications, and cytotoxicity of silicon and germanium nanocrystals. ChemPlusChem 82:60–73
43. Zhang, XD, Chen XK, Guo YX, Jia HR, Jiang YW, Wu FG (2020) Endosome/lysosome-detained supramolecular nanogels as an efflux retarder and autophagy inhibitor for repeated photodynamic therapy of multidrug-resistant cancer. Nanoscale Horiz 5:481–487
44. Chen XK, Zhang XD, Guo YX, Zhu YX, Liu XY, Chen Z, Wu FG (2019) Smart supramolecular "Trojan horse"-inspired nanogels for realizing light-triggered nuclear drug influx in drug-resistant cancer cells. Adv Funct Mater 29:1807772
45. Cheng XY, Guan B (2017) Optical biosensing and bioimaging with porous silicon and silicon quantum dots. Prog Electromagn Res 160:103–121
46. Xu XL, Ma SY, Xiao XC, Hu Y, Zhao D (2016) The preparation of high-quality water-soluble silicon quantum dots and their application in the detection of formaldehyde. RSC Adv 6:98899–98907

47. Chen XK, Zhang XD, Lin FM, Guo YX, Wu FG (2019) One-step synthesis of epoxy group-terminated organosilica nanodots: a versatile nanoplatform for imaging and eliminating multidrug-resistant bacteria and their biofilms. Small 15:1901647
48. Li Q, Jin RC (2017) Photoluminescence from colloidal silicon nanoparticles: significant effect of surface. Nanotechnol Rev 6:601–612
49. Oliinyk BV, Korytko D, Lysenko V, Alekseev S (2019) Are fluorescent silicon nanoparticles formed in a one-pot aqueous synthesis? Chem Mater 31:7167–7172
50. Chen XK, Zhang XD, Xia LY, Wang HY, Chen Z, Wu FG (2018) One-step synthesis of ultrasmall and ultrabright organosilica nanodots with 100% photoluminescence quantum yield: long-term lysosome imaging in living, fixed, and permeabilized cells. Nano Lett 18:1159–1167
51. McVey BFP, Tilley RD (2014) Solution synthesis, optical properties, and bioimaging applications of silicon nanocrystals. Acc Chem Res 47:3045–3051
52. Ravotto L, Chen Q, Ma YG, Vinogradov SA, Locritani M, Bergamini G, Negri F, Yu YX, Korgel BA, Ceroni P (2017) Bright long-lived luminescence of silicon nanocrystals sensitized by two-photon absorbing antenna. Chem 2:550–560
53. Hessel CM, Reid D, Panthani MG, Rasch MR, Goodfellow BW, Wei JW, Fujii H, Akhavan V, Korgel BA (2012) Synthesis of ligand-stabilized silicon nanocrystals with size-dependent photoluminescence spanning visible to near-infrared wavelengths. Chem Mater 24:393–401
54. Kelly JA, Shukaliak AM, Fleischauer MD, Veinot JGC (2011) Size-dependent reactivity in hydrosilylation of silicon nanocrystals. J Am Chem Soc 133:9564–9571
55. Warner JH, Rubinsztein-Dunlop H, Tilley RD (2005) Surface morphology dependent photoluminescence from colloidal silicon nanocrystals. J Phys Chem B 109:19064–19067
56. Fuzell J, Thibert A, Atkins TM, Dasog M, Busby E, Veinot JGC, Kauzlarich SM, Larsen DS (2013) Red states versus blue states in colloidal silicon nanocrystals: exciton sequestration into low-density traps. J Phys Chem Lett 4:3806–3812
57. English DS, Pell LE, Yu ZH, Barbara PF, Korgel BA (2002) Size tunable visible luminescence from individual organic monolayer stabilized silicon nanocrystal quantum dots. Nano Lett 2:681–685
58. Mastronardi ML, Maier-Flaig F, Faulkner D, Henderson EJ, Kubel C, Lemmer U, Ozin GA (2012) Size-dependent absolute quantum yields for size-separated colloidally-stable silicon nanocrystals. Nano Lett 12:337–342
59. Shen XB, Song B, Fang B, Yuan X, Li YY, Wang SY, Ji SJ, He Y (2018) Solvent polarity-induced photoluminescence enhancement (SPIPE): a method enables several-fold increase in quantum yield of silicon nanoparticles. Nano Res 12:315–322
60. Jurbergs D, Rogojina E, Mangolini L, Kortshagen U (2006) Silicon nanocrystals with ensemble quantum yields exceeding 60%. Appl Phys Lett 88:233116
61. Li Q, He Y, Chang J, Wang L, Chen HZ, Tan YW, Wang HY, Shao ZZ (2013) Surface-modified silicon nanoparticles with ultrabright photoluminescence and single-exponential decay for nanoscale fluorescence lifetime imaging of temperature. J Am Chem Soc 135:14924–14927
62. Li Q, Luo TY, Zhou M, Abroshan H, Huang JC, Kim HJ, Rosi NL, Shao ZZ, Jin RC (2016) Silicon nanoparticles with surface nitrogen: 90% quantum yield with narrow luminescence bandwidth and the ligand structure based energy law. ACS Nano 10:8385–8393
63. Dasog M, De los Reyes GB, Titova LV, Hegmann FA, Veinot JGC (2014) Size vs surface: tuning the photoluminescence of freestanding silicon nanocrystals across the visible spectrum via surface groups. ACS Nano 8:9636–9648
64. Hurley PT, Ribbe AE, Buriak JM (2003) Nanopatterning of alkynes on hydrogen-terminated silicon surfaces by scanning probe-induced cathodic electrografting. J Am Chem Soc 125:11334–11339
65. Chatterjee S, Mukherjee TK (2013) Size-dependent differential interaction of allylamine-capped silicon quantum dots with surfactant assemblies studied using photoluminescence spectroscopy and imaging technique. J Phys Chem C 117:10799–10808
66. Höhlein IMD, Kehrle J, Purkait TK, Veinot JGC, Rieger B (2015) Photoluminescent silicon nanocrystals with chlorosilane surfaces—synthesis and reactivity. Nanoscale 7:914–918
67. Zhou TL, Anderson RT, Li HS, Bell J, Yang YA, Gorman BP, Pylypenko S, Lusk MT, Sellinger A (2015) Bandgap tuning of silicon quantum dots by surface functionalization with conjugated organic groups. Nano Lett 15:3657–3663
68. Das P, Jana NR (2014) Highly colloidally stable hyperbranched polyglycerol grafted red fluorescent silicon nanoparticle as bioimaging probe. ACS Appl Mater Interfaces 6:4301–4309
69. Manhat BA, Brown AL, Black LA, Ross JBA, Fichter K, Vu T, Richman E, Goforth AM (2011) One-step melt synthesis of water soluble, photoluminescent, surface-oxidized silicon nanoparticles for cellular imaging applications. Chem Mater 23:2407–2418
70. Hsu CW, Septiadi D, Lai CH, Chen PK, Seeberger PH, De Cola L (2017) Glucose-modified silicon nanoparticles for cellular imaging. ChemPlusChem 82:660–667
71. Lai CH, Hutter J, Hsu CW, Tanaka H, Varela-Aramburu S, De Cola L, Lepenies B, Seeberger PH (2016) Analysis of carbohydrate-carbohydrate interactions using sugar-functionalized silicon nanoparticles for cell imaging. Nano Lett 16:807–811
72. Montalti M, Cantelli A, Battistelli G (2015) Nanodiamonds and silicon quantum dots: ultrastable

and biocompatible luminescent nanoprobes for long-term bioimaging. Chem Soc Rev 44:4853–4921
73. Su YY, Ji XY, He Y (2016) Water-dispersible fluorescent silicon nanoparticles and their optical applications. Adv Mater 28:10567–10574
74. Henderson EJ, Shuhendler AJ, Prasad P, Baumann V, Maier-Flaig F, Faulkner DO, Lemmer U, Wu XY, Ozin GA (2011) Colloidally stable silicon nanocrystals with near-infrared photoluminescence for biological fluorescence imaging. Small 7:2507–2516
75. Ji XY, Wang HY, Song B, Chu BB, He Y (2018) Silicon nanomaterials for biosensing and bioimaging analysis. Front Chem 6:38
76. Erogbogbo F, Yong KT, Hu R, Law WC, Ding H, Chang CW, Prasad PN, Swihart MT (2010) Biocompatible magnetofluorescent probes: luminescent silicon quantum dots coupled with superparamagnetic iron(III) oxide. ACS Nano 4:5131–5138
77. Tu CC, Chen KP, Yang TA, Chou MY, Lin LY, Li YK (2016) Silicon quantum dot nanoparticles with antifouling coatings for immunostaining on live cancer cells. ACS Appl Mater Interfaces 8:13714–13723
78. Dhenadhayalan N, Lee HL, Yadav K, Lin KC, Lin YT, Chang AHH (2016) Silicon quantum dot-based fluorescence turn-on metal ion sensors in live cells. ACS Appl Mater Interfaces 8:23953–23962
79. Erogbogbo F, Yong KT, Roy I, Xu GX, Prasad PN, Swihart MT (2008) Biocompatible luminescent silicon quantum dots for imaging of cancer cells. ACS Nano 2:873–878
80. Zhu H, Fan JL, Du JJ, Peng XJ (2016) Fluorescent probes for sensing and imaging within specific cellular organelles. Acc Chem Res 49:2115–2126
81. Choi J, Zhang Q, Reipa V, Wang NS, Stratmeyer ME, Hitchins VM, Goering PL (2009) Comparison of cytotoxic and inflammatory responses of photoluminescent silicon nanoparticles with silicon micron-sized particles in Raw 264.7 macrophages. J Appl Toxicol 29:52–60
82. Laskin DL, Laskin JD (1996) Macrophages, inflammatory mediators, and lung injury. Methods 10:61–70
83. Tu CQ, Ma XC, Pantazis P, Kauzlarich SM, Louie AY (2010) Paramagnetic, silicon quantum dots for magnetic resonance and two-photon imaging of macrophages. J Am Chem Soc 132:2016–2023
84. Pang JY, Su YY, Zhong YL, Peng F, Song B, He Y (2016) Fluorescent silicon nanoparticle-based gene carriers featuring strong photostability and feeble cytotoxicity. Nano Res 9:3027–3037
85. Song CX, Zhong YL, Jiang XX, Peng F, Lu YM, Ji XY, Su YY, He Y (2015) Peptide-conjugated fluorescent silicon nanoparticles enabling simultaneous tracking and specific destruction of cancer cells. Anal Chem 87:6718–6723
86. Odell ID, Cook D (2013) Immunofluorescence techniques. J Invest Dermatol 133:e4
87. Tu CC, Awasthi K, Chen KP, Lin CH, Hamada M, Ohta N, Li YK (2017) Time-gated imaging on live cancer cells using silicon quantum dot nanoparticles with long-lived fluorescence. ACS Photonics 4:1306–1315
88. Zhong YL, Peng F, Bao F, Wang SY, Ji XY, Yang L, Su YY, Lee ST, He Y (2013) Large-scale aqueous synthesis of fluorescent and biocompatible silicon nanoparticles and their use as highly photostable biological probes. J Am Chem Soc 135:8350–8356
89. Torchilin VP (2006) Multifunctional nanocarriers. Adv Drug Deliv Rev 58:1532–1555
90. Peer D, Karp JM, Hong S, Farokhzad OC, Margalit R, Langer R (2007) Nanocarriers as an emerging platform for cancer therapy. Nat Nanotechnol 2:751–760
91. Zhao QQ, Zhang R, Ye DX, Zhang S, Chen H, Kong JL (2017) Ratiometric fluorescent silicon quantum dots-Ce6 complex probe for the live cell imaging of highly reactive oxygen species. ACS Appl Mater Interfaces 9:2052–2058
92. Roy D, Fouzder C, Mukhuty A, Pal S, Mondal MK, Kundu R, Chowdhury P (2019) Designed synthesis of dual emitting silicon quantum dot for cell imaging: direct labeling of alpha 2-HS-glycoprotein. Bioconjug Chem 30:1575–1583
93. Chen XK, Zhang XD, Li CC, Sayed SM, Sun W, Lin FM, Wu FG (2019) Superbright organosilica nanodots as a universal sensor for fast discrimination and accurate quantification of live/dead cells. Sens Actuators B Chem 295:49–55
94. Zhao EG, Hong YN, Chen SJ, Leung CWT, Chan CYK, Kwok RTK, Lam JWY, Tang BZ (2014) Highly fluorescent and photostable probe for long-term bacterial viability assay based on aggregation-induced emission. Adv Healthc Mater 3:88–96
95. Nasu Y, Asaoka Y, Namae M, Nishina H, Yoshimura H, Ozawa T (2016) Genetically encoded fluorescent probe for imaging apoptosis in vivo with spontaneous GFP complementation. Anal Chem 88:838–844
96. Erogbogbo F, Tien CA, Chang CW, Yong KT, Law WC, Ding H, Roy I, Swihart MT, Prasad PN (2011) Bioconjugation of luminescent silicon quantum dots for selective uptake by cancer cells. Bioconjug Chem 22:1081–1088
97. Gao G, Jiang YW, Sun W, Wu FG (2018) Fluorescent quantum dots for microbial imaging. Chin Chem Lett 29:1475–1485
98. Lin FM, Li CC, Dong L, Fu DG, Chen Z (2017) Imaging biofilm-encased microorganisms using carbon dots derived from *L. plantarum*. Nanoscale 9:9056–9064
99. Zhang XD, Chen XK, Yang JJ, Jia HR, Li YH, Chen Z, Wu FG (2016) Quaternized silicon nanoparticles with polarity-sensitive fluorescence for selectively imaging and killing Gram-positive bacteria. Adv Funct Mater 26:5958–5970

100. Zhai X, Song B, Chu BB, Su YY, Wang HY, He Y (2018) Highly fluorescent, photostable, and biocompatible silicon theranostic nanoprobes against *Staphylococcus aureus* infections. Nano Res 11:6417–6427
101. Tang JL, Chu BB, Wang JH, Song B, Su YY, Wang HY, He Y (2019) Multifunctional nanoagents for ultrasensitive imaging and photoactive killing of Gram-negative and Gram-positive bacteria. Nat Commun 10:4057
102. Petchiappan A, Chatterji D (2017) Antibiotic resistance: current perspectives. ACS Omega 2:7400–7409
103. Blair JMA, Webber MA, Baylay AJ, Ogbolu DO, Piddock LJV (2015) Molecular mechanisms of antibiotic resistance. Nat Rev Microbiol 13:42–51
104. McCarthy MW, Kontoyiannis DP, Cornely OA, Perfect JR, Walsh TJ (2017) Novel agents and drug targets to meet the challenges of resistant fungi. J Infect Dis 216:S474–S483
105. Schachter B (2003) Slimy business—the biotechnology of biofilms. Nat Biotechnol 21:361–365
106. Gupta A, Das R, Tonga GY, Mizuhara T, Rotello VM (2018) Charge-switchable nanozymes for bioorthogonal imaging of biofilm-associated infections. ACS Nano 12:89–94
107. Liu Y, Busscher HJ, Zhao BR, Li YF, Zhang ZK, van der Mei HC, Ren YJ, Shi LQ (2016) Surface-adaptive, antimicrobially loaded, micellar nanocarriers with enhanced penetration and killing efficiency in staphylococcal biofilms. ACS Nano 10:4779–4789
108. Rogers SA, Huigens RW III, Melander C (2009) A 2-aminobenzimidazole that inhibits and disperses Gram-positive biofilms through a zinc-dependent mechanism. J Am Chem Soc 131:9868–9869
109. Rozenbaum RT, Su LZ, Umerska A, Eveillard M, Hakansson J, Mahlapuu M, Huang F, Liu JF, Zhang ZK, Shi LQ, van der Mei HC, Busscher HJ, Sharma PK (2019) Antimicrobial synergy of monolaurin lipid nanocapsules with adsorbed antimicrobial peptides against *Staphylococcus aureus* biofilms in vitro is absent in vivo. J Control Release 293:73–83
110. Hidalgo G, Burns A, Herz E, Hay AG, Houston PL, Wiesner U, Lion LW (2009) Functional tomographic fluorescence imaging of pH microenvironments in microbial biofilms by use of silica nanoparticle sensors. Appl Environ Microbiol 75:7426–7435
111. Dong RY, Li YJ, Li W, Zhang HR, Liu YL, Ma L, Wang XJ, Lei BF (2019) Recent developments in luminescent nanoparticles for plant imaging and photosynthesis. J Rare Earths 37:903–915
112. Carpita N, Sabularse D, Montezinos D, Delmer DP (1979) Determination of the pore size of cell walls of living plant cells. Science 205:1144–1147
113. Li YJ, Li W, Zhang HR, Dong RY, Li DN, Liu YL, Huang L, Lei BF (2019) Biomimetic preparation of silicon quantum dots and their phytophysiology effect on cucumber seedlings. J Mater Chem B 7:1107–1115
114. Karaman DŞ, Sarparanta MP, Rosenholm JM, Airaksinen AJ (2018) Multimodality imaging of silica and silicon materials in vivo. Adv Mater 30:1703651
115. Tu CQ, Ma XC, House A, Kauzlarich SM, Louie AY (2011) PET imaging and biodistribution of silicon quantum dots in mice. ACS Med Chem Lett 2:285–288
116. Zhou YF, Zhang Y, Zhong YL, Fu R, Wu SC, Wang Q, Wang HY, Su YY, Zhang HM, He Y (2018) The in vivo targeted molecular imaging of fluorescent silicon nanoparticles in *Caenorhabditis elegans*. Nano Res 11:2336–2346
117. Srivastava PK, Han SS, Tu CC, Jing LL (2019) Phototoxicity generated by silicon quantum dot nanoparticles on zebrafish embryos. ACS Appl Bio Mater 2:2872–2878
118. Chen F, Zhang XL, Ma K, Madajewski B, Benezra M, Zhang L, Phillips E, Turker MZ, Gallazzi F, Penate-Medina O, Overholtzer M, Pauliah M, Gonen M, Zanzonico P, Wiesner U, Bradbury MS, Quinn TP (2018) Melanocortin-1 receptor-targeting ultrasmall silica nanoparticles for dual-modality human melanoma imaging. ACS Appl Mater Interfaces 10:4379–4393
119. Joo J, Liu XY, Kotamraju VR, Ruoslahti E, Nam Y, Sailor MJ (2015) Gated luminescence imaging of silicon nanoparticles. ACS Nano 9:6233–6241
120. Ye HL, Cai SJ, Li S, He XW, Li WY, Li YH, Zhang YK (2016) One-pot microwave synthesis of water-dispersible, high fluorescence silicon nanoparticles and their imaging applications in vitro and in vivo. Anal Chem 88:11631–11638
121. Erogbogbo F, Yong KT, Roy I, Hu R, Law WC, Zhao WW, Ding H, Wu F, Kumar R, Swihart MT, Prasad PN (2011) In vivo targeted cancer imaging, sentinel lymph node mapping and multi-channel imaging with biocompatible silicon nanocrystals. ACS Nano 5:413–423

Fluorescent Metal Nanoclusters for Bioimaging

Jie Xu and Li Shang

1 Introduction

Fluorescent metal nanoclusters (MNCs), usually consisting of several to approximately a hundred metal atoms [1], have attracted extensive attention over the past few decades. MNCs have size down to less than 2 nm, which is comparable to the Fermi wavelength of electrons [2], resulting in the break up of the continuous density of states of the particles into discrete energy levels [1, 3]. MNCs exhibit distinct optical, electronic, and chemical properties, including strong photoluminescence, excellent photostability, and good biocompatibility. These unique properties make MNCs ideal probes for many applications in biological imaging and diagnosis.

Especially, near-infrared (NIR) fluorescent MNCs are promising probes for bioimaging, because biological tissues show very weak absorption and autofluorescence in the NIR spectrum window (650–900 nm wavelengths) [4, 5]. Also, NIR light can pass across several centimeters of heterogeneous living tissues [6]. Particularly, NIR-emitting MNC probes can alleviate several limitations of conventional NIR organic dyes and other nanoprobes like semiconductor quantum dots (QDs). Organic dyes show many drawbacks such as poor hydrophilicity and photostability, insufficient stability in biological systems, and weak multiplexing capability [7]. Most reported QDs display high inherent cytotoxicity and self-aggregation inside live cells, which limit their practical bio-applications [8].

Fluorescence lifetime imaging (FLIM) and two-photon imaging have been widely adopted in tissue and cell studies, and now have become powerful tools in early diseases diagnosis as well as guiding the disease treatment [9, 10]. Fluorescent MNCs possess much longer lifetime than that of cellular autofluorescence and most organic dyes, making them attractive markers for cellular FLIM applications, which is independent of fluorophore concentration and laser excitation intensity [11]. Although one-photon fluorescence imaging techniques are featured with good spatial resolution and high sensitivity, they hardly obtain anatomical or three-dimensional details of tumor tissues in vivo [12]. Compared to one-photon imaging, two-photon imaging is a powerful technique for enhanced tissue penetration depth

J. Xu
State Key Laboratory of Solidification Processing, Center for Nano Energy Materials, School of Materials Science and Engineering, Northwestern Polytechnical University and Shaanxi Joint Laboratory of Graphene (NPU), Xi'an, China

L. Shang (✉)
State Key Laboratory of Solidification Processing, Center for Nano Energy Materials, School of Materials Science and Engineering, Northwestern Polytechnical University and Shaanxi Joint Laboratory of Graphene (NPU), Xi'an, China

NPU-QMUL Joint Research Institute of Advanced Materials and Structures (JRI-AMAS), Northwestern Polytechnical University, Xi'an, China
e-mail: li.shang@nwpu.edu.cn

F.-G. Wu (ed.), *Fluorescent Materials for Cell Imaging*, https://doi.org/10.1007/978-981-15-5062-1_5

(>500 μm), low tissue autofluorescence, and self-absorption, as well as reduced photodamage [10, 13, 14]. With relatively good biocompatibility and large two-photon absorption (TPA) cross section, MNCs are also considered as ideal probes for two-photon imaging in biological system.

Besides fluorescence (FL) imaging, several other imaging techniques have also been used in the early-stage diagnosis of cancer, such as magnetic resonance imaging (MRI), X-ray computed tomography (CT), photoacoustic imaging (PAI), positron emission tomography (PET) imaging, and single-photon emission computed tomography (SPECT) [15, 16]. Each imaging modality has its own unique advantages along with intrinsic limitations [17]. For example, CT imaging can easily differentiate various tissue densities, and allow three-dimensional visual reconstructions of tissue, which suffers from poor sensitivity in soft tissues with limited density differences [18, 19]. MR imaging is able to provide high-quality 3D information of soft tissues and possesses high spatial resolution, but has the disadvantage of relatively low sensitivity [20–23]. In contrary, FL imaging has high sensitivity and resolution for imaging at the cellular level, but it cannot provide spatial resolution and 3D tissue detail [24]. Therefore, the rational combination of different modalities, known as "multimodal imaging," is a powerful method that can provide more reliable and accurate detection of disease sites [15, 25].

In this chapter, we mainly focus on the latest progress in fluorescent MNCs probes for biological imaging. Specifically, we summarize recent advances in the synthesis and applications of fluorescent MNCs (including Au, Ag, Cu, and alloy NCs) as novel bioimaging probes, including single-modal imaging (fluorescence intensity-based imaging, FLIM, two-photon imaging, PET imaging) probes and the combination of FL imaging with several other imaging techniques to form multimodal imaging (such as FL/CT/MRI, FL/PAI/MRI, FL/SPECT, etc.) probes. In the final section, we will give a brief outlook on the challenges and opportunities for fluorescent MNCs in bioimaging applications.

2 Synthesis of Fluorescent MNCs

Up to now, many different methods have been developed to synthesize MNCs with the photoluminescence (PL) property. Generally, these approaches can be classified into two groups, "bottom-up" and "top–down" [26]. In both strategies, surface ligands or templates play an important role in defining their final properties. Therefore, in the following, we will overview each synthetic strategy based on the type of templates or capping ligands (representative examples summarized in Table 1).

2.1 Thiols

Owing to the strong interaction between thiols and Au/Ag, small thiolate molecules are the most commonly adopted stabilizers in MNC synthesis [27]. Among them, glutathione (GSH) is the most commonly adopted one, and GSH-stabilized AuNCs with a maximum emission at 780 nm could be obtained via $NaBH_4$ reduction. These AuNCs display strong one- and two-photon emissions, good photostability and biocompatibility [28]. By employing GSH as reducing and protecting reagent simultaneously, Zheng and coworkers [29] successfully synthesized NIR-emitting GSH-AuNCs with a core size 2.5 nm at 90 °C. Besides, water-soluble GSH-capped AuNCs were also obtained by using tetrabutylammonium borohydride (TBAB) as a mild reductant, and the yielded GSH-AuNCs showed excellent PL properties and low cytotoxicity [30]. Wu et al. [31] developed a one-pot one-cluster synthesis method to prepare monosized Ag_{14}NCs capped with GSH. They found that the fluorescence quantum yield (QY) of $Ag_{14}(SG)_{11}$ NCs is strongly solvent-dependent, and the fluorescence intensity increases upon decreasing the solvent polarity or dielectric constant [32, 33]. Recently, a rapid sonochemical route to synthesize fluorescent AgNCs using hydrazine hydrate as reducing agent and GSH as capping agent was developed [34]. The as-prepared AgNCs show high photo-, time-,

Table 1 Summary of representative literatures on the synthesis of fluorescent MNCs

Metal	Capping agent	λ_{em} (nm)	QY	Size (HD)	Ref.
Au	GSH	780	–	1.1 nm∗	[28]
Au	GSH	810	~0.5%	3.3 nm (2.5 nm∗)	[29]
Au	GSH	650	1.6%	3.1 nm (1.9 nm∗)	[30]
Au	GSH	685	1.3%	–	[49]
Ag	GSH	670	–	~1.1 nm∗	[37]
Ag	GSH	720	2.8%	<2 nm∗	[50]
Ag	GSH	645	8.2%	~2 nm∗	[34]
Ag	GSH	640	–	~1 nm∗	[31]
Cu	GSH	430	~6%	~2.2 nm∗	[88]
Cu	GSH	610	5.0%	2.3 nm∗	[35]
Cu	GSH	610	4.5%	2.4 nm∗	[38]
Cu	GSH	585	2.1%	2.2 nm∗	[89]
Ag_2S	GSH	679/727	0.3%, 0.1%	3.0 nm∗, 3.7 nm∗	[40]
Ag_2S	3-MPA	795	14%	7.5 nm (2.5 nm∗)	[41]
AuCe	GSH	570	–	1.2–2.2 nm∗	[90]
AuAg	GSH	716	3.4%	1.8 nm∗	[42]
AuAg	LA	630	6.4%	3.6 nm (1.9 nm∗)	[91]
AuAg	PEI-LA	680	14.56%	–	[92]
ZnAg	L-cysteine, chicken egg white protein	657	13.3%	1.8 nm∗	[93]
Au	DHLA	684	~0.6%	3.2 nm	[11]
Au	DHLA	715	2.9%	3.3 nm (1.6 nm∗)	[44]
Au	DHLA	720	10%	1.4 nm∗	[45]
Au	DHLA	650	1–3%	<5 nm	[51]
Au	DHLA	650	~7%	2 nm∗	[52]
Ag	DHLA	630	2.4%	2.1 nm (1.3 nm∗)	[94]
Cu	DHLA	650	7.2%	1.9 nm∗	[46]
Cu	TA	430	14%	2.2 nm∗	[95]
Au	11-MUA	530	3.1%	1.33 nm∗	[96]
Au	11-MUA, histidine	600	13.06%	–	[97]
Au	DPA	610	1.3%	2.14 nm (1.8 nm∗)	[98]
Au	MSA/tiopronin	785	3.4%, 3.8%	~1.5 nm∗	[47]
Ag	TSA	612	25%	2–5 nm∗	[48]
Ag	MT	632	–	1.9 nm∗	[99]
Ag	Sodium cholate	406, 430	20.1%	<1 nm∗	[100]
Pt	MAA	470	18%	–	[84]
Au	BSA	710	–	~2.7 nm	[101]
Au	BSA	665	–	3.74 nm	[102]
Au	BSA	670	~6%	<3 nm∗	[103]
Au	BSA	~674	~6%	~1 nm∗	[104]
Au	BSA	660	~4%	1 nm∗	[65]
Cd	BSA	475	2.86%	7.5 nm (~1 nm∗)	[105]
Mg	BSA	465	17%	12 nm (~8.5 nm∗)	[106]
Ag	HSA, BSA	620, 510	13%, 10%	2.6 nm, 2 nm	[107]
Ag	dLys	640	–	–	[64]
Au	Human transferrin	710	~7.7%	2.6 nm∗	[57]
Au	Apoferritin	665	8.2%	1.2 nm∗	[58]
Au	Human transferrin	695	~4.3%	<2 nm∗	[59]
Cu	Peptide	418	–	2.97 nm∗	[108]
Cu	Lysozyme	450	18%	2.3 nm∗	[109]

(continued)

Table 1 (continued)

Metal	Capping agent	λ_{em} (nm)	QY	Size (HD)	Ref.
Cu	Transferrin	670	6.2%	2.99 nm∗	[63]
Au	Trypsin	690	6.5%	2.7 nm∗	[60]
Au	Human insulin	680	~10%	5.36 nm	[61]
AuAg	Chicken egg white protein	600	5.4%	4.4 nm∗	[110]
Au	Bovine pancreatic ribonuclease A	682	~12%	6.2 nm	[62]
Au	Peptide CCYTAT	677	11%	1.5 nm∗	[68]
Au	Tripeptide	680	12.4%	1.6 nm∗	[111]
Ag	ssDNA	705	34%	~2.5 nm∗	[71]
Ag	ssDNA	700	52%	3 nm	[72]
Ag	DNA	550	17.4%	~3 nm∗	[79]
Ag	DNA	550	–	~3 nm∗	[80]
Ag	DNA (AS1411)	635	40.1%	1.5 nm∗	[112]
Ag	C_{12} ssDNA	~700	17%	–	[76]
Ag	C_{24} ssDNA	715	14%	–	[77]
Ag	G-quadruplex (AS1411)	680	6.79%	<2 nm∗	[78]
Cu	DNA	584	–	–	[113]
Au	PTMP-PMAA	~660	4.8%	<3 nm	[81]
Au	PEG	810	–	5.5 nm (2.3 nm∗)	[82]
Au	PAMAM	458	25%	<2 nm∗	[86]
Au	PEI-LA	696	3.13%	–	[114]
Pt	PEI	560	6.8%	2 nm (1.4 nm∗)	[85]
Ag	SH-PEI	690	3%	12 nm (2.3 nm∗)	[83]
Cu	PVP	518	44.67%	2.28 nm∗	[115]

∗ core size, *HD* hydrodynamic diameter, *GSH* glutathione, *3-MPA* 3-mercaptopropionic acid, *LA* lipoic acid, *PEI* polyethyleneimine, *DHLA* dihydrolipoic acid, *TA* tannic acid, *11-MUA* 11-mercaptoundecanoic acid, *DPA* D-penicillamine, *MSA* 2-mercaptosuccinic acid, *tiopronin* N-(2-mercapto-propionyl) glycine, *TSA* thiosalicylic acid, *MT* metallothionein, *MAA* mercaptoacetic acid, *BSA* bovine serum albumin, *HSA* human serum albumin, *dLys* denatured lysozyme, *CCYTAT* H_2N–CCYRGRKKRRQRRR–COOH, *PTMP* pentaerythritol tetrakis 3-mercaptopropionate, *PMAA* poly(methacrylic acid), *PEG* poly(ethylene glycol), *PAMAM* poly(amidoamine), *SH-PEI* thiol-polyethyleneimine, *PVP* poly(vinylpyrrolidone)

pH-, and ions-stability in aqueous solution, and have been exploited as probes for monitoring Pb^{2+} in living cells. In another work, Song and coworkers [35] reported a one-step synthetic method to prepare GSH templated CuNCs. The resultant CuNCs contain 1–3 atoms and exhibit red fluorescence ($\lambda_{em} = 610$ nm) with high QY, up to 5.0%. Interestingly, the fluorescence signal of the CuNCs is reversibly responsive to the environmental temperature in the range of 15–80 °C.

Wang and coworkers [36] proposed a different strategy to in situ biosynthesize fluorescent AuNCs inside cancer cells and tumor tissues. They found that $HAuCl_4$ can undergo a more rapid and efficient spontaneous reduction into AuNCs inside cancerous cells than in normal ones, enabling self-bio-imaging of cancer cells and tumors by long-lasting fluorescent markers. Subsequently, they reported the intracellular biosynthesis of AgNCs by cancerous cells incubated with silver ions [37]. AgNCs were spontaneously biosynthesized in situ by HeLa cancer cells treated with a specific silver salt derivative $[Ag(GSH)]^+$ and exogenous GSH. Recently, the same group [38] explored the preparation of an intracellular temperature nanoprobe specifically by in situ biosynthesized fluorescent CuNCs in target cancer cells upon incubation with a special copper precursor (i.e., the complex solution of GSH and copper(II)). These fluorescent CuNCs could be biosynthesized spontaneously in MDA -MB-231 cancer cells through a particular molecular process, but not in normal cells (i.e., L02

cells). In a recent study, they demonstrated that fluorescent ZnO nanoclusters and magnetic Fe_3O_4 nanoclusters can also be synthesized in cancer cells [39].

Using GSH as a scaffold and sulfur–hydrazine hydrate complex ($S–N_2H_4·H_2O$) as the S^{2-} source, Wang et al. [40] developed a one-step approach to prepare water-soluble fluorescent Ag_2S NCs with tunable PL properties. By adjusting the amount of GSH and the ratio of Ag^+ to $S–N_2H_4·H_2O$, Ag_2S NCs with different PL wavelengths and sizes were obtained. Subsequently, Xian group [41] successfully synthesized NIR-emitting fluorescence Ag_2S QDs in aqueous solution using 3-mercaptopropionic acid (3-MPA) as sulfur source and stabilizer. Interestingly, the fluorescence intensity of Ag_2S QDs was obviously enhanced upon the addition of various rare earth ions, especially in the presence of Gd^{3+}. They speculated that the electrostatic interaction and coordination between rare earth ions and -COOH from MPA on Ag_2S QDs results in QDs aggregation and displays the feature of aggregation-induced emission (AIE).

Wang and coworkers [42] used a galvanic replacement reaction to prepare AgAu alloy NCs. In the first step, the template (i.e., AgNCs) was prepared by using GSH as the stabilizing agent and $N_2H_4·2H_2O$ as the reducing agent. Then, when the $AuCl_4^-$ ion and GSH were added to the aqueous solution of AgNCs, the galvanic replacement reaction occurred due to higher standard reduction potential of $AuCl_4^-$/Au pair (0.99 V vs SHE) than that of Ag^+/Ag pair (0.80 V vs SHE) [43]. The as-prepared AgAu alloy NCs displayed NIR fluorescence centered at 716 nm and showed tunable luminescence from visible red (614 nm) to NIR (716 nm) by controlling the Ag/Au ratios.

In addition to GSH, bidentate dihydrolipoic acid (DHLA) is another attractive ligand for MNCs synthesis due to its strong binding affinity to metal atoms. Shang et al. [11] synthesized NIR-emitting DHLA–AuNCs with a one-pot strategy by simply reducing a mixture of lipoic acid (LA) and gold salt with $NaBH_4$ in aqueous solution. The obtained AuNCs possess NIR emission and long fluorescence lifetime (>100 ns), making them attractive as markers for cellular FLIM applications. Afterwards, the same group developed a microwave-assisted strategy for synthesizing DHLA–AuNCs [44]. Particularly, irradiation with microwaves during the synthesis enhanced the fluorescence QY of AuNCs by about fivefold from ~0.6% to 2.9%, and it also shortened the reaction time from hours to several minutes. Moreover, by using microwave irradiation, the emission peak red shifts from 690 nm to 715 nm upon excitation at 580 nm. Later, via a slightly modified strategy, Nair et al. [45] reported the synthesis of NIR-emitting $(Au)_{18}(LA)_{14}$ NCs with a higher QY, 10%. Besides AuNCs, Ghosh and coworkers [46] reported the synthesis of brightly red fluorescent DHLA–CuNCs, in combination with biocompatible polymer poly(vinylpyrrolidone) (PVP) as stabilizers. The fluorescence of CuNCs was found to be pH sensitive, and the emission could be tuned reversibly according to the pH.

Besides GSH and DHLA, other thiols such as tiopronin and mercaptosuccinic acid (MSA) have also been used as stabilizers, which yielded AuNCs centered at 785 nm with QYs in the range of 3–4% [47]. Recently, Zhou et al. [48] synthesized hydrophobicity-guided self-assembled particles of AgNCs with AIE (Fig. 1). They adopted a hydrophobic ligand, thiosalicylic acid, as capping agent to prepare AgNCs which showed significant AIE behavior. This AIE property of AgNCs enables them to sensitively respond to multiple external stimuli such as solvent polarity, pH, and environmental temperature. The hydrophobic nature of thiosalicylic acid as the capping ligand of AgNCs drives the formation of self-assembled particles of AgNCs with bright luminescence.

In addition to the above-mentioned strategy by direct reduction of metal ions in the presence of thiols, fluorescent MNCs can also be prepared by etching large metal nanoparticles with thiols. $Au_{23}(SG)_{18}$ NCs (SG denotes GSH) were obtained via the interfacial etching process using $Au_{25}SG_{18}$ NCs as the precursor. For interfacial etching, an interface was created by making an immiscible biphasic mixture of toluene containing octanethiol (OT) and an aqueous solution of $Au_{25}SG_{18}$. A highly fluorescent, water-soluble $Au_{23}(SG)_{18}$ cluster was obtained by etching at 25 °C

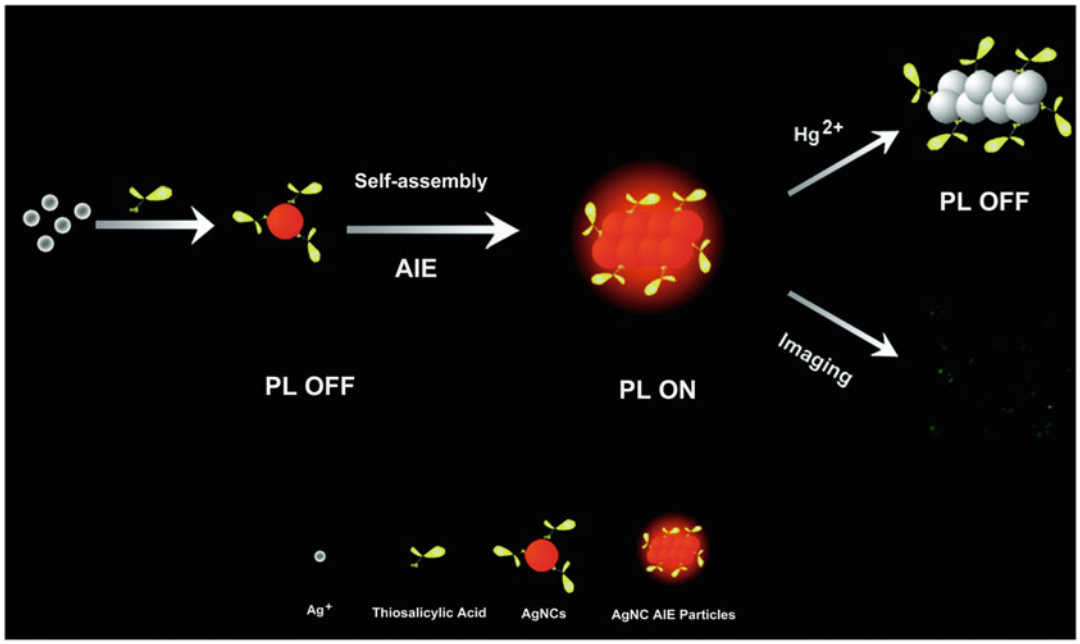

Fig. 1 Schematic of the fabrication of self-assembled particles of AgNCs with AIE and their use in quantifying mercuric ion and imaging cells. Reprinted with permission from Ref. [48]

[49]. Red-emitting AgNCs were produced by an interfacial etching route using GSH as a ligand etchant from MSA-protected AgNPs. These AgNCs show high photostability over time and a high stability for a wide pH range [50]. Lin and coworkers [51] developed a strategy to synthesize DHLA–AuNCs based on precursor-induced AuNPs etching in organic phase and ligand exchange with DHLA to transfer the particles into aqueous solution. Subsequently, the same group adopted a further 24 h thermal treatment at 70 °C to markedly increase the QY of AuNCs to nearly 7% [52].

2.2 Proteins, Peptides, and DNA Oligonucleotides

Biomacromolecules such as proteins and peptides have also been extensively utilized as templates for synthesizing fluorescent MNCs. Particularly, proteins possess abundant binding sites that can potentially bind and further reduce metal ions, thus offering promising scaffolds for template-driven formation of small MNCs [53, 54]. Notably, bovine serum albumin (BSA) was first reported by Xie et al. as an excellent scaffold for AuNCs due to the strong force of Au–S bonding and the steric protection (Fig. 2), where NIR-emitting AuNCs with maximum emission wavelength at about 640 nm can be obtained [55]. Recently, Yu et al. [56] reported a kind of novel hybrid membrane made with AuNC-embedded BSA (AuNCs@BSA) fibrils and activated graphene oxide (GO), which was used to remove heavy metal ions, Hg^{2+}, from water. Later, researchers also tried many other proteins, such as transferrin-family proteins [57–59], trypsin [60], insulin [61], and ribonuclease A [62], as potential bioscaffolds for synthesizing MNCs. For example, transferrin (Tf)-templated CuNCs have been synthesized at room temperature via a biomineralization process, where ascorbic acid was used as the reductant. The as-prepared Tf-CuNCs exhibited intense NIR fluorescence with a QY about 6.2% [63]. Using denatured lysozyme (dLys) as the capping agent, a ratiometric fluorescent AgNCs probe was

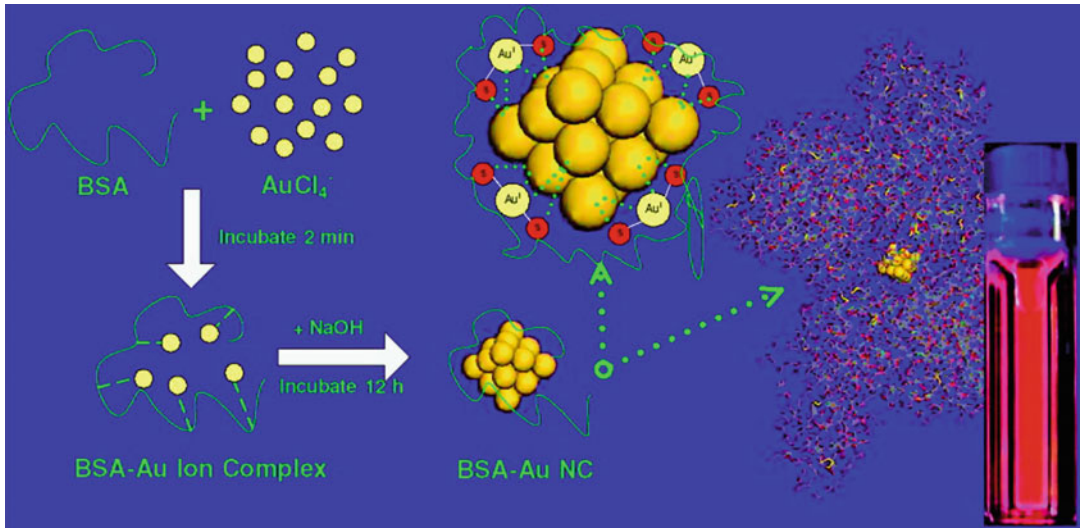

Fig. 2 Schematic of the formation of AuNCs in BSA solution under alkaline conditions. Reprinted with permission from Ref. [55]

developed [64]. This probe could be utilized for ratiometric detection of H_2O_2 and further exploited to H_2O_2–generated oxidase-based biosensing, such as glucose and acetylcholine chloride. Also, dual channel fluorescence confocal images of •OH in living cells was realized using the dLys-AgNCs probe. Besides their well-known roles as capping agents, proteins such as BSA can also function as etching agents for synthesizing fluorescent AuNCs in a few cases. For example, Pradeep et al. [65] employed a core etching method to synthesize BSA-AuNCs from MSA-capped AuNPs.

In addition to proteins, the integration of MNCs with peptides can also combine the distinct optical properties of MNCs with the biological functions of peptides [66, 67]. For example, Gao group [68] developed a one-step biomineralization method to produce AuNCs by using a bifunctional CCYTAT peptide, which contains one domain for biomineralizing and capturing AuNCs and another domain for targeting cell nuclei. The as-prepared AuNCs showed a maximum emission at 677 nm and possessed a high fluorescence QY of about 11%. Recently, by combining biomineralization and supramolecular self-assembly of motif-designed peptide constructs, researchers reported that the emission of peptide–AuNCs can be enhanced by nearly 70-fold, which largely increases their utility for biological applications [69].

DNA have been employed in the design and fabrication of various DNA-templated metal nanostructures owing to their distinct interactions with metal cations [70]. In 2008, Dickson group [71] first reported the use of ssDNA to synthesize AgNCs with fluorescence tunable throughout the visible and NIR range. Notably, these AgNCs possessed a high QY up to 34%. Sharma et al. [72] also reported four different DNA sequences as AgNC templates with emission at different wavelengths. The resulting NIR-emitting AgNCs had QY greater than 50% and were very promising as biolabels. It has been shown in earlier reports that Ag^+ has a higher binding affinity to cytosine bases than other bases [73–75]. Therefore, Dickson and coworkers [76, 77] reported NIR-emitting AgNCs creating in single-stranded oligo-DNA consisting of 12 or 24 cytosine bases. By using more advanced DNA structures, such as G-quadruplex, as the template, Wang group [78] reported the synthesis of fluorescent AgNCs made of 2–4 Ag atoms centered at 680 nm. Furthermore, intrinsically fluorescent AgNCs–aptamer assemblies for cell recognition were developed by Wang and coworkers

[79]. They employed a cancer-targeted DNA aptamer sequence (A-strand) and cytosine-rich sequence for templated synthesis of fluorescent AgNCs (C-strand). A fluorescent sgc8c–AgNCs assembly with relatively high luminescence has been achieved and exhibited specific binding to target CCRF-CEM cells by using a six-base adenine linker. Subsequently, adopting a similar method, the same group [80] reported a label-free and turn-on aptamer strategy for cancer cell detection based on the recognition-induced conformation alteration of aptamer and hybridization-induced fluorescence enhancement effect of DNA–AgNCs in proximity of guanine-rich DNA sequences (Fig. 3). In this strategy, two tailored DNA probes were designed, namely, a recognition probe (R-Probe) and a signal probe (S-Probe). In the presence of target cancer cells, recognizing and binding of the aptamer to the protein receptors on the cancer cells surface enforces the R-Probe to undergo a conformational alteration, causing the arm segment dissociation. The hybridization between the arm segment in the R-Probe and the link sequence in the S-Probe could then be initiated. Finally, the S-Probe-templated dark AgNCs are brought close to the guanine-rich DNA sequences and changed to bright AgNCs, leading to enhanced fluorescence readout.

2.3 Polymers

There are also efforts on using polymer as stabilizers for preparing fluorescent MNCs based on their capability of sequestering metal ions from solutions. Moreover, the terminal groups on the polymer periphery are very useful for the further bioconjugation of MNCs. For instance, Huang and coworkers [81] prepared NIR-emitting AuNCs by using multidentate polymer, thioether-terminated poly(methacrylic acid) (PTMP-PMAA), as ligands. In another report, fluorescent poly(ethylene glycol) (PEG)–AuNPs with an emission peak at 810 nm were created by thermally reducing $HAuCl_4$ in the presence of thiolated PEG ligands with a molecular weight (MW) of 1 kDa in aqueous solution [82]. Similarly, Wang et al. [83] reported a one-pot fabrication of thiol-terminated polyethyleneimine (SH-PEI) stabilized NIR-emitting AgNCs. SH-PEI not only acts as an excellent stabilizer for AgNCs but also facilitates post-surface modification with functional biomolecules. Inouye and coworkers [84] synthesized $Pt_5(MAA)_8$ NCs with an 18% QY in water. Upon bioconjugating an antibody, they successfully labeled chemokine receptors in living HeLa cells. Afterwards, the same group investigated the formation of yellow fluorescent PEI-protected PtNCs (PtNCs@PEI) [85]. They found that PtNCs were produced in the cavities formed by coiled PEI ligands and were mostly stabilized with the amino groups ($-NH_2$). The size and fluorescence properties of PtNCs@PEI are strongly related to the cavities formed by the coiled PEI ligands. As shown in Fig. 4, under alkaline pH conditions, PEI have the ability to coil around the surface of PtNCs to form the cavities. As for the neutral condition (all primary amines protonated), the hydrodynamic size of PtNCs is a little larger than ones produced under basic condition, resulting in the slight shift to longer emission wavelength. At acidic pH (most amines protonated), both PEI and PEI-capped NCs possess considerable positive charges, leading to an expansion of PEI chains because of the repulsion between the charged amines. The dimension of cavity in the acidic situation is much bigger than that in the basic situation, caused the larger PtNPs and no emitted fluorescence.

Recently, poly(amidoamine) (PAMAM) dendrimer-hosted Au_5NCs were successfully synthesized through a two-stage growth process with a high fluorescence QY up to 25% [86]. As shown in Fig. 5, stage I presented a simultaneous self-nucleation of Au_5NCs and subsequent PAMAM-hosted self-assembly with a rapid rate of fluorescence increase. At stage II, the fluorescence enhancement should be mainly dominated by the self-assembly of Au_5NCs in PAMAM matrix. First, the emission from self-assembled aggregates was attributed to ligand-to-metal–metal charge transfer (LMMCT) from electron-rich-NH_2 groups in PAMAM to Au atoms, which

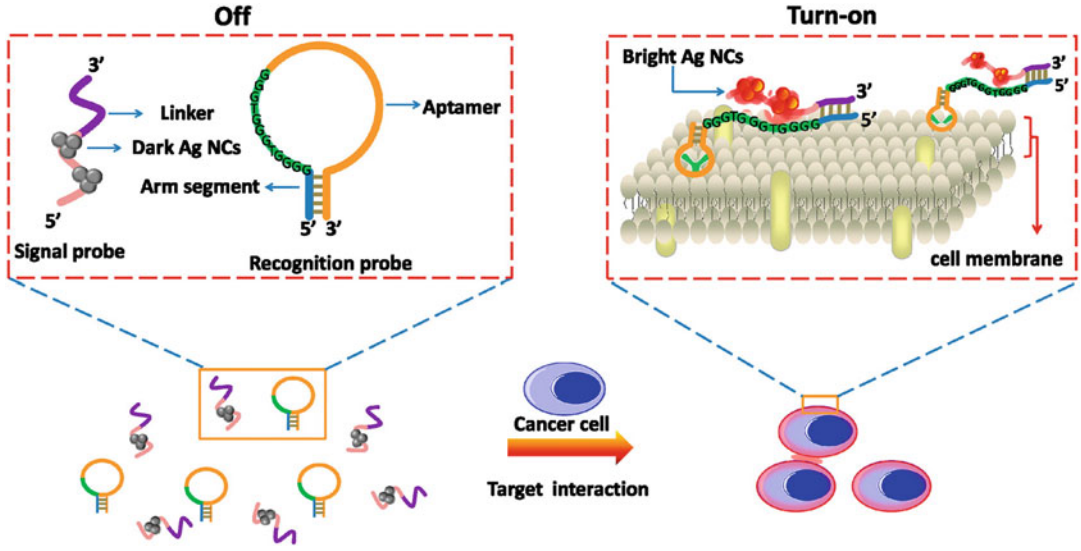

Fig. 3 Schematic representation of the label-free and turn-on aptamer strategy for cancer cell detection based on DNA–AgNCs fluorescence upon recognition-induced hybridization. Reprinted with permission from Ref. [80]

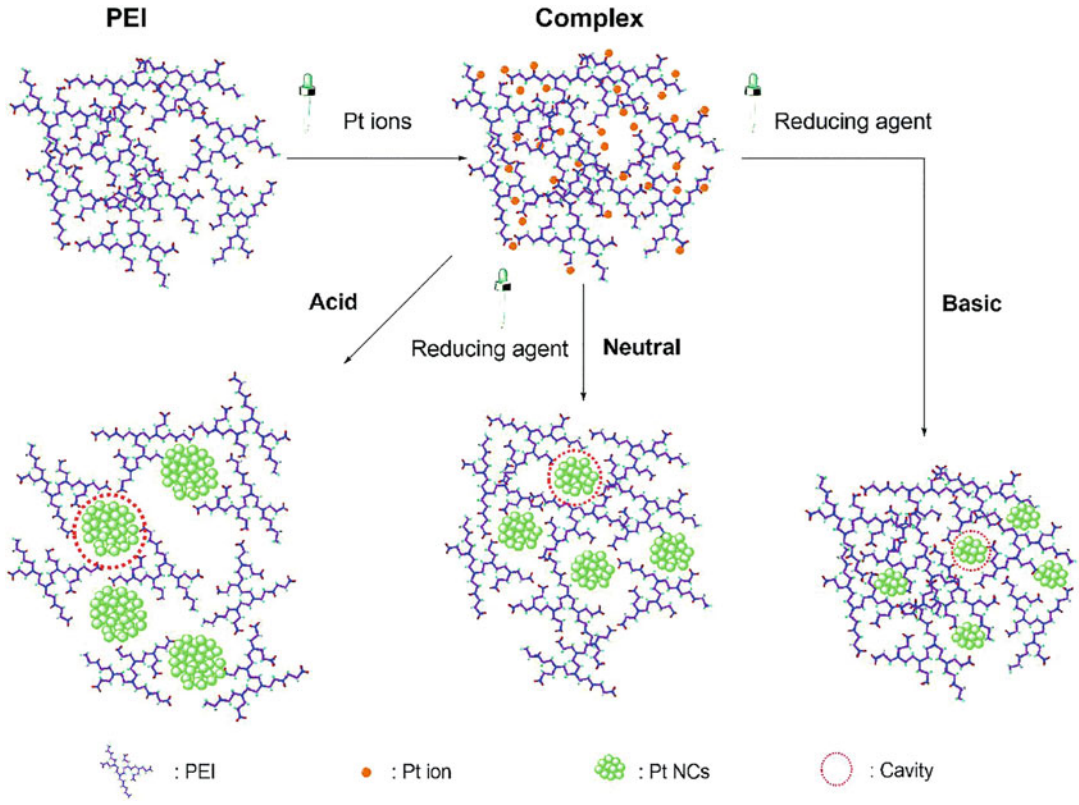

Fig. 4 Schematic formation of PEI chelation with Pt ions and reduced PtNCs in PEI cavities at different pH mediums. Reprinted with permission from Ref. [85]

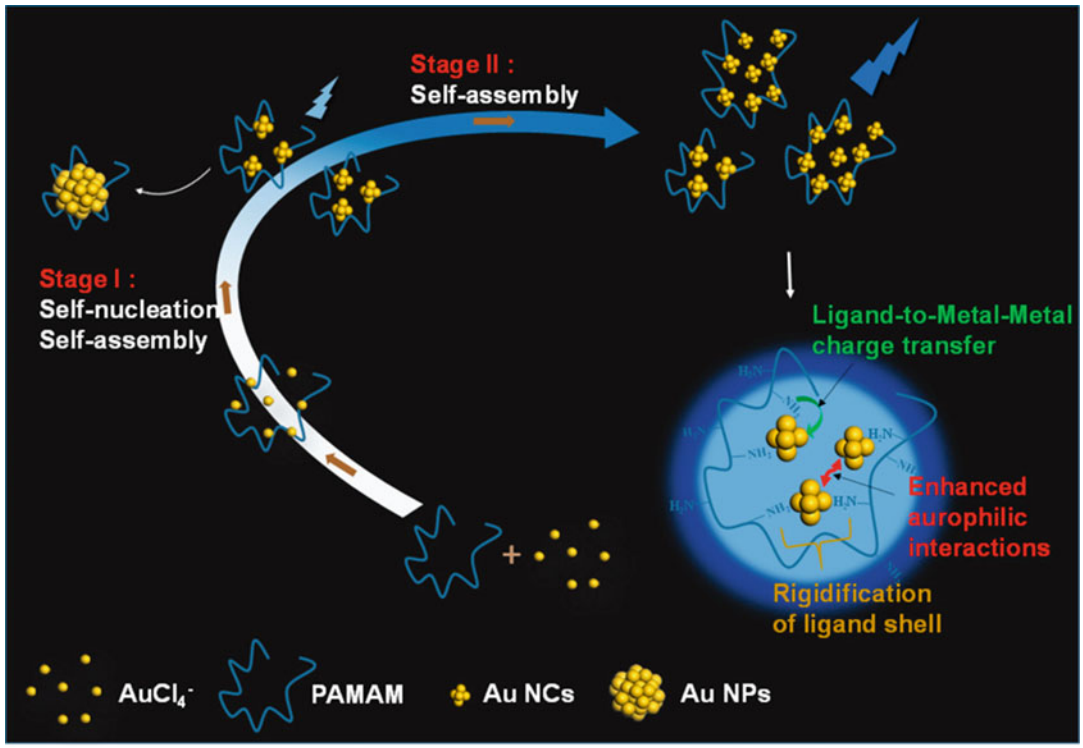

Fig. 5 Schematic illustration of growth process and the structure of Au_5NCs self-assemblies in PAMAM matrix. Reprinted with permission from Ref. [86]

generated radiative relaxation through a metal-centered triplet state. In addition, because PAMAM endowed AuNCs with stronger inner interactions compared to those isolated species, enhanced aurophilic interactions greatly promote excited-state relaxation dynamics and enhanced rigid structures reduced the level of nonradiative relaxation of excited states, which was also responsible for enhanced emission [87].

3 MNCs for Fluorescence Bioimaging

With many attractive features including ultrasmall size, good biocompatibility, brightness, and photostability, MNCs are promising fluorescence probes for biological imaging. Indeed, great progress has been achieved in recent years on employing fluorescent MNCs for biological imaging applications, as summarized in Table 2.

In 2012, Shang et al. [44] demonstrated the utilization of DHLA–AuNCs for imaging intracellular Hg^{2+} in living HeLa cells, where they observed the intracellular fluorescence quenching effect upon addition of Hg^{2+} ions. Subsequently, the same group [94] systematically investigated the interactions of AgNCs with human serum albumin (HSA). They found that protein adsorption markedly changes the uptake behavior as well the cytotoxicity of AgNCs. The amount of AgNCs internalized by the cells is substantially reduced in the presence of HSA. Moreover, the fluorescence from intracellular AgNCs is stronger than that from membrane-associated particles in both cases, the fluorescence decrease in the membrane region (ca. 13-fold) is much larger than for inside the cells (ca. sevenfold). Afterwards, they systematically varied the surface charge of HSA to examine the effect of Coulomb forces in modulating the biological interactions of AuNCs [116]. By utilizing confocal fluorescence

Table 2 Fluorescent MNCs as single-modal fluorescence imaging probes

Metal	Capping agent	Functionalization	λ_{em} (nm)	Imaging modal	Biosystems	Ref.
Au	DHLA	–	715	Intensity	HeLa cells	[44]
Au	DHLA	–	684	Intensity	HeLa cells	[116]
Au	CCYTAT	–	677	Intensity	HeLa cells	[68]
Ag	G-quadruplex (AS1411)	–	680	Intensity	HeLa cells	[78]
Ag	GSH	–	645	Intensity	HeLa cells	[34]
Ag	DHLA	–	630	Intensity	HeLa cells	[94]
AuAg	LA	–	630	Intensity	HeLa cells	[91]
Cu	Lysozyme	–	450	Intensity	HeLa cells	[109]
Cu	Transferrin	–	670	Intensity	HeLa cells	[63]
Cu	DHLA	–	650	Intensity	HeLa cells	[46]
Cu	GSH	–	585	Intensity	HeLa cells	[89]
Cu	GSH	–	430	Intensity	HeLa, MDAMB-231, A549 cells	[88]
Cu	GSH	–	610	Intensity	MC3T3-E1 cells	[35]
Cu	GSH	–	610	Intensity	MDA-MB-231 cancer cells	[38]
Cu	TA	–	430	Intensity	A549 cells	[95]
Mg	BSA	–	465	Intensity	A549 cells	[106]
Au	Human transferrin	–	695	Intensity	A549 lung tumor cells	[59]
Au	PTMP-PMAA	–	~660	Intensity	Hematopoietic cancer cells K562	[81]
Ag	GSH	–	720	Intensity	Epithelial lung cancer cells (A549)	[50]
Ag	GSH	–	640	Intensity	Lung cancer cells (A549)	[31]
Ag	TSA	–	612	Intensity	Human A549 cells	[48]
Ag	dLys	–	640	Intensity	PC-3 cells	[64]
Ag	Sodium cholate	–	406, 430	Intensity	Zebrafish embryos	[100]
Ag	DNA	–	550	Intensity	CCRF-CEM cancer cells	[80]
Ag	DNA (AS1411)	–	635	Intensity	MCF-7 human breast cancer cells	[112]
Ag_2S	GSH	–	679	Intensity	MC3T3-EI cells	[40]
Ag_2S	3-MPA	–	795	Intensity	MDA-MB-468 cells	[41]
AuAg	GSH	–	716	Intensity	CAL-27 cells	[42]
AuAg	PEI-LA	–	680	Intensity	B16F10, HeLa, and CHO cells, BALB/C nude mice	[92]
AuCe	GSH	–	570	Intensity	HeLa cells, cervical carcinoma tumor xenograft mice	[90]
AuCe	BSA	–	650	Intensity	HeLa cells	[127]
Au	BSA	–	710	Intensity	MDA-MB-45 tumor and Hela tumor xenograft mice	[101]
Au	Apoferritin	–	665	Intensity	Human Caco-2 cells, nude mice	[58]
Au	GSH	–	810	Intensity	MCF-7 tumor-bearing mice	[29]
Au	PEG	–	810	Intensity	MCF-7 tumor-bearing mice	[82]
Ag	GSH	–	670	Intensity	HeLa cells, tumor-bearing mice	[37]
Au	Human insulin	–	680	Intensity	Chondrocytes, mice	[61]
Au	BSA	FA	~674	Intensity	Oral carcinoma KB cells	[104]
Au	BSA	FA	660	Intensity	Oral carcinoma KB cells	[65]
Au	BSA	FA	665	Intensity	FR-positive tumor cells, tumor-bearing mice	[102]
Au	BSA	FA	655	Intensity	MCF-7 cells, MCF-7 xenograft tumors	[140]

(continued)

Table 2 (continued)

Metal	Capping agent	Functionalization	λ_{em} (nm)	Imaging modal	Biosystems	Ref.
Au	Ovalbumin	FA	626	Intensity	HeLa cells	[141]
Au	GSH	FA	642	Intensity	HeLa and KB cells	[142]
Au	LA	FA	720	Intensity	C6 rat glial cancer cells, subcutaneous C6 glial tumor mouse	[45]
Au	Trypsin	FA	690	Intensity	HeLa tumor-bearing mice	[60]
Ag	MT	FA	632	Intensity	HeLa cells	[99]
Ag	SH-PEI	FA	690	Intensity	MCF-7 cells; tumor-bearing mice	[83]
Cd	BSA	HA	475	Intensity	MCF-7 breast cancer cells	[105]
Au	GSH	Streptavidin	685	Intensity	Human hepatoma cells (HepG2)	[49]
Au	DHLA	Streptavidin	650	Intensity	Human hepatoma cells (HepG2)	[51]
Au	Bovine pancreatic ribonuclease A	Vitamin B_{12}	682	Intensity	Human Caco-2 cells	[62]
Au	BSA	SiO_2	670	Intensity	Lung tumor cells	[103]
Au	GSH	SiO_2	565	Intensity	HeLa cells	[126]
Au	Chitosan	TPP	440	Intensity	HeLa cells	[124]
Au	N-acetyl-L-cysteine	Chitosan	680	Intensity	HeLa cells	[122]
Pt	MAA	Anti-CXCR4-Ab antibody	470	Intensity	HeLa cells	[84]
Pt	PEI	Anti-CXCR4-Ab antibody	560	Intensity	HeLa cells	[85]
Ag	ssDNA	SWCNTs	620	Intensity	HeLa cells	[143]
Ag	DNA	Aptamer	595	Intensity	HeLa cells	[144]
Au	BSA	Met	655	Intensity	Met receptor positive tumor cells, tumor-bearing mice	[120]
Au	BSA	GSH	660	Intensity	4T1 breast cancer cells, 4T1 tumor-bearing mice	[121]
Au	Human transferrin	GO	710	Intensity	HeLa cells, HeLa tumor-bearing mice	[57]
Au	DHLA	Liposome	650	Intensity	Human endothelial cells, hindlimb ischemic mice	[52]
Cu	BSA	LHRH peptide	~410	PET	Orthotopic A549 lung tumor-bearing mice	[131]
^{64}CuAu	GSH	–	800	PET	BALB/c mice	[145]
^{64}CuAu	TA-PEG	Plerixafor	–	PET	4T1 tumor-bearing mice	[133]
Au	DHLA	–	684	FLIM	HeLa cells	[11]
Au	MSA/tiopronin	PEG	785	FLIM	HeLa cells	[47]
Au	LA	–	715	FLIM	HeLa cells	[136]
Au	BSA	Herceptin	640	FLIM	SK-BR3 cells	[137]
Ag	HSA, BSA	GO	620, 510	FLIM	K562 cells	[107]
Au	11-MUA	Dextran	530	Two-photon	Human mesenchymal stem cells (hMSCs)	[96]
Au	GSH	–	780	Two-photon	SH-SY5Y human neuroblastoma cells	[28]
Au	DPA	–	610	Two-photon	HeLa cells	[98]
Au	BSA	DOX	655	Two-photon	HeLa cells	[138]

(continued)

Table 2 (continued)

Metal	Capping agent	Functionalization	λ_{em} (nm)	Imaging modal	Biosystems	Ref.
Au	BSA	RGD	650	Two-photon	U87-MG cancer cells	[139]
Cu	Peptide	–	460	Two-photon	HeLa cells, A549 cells	[108]

DHLA dihydrolipoic acid, *LA* lipoic acid, *CCYTAT* H_2N–CCYRGRKKRRQRRR–COOH, *TA* tannic acid, *PTMP* pentaerythritol tetrakis 3-mercaptopropionate, *PMAA* poly(methacrylic acid), *GSH* glutathione, *PEG* poly(ethylene glycol), *TSA* thiosalicylic acid, *dLys* denatured lysozyme, *BSA* bovine serum albumin, *FA* folic acid, *PEI* polyethyleneimine, *LA* lipoic acid, *MT* metallothionein, *SH-PEI* thiol-polyethyleneimine, *HA* hyaluronic acid, *TPP* triphenylphosphonium, *MAA* mercaptoacetic acid, *PEI* polyethylenimine, *SWCNTs* single-walled carbon nanotubes; *Met* methionine, *GO* graphene oxide, *PET* positron emission tomography, *LHRH* luteinizing hormone releasing hormone, *TA-PEG* thioctic acid–polyethylene glycol, *MSA* 2-mercaptosuccinic acid, *tiopronin* N-(2-mercapto-propionyl) glycine, *FLIM* fluorescence lifetime imaging, *11-MUA* 11-mercaptoundecanoic acid, *DPA* D-penicillamine, *DOX* doxorubicin

microscopy to observe the uptake and localization of AuNCs in HeLa cells, they found distinct difference in the cellular uptake of AuNCs adsorbed with differently modified HSA (Fig. 6): nHSA (native HSA) suppressed cellular uptake, aHSA (HSA with more negative surface charges) showed negligible effect, and cHSA (HSA with more positive surface charges) enhanced cellular uptake. The results provide helpful information in designing NIR AuNCs aiming to highly efficient cell labeling applications.

Gao and coworkers [68] found that peptide–AuNCs with a bifunctional CCYTAT peptide could specifically target the nucleus of three different cell lines, including normal cells human gastric mucosa cells (GES-1), human embryonic lung fibroblast cells (MRC-5), and human cervical cancer cells (HeLa). Ai et al. [78] successfully employed G-quadruplex AS1411-templated AgNCs for specific bioimaging HeLa cells. Besides, Guével et al. [50] employed GSH-AgNCs as optical probes for NIR fluorescence imaging of epithelial lung cancer A549 cells. Confocal images showed that AgNCs were taken up in the cytoplasm and more specifically in the vesicles of A549 cells, but were absent in the nucleus. In contrast, Wang and coworkers [40, 42] observed that GSH-capped Ag_2S NCs and AgAu alloy NCs were distributed in both cytoplasm and the cellular nucleus of MC3T3-EI cells and CAL-27 cells. These differences in the intracellular localization of MNCs upon the internalization suggest that not only the surface ligands but also the cell types can influence their intracellular fate.

A large number of reports have also focused on tumor imaging in vivo currently. For example, Wu et al. [101] reported the first example of tumor imaging with BSA-AuNCs. Their in vivo tumor targeting and ex vivo imaging studies showed that these ultrasmall AuNCs were highly accumulated in the tumor areas (Fig. 7) due to the enhanced permeability and retention (EPR) effects. Sun and coworkers [58] achieved ferritin receptor-mediated targeting and bioimaging with far-red emitting paired AuNCs. These far-red luminescent AuNCs could act as an excellent probe for targeting ferritin receptor-overexpressed human Caco-2 cells and whole female nude mice body imaging with specific targeting to the kidney. In addition, renal-clearable NIR-emitting GSH-AuNCs and PEG-AuNCs have been reported for in vivo NIR tumor targeting of MCF-7 tumor-bearing mice [29, 82]. They not only exhibited efficient renal clearance and low reticuloendothelial system (RES) accumulation but also showed a much longer tumor retention time and faster normal tissue clearance.

Furthermore, Wang et al. [37] reported the use of biosynthesized NIR-emitting AgNCs for in situ imaging cancer cells and tumors, which did not occur in normal cells and tissues. The same group also explored the possibility of imaging cancer cells through in situ self-biosynthesized ZnNCs [117]. Particularly, in vivo imaging of

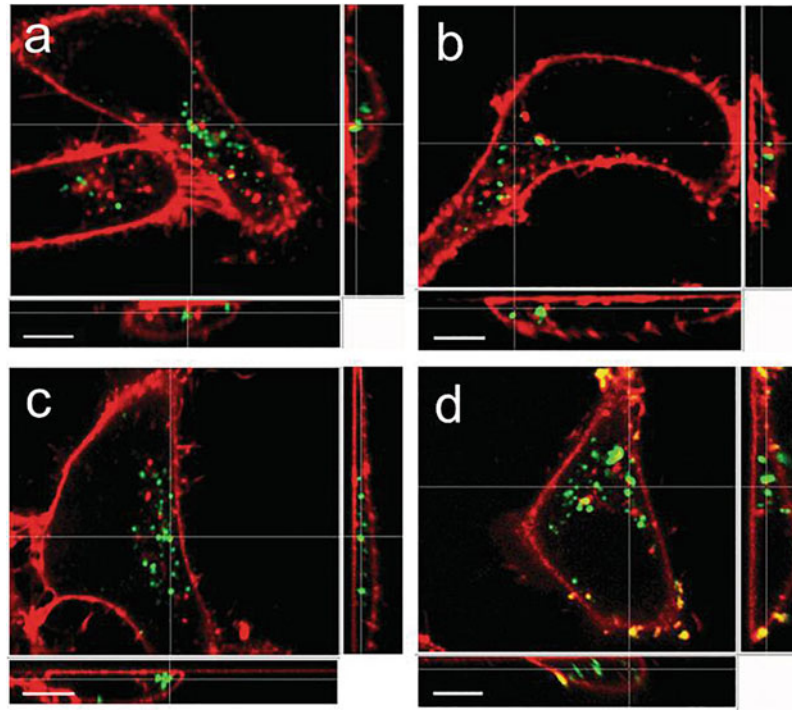

Fig. 6 Three-dimensional fluorescence confocal images of HeLa cells upon incubation with AuNCs (2.5 μM, green) for 2 h: (**a**) without proteins and with 2.5 μM (**b**) nHSA, (**c**) aHSA, and (**d**) cHSA. Cell membranes were stained with CellMask DeepRed (red). The data are shown as sections in the x-y plane (upper left), x-z plane (lower left), and y-z plane (right). Scale bar, 10 μm. Reprinted with permission from Ref. [116]

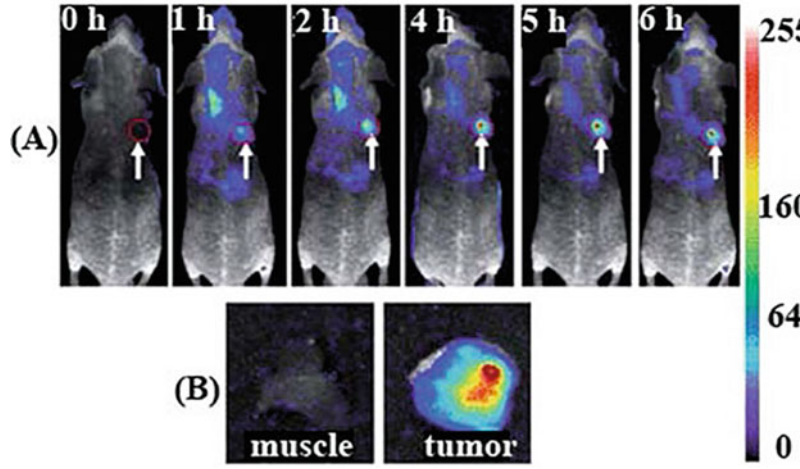

Fig. 7 (**a**) Fluorescence images of mice bearing an MDA-MB-45 tumor. Strong signal from AuNCs was observed in the tumor (marked by the red circle). The arrowheads indicated the tumor. (**b**) Ex vivo fluorescence image of the tumor tissue and the muscle tissue around the tumor from the mice used in A. Reprinted with permission from Ref. [101]

subcutaneous xenografted tumors in nude mice has also established the validity of this strategy for the rapid and precise target self-bioimaging of tumors by subcutaneous injections of zinc gluconate solutions, without significant dissemination to the surrounding normal tissues. Recently, they explored a facile and green strategy to in situ biosynthesize fluorescent CuNCs in cancer cells [38]. As shown in Fig. 8, it is evident that fluorescent CuNCs could be spontaneously biosynthesized in cancer cells for intracellular fluorescence imaging, which could not be biosynthesized in normal cells. More importantly, the relevant fluorescence intensity of the in situ

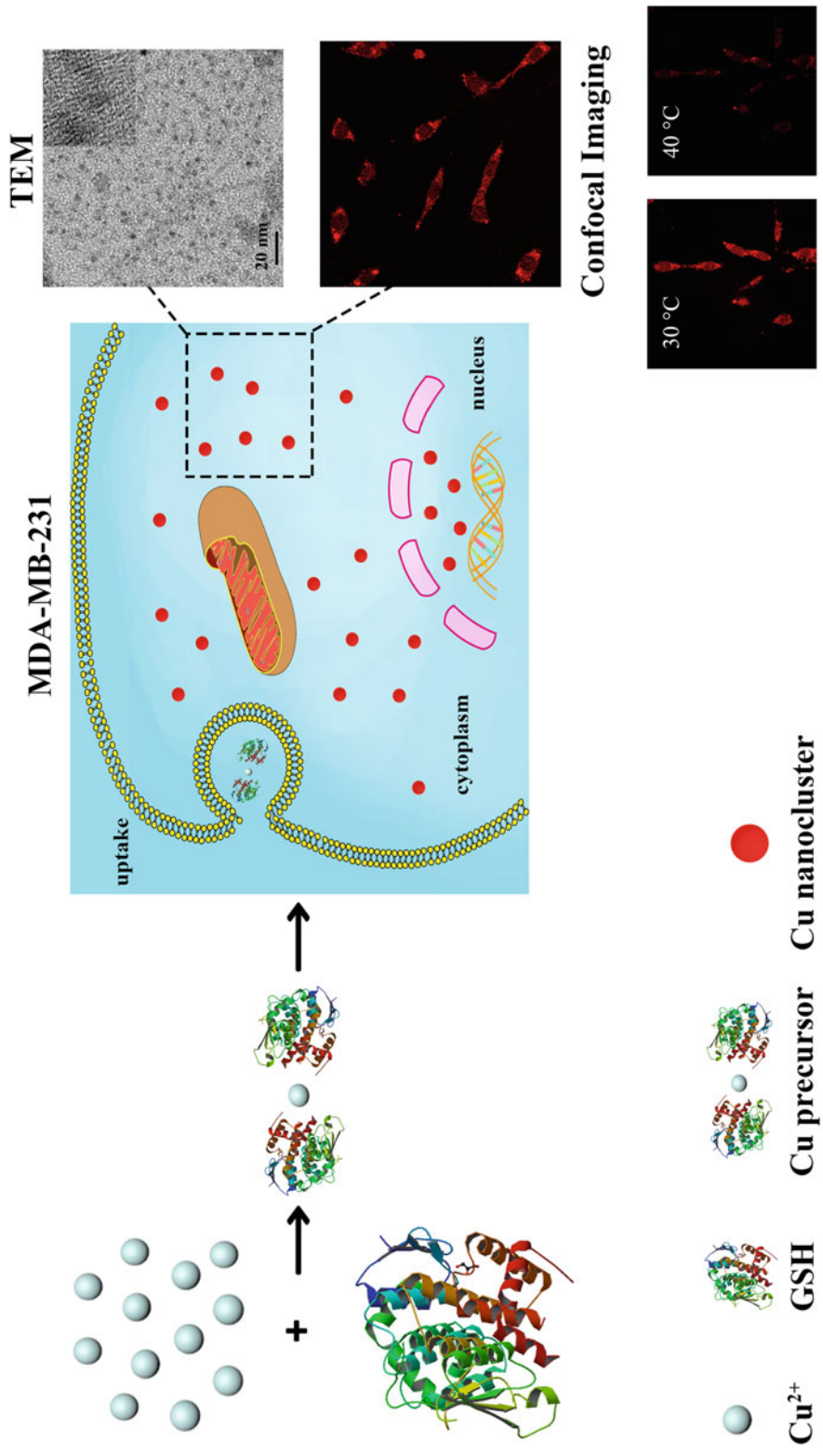

Fig. 8 Schematic illustration of the process for the spontaneous biosynthesis of fluorescent CuNCs in cancer cells for intracellular fluorescence imaging and temperature measurement. Reprinted with permission from Ref. [38]

biosynthesized CuNCs was reversibly and sensitively responsive to physiological temperature changes in MDA-MB-231 cancer cells. Besides, Liu et al. [61] successfully synthesized fluorescent human insulin–Au nanodots (NDs) for in vivo imaging of insulin metabolism. Investigations on mice ear and ex vivo assays on human fat tissues showed that cells with rich insulin receptors had higher uptake of administrated insulin.

For targeted imaging of cancer cells and tumors, MNCs are modified with specific recognition units such as folic acid (FA) and streptavidin. For example, targeted imaging of folate receptor (FR) positive oral carcinoma KB cells using FA-conjugated BSA-AuNCs has been reported [65, 104]. Tumor targeting and specific affinity of FA-conjugated AuNCs for FR over-expressed tumors facilitated the accumulation of AuNCs in the tumor site, which enhanced the fluorescence signal in the tumor site, enabling in vivo targeted imaging of tumors with high specificity and also the subsequent tumor therapy [45, 60, 102]. Recently, Wang et al. [83] reported the conjugation of PEI-AgNCs with FA for both in vitro and in vivo targeted imaging. Their results indicated that the clearance rate of FA-conjugated AgNCs in the tumor-bearing mice was much slower than that in the normal mice because the high affinity of FA to target tumors inhibited FA-AgNCs from being metabolized. Moreover, Chen et al. [118] synthesized core–shell structured multifunctional nanocarriers for targeted anticancer drug delivery, where FA-conjugated amphiphilic hyperbranched block copolymer was used as shell on the surface of AuNCs. The nanocarriers specifically targeted cancer cells because of the enhanced cell uptake mediated by FA moiety. Similarly, the multifunctional anticancer drug paclitaxel (PTX)-loaded AuNCs/FA-modified poly(DBAM-*co*-NAS-*co*-HEMA) (PDNH) core-satellites nanocomposites were fabricated, which possessed simultaneous cancer imaging, targeted drug delivery, and controlled anticancer drug release [119]. In vivo studies showed the selective accumulation of FA-conjugated nanocomposites in tumor tissues, and the drug delivery process could be continuously monitored by the imaging probes, AuNCs. Similarly, streptavidin-conjugated AuNCs have been reported to specifically label endogeneous biotin within human hepatoma cells (HepG2) using the specific interactions between streptavidin and biotin [49, 51].

Apart from FA and streptavidin, other functionalized molecules have also been used to conjugate with MNCs. For instance, Kong et al. [62] developed a multifunctional nanoprobe for simultaneous targeting and imaging of human colon carcinoma Caco-2 cells by conjugating vitamin B_{12} to the ribonuclease A–stabilized AuNCs. Chen et al. [120] fabricated a fluorescent nanoprobe capable of specifically targeting carcinoma cells and tumors by coupling methionine (Met) and an NIR organic fluorescent dye MPA to BSA-AuNCs (Au-Met-MPA). Cui et al. [121] synthesized well-defined AuNCs nanoassembly by the self-assembly of reduced AuNCs using GSH as linkers. The as-prepared nanoassembly displayed highly effective cellular uptake and precise tumor targeting for NIRFL imaging in vivo compared to that of individual AuNCs. Wang et al. [57] reported the fabrication of Tf-AuNCs/GO nanocomposite (Tf-AuNCs/GO) for turn-on NIR fluorescence bioimaging of transferrin receptor (TfR) over-expressed HeLa cells and HeLa tumor-bearing mice.

Duan et al. [122] applied chitosan grafted with N-acetyl-L-cysteine (NAC-CS) as the template to prepare NIR fluorescent AuNCs (AuNCs@NAC-CS), which possessed many advantages in cell imaging, such as low cytotoxicity, low sensitivity to tumor cells contents (H_2O_2 and protease), and long-time cell imaging. During in vivo experiments, the obvious fluorescence signal of AuNCs@NAC-CS appeared in the liver and kidney of the normal mice after 6 h injection. The ultrasmall NPs were efficiently cleared which overcomes the toxicity by nonspecific accumulation in healthy tissues/organs from renal in vivo [123]. Triphenylphosphonium (TPP), a kind of delocalized lipophilic cations capable of selectively accumulating into highly negatively charged mitochondria of living cells, has been employed in functionalizing chitosan–AuNC composites (AuNCs@CS-TPP) for targeted

mitochondrial imaging in living cells [124]. By functionalizing of TAT peptide on the surface of AuNCs, multifunctional TAT peptide–AuNCs are designed for simultaneous fluorescence imaging as well as NIR light activated nucleus-targeting photodynamic therapy [125]. Recently, by combining biomineralization and supramolecular self-assembly of motif-designed peptide constructs containing an RGD sequence, Su et al. [69] have demonstrated the utility of AuNC-incorporated peptide nanofibers for targeted imaging of cancer cells.

Taking advantage of their good cellular imaging properties, metal NC-based composites have been developed for real-time imaging of important physiological events in the intracellular environment. For instance, a novel nanocomposite has been developed through a crown-like assembly of dye-encapsulated silica particles decorated with satellite AuNCs for imaging of highly reactive oxygen species (hROS) in live cells [126]. This composite exhibits single-excitation and dual-emission fluorescent properties, one emission at 565 nm originating from the AuNCs, which fluorescence can be quenched substantially by hROS, and the other at 435 nm arising from the silica particles acting as an internal reference (Fig. 9a). When the composite-loaded cells were incubated with H_2O_2, a kind of weak ROS, strong fluorescence signals at both the blue and the red channels remained constant (Fig. 9b). However, a remarkable change was observed in the fluorescence images when the composite-loaded cells were incubated with hROS, such as HClO and $ONOO^-$, 3-morpholinosydnon-imine (SIN-1) can slowly releases $ONOO^-$. Chen et al. [127] reported a dual-emission BSA-templated (cerium) CeAuNCs probe for ratiometric determination of local pH values inside cells. Recently, Pan et al. [128] used viscosity-sensitive GSH-AuNCs with diffusion-dependent emission for viscosity imaging in live cells. Nystatin can induce mitochondrial malfunction by causing structural changes or swelling of mitochondria, resulting in a sharp increase of viscosity in the cells [129, 130]. A remarkable fluorescence enhancement effect can be observed for the cells successively treated with nystatin and AuNCs.

Gao et al. [131] first developed ultrasmall chelator-free radioactive [^{64}Cu]CuNCs using BSA as a scaffold for PET imaging in an orthotopic lung cancer model. By preconjugating tumor target peptide luteinizing hormone releasing hormone (LHRH) to the BSA shell, the prepared [^{64}Cu]CuNC@BSA-LHRH showed high uptake in A549 human lung tumor, high radiolabeling stability, and rapid renal clearance characteristics. After injecting via tail vein into mice bearing orthotopic A549 lung tumors, the orthotopic A549 tumors of the left lung were clearly delineated with very little local background in the whole-body PET imaging of mice injected with [^{64}Cu]CuNC@BSA-LHRH (Fig. 10b). It is noticeable, however, that a significant difference in [^{64}Cu]CuNCs uptake between [^{64}Cu]CuNC@BSA and [^{64}Cu]CuNC@BSA-LHRH is observable after 0.5–4 h post-injection. The [^{64}Cu]CuNC@BSA-LHRH was retained preferentially in the orthotopic lung tumor by combined active targeting and passive targeting after injection [132]. Although [^{64}Cu]CuNC@BSA also showed partial tumor localization due to passive targeting by the effective EPR effect [132], most of the [^{64}Cu]CuNC@BSA distributed in the kidney and bladder (Fig. 10a). In another study, Liu and coworkers [133] prepared ^{64}Cu doped AuNCs (^{64}CuAuNCs) functionalized with AMD3100 (or Plerixafor) for targeted PET imaging of CXCR4, an up-regulated receptor on primary tumor and lung metastasis in a mouse 4 T1 orthotopic breast cancer model. In contrast to the ligand tracer alone (^{64}Cu–AMD3100) and NCs (^{64}CuAuNCs) without the conjugation of AMD3100, the targeted ^{64}CuAuNCs–AMD3100 exhibited higher sensitivity, better accuracy, and much earlier detection of CXCR4 expression in lung metastasis. Radionuclide ^{64}Cu-doped alloy ^{64}CuAuNCs have also be used as targeted probes for PET imaging in U87MG glioblastoma xenografted mice [134] and prostate cancer bearing mice [135].

FLIM is a powerful technique for cell imaging, which can take advantage of MNCs that typically

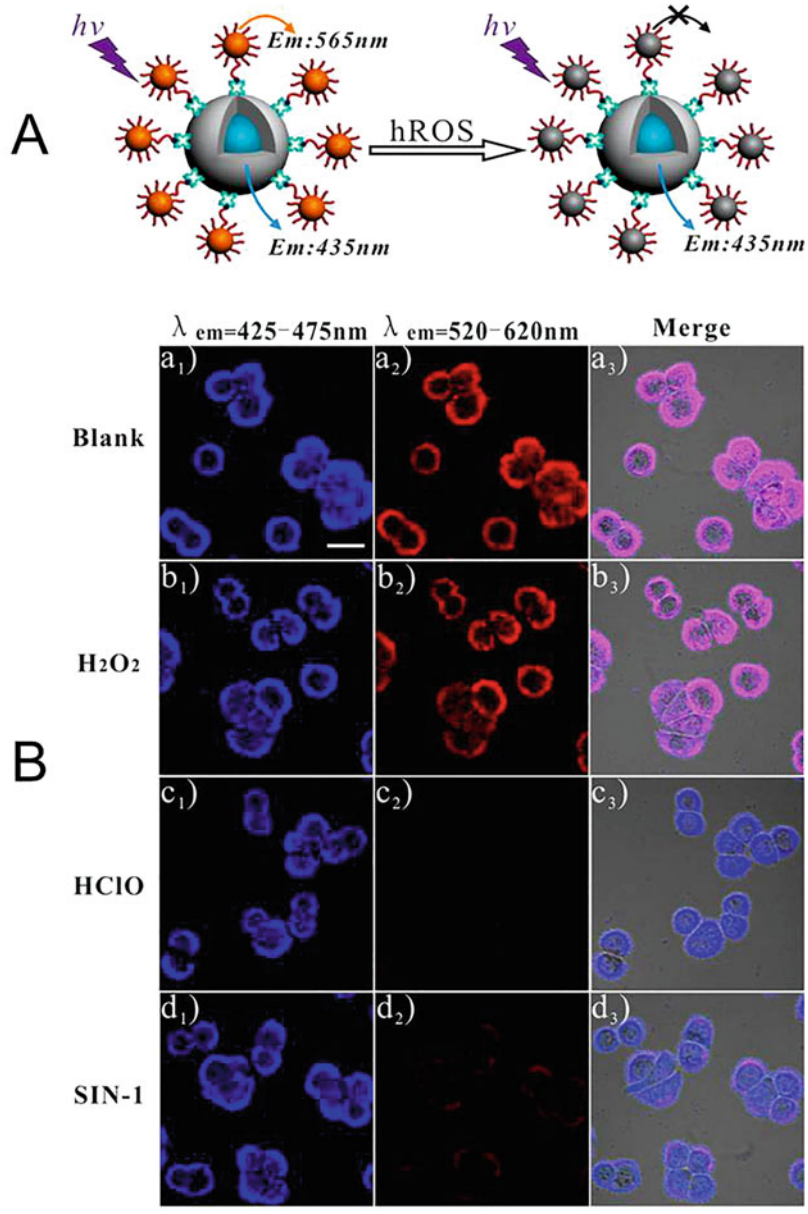

Fig. 9 (**a**) Schematic illustration of hROS detection using dye-encapsulated silica particles decorated with satellite AuNCs. (**b**) Confocal fluorescence microscopy images of HeLa cells after incubation with silica-AuNC composites for 1 h. Cells were (a) untreated or treated with (b) 1 mM H_2O_2 for 10 min, (c) 200 μM HClO for 5 min, and (d) 3 mM SIN-1 for 40 min. Reprinted with permission from Ref. [126]

possess longer fluorescence lifetime than the life time of the autofluorescence from cellular organelles, and thus they can easily be imaged by using lifetime gating. Upon FLIM imaging, the researchers observed that AuNCs located near the cell membrane displayed longer lifetimes than those internalized inside the cells [11], indicating that FLIM imaging not only reveals the cellular uptake of AuNCs but also provides information on their different local environment. Later, based on the fact that the fluorescence intensity as well as the lifetime of DHLA–AuNCs is highly dependent on the temperature, Shang et al. [136] demonstrated the utilization of AuNC-based FLIM imaging for temperature sensing in live cells. As shown in Fig. 11, with increasing the temperature, the fluorescence lifetime decreased markedly from 970 ns at 14 °C to 670 ns at 43 °C,

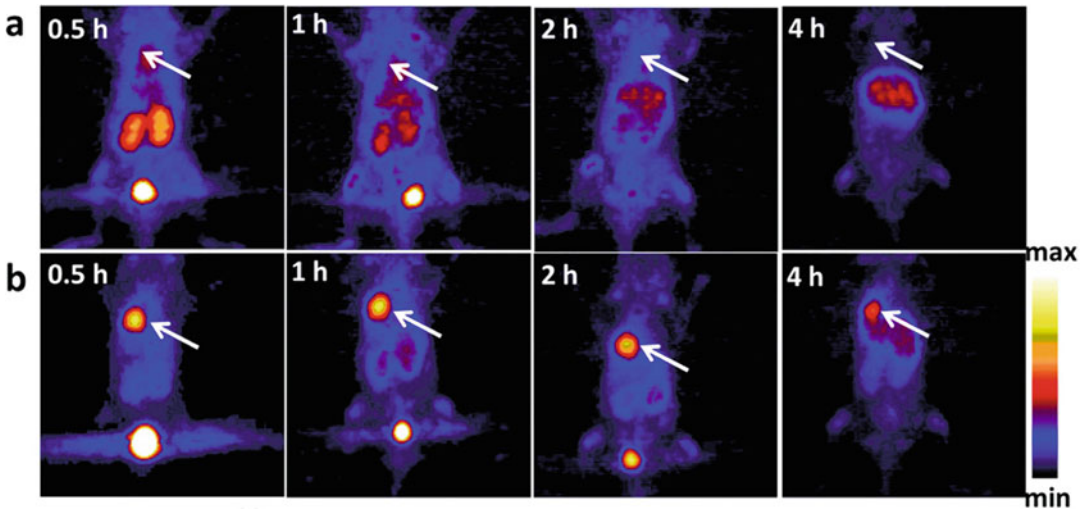

Fig. 10 In vivo PET imaging and biodistribution. Representative PET images of coronal single slices on orthotopic A549 lung tumor-bearing mice after intravenous injection of 6.7 MBq of [^{64}Cu]CuNC@BSA (**a**) and [^{64}Cu]CuNC@BSA-LHRH (**b**). Images were acquired at 0.5, 1, 2, and 4 h. White arrows indicate the lung tumor. Reprinted with permission from Ref. [131]

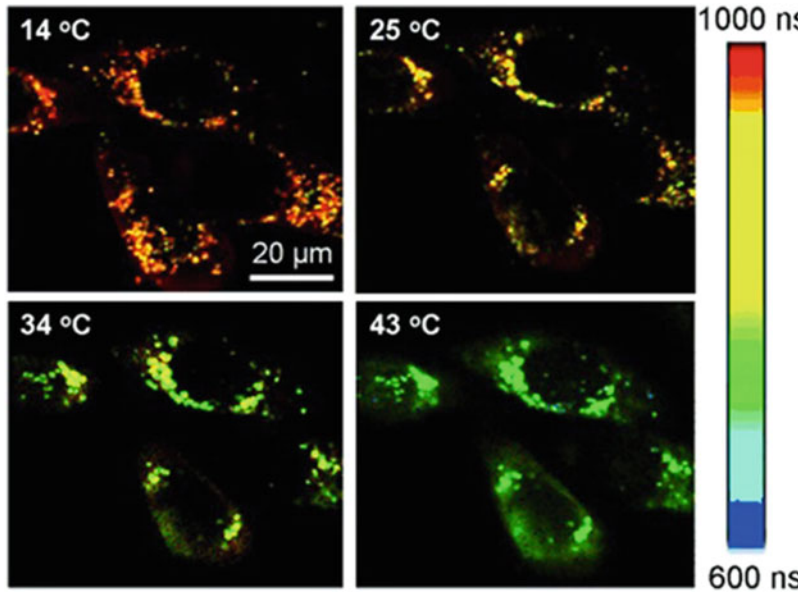

Fig. 11 Typical FLIM images of HeLa cells with internalized AuNCs at four different temperatures. Reprinted with permission from Ref. [136]

suggesting the potential of AuNC-based system for thermal sensing at the subcellular level via FLIM. In another report, Zhang and coworkers [47] demonstrated FLIM-based cellular imaging by using MSA- and tiopronin-capped AuNCs and further covalently bound PEG moieties to improve their capability of staining HeLa cells. Particularly, they observed that these PEGlyated

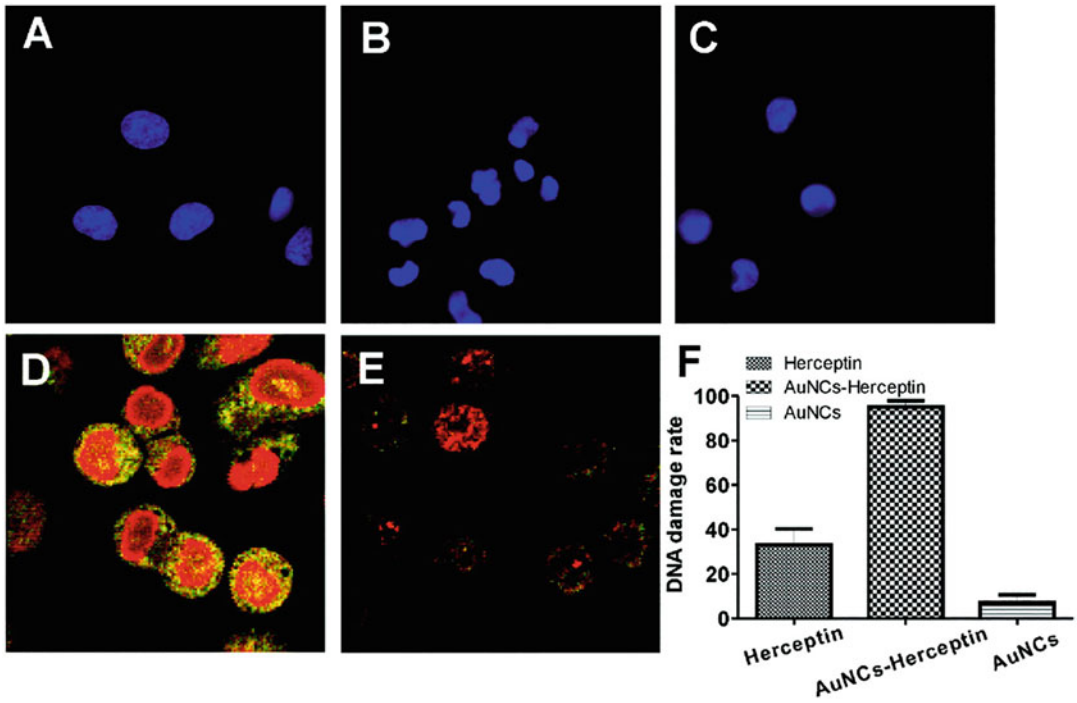

Fig. 12 Fluorescence images show the apoptosis induced by AuNCs alone (**a**), AuNCs-Her (**b**), and Herceptin (**c**) by staining the nucleus with Hoechst 33258 (excited by UV light and the emission is 460 nm). FLIM shows DNA damage of SK-BR3 cells induced by AuNCs-Her (**d**) and Herceptin alone (**e**) indicated by the bright yellow dots. Quantitative evaluation of DNA damage of cells as a percentage of the total number of cells for different treatments (**f**). Reprinted with permission from Ref. [137]

AuNCs widely distribute throughout the cells and especially accumulate in the areas close to the cell nucleus. Irudayaraj et al. [137] reported the use of Herceptin-conjugated BSA-AuNCs (AuNCs-Her) for simultaneous imaging and enhanced cancer therapy because of its ability to induce nuclear DNA damage and apoptosis. Importantly, they found that the endocytosed AuNCs-Her could escape the endolysosomal pathway and enter the nucleus of cancer cells to enhance the therapeutic efficacy of Herceptin. FLIM indicated that almost all of the cells cultured with AuNCs-Her had specific fluorescence staining, representing DNA damage (Fig. 12d). In contrast, only a small amount of cells treated with Herceptin alone shows DNA damage under the same condition (Fig. 12e). Quantification of apoptosis positive cells as a percentage of the total number of cells revealed that only 35% of the cells treated with Herceptin underwent apoptosis due to DNA damage compared to 95% of the AuNCs-Her (Fig. 12f) treated cells.

The outstanding TPA cross sections of MNCs make them good candidates for application in two-photon cellular imaging, which is another attractive imaging technique because of its ability of imaging depth inside tissues and low phototoxicity of NIR light. Polavarapu and coworkers [28] investigated the two-photon excitation fluorescence imaging of SH-SY5Y human neuroblastoma cells incubated with GSH-AuNCs under excitation of femtoseond laser pulses at 800 nm. The two-photon imaging and z-stack sectioning results clearly confirmed that AuNCs were internalized inside the cells. Khandelia et al. [138] reported the use of anticancer drug doxorubicin (DOX) loaded BSA-AuNCs for imaging HeLa cells by two-photon excitation at 730 nm. Their results demonstrated that DOX-loaded AuNCs not only helped in tracking the delivery

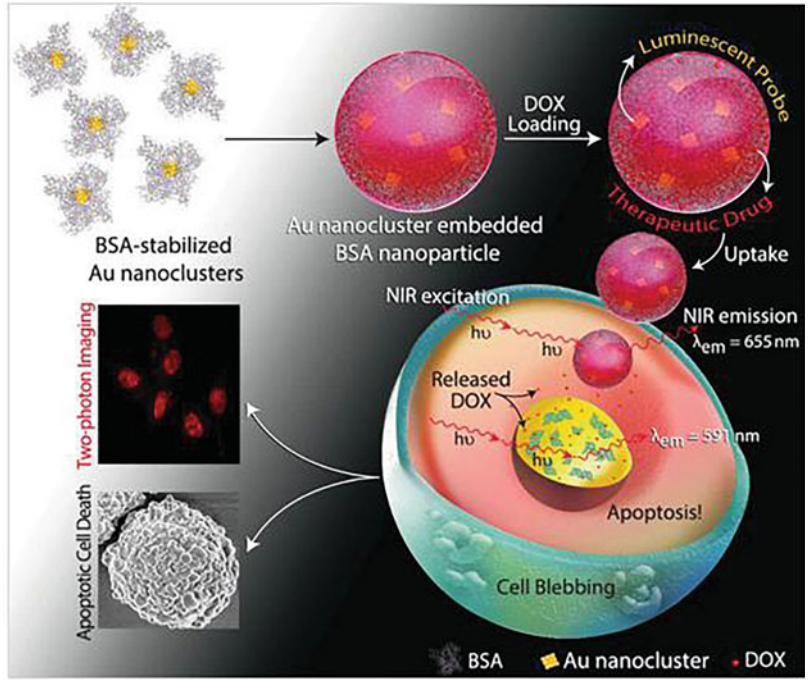

Fig. 13 A schematic illustration of the formation of DOX-loaded AuNC-embedded BSA nanoparticles, followed by uptake and release of DOX inside HeLa cells, leading to apoptotic cell death, as visualized by two-photon imaging. Reprinted with permission from Ref. [138]

but also released drugs to the cancer cells, leading to apoptotic cell death (Fig. 13). In a recent work, Gu et al. [139] prepared RGD conjugated BSA-AuNC nano-capsules for two-photon fluorescence imaging of U87-MG cancer cells. The Z-stack sectioning of two-photon images revealed that hybrid nano-capsules were mainly resided in the cytoplasm nearby the nucleus.

4 Fluorescent MNCs as Multimodal Bioimaging Probes

At present, multimodal imaging probes based on fluorescent AuNCs for tumor imaging have also attracted plenty of attention (see the summary in Table 3). In an early work, Zhou et al. [146] reported multimodal imaging of NIR-emitting radioactive GSH-AuNPs, which were incorporated with a gold radioisotope ^{198}Au. The ^{198}Au in GSH-[^{198}Au] AuNPs not only helps to quantify the pharmacokinetics of these NIR-emitting AuNPs rapidly but also allows their utility for in vivo SPECT imaging by emitting gamma rays. Thus these NIR-emitting radioactive AuNPs can serve as dual-modality imaging probes with both SPECT and FL imaging capabilities (Fig. 14). Chen and coworkers [147] recently fabricated a dual-modality FL/CT iodinated BSA-AuNCs for early accurate diagnosis of thyroid cancer. They accomplished in vivo FL and CT imaging via an orthotopic human thyroid cancer patient tissue derived xenograft (PDX) mouse model. Adopting the similar FL and CT dual-modal imaging techniques, insulin–AuNCs were used to distinguish the differentiated C2C12 myoblasts from undifferentiated ones [148]. Also, FA-conjugated GSH-AuNCs and lysozyme-AuNCs have been used for in vivo targeted dual-modal FL/CT imaging of MGC-803 tumor-bearing mice and HeLa tumor-bearing nude mice, respectively [30, 149]. Sarkar et al. [107] synthesized protein-capped AgNCs impregnated onto GO sheets for FLIM. Furthermore, AgNCs/GO assembly have a great potential as CT imaging contrasting agents, and CT images show significant contrast enhancement of bone tissues in mice models.

Table 3 Fluorescent MNCs as multimodal bioimaging probes

Metal	Capping agent	Functionalization	λ_{em} (nm)	Imaging modals	Biosystems	Ref.
Au	GSH	^{198}Au	810	NIRFL/SPECT	Live mouse	[146]
Au	BSA	Iodine	680	NIRFL/CT	Human thyroid cancer PDX nude mouse	[147]
Au	Insulin	–	670	NIRFL/CT	Differentiated C2C12 mouse myoblasts	[148]
Au	GSH	FA	650	NIRFL/CT	MGC-803 tumor-bearing mice	[30]
Au	Lysozyme	FA	690	NIRFL/CT	HeLa tumor-bearing nude mice	[149]
Ag	HSA, BSA	GO	620, 510	FL/CT	Swiss albino mice	[107]
Au	BSA	Gd(III)	700	NIRFL/MRI	U87-MG tumor-bearing mice	[150]
Au	Cyclodecapeptide	Gd(III)	~660	NIRFL/MRI	Kunming mouse	[151]
Au	GSH	Fe_3O_4 NPs	650	NIRFL/MRI	293 T cells	[152]
Au	BSA	Fe_3O_4 NPs	~650	NIRFL/MRI	H1650 cells	[153]
Au	BSA	Fe_3O_4 NPs, AuNRs	650	NIRFL/MRI	HeLa cells	[156]
Au	HSA	^{64}Cu	~667	NIRFL/PET	U87MG glioblastoma Xenograft mice	[134]
Au	Thioctic-zwitterion	–	~750	NIRFL/PAI	U87MG cells; mice	[164]
Au	GSH	Gd(III)	~652	NIRFL/CT/MRI	A549 tumor-bearing mice	[157]
Au	Albumin	DTPA–Gd(III)	660	NIRFL/CT/MRI	MCF-7 tumor-bearing mice	[158]
Au	BSA	Gd_2O_3, ICG	635	NIRFL/CT/MRI	Kunming mice	[159]
Au	BSA	Gd(III), FA	660	NIRFL/CT/MRI	KB tumor-bearing mice	[161]
Au	GSH	Gd^{3+}, SiO_2	595	FL/CT/MRI	MCF-7 cells, tumor-bearing BALB/c mice	[162]
Au	Triphenylphosphine	SiO_2	827	NIRFL/PAI/MRI	LS174T tumor-bearing mice	[163]

GSH glutathione, *BSA* bovine serum albumin, *FA* folic acid, *Cyclodecapeptide* c (Asp-Arg-Glu-Pro-Cys-Glu-Tyr-Asp-Pro-Cys), *HSA* human serum albumin, *GO* graphene oxide, *AuNRs* gold nanorods, *DTPA* diethylene triamine pentaacetic acid, *NIRFL* near-infrared fluorescence, *SPECT* single-photon emission computed tomography, *CT imaging* X-ray computed tomography imaging, *MRI* magnetic resonance imaging, *ICG* indocyanine green, *PET* positron emission tomography, *PAI* photoacoustic imaging

NIRFL and MR dual-modal imaging have been reported through coupling AuNCs with magnetic agents such as Gd_2O_3 and Fe_3O_4 NPs. For example, Sun et al. [150] employed Gd_2O_3 functionalized BSA-AuNCs as probes for dual-modal NIRFL and MR blood pool imaging in vivo. By further bioconjugation of BSA-Gd_2O_3/AuNCs with arginine–glycine–aspartic acid peptide (RGD), they can be used for in vivo targeted tumor imaging of U87-MG tumor-bearing mice. Liang and coworkers [151] constructed Gd^{3+}-functionalized AuNCs for dual-model NIRFL/MR imaging by using a cyclodecapeptide as the template. Recently, Wang et al. [152] demonstrated a facile strategy of fabricating GSH-AuNC probes decorated with magnetic Fe_3O_4 NPs for bimodal NIRFL/MR cell imaging. Alternatively, dual-modal bioimaging probes can be fabricated by conjugating biotinylated NIR fluorescent BSA-AuNCs to streptavidin functionalized Fe_3O_4 NPs [153].

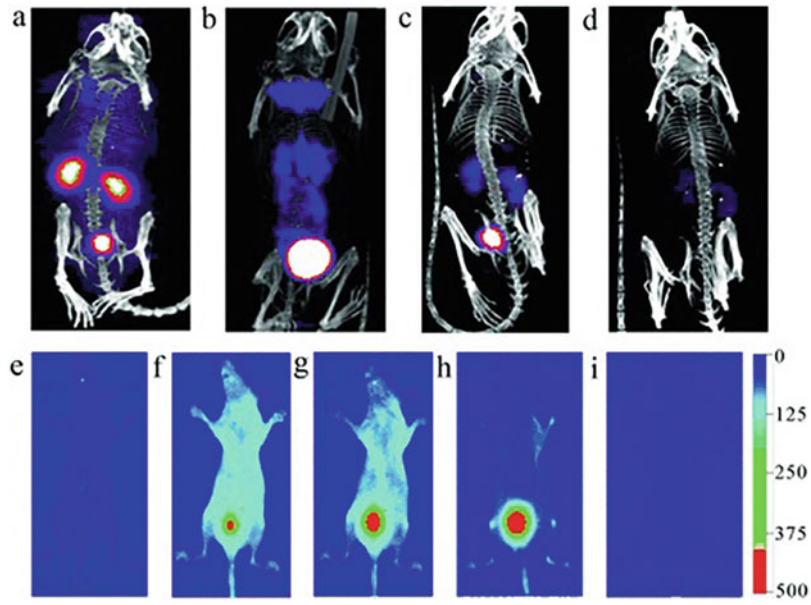

Fig. 14 Representative SPECT images (top row) of BALB/c mice injected with GSH-[^{198}Au] AuNPs. (**a**) 10 min, (**b**) 1 h, (**c**) 4 h, and (**d**) 24 h p.i.. In vivo FL imaging (bottom row) of a live mouse (**e**) pre-injection, and (**f**) 5 min, (**g**) 20 min, (**h**) 1 h, (**i**) 24 h after IV injection of GSH-[^{198}Au] AuNPs. Reprinted with permission from Ref. [146]

At present, multifunctional theranostic systems with strong clinical imaging-guided capability, phototherapy function, and target specificity have been developed for cancer therapy. Yang et al. [154] fabricated a new imaging-guided and multifunctional cancer therapy platform with multimodal imaging and dual phototherapy function by assembling the captopril-protected Au_{25}NCs ($Au_{25}(Capt)_{18}^{-}$) into mesoporous silica-coated Nd^{3+}-sensitized upconversion nanoparticles (UCNPs@SiO_2). Under 808 nm NIR irradiation, the UCNPs@SiO_2-$Au_{25}(Capt)_{18}^{-}$ nanocomposite can simultaneously exhibit tri-modal upconversion luminescence, photothermal, and photoacoustic imaging features in vivo. Besides, the composite can also present the MR and CT imaging effects due to the Gd^{3+} and Yb^{3+} ions in the UCNPs. Subsequently, the same group designed Fe_3O_4@ZIF-8-$Au_{25}(Capt)_{18}^{-}$ nanocomposites for multimodal imaging and synergistic cancer therapy [155]. Under 808 nm NIR irradiation, the attached photosensitizer agent $Au_{25}(Capt)_{18}^{-}$ clusters can produce highly reactive singlet oxygen ($^1O_2$) for photodynamic therapy (PDT). In addition, the magnetic properties of encapsulated Fe_3O_4 nanocrystals can simultaneously produce hyperthermal effects for photothermal therapy (PTT) and present targeting and MR imaging capability. Protein-based multifunctional nanocarriers (MFNCs) were successfully constructed by assembling gold nanorods, superparamagnetic iron oxide NPs, and AuNCs within BSA (Fig. 15) [156], without affecting their individual properties. The MFNCs showed simultaneous integration of corresponding plasmonic, magnetic, and luminescence properties, which can be used for plasmonic photothermal therapy (PPTT), two-photon and MR imaging in vitro. Moreover, the MFNCs demonstrated efficient loading and delivery of DOX to HeLa cells, resulting in efficient killing of cancer cells and tracking the delivery and release of the drug through confocal fluorescence microscopy.

In addition to the NIRFL and MRI contrasts offered by the probe, the green fluorescence of the endoperoxide triggered by $^1O_2$ can provide additional modality for live cell imaging [153]. With the co-existence of GSH-AuNCs and Gd^{3+} ions, the nanoprobes can act as a multifunctional nanoplatform for triple-modal NIRFL/CT/MR

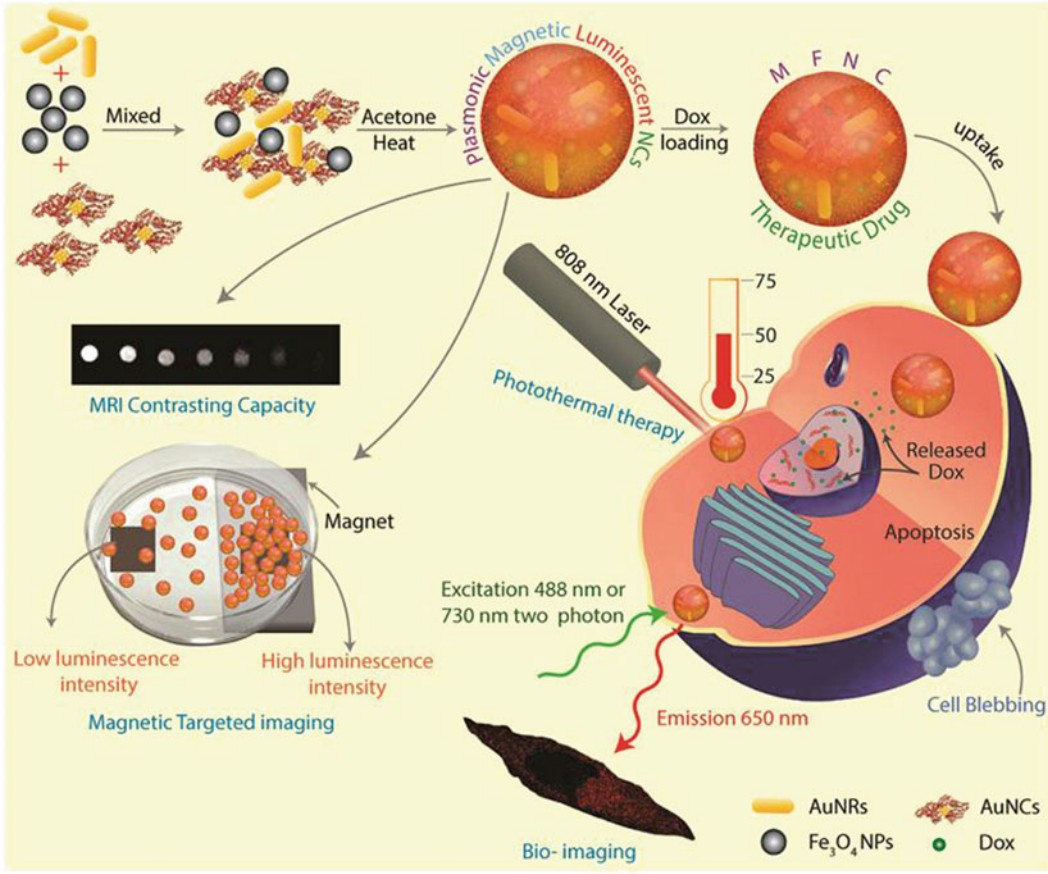

Fig. 15 Schematic depiction of preparing MFNCs, using for plasmonic photothermal therapy and two-photon/MR imaging in vitro, following successful loading and delivery of anticancer drug Dox induced cancer cells death. Reprinted with permission from Ref. [156]

imaging of A549 cancer cells and xenografted A549 tumor models [157]. Similarly, Hu and coworkers [158] prepared Au–Gd NC hybrids by using albumin as the stabilizer, which were suitable for in vivo triple-modal NIRFL/CT/MRI imaging of MCF-7 tumor-bearing mice (Fig. 16). Upon intravenously injected, the hybrid NCs were effectively accumulated in tumor tissues and quickly cleared by renal excretion, indicating their capacity of tumor targeting and low body residues. Recently, Wang and coworkers [159] developed a facile approach to construct BSA-stabilized Gd_2O_3-AuNCs nanoplatform for multimodal imaging and cancer therapy. The nanocomposites exhibit photoluminescent capability in NIR region, and are able to generate singlet oxygen ($^1O_2$) species under NIR laser irradiation at 808 nm for photodynamic therapy. After loading indocyanine green (ICG), the Gd_2O_3-AuNCs-ICG nanocomposites exhibited excellent in vivo triple-modal NIRFL/MR/CT imaging capability, as well as combined photodynamic and photothermal therapy. Wang et al. [160] reported a new method for targeted multimodal tumor bioimaging by using in situ self-biosynthesized AuNCs and iron complexes composites via simple introduction of $AuCl_4^-$ (i.e., $HAuCl_4$) and Fe^{2+} (i.e., $FeCl_2$) ions to the cancer cells or xenograft tumor mice model. In a recent study, the same group [39] explored a

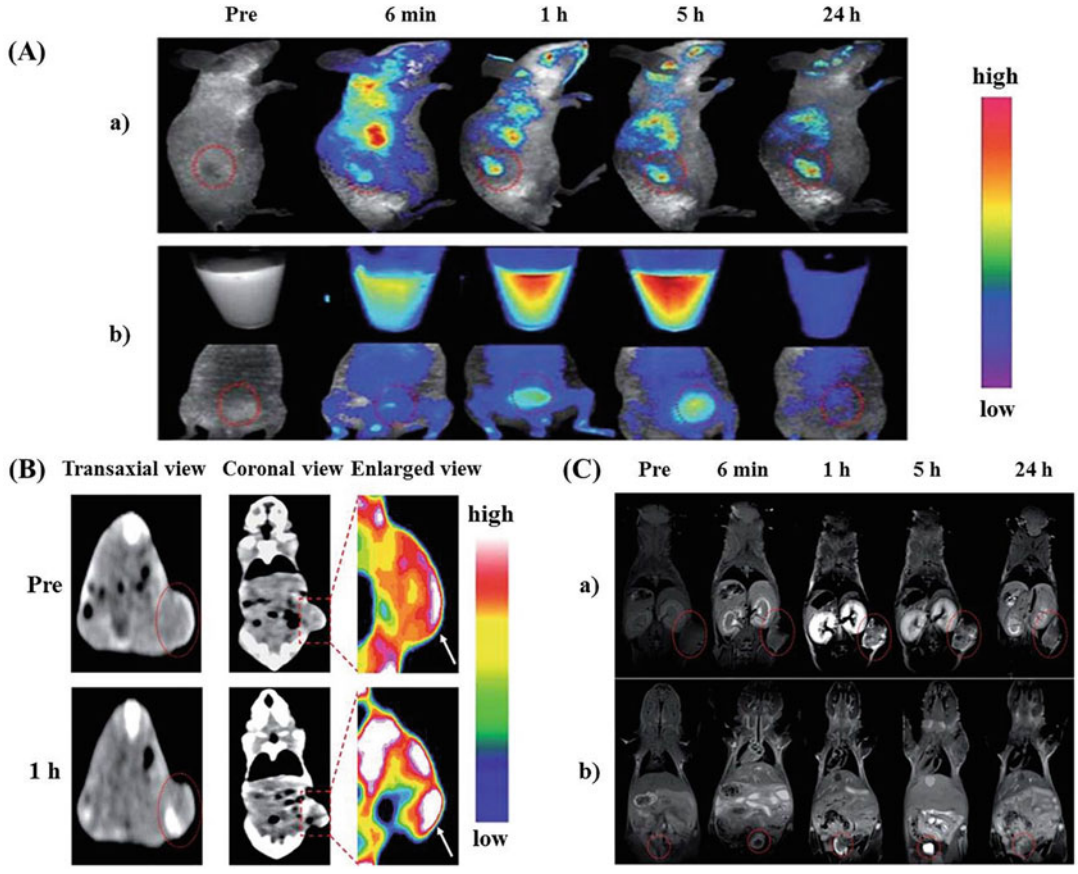

Fig. 16 (**a**) (a and b) In vivo FL imaging of MCF-7 tumor-bearing mice after the tail-vein injection of hybrid NCs. Inset image is the FL reflectance images of urine. (**b**) In vivo CT images of MCF-7 tumor-bearing mice injected with the hybrid Au–Gd NCs. The arrow and red dotted circle indicate the tumor site. (**c**) (a and b) In vivo MRI images of MCF-7 tumor-bearing mice injected with the hybrid Au–Gd NCs. The arrow and red dotted circle indicate the tumor (a) and bladder (b) sites, respectively. Reprinted with permission from Ref. [158]

novel in vivo multimodal NIRFL/MR/CT bioimaging method for the early detection of tumors based on in situ biosynthesized Zn&Fe oxide NCs. By introducing Zn^{2+} and Fe^{2+} ions via a single injection, fluorescent ZnO NCs and superparamagnetic Fe_3O_4 nanoparticles can be spontaneously self-biosynthesized in tumor cells/tissues. Xu et al. [161] synthesized AuNC-Gd_2O_3 integrated nanoprobe (denoted as AuGds) using BSA as the template via a biomineralization approach. After being chemically modified with FA, the FA-AuGds could specifically target FRs on KB tumor cells, and permitted in vivo NIRFL, MR, and CT imaging of xenografted KB tumor-bearing mice. Gd^{3+}-aggregated AuNCs encapsulated by SiO_2 shell (Gd^{3+}-AuNCs@SiO_2 NPs) were strategically designed and prepared. In the presence of Gd^{3+} ions, the GSH-capped AuNCs show aggregation-induced fluorescence (AEF) effect. The as-prepared composites can be used for in vitro and in vivo multimodal FL/MR/CT cancer imaging [162]. Hembury and coworkers [163] synthesized highly monodispersed SiO_2/AuNCs by nucleating gold within hollow mesoporous silica particles in a one-phase synthetic route. These SiO_2/AuNCs possessed stable NIR fluorescence and paramagnetism, thus it could be used as a promising probe

for in vivo NIRFL/PAI/MR imaging of colorectal carcinoma tumor (LS174T)-bearing mice.

5 Conclusions and Outlooks

In this chapter, we have systematically summarized recent advances in the synthesis strategies and bioimaging applications of fluorescent MNCs. In the past few years, fluorescent MNCs have been largely explored for bioimaging due to their ultrasmall size, good biocompatibility, and easy functionalization. Although a large number of researches have been reported about MNCs currently, there are still a lot of rooms to further improve and many unclear questions to reveal.

First of all, most MNCs possess a relatively low QY (usually less than 10%) in comparison to other fluorophores such as semiconductor QDs and many organic dyes. In addition, MNCs often show size heterogeneity in the crude product, and it still remains challenging to obtain atomically precise water-soluble MNCs suitable for bioimaging applications, which markedly precludes quantitative tracking in organisms. Therefore, researchers still need to make greater effort to explore more efficient synthesis routes for size-controllable fluorescent MNCs with relatively high QY and high purity [165, 166]. Second, the present bioimaging studies mainly concentrate on fluorescent AuNCs due to their good stability and easy synthesis. Considering gold is relatively expensive compared to other metals, it would be attractive to further exploit potential bioimaging applications of other MNCs or alloy NCs. Third, up to now, relatively little is known about the behavior of these ultrasmall MNCs within the complex biological environment [167], which is actually highly important regarding the safe as well as efficient use of MNCs in bioimaging applications. Thus, further study to understand the mechanism of cellular and intravital uptake of MNCs and long-term effect after entering into biosystems would be necessary and important. Furthermore, in order to advance potential utility of MNCs as multifunctional probes for applications besides imaging, more types of MNCs-based nanocomposites should be developed by integrating other functional nanomaterials.

In the past years, significant progress has been achieved in developing fluorescent MNCs for bioimaging, but many challenges still remain to face and resolve in the future. With continuing development and more efforts within the community, we believe that more robust fluorescent MNCs will be available, which will then further advance imaging-based applications of these novel nanoprobes in medical diagnose and therapy researches.

Acknowledgements This chapter was modified from the paper published by our group in Chinese Chemical Letters (Xu and Shang 2018; 29:1436–1444). The related contents are re-used with the permission.

References

1. Díez I, Ras RHA (2010) Few-atom silver clusters as fluorescent reporters. In: Advanced fluorescence reporters in chemistry and biology II. Springer, Dordrecht, pp 307–332
2. Zheng J, Nicovich PR, Dickson RM (2007) Highly fluorescent noble-metal quantum dots. Annu Rev Phys Chem 58:409–431
3. Díez I, Ras RHA (2011) Fluorescent silver nanoclusters. Nanoscale 3:1963–1970
4. He X, Wang K, Cheng Z (2010) In vivo near-infrared fluorescence imaging of cancer with nanoparticle-based probes. WIREs Nanomed Nanobiotechnol 2:349–366
5. Song F, Liang R, Deng J, Liu Z, Peng X (2017) Fine-tailoring the linker of near-infrared fluorescence probes for nitroreductase imaging in hypoxic tumor cells. Chin Chem Lett 28:1997–2000
6. Park H, Crozier KB (2013) Multispectral imaging with vertical silicon nanowires. Sci Rep 3:2460
7. He X, Gao J, Gambhir SS, Cheng Z (2010) Near-infrared fluorescent nanoprobes for cancer molecular imaging: status and challenges. Trends Mol Med 16:574–583
8. Weng J, Ren J (2006) Luminescent quantum dots: a very attractive and promising tool in biomedicine. Curr Med Chem 13:897–909
9. Berezin MY, Achilefu S (2010) Fluorescence lifetime measurements and biological imaging. Chem Rev 110:2641–2684
10. Helmchen F, Denk W (2005) Deep tissue two-photon microscopy. Nat Methods 2:932–940
11. Shang L, Azadfar N, Stockmar F, Send W, Trouillet V, Bruns M, Gerthsen D, Nienhaus GU

(2011) One-pot synthesis of near-infrared fluorescent gold clusters for cellular fluorescence lifetime imaging. Small 7:2614–2620
12. Yuan L, Lin W, Zheng K, He L, Huang W (2013) Far-red to near infrared analyte-responsive fluorescent probes based on organic fluorophore platforms for fluorescence imaging. Chem Soc Rev 42:622–661
13. Kim HM, Jung C, Kim BR, Jung SY, Hong JH, Ko YG, Lee KJ, Cho BR (2007) Environment-sensitive two-photon probe for intracellular free magnesium ions in live tissue. Angew Chem Int Ed 46:3460–3463
14. Zipfel WR, Williams RM, Webb WW (2003) Nonlinear magic: multiphoton microscopy in the biosciences. Nat Biotechnol 21:1369–1377
15. Lee DE, Koo H, Sun IC, Ryu JH, Kim K, Kwon IC (2012) Multifunctional nanoparticles for multimodal imaging and theragnosis. Chem Soc Rev 41:2656–2672
16. Li DZ, Chen HD, Bi F, Wang ZX (2016) Progress of multimodal molecular imaging technology in diagnosis of tumor. Chin J Anal Chem 44:1609–1618
17. Willmann JK, van Bruggen N, Dinkelborg LM, Gambhir SS (2008) Molecular imaging in drug development. Nature Rev Drug Discov 7:591–607
18. Zhou B, Zheng L, Peng C, Li D, Li J, Wen S, Shen M, Zhang G, Shi X (2014) Synthesis and characterization of PEGylated polyethylenimine-entrapped gold nanoparticles for blood pool and tumor CT imaging. ACS Appl Mater Interfaces 6:17190–17199
19. Peng C, Qin J, Zhou B, Chen Q, Shen M, Zhu M, Lu X, Shi X (2013) Targeted tumor CT imaging using folic acid-modified PEGylated dendrimer-entrapped gold nanoparticles. Polym Chem 4:4412–4424
20. Zhou J, Lu Z, Shan G, Wang S, Liao Y (2014) Gadolinium complex and phosphorescent probe-modified $NaDyF_4$ nanorods for T1- and T2-weighted MRI/CT/phosphorescence multimodality imaging. Biomaterials 35:368–377
21. Kim J, Piao Y, Hyeon T (2009) Multifunctional nanostructured materials for multimodal imaging, and simultaneous imaging and therapy. Chem Soc Rev 38:372–390
22. Tsotsalas M, Busby M, Gianolio E, Aime S, De Cola L (2008) Functionalized nanocontainers as dual magnetic and optical probes for molecular imaging applications. Chem Mater 20:5888–5893
23. Lee JH, Huh YM, Jun YW, Seo JW, Jang JT, Song HT, Kim S, Cho EJ, Yoon HG, Suh JS, Cheon J (2007) Artificially engineered magnetic nanoparticles for ultra-sensitive molecular imaging. Nat Med 13:95–99
24. Michaelis J, Hettich C, Mlynek J, Sandoghdar V (2000) Optical microscopy using a single-molecule light source. Nature 405:325–328
25. Louie A (2010) Multimodality imaging probes: design and challenges. Chem Rev 110:3146–3195
26. Lu Y, Chen W (2012) Sub-nanometre sized metal clusters: from synthetic challenges to the unique property discoveries. Chem Soc Rev 41:3594–3623
27. Jin R (2010) Quantum sized, thiolate-protected gold nanoclusters. Nanoscale 2:343–362
28. Polavarapu L, Manna M, Xu QH (2011) Biocompatible glutathione capped gold clusters as one- and two-photon excitation fluorescence contrast agents for live cells imaging. Nanoscale 3:429–434
29. Liu J, Yu M, Zhou C, Yang S, Ning X, Zheng J (2013) Passive tumor targeting of renal-clearable luminescent gold nanoparticles: long tumor retention and fast normal tissue clearance. J Am Chem Soc 135:4978–4981
30. Zhang C, Zhou Z, Qian Q, Gao G, Li C, Feng L, Wang Q, Cui D (2013) Glutathione-capped fluorescent gold nanoclusters for dual-modal fluorescence/X-ray computed tomography imaging. J Mater Chem B 1:5045–5053
31. Yang J, Xia N, Wang X, Liu X, Xu A, Wu Z, Luo Z (2015) One-pot one-cluster synthesis of fluorescent and bio-compatible Ag_{14} nanoclusters for cancer cell imaging. Nanoscale 7:18464–18470
32. Pyo K, Thanthirige VD, Kwak K, Pandurangan P, Ramakrishna G, Lee D (2015) Ultrabright luminescence from gold nanoclusters: rigidifying the Au(I)-thiolate shell. J Am Chem Soc 137:8244–8250
33. Li Y, Wang X, Xu S, Xu W (2013) The solvent effect on the luminescence of silver nanoclusters. Phys Chem Chem Phys 15:2665–2668
34. Wang C, Wu J, Jiang K, Humphrey MG, Zhang C (2017) Stable Ag nanoclusters-based nano-sensors: rapid sonochemical synthesis and detecting Pb^{2+} in living cells. Sens Actuators B Chem 238:1136–1143
35. Wang C, Ling L, Yao Y, Song Q (2015) One-step synthesis of fluorescent smart thermo-responsive copper clusters: a potential nanothermometer in living cells. Nano Res 8:1975–1986
36. Wang J, Zhang G, Li Q, Jiang H, Liu C, Amatore C, Wang X (2013) In vivo self-bio-imaging of tumors through in situ biosynthesized fluorescent gold nanoclusters. Sci Rep 3:1157
37. Gao S, Chen D, Li Q, Ye J, Jiang H, Amatore C, Wang X (2014) Near-infrared fluorescence imaging of cancer cells and tumors through specific biosynthesis of silver nanoclusters. Sci Rep 4:4384
38. Ye J, Dong X, Jiang H, Wang X (2017) An intracellular temperature nanoprobe based on biosynthesized fluorescent copper nanoclusters. J Mater Chem B 5:691–696
39. Du T, Zhao C, ur Rehman F, Lai L, Li X, Sun Y, Luo S, Jiang H, Selke M, Wang X (2017) Rapid and multimodal in vivo bioimaging of cancer cells through in situ biosynthesis of Zn&Fe nanoclusters. Nano Res 10:2626–2632
40. Wang C, Wang Y, Xu L, Zhang D, Liu M, Li X, Sun H, Lin Q, Yang B (2012) Facile aqueous-phase synthesis of biocompatible and fluorescent Ag_2S nanoclusters for bioimaging: tunable

photoluminescence from red to near infrared. Small 8:3137–3142
41. Ding C, Cao X, Zhang C, He T, Hua N, Xian Y (2017) Rare earth ions enhanced near infrared fluorescence of Ag_2S quantum dots for the detection of fluoride ions in living cells. Nanoscale 9:14031–14038
42. Wang C, Xu L, Xu X, Cheng H, Sun H, Lin Q, Zhang C (2014) Near infrared Ag/Au alloy nanoclusters: tunable photoluminescence and cellular imaging. J Colloid Interface Sci 416:274–279
43. Sun Y, Xia Y (2004) Mechanistic study on the replacement reaction between silver nanostructures and chloroauric acid in aqueous medium. J Am Chem Soc 126:3892–3901
44. Shang L, Yang L, Stockmar F, Popescu R, Trouillet V, Bruns M, Gerthsen D, Nienhaus GU (2012) Microwave-assisted rapid synthesis of luminescent gold nanoclusters for sensing Hg^{2+} in living cells using fluorescence imaging. Nanoscale 4:4155–4160
45. Nair LV, Nazeer SS, Jayasree RS, Ajayaghosh A (2015) Fluorescence imaging assisted photodynamic therapy using photosensitizer-linked gold quantum clusters. ACS Nano 9:5825–5832
46. Ghosh R, Goswami U, Ghosh SS, Paul A, Chattopadhyay A (2015) Synergistic anticancer activity of fluorescent copper nanoclusters and cisplatin delivered through a hydrogel nanocarrier. ACS Appl Mater Interfaces 7:209–222
47. Zhang J, Fu Y, Conroy CV, Tang Z, Li G, Zhao RY, Wang G (2012) Fluorescence intensity and lifetime cell imaging with luminescent gold nanoclusters. J Phys Chem C 116:26561–26569
48. Pan S, Liu W, Tang J, Yang Y, Feng H, Qian Z, Zhou J (2018) Hydrophobicity-guided self-assembled particles of silver nanoclusters with aggregation-induced emission and their use in sensing and bioimaging. J Mater Chem B 6:3927–3933
49. Muhammed MAH, Verma PK, Pal SK, Kumar RCA, Paul S, Omkumar RV, Pradeep T (2009) Bright, NIR-emitting Au_{23} from Au_{25}: characterization and applications including biolabeling. Chem Eur J 15:10110–10120
50. Le Guével X, Spies C, Daum N, Jung G, Schneider M (2012) Highly fluorescent silver nanoclusters stabilized by glutathione: a promising fluorescent label for bioimaging. Nano Res 5:379–387
51. Lin CAJ, Yang TY, Lee CH, Huang SH, Sperling RA, Zanella M, Li JK, Shen JL, Wang HH, Yeh HI (2009) Synthesis, characterization, and bioconjugation of fluorescent gold nanoclusters toward biological labeling applications. ACS Nano 3:395–401
52. Wang HH, Lin CAJ, Lee CH, Lin YC, Tseng YM, Hsieh CL, Chen CH, Tsai CH, Hsieh CT, Shen JL, Chan WH, Chang WH, Yeh HI (2011) Fluorescent gold nanoclusters as a biocompatible marker for in vitro and in vivo tracking of endothelial cells. ACS Nano 5:4337–4344
53. Shang L, Dong S, Nienhaus GU (2011) Ultra-small fluorescent metal nanoclusters: synthesis and biological applications. Nano Today 6:401–418
54. Shang L, Nienhaus GU (2015) Biomineralization: nanocrystals by design. Nat Chem 7:769–770
55. Xie J, Zheng Y, Ying JY (2009) Protein-directed synthesis of highly fluorescent gold nanoclusters. J Am Chem Soc 131:888–889
56. Yu X, Liu W, Deng X, Yan S, Su Z (2018) Gold nanocluster embedded bovine serum albumin nanofibers-graphene hybrid membranes for the efficient detection and separation of mercury ion. Chem Eng J 335:176–184
57. Wang Y, Chen JT, Yan XP (2013) Fabrication of transferrin functionalized gold nanoclusters/graphene oxide nanocomposite for turn-on near-infrared fluorescent bioimaging of cancer cells and small animals. Anal Chem 85:2529–2535
58. Sun C, Yang H, Yuan Y, Tian X, Wang L, Guo Y, Xu L, Lei J, Gao N, Anderson GJ, Liang XJ, Chen C, Zhao Y, Nie G (2011) Controlling assembly of paired gold clusters within apoferritin nanoreactor for in vivo kidney targeting and biomedical imaging. J Am Chem Soc 133:8617–8624
59. Le Guevel X, Daum N, Schneider M (2011) Synthesis and characterization of human transferrin-stabilized gold nanoclusters. Nanotechnology 22:275103
60. Liu JM, Chen JT, Yan XP (2013) Near infrared fluorescent trypsin stabilized gold nanoclusters as surface plasmon enhanced energy transfer biosensor and in vivo cancer imaging bioprobe. Anal Chem 85:3238–3245
61. Liu CL, Liu TM, Hsieh TY, Liu HW, Chen YS, Tsai CK, Chen HC, Lin JW, Hsu RB, Wang TD, Chen CC, Sun CK, Chou PT (2013) In vivo metabolic imaging of insulin with multiphoton fluorescence of human insulin-Au nanodots. Small 9:2103–2110
62. Kong Y, Chen J, Gao F, Brydson R, Johnson B, Heath G, Zhang Y, Wu L, Zhou D (2013) Near-infrared fluorescent ribonuclease-A-encapsulated gold nanoclusters: preparation, characterization, cancer targeting and imaging. Nanoscale 5:1009–1017
63. Zhao T, He XW, Li WY, Zhang YK (2015) Transferrin-directed preparation of red-emitting copper nanoclusters for targeted imaging of transferrin receptor over-expressed cancer cells. J Mater Chem B 3:2388–2394
64. Liu F, Bing T, Shangguan D, Zhao M, Shao N (2016) Ratiometric fluorescent biosensing of hydrogen peroxide and hydroxyl radical in living cells with lysozyme-silver nanoclusters: lysozyme as stabilizing ligand and fluorescence signal unit. Anal Chem 88:10631–10638
65. Muhammed MAH, Verma PK, Pal SK, Retnakumari A, Koyakutty M, Nair S, Pradeep T (2010) Luminescent quantum clusters of gold in

bulk by albumin-induced core etching of nanoparticles: metal ion sensing, metal-enhanced luminescence, and biolabeling. Chem Eur J 16:10103–10112
66. Yuan Q, Wang Y, Zhao L, Liu R, Gao F, Gao L, Gao X (2016) Peptide protected gold clusters: chemical synthesis and biomedical applications. Nanoscale 8:12095–12104
67. Yu X, Wang Z, Su Z, Wei G (2017) Design, fabrication, and biomedical applications of bioinspired peptide–inorganic nanomaterial hybrids. J Mater Chem B 5:1130–1142
68. Wang Y, Cui Y, Zhao Y, Liu R, Sun Z, Li W, Gao X (2012) Bifunctional peptides that precisely biomineralize Au clusters and specifically stain cell nuclei. Chem Commun 48:871–873
69. Zhang W, Lin D, Wang H, Li J, Nienhaus GU, Su Z, Wei G, Shang L (2017) Supramolecular self-assembly bioinspired synthesis of luminescent gold nanocluster-embedded peptide nanofibers for temperature sensing and cellular imaging. Bioconjug Chem 28:2224–2229
70. Pitchiaya S, Krishnan Y (2006) First blueprint, now bricks: DNA as construction material on the nanoscale. Chem Soc Rev 35:1111–1121
71. Richards CI, Choi S, Hsiang JC, Antoku Y, Vosch T, Bongiorno A, Tzeng YL, Dickson RM (2008) Oligonucleotide-stabilized Ag nanocluster fluorophores. J Am Chem Soc 130:5038–5039
72. Sharma J, Yeh HC, Yoo H, Werner JH, Martinez JS (2010) A complementary palette of fluorescent silver nanoclusters. Chem Commun 46:3280–3282
73. Shukla S, Sastry M (2009) Probing differential Ag +−nucleobase interactions with isothermal titration calorimetry (ITC): towards patterned DNA metallization. Nanoscale 1:122–127
74. Soto-Verdugo V, Metiu H, Gwinn E (2010) The properties of small Ag clusters bound to DNA bases. J Chem Phys 132:195102
75. Schultz D, Gwinn E (2011) Stabilization of fluorescent silver clusters by RNA homopolymers and their DNA analogs: C,G versus A,T(U) dichotomy. Chem Commun 47:4715–4717
76. Vosch T, Antoku Y, Hsiang JC, Richards CI, Gonzalez JI, Dickson RM (2007) Strongly emissive individual DNA-encapsulated Ag nanoclusters as single-molecule fluorophores. Proc Natl Acad Sci U S A 104:12616–12621
77. Antoku Y, Hotta J, Mizuno H, Dickson RM, Hofkens J, Vosch T (2010) Transfection of living HeLa cells with fluorescent poly-cytosine encapsulated Ag nanoclusters. Photochem Photobiol Sci 9:716–721
78. Ai J, Guo W, Li B, Li T, Li D, Wang E (2012) DNA G-quadruplex-templated formation of the fluorescent silver nanocluster and its application to bioimaging. Talanta 88:450–455
79. Yin J, He X, Wang K, Qing Z, Wu X, Shi H, Yang X (2012) One-step engineering of silver nanoclusters-aptamer assemblies as luminescent labels to target tumor cells. Nanoscale 4:110–112
80. Yin J, He X, Wang K, Xu F, Shangguan J, He D, Shi H (2013) Label-free and turn-on aptamer strategy for cancer cells detection based on a DNA-silver nanocluster fluorescence upon recognition-induced hybridization. Anal Chem 85:12011–12019
81. Huang X, Luo Y, Li Z, Li B, Zhang H, Li L, Majeed I, Zou P, Tan B (2011) Biolabeling hematopoietic system cells using near-infrared fluorescent gold nanoclusters. J Phys Chem C 115:16753–16763
82. Liu J, Yu M, Ning X, Zhou C, Yang S, Zheng J (2013) PEGylation and zwitterionization: pros and cons in the renal clearance and tumor targeting of near-IR-emitting gold nanoparticles. Angew Chem Int Ed 52:12572–12576
83. Wang Y, Dai C, Yan XP (2014) Fabrication of folate bioconjugated near-infrared fluorescent silver nanoclusters for targeted in vitro and in vivo bioimaging. Chem Commun 50:14341–14344
84. Tanaka S, Miyazaki J, Tiwari DK, Jin T, Inouye Y (2011) Fluorescent platinum nanoclusters: synthesis, purification, characterization, and application to bioimaging. Angew Chem Int Ed 50:431–435
85. Huang X, Ishitobi H, Inouye Y (2016) Formation of fluorescent platinum nanoclusters using hyperbranched polyethylenimine and their conjugation to antibodies for bio-imaging. RSC Adv 6:9709–9716
86. Yang L, Wang H, Li D, Li L, Lou X, Liu H (2018) Self-nucleation and self-assembly of highly fluorescent Au_5 nanoclusters for bioimaging. Chem Mater 30:5507–5515
87. Yam VWW, Cheng ECC, Zhou ZY (2000) A highly soluble luminescent decanuclear gold(I) complex with a propeller-shaped structure. Angew Chem Int Ed 39:1683–1685
88. Das NK, Ghosh S, Priya A, Datta S, Mukherjee S (2015) Luminescent copper nanoclusters as a specific cell-imaging probe and a selective metal ion sensor. J Phys Chem C 119:24657–24664
89. Kong L, Chu X, Liu W, Yao Y, Zhu P, Ling X (2016) Glutathione-directed synthesis of Cr(vi)-and temperature-responsive fluorescent copper nanoclusters and their applications in cellular imaging. New J Chem 40:4744–4750
90. Ge W, Zhang Y, Ye J, Chen D, Rehman FU, Li Q, Chen Y, Jiang H, Wang X (2015) Facile synthesis of fluorescent Au/Ce nanoclusters for high-sensitive bioimaging. J Nanobiotechnol 13:8
91. Huang H, Li H, Feng JJ, Wang AJ (2016) One-step green synthesis of fluorescent bimetallic Au/Ag nanoclusters for temperature sensing and in vitro detection of Fe^{3+}. Sens Actuators B Chem 223:550–556
92. Wang P, Lin L, Guo Z, Chen J, Tian H, Chen X, Yang H (2016) Highly fluorescent gene carrier based on Ag-Au alloy nanoclusters. Macromol Biosci 16:160–167

93. Desai ML, Jha S, Basu H, Singhal RK, Sharma PK, Kailasa SK (2018) Chicken egg white and L-cysteine as cooperative ligands for effective encapsulation of Zn-doped silver nanoclusters for sensing and imaging applications. Colloid Surface A 559:35–42
94. Shang L, Dörlich RM, Trouillet V, Bruns M, Nienhaus GU (2012) Ultrasmall fluorescent silver nanoclusters: protein adsorption and its effects on cellular responses. Nano Res 5:531–542
95. Cao H, Chen Z, Zheng H, Huang Y (2014) Copper nanoclusters as a highly sensitive and selective fluorescence sensor for ferric ions in serum and living cells by imaging. Biosens Bioelectron 62:189–195
96. Liu CL, Ho ML, Chen YC, Hsieh CC, Lin YC, Wang YH, Yang MJ, Duan HS, Chen BS, Lee JF, Hsiao JK, Chou PT (2009) Thiol-functionalized gold nanodots: two-photon absorption property and imaging in vitro. J Phys Chem C 113:21082–21089
97. Bian P, Zhou J, Liu Y, Ma Z (2013) One-step fabrication of intense red fluorescent gold nanoclusters and their application in cancer cell imaging. Nanoscale 5:6161–6166
98. Shang L, Dorlich RM, Brandholt S, Schneider R, Trouillet V, Bruns M, Gerthsen D, Nienhaus GU (2011) Facile preparation of water-soluble fluorescent gold nanoclusters for cellular imaging applications. Nanoscale 3:2009–2014
99. Hu S, Ye B, Yi X, Cao Z, Wu D, Shen C, Wang J (2016) Dumbbell-shaped metallothionein-templated silver nanoclusters with applications in cell imaging and Hg^{2+} sensing. Talanta 155:272–277
100. Chandirasekar S, Chandrasekaran C, Muthukumarasamyvel T, Sudhandiran G, Rajendiran N (2015) Sodium cholate-templated blue light-emitting Ag subnanoclusters: in vivo toxicity and imaging in zebrafish embryos. ACS Appl Mater Interfaces 7:1422–1430
101. Wu X, He X, Wang K, Xie C, Zhou B, Qing Z (2010) Ultrasmall near-infrared gold nanoclusters for tumor fluorescence imaging in vivo. Nanoscale 2:2244–2249
102. Chen H, Li S, Li B, Ren X, Li S, Mahounga DM, Cui S, Gu Y, Achilefu S (2012) Folate-modified gold nanoclusters as near-infrared fluorescent probes for tumor imaging and therapy. Nanoscale 4:6050–6064
103. Le Guével X, Hötzer B, Jung G, Schneider M (2011) NIR-emitting fluorescent gold nanoclusters doped in silica nanoparticles. J Mater Chem 21:2974–2981
104. Retnakumari A, Setua S, Menon D, Ravindran P, Muhammed H, Pradeep T, Nair S, Koyakutty M (2010) Molecular-receptor-specific, non-toxic, near-infrared-emitting Au cluster-protein nanoconjugates for targeted cancer imaging. Nanotechnology 21:055103
105. Sarparast M, Noori A, Ilkhani H, Bathaie SZ, El-Kady MF, Wang LJ, Pham H, Marsh KL, Kaner RB, Mousavi MF (2016) Cadmium nanoclusters in a protein matrix: synthesis, characterization, and application in targeted drug delivery and cellular imaging. Nano Res 9:3229–3246
106. Pandya A, Tripathi A, Purohit R, Singh S, Nandasiri MI, Karakoti A, Singh SP, Shanker R (2015) Fluorescent magnesium nanocomplex in a protein scaffold for cell nuclei imaging applications. RSC Adv 5:94236–94240
107. Kundu N, Mukherjee D, Maiti TK, Sarkar N (2017) Protein-guided formation of silver nanoclusters and their assembly with graphene oxide as an improved bioimaging agent with reduced toxicity. J Phys Chem Lett 8:2291–2297
108. Wang Y, Cui Y, Liu R, Wei Y, Jiang X, Zhu H, Gao L, Zhao Y, Chai Z, Gao X (2013) Blue two-photon fluorescence metal cluster probe precisely marking cell nuclei of two cell lines. Chem Commun 49:10724–10726
109. Ghosh R, Sahoo AK, Ghosh SS, Paul A, Chattopadhyay A (2014) Blue-emitting copper nanoclusters synthesized in the presence of lysozyme as candidates for cell labeling. ACS Appl Mater Interfaces 6:3822–3828
110. Tian L, Li Y, Ren T, Tong Y, Yang B, Li Y (2017) Novel bimetallic gold-silver nanoclusters with "Synergy"-enhanced fluorescence for cyanide sensing, cell imaging and temperature sensing. Talanta 170:530–539
111. Wang X, Wang Y, He H, Ma X, Chen Q, Zhang S, Ge B, Wang S, Nau WM, Huang F (2017) Deep-red fluorescent gold nanoclusters for nucleoli staining: real-time monitoring of the nucleolar dynamics in reverse transformation of malignant cells. ACS Appl Mater Interfaces 9:17799–17806
112. Li J, Zhong X, Cheng F, Zhang JR, Jiang LP, Zhu JJ (2012) One-pot synthesis of aptamer-functionalized silver nanoclusters for cell-type-specific imaging. Anal Chem 84:4140–4146
113. Zhu X, Shi H, Shen Y, Zhang B, Zhao J, Li G (2015) A green method of staining DNA in polyacrylamide gel electrophoresis based on fluorescent copper nanoclusters synthesized in situ. Nano Res 8:2714–2720
114. Tian H, Guo Z, Chen J, Lin L, Xia J, Dong X, Chen X (2012) PEI conjugated gold nanoparticles: efficient gene carriers with visible fluorescence. Adv Healthc Mater 1:337–341
115. Li Y, Feng L, Yan W, Hussain I, Su L, Tan B (2019) PVP-templated highly luminescent copper nanoclusters for sensing trinitrophenol and living cell imaging. Nanoscale 11:1286–1294
116. Shang L, Yang L, Seiter J, Heinle M, Brenner-Weiss-G, Gerthsen D, Nienhaus GU (2014) Nanoparticles interacting with proteins and cells: a systematic study of protein surface charge effects. Adv Mater Interfaces 1:1300079
117. Su M, Ye J, Li Q, Ge W, Zhang Y, Jiang H, Amatore C, Wang X (2015) In vivo accurate target bio-marking of tumors through in situ biosynthesized fluorescent zinc nanoclusters. RSC Adv 5:74844–74849
118. Chen T, Xu S, Zhao T, Zhu L, Wei D, Li Y, Zhang H, Zhao C (2012) Gold nanocluster-conjugated

amphiphilic block copolymer for tumor-targeted drug delivery. ACS Appl Mater Interfaces 4:5766–5774
119. Chen D, Luo Z, Li N, Lee JY, Xie J, Lu J (2013) Amphiphilic polymeric nanocarriers with luminescent gold nanoclusters for concurrent bioimaging and controlled drug release. Adv Funct Mater 23:4324–4331
120. Chen H, Li B, Ren X, Li S, Ma Y, Cui S, Gu Y (2012) Multifunctional near-infrared-emitting nanoconjugates based on gold clusters for tumor imaging and therapy. Biomaterials 33:8461–8476
121. Cui HD, Hu DH, Zhang JN, Gao GH, Zheng CF, Gong P, Xi XH, Sheng ZH, Cai LT (2017) Theranostic gold cluster nanoassembly for simultaneous enhanced cancer imaging and photodynamic therapy. Chin Chem Lett 28:1391–1398
122. Duan Y, Duan R, Liu R, Guan M, Chen W, Ma J, Chen M, Du B, Zhang Q (2018) Chitosan-stabilized self-assembled fluorescent gold nanoclusters for cell imaging and biodistribution in vivo. ACS Biomater Sci Eng 4:1055–1063
123. Wei Q, Chen Y, Ma X, Ji J, Qiao Y, Zhou B, Ma F, Ling D, Zhang H, Tian M, Tian J, Zhou M (2018) High-efficient clearable nanoparticles for multimodal imaging and image-guided cancer therapy. Adv Funct Mater 28:1704634
124. Zhuang Q, Jia H, Du L, Li Y, Chen Z, Huang S, Liu Y (2014) Targeted surface-functionalized gold nanoclusters for mitochondrial imaging. Biosens Bioelectron 55:76–82
125. Vankayala R, Kuo CL, Nuthalapati K, Chiang CS, Hwang KC (2015) Nucleus-targeting gold nanoclusters for simultaneous in vivo fluorescence imaging, gene delivery, and NIR-light activated photodynamic therapy. Adv Funct Mater 25:5934–5945
126. Chen T, Hu Y, Cen Y, Chu X, Lu Y (2013) A dual-emission fluorescent nanocomplex of gold-cluster-decorated silica particles for live cell imaging of highly reactive oxygen species. J Am Chem Soc 135:11595–11602
127. Chen YN, Chen PC, Wang CW, Lin YS, Ou CM, Ho LC, Chang HT (2014) One-pot synthesis of fluorescent BSA-Ce/Au nanoclusters as ratiometric pH probes. Chem Commun 50:8571–8574
128. Pan S, Zhou J, Liu W, Ye Y, Chen G, Xu J, Qian Z, Chen J, Feng H (2019) Viscosity-sensitive thiolated gold nanoclusters with diffusion-controlled emission for intracellular viscosity imaging. Analyst 144:4483–4487
129. Ma Y, Zhao Y, Guo R, Zhu L, Lin W (2018) A near-infrared emission fluorescent probe with multi-rotatable moieties for highly sensitive detection of mitochondrial viscosity in an inflammatory cell model. J Mater Chem B 6:6212–6216
130. Yang Z, He Y, Lee JH, Park N, Suh M, Chae WS, Cao J, Peng X, Jung H, Kang C, Kim JS (2013) A self-calibrating bipartite viscosity sensor for mitochondria. J Am Chem Soc 135:9181–9185
131. Gao F, Cai P, Yang W, Xue J, Gao L, Liu R, Wang Y, Zhao Y, He X, Zhao L (2015) Ultrasmall [^{64}Cu]Cu nanoclusters for targeting orthotopic lung tumors using accurate positron emission tomography imaging. ACS Nano 9:4976–4986
132. McDonald DM, Baluk P (2002) Significance of blood vessel leakiness in cancer. Cancer Res 62:5381–5385
133. Zhao Y, Detering L, Sultan D, Cooper ML, You M, Cho S, Meier SL, Luehmann H, Sun G, Rettig M, Dehdashti F, Wooley KL, DiPersio JF, Liu Y (2016) Gold nanoclusters doped with ^{64}Cu for CXCR4 positron emission tomography imaging of breast cancer and metastasis. ACS Nano 10:5959–5970
134. Hu H, Huang P, Weiss OJ, Yan X, Yue X, Zhang MG, Tang Y, Nie L, Ma Y, Niu G, Wu K, Chen X (2014) PET and NIR optical imaging using self-illuminating ^{64}Cu-doped chelator-free gold nanoclusters. Biomaterials 35:9868–9876
135. Zhao Y, Sultan D, Detering L, Luehmann H, Liu Y (2014) Facile synthesis, pharmacokinetic and systemic clearance evaluation, and positron emission tomography cancer imaging of ^{64}Cu-Au alloy nanoclusters. Nanoscale 6:13501–13509
136. Shang L, Stockmar F, Azadfar N, Nienhaus GU (2013) Intracellular thermometry by using fluorescent gold nanoclusters. Angew Chem Int Ed 52:11154–11157
137. Wang Y, Chen J, Irudayaraj J (2011) Nuclear targeting dynamics of gold nanoclusters for enhanced therapy of HER2$^+$ breast cancer. ACS Nano 5:9718–9725
138. Khandelia R, Bhandari S, Pan UN, Ghosh SS, Chattopadhyay A (2015) Gold nanocluster embedded albumin nanoparticles for two-photon imaging of cancer cells accompanying drug delivery. Small 11:4075–4081
139. Gu W, Zhang Q, Zhang T, Li Y, Xiang J, Peng R, Liu J (2016) Hybrid polymeric nano-capsules loaded with gold nanoclusters and indocyanine green for dual-modal imaging and photothermal therapy. J Mater Chem B 4:910–919
140. Hu D, Sheng Z, Fang S, Wang Y, Gao D, Zhang P, Gong P, Ma Y, Cai L (2014) Folate receptor-targeting gold nanoclusters as fluorescence enzyme mimetic nanoprobes for tumor molecular colocalization diagnosis. Theranostics 4:142–153
141. Qiao J, Mu X, Qi L, Deng J, Mao L (2013) Folic acid-functionalized fluorescent gold nanoclusters with polymers as linkers for cancer cell imaging. Chem Commun 49:8030–8032
142. Pyo K, Ly NH, Yoon SY, Shen Y, Choi SY, Lee SY, Joo SW, Lee D (2017) Highly luminescent folate-functionalized Au_{22} nanoclusters for bioimaging. Adv Healthc Mater 6:1700203
143. Jiang H, Xu G, Sun Y, Zheng W, Zhu X, Wang B, Zhang X, Wang G (2015) A "turn-on" silver nanocluster based fluorescent sensor for folate

receptor detection and cancer cell imaging under visual analysis. Chem Commun 51:11810–11813
144. Li J, You J, Zhuang Y, Han C, Hu J, Wang A, Xu K, Zhu JJ (2014) A "light-up" and "spectrum-shift" response of aptamer-functionalized silver nanoclusters for intracellular mRNA imaging. Chem Commun 50:7107–7110
145. Chen F, Goel S, Hernandez R, Graves SA, Shi S, Nickles RJ, Cai W (2016) Dynamic positron emission tomography imaging of renal clearable gold nanoparticles. Small 12:2775–2782
146. Zhou C, Hao G, Thomas P, Liu J, Yu M, Sun S, Oz OK, Sun X, Zheng J (2012) Near-infrared emitting radioactive gold nanoparticles with molecular pharmacokinetics. Angew Chem Int Ed 51:10118–10122
147. Chen X, Zhu H, Huang X, Wang P, Zhang F, Li W, Chen G, Chen B (2017) Novel iodinated gold nanoclusters for precise diagnosis of thyroid cancer. Nanoscale 9:2219–2231
148. Liu CL, Wu HT, Hsiao YH, Lai CW, Shih CW, Peng YK, Tang KC, Chang HW, Chien YC, Hsiao JK, Cheng JT, Chou PT (2011) Insulin-directed synthesis of fluorescent gold nanoclusters: preservation of insulin bioactivity and versatility in cell imaging. Angew Chem Int Ed 50:7056–7060
149. Liu Y, Tian GF, He XW, Li WY, Zhang YK (2016) Microwave-assisted one-step rapid synthesis of near-infrared gold nanoclusters for NIRF/CT dual-modal bioimaging. J Mater Chem B 4:1276–1283
150. Sun SK, Dong LX, Cao Y, Sun HR, Yan XP (2013) Fabrication of multifunctional Gd_2O_3/Au hybrid nanoprobe via a one-step approach for near-infrared fluorescence and magnetic resonance multimodal imaging in vivo. Anal Chem 85:8436–8441
151. Liang G, Ye D, Zhang X, Dong F, Chen H, Zhang S, Li J, Shen X, Kong J (2013) One-pot synthesis of Gd^{3+}-functionalized gold nanoclusters for dual model (fluorescence/magnetic resonance) imaging. J Mater Chem B 1:3545–3552
152. Wang C, Yao Y, Song Q (2015) Gold nanoclusters decorated with magnetic iron oxide nanoparticles for potential multimodal optical/magnetic resonance imaging. J Mater Chem C 3:5910–5917
153. Shibu ES, Sugino S, Ono K, Saito H, Nishioka A, Yamamura S, Sawada M, Nosaka Y, Biju V (2013) Singlet-oxygen-sensitizing near-infrared-fluorescent multimodal nanoparticles. Angew Chem Int Ed 52:10559–10563
154. He F, Yang G, Yang P, Yu Y, Lv R, Li C, Dai Y, Gai S, Lin J (2015) A new single 808 nm NIR light-induced imaging-guided multifunctional cancer therapy platform. Adv Funct Mater 25:3966–3976
155. Yang D, Yang G, Gai S, He F, An G, Dai Y, Lv R, Yang P (2015) Au_{25} cluster functionalized metal-organic nanostructures for magnetically targeted photodynamic/photothermal therapy triggered by single wavelength 808 nm near-infrared light. Nanoscale 7:19568–19578
156. Pan UN, Khandelia R, Sanpui P, Das S, Paul A, Chattopadhyay A (2016) Protein-based multifunctional nanocarriers for imaging, photothermal therapy, and anticancer drug delivery. ACS Appl Mater Interfaces 9:19495–19501
157. Hou W, Xia F, Alfranca G, Yan H, Zhi X, Liu Y, Peng C, Zhang C, de la Fuente JM, Cui D (2017) Nanoparticles for multi-modality cancer diagnosis: simple protocol for self-assembly of gold nanoclusters mediated by gadolinium ions. Biomaterials 120:103–114
158. Hu DH, Sheng ZH, Zhang PF, Yang DZ, Liu SH, Gong P, Gao DY, Fang ST, Ma YF, Cai LT (2013) Hybrid gold-gadolinium nanoclusters for tumor-targeted NIRF/CT/MRI triple-modal imaging in vivo. Nanoscale 5:1624–1628
159. Han L, Xia JM, Hai X, Shu Y, Chen XW, Wang JH (2017) Protein-stabilized gadolinium oxide-gold nanoclusters hybrid for multimodal imaging and drug delivery. ACS Appl Mater Interfaces 9:6941–6949
160. Zhao C, Du T, Rehman F, Lai L, Liu X, Jiang X, Li X, Chen Y, Zhang H, Sun Y, Luo S, Jiang H, Selke M, Wang X (2016) Biosynthesized gold nanoclusters and iron complexes as scaffolds for multimodal cancer bioimaging. Small 12:6255–6265
161. Xu C, Wang Y, Zhang C, Jia Y, Luo Y, Gao X (2017) AuGd integrated nanoprobes for optical/MRI/CT triple-modal in vivo tumor imaging. Nanoscale 9:4620–4628
162. Wu X, Li C, Liao S, Li L, Wang T, Su Z, Wang C, Zhao J, Sui C, Lin J (2014) Silica-encapsulated Gd^{3+}-aggregated gold nanoclusters for in vitro and in vivo multimodal cancer imaging. Chem Eur J 20:8876–8882
163. Hembury M, Chiappini C, Bertazzo S, Kalber TL, Drisko GL, Ogunlade O, Walker-Samuel S, Krishna KS, Jumeaux C, Beard P, Kumar CS, Porter AE, Lythgoe MF, Boissiere C, Sanchez C, Stevens MM (2015) Gold-silica quantum rattles for multimodal imaging and therapy. Proc Natl Acad Sci U S A 112:1959–1964
164. Shen D, Henry M, Trouillet V, Comby-Zerbino C, Bertorelle F, Sancey L, Antoine R, Coll JL, Josserand V, Le Guével X (2017) Zwitterion functionalized gold nanoclusters for multimodal near infrared fluorescence and photoacoustic imaging. APL Mater 5:053404
165. Jin R, Zeng C, Zhou M, Chen Y (2016) Atomically precise colloidal metal nanoclusters and nanoparticles: fundamentals and opportunities. Chem Rev 116:10346–10413
166. Wang S, Meng X, Das A, Li T, Song Y, Cao T, Zhu X, Zhu M, Jin R (2014) A 200-fold quantum yield boost in the photoluminescence of silver-doped Ag_xAu_{25-x} nanoclusters: the 13 th silver atom matters. Angew Chem Int Ed 53:2376–2380
167. Shang L, Nienhaus GU (2017) Research Update: Interfacing ultrasmall metal nanoclusters with biological systems. APL Mater 5:053101

Lanthanide-Based Upconversion Nanoparticles for Bioimaging Applications

Youbin Li, Songjun Zeng, and Jianhua Hao

1 Introduction

Luminescent materials are often referred to the matters that can convert a particular type of energy into light emission [1]. Especially, lanthanide (Ln^{3+}) activated UC materials, which utilize the photon UC process to convert the NIR light into short wavelength emission (e.g., UV, visible and NIR emission with the wavelength usually shorter than 800 nm), have played an important role as promising candidates in solid-state lasers (lighting) [2–5], temperature sensors [6], and biomedical field [7–14]. Owing to the rich *f*-orbital configurations of the Ln^{3+} ions, efficient fluorescence emissions ranging from UV to NIR region raised from the *f-f* transition are routinely obtained. Thus, these ions are the most widely used in phosphors among all the existing phosphors. However, direct excitation of Ln^{3+} ions was proved to be an inefficient process due to the existence of forbidden properties of 4*f* transitions. Therefore, a doping strategy, which incorporates different elements into the host matrix, is widely adopted to construct desirable Ln^{3+}-doped hybrid materials with desirable fluorescence properties. Among all the developed lanthanide-doped hosts, the $NaLnF_4$ host is considered as the most efficient host for Ln^{3+} emitter. The Ln-based materials usually possess narrow band emission (~10–20 nm), which results in the rich and resolvable bands in the same spectral region [15, 16]. And, the lanthanide materials usually exhibit low photo-bleaching. Thus, when compared to the conventional semiconductor quantum dots (QDs) and organic dyes, the rare earth-based materials with advantages of large stokes shifts, low photo-bleaching, and low phototoxicity [17–19] are regarded as a new type of luminescence nanoprobes for widely used in the fields of sensors and biomedical imaging applications [7, 8, 10–14, 20–24]. Up to now, great efforts have been devoted to the lanthanide-based biomedical applications, including cell tracking, tumor targeted imaging, vascular imaging, and multimodal imaging [20–33].

In view of the rapid development of UCNPs in the biomedical field, it is essential to discuss the recent development in the design of UCNPs for various bioimaging applications. Here, we will focus on the discussion of the recent progress of the design and synthesis of rare-earth nanoparticles. Different Ln^{3+}-sensitized systems will be classified and then discussed accordingly.

Y. Li · S. Zeng (✉)
Key Laboratory of Low-dimensional Quantum Structures and Quantum Control of Ministry of Education, School of Physics and Electronics, Hunan Normal University, Changsha, PR China

Key Laboratory for Matter Microstructure and Function of Hunan Province, School of Physics and Electronics, Hunan Normal University, Changsha, PR China
e-mail: songjunz@hunnu.edu.cn

J. Hao
Department of Applied Physics, The Hong Kong Polytechnic University, Hong Kong, PR China
e-mail: jh.hao@polyu.edu.hk

F.-G. Wu (ed.), *Fluorescent Materials for Cell Imaging*, https://doi.org/10.1007/978-981-15-5062-1_6

Finally, we summarize the recent research progress of the UCNPs for cellular and deep tissue imaging, particularly the latest development of NIR-II (1000–1700 nm) bioimaging.

2 Lanthanide-Based Upconversion Luminescence Processes

As is known, Auzel and co-workers had reported an original work on the Yb-sensitized Er^{3+}-based upconversion luminescence (UCL) in a glass matrix [34]. UC materials were found to emit high energy visible light under NIR excitation and primarily applied in optical devices [35]. By utilizing the long lifetime and real ladder-like energy levels of Ln^{3+} ions in the inorganic host lattice, the UC materials are capable of generating high energy anti-stokes emission. As the UC emission of the rare earth is mainly based on the transition between 4*f* electrons of the Ln^{3+}, thus, the mechanism of the lanthanide-doped UCL is mainly focused on the transition of the 4*f* shell. The crystal field action has little effect on the transition of the electronic states owing to the shielding effect of the $5S^2$ and $5P^6$ shells on the 4f electron layer. Also, the fluorescence of the crystal field on the energy level position is in the range of 100 wavenumbers, so the spectra from this class of Ln^{3+} are very similar to those of free ions. The luminescence process of UCNPs can be mainly divided into three steps: the excitation energy is first introduced into the matrix lattice and then moved to the activated ions, and eventually the excited ions emit fluorescence and the energy of electrons is transferred from the excited state to the ground state. The mechanism of UC processes is mainly based on the following excited state absorption (ESA), energy transfer upconversion (ETU), and photon avalanche (PA) [36]. As shown in Fig. 1a, the same ions are sequentially absorbed by a continuous multi-photon and the electrons of the ions jump to an excited state energy level from the ground state energy level and then return to the ground state to generate a UC emission, which is also the most basic process of the UCL. In ETU (Fig. 1b),

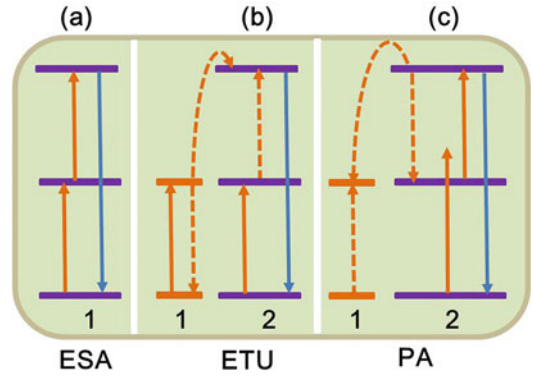

Fig. 1 Simplified energy level diagrams of UC processes including: (a) ESA, (b) ETU, and (c) PA

activator and neighboring sensitizer both absorb one photon at first, then the energy is transferred between sensitizer and activator, resulting in a population of emitting ions in a highly excited state. PA (Fig. 1c) is a combination of excited state absorption and energy transfer process. Moreover, the PA-induced UC emission [13] has mainly relied on pumping power. The UC emission intensity is significantly increased when the power threshold is enhanced. The fluorescence emission intensity of Pr^{3+}-doped lanthanide nanocrystals was significantly increased (~1000 times) when the laser-pump radiation was improved to a threshold of power.

In addition, the UCL properties of the rare-earth nanoparticles are mainly dependent on the host matrix, sensitizer, and activator. Thus, how to select a matrix material is vitally important for the UC emission efficiency. The UC emission is known to be significantly affected by the phonon energy of the host matrix. In the matrix with lower phonon energy, the probability of the non-radiative relaxation can be effectively reduced, resulting in the high UC efficiency of the UCNPs. When compared with the commonly used oxide matrix materials [37–44], the $NaLnF_4$ system with lower phonon energy, higher reflection coefficient, and relatively lower crystallization temperature is expected to be an ideal UC matrix material [45]. In fact, due to the efficient UC emission properties of the lanthanide-doped $NaLnF_4$ nanocrystals, including the high quantum yield (QY), narrow band emission, long lifetime,

and high emission intensity [46], the $NaLnF_4$ nanocrystals are widely applied in the optical amplifier, laser [47–50], and biomedical field [51–55]. It should be pointed out that the optical, magnetic, and chemical properties of the nanocrystals are strongly dependent on the morphology, size, and varied chemical components of the nanocrystals. Notably, the monodispersed nanocrystals always exhibit specific size and surface effects differing from the conventional bulk materials due to the uniform size, thus they exhibit interesting physical and chemical properties. Recently, growing endeavors are devoted to fabricating uniformly monodispersed nanocrystals with controlled phase and size, including the co-precipitation [56–58], thermal decomposition [59–61], hydro (solve)-thermal synthesis [13, 62, 63], and sol-gel process [64–66]. And, various Ln^{3+}-sensitized (Ln = Yb, Nd, Er, Tm) and organic dye-sensitized UC systems were developed for bioimaging.

3 Yb^{3+}-Sensitized UCNPs for Imaging

As is known, the UC processes are mainly relied on the energy transfer between activators and sensitizers. The UC efficiency of the different host materials has been explored in depth. Up to now, $NaYF_4$, $NaYbF_4$, $NaGdF_4$, $NaLaF_4$, LaF_3, GdF_3, GdOF, La_2O_3, Lu_2O_3, Y_2O_3, Y_2O_2S have been extensively studied as host materials [67]. As aforementioned, the host lattice dramatically affects the energy exchange interactions between dopant ions, thus host materials with low phonon energies are required to reduce the non-radiative losses and hence maximize the radiative emission. Among these host materials, fluorides with low phonon energies (~350 cm^{-1}) have been widely applied [67]. Typically, the Er^{3+}, Tm^{3+}, and Ho^{3+} ions are frequently used as activators to entrap the energy from the sensitizers and then generate UCL owing to their ladder-like configuration of energy levels [68]. Conventional 980 nm excited UCL process generally utilizes the Yb^{3+} ion as a sensitizer to harvest the 980 nm photon energy due to its large absorption cross-section at 980 nm than other lanthanide ions. In the Yb/Er co-doped UCNPs system, the green emission bands at 510/550 nm are attributed to the energy transitions from the $^2H_{11/2}$ and $^4S_{3/2}$ state to the $^4I_{15/2}$ state of Er^{3+}; the red emission band at 660 nm is ascribed to the $^4F_{9/2}$ excited state to the ground state $^4I_{15/2}$ of Er^{3+} [68–72]. Similarly, in the Yb/Tm co-doped UCNPs, the UCL emission peaks at 451, 481, 646, and 800 nm are attributed to the energy transitions of $^1D_2$-$^3F_4$, $^1G_4$-$^3H_6$, $^1G_4$-$^3F_4$, and $^3H_4$-$^3H_6$ from Tm^{3+}, respectively [73–76]. Yb/Ho co-doped UCNPs mainly showed UCL emission peaks at 541, 647, and 751 nm, which are ascribed to the transitions from $^5S_2$, $^5F_5$, and $^5F_4$ excited states to the $^5I_8$ ground state of Ho^{3+}, respectively [76–79].

In 1999, Zijimans and co-workers [80] introduced the submicron-sized Y_2O_2S:Yb^{3+}/Tm^{3+} particles for UC bioimaging. High-performance and non-bleaching imaging was achieved with 980 nm laser as a light resource. After that, lanthanide-based UC bioimaging is also successfully demonstrated by using oxide nanomaterials [81, 82]. To make UCNPs suitable for biomedical applications, several material's characterizers should be met. First, the bioprobes should possess suitable nanosize and uniform structure. The formed crystal structure has a positive impact on the host materials parameters. As the size of the conventional oxides particles is too large at the submicron level, which is unsuitable for biomedical applications. Secondly, adequate dispersibility and high fluorescence emission efficiency are required. Recently, significant efforts have been devoted to developing high-efficiency UCNPs for biomedical applications.

As aforementioned, compared with the oxide-based host materials, fluorides are more suitable host materials for the doping of lanthanide ions to generate UC emissions, owing to their low phonon energy. In 2008, a breakthrough was demonstrated by Chatterjee et al. [83], and they performed the multiphoton-excited fluorescence imaging by using the UCNPs as bioprobes (Fig. 2). The as-prepared PEI-coated and folic

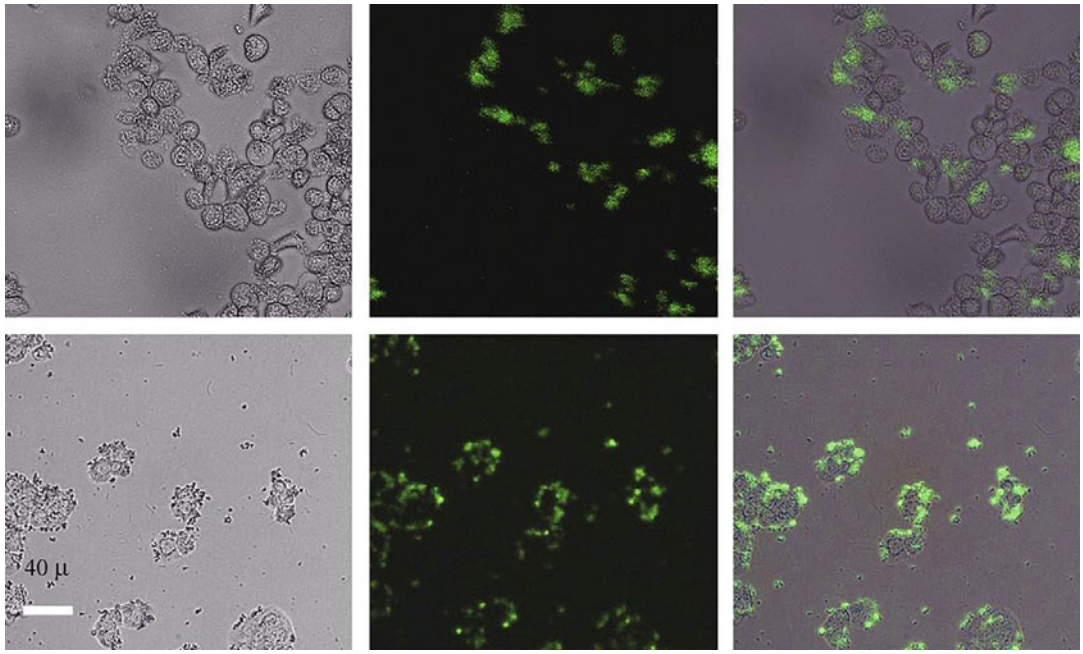

Fig. 2 Bright field, confocal, and superimposed images of live human ovarian carcinoma cells (OVCAR3, top row) and human colonic adenocarcinoma cells (HT29, bottom row), by using $NaYF_4$ nanoparticles. Reprinted with permission from Ref. [83]. Copyright© 2007 Elsevier Ltd

acid conjugated $NaYF_4$:Yb^{3+}/Er^{3+} nanocrystals showed highly targeted efficiency to the human HT29 adenocarcinoma cells and human OVCAR3 ovarian carcinoma, which possess high levels of folate receptors on the surface. Similarly, our group [30] also reported a PEG-modified $BaGdF_5$:Yb/Er UCNPs with suitable particle size and NIR-to-visible emission for imaging of HeLa cells (Fig. 3).

However, though the NIR excitation system holds excellent advantages for deep tissue bioimaging, the green optical-guided cellular and tissue imaging are still limited for further application in deep biological tissues. For deep tissue imaging, the NIR-to-NIR system should be more attractive. The NIR-to-NIR UC process enables deep tissue penetration and high signal-to-noise ratio owing to the largely decreased autofluorescence background and minimized light scattering. Nyk et al. [84] reported the 980 nm light-activated Tm-based UCNPs system with 790 nm emission for cellular and tissue imaging. The doped Tm^{3+} ions are frequently used as an activator to generate NIR emission around 800 nm due to the transition from $^3H_4$ to $^3H_6$ under continuous 980 nm laser excitation. High-performance imaging was successfully achieved since both the excitation and emission bands were located within the NIR region.

It should be noted that the hexagonal phase structure shows an enhanced UCL emission compared with the cubic phase. For nanoparticles, doping has played an important effect on the crystallographic phase, size, and emission efficiency. In 2010, Liu's group [12] realized the simultaneous phase and size control of UCNPs with doping lanthanide Gd^{3+}, paving the convenient way of designing the highly uniform structure of $NaLnF_4$ nanocrystals with hexagonal phase. In 2011, Liu and co-workers [85] reported the sub-10 nm Gd^{3+}-doped hexagonal phase $NaLuF_4$ nanoparticles with NIR emission for cellular and deep tissue imaging (Fig. 4). Subsequently, many groups synthesized a series of Yb/Tm co-doped UCNPs, such as $NaYF_4$, [86] $NaGdF_4$, [87] $NaLuF_4$, [23], and $NaYbF_4$ [88] for bioimaging application.

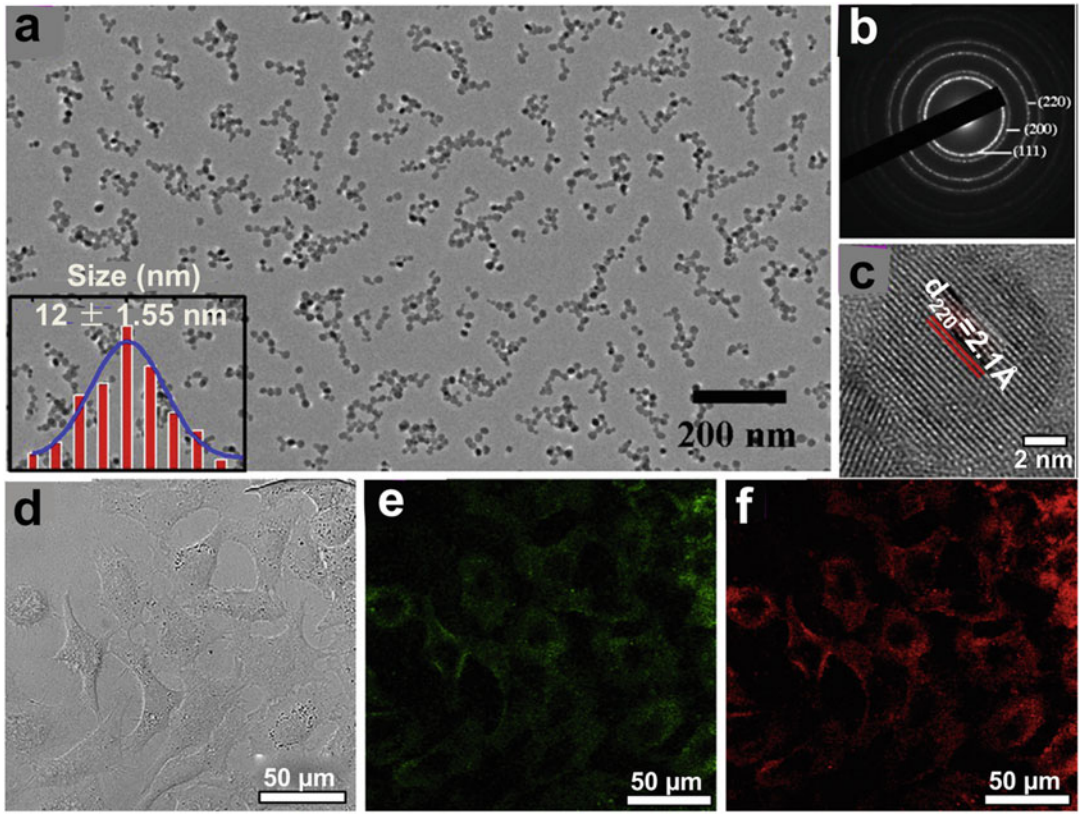

Fig. 3 TEM and XRD results of the PEG-modified $BaGdF_5$:Yb/Er UCNPs: (a) Typical TEM image, (b) Corresponding SAED pattern, (c) HRTEM image. In vitro bioimaging of the PEG-modified $BaGdF_5$:Yb/Er colloidal UCNPs in HeLa cells: (d) bright field image of HeLa cells, (e) corresponding green UC fluorescent image (500-600 nm), (f) the red emission UC fluorescent image (600-700 nm). Reprinted with permission from Ref. [30]. Copyright © 2013 Elsevier Ltd

In general, the spectral region located in 600–800 nm is often defined as "biological transparent window" [50] for cellular and biomedical application, owing to the deep tissue penetration and low background noise. Consequently, it is a great challenge to explore nanoprobes with NIR-to-NIR properties for high-performance bioimaging. Except for the Tm-based UCNPs system, the Yb/Er and Yb/Ho co-doped UCNPs systems with red UC emission centered at 650 nm are also beneficial for the red UC optical-guided bioimaging. Thus, there has been an increasing focus on the engineering of UCNPs with pure single band red UC emission for bioimaging applications. However, owing to the multiple metastable excited state of the lanthanide ions, it is still a challenge to achieve the pure single band red emissive UCNPs.

Wang et al. [50] reported a Yb^{3+}-doped mechanism to achieve high red-to-green (R/G) ratio emissive UCNPs. However, high Yb^{3+} concentration usually induces the decreased interatomic distance, thus resulting in the unavoidable back energy losses. Thus, the population of the excited levels of $^2H_{9/2}$, $^2H_{11/2}$, and $^4S_{3/2}$ was suppressed, leading to the weak blue ($^2H_{9/2}$-$^4I1_{5/2}$) and green ($^2H_{11/2}$,$^4S_{3/2}$-$^4I_{15/2}$) emission intensity and high R/G ratio [89, 90]. Xie et al. [91] presented the MnF_2:Yb/Er UCNPs with strong red emission and a dimmed green emission. The Mn^{2+} possesses a metastable level $^4T_1$, the energy transfer between the Er and Mn occurred rapidly under high energy excitation. And, the energy

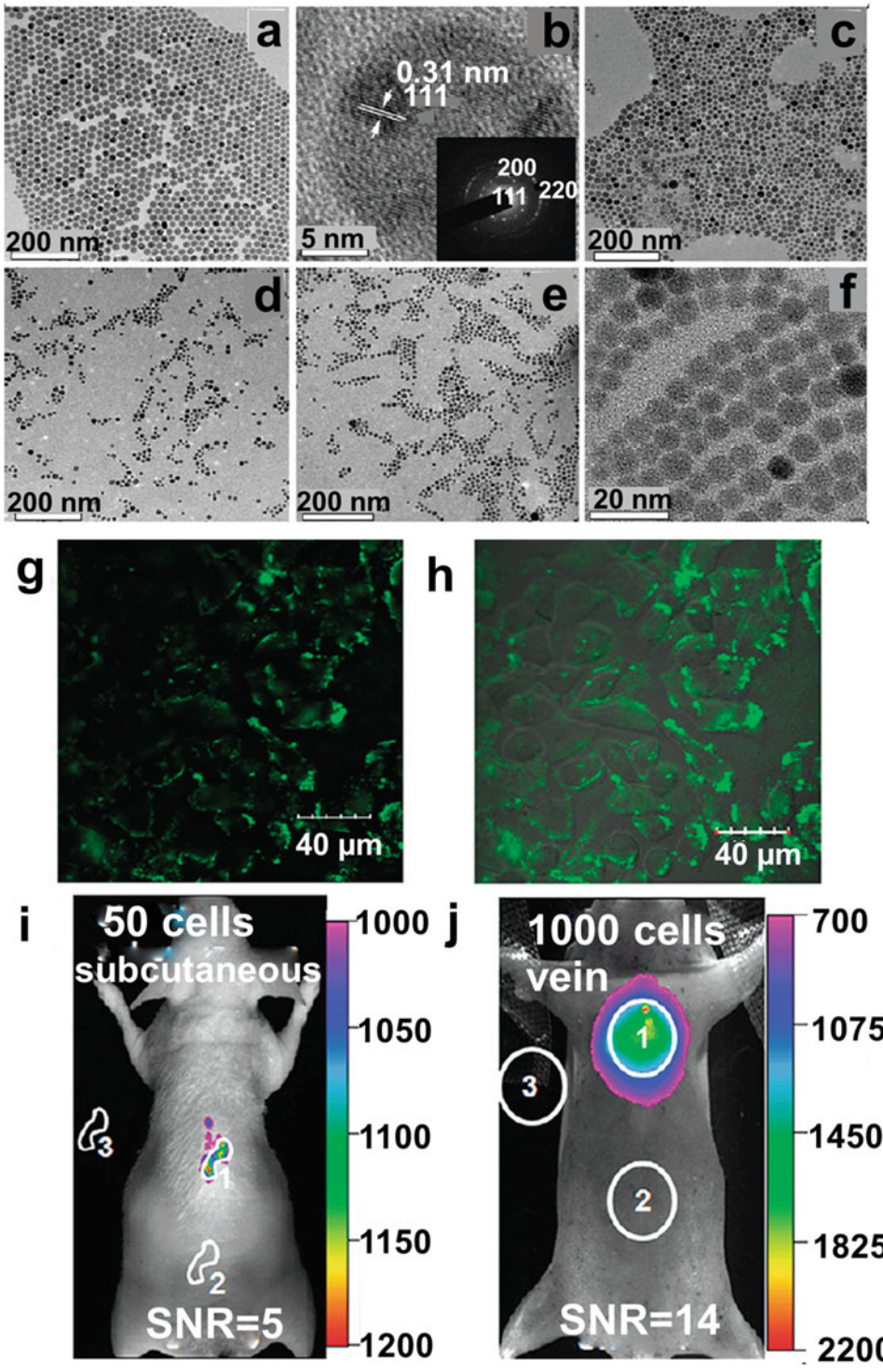

Fig. 4 TEM images of (**a**) Lu1, (**c**) Lu2, (**d**) Lu5, and (**e**, **f**) Lu6. (**b**) HRTEM image and (inset) SAED pattern of Lu1. (**g**) Confocal UCL image and (**h**) its overlay with a bright field image of cells (λex = 980 nm, λem = 450–490 nm). (**i**, **j**) In vivo UCL imaging of athymic nude mice after (**i**) subcutaneous injection of 50 KB cells and (**j**) vein injection of 1000 cells. Reprinted with permission from Ref. [85]. Copyright © 2011 American Chemical Society

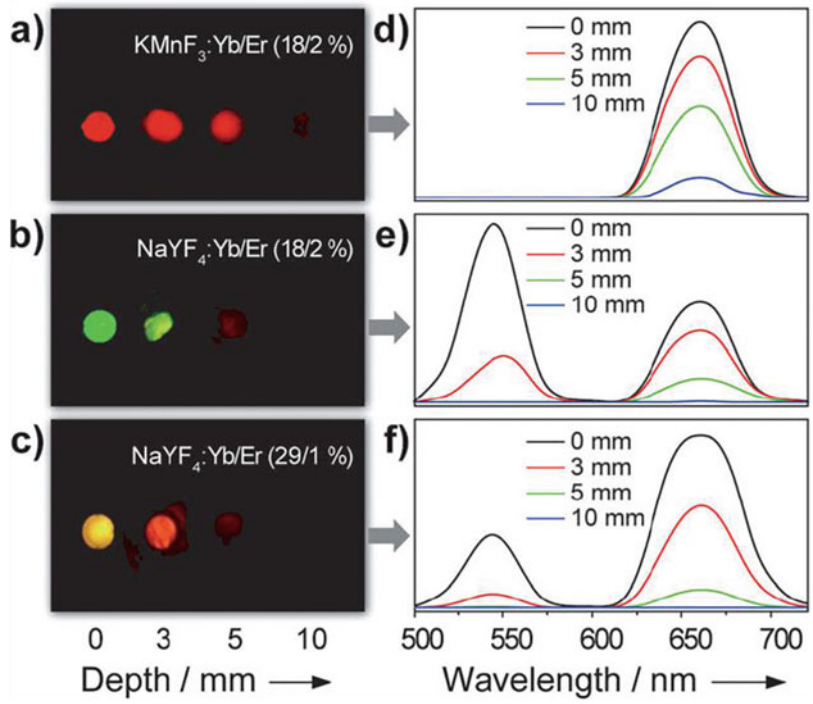

Fig. 5 Luminescence images of pork muscle tissues injected with different UC nanocrystals. (**a**) $KMnF_3$:Yb/Er (18:2 mol%), (**b**) $NaYF_4$:Yb/Er (18:2 mol%), (**c**) $NaYF_4$:Yb/Er (29:1 mol%). (**d**–**f**) Corresponding emission luminescence spectra of (**a**–**c**). Reprinted with permission from Ref. [93]. Copyright © 2011 Wiley-VCH Verlag GmbH & Co. KGaA, Weinheim

of $^4S_{3/2}$ (Er^{3+}) state is a little higher than $^4T_1$ (Mn^{2+}) state. The energy was then transferred from the $^4S_{3/2}$ state to Mn^{2+} ion through energy relaxation, later, the energy of Mn^{2+} can easily transfer back to the $^4F_{9/2}$ state of Er^{3+}, resulting in the generation of highly dominated red band emission. Similarly, the Yb/Er co-doped $KMnF_3$ UCNPs [92] with high R/G ratio UC emission were also achieved.

Though high R/G ratio UCNPs were achieved, single band red-emissive UCNPs have not yet been reported. Liu's group [93] provided a novel oil-based method for the synthesis of the lanthanide (Er^{3+}, Ho^{3+}, and Tm^{3+})-doped $KMnF_4$ UCNPs with single band emission for deep tissue imaging. As demonstrated in Fig. 5, the blue and green emissions of Er^{3+} completely disappeared, suggesting the efficient exchange-energy transfer from Er^{3+} to Mn^{2+}. The pure red emission is mainly attributed to the close proximity and effective mixing of wave functions of the Er^{3+} and Mn^{2+} ions in the crystal host lattices. Due to their special single band UC emission, these UCNPs can be used as good candidates for imaging at different tissue depths.

Inspired by these results, Zhao's group [94] demonstrated a Mn^{2+}-doping strategy for precise control of the R/G ratio and the pure red-emissive $NaYF_4$:Yb/Er UCNPs (Fig. 6). In this work, Mn^{2+} ion doping has played a positive effect on controlling the phase and size of the synthesized $NaYF_4$. The cubic phase small $NaYF_4$ nanocrystals were obtained when doping 5% mol Mn^{2+}, and no phase change was observed when the Mn^{2+}-doping content reached up to 30%, revealing the successful formation of Y-Mn solid solution structure. More importantly, the R/G ratio was dramatically improved from 0.83 to 163.78 with increasing the Mn^{2+}-doping concentration. The fine control of the R/G ratio was performed through Mn^{2+} doping, further proving the high-efficiency energy transfer of Mn^{2+} and Er^{3+}. Thus, these UCNPs with greatly enhanced red emissions were ideal bioprobes for cellular and red UC optical imaging. Later, our group [33] proposed a strategy to simultaneously

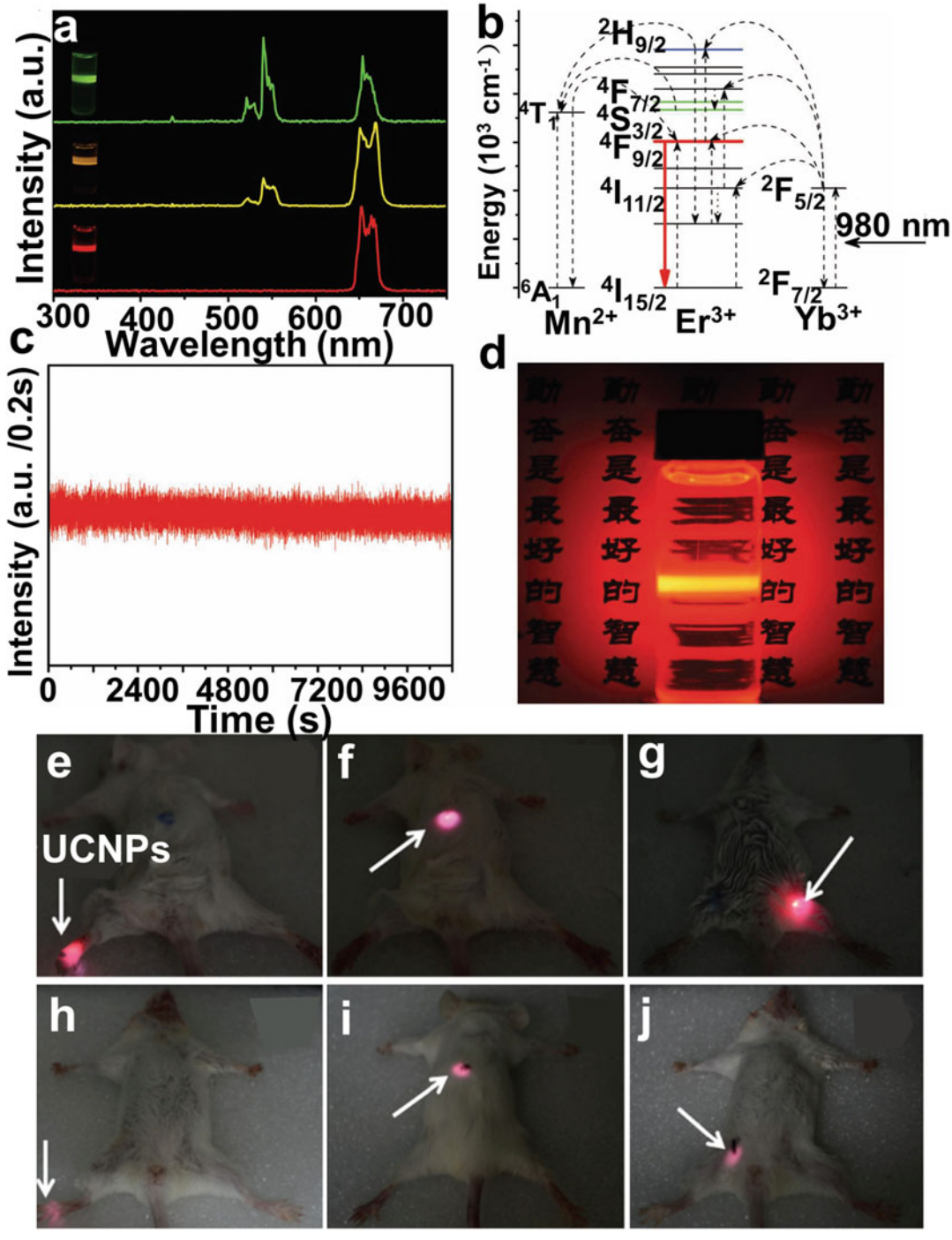

Fig. 6 Photoluminescence studies of $NaYF_4$:Yb/Er (18/2 mol%) nanoparticles with varying Mn^{2+} dopant concentrations. (**a**) UC emission spectra of $NaYF_4$: Yb/Er (18/2 mol%) nanocrystals with 0, 5, and 30 mol% Mn^{2+} dopant ions dispersed in cyclohexane (1 mg/mL), respectively; inset: luminescent photographs of the corresponding samples. (**b**) Schematic energy level diagram showing the possible UC mechanism. (**c**) The luminescence time traces acquired with 200 ms time under continuous 980 nm laser illumination for more than 3 h. (**d**) Luminescent photograph of 30 mol% Mn^{2+}-doping UCNPs dispersed in cyclohexane (2 mg/mL). In vivo UC

realize phase and size control and enhanced UCL emission in the $NaLnF_4$ (Ln = Lu, Gd, Yb) system through Mn^{2+} doping (Fig. 7). Moreover, the overall UCL emission intensity was greatly improved by doping Mn^{2+} ions (~59.1 times for $NaLuF_4$ host, ~39.3 times for $NaYbF_4$ host compared to the UCNPs without Mn^{2+} doping) owing to the remarkably enhanced red UCL emission. Apart from the Mn^{2+}-doping induced enhancement of red UCL emission, Rai et al. presented $NaSc_{0.75}Er_{0.02}Yb_{0.18}Gd_{0.05}F_4$@AuNPs nanoparticles with greatly enhanced red UCL emission for red optical-guided cellular imaging [95]. The R/G ratio was greatly improved (~20 times), due to the resonance energy and plasmonic effect of Au. The synthesized nanoparticles with red UC emission were promising candidates for imaging applications. Chen et al. also reported the $LiYF_4$:Er nanoparticles with highly improved QY under 1490 nm laser excitation [96]. When compared with the conventional Er-based UNCPs with QY of 0.3%, the QY of the reported nanocrystals under 1490 nm laser excitation was measured to be about 1.2%, which is almost four times than that under 980 nm laser excitation. Recently, Zhang and co-workers have presented a new type of Er^{3+}-sensitized UCNPs with excitation wavelength and emission wavelength beyond 1000 nm for in vivo biosensing [53]. With both excitation wavelength and emission wavelength beyond 1000 nm, deep penetration and greatly decreased autofluorescence optical imaging were achieved.

As mentioned above, the UC photoluminescence mechanism of the Yb-Er/Tm-based UCNPs is based on the absorption of 980 nm photons by the sensitizers of Yb^{3+} ions due to the high absorption efficiency of Yb^{3+} at 980 nm. After absorption of 980 nm photons, the subsequent energy transfer is occurred to realize the two-photon excitation of the lanthanide emitters such as Er or Tm, which is attributed to the long life-time of the abundant intermediate excited state of the lanthanide emitters. Thus, the two-photon microscopy imaging of UCNPs can be easily realized by a cheap 980 nm laser. Moreover, the UCNPs feature high photostability, and low autofluorescence under NIR laser excitation, making them ideal probes for two-photon microscopy imaging of cell.

4 Nd^{3+}-Sensitized UCNPs for Imaging

Typically, lanthanide-doped UCNPs with various compositions have been widely studied. These nanoparticles are usually doped with Yb^{3+} ions as a sensitizer to absorb the 980 nm laser irradiation. However, the 980 nm wavelength overlaps with the absorption wavelength of water, leading to the overheating effect in bio-tissues. To address this problem, the Nd^{3+} ions were introduced to act as NIR absorbers and sensitizers in the lanthanide-doped UCNPs system. Notably, Nd^{3+} possesses a shorter absorption wavelength at 808 nm than Yb^{3+} at 980 nm [97–102]. Moreover, the water absorption coefficient at 808 nm (0.02 cm^{-1}) is relatively lower than it at 980 nm (0.48 cm^{-1}). Besides, the Nd^{3+} ion also has a large absorption cross-section at 808 nm, which is ten times higher than that of Yb^{3+} at 980 nm [103]. It is expected that the Nd-sensitized UCNPs system can simultaneously improve the UC emission efficiency and solve the 980 nm laser-induced overheating issues.

In 2013, Shen et al. [104] reported an 808 nm light-triggered $Nd^{3+}/Yb^{3+}/Er^{3+}(Tm^{3+})$ tri-doped core/shell $NaYF_4$ UCNPs with a visible emission. In the tri-doped cascade sensitized UC system, the Nd^{3+} ions in the core act as the sensitizer to

Fig. 6 (continued) luminescence animal imaging study. PEG-UCNPs were injected into (**e**, **h**) translucent foot, (**f**, **i**) below the skin of back or (**g**, **j**) thigh muscles of mice show effective luminescence. Reprinted with permission from Ref. [94]. Copyright © 2012 WILEY-VCH Verlag GmbH & Co. KGaA, Weinheim

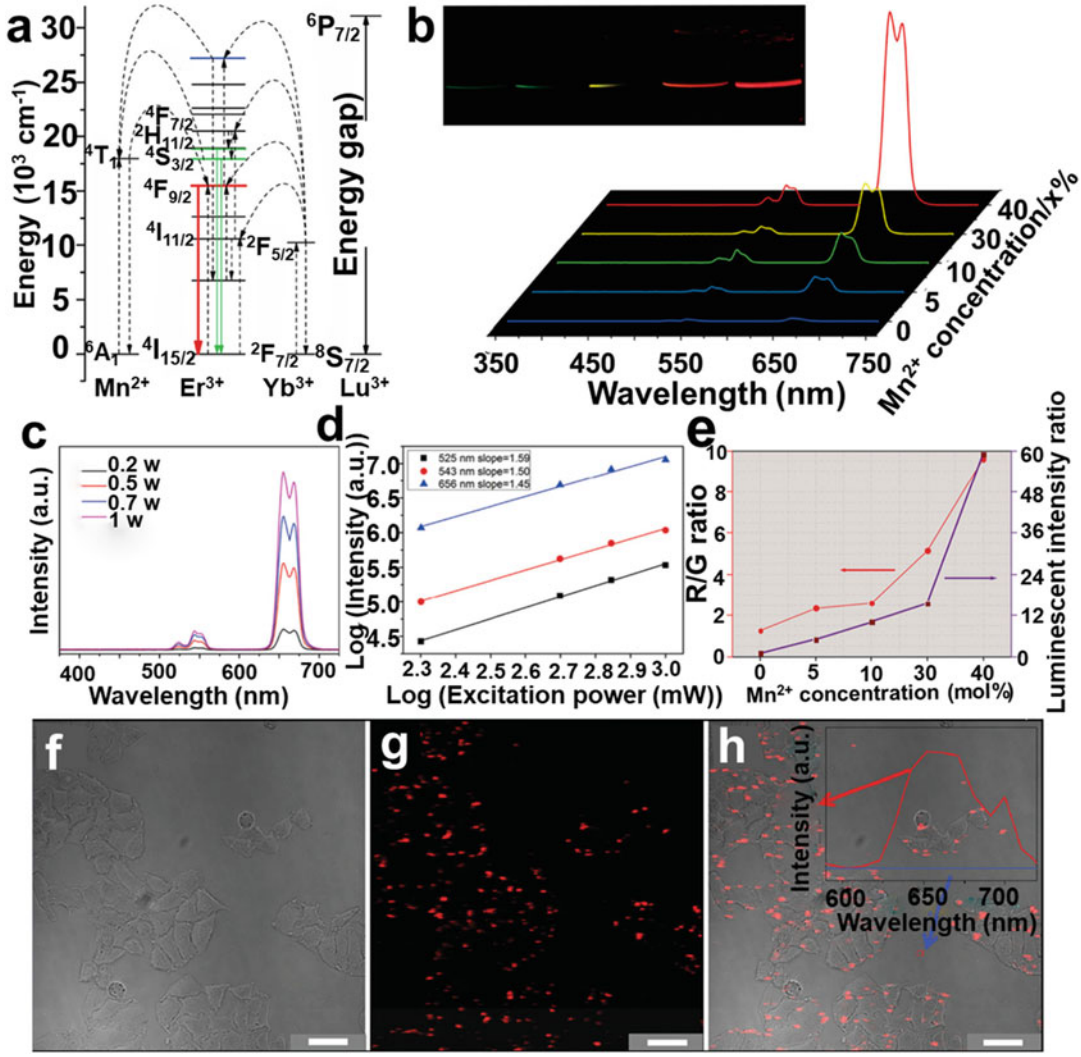

Fig. 7 UCL studies of $NaLuF_4$:Mn/Yb/Er (x/18/2 mol%) UCNPs. (**a**) Proposed energy transfer mechanisms, (**b**) UCL spectra of the as-synthesized UCNPs doped with different content of Mn^{2+}, (**c**) power dependent UCL spectra, (**d**) the corresponding plots of Log (UC intensity) vs Log (excitation power), (**e**) the calculated R/G ratio (red curve) and the whole UCL intensity (purple curve). The insets of b show the corresponding digital photographs of cyclohexane solutions containing 1 wt% UCNPs doped with 0, 5, 10, 30, and 40% Mn^{2+}, respectively. In vitro bioimaging of HeLa cells treated with $NaLuF_4$:Mn/Yb/Er UCNPs. (**f**) Bright field image of HeLa cells, (**g**) fluorescent image (λex = 980 nm, emission filter range: 600–700 nm), (**h**) overlay image, and the inset of which shows the localized UCL spectra taken from HeLa cells and background. Scale bars are 50 μm for all images. Reprinted with permission from Ref. [33]. Copyright © 2014 WILEY-VCH Verlag GmbH & Co. KGaA, Weinheim

absorb the photon at 808 nm, as well as Yb^{3+} ions take the role of bridging ions to transfer the energy of Nd^{3+} ions to the emitters. A ~ 28.7 times enhancement of the green emission was achieved by doping 0.5% Nd^{3+} in the core. The emission intensity was gradually decreased at a high Nd^{3+}-doping concentration owing to the concentration quenching effect. Notably, the design allows for only low Nd^{3+}-doping content, resulting in low UC emission efficiency.

Fortunately, Liu's group [103] has introduced a novelty core–shell strategy with 1% Nd in core and 20% Nd in the shell to enhance the UC emission (Fig. 8). The absorption intensity of the 20% Nd^{3+} doped UCNPs in the shell layer was greatly improved (17 times) when compared with the Nd^{3+} free UCNPs. This study simultaneously addresses the high Nd^{3+}-doping induced concentration quenching issues, and greatly improves the UC emission efficiency of the Nd-based UCNPs system.

In addition, Yan's group [105] also designed a core–shell structure ($NaGdF_4$:Yb,Er@$NaGdF_4$:Nd,Yb) with Nd^{3+} ions in the shell layer to address the concentration quenching issues as well as deleterious energy transfer between activators and Nd^{3+}. As shown in Fig. 9, high quality in vivo NIR imaging with 808 nm light-triggered UCNPs system was successfully demonstrated without the concern of overheating issues. Notably, great progress has been made to enhance the UCL efficiency in the 808 nm excited system by separating the activator ions (Er, Tm, Ho, etc.) and sensitizer Nd^{3+}. However, recent studies have shown that the energy back transfer mainly aroused the undesirable UCL decrease. The electron energy of the activator can be efficiently transferred back to Nd^{3+}, leading to the unavoidable energy quenching. There is still much room to eliminate the quenching interactions between the Nd^{3+} and activators to obtain the maximum harvest of 808 nm photons.

In 2014, Zhong et al. [106] demonstrated a quenching-shield sandwich structure for 800 nm excited UCL of Nd^{3+}-sensitized nanoparticles. The fabricated $NaYF_4$:Yb,X@$NaYF_4$:Yb@$NaNdF_4$:Yb nanoparticles successfully separate the activators (X = Er^{3+}/Tm^{3+}/Ho^{3+} ions in the core) and sensitizers (Nd^{3+} in the out layer). The Nd^{3+} as a sensitizer in the out layer can harvest the 808 nm photons, leading to the population of $^4F_{5/2}$ state of Nd^{3+}. The energy was then transferred to Yb^{3+} through the cross-relaxation [($^4F_{3/2}$) Nd, ($^2F_{7/2}$) Yb] → [($^4I_{9/2}$) Nd, ($^2F_{5/2}$) Yb], then the energy was embedded in the core by the activator Er^{3+} ions. The transition layer between the core and out layer has played the role as a shield to block the back energy transfer from Er^{3+} to Nd^{3+}, thus leading to the minimum detrimental relaxation pathway at high Nd^{3+} ions doping concentration (90%) in the out layer.

Wang and co-workers [107] have designed a $NaGdF_4$: A (A = Eu, Tb)@$NaGdF_4$: Yb/Tm@$NaGdF_4$: Yb/Nd core–shell–shell structure. The nanoparticle exhibits multicolor emission. In the designed structure, intense UC emission was achieved for activators without long-lived intermediate states through Gd^{3+}-mediated energy migration under 808 nm laser excitation. The sensitizers of Nd^{3+} ions, accumulators of Tm^{3+}, and activators of Eu^{3+} and Tb^{3+} were doped into different layers to avoid non-radiative decay, thus high Nd^{3+}-doping concentration was allowed to harvest the 808 nm photons. As a result, the Nd^{3+}-trinity system with three layers was introduced to increase the absorption of 808 nm photons through high Nd^{3+}-doping contents as well as block the back energy transfer. The designed system with excellent UC emission, prolonged lifetime, and minimized overheating effect under 808 nm irradiation is an ideal probe for biomedical application. Wen et al. [108] reported a sandwich-like core–shell nanostructure with enhanced UCL intensity, which showed that the UCL emission intensity was related to the size of the inner core. When the diameter of the core increased while the shell layer compressed, the distance for the sensitizers Nd^{3+} ions to the activators reduced, resulting in the enhanced UCL emission intensity.

5 Organic Dyes-Sensitized UCNPs

Although great progress has been made on size, shape, and emission-controlled UCNPs, the low UCL efficiency still limits the application of the UCNPs. Commonly, in the 980 nm laser-excited system, Yb^{3+} ions were employed as a sensitizer to harvest the excitation photons and then transfers its excitation energy to the activators

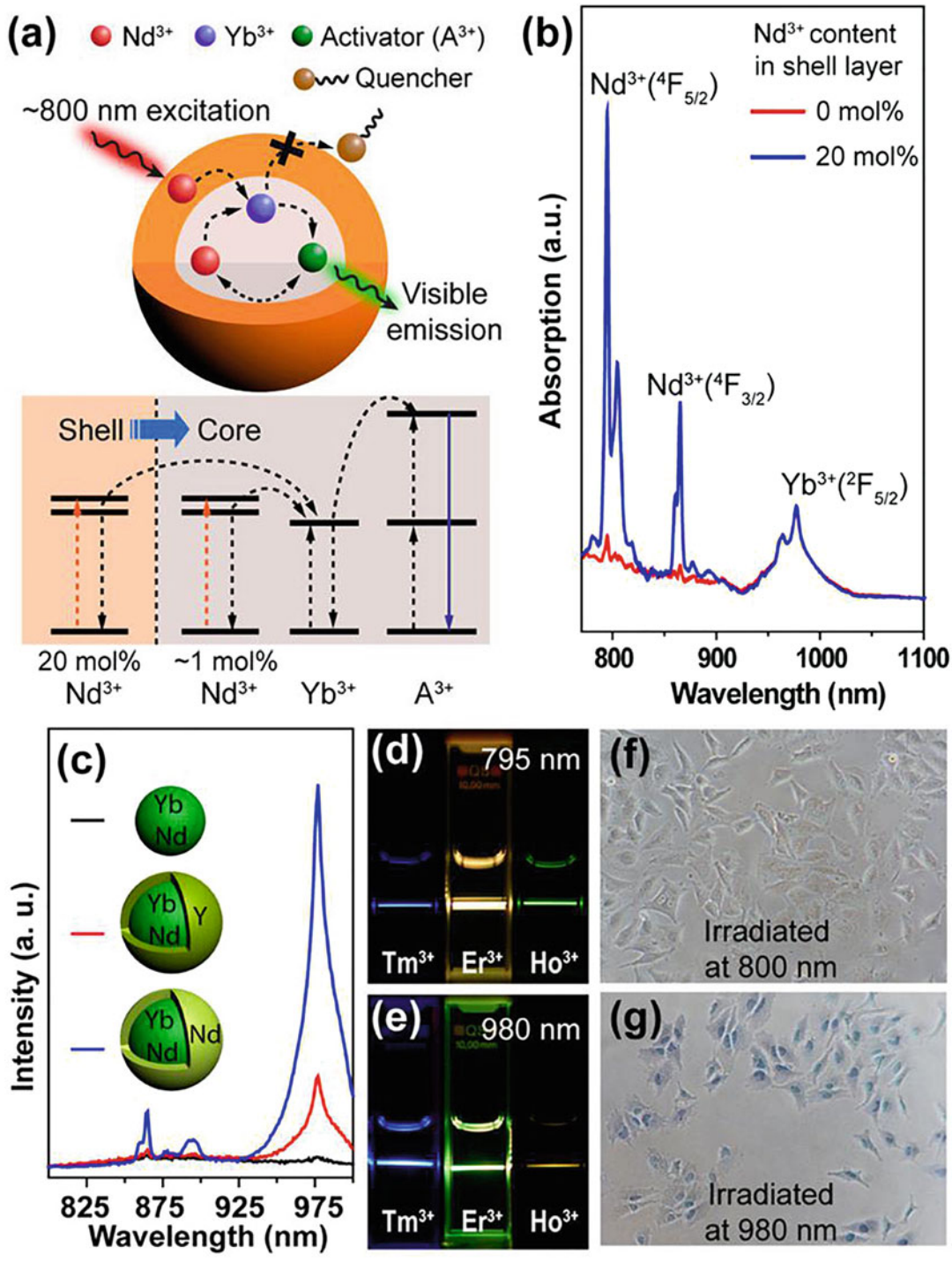

Fig. 8 (**a**) Schematic design (top) and simplified energy level diagram (bottom) of a core−shell nanoparticle for photon UC under 800 nm excitation. (**b**) NIR absorption spectra of $NaYF_4$:Yb/Nd (30/1%) nanoparticles coated with an inert $NaYF_4$ shell or an active $NaYF_4$:Nd (20%) shell. The absorption spectra were normalized at 976 nm for comparison. (**c**) NIR photoluminescence spectra of the nanoparticles. (**d**, **e**) Luminescence photographs of activator emissions (Tm 0.5%, Er 0.5%, Ho 1%) for Nd^{3+}-sensitized and Yb^{3+}-sensitized nanoparticles under 795 and 980 nm irradiation, respectively (laser power: 100 mW). (**f**, **g**) Optical microscopy images of trypan blue treated HeLa cells recorded after irradiation for 5 min at 800 and 980 nm, respectively. Reprinted with permission from Ref. [103]. Copyright © 2013 American Chemical Society

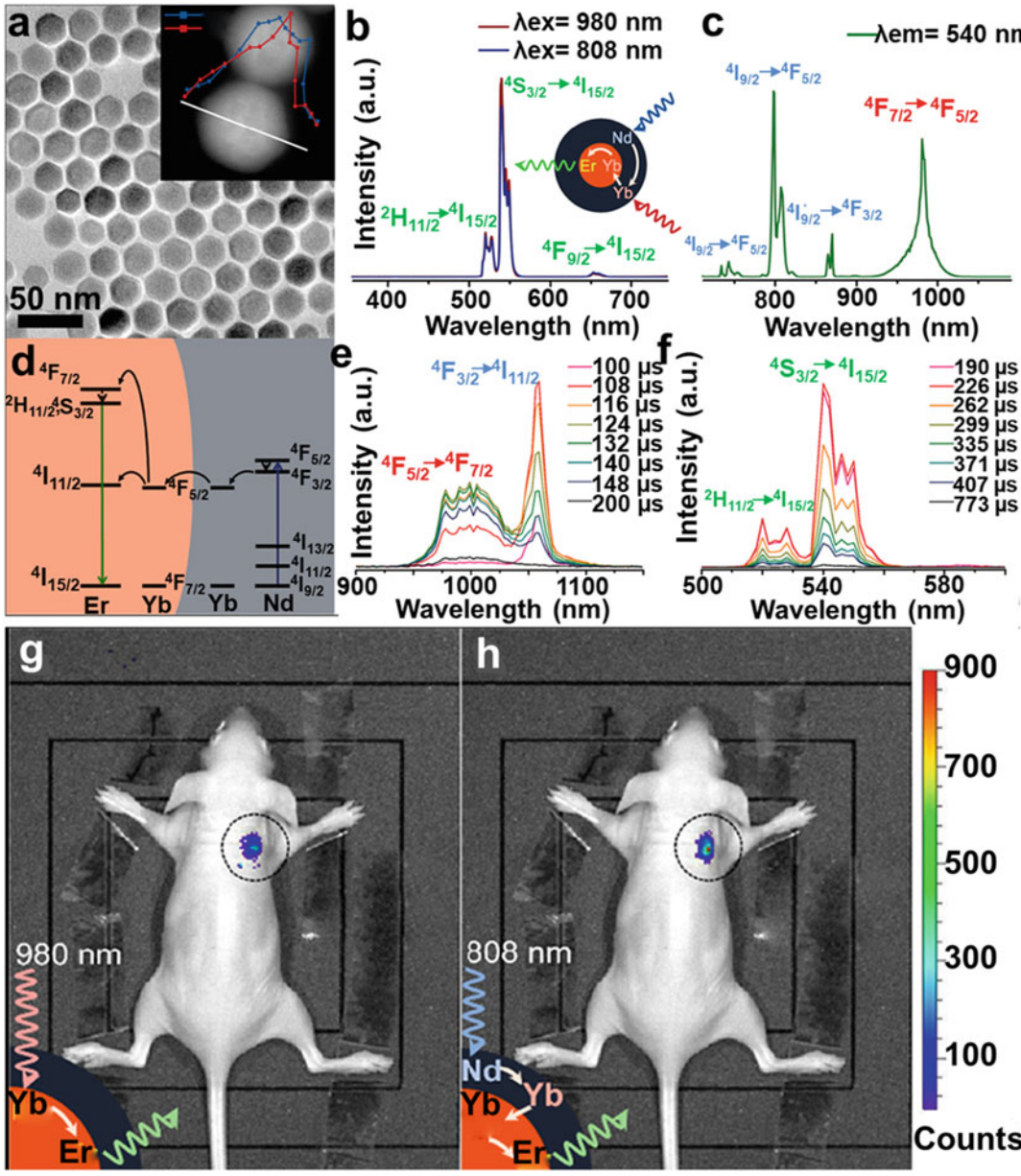

Fig. 9 (**a**) TEM image of Er@Nd NPs (Inset: EDS line-scan profile of a single particle). (**b**) UC emission spectra of Er@Nd NPs under 980 and 808 nm excitation. (**c**) Excitation spectrum of Er@Nd NPs (λem = 540 nm). (**d**) Energy transfer pathway under 808 nm excitation. (**e**, **f**) Time-resolved emission spectra of Er@Nd NPs under 808 nm excitation. In vivo UC imaging of a nude mouse subcutaneously injected with Er@Nd NPs. The images were obtained with 980 nm laser (**g**) and 808 nm laser (**h**) irradiation. Reprinted with permission from Ref. [105]. Copyright © 2013 American Chemical Society

ions (Er^{3+}, Tm^{3+}, Ho^{3+}). However, the Yb^{3+} was proved to possess a narrow absorption band of ~10,260–10,660 cm^{-1} and a relatively small absorption cross-section of ~10^{-20} cm^2, which is ten times narrower and ~1000–10,000 times smaller than the organic dyes [102, 109], respectively. Such a fundamental characteristic largely restricts the conventional Yb^{3+}-sensitized UCNPs in producing highly efficient UCL emission. Recently, some lanthanide coordination complexes utilize organic dyes as the sensitizer to obtain the UC emission. Inspired by these results, dye-sensitized UCNPs were explored to enhance the UC emission intensity. Up to present, numerous organic dyes have been utilized to sensitize the Yb^{3+} (~980 nm) and Nd^{3+} (740/810 nm), such as IR-783 [110], IR 806 [102], IR 808 [109], IR 820 [109], IR 845 [110], ICG [111, 112], etc. In addition, organic dyes with absorption and emission wavelength in the range of visible regions are typically sensitized to the Eu^{3+} and Tb^{3+} ions.

In 2012, Zou and co-workers [102] reported a new type of materials where an organic dye (IR 806) acted as an antenna to absorb NIR (980 nm) light and then transferred it to the hexagonal phase $NaYF_4$:Yb/Er UCNPs to produce the UC emission. The emission wavelengths overlap with the absorption of Yb^{3+}, resulting in the Forster-type energy transfer from the IR 806 to Yb^{3+} ions, then the Er^{3+} is activated to generate UC emission (510/540 and 650 nm). Owing to the increased absorptivity and overall broadening of the absorption spectrum of the upconverter, the UC emission intensity of the dye-sensitized UCNPs is dramatically improved (by a factor of ~3000 folders). However, the UC efficiency of UCNPs was still not high enough because of the mismatched spectral region between the NIR dye and Yb^{3+} and the core-only nanoparticle-induced surface-related luminescence quenching effect. To address this issue, a NIR dye-sensitized core–shell nanostructure was introduced. Prasad's group [109] has proposed a multistep cascade energy transfer strategy. The infrared organic dyes were decorated on the shell, and then a sequential non-radiative energy transfer to upconverting ion pairs in the core happened (Fig. 10). The IR 808 dye-sensitized core–shell $NaYbF_4$:Tm@$NaYF_4$:Nd nanoparticles were designed. The Nd^{3+} in the shell layer acted as a mediate sensitizer 1, and the Yb^{3+} and Tm^{3+} ions in the core served as sensitizer 2 and activator, respectively. Broadly absorbing NIR dyes (IR 808) are expected to harvest the 808 nm photons efficiently and non-radiatively transfer to the Nd^{3+} in shell. And finally, the energy is transferred to Yb^{3+} in the core to activate Tm^{3+} ion to produce multiphoton UC emission. The UC QY was greatly enhanced (19%), which was nearly 100 times larger than the typically reported 808 nm excited UCNPs system.

After that, Han's group [110, 113] has presented a dye-sensitizing and core–shell enhancement strategy with significantly enhanced UC emission. By using the dye-sensitized core/active shell UCNPs system [113], they have successfully activated the neurons (Fig. 11) under 808 nm laser excitation with eliminated overheating effect. These results further demonstrated the feasibility of the dye-sensitized UCNPs for biomedical cell imaging.

6 Lanthanide-Based Nanocrystals for NIR-II Bioimaging

As aforementioned, lanthanide-based UCNPs usually generate high-efficiency UC emission under 980/808 nm laser irradiation. And the UCNPs show some unique optical properties, such as narrow band emission (full width at half maximum, FWHM ~12 nm), long lifetime, low photobleaching, no blinking, and high biocompatibility for bioimaging [114]. During recent years, lanthanide UCNPs, which exhibit efficient NIR-to-Visible/NIR emission, have been widely explored as labels for living cell imaging. Although high contrast cellular imaging was successfully achieved by using the lanthanide UCNPs, however, it was still limited by the undesirable imaging resolution. This was mainly attributed to the relatively large photon scattering losses. Thus, designing UCNPs with new

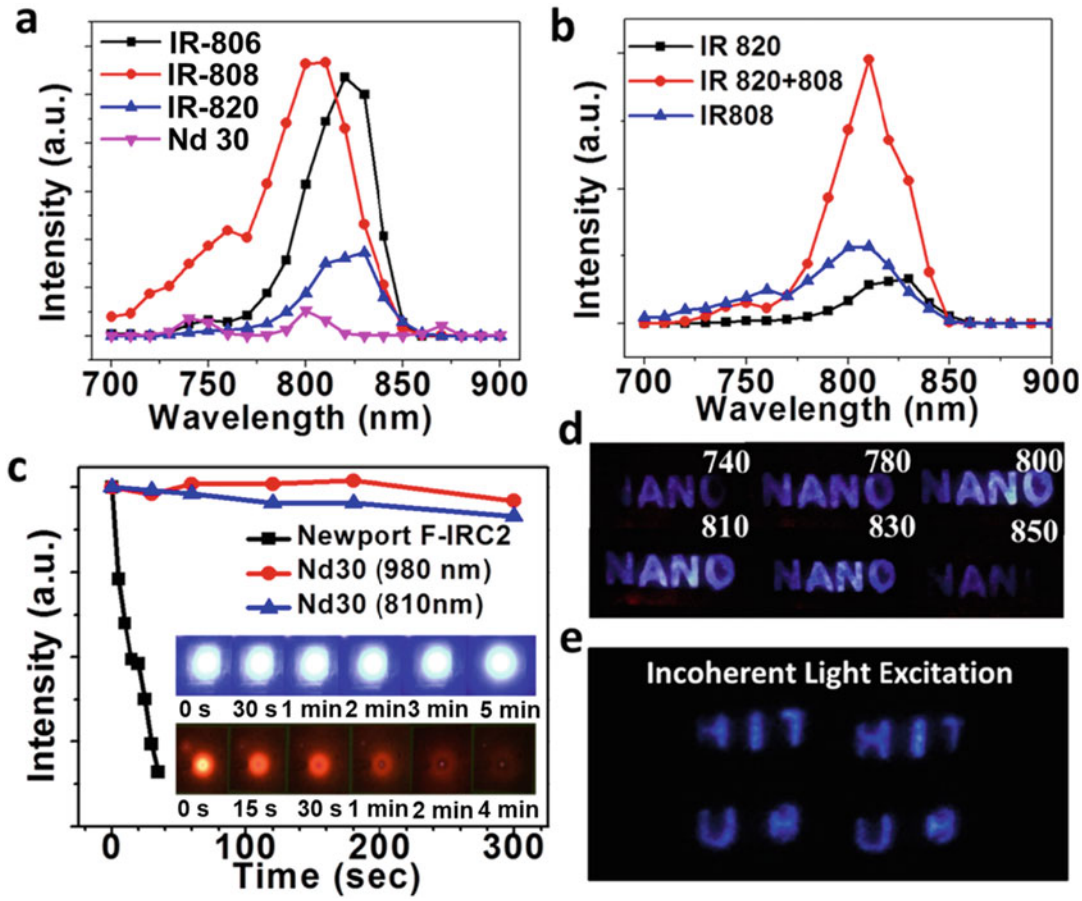

Fig. 10 Co-sensitization and applications of an inorganic fluoride core/shell nanostructure. (**a**) Excitation spectra of UCL peaked at 350 nm from the core/shell ($NaYbF_4$:Tm^{3+} 0.5%)@$NaYF_4$:Nd^{3+}30% nanoparticles (Nd 30) as well as from the IR 808-sensitized (IR 808), the IR 806-sensitized (IR 806), and the IR 820-sensitized (IR 820) core/shell ($NaYbF_4$:Tm^{3+} 0.5%)@$NaYF_4$:Nd^{3+} 30% nanoparticles. (**b**) Excitation spectra of UCL peaked at 350 nm from IR 808-sensitized, IR 820-sensitized, as well as the IR 808 and IR 820-co-sensitized core/shell ($NaYbF_4$:Tm^{3+} 0.5%)@ $NaYF_4$:Nd^{3+} 30% nanoparticles. (**c**) Photostability of UCL from a homemade IR card and a commercial IR card (Newport F-IRC2, Irvine, CA) excited at 810 nm, 1 W/cm^2. The inset shows the photographic images of both cards taken at different time points. (**d**) Blue UC from regular letters printed using an upconverting ink made by the IR-808-sensitized core/shell nanoparticles and polystyrene. (**e**) UC of incoherent light (halogen lamp) by the IR-808 and IR-820 co-sensitized $NaYbF_4$:Tm^{3+}@$NaYF_4$:Nd^{3+} core/shell nanoparticles. Reprinted with permission from Ref. [109]. Copyright © 2015 American Chemical Society

imaging wavelengths possessing low scattering losses is highly desirable for in vivo deep tissue bioimaging.

Recently, optical simulations have provided a novelty of optical imaging window (1000–1700 nm, SWIR, also named NIR-II). NIR-II bioimaging technique enjoying the features of greater penetration, high resolution, high sensitivity, and near-zero background is emerged as the next generation optical imaging method [115, 116]. Notably, except for the excellent UC optical properties of UCNPs in the NIR region [25], the lanthanide-based nanoparticles are also capable of simultaneously generating high-efficiency down-shifting NIR-II emission, leading to the significant reduction in photon scattering than the UC NIR-I/visible region [26, 117]. Recently, some attempts have been made to explore the down-shifting optical property of the traditional UCNPs. Moghe's group

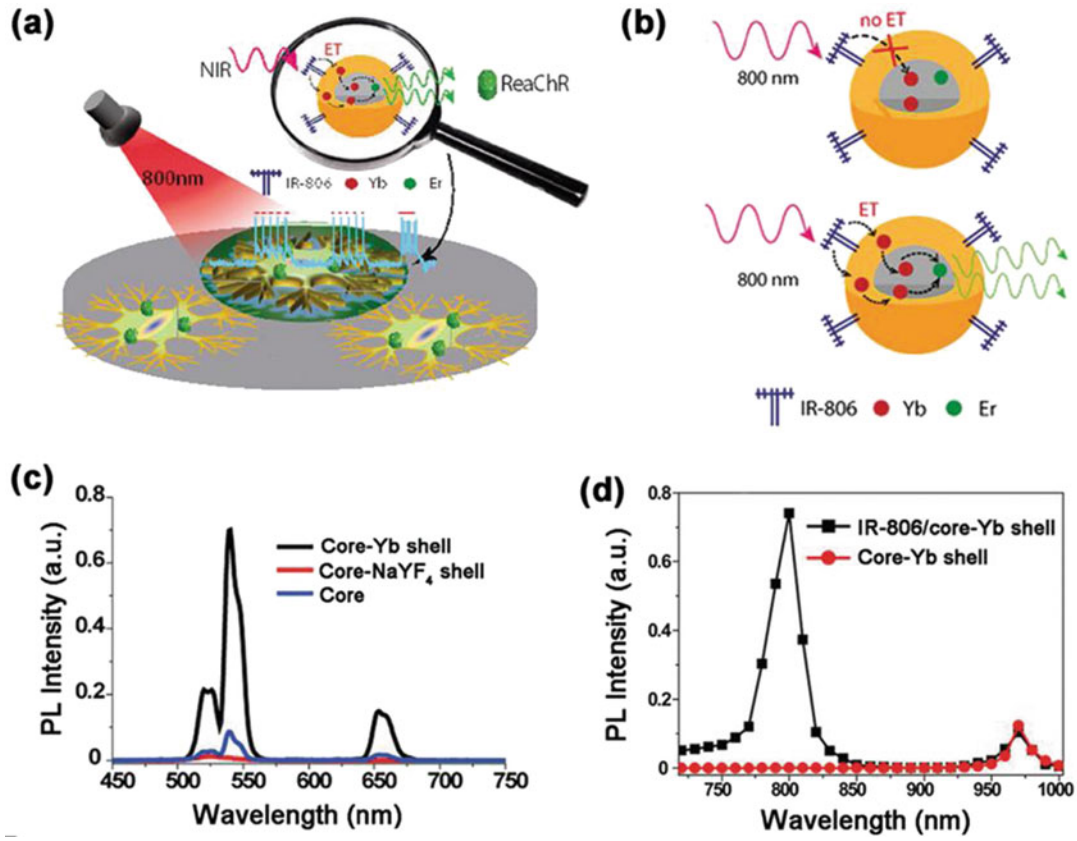

Fig. 11 (**a**) Schematic illustration of dye-sensitized core–shell UCNPs for optogenetics and bioimaging applications. (**b**) Schematic showing the proposed ET mechanism for core–shell UCNPs without (top) and with (bottom) Yb^{3+} doping. (**c**) Emission spectra of IR-806-sensitized core only, core–$NaYF_4$ shell, and core–Yb^{3+} shell. (**d**) Excitation spectra of core–Yb^{3+} active shell NP with and without IR-806 dye sensitization. Reprinted with permission from Ref. [113]. Copyright © 2016 American Chemical Society

[116] has demonstrated an innovative work on the evaluation of short-wave infrared (SWIR, 1000–1700 nm) properties of lanthanide nanoparticles. As shown in Fig. 12, disease detection by using the SWIR-imaging platform was demonstrated. And a library of lanthanide nanoparticles (Er, Ho, Pr, Tm) with tunable SWIR emission under 980 nm laser excitation was developed for real-time and multispectral SWIR bioimaging. These findings demonstrate that the SWIR imaging with the merits of high sensitivity, high spatial resolution, and large penetration depth is more beneficial for biomedical imaging application.

Among the whole NIR-II emitting region, the emission located around 1400 ~ 1600 nm emerges as the NIR-IIb imaging region [117–119] owing to the lower photon scattering than 1000–1400 nm. Thus, NIR-II fluorescence probes emitting in the 1400 ~ 1600 nm are urgently needed for high spatial resolution imaging. Recently, Dai's group [120] has reported the down-shifting Ce/Er doped rare-earth nanoparticles with NIR-IIb emission beyond 1500 nm. As shown in Fig. 13, NIR-IIb emission centered at 1525 nm was boosted by 9-fold with suppressing the UC pathway by the Ce-doping strategy. By using the rare earth-based probes, fast in vivo imaging of brain vascular was successfully achieved, presenting intriguing findings of short exposure time, high spatial resolution, and high sensitivity. Inspired by these results, our group [121] has explored the high-performance $NaLnF_4$ (Ln = Y, Yb, Lu) nanorods with enhanced NIR-IIb emission, high quantum

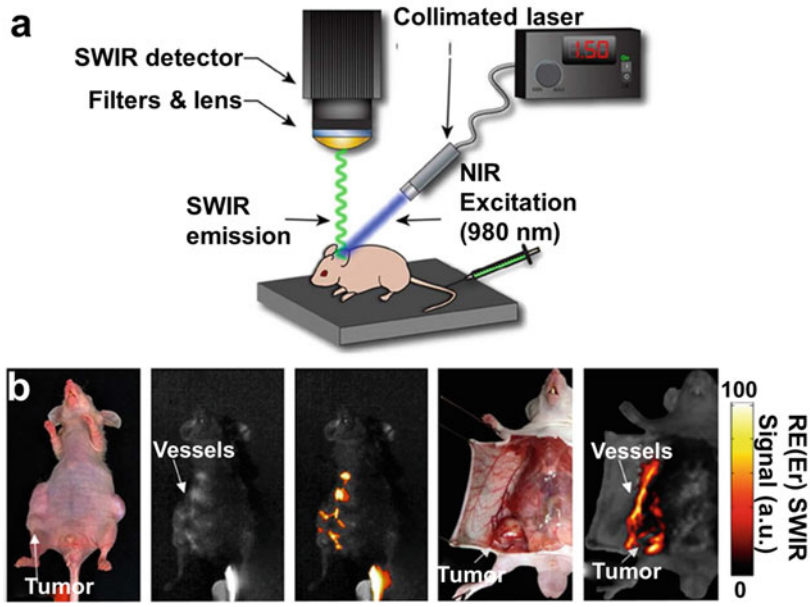

Fig. 12 (**a**) Schematic of the portable SWIR-imaging prototype. (**b**) Nude mice bearing melanoma xenografts were intravenously injected with rare-earth nanomaterials and imaged near surrounding tumor regions before dissection from the ventral aspect. Reprinted with permission from Ref. [116]. Copyright © 2013 Springer Nature

yield, and high biocompatibility via the Ce doping for NIR-IIb bioimaging. Small tumor/metastatic tumor detection with high sensitivity and tumor vascular imaging (Fig. 14) with the high spatial resolution were achieved by using the bright NIR-IIb emissive nanorods.

The aforementioned NIR-II bioimaging presents highly sensitive tumor vascular imaging with high spatial resolution and low background autofluorescence. Therefore, NIR-II imaging-guided surgical resection of the ultra-small tumor and metastasis tumor without background interference is urgently needed. Zhang's group [122] has presented an in vivo assembly of Er-based NIR-II emitting nanoprobe with DNA and targeting peptides for NIR-IIb (>1500 nm) imaging-guided metastatic ovarian cancer resection (Fig. 15). In this approach, RES retention induced long-term toxicity problem was largely solved by a two-staged in sequence injection approach. The nanoparticles were specially assembled in the tumor site, thus resulting in weak background signals in the liver and spleen. A high T/N ratio was achieved to highlight the outline of the ovarian metastases tumor ($\leq$1 mm) for precise tumor resection.

Although significant progress is achieved in NIR-II imaging by using 980 nm laser irradiation, the tissue overheating problem induced by 980 nm laser still cannot be ignored. Due to the low absorption coefficients of water and bio-tissue at 800 nm light, it is necessary to develop a new lanthanide-based NIR-II emitter with an optimized excitation wavelength. Zhang's group [26] has proposed the Nd-sensitized Er-based core–shell nanoparticles with an efficient 1525 nm emission for bioimaging under 808 nm laser excitation. With efficient 1525 nm emission, NIR-II bioimaging with large penetration depth (~18 mm) and low detection threshold concentration was achieved.

7 Conclusions and Perspective

In this chapter, we have reported the recent advancement in the design, synthesis, and application of the lanthanide UCNPs. In recent years,

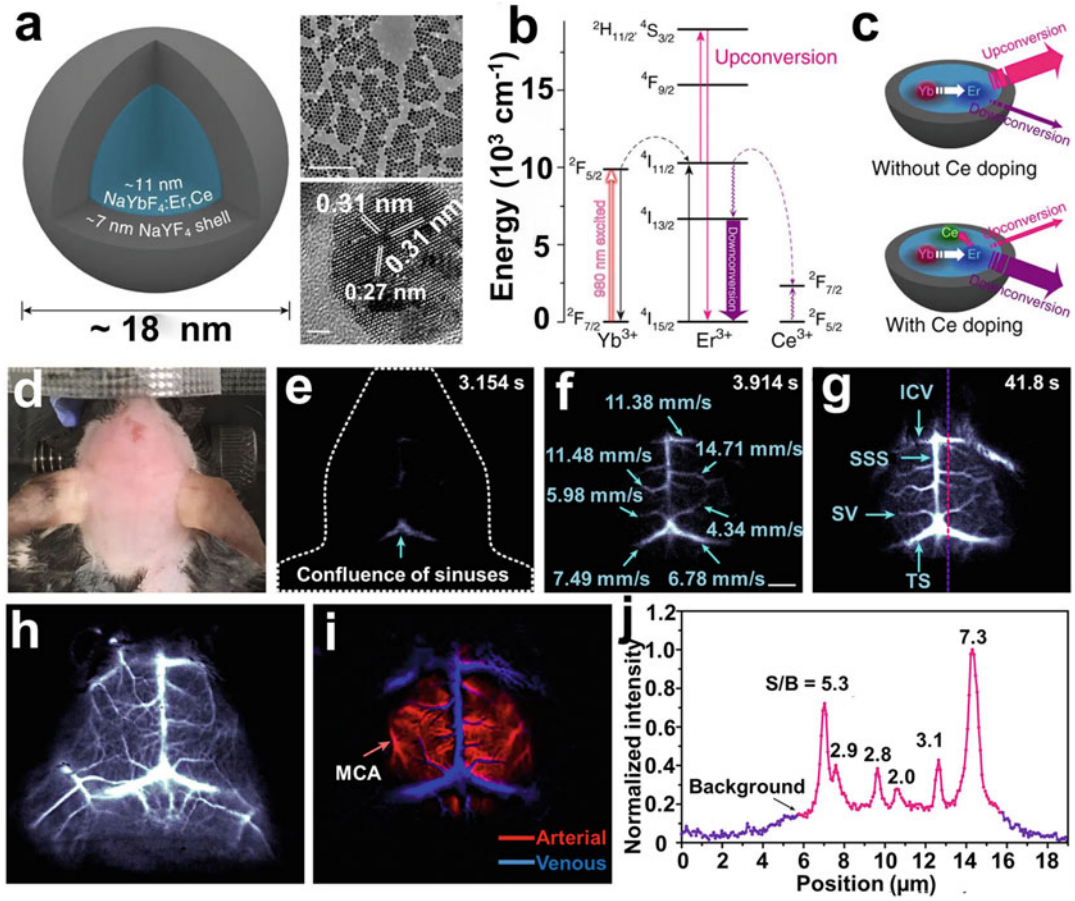

Fig. 13 Ce^{3+} doped rare-earth nanoparticles with enhanced NIR-II luminescence. (**a**) Schematic design of a $NaYbF_4$:Er,Ce@$NaYF_4$ core–shell nanoparticle (left) with corresponding TEM image (scale bar = 200 nm) and HRTEM image (scale bar = 2 nm). (**b**) Simplified energy level diagrams. (**c**) Schematic illustration of the proposed energy transfer mechanisms. Fast in vivo brain imaging with Er-RENPs@PMH-PEG in the NIR-II region. (**d**) Color photograph of a C57Bl/6 mouse (with hair shaved off) preceding NIR-II fluorescence imaging. (**e**–**g**) Time course NIR-II brain fluorescence images (exposure time: 20 ms). (**h**, **i**) Cerebral vascular image (exposure time: 20 ms) in NIR-II region with corresponding PCA overlaid image i showing arterial (red) and venous (blue) vessels. (**j**) SBR analysis of NIR-II cerebrovascular image g by plotting the cross-sectional intensity profiles. Reprinted with permission from Ref. [120]. Copyright © 2017 Springer Nature

lanthanide-based UCNPs have been considered as promising luminescent probe for bioimaging applications owing to their intriguing optical properties. In particular, when compared with the organic dye and QDs, under continuous-wave excitation at 980 nm, lanthanide-doped nanoparticles showed unique UCL properties, such as narrow band emission, long lifetimes, large anti-stokes shift, and non-blinking. However, traditional Yb^{3+}-sensitized UCNPs present low photon harvesting capability owing to the weak NIR absorption, subsequently leading to low UCL efficiency. To improve the UCL efficiency, Nd-sensitized and dye-sensitized UCNPs have been demonstrated in this chapter, which greatly alleviates the insufficient light-harvesting problem. Finally, by combining the advantages of both organic dye-sensitized and Yb/Nd-sensitized strategies, the superb next generation lanthanide-based materials with remarkabley enhanced UCL

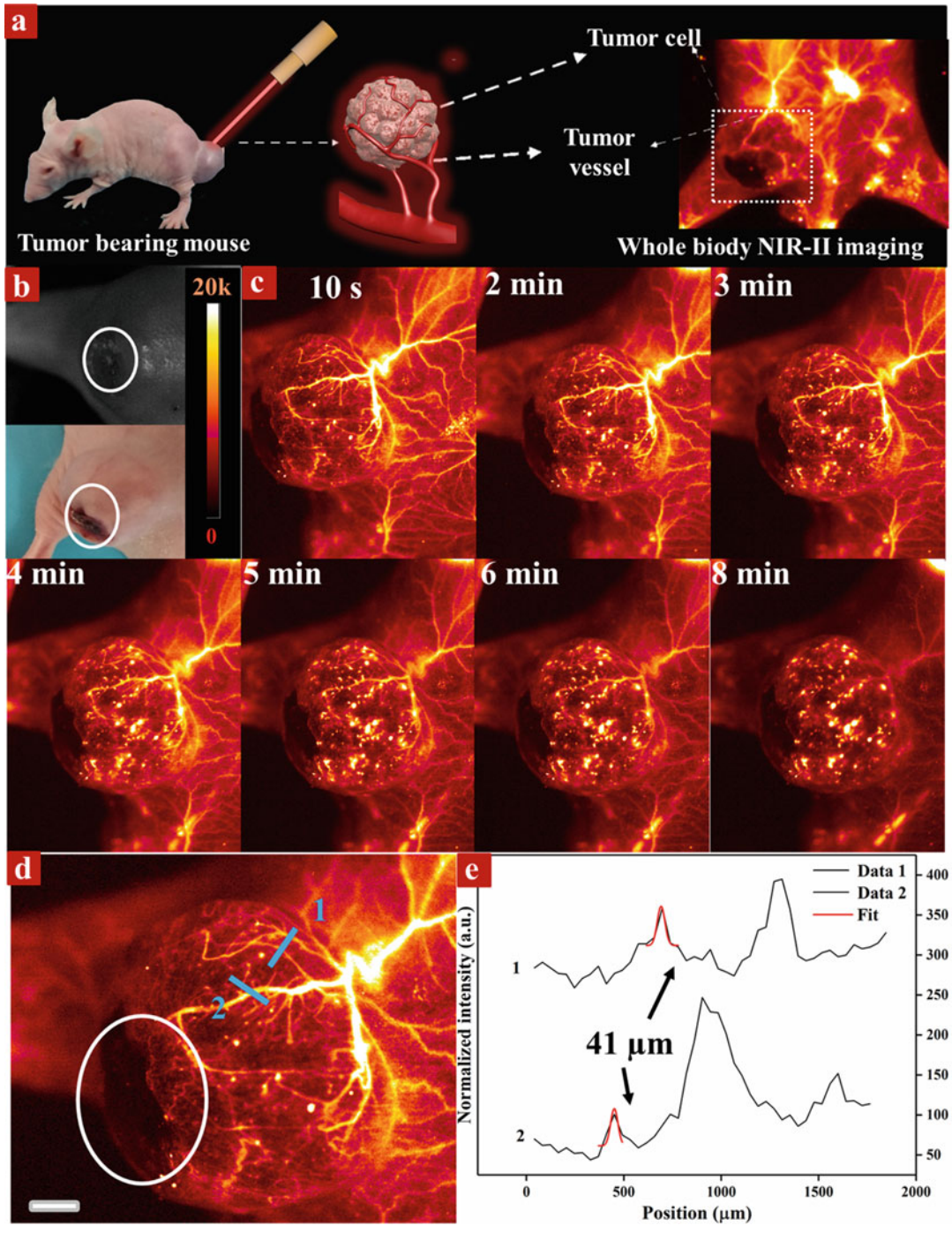

Fig. 14 (**a**) Schematic illustration of in vivo NIR-II bioimaging of the tumor. (**b**) A bright field image (up) and digital photograph of the tumor. (**c**) A time course of NIR-II images recorded at 980 nm laser excitation of a mouse tumor. (**d**) A high magnification tumor vascular image. (**e**) The corresponding zoom-in image of the marked vessel in (**d**) and the cross-sectional fluorescence intensity profiles along white line. The scale bar is 2 mm. Reprinted with permission from Ref. [121]. Copyright © 2019 American Chemical Society

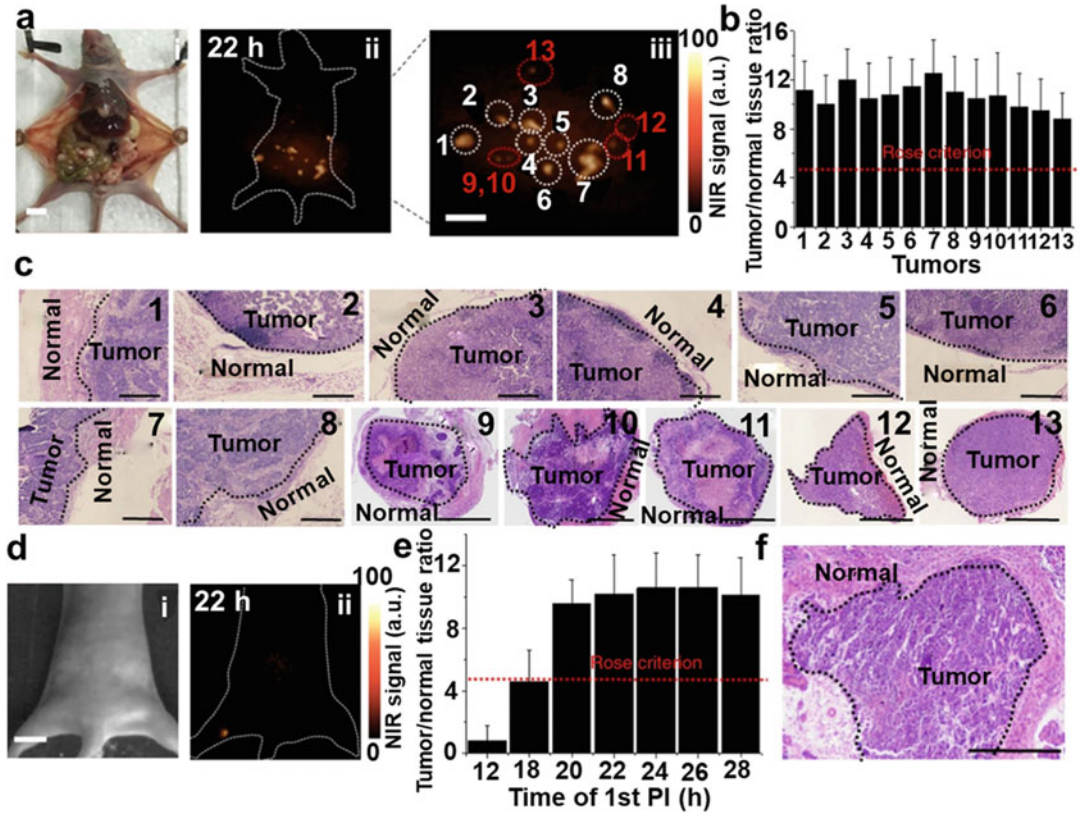

Fig. 15 NIR-II image-guided surgery. (**a**) Optical photo of human ovarian adenocarcinoma peritoneal metastases model and the corresponding NIR-II fluorescence bioimaging (1000 nm long-pass filter) results (Scale bar, 1 cm). (**b**) T/N ratios plotted as a function of different labeled peritoneal metastatic tumors, red dotted line is according to the Rose criterion. (**c**) H&E staining results of tumor margin in Nos. 1–8 (scale bars, 0.2 mm) and metastatic lesions in Nos. 9–13 (Scale bars, 0.5 mm). (**d**) NIR-II fluorescence bioimaging results of the popliteal lymph node metastasis at 22 h PI. Scale bar, 1 cm. (**e**) T/N ratios plotted as a function of different PI of the first injection, red dotted line is according to the Rose criterion. (**f**) H&E staining results of popliteal lymph node metastasis (Scale bar, 0.5 mm). Tumors were resected under NIR-II fluorescence bioimaging guidance. Reprinted with permission from Ref. [122]. Copyright © 2018 Springer Nature

brightness can be envisaged for cellular and in vivo bioimaging. However, for real applications in cellular and in vivo bioimaging, there are still many problems and challenges needed to be addressed. We summarize the problems and potential development directions of UCNPs for application in cellular and biomedical imaging in vivo as follows:

1. Although great progress has been achieved, the development of UCNPs for biomedical and cellular imaging is still limited by the relatively low QY, leading to an undesirable penetration depth (<1 cm). Recently, many strategies have been adopted to increase the QY, such as core–shell–shell strategy and efficient organic dye-sensitization strategy, subsequently leading to the enhancement in particle size, which may be unsuitable for fast excretion in vivo bioimaging. Therefore, searching for some new approaches is essential to improve the QY of the ultra-small UCNPs (sub-10 nm).
2. The surface defects and surface groups of UCNPs may significantly affect their quantum efficiency and biocompatibility. For nanosized UCNPs, the nonspecific biomolecules decorated on the UCNPs have played an

important role in decreasing the surface effect (high UC efficiency) and improving the solubility (long-term stability) for bioimaging. There is still much room to study the interface between the surface ligands and UCNPs.

3. The toxicity of UCNPs is one of the main issue in cellular and bioimaging application. Due to the unknown long-term toxicity of UCNPs in vivo, a key factor for UCNPs in the biomedical application is rapid excretion. However, most of the developed image probes were uptaken by the nonspecific organ (liver and spleen), leading to a long time excreting rate and unknown long-term toxicity. Therefore, the development of high-efficiency sub-5 nm UCNPs with the rapid renal filtration (<renal filtration threshold: 40 kD) effect is highly desirable for in vivo bioimaging.
4. Currently, great efforts have been devoted to developing lanthanide-based nanoprobes with excitation (Nd/organic dyes: 808 nm; Yb: 980 nm) and emission wavelength (Er/Tm/Ho: visible and NIR) at the visible and NIR region for biological imaging application. Owing to the rich spectrum of rare earth, the penetration depth can be further improved by using NIR-II excitation (Tm: 1208 nm; Er: 1525 nm) or emission (Nd: 1050 nm; Er: 1525 nm; Tm: 1475 nm) in lanthanide nanocrystals. Therefore, developing lanthanide-based nanocrystals with tunable excitation and emission wavelength beyond 1000 nm is highly desirable for cellular and in vivo biomedical optical imaging.

Acknowledgment The related contents are re-used with permission.

References

1. Poddar A, Gedam SC, Dhoble SJ (2013) Photoluminescence study of $KMgSO_4F$:X (X=Cu^+ or Dy^{3+} or Eu^{3+}) halosulfate phosphor. J Lumin 143:579–582
2. Downing E, Hesselink L, Ralston J, Macfarlane R (1996) A three-color, solid-state, three-dimensional display. Science 273:1185–1189
3. Hutchinson JA, Allik TH (1992) Diode array-pumped Er, Yb: phosphate glass laser. Appl Phys Lett 60:1424–1426
4. Joubert MF (1999) Photon avalanche upconversion in rare earth laser materials. Opt Mater 11:181–203
5. Stoneman RC, Esterowitz L (1992) Efficient resonantly pumped 2.8-μm Er^{3+}: GSGG laser. Opt Lett 17:816–818
6. Berthou H, Jörgensen CK (1990) Optical-fiber temperature sensor based on upconversion-excited fluorescence. Opt Lett 15:1100–1102
7. Chatterjee DK, Gnanasammandhan MK, Zhang Y (2010) Small upconverting fluorescent nanoparticles for biomedical applications. Small 6:2781–2795
8. Fischer LH, Harms GS, Wolfbeis OS (2011) Upconverting nanoparticles for nanoscale thermometry. Angew Chem Int Ed 50:4546–4551
9. Gai SL, Li CX, Yang PP, Lin J (2014) Recent progress in rare earth micro/nanocrystals: soft chemical synthesis, luminescent properties, and biomedical applications. Chem Rev 114:2343–2389
10. Li CX, Lin J (2010) Rare earth fluoride nano−/microcrystals: synthesis, surface modification and application. J Mater Chem 20:6831–6847
11. Wang F, Banerjee D, Liu YS, Chen XY, Liu XG (2010) Upconversion nanoparticles in biological labeling, imaging, and therapy. Analyst 135:1839–1854
12. Wang F, Han Y, Lim CS, Lu YH, Wang J, Xu J, Chen HY, Zhang C, Hong MH, Liu XG (2010) Simultaneous phase and size control of upconversion nanocrystals through lanthanide doping. Nature 463:1061–1065
13. Wang GF, Peng Q, Li YD (2009) Upconversion luminescence of monodisperse CaF_2:Yb^{3+}/Er^{3+} nanocrystals. J Am Chem Soc 131:14200–14201
14. Zhang C, Sun LD, Zhang YW, Yan CH (2010) Rare earth upconversion nanophosphors: synthesis, functionalization and application as biolabels and energy transfer donors. J Rare Earths 28:807–819
15. Chan WCW, Nie SM (1998) Quantum dot bioconjugates for ultrasensitive nonisotopic detection. Science 281:2016–2018
16. Han MY, Gao XH, Su JZ, Nie SM (2001) Quantum-dot-tagged microbeads for multiplexed optical coding of biomolecules. Nat Biotechnol 19:631–635
17. Goldys EM, Drozdowicz-Tomsia K, Sun JJ, Dosev D, Kennedy IM, Yatsunenko S, Godlewski M (2006) Optical characterization of Eu-doped and undoped Gd_2O_3 nanoparticles synthesized by the hydrogen flame pyrolysis method. J Am Chem Soc 128:14498–14505
18. Gordon WO, Carter JA, Tissue BM (2004) Long-lifetime luminescence of lanthanide-doped gadolinium oxide nanoparticles for immunoassays. J Lumin 108:339–342
19. Nichkova M, Dosev D, Gee SJ, Hammock BD, Kennedy IM (2005) Microarray immunoassay for phenoxybenzoic acid using polymer encapsulated

Eu:Gd_2O_3 nanoparticles as fluorescent labels. Anal Chem 77:6864–6873
20. Bünzli JCG (2010) Lanthanide luminescence for biomedical analyses and imaging. Chem Rev 110:2729–2755
21. Eliseeva SV, Bünzli JCG (2010) Lanthanide luminescence for functional materials and bio-sciences. Chem Soc Rev 39:189–227
22. Hoppe HA (2009) Recent developments in the field of inorganic phosphors. Angew Chem Int Ed 48:3572–3582
23. Xia A, Chen M, Gao Y, Wu DM, Feng W, Li FY (2012) Gd^{3+} complex-modified $NaLuF_4$-based upconversion nanophosphors for trimodality imaging of NIR-to-NIR upconversion luminescence, X-ray computed tomography and magnetic resonance. Biomaterials 33:5394–5405
24. Zhou J, Yu MX, Sun Y, Zhang XZ, Zhu XJ, Wu ZH, Wu DM, Li FY (2011) Fluorine-18-labeled Gd^{3+}/Yb^{3+}/Er^{3+} co-doped $NaYF_4$ nanophosphors for multimodality PET/MR/UCL imaging. Biomaterials 32:1148–1156
25. Wang HB, Lu W, Zeng TM, Yi ZG, Rao L, Liu HR, Zeng SJ (2014) Multi-functional $NaErF_4$:Yb nanorods: enhanced red upconversion emission, in vitro cell, in vivo X-ray, and T_2-weighted magnetic resonance imaging. Nanoscale 6:2855–2860
26. Wang R, Li XM, Zhou L, Zhang F (2014) Epitaxial seeded growth of rare-earth nanocrystals with efficient 800 nm near-infrared to 1525 nm short-wavelength infrared downconversion photoluminescence for in vivo bioimaging. Angew Chem Int Ed 53:12086–12090
27. Yi ZG, Li XL, Xue ZL, Liang X, Lu W, Peng H, Liu HR, Zeng SJ, Hao JH (2015) Remarkable NIR enhancement of multifunctional nanoprobes for in vivo trimodal bioimaging and upconversion optical/T_2-weighted MRI-guided small tumor diagnosis. Adv Funct Mater 25:7119–7129
28. Yi ZG, Lu W, Liu HR, Zeng SJ (2015) High quality polyacrylic acid modified multifunction luminescent nanorods for tri-modality bioimaging, in vivo long-lasting tracking and biodistribution. Nanoscale 7:542–550
29. Yi ZG, Lu W, Xu YR, Yang J, Deng L, Qian C, Zeng TM, Wang HB, Rao L, Liu HR, Zeng SJ (2014) PEGylated $NaLuF_4$:Yb/Er upconversion nanophosphors for in vivo synergistic fluorescence/X-ray bioimaging and long-lasting, real-time tracking. Biomaterials 35:9689–9697
30. Zeng SJ, Tsang MK, Chan CF, Wong KL, Hao JH (2012) PEG modified $BaGdF_5$:Yb/Er nanoprobes for multi-modal upconversion fluorescent, in vivo X-ray computed tomography and biomagnetic imaging. Biomaterials 33:9232–9238
31. Zeng SJ, Wang HB, Lu W, Yi ZG, Rao L, Liu HR, Hao JH (2014) Dual-modal upconversion fluorescent/X-ray imaging using ligand-free hexagonal phase $NaLuF_4$: Gd/Yb/Er nanorods for blood vessel visualization. Biomaterials 35:2934–2941
32. Zeng SJ, Xiao JJ, Yang QB, Hao JH (2012) Bi-functional $NaLuF_4$:Gd^{3+}/Yb^{3+}/Tm^{3+} nanocrystals: structure controlled synthesis, near-infrared upconversion emission and tunable magnetic properties. J Mater Chem 22:9870–9874
33. Zeng SJ, Yi ZG, Lu W, Qian C, Wang HB, Rao L, Zeng TM, Liu HR, Liu HJ, Fei B, Hao JH (2014) Simultaneous realization of phase/size manipulation, upconversion luminescence enhancement, and blood vessel imaging in multifunctional nanoprobes through transition metal Mn^{2+} doping. Adv Funct Mater 24:4051–4059
34. Auzel F (2004) Upconversion and anti-stokes processes with f and d ions in solids. Chem Rev 104:139–173
35. Esterowitz L, Schnitzler A, Noonan J, Bahler J (1968) Rare earth infrared quantum counter. Appl Opt 7:2053–2070
36. Haase M, Schäfer H (2011) Upconverting nanoparticles. Angew Chem Int Ed 50:5808–5829
37. Chen GY, Liu Y, Zhang YG, Somesfalean G, Zhang ZG, Sun Q, Wang FP (2007) Bright white upconversion luminescence in rare-earth ion doped Y_2O_3 nanocrystals. Appl Phys Lett 91:133103
38. Chen GY, Zhang YG, Somesfalean G, Zhang ZG, Sun Q, Wang FP (2006) Two-color upconversion in rare-earth-ion-doped ZrO_2 nanocrystals. Appl Phys Lett 89:163105
39. Konrad A, Fries T, Gahn A, Kummer F, Herr U, Tidecks R, Samwer K (1999) Chemical vapor synthesis and luminescence properties of nanocrystalline cubic Y_2O_3:Eu. J Appl Phys 86:3129–3133
40. Kottaisamy M, Jeyakumar D, Jagannathan R, Rao MM (1996) Yttrium oxide:Eu^{3+} red phosphor by self-propagating high temperature synthesis. Mater Res Bull 31:1013–1020
41. Matsuura D (2002) Red, green, and blue upconversion luminescence of trivalent-rare-earth ion-doped Y_2O_3 nanocrystals. Appl Phys Lett 81:4526–4528
42. Murugana AV, Viswanath AK, Ravi V, Kakade BA, Saaminathan V (2006) Photoluminescence studies of Eu^{3+} doped Y_2O_3 nanophosphor prepared by microwave hydrothermal method. Appl Phys Lett 89:123120
43. Tao Y, Zhao GW, Zhang WP, Xia SD (1997) Combustion synthesis and photoluminescence of nanocrystalline Y_2O_3:Eu phosphors. Mater Res Bull 32:501–506
44. Vetrone F, Boyer JC, Capobianco JA, Speghini A, Bettinelli, M (2003) Effect of Yb^{3+} codoping on the upconversion emission in nanocrystalline Y_2O_3:Er^{3+}. J Phys Chem B 107:1107–1112
45. Krämer KW, Biner D, Frei G, Güdel HU, Hehlen MP, Lüthi SR (2004) Hexagonal sodium yttrium fluoride based green and blue emitting upconversion phosphors. Chem Mater 16:1244–1251
46. Carlos LD, Ferreira RAS, Bermudez VDZ, Ribeiro SJL (2009) Lanthanide-containing light-emitting organic-inorganic hybrids: a bet on the future. Adv Mater 21:509–534

47. Sivakumar S, van Veggel FCJM, Raudsepp M (2005) Bright white light through up-conversion of a single NIR source from sol−gel-derived thin film made with Ln^{3+}-doped LaF_3 nanoparticles. J Am Chem Soc 127:12464–12465
48. Sudarsan V, Sivakumar S, van Veggel FCJM, Raudsepp M (2005) General and convenient method for making highly luminescent sol−gel derived silica and alumina films by using LaF_3 nanoparticles doped with lanthanide ions (Er^{3+}, Nd^{3+}, and Ho^{3+}). Chem Mater 17:4736–4742
49. Wang F, Fan XP, Wang MQ, Zhang Y (2007) Multicolour PEI/$NaGdF_4$:Ce^{3+}/Ln^{3+} nanocrystals by single-wavelength excitation. Nanotechnology 18:025701
50. Wang F, Liu XG (2008) Upconversion multicolor fine-tuning: visible to near-infrared emission from lanthanide-doped $NaYF_4$ nanoparticles. J Am Chem Soc 130:5642–5643
51. Jiang S, Zhang Y, Lim KM, Sim EKW, Ye L (2009) NIR-to-visible upconversion nanoparticles for fluorescent labeling and targeted delivery of siRNA. Nanotechnology 20:155101
52. Li YB, Li XL, Xue ZL, Jiang MY, Zeng SJ, Hao JH (2017) M^{2+} doping induced simultaneous phase/size control and remarkable enhanced upconversion luminescence of $NaLnF_4$ probes for optical-guided tiny tumor diagnosis. Adv Healthc Mater 6:1601231
53. Liu L, Wang SF, Zhao BZ, Pei P, Fan Y, Li XM, Zhang F (2018) Er^{3+} sensitized 1530 nm to 1180 nm second near-infrared window upconversion nanocrystals for in vivo biosensing. Angew Chem Int Ed 57:7518–7522
54. Xue ZL, Yi ZG, Li XL, Li YB, Jiang MY, Liu HR, Zeng SJ (2017) Upconversion optical/magnetic resonance imaging-guided small tumor detection and in vivo tri-modal bioimaging based on high-performance luminescent nanorods. Biomaterials 115:90–103
55. Yi GS, Lu HC, Zhao SY, Ge Y, Yang WJ, Chen DP, Guo LH (2004) Synthesis, characterization, and biological application of size-controlled nanocrystalline $NaYF_4$:Yb,Er infrared-to-visible up-conversion phosphors. Nano Lett 4:2191–2196
56. Heer S, Kömpe K, Gudel HU, Haase M (2004) Highly efficient multicolour upconversion emission in transparent colloids of lanthanide-doped $NaYF_4$ nanocrystals. Adv Mater 16:2102–2105
57. Li ZQ, Zhang Y (2006) Monodisperse silica-coated polyvinylpyrrolidone/$NaYF_4$ nanocrystals with multicolor upconversion fluorescence emission. Angew Chem Int Ed 45:7732–7735
58. Zeng JH, Su J, Li ZH, Yan RX, Li YD (2005) Synthesis and upconversion luminescence of hexagonal-phase $NaYF_4$:Yb, Er^{3+} phosphors of controlled size and morphology. Adv Mater 17:2119–2123
59. Boyer JC, Cuccia LA, Capobianco JA (2007) Synthesis of colloidal upconverting $NaYF_4$: Er^{3+}/Yb^{3+} and Tm^{3+}/Yb^{3+} monodisperse nanocrystals. Nano Lett 7:847–852
60. Mai HX, Zhang YW, Si R, Yan ZG, Sun LD, You LP, Yan CH (2006) High-quality sodium rare-earth fluoride nanocrystals: controlled synthesis and optical properties. J Am Chem Soc 128:6426–6436
61. Mai HX, Zhang YW, Sun LD, Yan CH (2007) Highly efficient multicolor up-conversion emissions and their mechanisms of monodisperse $NaYF_4$:Yb,Er core and core/shell-structured nanocrystals. J Phys Chem C 111:13721–13729
62. Wang LY, Li YD (2006) $Na(Y_{1.5}Na_{0.5})F_6$ single-crystal nanorods as multicolor luminescent materials. Nano Lett 6:1645–1649
63. Zhang F, Li J, Shan J, Xu L, Zhao DY (2009) Shape, size, and phase-controlled rare-earth fluoride nanocrystals with optical upconversion properties. Chem Eur J 15:11010–11019
64. Jayasankar CK, Kumar KU, Venkatramu V, Babu P, Tröster T, Sievers W, Wortmann G (2008) Effect of pressure on luminescence properties of Sm^{3+} ions in potassium niobate tellurite glass. J Lumin 128:718–720
65. Patra A, Friend CS, Kapoor R, Prasad PN (2002) Upconversion in Er^{3+}:ZrO_2 nanocrystals. J. Phys Chem B 106:1909–1912
66. Patra A, Friend CS, Kapoor R, Prasad PN (2003) Fluorescence upconversion properties of Er^{3+}-doped TiO_2 and $BaTiO_3$ nanocrystallites. Chem Mater 15:3650–3655
67. Zhou J, Liu Z, Li FY (2012) Upconversion nanophosphors for small-animal imaging. Chem Soc Rev 41:1323–1349
68. Yi GS, Chow GM (2006) Synthesis of hexagonal-phase $NaYF_4$:Yb,Er and $NaYF_4$:Yb,Tm nanocrystals with efficient up-conversion fluorescence. Adv Funct Mater 16:2324–2329
69. Chen GY, Qiu HL, Fan RW, Hao SW, Tan S, Yang CH, Han G (2012) Lanthanide-doped ultrasmall yttrium fluoridenanoparticles with enhanced multicolor upconversion photoluminescence. J Mater Chem 22:20190–20196
70. Li FF, Li CG, Liu XM, Chen Y, Bai TY, Wang L, Shi Z, Feng SH (2012) Hydrophilic, upconverting, multicolor, lanthanide-doped $NaGdF_4$ nanocrystals as potential multifunctional bioprobes. Chem Eur J 18:11641–11646
71. Li ZQ, Zhang Y (2008) An efficient and user-friendly method for the synthesis of hexagonal-phase $NaYF_4$: Yb, Er/Tm nanocrystals with controllable shape and upconversion fluorescence. Nanotechnology 19:345606
72. Qiu HL, Chen GY, Sun L, Hao SW, Han G, Yang CH (2011) Ethylenediaminetetraacetic acid (EDTA)-controlled synthesis of multicolor lanthanide doped $BaYF_5$ upconversion nanocrystals. J Mater Chem 21:17202–17208
73. Boyer JC, Vetrone F, Cuccia LA, Capobianco JA (2006) Synthesis of colloidal upconverting $NaYF_4$ nanocrystals doped with Er^{3+}, Yb^{3+} and Tm^{3+}, Yb^{3+} via thermal decomposition of lanthanide trifluoroacetate precursors. J Am Chem Soc 128:7444–7445

74. Chai RT, Lian HZ, Hou ZY, Zhang CM, Peng C, Lin J (2010) Preparation and characterization of upconversion luminescent $NaYF_4:Yb^{3+},Er^{3+}(Tm^{3+})$/PMMA bulk transparent nanocomposites through in situ photopolymerization. J Phys Chem C 114:610–616
75. Ehlert O, Thomann R, Darbandi M, Nann T (2008) A four-color colloidal multiplexing nanoparticle system. ACS Nano 2:120–124
76. Yi GS, Chow GM (2005) Colloidal LaF_3:Yb,Er, LaF_3:Yb, Ho and LaF_3:Yb, Tm nanocrystals with multicolor upconversion fluorescence. J Mater Chem 15:4460–4464
77. Huang SH, Xu J, Zhang ZG, Zhang X, Wang LZ, Gai SL, He F, Niu N, Zhang ML, Yang PP (2012) Rapid, morphologically controllable, large-scale synthesis of uniform $Y(OH)_3$ and tunable luminescent properties of $Y_2O_3:Yb^{3+}/Ln^{3+}$ (Ln = Er, Tm and Ho). J Mater Chem 22:16136–16144
78. Niu WB, Wu SL, Zhang SF, Li L (2010) Synthesis of colour tunable lanthanide-ion doped $NaYF_4$ upconversion nanoparticles by controlling temperature. Chem Commun 46:3908–3910
79. Ye XC, Collins JE, Kang YJ, Chen J, Chen DTN, Yodh AG, Murray CB (2010) Morphologically controlled synthesis of colloidal upconversion nanophosphors and their shape-directed self-assembly. Proc Natl Acad Sci U S A 107:22430–22435
80. Zijlmans HJMAA, Bonnet J, Burton J, Kardos K, Vail T, Niedbala RS, Tanke HJ (1999) Detection of cell and tissue surface antigens using up-converting phosphors: a new reporter technology. Anal Biochem 267:30–36
81. Hilderbrand SA, Shao FW, Salthouse C, Mahmood U, Weissleder R (2009) Upconverting luminescent nanomaterials: application to in vivo bioimaging. Chem Commun 4188–4190
82. Zhou LJ, Gu ZJ, Liu XX, Yin WY, Tian G, Yan L, Jin S, Ren WL, Xing GM, Li W, Chang XL, Hu ZB, Zhao YL (2012) Size-tunable synthesis of lanthanide-doped Gd_2O_3 nanoparticles and their applications for optical and magnetic resonance imaging. J Mater Chem 22:966–974
83. Chatterjee DK, Rufalhah AJ, Zhang Y (2008) Upconversion fluorescence imaging of cells and small animals using lanthanide doped nanocrystals. Biomaterials 29:937–943
84. Nyk M, Kumar R, Ohulchanskyy TY, Bergey EJ, Prasad PN (2008) High contrast in vitro and in vivo photoluminescence bioimaging using near infrared to near infrared up-conversion in Tm^{3+} and Yb^{3+} doped fluoride nanophosphors. Nano Lett 8:3834–3838
85. Liu Q, Sun Y, Yang TS, Feng W, Li CG, Li FY (2011) Sub-10 nm hexagonal lanthanide-doped $NaLuF_4$ upconversion nanocrystals for sensitive bioimaging in vivo. J Am Chem Soc 133:17122–17125
86. Xia A, Gao Y, Zhou J, Li CY, Yang TS, Wu DM, Wu LM, Li FY (2011) Core–shell $NaYF_4:Yb^{3+}$, $Tm^{3+}@Fe_xO_y$ nanocrystals for dual-modality T_2-enhanced magnetic resonance and NIR-to-NIR upconversion luminescent imaging of small-animal lymphatic node. Biomaterials 32:7200–7208
87. Zhou J, Sun Y, Du XX, Xiong LQ, Hu H, Li FY (2010) Dual-modality in vivo imaging using rare-earth nanocrystals with near-infrared to near-infrared (NIR-to-NIR) upconversion luminescence and magnetic resonance properties. Biomaterials 31:3287–3295
88. Xing HY, Bu WB, Ren QG, Zheng XP, Li M, Zhang SJ, Qu HY, Wang Z, Hua YQ, Zhao KL, Zhou LP, Peng WJ, Shi JL (2012) A $NaYbF_4$: Tm^{3+} nanoprobe for CT and NIR-to-NIR fluorescent bimodal imaging. Biomaterials 33:5384–5393
89. Flaherty JM, Bartolo BD (1973) Radiative and radiationless processes of Er^{3+} in MnF_2. J Lumin 8:51–70
90. Sell DD, Greene RL, White RM (1967) Optical exciton-magnon absorption in MnF_2. Phys Rev 158:489–510
91. Xie MY, Peng XN, Fu XF, Zhang JJ, Li GL, Yu XF (2009) Synthesis of Yb^{3+}/Er^{3+} co-doped MnF_2 nanocrystals with bright red up-converted fluorescence. Script Mater 60:190–193
92. Zeng JH, Xie T, Li ZH, Li YD (2007) Monodispersed nanocrystalline fluoroperovskite up-conversion phosphors. Cryst Growth Des 7:2774–2777
93. Wang J, Wang F, Wang C, Liu Z, Liu XG (2011) Single-band upconversion emission in lanthanide-doped $KMnF_3$ nanocrystals. Angew Chem Int Ed 50:10369–10372
94. Tian G, Gu ZJ, Zhou LJ, Yin WY, Liu XX, Yan L, Jin S, Ren WL, Xing GM, Li SJ, Zhao YL (2012) Mn^{2+} dopant-controlled synthesis of $NaYF_4$:Yb/Er upconversion nanoparticles for in vivo imaging and drug delivery. Adv Mater 24:1226–1231
95. Rai M, Singh SK, Singh AK, Prasad R, Koch B, Mishra K, Rai SB (2015) Enhanced red upconversion emission, magneto luminescent behavior, and bioimaging application of $NaSc_{0.75}Er_{0.02}Yb_{0.18}Gd_{0.05}F_4$@AuNPs nanoparticles. ACS Appl Mater Interfaces 7:15339–15350
96. Chen GY, Ohulchanskyy TY, Kachynski A, Ågren H, Prasad PN (2011) Intense visible and near-infrared upconversion photoluminescence in colloidal $LiYF_4:Er^{3+}$ nanocrystals under excitation at 1490 nm. ACS Nano 5:4981–4986
97. Balda R, Peña JI, Arriandiaga MA, Fernandez J (2010) Efficient $Nd^{3+}\rightarrow Yb^{3+}$ energy transfer in $0.8CaSiO_3$-$0.2Ca_3(PO_4)_2$ eutectic glass. Opt Express 18:13842–13850
98. Liu YX, Wang DS, Shi JX, Peng Q, Li YD (2013) Magnetic tuning of upconversion luminescence in lanthanide-doped bifunctional nanocrystals. Angew Chem Int Ed 52:4366–4369
99. Zhan QQ, Qian J, Liang HJ, Somesfalean G, Wang D, He SL, Zhang ZG, Andersson-Engels S (2011) Using 915 nm laser excited $Tm^{3+}/Er^{3+}/Ho^{3+}$-doped $NaYbF_4$ upconversion nanoparticles for in vitro and deeper in vivo bioimaging without overheating irradiation. ACS Nano 5:3744–3757

100. Zhan QQ, He SL, Qian J, Cheng H, Cai FH (2013) Optimization of optical excitation of upconversion nanoparticles for rapid microscopy and deeper tissue imaging with higher quantum yield. Theranostics 3:306–316
101. Zhou JJ, Shirahata N, Sun HT, Ghosh B, Ogawara M, Teng Y, Zhou SF, Chu RGS, Fujii M, Qiu JR (2013) Efficient dual-modal NIR-to-NIR emission of rare earth ions co-doped nanocrystals for biological fluorescence imaging. J Phys Chem Lett 4:402–408
102. Zou WQ, Visser C, Maduro JA, Pshenichnikov MS, Hummelen JC (2012) Broadband dye-sensitized upconversion of near-infrared light. Nat Photonics 6:560–564
103. Xie XJ, Gao NY, Deng RR, Sun Q, Xu QH, Liu XG (2013) Mechanistic investigation of photon upconversion in Nd^{3+}-sensitized core–shell nanoparticles. J Am Chem Soc 135:12608–12611
104. Shen J, Chen GY, Vu AM, Fan W, Bilsel OS, Chang CC, Han G (2013) Engineering the upconversion nanoparticle excitation wavelength: cascade sensitization of tri-doped upconversion colloidal nanoparticles at 800 nm. Adv Opt Mater 1:644–650
105. Wang YF, Liu GY, Sun LD, Xiao JW, Zhou JC, Yan CH (2013) Nd^{3+}-sensitized upconversion nanophosphors: efficient in vivo bioimaging probes with minimized heating effect. ACS Nano 7:7200–7206
106. Zhong YT, Tian G, Gu ZJ, Yang YJ, Gu L, Zhao YL, Ma Y, Yao JN (2014) Elimination of photon quenching by a transition layer to fabricate a quenching-shield sandwich structure for 800 nm excited upconversion luminescence of Nd^{3+}-sensitized nanoparticles. Adv Mater 26:2831–2837
107. Wang T, Zhou HF, Yu ZC, Zhou GJ, Zhou J, Huang DP, Sun LL, Gao P, Sun YZ, Hu JF (2018) 808 nm excited multicolor upconversion tuning through energy migration in core–shell–shell nanoarchitecture. J Phys Chem C 122:10113–10124
108. Wen HL, Zhu H, Chen X, Hung TF, Wang BL, Zhu GY, Yu SF, Wang F (2013) Upconverting near-infrared light through energy management in core–shell–shell nanoparticles. Angew Chem Int Ed 52:13419–13423
109. Chen GY, Damasco J, Qiu HL, Shao W, Ohulchanskyy TY, Valiev RR, Wu X, Han G, Wang Y, Yang CH, Ågren H, Prasad PN (2015) Energy-cascaded upconversion in an organic dye-sensitized core/shell fluoride nanocrystal. Nano Lett 15:7400–7407
110. Wu X, Lee H, Bilsel O, Zhang YW, Li ZJ, Chen T, Liu Y, Duan CY, Shen J, Punjabi A, Han G (2015) Tailoring dye-sensitized upconversion nanoparticle excitation bands towards excitation wavelength selective imaging. Nanoscale 7:18424–18428
111. Chen GY, Shao W, Valiev RR, Ohulchanskyy TY, He GS, Ågren H, Prasad PN (2016) Efficient broadband upconversion of near-infrared light in dye-sensitized core/shell nanocrystals. Adv Opt Mater 4:1760–1766
112. Wei W, Chen GY, Baev A, He GS, Shao W, Damasco J, Prasad PN (2016) Alleviating luminescence concentration quenching in upconversion nanoparticles through organic dye sensitization. J Am Chem Soc 138:15130–15133
113. Wu X, Zhang YW, Takle K, Bilsel O, Li ZJ, Lee H, Zhang ZJ, Li DS, Fan W, Duan CY, Chan EM, Lois C, Xiang Y, Han G (2016) Dye-sensitized core/active shell upconversion nanoparticles for optogenetics and bioimaging applications. ACS Nano 10:1060–1066
114. Yu MX, Li FY, Chen ZG, Hu H, Zhan C, Yang H, Huang CH (2009) Laser scanning up-conversion luminescence microscopy for imaging cells labeled with rare-earth nanophosphors. Anal Chem 81:930–935
115. Lim YT, Kim S, Nakayama A, Stott NE, Bawendi MG, Frangioni JV (2003) Selection of quantum dot wavelengths for biomedical assays and imaging. Mol Imaging 2:50–64
116. Naczynski DJ, Tan MC, Zevon M, Wall B, Kohl J, Kulesa A, Chen S, Roth CM, Riman RE, Moghe PV (2013) Rare-earth-doped biological composites as in vivo shortwave infrared reporters. Nat Commun 4:2199
117. Xue ZL, Zeng SJ, Hao JH (2018) Non-invasive through-skull brain vascular imaging and small tumor diagnosis based on NIR-II emissive lanthanide nanoprobes beyond 1500 nm. Biomaterials 171:153–163
118. Diao S, Hong GS, Antaris AL, Blackburn JL, Cheng K, Cheng Z, Dai HJ (2015) Biological imaging without autofluorescence in the second near-infrared region. Nano Res 8:3027–3034
119. Hong GS, Antaris AL, Dai HJ (2017) Near-infrared fluorophores for biomedical imaging. Nat Biomed Eng 1:0010
120. Zhong YT, Ma ZR, Zhu SJ, Yue JY, Zhang MX, Antaris AL, Yuan J, Cui R, Wan H, Zhou Y, Wang WZ, Huang NF, Luo J, Hu ZY, Dai HJ (2017) Boosting the down-shifting luminescence of rare-earth nanocrystals for biological imaging beyond 1500 nm. Nat Commun 8:737
121. Li YB, Zeng SJ, Hao JH (2019) Non-invasive optical guided tumor metastasis/vessel imaging by using lanthanide nanoprobe with enhanced down-shifting emission beyond 1500 nm. ACS Nano 13:248–259
122. Wang PY, Fan Y, Lu LF, Liu L, Fan LL, Zhao MY, Xie Y, Xu CJ, Zhang F (2018) NIR-II nanoprobes in-vivo assembly to improve image-guided surgery for metastatic ovarian cancer. Nat Commun 9:2898

Conjugated Polymers and Polymer Dots for Cell Imaging

Tingting Sun and Zhigang Xie

1 Introduction

Conjugated polymers (CPs) as a class of excellent conducting materials have been widely employed in optoelectronic devices, such as photovoltaic cells, light-emitting diodes, and field effect transistors, due to their large π-conjugated backbones and delocalized electronic structures [1]. In addition, the inherent light-harvesting and light-amplifying qualities of CPs also render them as promising fluorescent probes in biological field. To make them applicable in biological environment, CPs should be dissolved or dispersed in aqueous media, thus water-soluble conjugated polymers (WSCPs) or conjugated polymer nanoparticles (CPNs) are developed. WSCPs are designed via modifying the side chains and applied in diagnostics, in vitro or ex/in vivo imaging, drug/gene delivery, and photodynamic therapy [2–4]. However, several limitations still exist in their practical application, including complicated conjugation and purification steps, undesirable self-aggregation behaviors, low quantum yield (QY) of most near-infrared (NIR) WSCPs, and potential toxicity in vivo [4]. To solve these problems, CPNs have been proposed to be promising nanomaterial for biomedical application [5–16]. CPNs have many advantages, such as easy preparation, high brightness, excellent biocompatibility, and photostability [17].

Small fluorescent nanoparticles are especially attractive for most biological applications, such as semiconductor quantum dots (Qdots) [18–20], silicon dots [21, 22], carbon dots [23–26], and dye-doped silica dots [27], in which "dot" refers to their small particle size [28]. In consistence with these small dots, polymer dots (Pdots) are viewed as a subset of CPNs with both small particle size (less than 20–30 nm in diameter, preferably in the 5–20 nm range) and high brightness [28, 29]. There should be more than 50% and preferably greater than 80% CPs in Pdots, because the fluorescence brightness is largely determined by the weight or volume fraction of CPs [28, 29]. Moreover, Pdots should possess a hydrophobic polymer interior to ensure colloidal stability and the fluorescence brightness [30]. As fluorescent probes, Pdots exhibit many excellent characteristics, such as fast emission rate, high fluorescence brightness, excellent photostability, as well as nonblinking and nontoxic features [30–49].

Although some reviews have summarized the synthesis, properties, and biological applications of CPNs and Pdots, respectively [4, 7–9, 12–15, 17, 28, 29, 50], a comprehensive summary about CPNs and Pdots as new fluorescent materials for cell imaging does not exist yet. To further promote the development and application of CPNs and Pdots in biomedical fields, in this chapter, we

T. Sun · Z. Xie (✉)
State Key Laboratory of Polymer Physics and Chemistry, Changchun Institute of Applied Chemistry, Chinese Academy of Sciences, Changchun, Jilin, People's Republic of China
e-mail: xiez@ciac.ac.cn

F.-G. Wu (ed.), *Fluorescent Materials for Cell Imaging*, https://doi.org/10.1007/978-981-15-5062-1_7

will summarize the developments of CPNs and Pdots from design and synthesis to their applications in cell imaging.

2 Conjugated Polymer Nanoparticles (CPNs)

In 2013, Wang's group systematically reviewed the biological applications of CPNs on fluorescence imaging, anti-microorganism and antitumor, as well as gene delivery and drug delivery/release [7]. CPNs have been developed very fast, and some other reviews have also summarized the synthesis, properties, and biological applications of CPNs [51–54]. Lately, Wang et al. have summarized more progresses of CPNs including multimode molecular and cell imaging, anti-microorganism/anticancer therapy, and cell activity regulation, besides previously reported sensing, fluorescence imaging, and photodynamic therapy [17]. Compared to small organic molecule dyes, CPs have a larger optical cross section, because their backbones behave as numerous light-harvesting units [8]. CPNs have been widely used in cell imaging due to their facile chemical synthesis, large extinction coefficients, tunable spectral properties, high brightness, superior photostability, versatile surface modification, and low cytotoxicity [33, 37].

2.1 Synthesis of CPs and Preparation of CPNs

Typical CPs primarily include four basic types, namely poly(fluorene) (PF) and its derivatives, poly(thiophene) (PT) and its derivatives, poly (p-phenylenevinylene) (PPV) and its derivatives, as well as poly(p-phenyleneethynylene) (PPE) and its derivatives, which are mainly synthesized by Suzuki coupling, oxidative polymerization, Heck and Sonogashira coupling, respectively [7]. Recently, NIR absorption is required for CPNs to be applied in biomedical research due to the deep tissue penetration and low phototoxicity in biology system of NIR light [55–58]. Therefore, it has become a trend to synthesize more and more donor-acceptor (D-A)-structured CPs via Suzuki or Stille polymerization to obtain the red-shifted absorption by utilizing intramolecular charge transfer to lower the bandgap of polymers [59]. Wang and coworkers have summarized the structures of relevant CPs used for biomedical applications [17].

To prepare CPNs, the commonly used methods are nanoprecipitation, miniemulsion, and self-assembly [7, 17]. For nanoprecipitation method, which is the mostly used one, CPs alone or with amphiphilic polymers are dissolved in a water-miscible "good" solvent (generally tetrahydrofuran), and then rapidly added to excess "poor" solvent (generally ultrapure water) under ultrasonication. CPNs are obtained after the evaporation of organic solvent. Many studies indicate that the particle diameter is dependent on the starting concentration of the CPs in good organic solvents, and the sizes of particles will increase with the starting concentrations of CPs in organic solvents [31, 60]. For miniemulsion method, unlike nanoprecipitation method, water-immiscible organic solvent (such as dichloromethane) is used, and additional surfactant is added to avoid coalescence of emulsion droplets [61, 62]. CPs are dissolved in organic solvent and then added to aqueous solution with surfactants under sonication, forming a homogeneous emulsion. CPNs are formed by removing the organic solvent from the emulsion. For self-assembly method, oppositely charged or amphiphilic CPs and co-assembling reagents are dissolved in water independently, and blended together under stirring to prepare CPNs [63–65].

2.2 CPNs for Fluorescence Imaging

Bioimaging is an effective approach to observe the morphological details of cells and tissues, which is a powerful tool in biological research and life sciences. Recently, increasing attention has been paid on various imaging techniques, including fluorescence imaging [66–75], positron emission tomography [76–78], computed tomography [79–82], magnetic resonance imaging [83–85], single photon emission computed

tomography [86–88], and photoacoustic/ultrasound imaging [89–93]. Among these technologies, fluorescence imaging possesses many advantages, including easy operation, high contrast and sensitivity, good temporal resolution, and minimal invasiveness. Fluorescence imaging agents, such as Qdots [94–96], carbon dots [25, 26, 97], fluorescent proteins [98–100], and organic fluorescent dyes [101–105] have been extensively studied in the past decade. However, there are many limitations for their application in bioimaging, such as short Stokes shift, poor stability or biocompatibility, and photodegradation under repeated excitation. Fluorescent CPNs have acquired great promise for bioimaging due to their easy modification, large extinction coefficients, high fluorescence brightness, superior photostability, and low cytotoxicity.

It is an essential way to study the dynamic and complex cellular processes via fluorescent labeling in live cells [106]. In 2007, Moon et al. introduced fluorescent CPNs that were easily synthesized and capable of fluorescence imaging of live cells without obvious toxicity [107]. An amine containing poly(p-phenylene ethynylene) (PPE) was synthesized via the palladium/copper-catalyzed cross-coupling reaction (Fig. 1a). The amine groups were introduced at the end of ethylene oxide to minimize the π-stacking of aromatic backbones in aqueous solution. Stable nanometer-sized particles with an average size of 97 nm were fabricated by sequential ultrafiltration with acetic acid, ethylenediaminetetraacetic acid, and water. It could be seen from the microscopic images of live BALB/C 3T3 cells (mouse embryonic fibroblast) stained by the CPNs

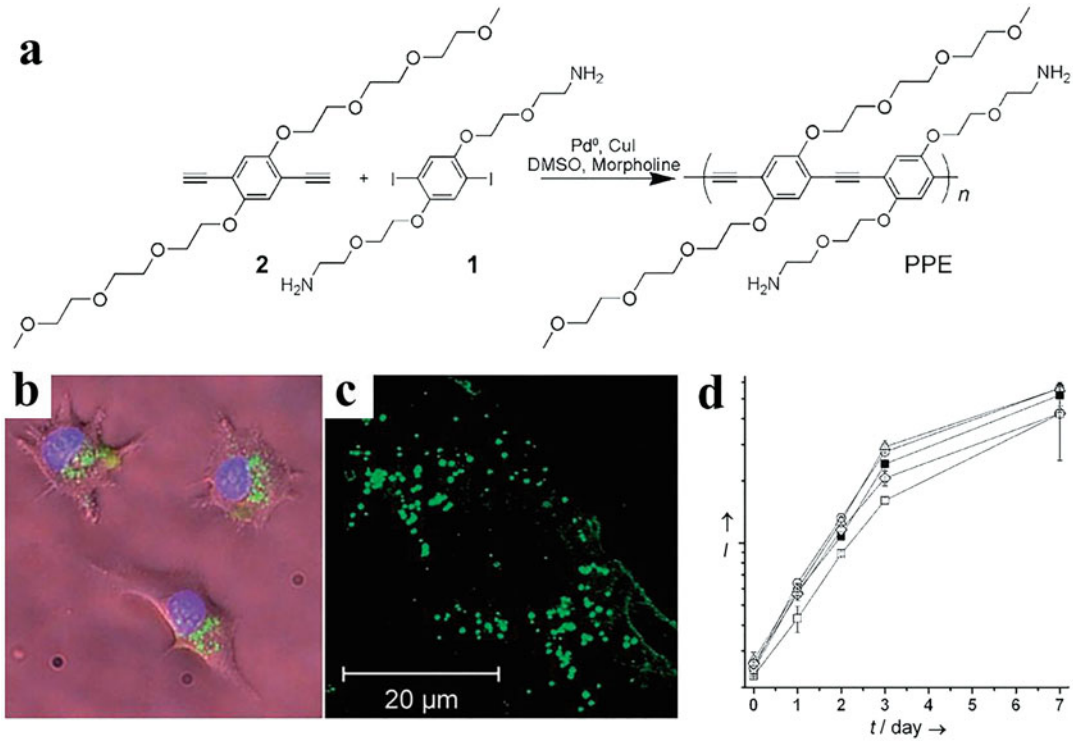

Fig. 1 (**a**) Synthetic route of PPE from diiodoarene (1) and diyne (2). (**b**) Fluorescence images of live BALB/C 3 T3 cells incubated sequentially with CPNs (green) and Hoechst dye (blue). (**c**) Fluorescence images of fixed BALB/C 3T3 cells. Live cells were incubated with CPNs and fixed for confocal microscopic study. (**d**) Viability of BHK cells incubated with various concentrations of CPNs for different days. ■ no CPN; ○ 33 μM; Δ 66 μM; ◊ 132 μM; □ 264 μM of CPNs. (Reprinted with permission from Ref. [107]. Copyright © 2007 Wiley-VCH Verlag GmbH & Co. KGaA, Weinheim)

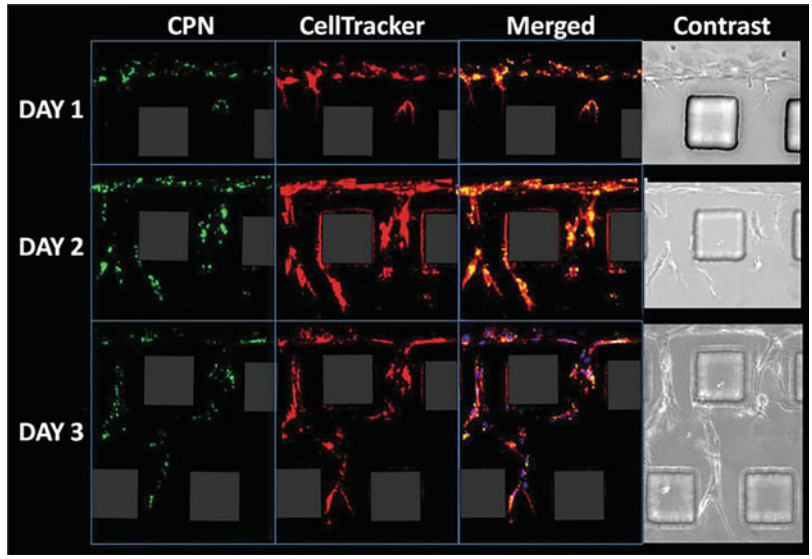

Fig. 2 Fluorescence images of cultured cells (day 1, 2, and 3) in a microfluidic device. The cell nuclei of cells in day-3 image (merged) were stained with DAPI (blue) to further demonstrate the growth of cells. The last column shows corresponding phase-contrast images. The gray squares in fluorescence images represent posts in the device. (Reprinted with permission from Ref. [108]. Copyright © 2009 Wiley-VCH Verlag GmbH & Co. KGaA, Weinheim)

overnight that CPNs were distributed in the cytoplasm, and especially around the perinuclear region (Fig. 1b). A confocal microscopic image of fixed 3T3 cells (Fig. 1c) suggested that CPNs were mainly accumulated in vesicular structures, such as early or late endosomes. The viabilities of cells treated with CPNs were compared to the control groups without CPNs (Fig. 1d), demonstrating good biocompatibility of CPNs. CPNs have a high quantum yield and better photostability than representative fluorescent dyes. Study of the cellular uptake and location of CPNs will lay the foundation of more fluorescence-imaging-based applications, such as delivery of bioactive molecules.

After that, they reported the two-photon fluorescent imaging characteristics of CPNs based on PPE [108]. Two-photon fluorescent imaging is promising for in vivo microscopic physiological studies in many areas, such as immunology, neurobiology, and tissue engineering [109–111]. Advances in the design of two-photon endomicroscope have further made it possible to develop noninvasive diagnostic procedures to detect the malignancy in organs, such as the intestine and the oral cavity [110, 112, 113]. Although high two-photon action cross-sections have been realized in some organic fluorophores [33, 34, 114–116] and Qdots [20], the application of these probes in biomedical fields also has many limitations, such as the hydrophobicity and cytotoxicity of organic fluorophores, as well as the existence of "dark" dots [117] and heavy-metal core-related cytotoxicity of Qdots. CPs can well resolve the above problems and meet the requirements for two-photon fluorescent imaging. Moon et al. used CPNs for two-photon imaging of endothelial cells in a model-tissue culture system. They improved the preparation methods of CPNs, thus significantly reducing the size of them to 8 nm. CPNs exhibit large two-photon cross-sections and high photostability comparable to Qdots. More importantly, the nontoxicity and hydrophilicity of CPNs enabled them for long-term monitoring of angiogenesis by endothelial cells in a tissue model (Fig. 2), revealing the potential of CPNs in biomedical applications.

The prevalent polyvalent interactions in the nature play an important role in maintaining some biological functions, such as signal transduction, gene regulation, cell-cell recognition, cell adhesion and proliferation [118]. Therefore, synthetic ligands with multivalent recognition elements might bind to cell-surface receptors or other components of the extracellular matrix

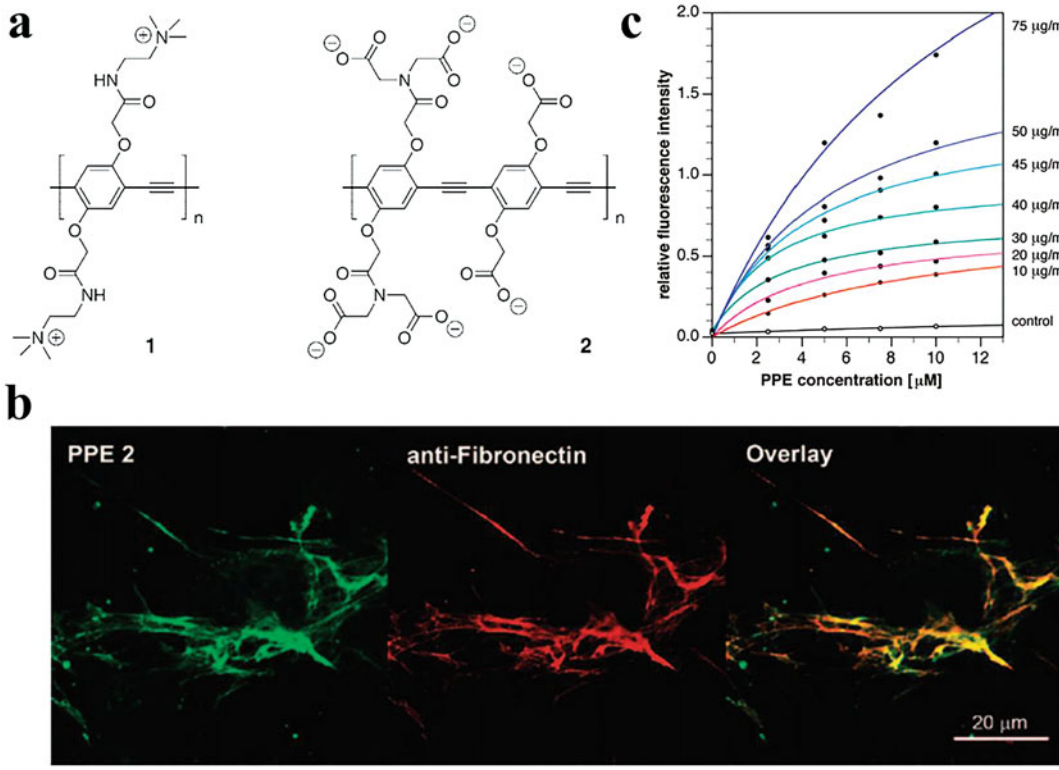

Fig. 3 (**a**) Structures of PPE 1 and PPE 2. (**b**) Immunofluorescence staining of PPE 2 with an antibody against fibronectin (NIH 3 T3 cells). Images from left to right: Fluorescence images of cells stained with PPE 2 (green), anti-fibronectin (red), and overlay of the both. (**c**) Binding assay of PPE 2 with surface-adsorbed different concentrations (as shown on the right of the graph) of fibronectin. (Reprinted with permission from Ref. [122]. Copyright © 2008 American Chemical Society)

selectively, and thus serve as selective effectors or inhibitors to these processes [119]. Bunz and Fahrni wanted to explore whether a ligand with multiple nonspecific interactions could selectively recognize the components in extracellular matrix of live cells. In their work, PPE was also selected as the backbone, and functionalized either with positively charged tetraalkylammonium groups (PPE 1) [120] or with negatively charged carboxylates (PPE 2) [120, 121] (Fig. 3a) as nonspecific low-affinity binding elements [122]. The two polymers showed distinctly different behaviors when added to live NIH 3T3 fibroblast cells in growth medium for 4 h. PPE 1 with positive charge exhibited punctate staining of endocytic vesicles, while anionic PPE 2 showed a characteristic filamentous extracellular staining pattern. Fibronectin is an extracellular matrix protein, which interacts with actin filaments at specific locations within the extracellular matrix. Immunofluorescence staining demonstrated that the fluorescence of PPE 2 almost perfectly co-localized with that of commercial antibody against fibronectin, as shown in Fig. 3b. In vitro binding assay was performed to probe the interaction between PPE 2 and fibronectin, as illustrated in Fig. 3c, the fluorescence intensity increased not only with increasing polymer concentration but also with the increase of fibronectin surface density, and the avidity of the polymer-fibronectin complex lies in a similar range compared to the multivalent carbohydrate–lectin interactions [123]. In addition, both polymers possessed bright fluorescence emission and good photostability, rendering them suitable for two-photon excitation microscopy. In

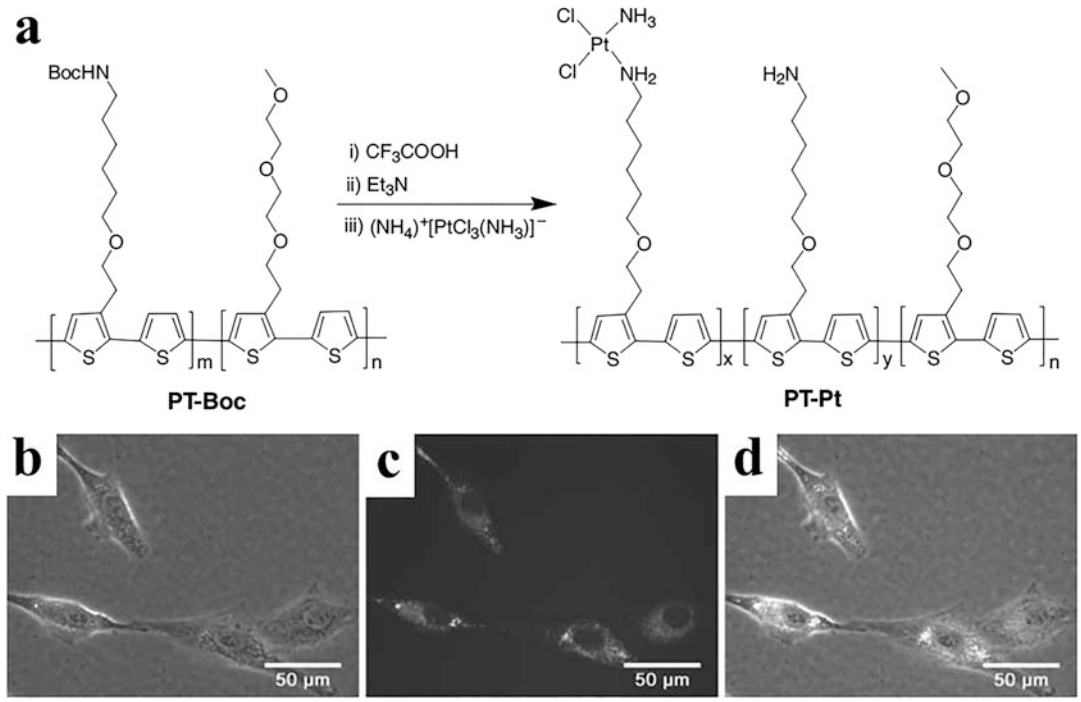

Fig. 4 (**a**) The synthetic route of cisplatin-functionalized polythiophene (PT-Pt). Fluorescence images of human pulmonary carcinoma (A549) cells incubated with 16 μg mL^{-1} of PT-Pt; (**b**) phase-contrast image; (**c**) fluorescence image; (**d**) overlap of phase-contrast image and fluorescence image. (Reprinted with permission from Ref. [127]. Copyright © 2011 Wiley-VCH Verlag GmbH & Co. KGaA, Weinheim)

view of the biological importance of fibronectin, this work underscores the efficacy of weak non-specific polyvalent interactions on the design of new synthetic ligands.

CPs can also be used for imaging the cellular distribution of anticancer drugs. Cisplatin has been one of the widely used anticancer agents nowadays, while its application is also limited by drug resistance and side effects [124]. Therefore, it is necessary to get more information on how cells process the internalized platinum drugs to improve the properties of platinum-based drugs. Methods for studying the distribution of platinum drugs in cells mainly include fluorescent-dye labeling approaches and atom-based analytical techniques [125, 126]. Wang and coworkers synthesized an amphiphilic polythiophene derivative (PT-Boc), and the polymer could form nanoaggregates in water, which exhibited good photostability and biocompatibility [127]. The nanoaggregates could easily enter cytoplasm and be used for cell imaging. Then the polythiophene-cisplatin conjugate (PT-Pt) was synthesized by coordinated interaction between cisplatin and the amine group of the side chain of polythiophene (Fig. 4a). The PT-Pt could be used for monitoring the distribution of cisplatin in cells (Fig. 4b–d). It is expected that the good reactivity of the amine group in the polythiophene side chain shows great promise for fluorescence imaging of similar drugs in living cells.

One of the main limitations in the application of CPs for cell imaging is their inadequate water solubility. Introducing ionic or hydrophilic functional groups to CPs is one strategy to address this issue, while the synthetic procedures usually require many procedures, which are time-consuming. In addition to the complex modification of polymer structures, to prepare CPs based nanoparticles through nanoprecipitation method is an easier way. By controlling the experimental conditions precisely, the prepared CPNs with

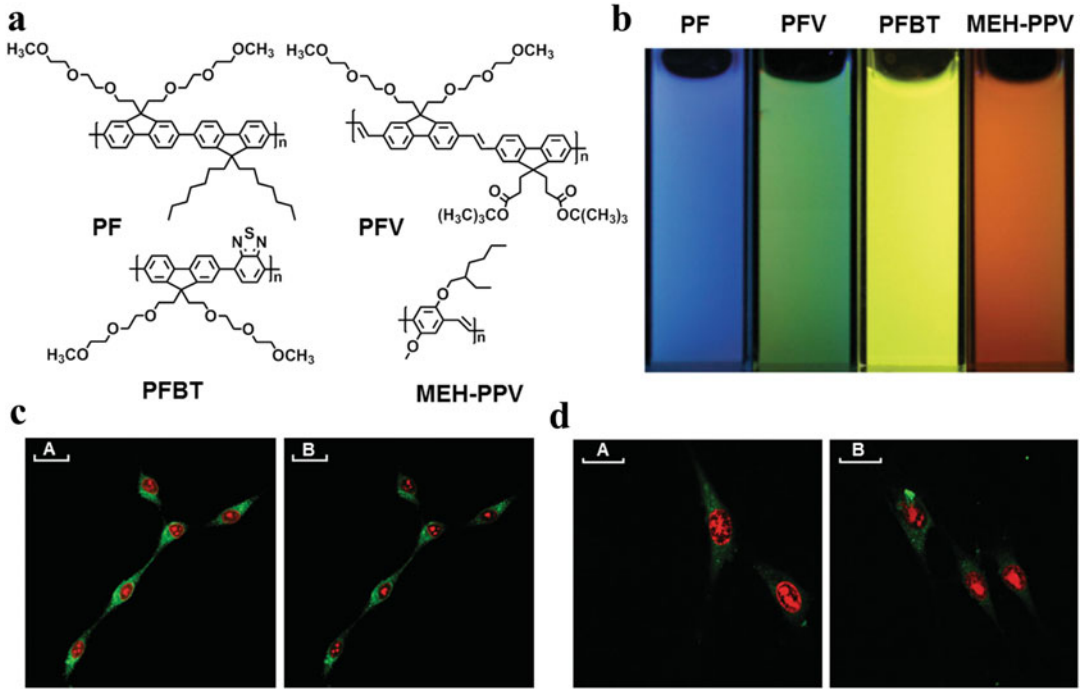

Fig. 5 (**a**) Structures of PF, PFV, PFBT, and MEH-PPV. (**b**) A photograph of CPL NPs (PF, PFV, PFBT, and MEH-PPV) under a hand-held UV lamp captured by digital camera. (**c**) CLSM images of MCF-7 cells after 2.5 h incubation with the FA PFV-loaded PLGA NPs (87.5 nM PFV). The images are obtained under continuous excitation of 405 nm laser (5% laser power) for (A) 0 and (B) 20 min. (**d**) CLSM images of NIH/3T3 cells after 2.5 h incubation with (A) the PFV-loaded PLGA NPs and (B) FA PFV-loaded PLGA NPs (87.5 nM PFV). The images are obtained under continuous excitation of 405 nm laser (5% laser power). (Reprinted with permission from Ref. [62]. Copyright © 2009 Wiley-VCH Verlag GmbH & Co. KGaA, Weinheim)

different sizes showed limited blinking and high fluorescence [31, 34]. However, to provide these nanoparticles with functional surfaces, further encapsulation is necessary. Liu's group used poly(DL-lactide-co-glycolide) (PLGA) as the matrix polymer, and reported a simple strategy for the preparation of biocompatible and surface-functionalizable CPs based nanoparticles in one step [62]. CP-loaded PLGA NPs (CPL NPs) were prepared via a modified solvent extraction/evaporation single-emulsion method with poly(vinyl alcohol) as emulsifier [128]. The obtained NPs are stable with biocompatible and functionalized surfaces. Moreover, the fluorescence properties of the CPL NPs could be adjusted by loading different types of CPs (Fig. 5a, b). The ability of CPL NPs for bioimaging was verified through incubation with human breast cancer (MCF-7) cells. Confocal laser scanning microscopy (CLSM) studies reveal that the CPL NPs could be internalized by cells with intense fluorescence. After conjugation with folic acid (FA), the surface-functionalized CPL NPs exhibited greatly enhanced cellular uptake by MCF-7 cells (Fig. 5c) via receptor-mediated endocytosis, as compared to that by NIH/3 T3 cells (Fig. 5d), indicating a selectively targeted cell imaging effect of the FA functionalized CPL NPs. The surface-functionalized CPL NPs inspire new strategies for specific biological imaging and cancer detection.

Recently, multiplex biological analysis and imaging have become more and more important in drug discovery, gene profiling, and clinical diagnostics [129–131]. CPNs have been developed for cell imaging due to their high fluorescence brightness, low toxicity, and excellent photostability. Nevertheless, CPNs themselves

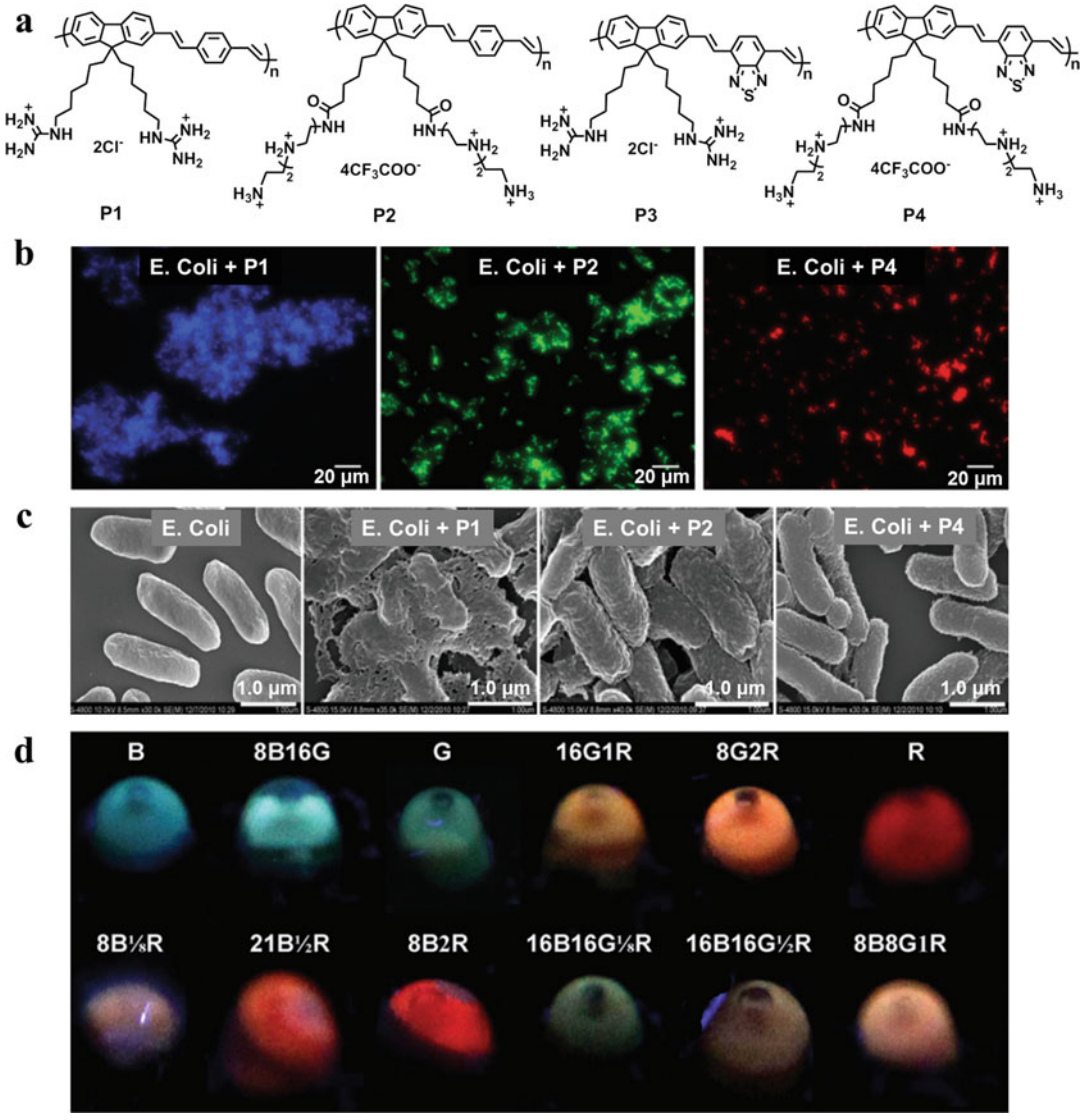

Fig. 6 (**a**) Chemical structures of four cationic CPs (P1, P2, P3, and P4). (**b**) Fluorescence images of *E. coli*-CPN microparticles. (**c**) SEM images of *E. coli* and *E. coli*-CPN microparticles. Scale bars: 1.0 μm. (**d**) The images of various color-barcoded microparticles obtained from mixing the *E. coli* and CPNs under 365 nm UV light. (Reprinted with permission from Ref. [132]. Copyright © 2012 Wiley-VCH Verlag GmbH & Co. KGaA, Weinheim)

have limited numbers of colors. Therefore, in order to meet the requirements of multiplexed biological analysis and imaging, it is necessary to find an effective method to achieve multicolor regulation. Wang and Zhu et al. developed a novel technique for preparing encoded multicolor CPNs via the self-assembly of *E. coli* and CPNs by simply mixing them together [132]. In their work, four cationic CPNs with different colors (blue, green, yellow, and red) have been prepared (Fig. 6a). With *E. coli* TOP10 as the assembly vector, *E. coli*-CPN microparticles in three basic

colors were prepared by merely mixing the *E. coli* with P1 (blue), P2 (green), or P4 (red) followed by centrifugation. The outlines of *E. coli* were observed in blue, green, and red fluorescence with 1–3 μm length and 0.5 μm diameters in size (Fig. 6b). As shown in scanning electron microscopy (SEM) images (Fig. 6c), upon coating with CPNs, the smooth outer surface of *E. coli* changed to be coarse, showing a continuous layer of CPNs. Multicolor could be adjusted through fine-tuning fluorescence resonance energy transfer (FRET) among the three CPNs, and 12 color-encoded microparticles could be easily prepared under one excitation (Fig. 6d). These multicolor particles did not show toxicity towards A549 cells, and were successfully applied for imaging and optical barcoding. This effective method opens up the possibility of CPNs for multiplex biological analysis and imaging.

Targeted imaging of tumor cells is of great importance for the diagnosis and treatment of cancer. In consideration that every commercial optical instrument has its own excitation source, it is imperative to develop a targeted fluorescent material which could match different excitation sources and show multicolor emission [17]. Wang and coworkers introduced a method of targeted imaging of tumor cells based on multicolor CPNs due to their simple synthesis and all-round surface modification [133]. Four CPs with blue (P1), green (P2), yellow (P3), and red (P4) emissions were designed and synthesized (Fig. 7a), and carboxyl functionalized CPNs were prepared via a modified co-precipitation method on the basis of hydrophobic interactions between the CPs and poly(styrene-co-maleic anhydride) (PSMA) as the source of carboxyl functionalities. The carboxyl groups on the surface could be further modified with antibodies through amide coupling (Fig. 7b). Multicolor P1–4/PSMA CPNs obtained from co-precipitation of P1, P2, P3, P4, and PSMA (Fig. 7c) showed entire visible region emission based on FRET mechanism. After modification with the primary antibody to epithelial cell-surface receptor (anti-EpCAM), multicolor (blue, green, and red) fluorescence images of MCF-7 cells incubated with P1–4/PSMA CPNs were observed upon excitation at 405, 488, and 559 nm (Fig. 7d). To address the limited specificity of single antibody-labeled for tumor cells, much better specificity was achieved by using two CPNs labeled with different antibodies to detect one tumor cell. The multicolor CPNs in this work match well to those available in commercial fluorescence instruments, showing the potential of CPNs in targeted cell imaging and detection of tumor cells.

CPNs hold great potential for in vivo application owing to their good water dispersibility, organic nature of chemical constitution, low cytotoxicity, and high light absorbing ability, although it is more difficult for in vivo imaging than in vitro cell imaging due to the complicated biological environments and multiple biological barriers [7]. In 2010, Kim et al. realized in vivo application of cyanovinylene-backboned CPNs for real-time sentinel lymph node (SLN) imaging by intradermal injection [134]. The chemically and colloidally stable CPNs were easily prepared via single-step in situ polymerization in solvent-free micelles under mild conditions, and provided high nanoscopic chromophore density and outstanding signal brightness. The utility of CPNs in effective SLN mapping can provide guidance on noninvasively identifying superficial SLNs or revealing deep SLNs by tracing the lymphatics during surgery.

It is highly important to understand the life-threatening pathological processes like cancer metastasis and optimize cell-based therapeutics via noninvasively monitoring the transplanted cells in vivo [135–137]. Rao et al. reported phosphorylcholine-coated NIR semiconducting polymer nanoparticles (SPNs) for rapid and efficient in vivo cell tracking [138]. The zwitterionic SPN (SPN_{RD}) was yielded via co-precipitation of poly [2,7-(9,9-dioctylfluorene)-alt-4,7-bis(thiophen-2-yl) benzothiadiazole] (PFODBT) and 1,2-dipalmitoyl-sn-glycero-3-phosphocholine (DPPC). SPN_{RD} could enter different cells in complete culture medium within 30 min of incubation, which demonstrated its potential as a general cell tracker. The far-red absorbing and NIR emitting

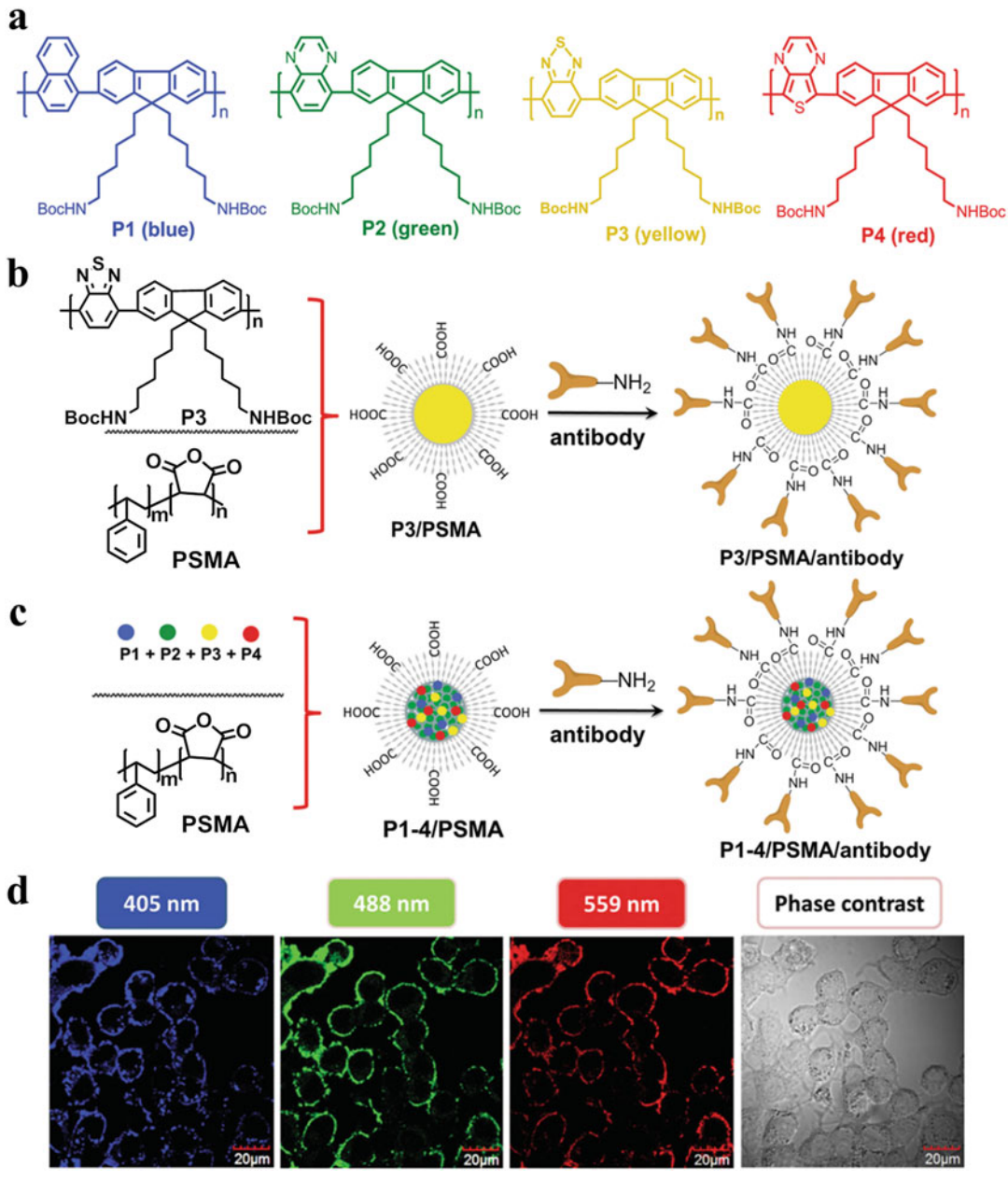

Fig. 7 (**a**) Chemical structures of four CPs (P1, P2, P3, and P4) in different colors. Schematic illustration of (**b**) the general preparation of CPNs (P3/PSMA) and their modification with an antibody, as well as (**c**) the preparation of multicolor CPNs (P1–4/PSMA) and relative modification with an antibody. (**d**) Multi-channel fluorescence images of MCF-7 cells incubated with P1–4/PSMA/anti-EpCAM CPNs and excited by laser at 405, 488, and 559 nm. (Reprinted with permission from Ref. [133]. Copyright © 2014 Wiley-VCH Verlag GmbH & Co. KGaA, Weinheim)

of SPN_{RD} rendered it clearly visible at least within 0.5 cm of tissue penetration depth in spite of its relatively low quantum yield, which was hardly achievable for the highly fluorescent green SPN (SPN_G). The SPN_{RD} permitted in vivo tracking of human renal cell carcinoma cells in living

mice at a lower detection limit of 10,000 of cells, and no obvious alteration of cell phenotype could be observed after 12 days. Thus, SPNs as a cell tracking label could provide unique opportunities for optimizing cellular therapy and deciphering pathological processes.

To address the limitation of autofluorescence and penetration depth of biological tissues, in vivo biological imaging in the second near-infrared window (NIR-II, 1.0–1.7 μm) has attracted increasing interest [139–144] due to its distinct advantages over that in the visible (400–750 nm) or the conventional NIR (750–900 nm) regions. The first example of NIR-II biological imaging was reported by Dai's group for ultrafast fluorescence in vivo imaging [145]. A brightly fluorescent D-A structured copolymer poly(benzo[1,2-b:3,4-b']difuran-alt-fluorothieno-[3,4-b]thiophene) (pDA) was synthesized via alternating copolymerization (Fig. 8a). The stable CPNs with fluorescence emission at around 1050 nm were prepared with PEGylated phospholipid (DSPE-mPEG) as the biocompatible surfactant (Fig. 8b). After modification with targeted Cetuximab (Erbitux) antibody (pDA-PEG-Erbitux, Fig. 8c), the nanoparticles realized specific imaging of EGFR-positive breast tumor MDA-MB-468 cells in NIR-II window (Fig. 8d). They achieved ultrafast blood flow imaging of mouse femoral arterial with NIR-II pDA-PEG (Fig. 8e), and also the first in vivo blood flow velocity measurement on the millisecond scale. After that, more and more NIR-II fluorescence agents have been developed to acquire high spatial and temporal resolutions and could eventually be suitable for clinic use.

3 Conjugated Polymer Dots (Pdots)

In recent years, Pdots, which are primarily consist of π-CPs and possess small particle size, high brightness as well as excellent photostability, have demonstrated wide applications in many areas including fluorescence imaging. Chiu and Wu carried out a systematic characterization of the optical properties and performance of Pdots for fluorescence imaging and flow cytometry, in which they found that either the single-particle brightness or the cell-labeling brightness of Pdots is much higher than that of Qdots with comparable particle size, even more than an order of magnitude [39, 41]. To control the surface chemistry of Pdots and introduce functional groups to them, some simple but powerful approaches have been developed [30, 38–42, 44, 46–48], which is a prerequisite in employing more novel Pdots for biomedical applications. Since the first-generation of Pdots which exhibit broad emission spectra, more types of Pdots such as narrow emissive Pdots [49, 146–150], NIR-emissive Pdots [146, 150–155], long luminescence lifetime emissive Pdots [147, 149], single-chain and monovalent Pdots [156], photoswitchable Pdots [157–160], and electro−/chemiluminescent Pdots [161–163] have been developed, and the performance of Pdots has been gradually improved [29]. Pdots have been well developed for bioimaging [147, 148, 155], biosensing [164–169], and phototherapy of cancer [82, 170–173], and we will summarize their application in fluorescence imaging in this section.

3.1 Preparation and Properties of Pdots

Two main preparation methods of CPNs are miniemulsion approach and reprecipitation method, among which the latter could generate Pdots with sizes of about 5–30 nm, whereas the former usually produces particles with larger diameters from 40 to 500 nm [30, 46–48]. The particle size can be tuned by adjusting the concentration of polymer in the solution because of the competition between interchain aggregation and intrachain collapse during reprecipitation process. The internal structures of Pdots are typically densely packed with hydrophobic CPs due to the strong hydrophobic interactions, which can be seen by the highly efficient energy transfer inside the NPs [30, 36, 42, 48]. The Pdots are

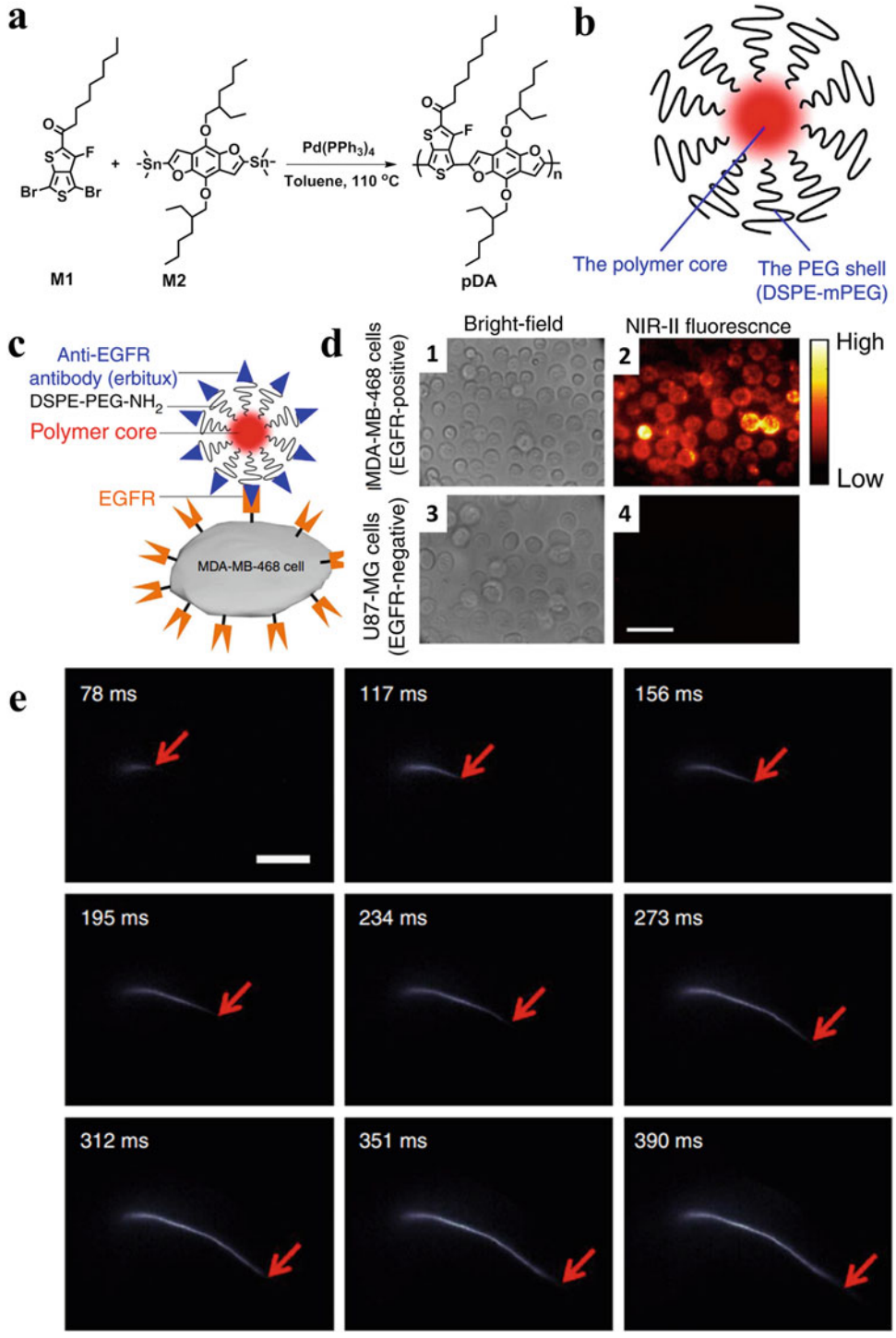

Fig. 8 (**a**) The synthetic route of the polymer (pDA). Schematic illustration of (**b**) the pDA-PEG nanoparticle with a hydrophilic PEG shell and a hydrophobic polymer core, and (**c**) pDA-PEG-Erbitux (the anti-EGFR antibody) bioconjugate. (**d**) Bright-field (1, 3) and NIR-II fluorescence (2, 4) images of EGFR-positive MDA-MB-468 cells (1, 2) and EGFR-negative U87-MG cells (3, 4) treated with pDA-PEG-Erbitux bioconjugate. (**e**) NIR-II fluorescence images of blood flow moving in the femoral artery of a mouse hindlimb after injection of pDA-PEG. (Reprinted with permission from Ref. [145]. Copyright © 2014 Springer Nature)

typically in glassy phase, and the crystalline phase can be partially formed in the glassy matrix in certain polymers, such as PFO [35]. The performance of nanoparticle probe in biological applications is highly related to its physical size, and most imaging and bioassays require small nanoparticle labels [28]. According to the fluorescence brightness of per-particle, the number of fluorophores in each particle increases with the volume at a given fluorophore packing density. The absorption cross section of the nanoparticles is highly related to the particle size and the fluorophore packing density, so Pdots have a significant advantage due to their densely packed chromophoric structures [28].

For the utility as fluorescent labels, the optical properties of Pdots have been systematically evaluated [30, 31, 33, 34, 39–41, 48, 174]. Pdots prepared via reprecipitation methods generally exhibit blue-shifted and broadened absorption spectra in comparison with that of the polymer in tetrahydrofuran [174]. McNeill and coworkers have reported for the first time that Pdots exhibit two-photon absorption cross-sections up to 2.0×10^5 GM, which is benefit for their two-photon fluorescence applications [33]. In addition, the fluorescence lifetime of Pdots from different CPs determined by the time-correlated single-photon counting technique generally differs from 100 ps to 1 ns [28, 34]. Pdots exhibit a fluorescence radiative rate constant (k_R) in the range of 10^8–10^9 s^{-1}, which is similar to or higher than that of typical fluorescent dyes (ca. 10^8 s^{-1}), and about two orders of magnitude higher than that of single quantum dot [175]. The photostability of Pdots is higher than that of typical fluorescent dyes [34, 39].

Colloidal and chemical stability are also of great significance for the biological applications of Pdots. Bare Pdots can hold great colloidal stability in deionized water for a long time without aggregation or precipitation, while the existence of either moderate ionic strength or divalent metal ions will cause the aggregation of them [46]. For the chemical stability of Pdots, the fluorescence of them was not affected by any tested biologically relevant ions and common reactive oxygen species, demonstrating the significant advantage of Pdots for in vivo imaging [28].

3.2 Pdots for Fluorescence Imaging

The extraordinary fluorescence brightness, stable and fast emission rate, as well as excellent photo, colloidal and chemical stability of Pdots lay a solid foundation for their biological applications. In vitro cell imaging applications of Pdots were initially conducted by a nonspecific labeling method [34]. Due to their high fluorescence brightness, Pdots could be used for imaging at a low concentration [176]. Different from endocytosis-based labeling, cell imaging based on antigen-antibody interactions can realize specific cellular targeting. By introducing a small amount of amphiphilic polymer with functional groups into the majority of CPs during nanoparticle formation, the nanoparticle surface can be modified for covalent conjugation to bioactive molecules, such as immunoglobulin G (IgG) and streptavidin. The bioconjugates of Pdots could specifically label cell surface marker in MCF-7 cells without any detectable nonspecific binding, and the fluorescence brightness of Pdots was much higher than that of quantum dot probes and Alexa dyes [39]. Chiu et al. also realized specific subcellular imaging of Pdots after successful functionalization and bioconjugation, revealing the great promise of Pdots for bioanalytical applications and biological imaging [47].

The photon-limiting interferences such as scattering, absorption, and autofluorescence are main limitations for fluorescence imaging to be translated into the clinic. In this context, Pdots show great potential for in vivo application due to their organic chemical constitution, water dispersibility, and superior light absorbing ability generated from their high chromophore density. Kim and coworkers have successfully demonstrated the in vivo mapping of cyanovinylene-backboned polymer dots (cvPDs) to SLN [134]. Surfactant-stabilized cvPDs were synthesized via in situ Knoevenagel polymerization in the organic solvent-free aqueous phase

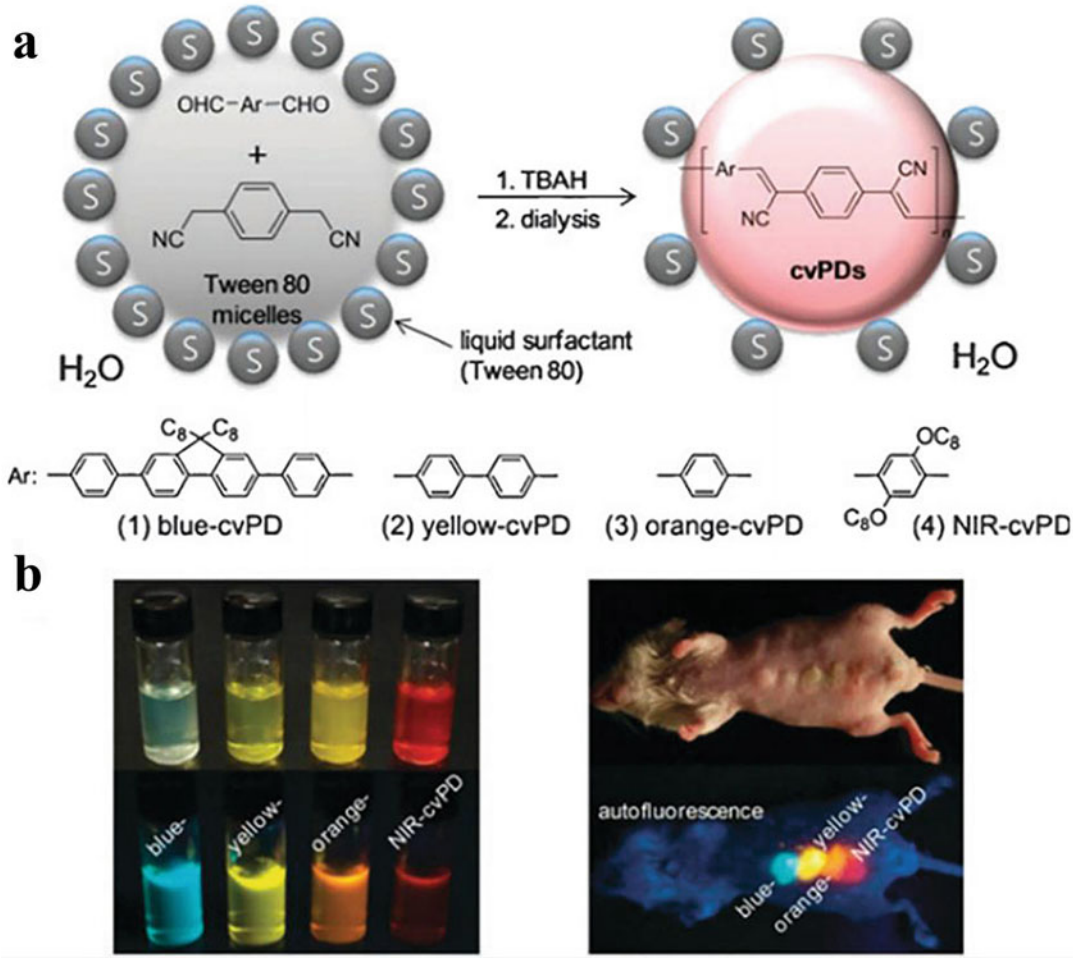

Fig. 9 (**a**) Schematic illustration of colloidal synthesis of cvPDs via Knoevenagel condensation catalyzed by tetrabutylammonium hydroxide (TBAH) in the hydrophobic core of micelles in aqueous solution. (**b**) True-color photographs of cvPDs in water (left) and a live mouse injected with cvPDs (right) under room light (top) and UV excitation (365 nm) for fluorescence (bottom). (Reprinted with permission from Ref. [134]. Copyright © 2010 Royal Society of Chemistry)

(Fig. 9a). Similar to Qdots [177], multicolor fluorescence was observed under single-wavelength excitation due to the broad absorption profiles of cvPDs, which was beneficial for simultaneous imaging of diversiform molecular targets (Fig. 9b). To demonstrate their potential for application in multicolor in vivo imaging, a live mouse was subcutaneously injected with cvPDs, and the fluorescence spots were clearly distinguished from the background according to the color and brightness even under UV excitation, by which the autofluorescence of a live mouse should be significant (Fig. 9b). After the intradermal injection of NIR-cvPDs into the forepaw pad of a mouse, clear-cut imaging of SLN was observed, which provides a possibility for precisely identifying SLNs by real-time optical guidance during surgery.

Although various efforts had been paid by researchers, there were still a few challenges for Pdots to be used as in vivo probes at that time, such as the limited fluorescence brightness of Pdots in the red and NIR, as well as the uncertainty of whether Pdots could be specifically

delivered to tumor tissues in vivo. To address these concerns, Chiu et al. prepared highly fluorescent Pdots consisting of optimally tailored CP blends for in vivo brain tumor targeting [41]. On account of the efficient intra-particle energy transfer in Pdots [135], the polymer-blend dots (PBdots) were designed with a visible-light-harvesting polymer (PFBT) as the donor and an efficient deep-red emitting polymer (PF-DBT5) as the acceptor (Fig. 10a). Due to the close stacking of the donor/acceptor polymers into single dots, the intra-particle energy transfer led to complete quenching of the donor fluorescence and intense fluorescence from the acceptor (PF-DBT5) alone. The PBdots were the brightest at that time among different fluorescent nanoparticles of similar size. Chlorotoxin (CTX), a 36-amino acid peptide with strong affinity to tumors of neuroectodermal origin, was selected as the tumor-targeting ligand [136]. The PBdots were covalently conjugated to CTX (PBdot-CTX), then the results from biophotonic imaging (Fig. 10b and c) and histological analyses (Fig. 10d) certified their specific targeting to malignant brain tumors. This study as the first demonstration of targeted delivery of Pdots to diseased tissues, suggests a great promise of Pdot-based probes for clinical cancer diagnostics and therapeutics.

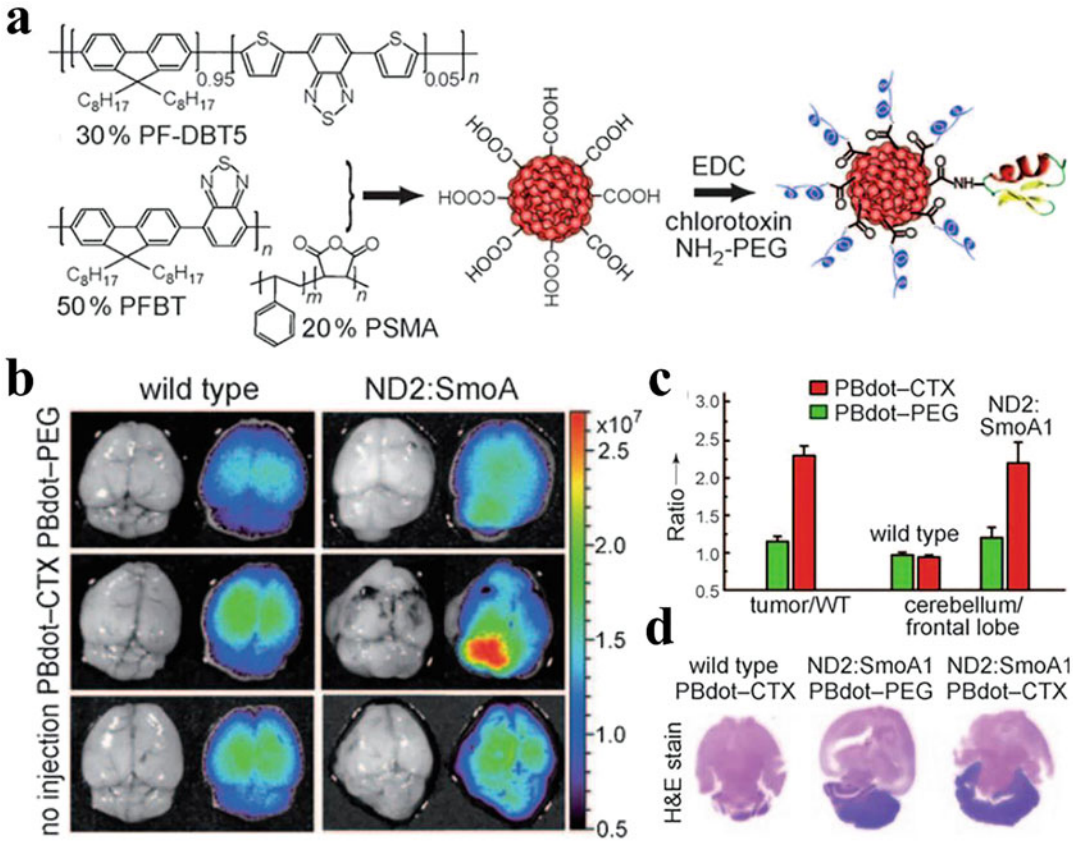

Fig. 10 (**a**) The preparation of PBdots as well as their functionalization and CTX conjugation. (**b**) Fluorescence imaging of healthy brains in wild-type mice (left) and medulloblastoma tumors in ND2:SmoA1 mice (right). The mice were injected with either nontargeting PBdot-PEG (top) or targeting PBdot-CTX (middle), and the mice without injection (bottom) served as control. (**c**) Tumor-targeting efficiency quantified by fluorescence signals in ND2:SmoA1 versus wild-type mice and cerebellum versus frontal lobe. (**d**) Histological analyses of the mouse brains in (**b**). (Reprinted with permission from Ref. [41]. Copyright © 2011 Wiley-VCH Verlag GmbH & Co. KGaA, Weinheim)

Despite the progress, the conventional Pdots generally show broad emission spectra, which are severe limitations for their usefulness in many biological applications especially in multiplex detections, such as in vitro/in vivo imaging, flow cytometry and cell sorting, Western blot analysis, and nucleic acid analysis [29]. In order to address this limitation and design Pdots with narrow emission, Chiu group employed donor-acceptor strategy and developed a series of boron dipyrromethene (BODIPY)-based Pdots, in which BODIPY monomers were covalently introduced into the polymer and used as narrow emissive species [49, 148, 150]. The reason to select BODIPY dyes was that they possess high absorption coefficients and quantum yields, sharp emission peaks, and good photostability [178–180]. The emission FWHM (full width at half maximum) values of these Pdots are about 40–55 nm (Fig. 11a), which are 1.5–2 times narrower than those of conventional Pdots [49]. Due to the carboxylate groups in the monomers, it is convenient to conjugate the Pdots with biological molecules like streptavidin (SA). The flow cytometry results (Fig. 11b–d) proved that all Pdot-SA probes and Qdot 525-SA probes could effectively label EpCAM receptors on the MCF-7 cell surface, while the groups treated with identical conditions but without incubation of primary biotinylated antibody

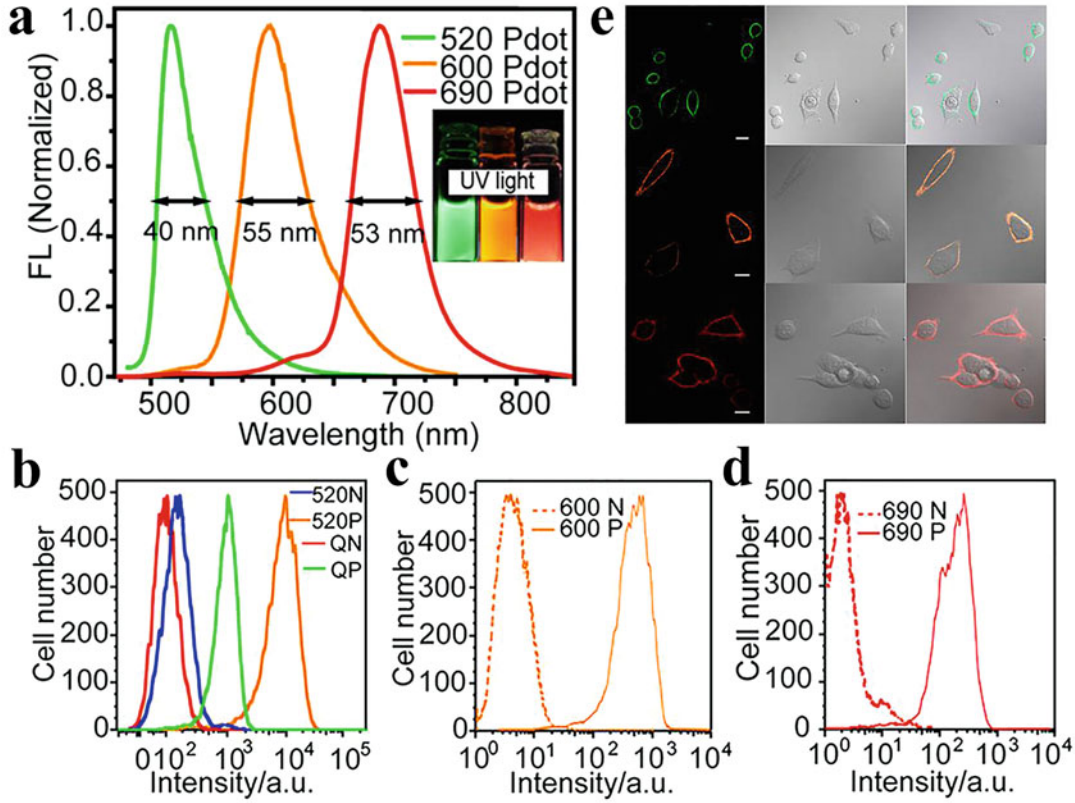

Fig. 11 (**a**) Fluorescence spectra of BODIPY 520 Pdots, BODIPY 600 Pdots, and BODIPY 690 Pdots in aqueous solution. Flow cytometry results of MCF-7 cells labeled with (**b**) Qdots 525 and BODIPY 520 Pdots, (**c**) BODIPY 600 Pdots, and (**d**) BODIPY 690 Pdots via nonspecific binding (N, negative control) or positive specific targeting (P, positive). All Pdots and Qdots were labeled with SA. (**e**) Confocal fluorescence images of MCF-7 cells incubated with BODIPY Pdot-SA probes (from top to bottom: BODIPY 520 Pdot-SA, BODIPY 600 Pdot-SA, and BODIPY 690 Pdot-SA). Scale bars: 20 μm. (Reprinted with permission from Ref. [49]. Copyright © 2013 American Chemical Society)

could not label the cells. The comparison between BODIPY 520 Pdots and commercial Qdots 525 under the same conditions (Fig. 11b) proved that BODIPY 520 Pdots were about an order of magnitude brighter than Qdot 525. The result was consistent with the single-particle brightness measurements. The confocal fluorescence imaging results further confirmed the specific cellular labeling by these BODIPY Pdot-SA probes (Fig. 11e), which indicated that the narrow emissive Pdots showed great promise for many multiplexed biological detections.

To efficiently select and isolate cells of interest from a mixed population is of great significance in biomedical and clinical research. Usually, the selected cells are subjected to cell expansion [181], transplantation [182], and genetic analysis [183]. Among various methods to select cells, fluorescence activated cell sorting (FACS), in which individual cells of interest are sorted based on fluorescence recognition of specific biomarkers, perhaps is the most powerful approach because it can offer high throughput and much information with single-cell sensitivity [184]. However, FACS is used to isolate cells from a suspension of cells, so the adherent cells in solid tumors or intact tissues must be separated by enzymatic dissociation firstly and then sorted [185, 186]. To exclude this limitation of FACS, Chiu et al. employed photoswitchable Pdots as an optical "painting" tool during imaging, which enabled the optical marking of individual cells, and the marked cells could be isolated via FACS [158]. As shown in Fig. 12a, a new type of photoswitchable Pdots was designed and synthesized, which was reversibly switchable between the bright (ON) and dark (OFF) states. MCF-7 cells were firstly labeled with photoswitchable Pdot-streptavidin via biotinylated antibody against cell-surface receptors, and then cells of interest were optically painting with a focused 633-nm laser beam for subsequent FACS analysis and isolation. To demonstrate a complete cycle of photoswitching, cells were first labeled with ON-state Pdots (Fig. 12b and c), and became non-fluorescent after irradiation with UV light (Fig. 12d). While the orange fluorescence was recovered after the cells were irradiated with red light-emitting diode (Fig. 12e). Moreover, illumination with a focused 633-nm laser spot (10 μm) could achieve high-precision single-cell painting (Fig. 12f). This method extends the application of FACS to adherent cells and shows the potential in achieving high throughput marking and sorting of individual adherent cells.

NIR-emissive fluorescence probes are especially needed for in vivo imaging, because the NIR region possesses maximal penetration into biological tissues, less influence from autofluorescence and scattering in organisms [29]. The self-quenching phenomenon of most NIR emitters caused by their poor solubility in aqueous solution and the increased tendency to aggregate can be partly overcome by Pdots, because the interior of Pdots is hydrophobic and thus acts as a good environment to host NIR chromophores. Therefore, through the researchers' effort, NIR BODIPY-based [150] and squaraine-based [146] Pdots with NIR emission were developed by tuning the structure of the emitters. Both types of Pdots exhibit a large Stokes shift (>300 nm), while the molecular mechanism for efficient energy transfer and such a large Stokes shift may be different. For BODIPY Pdots, it was generated from cascade FRET [150]. But for squaraine Pdots, efficient energy transfer could be observed in spite of the minimal spectral overlap between donor and acceptor, which is an essential requirement for FRET. Thus, the authors hypothesized that energy transfer occurred via efficient exciton diffusion along the polymer chain, followed by through bond energy transfer between fluorene (the donor) and squaraine (the acceptor) [146]. This mechanism will inspire researchers to develop more narrow emissive NIR Pdots with high quantum yield and large Stokes shift, even without significant spectral overlap between the donor and acceptor [29].

Moreover, some other interesting studies about NIR-emissive Pdots have been reported by other research groups [151–155, 187–191]. To obtain NIR-emissive Pdots with both good photostability and high brightness, Chan group has compared two strategies to overcome

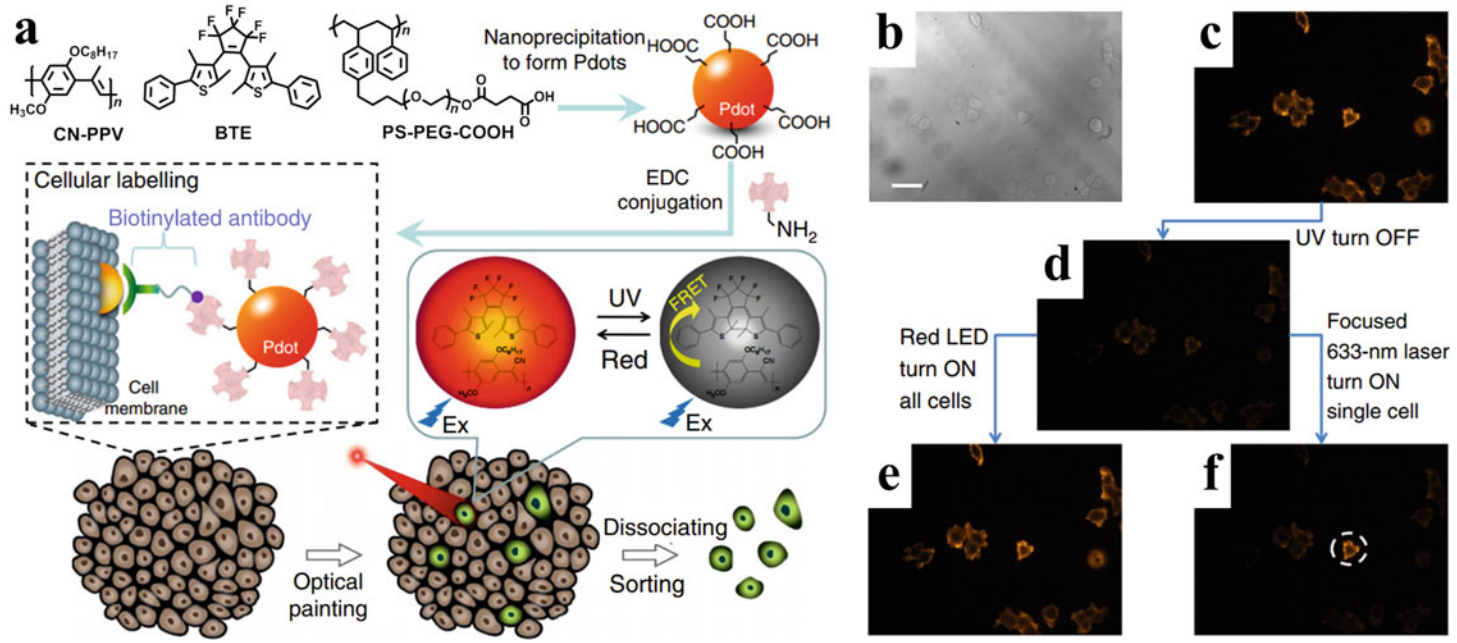

Fig. 12 (**a**) Schematic illustration of the preparation of Pdots, cellular labeling with Pdots and optical "painting" of labeled cells, followed by sorting and dissociating of painted cells. (**b**) Bright-field image of MCF-7 cells. (**c**–**f**) Fluorescence images showing the painting of (**e**) all cells or (**f**) a single cell. The cell exposed to a focused 633-nm laser turned bright (white dashed circle), while the other cells remained dark. The UV treatment was carried out with a hand-held UV lamp for 20 s. The single-cell painting was gotten by exposure to a focused 633-nm laser for 10 s. Wide-area illumination with a red diode light for 3 min leads to the turning ON of all cells. (Reprinted with permission from Ref. [158]. Copyright © 2016 Nature Publishing Group)

the aggregation-caused quenching (ACQ) effect in NIR-emissive Pdots: aggregation-induced emission (AIE) and anti-ACQ [192]. They designed two donor-type monomers with opposite characteristics, a tetraphenylethene (TPE)-based AIE fluorogen and a rigid three-dimensional pentiptycene (Pttc)-based moiety. The theoretical and experimental results show that the bulky steric hindrance could efficiently inhibit the ACQ effect, leading to an improved quantum yield of over 7 times higher than that of the planar structure, or about 1.4 times higher than that of the AIE-based conformation. In vitro and in vivo specific imaging was also realized by using these Pdots after bioconjugation. These results will provide valuable information for designing highly fluorescent Pdots.

4 Final Remarks and Future Perspective

In this chapter, we have comprehensively overviewed the recent advancements of CPNs and Pdots in the area of cell imaging. Great advances have been made in CPNs and Pdots due to their fascinating properties such as large extinction coefficients, high brightness, good photostability, and biocompatibility. The application of CPNs and Pdots has extended from in vitro to in vivo, from visible to NIR light, and their properties and functionalities can be tuned via structure design and surface modification.

Although a plenty of works have devoted to improving the performance of CPNs and Pdots, more efforts should be made for their real clinical applications. Firstly, in order to ensure the long-term biosafety of CPNs and Pdots in human body, their biodistribution as well as the biodegradation time and progress need further investigations. Secondly, more novel CPNs or Pdots with outstanding properties should be designed, for example, the biological imaging of CPNs or Pdots in NIR-II window could address the limitation of autofluorescence and penetration depth of biological tissues. Finally, targeted imaging is always needed for real application, so the surface modification methods should be expanded and further improved. We believe that the development of CPNs and Pdots continues to be an active area in fluorescence imaging, and has promising application foreground.

References

1. Heeger AJ (2001) Semiconducting and metallic polymers: the fourth generation of polymeric materials (Nobel Lecture). Angew Chem Int Ed 40:2591–2611
2. Thomas SW, Joly GD, Swager TM (2007) Chemical sensors based on amplifying fluorescent conjugated polymers. Chem Rev 107:1339–1386
3. Feng X, Liu L, Wang S, Zhu D (2010) Water-soluble fluorescent conjugated polymers and their interactions with biomacromolecules for sensitive biosensors. Chem Soc Rev 39:2411–2419
4. Zhu C, Liu L, Yang Q, Lv F, Wang S (2012) Water-soluble conjugated polymers for imaging, diagnosis, and therapy. Chem Rev 112:4687–4735
5. Tuncel D, Demir HV (2010) Conjugated polymer nanoparticles. Nanoscale 2:484–494
6. Li K, Liu B (2012) Polymer encapsulated conjugated polymer nanoparticles for fluorescence bioimaging. J Mater Chem 22:1257–1264
7. Feng L, Zhu C, Yuan H, Liu L, Lv F, Wang S (2013) Conjugated polymer nanoparticles: preparation, properties, functionalization and biological applications. Chem Soc Rev 42:6620–6633
8. Tang R, Feng X (2013) Highly luminescent conjugated polymer nanoparticles for imaging and therapy. Can Chem Trans 1:78–84
9. Li K, Liu B (2014) Polymer-encapsulated organic nanoparticles for fluorescence and photoacoustic imaging. Chem Soc Rev 43:6570–6597
10. Xu H, Li Q, Wang L, He Y, Shi J, Tang B, Fan C (2014) Nanoscale optical probes for cellular imaging. Chem Soc Rev 43:2650–2661
11. Massey M, Wu M, Conroy EM, Algar WR (2015) Mind your P's and Q's: the coming of age of semiconducting polymer dots and semiconductor quantum dots in biological applications. Curr Opin Biotechnol 34:30–40
12. Chan YH, Wu PJ (2015) Semiconducting polymer nanoparticles as fluorescent probes for biological imaging and sensing. Part Part Syst Charact 32:11–28
13. Wolfbeis OS (2015) An overview of nanoparticles commonly used in fluorescent bioimaging. Chem Soc Rev 44:4743–4768
14. Peng HS, Chiu DT (2015) Soft fluorescent nanomaterials for biological and biomedical imaging. Chem Soc Rev 44:4699–4722
15. Pu K, Chattopadhyay N, Rao J (2016) Recent advances of semiconducting polymer nanoparticles

in in vivo molecular imaging. J Control Release 240:312–322
16. Zhang W, Lin W, Wang X, Li C, Liu S, Xie Z (2019) Hybrid nanomaterials of conjugated polymers and albumin for precise photothermal therapy. ACS Appl Mater Interfaces 11:278–287
17. Wang Y, Feng L, Wang S (2019) Conjugated polymer nanoparticles for imaging, cell activity regulation, and therapy. Adv Funct Mater 29:1806818
18. Bruchez M, Moronne M, Gin P, Weiss S, Alivisatos AP (1998) Semiconductor nanocrystals as fluorescent biological labels. Science 281:2013–2016
19. Chan WCW, Nie S (1998) Quantum dot bioconjugates for ultrasensitive nonisotopic detection. Science 281:2016–2018
20. Michalet X, Pinaud FF, Bentolila LA, Tsay JM, Doose S, Li JJ, Sundaresan G, Wu AM, Gambhir SS, Weiss S (2005) Quantum dots for live cells, in vivo imaging, and diagnostics. Science 307:538–544
21. Warner JH, Hoshino A, Yamamoto K, Tilley RD (2005) Water-soluble photoluminescent silicon quantum dots. Angew Chem Int Ed 44:4550–4554
22. He Y, Zhong Y, Peng F, Wei X, Su Y, Lu Y, Su S, Gu W, Liao L, Lee ST (2011) One-pot microwave synthesis of water-dispersible, ultraphoto- and pH-stable, and highly fluorescent silicon quantum dots. J Am Chem Soc 133:14192–14195
23. Sun YP, Zhou B, Lin Y, Wang W, Fernando KAS, Pathak P, Meziani MJ, Harruff BA, Wang X, Wang H, Luo PG, Yang H, Kose ME, Chen B, Veca LM, Xie SY (2006) Quantum-sized carbon dots for bright and colorful photoluminescence. J Am Chem Soc 128:7756–7757
24. Baker SN, Baker GA (2010) Luminescent carbon nanodots: emergent nanolights. Angew Chem Int Ed 49:6726–6744
25. Zheng M, Ruan S, Liu S, Sun T, Qu D, Zhao H, Xie Z, Gao H, Jing X, Sun Z (2015) Self-targeting fluorescent carbon dots for diagnosis of brain cancer cells. ACS Nano 9:11455–11461
26. Zheng M, Liu S, Li J, Qu D, Zhao H, Guan X, Hu X, Xie Z, Jing X, Sun Z (2014) Integrating oxaliplatin with highly luminescent carbon dots: an unprecedented theranostic agent for personalized medicine. Adv Mater 26:3554–3560
27. Ow H, Larson DR, Srivastava M, Baird BA, Webb WW, Wiesner U (2005) Bright and stable core-shell fluorescent silica nanoparticles. Nano Lett 5:113–117
28. Wu C, Chiu DT (2013) Highly fluorescent semiconducting polymer dots for biology and medicine. Angew Chem Int Ed 52:3086–3109
29. Yu J, Rong Y, Kuo CT, Zhou XH, Chiu DT (2017) Recent advances in the development of highly luminescent semiconducting polymer dots and nanoparticles for biological imaging and medicine. Anal Chem 89:42–56
30. Zhang X, Yu J, Wu C, Jin Y, Rong Y, Ye F, Chiu DT (2012) Importance of having low-density functional groups for generating high-performance semiconducting polymer dots. ACS Nano 6:5429–5439
31. Szymanski C, Wu C, Hooper J, Salazar MA, Perdomo A, Dukes A, McNeill J (2005) Single molecule nanoparticles of the conjugated polymer MEH-PPV, preparation and characterization by near-field scanning optical microscopy. J Phys Chem B 109:8543–8546
32. Wu C, Peng H, Jiang Y, McNeill J (2006) Energy transfer mediated fluorescence from blended conjugated polymer nanoparticles. J Phys Chem B 110:14148–14154
33. Wu C, Szymanski C, Cain Z, McNeill J (2007) Conjugated polymer dots for multiphoton fluorescence imaging. J Am Chem Soc 129:12904–12905
34. Wu C, Bull B, Szymanski C, Christensen K, McNeill J (2008) Multicolor conjugated polymer dots for biological fluorescence imaging. ACS Nano 2:2415–2423
35. Wu C, McNeill J (2008) Swelling-controlled polymer phase and fluorescence properties of polyfluorene nanoparticles. Langmuir 24:5855–5861
36. Wu C, Bull B, Christensen K, McNeill J (2009) Ratiometric single-nanoparticle oxygen sensors for biological imaging. Angew Chem Int Ed 48:2741–2745
37. Yu J, Wu C, Sahu SP, Fernando LP, Szymanski C, McNeill J (2009) Nanoscale 3D tracking with conjugated polymer nanoparticles. J Am Chem Soc 131:18410–18414
38. Wu C, Jin Y, Schneider T, Burnham DR, Smith PB, Chiu DT (2010) Ultrabright and bioorthogonal labeling of cellular targets using semiconducting polymer dots and click chemistry. Angew Chem Int Ed 49:9436–9440
39. Wu C, Schneider T, Zeigler M, Yu J, Schiro PG, Burnham DR, McNeill JD, Chiu DT (2010) Bioconjugation of ultrabright semiconducting polymer dots for specific cellular targeting. J Am Chem Soc 132:15410–15417
40. Ye F, Wu C, Jin Y, Chan YH, Zhang X, Chiu DT (2011) Ratiometric temperature sensing with semiconducting polymer dots. J Am Chem Soc 133:8146–8149
41. Wu C, Hansen SJ, Hou Q, Yu J, Zeigler M, Jin Y, Burnham DR, McNeill JD, Olson JM, Chiu DT (2011) Design of highly emissive polymer dot bioconjugates for in vivo tumor targeting. Angew Chem Int Ed 50:3430–3434
42. Jin Y, Ye F, Zeigler M, Wu C, Chiu DT (2011) Near-infrared fluorescent dye-doped semiconducting polymer dots. ACS Nano 5:1468–1475
43. Chan YH, Wu C, Ye F, Jin Y, Smith PB, Chiu DT (2011) Development of ultrabright semiconducting polymer dots for ratiometric pH sensing. Anal Chem 83:1448–1455
44. Chan YH, Jin Y, Wu C, Chiu DT (2011) Copper (II) and iron(II) ion sensing with semiconducting polymer dots. Chem Commun 47:2820–2822

45. Yu J, Wu C, Tian Z, McNeill J (2012) Tracking of single charge carriers in a conjugated polymer nanoparticle. Nano Lett 12:1300–1306
46. Jin Y, Ye F, Wu C, Chan YH, Chiu DT (2012) Generation of functionalized and robust semiconducting polymer dots with polyelectrolytes. Chem Commun 48:3161–3163
47. Ye F, Wu C, Jin Y, Wang M, Chan YH, Yu J, Sun W, Hayden S, Chiu DT (2012) A compact and highly fluorescent orange-emitting polymer dot for specific subcellular imaging. Chem Commun 48:1778–1780
48. Yu J, Wu C, Zhang X, Ye F, Gallina ME, Rong Y, Wu IC, Sun W, Chan YH, Chiu DT (2012) Stable functionalization of small semiconducting polymer dots via covalent cross-linking and their application for specific cellular imaging. Adv Mater 24:3498–3504
49. Rong Y, Wu C, Yu J, Zhang X, Ye F, Zeigler M, Gallina ME, Wu IC, Zhang Y, Chan YH, Sun W, Uvdal K, Chiu DT (2013) Multicolor fluorescent semiconducting polymer dots with narrow emissions and high brightness. ACS Nano 7:376–384
50. Guo L, Ge J, Wang P (2018) Polymer dots as effective phototheranostic agents. Photochem Photobiol 94:916–934
51. Lyu Y, Pu K (2017) Recent advances of activatable molecular probes based on semiconducting polymer nanoparticles in sensing and imaging. Adv Sci 4:1600481
52. Jiang Y, Pu K (2018) Multimodal biophotonics of semiconducting polymer nanoparticles. Acc Chem Res 51:1840–1849
53. Li J, Rao J, Pu K (2018) Recent progress on semiconducting polymer nanoparticles for molecular imaging and cancer phototherapy. Biomaterials 155:217–235
54. Miao Q, Pu K (2018) Organic semiconducting agents for deep-tissue molecular imaging: second near-infrared fluorescence, self-luminescence, and photoacoustics. Adv Mater 30:1801778
55. Yin C, Zhen X, Zhao H, Tang Y, Ji Y, Lyu Y, Fan Q, Huang W, Pu K (2017) Amphiphilic semiconducting oligomer for near-infrared photoacoustic and fluorescence imaging. ACS Appl Mater Interfaces 9:12332–12339
56. Sun T, Dou JH, Liu S, Wang X, Zheng X, Wang Y, Pei J, Xie Z (2018) Second near-infrared conjugated polymer nanoparticles for photoacoustic imaging and photothermal therapy. ACS Appl Mater Interfaces 10:7919–7926
57. Sun T, Han J, Liu S, Wang X, Wang ZY, Xie Z (2019) Tailor-made semiconducting polymers for second near-infrared photothermal therapy of orthotopic liver cancer. ACS Nano 13:7345–7354
58. Sun T, Chen X, Wang X, Liu S, Liu J, Xie Z (2019) Enhanced efficacy of photothermal therapy by combining a semiconducting polymer with an inhibitor of a heat shock protein. Mater Chem Front 3:127–136
59. Lu X, Yuan P, Zhang W, Wu Q, Wang X, Zhao M, Sun P, Huang W, Fan Q (2018) A highly water-soluble triblock conjugated polymer for in vivo NIR-II imaging and photothermal therapy of cancer. Polym Chem 9:3118–3126
60. Kurokawa N, Yoshikawa H, Hirota N, Hyodo K, Masuhara H (2004) Size-dependent spectroscopic properties and thermochromic behavior in poly (substituted thiophene) nanoparticles. ChemPhysChem 5:1609–1615
61. Howes P, Green M, Levitt J, Suhling K, Hughes M (2010) Phospholipid encapsulated semiconducting polymer nanoparticles: their use in cell imaging and protein attachment. J Am Chem Soc 132:3989–3996
62. Li K, Pan J, Feng SS, Wu AW, Pu KY, Liu Y, Liu B (2009) Generic strategy of preparing fluorescent conjugated-polymer-loaded poly(DL-lactide-*co*-glycolide) nanoparticles for targeted cell imaging. Adv Funct Mater 19:3535–3542
63. Xing C, Xu Q, Tang H, Liu L, Wang S (2009) Conjugated polymer/porphyrin complexes for efficient energy transfer and improving light-activated antibacterial activity. J Am Chem Soc 131:13117–13124
64. Chong H, Nie C, Zhu C, Yang Q, Liu L, Lv F, Wang S (2012) Conjugated polymer nanoparticles for light-activated anticancer and antibacterial activity with imaging capability. Langmuir 28:2091–2098
65. Yang G, Liu L, Yang Q, Lv F, Wang S (2012) A multifunctional cationic pentathiophene: synthesis, organelle-selective imaging, and anticancer activity. Adv Funct Mater 22:736–743
66. Quan L, Liu S, Sun T, Guan X, Lin W, Xie Z, Huang Y, Wang Y, Jing X (2014) Near-infrared emitting fluorescent BODIPY nanovesicles for in vivo molecular imaging and drug delivery. ACS Appl Mater Interfaces 6:16166–16173
67. Quan L, Sun T, Lin W, Guan X, Zheng M, Xie Z, Jing X (2014) BODIPY fluorescent chemosensor for Cu^{2+} detection and its applications in living cells: fast response and high sensitivity. J Fluoresc 24:841–846
68. Sun T, Li Z, Xie Z, Jing X (2015) Amphiphilic cyanine-platinum conjugates as fluorescent nanodrugs. Chem Asian J 11:221–225
69. Sun T, Lin W, Zhang W, Xie Z (2016) Self-assembly of amphiphilic drug-dye conjugates into nanoparticles for imaging and chemotherapy. Chem Asian J 11:3174–3177
70. Zhang T, Ma C, Sun T, Xie Z (2019) Unadulterated BODIPY nanoparticles for biomedical applications. Coord Chem Rev 390:76–85
71. Lin W, Sun T, Xie Z, Gu J, Jing X (2016) A dual-responsive nanocapsule via disulfide-induced self-assembly for therapeutic agent delivery. Chem Sci 7:1846–1852
72. Li J, Pu K (2019) Development of organic semiconducting materials for deep-tissue optical imaging, phototherapy and photoactivation. Chem Soc Rev 48:38–71

73. Miao Q, Yeo DC, Wiraja C, Zhang J, Ning X, Xu C, Pu K (2018) Near-infrared fluorescent molecular probe for sensitive imaging of keloid. Angew Chem Int Ed 57:1256–1260
74. Wang X, Li P, Ding Q, Wu C, Zhang W, Tang B (2019) Observation of acetylcholinesterase in stress-induced depression phenotypes by two-photon fluorescence imaging in the mouse brain. J Am Chem Soc 141:2061–2068
75. Li X, Bottini M, Zhang L, Zhang S, Chen J, Zhang T, Liu L, Rosato N, Ma X, Shi X, Wu Y, Guo W, Liang XJ (2019) Core-satellite nanomedicines for in vivo real-time monitoring of enzyme-activatable drug release by fluorescence and photoacoustic dual-modal imaging. ACS Nano 13:176–186
76. Grayson PC, Alehashemi S, Bagheri AA, Civelek AC, Cupps TR, Kaplan MJ, Malayeri AA, Merkel PA, Novakovich E, Bluemke DA, Ahlman MA (2018) ^{18}F-fluorodeoxyglucose-positron emission tomography as an imaging biomarker in a prospective, longitudinal cohort of patients with large vessel vasculitis. Arthritis Rheumatol 70:439–449
77. Rauscher I, Eiber M, Weber WA, Gschwend JE, Horn T, Maurer T (2018) Positron-emission tomography imaging in urological oncology: current aspects and developments. Int J Urol 25:912–921
78. Shi Y, Li J, Zhang Z, Duan D, Zhang Z, Liu H, Liu T, Liu Z (2018) Tracing boron with fluorescence and positron emission tomography imaging of boronated porphyrin nanocomplex for imaging-guided boron neutron capture therapy. ACS Appl Mater Interfaces 10:43387–43395
79. Zhang G, Naha PC, Gautam P, Cormode DP, Chan JMW (2018) Water-dispersible bismuth-organic materials with computed tomography contrast properties. ACS Appl Bio Mater 1:1918–1926
80. Zhang M, Zou Y, Zhong Y, Liao G, Yu C, Xu Z (2019) Polydopamine-based tumor-targeted multifunctional reagents for computer tomography/fluorescence dual-mode bioimaging-guided photothermal therapy. ACS Appl Bio Mater 2:630–637
81. Chu Z, Chen L, Wang X, Yang Q, Zhao Q, Huang C, Huang Y, Yang DP, Jia N (2019) Ultrasmall Au-Ag alloy nanoparticles: protein-directed synthesis, biocompatibility, and X-ray computed tomography imaging. ACS Biomater Sci Eng 5:1005–1015
82. Wang Y, Sun Z, Chen Z, Wu Y, Gu Y, Lin S, Wang Y (2019) In vivo photoacoustic/single-photon emission computed tomography imaging for dynamic monitoring of aggregation-enhanced photothermal nanoagents. Anal Chem 91:2128–2134
83. Martins AF, Clavijo Jordan V, Bochner F, Chirayil S, Paranawithana N, Zhang S, Lo ST, Wen X, Zhao P, Neeman M, Sherry AD (2018) Imaging insulin secretion from mouse pancreas by MRI is improved by use of a zinc-responsive MRI sensor with lower affinity for Zn^{2+} ions. J Am Chem Soc 140:17456–17464
84. Akazawa K, Sugihara F, Nakamura T, Matsushita H, Mukai H, Akimoto R, Minoshima M, Mizukami S, Kikuchi K (2018) Perfluorocarbon-based ^{19}F MRI nanoprobes for in vivo multicolor imaging. Angew Chem Int Ed 57:16742–16747
85. Qiu K, Wang J, Rees TW, Ji L, Zhang Q, Chao H (2018) A mitochondria-targeting photothermogenic nanozyme for MRI-guided mild photothermal therapy. Chem Commun 54:14108–14111
86. Li J, Peng C, Guo Z, Shi C, Zhuang R, Hong X, Wang X, Xu D, Zhang P, Zhang D, Liu T, Su X, Zhang X (2018) Radioiodinated pentixather for SPECT imaging of expression of the chemokine receptor CXCR4 in rat myocardial-infarction-reperfusion models. Anal Chem 90:9614–9620
87. Wen X, Shi C, Xu D, Zhang P, Li Z, Li J, Su X, Zhuang R, Liu T, Guo Z, Zhang X (2019) Radioiodinated portable albumin binder as a versatile agent for in vivo imaging with single-photon emission computed tomography. Mol Pharm 16:816–824
88. Zhang X, Ruan Q, Duan X, Gan Q, Song X, Fang S, Lin X, Du J, Zhang J (2018) Novel ^{99m}Tc-labeled glucose derivative for single photon emission computed tomography: a promising tumor imaging agent. Mol Pharm 15:3417–3424
89. Zhang J, Zhen X, Upputuri PK, Pramanik M, Chen P, Pu K (2017) Activatable photoacoustic nanoprobes for in vivo ratiometric imaging of peroxynitrite. Adv Mater 29:1604764
90. Li Y, Chen Y, Du M, Chen ZY (2018) Ultrasound technology for molecular imaging: from contrast agents to multimodal imaging. ACS Biomater Sci Eng 4:2716–2728
91. Tang W, Yang Z, Wang S, Wang Z, Song J, Yu G, Fan W, Dai Y, Wang J, Shan L, Niu G, Fan Q, Chen X (2018) Organic semiconducting photoacoustic nanodroplets for laser-activatable ultrasound imaging and combinational cancer therapy. ACS Nano 12:2610–2622
92. Zhang L, Yin T, Li B, Zheng R, Qiu C, Lam KS, Zhang Q, Shuai X (2018) Size-modulable nanoprobe for high-performance ultrasound imaging and drug delivery against cancer. ACS Nano 12:3449–3460
93. Zhu H, Qin D, Wu Y, Jing B, Liu J, Hazlewood D, Zhang H, Feng Y, Yang X, Wan M, Wu D (2018) Laser-activated bioprobes with high photothermal conversion efficiency for sensitive photoacoustic/ultrasound imaging and photothermal sensing. ACS Appl Mater Interfaces 10:29251–29259
94. Chen D, Zhao J, Zhang L, Liu R, Huang Y, Lan C, Zhao S (2018) Capsicum-derived biomass quantum dots coupled with alizarin red S as an inner-filter-mediated illuminant nanosystem for imaging of intracellular calcium ions. Anal Chem 90:13059–13064
95. Mallick S, Kumar P, Koner AL (2019) Freeze-resistant cadmium-free quantum dots for live-cell imaging. ACS Appl Nano Mater 2:661–666
96. Zhou R, Sun S, Li C, Wu L, Hou X, Wu P (2018) Enriching Mn-doped ZnSe quantum dots onto

mesoporous silica nanoparticles for enhanced fluorescence/magnetic resonance imaging dual-modal bio-imaging. ACS Appl Mater Interfaces 10:34060–34067
97. Zheng M, Li Y, Liu S, Wang W, Xie Z, Jing X (2016) One-pot to synthesize multifunctional carbon dots for near infrared fluorescence imaging and photothermal cancer therapy. ACS Appl Mater Interfaces 8:23533–23541
98. Hudson DA, Caplan JL, Thorpe C (2018) Designing flavoprotein-GFP fusion probes for analyte-specific ratiometric fluorescence imaging. Biochemistry 57:1178–1189
99. Nasu Y, Asaoka Y, Namae M, Nishina H, Yoshimura H, Ozawa T (2016) Genetically encoded fluorescent probe for imaging apoptosis in vivo with spontaneous GFP complementation. Anal Chem 88:838–844
100. Wedeking T, Löchte S, Richter CP, Bhagawati M, Piehler J, You C (2015) Single cell GFP-trap reveals stoichiometry and dynamics of cytosolic protein complexes. Nano Lett 15:3610–3615
101. Glembockyte V, Frenette M, Mottillo C, Durantini AM, Gostick J, Štrukil V, Friščić T, Cosa G (2018) Highly photostable and fluorescent microporous solids prepared via solid-state entrapment of boron dipyrromethene dyes in a nascent metal-organic framework. J Am Chem Soc 140:16882–16887
102. Macdonald PJ, Gayda S, Haack RA, Ruan Q, Himmelsbach RJ, Tetin SY (2018) Rhodamine-derived fluorescent dye with inherent blinking behavior for super-resolution imaging. Anal Chem 90:9165–9173
103. Mahalingam SM, Dip F, Castillo M, Roy M, Wexner SD, Rosenthal RJ, Low PS (2018) Intraoperative ureter visualization using a novel near-infrared fluorescent dye. Mol Pharm 15:3442–3447
104. Petreto A, Dos Santos MC, Lefebvre O, Dos Santos GR, Ponzellini P, Garoli D, De Angelis F, Ammar M, Hildebrandt N (2018) Optimizing FRET on aluminum surfaces via controlled attachment of fluorescent dyes. ACS Omega 3:18867–18876
105. Kim Y, Li W, Shin S, Lee M (2013) Development of toroidal nanostructures by self-assembly: rational designs and applications. Acc Chem Res 46:2888–2897
106. Giepmans BNG, Adams SR, Ellisman MH, Tsien RY (2006) The fluorescent toolbox for assessing protein location and function. Science 312:217–224
107. Moon JH, McDaniel W, MacLean P, Hancock LF (2007) Live-cell-permeable poly(*p*-phenylene ethynylene). Angew Chem Int Ed 46:8223–8225
108. Rahim NAA, McDaniel W, Bardon K, Srinivasan S, Vickerman V, So PTC, Moon JH (2009) Conjugated polymer nanoparticles for two-photon imaging of endothelial cells in a tissue model. Adv Mater 21:3492–3496
109. Miller MJ, Wei SH, Parker I, Cahalan MD (2002) Two-photon imaging of lymphocyte motility and antigen response in intact lymph node. Science 296:1869–1873
110. Denk W, Strickler JH, Webb WW (1990) Two-photon laser scanning fluorescence microscopy. Science 248:73–76
111. Agarwal A, Coleno ML, Wallace VP, Wu WY, Sun CH, Tromberg BJ, George SC (2001) Two-photon laser scanning microscopy of epithelial cell-modulated collagen density in engineered human lung tissue. Tissue Eng 7:191–202
112. Fu L, Jain A, Cranfield C, Xie H, Gu M (2007) Three-dimensional nonlinear optical endoscopy. J Biomed Opt 12:040501
113. Jung W, Tang S, McCormic DT, Xie T, Ahn YC, Su J, Tomov IV, Krasieva TB, Tromberg BJ, Chen Z (2008) Miniaturized probe based on a microelectromechanical system mirror for multiphoton microscopy. Opt Lett 33:1324–1326
114. Bhawalkar JD, He GS, Prasad PN (1996) Nonlinear multiphoton processes in organic and polymeric materials. Rep Prog Phys 59:1041–1070
115. Albota M, Beljonne D, Brédas JL, Ehrlich JE, Fu JY, Heikal AA, Hess SE, Kogej T, Levin MD, Marder SR, McCord-Maughon D, Perry JW, Röckel H, Rumi M, Subramaniam G, Webb WW, Wu XL, Xu C (1998) Design of organic molecules with large two-photon absorption cross sections. Science 281:1653–1656
116. Cao L, Wang X, Meziani MJ, Lu F, Wang H, Luo PG, Lin Y, Harruff BA, Veca LM, Murray D, Xie SY, Sun YP (2007) Carbon dots for multiphoton bioimaging. J Am Chem Soc 129:11318–11319
117. Yao J, Larson DR, Vishwasrao HD, Zipfel WR, Webb WW (2005) Blinking and nonradiant dark fraction of water-soluble quantum dots in aqueous solution. Proc Natl Acad Sci U S A 102:14284–14289
118. Mammen M, Choi SK, Whitesides GM (1998) Polyvalent interactions in biological systems: implications for design and use of multivalent ligands and inhibitors. Angew Chem Int Ed 37:2754–2794
119. Kiessling LL, Gestwicki JE, Strong LE (2000) Synthetic multivalent ligands in the exploration of cell-surface interactions. Curr Opin Chem Biol 4:696–703
120. Miranda OR, You CC, Phillips R, Kim IB, Ghosh PS, Bunz UHF, Rotello VM (2007) Array-based sensing of proteins using conjugated polymers. J Am Chem Soc 129:9856–9857
121. Kim IB, Phillips R, Bunz UHF (2007) Carboxylate group side-chain density modulates the pH-dependent optical properties of PPEs. Macromolecules 40:5290–5293
122. McRae RL, Phillips RL, Kim IB, Bunz UHF, Fahrni CJ (2008) Molecular recognition based on low-affinity polyvalent interactions: selective binding

of a carboxylated polymer to fibronectin fibrils of live fibroblast cells. J Am Chem Soc 130:7851–7853
123. Liang PH, Wang SK, Wong CH (2007) Quantitative analysis of carbohydrate-protein interactions using glycan microarrays: determination of surface and solution dissociation constants. J Am Chem Soc 129:11177–11184
124. Sun T, Guan X, Zheng M, Jing X, Xie Z (2015) Mitochondria-localized fluorescent BODIPY-platinum conjugate. ACS Med Chem Lett 6:430–433
125. Klein AV, Hambley TW (2009) Platinum drug distribution in cancer cells and tumors. Chem Rev 109:4911–4920
126. Wang D, Lippard SJ (2005) Cellular processing of platinum anticancer drugs. Nat Rev Drug Discov 4:307–320
127. Tang H, Xing C, Liu L, Yang Q, Wang S (2011) Synthesis of amphiphilic polythiophene for cell imaging and monitoring the cellular distribution of a cisplatin anticancer drug. Small 7:1464–1470
128. Yin Win K, Feng SS (2005) Effects of particle size and surface coating on cellular uptake of polymeric nanoparticles for oral delivery of anticancer drugs. Biomaterials 26:2713–2722
129. Han M, Gao X, Su JZ, Nie S (2001) Quantum-dot-tagged microbeads for multiplexed optical coding of biomolecules. Nat Biotechnol 19:631–635
130. Wilson R, Cossins AR, Spiller DG (2006) Encoded microcarriers for high-throughput multiplexed detection. Angew Chem Int Ed 45:6104–6117
131. Lee H, Kim J, Kim H, Kim J, Kwon S (2010) Colour-barcoded magnetic microparticles for multiplexed bioassays. Nat Mater 9:745–749
132. Feng X, Yang G, Liu L, Lv F, Yang Q, Wang S, Zhu D (2012) A convenient preparation of multi-spectral microparticles by bacteria-mediated assemblies of conjugated polymer nanoparticles for cell imaging and barcoding. Adv Mater 24:637–641
133. Feng L, Liu L, Lv F, Bazan GC, Wang S (2014) Preparation and biofunctionalization of multicolor conjugated polymer nanoparticles for imaging and detection of tumor cells. Adv Mater 26:3926–3930
134. Kim S, Lim CK, Na J, Lee YD, Kim K, Choi K, Leary JF, Kwon IC (2010) Conjugated polymer nanoparticles for biomedical in vivo imaging. Chem Commun 46:1617–1619
135. de Vries IJM, Lesterhuis WJ, Barentsz JO, Verdijk P, van Krieken JH, Boerman OC, Oyen WJG, Bonenkamp JJ, Boezeman JB, Adema GJ, Bulte JWM, Scheenen TWJ, Punt CJA, Heerschap A, Figdor CG (2005) Magnetic resonance tracking of dendritic cells in melanoma patients for monitoring of cellular therapy. Nat Biotechnol 23:1407–1413
136. Lewin M, Carlesso N, Tung CH, Tang XW, Cory D, Scadden DT, Weissleder R (2000) Tat peptide-derivatized magnetic nanoparticles allow in vivo tracking and recovery of progenitor cells. Nat Biotechnol 18:410–414
137. Dudley ME, Rosenberg SA (2003) Adoptive-cell-transfer therapy for the treatment of patients with cancer. Nat Rev Cancer 3:666–675
138. Pu K, Shuhendler AJ, Valta MP, Cui L, Saar M, Peehl DM, Rao J (2014) Phosphorylcholine-coated semiconducting polymer nanoparticles as rapid and efficient labeling agents for in vivo cell tracking. Adv Healthc Mater 3:1292–1298
139. Welsher K, Liu Z, Sherlock SP, Robinson JT, Chen Z, Daranciang D, Dai H (2009) A route to brightly fluorescent carbon nanotubes for near-infrared imaging in mice. Nat Nanotechnol 4:773–780
140. Naczynski DJ, Tan MC, Zevon M, Wall B, Kohl J, Kulesa A, Chen S, Roth CM, Riman RE, Moghe PV (2013) Rare-earth-doped biological composites as in vivo shortwave infrared reporters. Nat Commun 4:2199
141. Dong B, Li C, Chen G, Zhang Y, Zhang Y, Deng M, Wang Q (2013) Facile synthesis of highly photoluminescent Ag_2Se quantum dots as a new fluorescent probe in the second near-infrared window for in vivo imaging. Chem Mater 25:2503–2509
142. Hong G, Robinson JT, Zhang Y, Diao S, Antaris AL, Wang Q, Dai H (2012) In vivo fluorescence imaging with Ag_2S quantum dots in the second near-infrared region. Angew Chem Int Ed 51:9818–9821
143. Yi H, Ghosh D, Ham MH, Qi J, Barone PW, Strano MS, Belcher AM (2012) M13 phage-functionalized single-walled carbon nanotubes as nanoprobes for second near-infrared window fluorescence imaging of targeted tumors. Nano Lett 12:1176–1183
144. Won N, Jeong S, Kim K, Kwag J, Park J, Kim SG, Kim S (2012) Imaging depths of near-infrared quantum dots in first and second optical windows. Mol Imaging 11:338–352
145. Hong G, Zou Y, Antaris AL, Diao S, Wu D, Cheng K, Zhang X, Chen C, Liu B, He Y, Wu JZ, Yuan J, Zhang B, Tao Z, Fukunaga C, Dai H (2014) Ultrafast fluorescence imaging in vivo with conjugated polymer fluorophores in the second near-infrared window. Nat Commun 5:4206
146. Wu IC, Yu J, Ye F, Rong Y, Gallina ME, Fujimoto BS, Zhang Y, Chan YH, Sun W, Zhou XH, Wu C, Chiu DT (2015) Squaraine-based polymer dots with narrow, bright near-infrared fluorescence for biological applications. J Am Chem Soc 137:173–178
147. Sun W, Yu J, Deng R, Rong Y, Fujimoto B, Wu C, Zhang H, Chiu DT (2013) Semiconducting polymer dots doped with europium complexes showing ultranarrow emission and long luminescence lifetime for time-gated cellular imaging. Angew Chem Int Ed 52:11294–11297
148. Rong Y, Yu J, Zhang X, Sun W, Ye F, Wu IC, Zhang Y, Hayden S, Zhang Y, Wu C, Chiu DT (2014) Yellow fluorescent semiconducting polymer dots with high brightness, small size, and narrow

emission for biological applications. ACS Macro Lett 3:1051–1054
149. Li Q, Zhang J, Sun W, Yu J, Wu C, Qin W, Chiu DT (2014) Europium-complex-grafted polymer dots for amplified quenching and cellular imaging applications. Langmuir 30:8607–8614
150. Zhang X, Yu J, Rong Y, Ye F, Chiu DT, Uvdal K (2013) High-intensity near-IR fluorescence in semiconducting polymer dots achieved by cascade FRET strategy. Chem Sci 4:2143–2151
151. Chen CP, Huang YC, Liou SY, Wu PJ, Kuo SY, Chan YH (2014) Near-infrared fluorescent semiconducting polymer dots with high brightness and pronounced effect of positioning alkyl chains on the comonomers. ACS Appl Mater Interfaces 6:21585–21595
152. Liu HY, Wu PJ, Kuo SY, Chen CP, Chang EH, Wu CY, Chan YH (2015) Quinoxaline-based polymer dots with ultrabright red to near-infrared fluorescence for in vivo biological imaging. J Am Chem Soc 137:10420–10429
153. Xiong L, Guo Y, Zhang Y, Cao F (2016) Highly luminescent and photostable near-infrared fluorescent polymer dots for long-term tumor cell tracking in vivo. J Mater Chem B 4:202–206
154. Liou SY, Ke CS, Chen JH, Luo YW, Kuo SY, Chen YH, Fang CC, Wu CY, Chiang CM, Chan YH (2016) Tuning the emission of semiconducting polymer dots from green to near-infrared by alternating donor monomers and their applications for in vivo biological imaging. ACS Macro Lett 5:154–157
155. Xiong L, Cao F, Cao X, Guo Y, Zhang Y, Cai X (2015) Long-term-stable near-infrared polymer dots with ultrasmall size and narrow-band emission for imaging tumor vasculature in vivo. Bioconjug Chem 26:817–821
156. Ye F, Sun W, Zhang Y, Wu C, Zhang X, Yu J, Rong Y, Zhang M, Chiu DT (2015) Single-chain semiconducting polymer dots. Langmuir 31:499–505
157. Chan YH, Gallina ME, Zhang X, Wu IC, Jin Y, Sun W, Chiu DT (2012) Reversible photoswitching of spiropyran-conjugated semiconducting polymer dots. Anal Chem 84:9431–9438
158. Kuo CT, Thompson AM, Gallina ME, Ye F, Johnson ES, Sun W, Zhao M, Yu J, Wu IC, Fujimoto B, DuFort CC, Carlson MA, Hingorani SR, Paguirigan AL, Radich JP, Chiu DT (2016) Optical painting and fluorescence activated sorting of single adherent cells labelled with photoswitchable Pdots. Nat Commun 7:11468
159. Chen J, Wang D, Turshatov A, Muñoz-Espí R, Ziener U, Koynov K, Landfester K (2013) One-pot fabrication of amphiphilic photoswitchable thiophene-based fluorescent polymer dots. Polym Chem 4:773–781
160. Osakada Y, Hanson L, Cui B (2012) Diarylethene doped biocompatible polymer dots for fluorescence switching. Chem Commun 48:3285–3287
161. Dai R, Wu F, Xu H, Chi Y (2015) Anodic, cathodic, and annihilation electrochemiluminescence emissions from hydrophilic conjugated polymer dots in aqueous medium. ACS Appl Mater Interfaces 7:15160–15167
162. Feng Y, Dai C, Lei J, Ju H, Cheng Y (2016) Silole-containing polymer nanodot: an aqueous low-potential electrochemiluminescence emitter for biosensing. Anal Chem 88:845–850
163. Chen H, Lu Q, Liao J, Yuan R, Chen S (2016) Anodic electrogenerated chemiluminescence behavior and the choline biosensing application of blue emitting conjugated polymer dots. Chem Commun 52:7276–7279
164. Sun K, Tang Y, Li Q, Yin S, Qin W, Yu J, Chiu DT, Liu Y, Yuan Z, Zhang X, Wu C (2016) In vivo dynamic monitoring of small molecules with implantable polymer-dot transducer. ACS Nano 10:6769–6781
165. Zhao Q, Zhou X, Cao T, Zhang KY, Yang L, Liu S, Liang H, Yang H, Li F, Huang W (2015) Fluorescent/phosphorescent dual-emissive conjugated polymer dots for hypoxia bioimaging. Chem Sci 6:1825–1831
166. Lin Z, Zhang G, Yang W, Qiu B, Chen G (2012) CEA fluorescence biosensor based on the FRET between polymer dots and Au nanoparticles. Chem Commun 48:9918–9920
167. Wu PJ, Chen JL, Chen CP, Chan YH (2013) Photoactivated ratiometric copper(II) ion sensing with semiconducting polymer dots. Chem Commun 49:898–900
168. Zhao Q, Zhang C, Liu S, Liu Y, Zhang KY, Zhou X, Jiang J, Xu W, Yang T, Huang W (2015) Dual-emissive polymer dots for rapid detection of fluoride in pure water and biological systems with improved reliability and accuracy. Sci Rep 5:16420
169. Wang C, Sun J, Mei H, Gao F (2016) Semiconducting-polymer-dot based fluorescent probe for turn-on sensing of phytic acid. Anal Methods 8:7755–7761
170. Shi H, Ma X, Zhao Q, Liu B, Qu Q, An Z, Zhao Y, Huang W (2014) Ultrasmall phosphorescent polymer dots for ratiometric oxygen sensing and photodynamic cancer therapy. Adv Funct Mater 24:4823–4830
171. Zhou X, Liang H, Jiang P, Zhang KY, Liu S, Yang T, Zhao Q, Yang L, Lv W, Yu Q, Huang W (2016) Multifunctional phosphorescent conjugated polymer dots for hypoxia imaging and photodynamic therapy of cancer cells. Adv Sci 3:1500155
172. Zhang D, Wu M, Zeng Y, Liao N, Cai Z, Liu G, Liu X, Liu J (2016) Lipid micelles packaged with semiconducting polymer dots as simultaneous MRI/photoacoustic imaging and photodynamic/photothermal dual-modal therapeutic agents for liver cancer. J Mater Chem B 4:589–599
173. Li S, Chang K, Sun K, Tang Y, Cui N, Wang Y, Qin W, Xu H, Wu C (2016) Amplified singlet oxygen generation in semiconductor polymer dots for

photodynamic cancer therapy. ACS Appl Mater Interfaces 8:3624–3634
174. Wu C, Szymanski C, McNeill J (2006) Preparation and encapsulation of highly fluorescent conjugated polymer nanoparticles. Langmuir 22:2956–2960
175. Dahan M, Laurence T, Pinaud F, Chemla DS, Alivisatos AP, Sauer M, Weiss S (2001) Time-gated biological imaging by use of colloidal quantum dots. Opt Lett 26:825–827
176. Fernando LP, Kandel PK, Yu J, McNeill J, Ackroyd PC, Christensen KA (2010) Mechanism of cellular uptake of highly fluorescent conjugated polymer nanoparticles. Biomacromolecules 11:2675–2682
177. Gao X, Cui Y, Levenson RM, Chung LWK, Nie S (2004) In vivo cancer targeting and imaging with semiconductor quantum dots. Nat Biotechnol 22:969–976
178. Li Z, Li LJ, Sun T, Liu L, Xie Z (2016) Benzimidazole-BODIPY as optical and fluorometric pH sensor. Dyes Pigments 128:165–169
179. Li Z, Zheng M, Guan X, Xie Z, Huang Y, Jing X (2014) Unadulterated BODIPY-dimer nanoparticles with high stability and good biocompatibility for cellular imaging. Nanoscale 6:5662–5665
180. Loudet A, Burgess K (2007) BODIPY dyes and their derivatives: syntheses and spectroscopic properties. Chem Rev 107:4891–4932
181. Xu W, Sims CE, Allbritton NL (2010) Microcup arrays for the efficient isolation and cloning of cells. Anal Chem 82:3161–3167
182. Wang Y, Phillips CN, Herrera GS, Sims CE, Yeh JJ, Allbritton NL (2013) Array of biodegradable microraftsfor isolation and implantation of living, adherent cells. RSC Adv 3:9264–9272
183. Lee JY, Jones C, Zern MA, Revzin A (2006) Analysis of local tissue-specific gene expression in cellular micropatterns. Anal Chem 78:8305–8312
184. Herzenberg LA, Parks D, Sahaf B, Perez O, Roederer M, Herzenberg LA (2002) The history and future of the fluorescence activated cell sorter and flow cytometry: a view from Stanford. Clin Chem 48:1819–1827
185. Cruz FC, Koya E, Guez-Barber DH, Bossert JM, Lupica CR, Shaham Y, Hope BT (2013) New technologies for examining the role of neuronal ensembles in drug addiction and fear. Nat Rev Neurosci 14:743–754
186. Guez-Barber D, Fanous S, Harvey BK, Zhang Y, Lehrmann E, Becker KG, Picciotto MR, Hope BT (2012) FACS purification of immunolabeled cell types from adult rat brain. J Neurosci Methods 203:10–18
187. Xiong L, Shuhendler AJ, Rao J (2012) Self-luminescing BRET-FRET near-infrared dots for in vivo lymph-node mapping and tumour imaging. Nat Commun 3:1193
188. Wu PJ, Kuo SY, Huang YC, Chen CP, Chan YH (2014) Polydiacetylene-enclosed near-infrared fluorescent semiconducting polymer dots for bioimaging and sensing. Anal Chem 86:4831–4839
189. Guo Y, Li Y, Yang Y, Tang S, Zhang Y, Xiong L (2018) Multiscale imaging of brown adipose tissue in living mice/rats with fluorescent polymer dots. ACS Appl Mater Interfaces 10:20884–20896
190. Cao F, Guo Y, Li Y, Tang S, Yang Y, Yang H, Xiong L (2018) Fast and accurate imaging of lymph node metastasis with multifunctional near-infrared polymer dots. Adv Funct Mater 28:1707174
191. Wang S, Liu J, Feng G, Ng LG, Liu B (2019) NIR-II excitable conjugated polymer dots with bright NIR-I emission for deep in vivo two-photon brain imaging through intact skull. Adv Funct Mater 29:1808365
192. Tsai WK, Wang CI, Liao CH, Yao CN, Kuo TJ, Liu MH, Hsu CP, Lin SY, Wu CY, Pyle JR, Chen J, Chan YH (2019) Molecular design of near-infrared fluorescent Pdots for tumor targeting: aggregation-induced emission versus anti-aggregation-caused quenching. Chem Sci 10:198–207

Aggregation-Induced Emission (AIE) Probes for Cell Imaging

Engui Zhao and Xinggui Gu

1 Introduction

Fluorescent materials are gaining increasing attention from biological researchers. By endowing the transparent biological subjects with distinct fluorescence signal, fluorescent materials highlight the targets with increased contrast, and thus enable visualizing subcellular structures and tracking of their biological processes. Organic fluorescent materials are widely used in biological researches, due to their advantageous properties of simple operation, good biocompatibility, and large structural diversity and emission variety.

However, most organic fluorescent probes are used molecularly and can be easily photobleached by continuous irradiation of excitation light. Increasing their working concentration can relieve the problem, but also results in fluorescence quenching due to the aggregation-caused quenching (ACQ) effect. ACQ effect was firstly disocovered by Förster and Kasper in 1954, which describes the emission properties of most conventional luminogens. Materials with ACQ effect emit intensely in their solutions, but show decreased emission intensity when they agglomerate together to form aggregates. Taking *N*,*N*-dicyclohexyl-1,7-dibromo-3,4,9,10-perylenetetracarboxylic diimide (DDPD) as an example (Fig. 1a), it fluoresces brightly when molecularly dissolved in a THF solution [1]. However, its fluorescence is quenched gradually with the increase in the volume ratio of the poor solvent of DDPD (water), demonstrating the phenomenon of ACQ. The mechanism governing ACQ effect has been well studied. Most conventional luminogens are disc-shaped. The disc-shaped molecules experience strong π–π stacking interactions (Fig. 1b), which promote the formation of aggregates. The excited states of the aggregates often favor the formation of excimeric species that decay through non-radiative relaxation pathways [2–6]. The ACQ effect is a great hurdle for the practical applications of these fluorescent materials, as luminophores are often used in the solid state, for example, as thin films in organic light-emitting diodes (OLEDs). Besides, most conventional luminophores, including these for medical diagnosis, contain hydrophobic aromatic rings. Such hydrophobic molecules tend to form aggregates in aqueous solutions and thus suffer from the ACQ effect. Great effort has been devoted to migrate the ACQ effect. Chemists introduced bulky wedges to aromatic ring to inhibit intermolecular interactions, while chemical engineers physically encapsulated the fluorophores with amphiphilic surfactants or dispersed the

E. Zhao
School of Chemical Engineering and Energy Technology, Dongguan University of Technology, Dongguan, China
e-mail: zhaoeg@dgut.edu.cn

X. Gu (✉)
Beijing Advanced Innovation Center for Soft Matter Science and Engineering, Beijing University of Chemical Technology, Beijing, China
e-mail: guxinggui@mail.buct.edu.cn

F.-G. Wu (ed.), *Fluorescent Materials for Cell Imaging*, https://doi.org/10.1007/978-981-15-5062-1_8

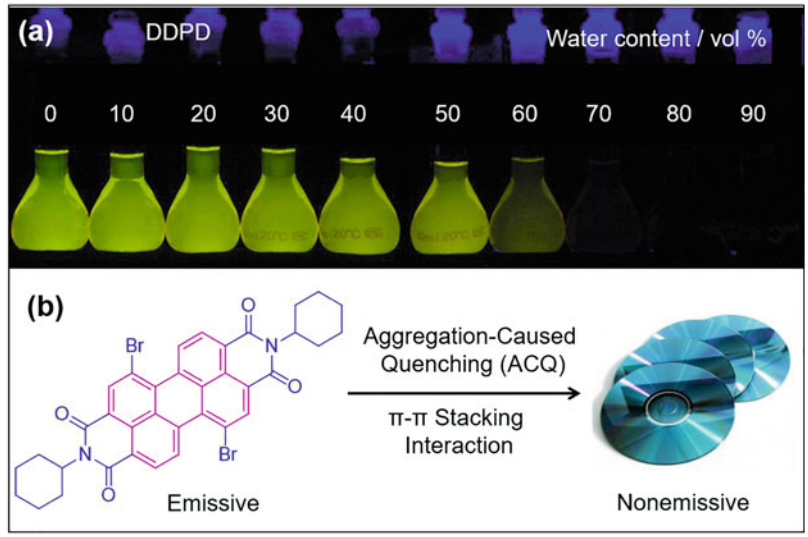

Fig. 1 (**a**) Fluorescence photographs of a luminophore with ACQ effect (DDPD) in THF/water mixtures with different water contents. (**b**) The disc-shaped DDPD molecules are non-fluorescent in the aggregated state because of the involved strong π–π stacking interaction. Reprinted with permission from Ref. [1]. Copyright © 2011 The Royal Society of Chemistry

fluorophores in polymers to insulate the fluorophores [2]. In contrast with the tremendous effort spent is the limited outcome. The chemists suffered from synthetic difficulties, while engineers only obtained unsatisfactory performances due to insulator and phase disengagement. Since aggregation is a natural inherent effect, fighting against the effect will be a tough journey. It would be helpful and cheerful if a fluorescent material can emit light in its aggregated state.

2 Aggregation-Induced Emission (AIE) Effect: Phenomenon and Mechanism

In 2001, Tang et al. observed a phenomenon that was completely opposite to the ACQ effect [1, 7, 8]. A species of propeller-shaped molecules emit weakly in their solutions, but are triggered to fluoresce intensely upon forming aggregates. They termed the phenomenon as aggregation-induced emission (AIE) effect [7]. Such luminogens with AIE attributes have been referred to as AIEgens. Typical examples of AIEgens are hexaphenylsilole (HPS) and tetraphenylethylene (TPE). As shown in Fig. 2, HPS is non-emissive when its molecules are dissolved in a good solvent, such as tetrahydrofuran (THF) or a THF/water mixture with a water fraction (f_w) of lower than 80 vol% [9]. Its fluorescence is turned on when f_w reaches 80 vol%. Further increasing water content leads to dramatically intensified emission, because of the more compact packing of these molecules in the aqueous mixtures with poor solvating power.

Such AIEgens with strong solid-state or aggregated-state emission perfectly solve the ACQ problems and may lead to technological innovation in the application field of fluorescence. Thus, there have been stirring of research interest in this area and increasing research effort has been spent to explore the underlying mechanism and potential applications of AIEgens. The former uncovered the working principles of AIEgens and built up the structure–property relationship of AIEgens, while the latter enriched the species of AIEgens and widened their application fields.

With the great research endeavor, the mechanism governing the AIE effect was uncovered. Fundamental physics teaches us that any molecular movements (rotation, vibration, etc.) consume energy [8]. The four phenyl peripheries in TPE can dynamically rotate with respect to the double bond (Fig. 3). In dilute solutions, the active intramolecular rotation can consume the excited-state

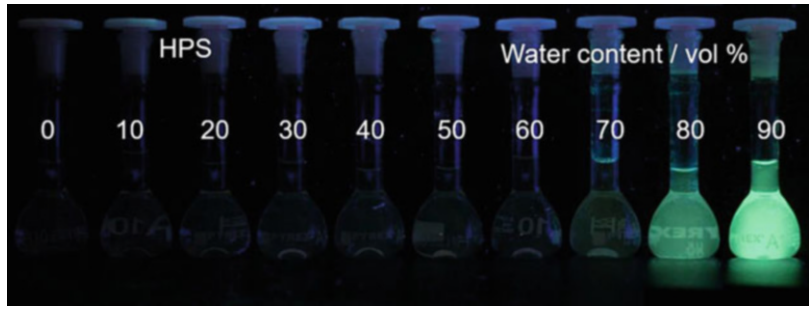

Fig. 2 Fluorescence photographs of HPS in THF/water mixtures with different water contents. Reprinted with permission from Ref. [9]. Copyright © 2014 WILEY-VCH Verlag GmbH & Co. KGaA, Weinheim

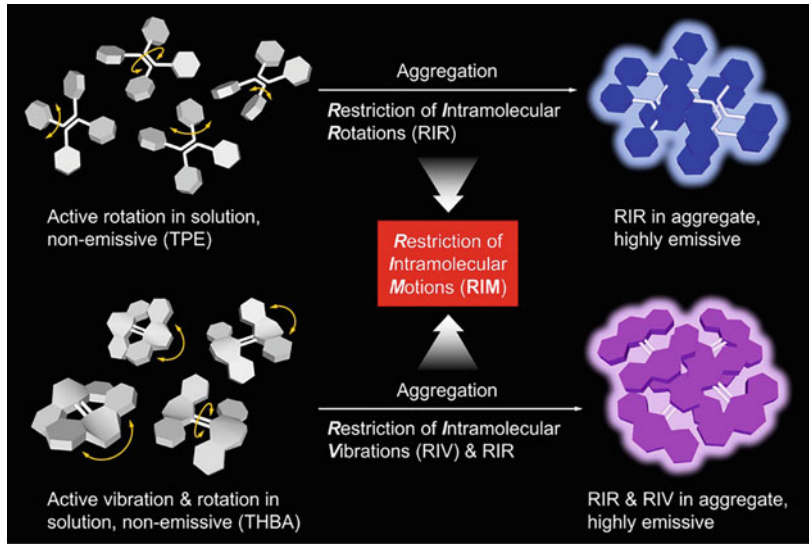

Fig. 3 Illustration on the RIR process of TPE and the RIV process of THBA

energy through non-radiative relaxation pathway and thus quenches the fluorescence of TPE. In the aggregated state, however, such rotation is restricted due to the physical constraint from adjacent molecules. Besides, there is no π–π stacking interaction due to the propeller-like conformation of these molecules. Thus, the non-radiative relaxation pathway is blocked and excitons are allowed to decay radiatively from the excited state. In general, AIE effect arises from restriction of intramolecular motions (RIM), which includes restriction of intramolecular rotations (RIR) and restriction of intramolecular vibrations (RIV) [10, 11].

The RIM process is in essence structural rigidification. Depending on molecular structure, luminescence pathways can be classified into several categories (Fig. 3). Propeller-shaped molecules such as HPS and TPE are AIE active due to the RIR process. 10,10′,11,11′-Tetrahydro-5,5′-bidibenzo[a,d] annulenylidene (THBA), a shell-like molecule with phenyl rings linked to a bendable flexure, can dynamically vibrate in solution, which effectively quenches the light-emitting process. Upon forming aggregates, the RIV process is activated, which turns on its fluorescence.

AIEgens are highly luminescent, photostable, and biocompatible and are thus promising for bioimaging applications. Generally, they enjoy the following advantages when applied in biological researches: (1) Low background emission: The non-emissive characteristic of AIEgens in the solution state provides low background emission in imaging applications, which greatly increases the sensitivity in sensory applications

and elevates the resolution. (2) Simple structural design: Anything that activates the RIM process can be utilized in the molecular design of AIEgens. By attaching recognition groups to AIEgens, biological sensors can be easily achieved. (3) High brightness: When fabricated into particles or bound to targets, AIEgens emit strong light under photoexcitation, making them ideal candidates for deep-tissue imaging. (4) Excellent photostability: The particles fabricated from AIEgens are more resistant to photobleaching than molecular probes. The good photostability of AIEgens is highly advantageous in tracking biological processes and conducting photo-therapeutic applications. (5) Good biocompatibility: The good biocompatibility ensures their in situ workability. Inspired by the bright future of employing AIEgens in solving the biological problems, lots of applications have been made with the AIEgens. We selected some representative examples to illustrate how these AIEgens contribute to biological researches.

3 AIE Materials for Imaging of Subcellular Structures

3.1 Mitochondrion Imaging

Mitochondrion is the powerhouse of cells and plays a vital role in their life and death. In mitochondria, a large number of proteins and enzymes exist and extract energy from the sugar and fat in the form of ATP, without which cell metabolic and normal functions are impossible. The large numbers of proteins and enzymes inside the cells are also responsible for maintaining the morphology of mitochondria. Abnormal morphology of mitochondria is indicative of its unhealthiness and malfunctions, thus tracking the morphology changes of mitochondrion may provide insight for mitochondrial healthiness.

Tang et al. construct a mitochondrial stain (TPE-TPP; Fig. 4a) by attaching triphenylphosphonium groups to TPE, which endow the TPE core with positive charges [12]. The large negative-inside transmembrane potential (−180 mV) of mitochondria drives the positively charged TPE-TPP to the organelle. Upon irradiation of excitation light, these TPE-TPP become fluorescent and light up the mitochondria (Fig. 4b). The mitochondrion specificity of TPE-TPP is evaluated by costaining with MitoTracker Red® FM (MT) (Fig. 4c), a commercially available mitochondrial stain, and high colocalization coefficiency is obtained, which proves the high specificity of TPE-TPP towards mitochondria. With the AIE property, TPE-TPP exhibits high photostability (Fig. 4e). The signal loss of TPE-TPP after 50 scans is less than 10%, while the fluorescence signal of MT drops by 80% after six scans. The excellent photostability of TPE-TPP enables its potential applications in monitoring the dynamic motions of mitochondrion in real time. Besides, TPE-TPP exhibits good tolerance to the microenvironmental changes of mitochondria. Treating the cells with carbonyl cyanide m-chlorophenylhydrazone (CCCP) can decrease the mitochondrial transmembrane potential, thus MT loses its targeting in CCCP treated cells. However, TPE-TPP remains its specificity to mitochondrion in CCCP treated cells. The good photostability and tolerance to microenvironment change properties of TPE-TPP make it a potential candidate for tracking mitochondrion.

Inspired by this work, a number of new AIE-active mitochondrion-specific probes are obtained by constructing AIEgens with positive charges and selected examples are shown in Fig. 5. By directly conjugating a pyridinium salt to TPE, TPE-Py (Fig. 5a) is obtained [13]. The pyridinium salt with positive charge is strongly electron-withdrawing, while TPE is moderately electron-donating. The donor–acceptor interaction lowers the energy gap and leads to the bathochromic shift in both absorption and emission spectra. Attracted by the negative-inside transmembrane potential of mitochondria, TPE-Py can enter the cell and selectively light up the mitochondria with yellow fluorescence and in high contrast (Fig. 5b). When TPE-Py is costained with MT, the fluorescence signal of TPE-Py overlaps perfectly with that of MT,

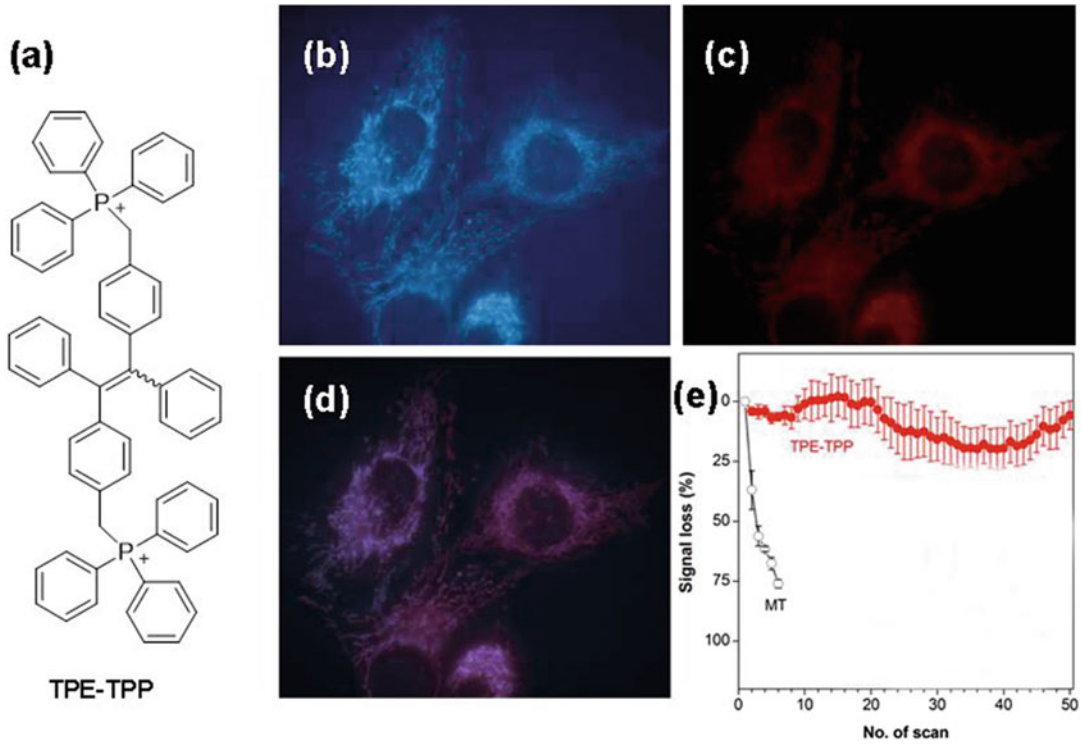

Fig. 4 (**a**) Molecular structure of TPE-TPP. (**b**–**c**) Fluorescence images of HeLa cells costained with (**b**) TPE-TPP (5 μM) for 1 h and (**c**) MT (50 nM) for 15 min. (**d**) Merged image of (**b**, **c**). (**e**) Change of fluorescence intensity with number of scans. Reprinted with permission from Ref. [12]. Copyright © 2013, American Chemical Society

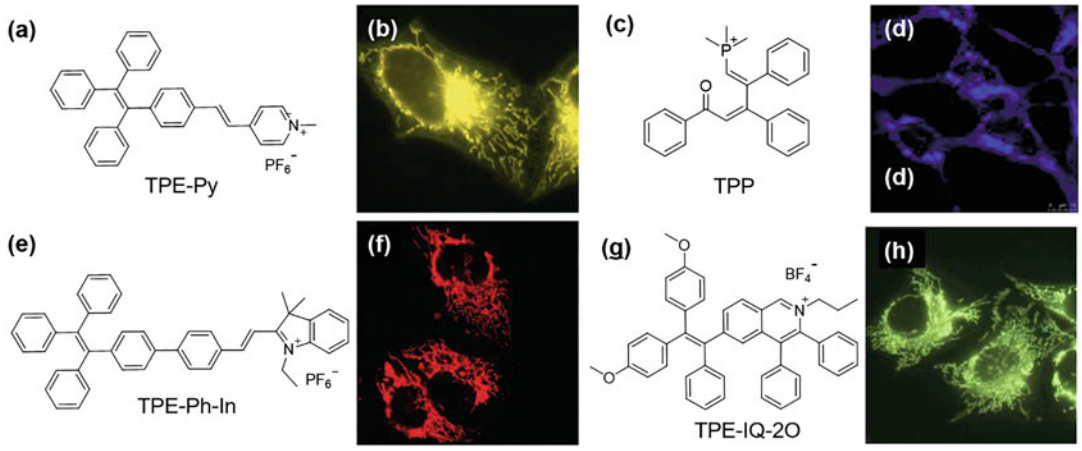

Fig. 5 (**a**, **c**, **e**, **g**) Molecular structures of (**a**) TPE-Py, (**c**) TPP, (**e**) TPE-Ph-In, and (**g**) TPE-IQ-2O. (**b**, **d**, **f**, **h**) Fluorescence images of (**b**) HeLa cells stained with TPE-Py, (**d**) HEK-293 cells stained with TPP, (**f**) HeLa cells stained with TPE-Ph-In, and (**h**) HeLa cell stained with TPE-IQ-2O. Reprinted with permission from Ref. [13]. Copyright © 2014, Royal Society of Chemistry. Reprinted with permission from Ref. [14]. Copyright © 2013 Elsevier B.V. All rights reserved. Reprinted with permission from Ref. [15]. Copyright © 2014, Royal Society of Chemistry

which proves the mitochondrial targeting of TPE-Py. In addition, TPE-Py also demonstrates very good photostability, with only 30% drop in emission intensity after continuous irradiation for 180 s, while MT loses 80% of its fluorescence owing to photobleaching. Gong and Ning et al. construct a conjugated phosphonium salt (TPP, Fig. 5c), which also demonstrates mitochondrial specificity (Fig. 5d) [14]. TPP selectively accumulates in the mitochondria of HEK-293 cells. Tang et al. construct a red AIE probe with mitochondrial specificity, TPE-Ph-In (Fig. 5e) and employ it for the evaluation of mouse sperm vitality [15]. Energetic sperms exhibit bright red fluorescence, while unvital mouse sperms emit faintly or demonstrate even no red fluorescence. That is because energetic cells maintain larger mitochondrial transmembrane potential to generate more ATP and thus attract more TPE-Ph-In molecules than unvital sperms. Another probe, TPE-IQ-2O (Fig. 5g) also demonstrates sensitivity to mitochondrial transmembrane potential.[16] As cancerous cells possess larger mitochondrial transmembrane potential than normal cells, TPE-IQ-2O selectively stains cancerous cells. Moreover, as TPE-IQ-2O can sensitize the generation of reactive oxygen species, which is toxic to cells. TPE-IQ-2O is employed to selectively kill cancerous cells over normal cells by photodynamic therapy.

Tang et al. report a photoactivable probe, *o*-TPE-ON+, with mitochondrial specificity [17] and apply it in super-resolved imaging. *o*-TPE-ON+ undergoes photocyclodehydrogenation reaction to form a more conjugated structure, *c*-TPE-ON+ with bright fluorescence (Fig. 6a). *o*-TPE-ON+ emits faintly in both solution and aggregated states due to the intermolecular motions of phenyl rings and twisted intramolecular charge transfer (TICT) effect. Upon photoirradiation, photocyclodehydrogenation reaction takes places [18], and *o*-TPE-ON+ is

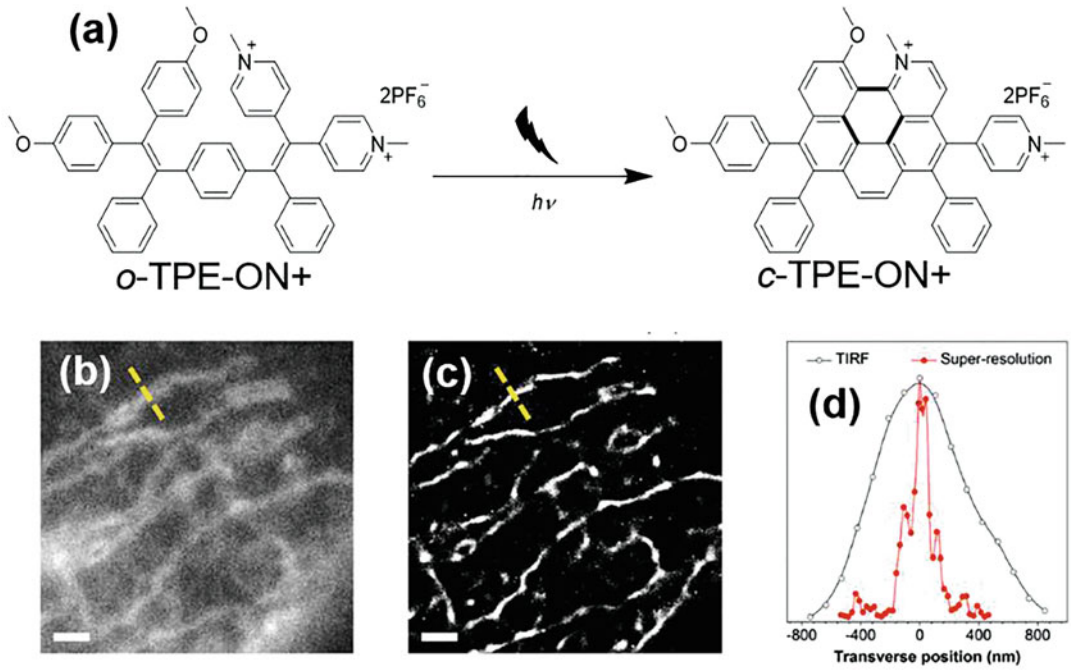

Fig. 6 (**a**) Photocyclodehydrogenation process of *o*-TPE-ON+. (**b**) Diffraction-limited TIRF image of a fixed HeLa cell with totally blurred structure. (**c**) Super-resolution image in the same region as (**b**). (**d**) Fluorescence intensity profiles of the single mitochondrion along the yellow dotted line marked in the images (**b**) and (**c**). Scale bar: 2 μm. Reprinted with permission from Ref. [17]. Copyright © 2016, WILEY-VCH Verlag GmbH & Co. KGaA, Weinheim

transformed to a strong emitter, *c*-TPE-ON+, and thus lights up mitochondria in a photoactivation manner. *o*-TPE-ON+ is examined under a stochastic optical reconstruction microscopy (STORM) to evaluate its photoswitching ability and it exhibits spontaneous blinking under continuous illumination with 561 nm laser. By tracking the intensity trace of each single molecule, the photon counts are determined to be 411 per molecule per switching, and the fluorescence on-time is measured to be 26 ms. The high photon counts and low fluorescence on-time are beneficial for achieving high resolution. As *o*-TPE-ON+ is mitochondrial specific, it is used for examining the morphology of mitochondria. With diffraction-limited total internal reflection fluorescence (TIRF) technique, only blurred image could be achieved (Fig. 6b), while STORM reveals the precise structure of mitochondrial (Fig. 6c). The transverse profile of a single mitochondrion is determined to be 697.1 nm with epifluorescent image and 104.5 nm with super-resolution image (Fig. 6d). As compared with previous photoactivation mechanism, this photocyclodehydrogenation reaction does not require any additives, such as thiols or oxygen scavenger, which are commonly applied in STORM. This enables *o*-TPE-ON+ to be applied in live-cell imaging. By continuous monitoring of the mitochondria, their dynamic fission and fusion processes are visualized in real time and with high resolution.

3.2 Nucleus Imaging

Nucleus is the organelle where genetic materials are held in eukaryotic cells. The genetic materials inside nucleus contain all the information that determines the structure and nature of cell substances. The function of nucleus is to maintain the integrity of these genetic materials and to control the activities of cell by regulating gene expression. Investigation on cell nucleus is thus of paramount importance. Clinical detection of nucleic acid is also very important, due to its implications in genetic engineering, forensics, and bioinformatics. Fluorescent probes that can detect DNA and image cell nucleus are thus hot pursuit of researchers.

Zhou et.al report a new AIEgen (FcPy, Fig. 7a) for nucleic acid detection and cell nucleus

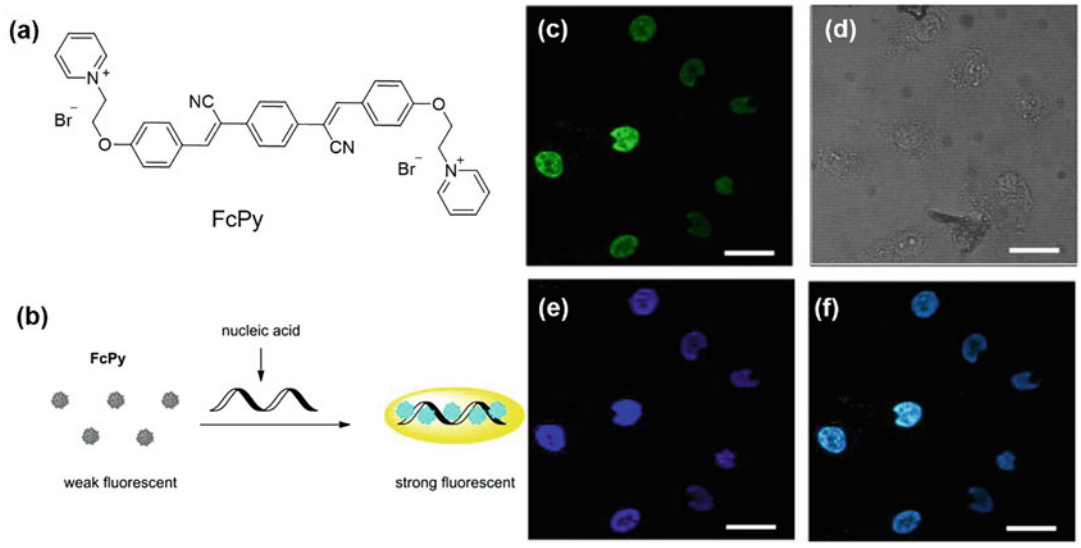

Fig. 7 (**a**) Molecular structure of FcPy. (**b**) Illustration of the fluorescence turn-on detection of nucleic acid. (**c**, **e**) Fluorescence images of HeLa cells stained with (**c**) FcPy and (**e**) Hoechst 33258. (**d**) Bright-field image of HeLa cells. (**f**) Merged image of (**c**) and (**e**). Scale bars: 20 μm. Reprinted with permission from Ref. [19]. Copyright © 2014, Elsevier Ltd. All rights reserved

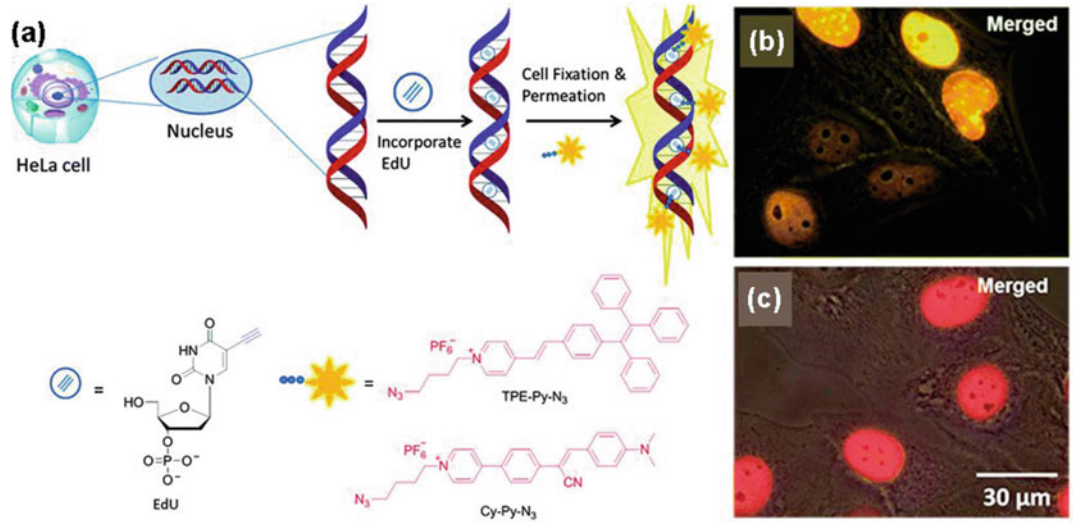

Fig. 8 (**a**) Illustrations of DNA synthesis detection by AIEgen through EdU assay. (**b**, **c**) Merged images of bright-field and fluorescence images of fixed HeLa cells stained with (**b**) TPE–Py–N_3 and (**c**) Cy–Py–N_3 in Tris buffer for 30 min. Reprinted with permission from Ref. [20]. Copyright © 2015 The Royal Society of Chemistry

imaging [19]. FcPy binds to both DNA and RNA in a fluorescence turn-on manner (Fig. 7b) along with hyperchromic shift of its emission peak from 505 nm to 475 nm. FcPy has no selectivity towards DNA and RNA, but its detection range towards RNA is larger than that of towards DNA. FcPy can also be applied as nucleic acid stain in gel electrophoresis and the detection limit is determined to be 1 μg. Interestingly, FcPy can enter cell and accumulate in nucleus region. To demonstrate the nucleus targeting of FcPy, HeLa cell is costained with FcPy and Hoechst 33258, which is a widely used cell nucleus probe. The fluorescence image from these two probes overlaps very well, which proves the nucleus targeting of FcPy (Fig. 7f).

During cell proliferation, DNA duplicates to ensure that each new cells can obtain correct number of chromosome. During the DNA replication process, nucleotides are necessary building blocks for new DNAs. Taking advantages of the DNA replication process, Tang et al. report another strategy to investigate nucleus activity [20]. Acetylene functionalized deoxyuridine (5-ethynyl-2′-deoxyuridine, EdU) is utilized for cell culture, and thus EdU can be incorporated into the DNA of cells (Fig. 8a). Afterwards, the cells are fixed, and azide functionalized AIEgens can be employed to react with the EdU. After washing away the unbounded fluorescent molecules, bright emission can be observed in the cell nucleus. By changing the core of the AIEgen, two probes TPE-Py-N_3 and Cy-Py-N_3 are obtained, which endow cells with yellow and red fluorescence, respectively, after the EdU assay. Thanks to the AIE characteristics of these fluorophores, the cells demonstrate high brightness and good photostability, which is superior to commercially available Alexa-azide dyes.

3.3 Lysosome Imaging

Lysosome is a type of membrane-bound organelle that is present in animal cells. It contains acid hydrolases, which can digest macromolecules. With these acid hydrolases, lysosome uptakes the duty of recycling nutritions from useless or dysfunctional cell components, as well as digesting foreign molecules. Meanwhile, increasing evidences have shown that lysosomes are also involved in various pathologies including inflammation, tumor formation, and several neurodegenerative diseases. Thus, visualizing the lysosome is of great importance for investigating

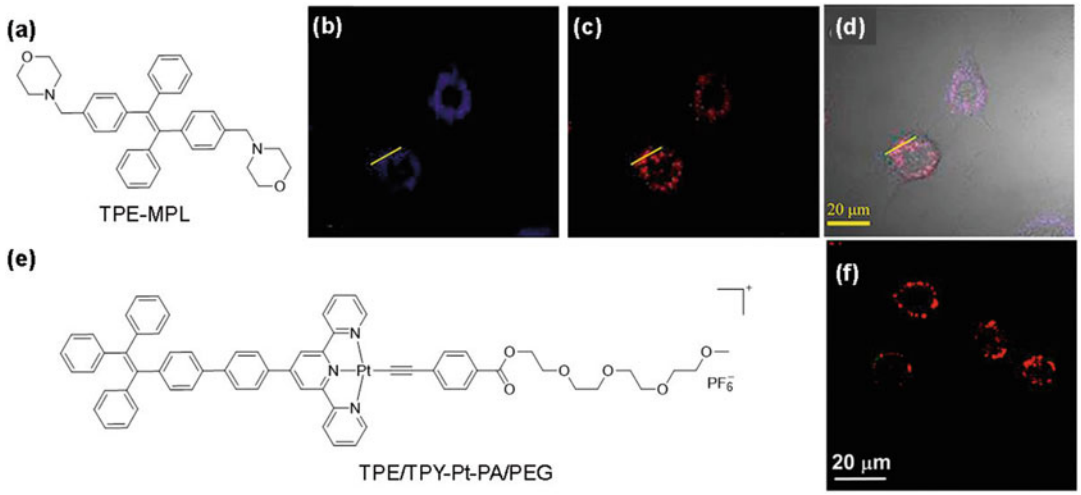

Fig. 9 (**a**, **e**) Molecular structures of TPE-MPL and TPE/TPY-Pt-PA/PEG, respectively. (**b**, **c**) Fluorescence images of L929 cells stained with (**b**) TPE-MPL (10 μM) for 30 min, (**c**) LysoTracker Red (LTR, 50 nM) for 30 min. (**d**) Merged image of panel **b** and panel **c** in bright field. λ_{ex}: 405 nm for TPE-MPL and 560 nm for LTR. (**f**) Merged fluorescence images of HeLa cells incubated with 100 nM LysoTracker Green for 30 min and 20 μM TPE/TPY-Pt-PA/PEG NPs. Reprinted with permission from Ref. [21]. Copyright © 2016, Elsevier Ltd. All rights reserved. Reprinted with permission from Ref. [22]. Copyright © 2018, Copyright © 2015 The Royal Society of Chemistry

intracellular metabolism and evaluating drug and gene delivery.

Liu et al. develop an AIE-active fluorogen for visualizing lysosome [21]. By attaching morpholine to TPE, TPE-MPL is obtained (Fig. 9a). With the weakly alkaline morpholine groups, TPE-MPL tends to accumulate in the lysosome of cells. The specificity of TPE-MPL towards lysosome is evaluated with a commercially available probe, LysoTracker Red (LTR), and high colocalization is obtained, indicative of the lysosome targeting of TPE-MPL. Besides, TPE-MPL demonstrates high photostability with less than 25% signal loss after 195 continuous scans, while LTR loses more than 75% of its fluorescence under the same treatment. Besides, TPE-MPL shows better tolerance to the pH change than LTR. Upon treating the cells with NH_4Cl, LTR loses its specificity, while TPE-MPL retains inside the lysosome. Such lysosome probe is expected to enable the accurate monitoring of lysosome activity.

Song, Qu, and Wong et al. report an AIE probe that fluoresces in the near-infrared region (Fig. 9e) [22]. TPE/TPY-Pt-PA/PEG can self-assemble to form nanoaggregates in aqueous solution. Upon incubation with HeLa cells, these nanoaggregates can enter the cells and accumulate in the lysosome of HeLa cells. The lysosome specificity of TPE/TPY-Pt-PA/PEG is proved by costaining with the commercially available probe LysoTracker Green. Besides, TPE/TPY-Pt-PA/PEG also demonstrates good biocompatibility, which enables its long-term tracking of cells and sheds light on the lysosome-storage associated diseases.

3.4 Lipid Droplet Imaging

Lipid droplets (LDs) are the main reservoir for neutral lipid storage and extensively exist in eukaryotic and prokaryotic cells. For a long period of time, lipid droplets have been simply regarded as a place for energy storage and deemed as an inert cell inclusion. However, the emergence of a series of LD proteins implies that the functions of LDs are more than lipid storage. Recent discoveries reveal that LDs are closely related to many metabolic diseases such as fatty

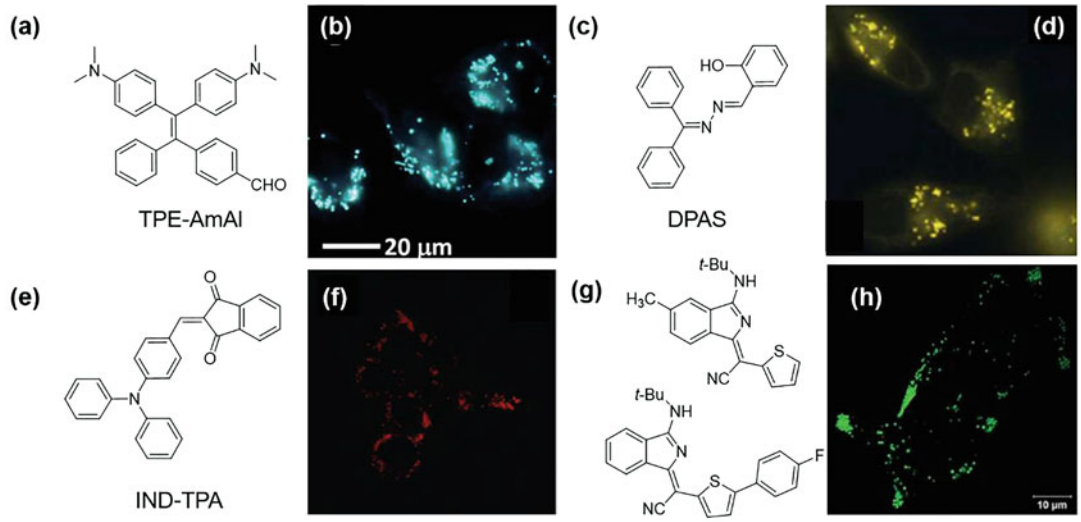

Fig. 10 (**a**, **c**, **e**, **g**) Molecular structures of lipid droplet specific bioprobes. (**b**, **d**, **f**, **h**) Fluorescence images of (**b**) HeLa cells stained with TPE-AmAl after treatment with 50 μM oleic acid for 6 h, (**d**) HeLa cells stained with DPAS for 15 min, (**f**) HCC827 cells stained with IND-TPA for 15 min, and (**h**) HeLa cells stained with 1H isoindole derivative (top in panel **g**) for 15 min. Reprinted with permission from Ref. [23]. Copyright © 2016, American Chemical Society. Reprinted with permission from Ref. [24]. Copyright © 2015 The Royal Society of Chemistry. Reprinted with permission from Ref. [25]. Copyright © 2017 The Royal Society of Chemistry

liver disease, atherosclerosis, type II diabetes, and hyperlipidemia. Monitoring and localizing the accumulation and abnormal level of LDs are thus of particular importance for biomedical research and early diagnosis.

Tang et al. develop a LD-targeting bioprobe (TPE-AmAl; Fig. 10a) that can be selectively delivered to the LDs of liver cells and light up the subcellular structure [23]. Compared with the widely used LD probe, Nile Red, TPE-AmAl demonstrates the advantages of low background, short staining time, high selectivity, excellent biocompatibility, and good photostability. In addition, it can also image the LDs in green algae, indicating its potential applications in the high-throughput screening of high-value microalgae as a preferential biofuel source. TPE-AmAl fluoresces in the blue region. Through molecular engineering, a series of AIE-active probes with yellow (DPAS, Fig. 10c) [24], red (IND-TPA, Fig. 10f) [25], and green (Fig. 10g up) [26] fluorescence are also reported.

Tang and Qin et al. report a photoactivable AIE probe for lipid droplet imaging [27]. DHAF does not emit light, but can easily undergo photo-oxidative dehydrogenation to form AF, which exhibits AIE characteristics (Fig. 11a). Interestingly, upon incubation with HCC827 cells, DHAF can pass through cell membrane and accumulate inside lipid droplets. Initially, no emission can be observed, since DHAF does not emit light. However, with continuous light irradiation, the emission from lipid droplets becomes increasingly brighter and the round-shaped lipid droplet can be distinguished obviously (Figs. 10d and 11b). Its specificity towards lipid droplet is proved by costaining with a commercially available lipid droplet probe, BODIPY493/503 Green, and high overlap coefficient of 0.99 is obtained. Besides, DHAF shows high photoactivation coefficiency, after three scans, the emission intensity is more than 200 times higher than of the control group. DHAF with easy preparation and cell uptake,

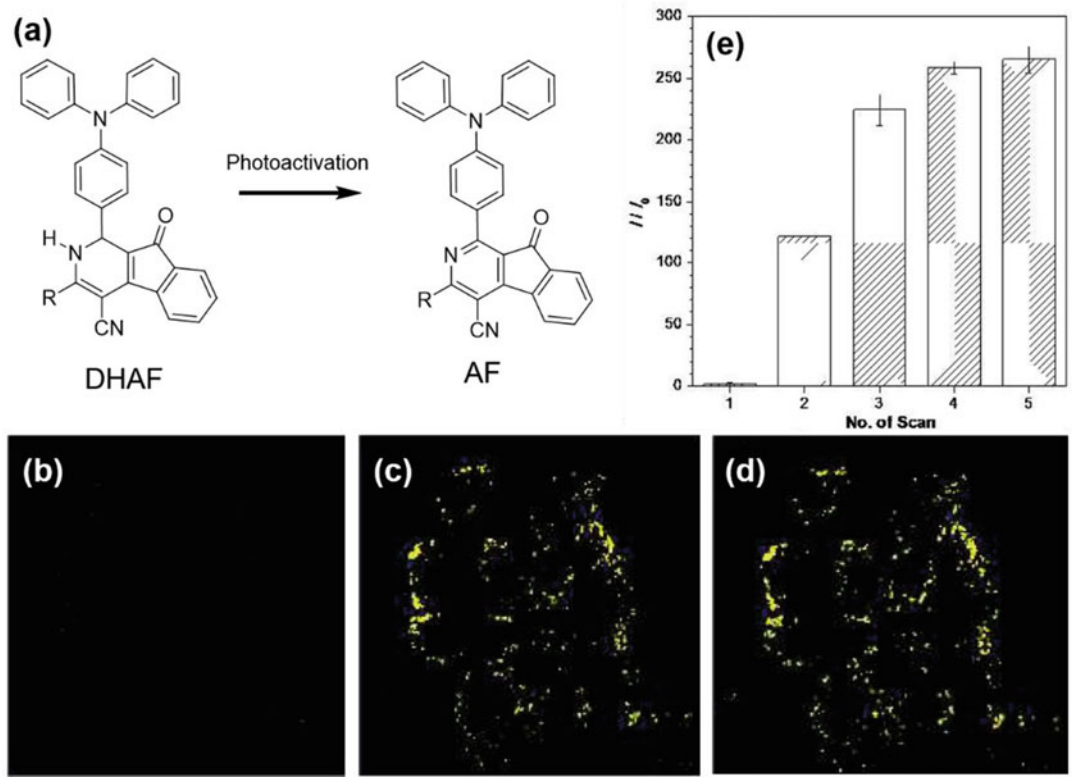

Fig. 11 (**a**) Illustration of the photoactivation process of DACF to AF. (**b**–**d**) Fluorescence images of live HCC827 cells taken under white light illumination and increasing scans at 405 nm with laser power of 1% (the scanning rate was 22.4 s per frame). The number of scan is (**b**) 1, (**c**) 3, (**d**) 5, respectively. (**e**) Plot of fluorescence enhancement (I/I_0) of HCC827 cells with number of scan

low cytotoxicity, and excellent photoactivation efficiency is expected to have broad applications in biological studies of LDs.

3.5 Cell Membrane Imaging

Cell membrane is a biological membrane that separates the interior of cells from outside environment, which protects the integrity of the interior of cell by allowing certain substances into the cell and keeping other substances out. Damage of cell membrane can lead to necrosis and is generally regarded as the benchmark of cell death. Cell membrane also maintains the shape of cell by anchoring cytoskeleton and groups cells together to form tissues by attaching to extracellular matrix. Besides, cell membrane is also associated with intercellular communication.

Li and his colleagues report a new AIE-active fluorophore (FD-9, Fig. 12a) that can selectively accumulate on cell membrane [28]. FD-9 is non-emissive in neither methanol nor THF. Addition of water into its methanol or THF solution can lead to aggregate formation and turn on its fluorescence, demonstrating a typical feature of AIE. Interestingly, FD-9 can selectively accumulate on cell membrane and light up the periphery of cell boundary. The high selectivity is proven by costaining with Dil, a widely used cell-membrane fluorescent probe. FD-9 also demonstrates the virtue attributes of good biocompatibility and excellent photostability. After incubation with FD-9 for 24 h, the viability of HepG-2 cell remains higher than 90%. The fluorescence intensity of cells stained by FD-9 remains higher than 50% of its initial intensity after continuous irradiation for 1500 s, while

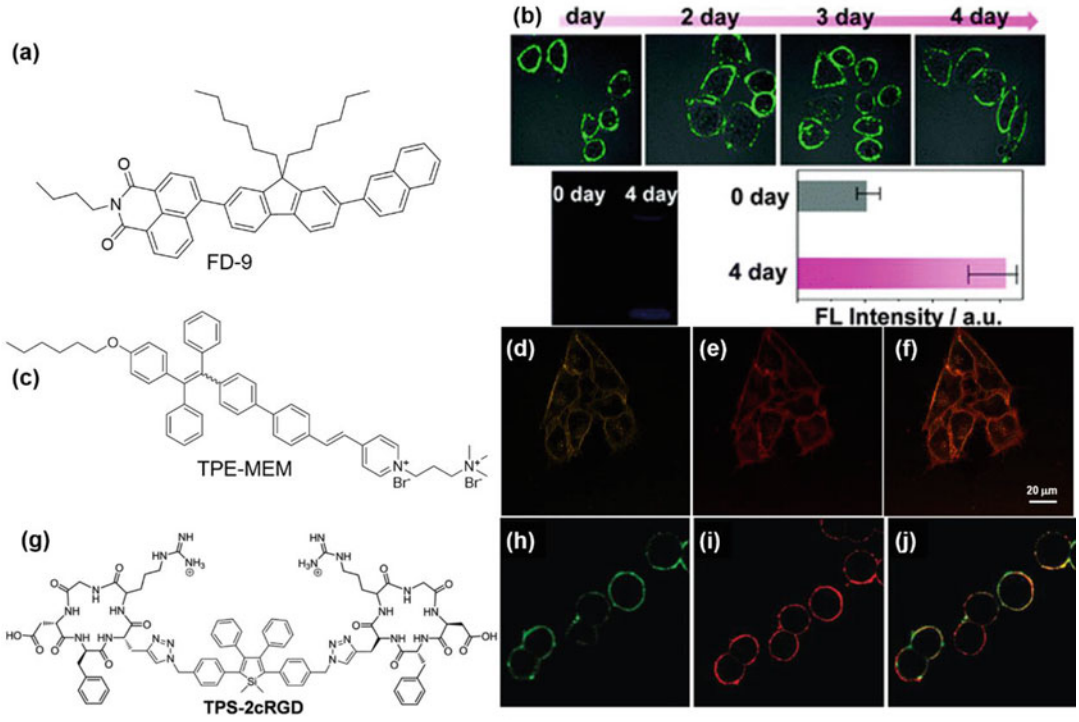

Fig. 12 (**a**, **c**, **g**) Molecular structures of FD-9, TPE-MEM, and TPS-2cRGD, respectively. (**b**) Merged images of fluorescence and bright-field image of HepG-2 cell stained with/without FD-9 and normalized fluorescence intensity of living HepG-2 cells incubated without FD-9 (0 day) and with FD-9 after 4 days. (**d**–**e**) Fluorescence images of HeLa cells stained with (**d**) TPE-MEM and (**e**) Cell Mask™ Deep Red plasma membrane stain. (**f**) Merged image of (**d**) and (**e**). (**h**–**j**) Fluorescence images of HT-29 cells stained by (**h**) TPS-2cRGD and (**i**) membrane tracker, with (**j**) their overlay images. Reprinted with permission from Ref. [28]. Copyright © 2013 Royal Society of Chemistry. Reprinted with permission from Ref. [29]. Copyright © 2019, American Chemical Society. Reprinted with permission from Ref. [30]. Copyright © 2012, American Chemical Society

Dil loses 65% of its signal after irradiation for 200 s. FD-9 also demonstrates high retainability on cell membrane. It can track the membrane of living cell for more than 100 h without decrease in specificity (Fig. 12b). The excellent biocompatibility, good photostability, and high cell-membrane retainability guarantee its feasibility in long-term tracking of cell membrane.

Tang et al. report an AIE-active probe for cell imaging [29]. By functionalizing TPE core with a hydrophobic alkyl tail and hydrophilic pyridium salt, TPE-MEM (Fig. 12c) mimics the structure of phospholipid and can easily enter and retain in the cell membrane. TPE-MEM is costained with Cell Mask™ Deep Red plasma membrane stain, a commercially available probe for cell membrane, and high colocalization coefficient is obtained, which proves its specificity. Interestingly, TPE-MEM demonstrates photosensitizing ability and can facilitate the production of reactive oxygen species and can be applied to photodynamic killing of cancer cells. Tang and Liu et al. report another strategy for cell membrane labeling [30]. cRGD recognizes and selectively binds to integrin $\alpha_v\beta_3$, which is overexpressed in plasma membrane of tumor cell of different origin. By conjugating cRGD to AIE fluorogen, tetraphenylsilole, TPS-2cRGD is obtained (Fig. 12g). By taking advantage of the AIE characteristics, the emission of TPE-2cRGD is turned on upon binding to integrin $\alpha_v\beta_3$. Such plasma membrane specific probe with AIE characteristics provides simple and economic solution to protein biomarker detection.

4 Long-Term Cell Tracking

By virtue of the strong solid-state emission of AIEgens, they can be easily fabricated into nanoparticles to prepare highly emissive AIE dots. Compared with molecular probes, AIE dots enjoy the following advantages: (1) Good photostability: Even if the molecules on the surface of AIE dots are photobleached by strong excitation light, the molecules inside AIE dots remain fluorescent. (2) Large variety: The surface of AIE dots can be facilely modified with different recognition groups to target different cell lines or subcellular structures. (3) Controllable in vivo retention: The size of AIE dots can be precisely controlled to manipulate their circulation time in the body of living animals. (4) Stimuli responsive: By controlling the particle formation and dissociation process, delivery and specific sensing can be realized.

Cell transplantation, migration, division, fusion, and lysis are important cell behaviors, which have great implications in studying cancer pathogenesis, invasion, and metastasis. Long-term tracking of cell is thus of great importance for both fundamental researches and practical applications. Long-term tracking studies, however, pose harsh requirement on the probes, such as excellent biocompatibility, good photostability, and semi-permanent immobilization inside the cell. In 2011, Tang et al. reported a cytophilic AIEgen (DEA-TPS; Fig. 13a) for long-term cell imaging [31]. DEA-TPS forms nanoparticles in aqueous solution. Once internalized into cells, DEA-TPS will stay inside live cells rather than leak out to the culture media, which enables its potential in long-term cell tracking. As shown in Fig. 13b, the fluorescence of HeLa cell stained by nanoaggregates of DEA-TPS pertains for more than four passages, while that of MitoTracker Green (MTG) only lasts for two passages. Because of their outstanding intracellular retention, the nanoaggregates of DEA-TPS inside a certain cell line do not leak out to contaminate cells of a different type in a co-culture system, hence permitting growth tracking of a specific cell line in complicated systems.

Recently, chitosan is functionalized with TPE, yielding bright chitosan (TPE-CS; Fig. 14a) [32]. TPE-CS inherits the AIE characteristic from TPE and thus demonstrates strong solid-state emission. TPE-CS is soluble in aqueous medium and can easily enter cells. Once inside the cell, they aggregate together to form large particles (Fig. 14b, c). These large particles cannot be externalized from cells, because their large

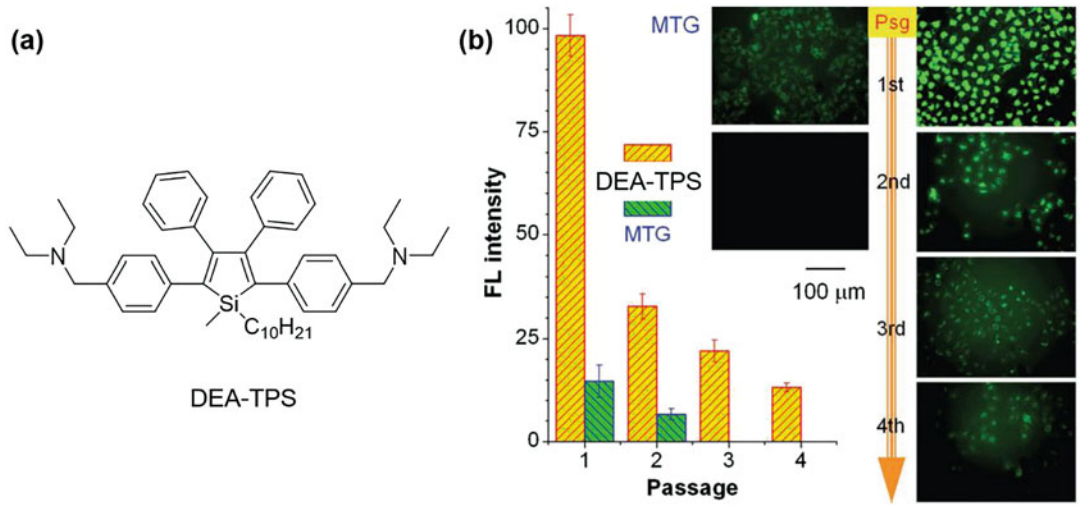

Fig. 13 (**a**) Molecular structure of DEA-TPS. (**b**) Fluorescence intensities and images of living HeLa cells stained by 5 μM of DEA-TPS and 200 nM of MTG at different passages (psg). Reprinted with permission from Ref. [31]. Copyright © 2011 WILEY-VCH Verlag GmbH & Co. KGaA, Weinheim

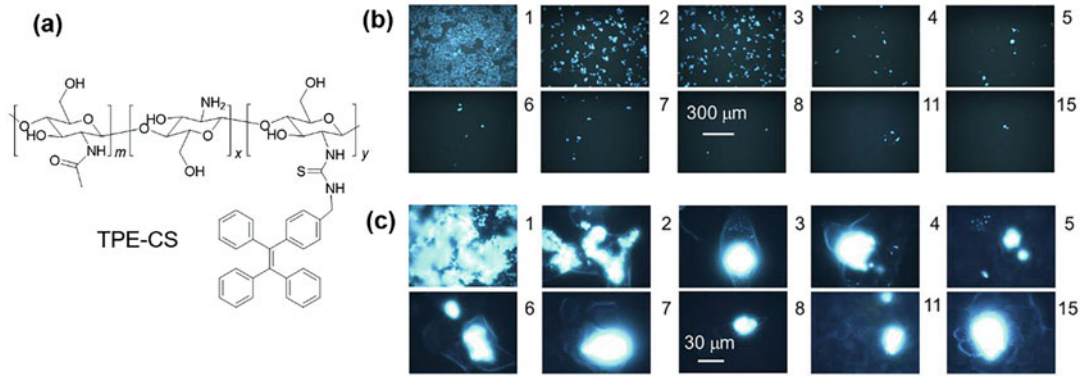

Fig. 14 (**a**) Molecular structure of TPE-CS. (**b**, **c**) Fluorescence images of HeLa cells stained by the aggregates of TPE-CS at different passages taken at magnifications of (**b**) × 100 and (**c**) × 1000. The numbers at the right side of images denote passages. Reprinted with permission from Ref. [32]. Copyright © 2013, American Chemical Society

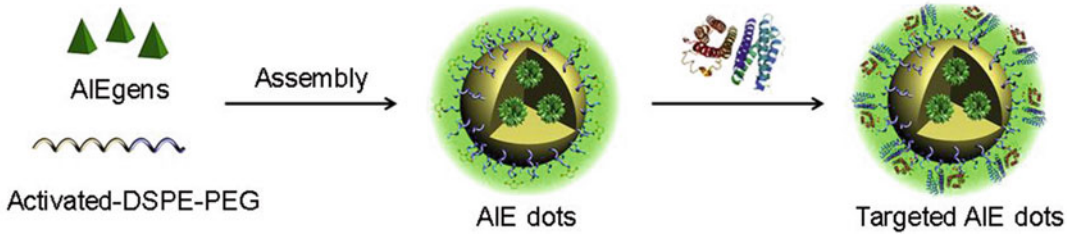

Fig. 15 Schematic diagram for fabrication of targeted AIE dots

size does not allow exclusion by exocytosis process. In addition, the β-(1-4) linkage between D-glucosamine is resistant to cleavage by the enzyme inside mammalian cells, so the big aggregates cannot be degraded. Thus, these aggregates can retain inside cell without decrease in size for quite a long period of time. During cell division process, the aggregates cannot be separated and thus cytoplasm distributes unevenly in the two cells, generating one highly emissive and one non-emissive cell. This guarantees that fluorescence is not diluted by cell division. Highly emissive cells can still be observed after 15 passages. Notably, after 15 passages, bright cells still exist, but it is very difficult to locate them from the large number of cells that are generated during cell division.

In the above two works of utilizing AIE dots for long-term cell imaging, the AIE dots are generated by either natural addition of their solutions into aqueous medium or allowing the soluble AIEgens to aggregate after entering cell, thus the size and targetability of these AIE dots are not well controlled. To resolve these issues, targeted AIE dots are designed and prepared. AIEgens are firstly encapsulated into lipid or bovine serum albumin (BSA) by means of the nanoprecipitation route (Fig. 15). The resulting AIE dots can be further decorated with functional groups to increase their cellular uptake or specificity, yielding targeted AIE dots. The AIE dots are highly luminescent, photostable, and biocompatible, and more importantly can retain inside the targeted cell without leakage for a long period of time. Such targeted AIE dots are promising for bioimaging applications.

By employing the method mentioned above, ultrabright AIE dots are obtained from BTPEBT (Fig. 16a), using DSPE-PEG2000 and DSPE-PEG2000-Mal as encapsulation agents [33]. The

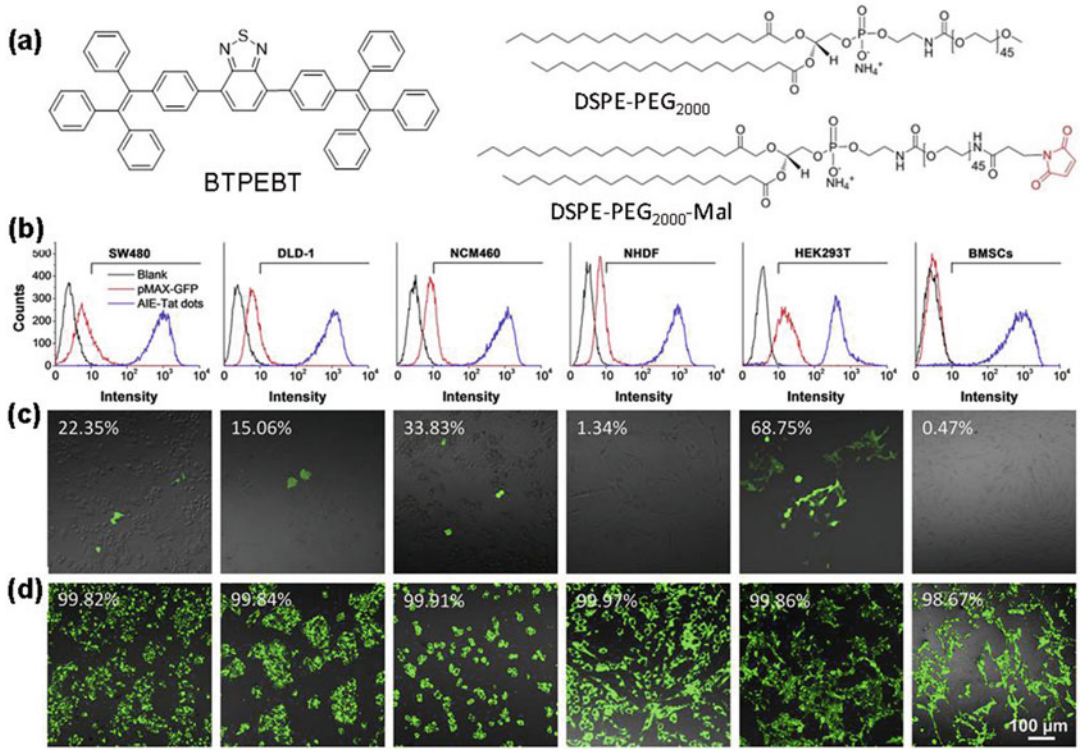

Fig. 16 (**a**) Molecular structures of BTPEBT, DSPE-PEG2000, and DSPE-PEG2000-Mal. (**b**) Flow cytometry histograms of different cell lines after GFP expression (red lines), AIE-Tat green dots staining (blue lines) or without treatment (black lines). (**c**, **d**) The corresponding fluorescence/transmission overlay images of (c) GFP expressed cells and (**d**) AIE-Tat green dots labeled cells, respectively. The fluorescence images in (**c**, **d**) are correlated to the flow cytometry results. Insets are labeling rates measured by flow cytometry. Reprinted with permission from Ref. [33]. Copyright © 2016, Elsevier Ltd. All rights reserved

maleimide group on the AIE dots can further react with the thiol group of HIV-1 transactivator of transcription (Tat) to increase the cellular uptake of AIE dots. The obtained AIE-Tat green dots demonstrate excellent biocompatibility, high cellular uptake, and long retention time inside cells. After incubation with 10 nM of AIE-Tat green dots for 48 h, the viability of HEK-293T remains higher than 90%. AIE-Tat green dots can label all the tested cell line with high labeling ratios of nearly 100%. Under similar conditions, GFP transfection only works well on HEK-293T with labeling efficiency of 70% and is less effective on other tested cell lines whose labeling efficiencies fall in the range of 0–30% (Fig. 16b). Their different performances in cell labeling can be clearly visualized under the fluorescence microscope. As shown in Fig. 16c, only a small fraction of cells are emissive after GFP transfection in most of the tested cell lines. However, after AIE-Tat green dots treatment, almost all the cells are endowed with green color (Fig. 16d). The high labeling efficiency of AIE-Tat dots enables their applications in almost all the cell lines without variation.

5 Intracellular Microenvironment Imaging

5.1 Intracellular pH

Even though the blood pH maintains rather stable within 7.35–7.45, the intracellular pH can vary from 4.7 in lysosome to 8.0 in mitochondria in a typical mammalian cell, arising from the

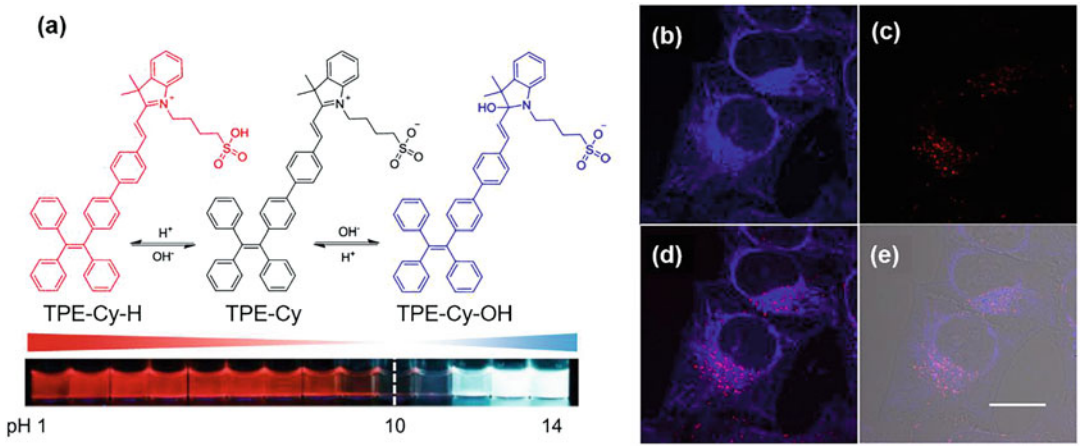

Fig. 17 (**a**) Fluorescence responses of TPE-Cy to pH changes. (**b**, **c**) Confocal images of HeLa cells stained with TPE-Cy taken under excitation of (**b**) 405 and (**c**) 488 nm, respectively. (**d**) Merged image of (**b**, **c**). (**e**) Merged image of (**d**) and its bright-field image. Scale bar: 20 μm. Reprinted with permission from Ref. [34]. Copyright © 2013, American Chemical Society

intracellular membrane structures, which divide the cell into small compartments. Abnormal pH is a hallmark of many common diseases such as cancer, stroke, and Alzheimer's disease. Sensing and monitoring pH changes inside the living cells are thus of great importance for studying cellular metabolisms and gaining insights into the physiological and pathological processes.

Recently, a pH sensitive AIEgen (TPE-Cy; Fig. 17a) composed of TPE and cyanine (Cy) units is prepared [34]. In acidic conditions, TPE-Cy is protonated (TPE-Cy-H) and its solubility is decreased, resulting in its aggregation in these solutions. In alkaline solutions, addition of hydroxyl group breaks the conjugation of Cy group (TPE-Cy-OH) and the strong donor–acceptor interaction between TPE and Cy is destroyed, resulting in a new emission peak in the blue region (Fig. 17a). In this way, TPE-Cy shows ratiometric response to a broad range of pH values without suffering from the ACQ effect.

TPE-Cy is an amphiphilic molecule and can enter cells easily. Once entered cells, the pH transition point of fluorescence is shifted from extracellular pH 10 to intracellular pH 6.5, presumably due to its interaction with the lipids inside cells, and a linear relationship of its fluorescence intensity with pH is established in the physiological range (pH 5.0 ~ 7.4). Such a broad range of fluorescence response and dramatic fluorescence change facilitate full-range intracellular pH sensing in a ratiometric manner. TPE-Cy can enter most of the organelles inside the cell, but exhibits different fluorescence response. In acidic lysosome, it fluoresces in the red region, while in other organelles it emits blue light. By employing different excitation and emission channels, lysosome can be differentiated from other organelles (Fig. 17b–e). In addition, the overall intracellular pH can be sensed by TPE-Cy. Through adjusting the pH of buffer solution, the intracellular pH can be tuned and the change of intracellular pH can be facilely determined by tracking the fluorescence of TPE-Cy. The fluorescence responses are monitored by using fluorescence microscope as well as flow cytometry. All these attributes endow TPE-Cy the potential for high-resolution and high-throughput analysis of intracellular environments, which may find an array of biomedical applications in cancer diagnosis and drug screening.

5.2 Intracellular Viscosity

Determination of intracellular viscosity is of crucial importance for the investigation of many biological processes. It controls the speed of

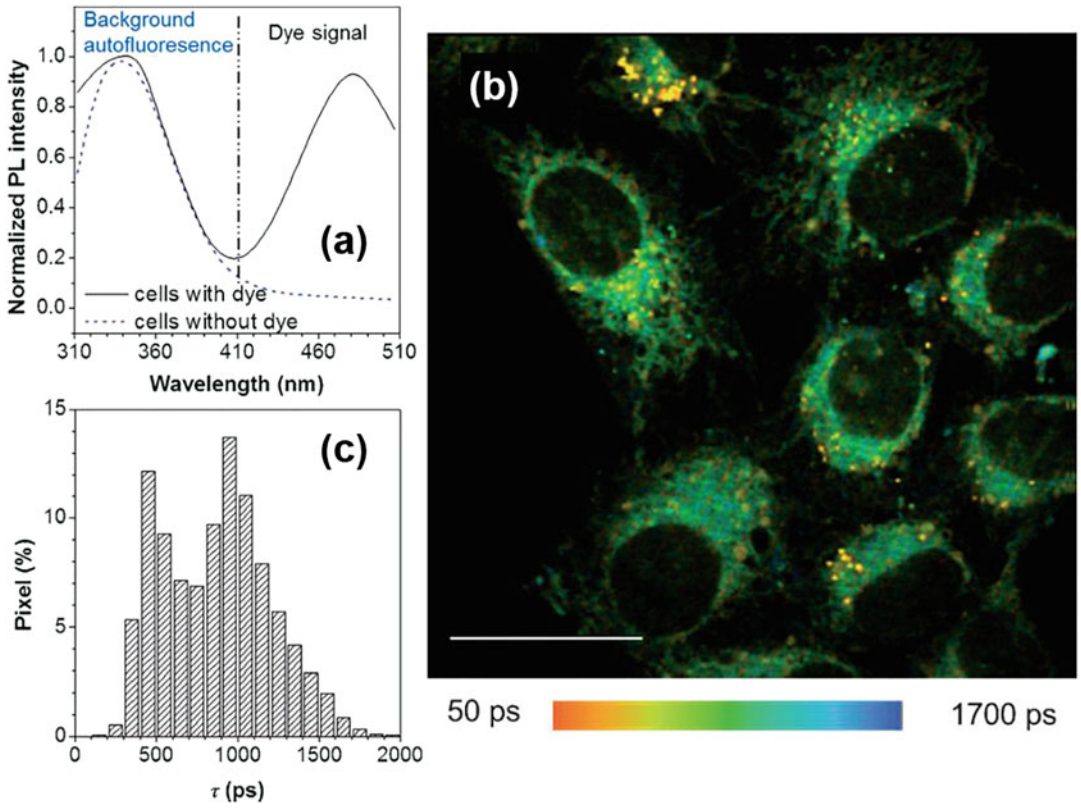

Fig. 18 (**a**) Comparison of photoluminescence signals from cell autofluorescence and cells stained with TPE-Cy upon two-photon excitation. (**b**) Fluorescence lifetime imaging microscopy images and (**c**) fluorescence lifetime distribution histogram of HeLa cells stained with TPE-Cy. Scale bar: 30 mm. Two-photon excitation wavelength: 600 nm. Reprinted with permission from Ref. [35]. Copyright © 2015 WILEY-VCH Verlag GmbH & Co. KGaA, Weinheim

biomass transportation as well as signal transduction in living systems. The changes in the intracellular viscosity have been regarded as indicators for a large variety of diseases such as atherosclerosis, diabetes, and Alzheimer's disease.

Recently, an AIE bioprobe (TPE-Cy, Fig. 17a) is applied to map the intracellular viscosity distribution [35]. Viscosity influences the rotational motion of TPE-Cy and it exhibits varied brightness and fluorescence lifetimes in different cellular environments. In cellular environment with high viscosity, its emission is intense with long lifetime, while in the low-viscosity environment, its emission is weak with short lifetime. In this way, information on the intracellular viscosity distribution can be transformed to fluorescence signal, which is valuable for identification of the health status of cell. As shown in Fig. 18a, the fluorescence signal of TPE-Cy can be clearly distinguished from autofluorescence in the visible light region under 600 nm two-photon excitation. Once entered cells, TPE-Cy is mainly located at membrane-bound organelles such as mitochondria and lipid droplets. In different subcellular organelles, it displays varied lifetime from 300 ps to 1500 ps. In the organelles with loose packing of phospholipid, such as lipid droplet, its lifetime is short (~500 ps), while in the organelles with tight packing of the phospholipid, such as mitochondria, its lifetime is long (~1000 ps). The broad distribution of the lifetime of TPE-Cy in different organelles reflects their different fluidity of the microenvironments. This method can be applied in other biological systems

as well as in screening drugs that can alter the intracellular viscosity.

6 Intracellular Substance Imaging

6.1 Imaging of Reactive Oxygen Species

Reactive oxygen species (ROS) are a species of chemically reactive molecules that contain oxygen, which play important roles in regulating physiological events in living organism. The amount of ROS in living organism should be maintained in a reasonable range. Overproduced ROS may lead to a number of diseases, such as cancer, neurodegenerative diseases, and inflammation. Detection of ROS level may thus provide insight into these physiological processes. Superoxide is one of the ROS and is generally considered to be the precursor of other ROS, including hydroxyl radical and hydrogen peroxide. Besides, superoxide is also actively involved in cell signaling process. Therefore, it is very essential to design and develop appropriate analysis tools for the detection of the superoxide anion in cells.

Hua et al. develop a near-infrared AIE-active fluorescence probe, BDP (Fig. 19a), for superoxide detection [36]. BDP is a weak emitter, due to the presence of cationic pyridium group, which leads to strong intramolecular charge transfer and fluorescence quenching. Reaction with superoxide changes the cationic pyridium group to neutral pyridium group (BD). BD with reduced intramolecular charge transfer effect fluoresces intensely with emission peak at 716 nm. Since the reaction is highly selective, other ROS or metal ion does not interference with the detection of superoxide. BDP shows good biocompatibility and is applied to imaging the superoxide in cells. Normal cells possess low superoxide concentration, so the cells are non-emissive (Fig. 19b–d). Phorbol-12-myristate-13-acetate (PMA) can elevate the superoxide level in cells, thus BDP stained HepG2 cells show increased fluorescence after incubation with PMA, which further proves that BDP can detect superoxide in cells. During

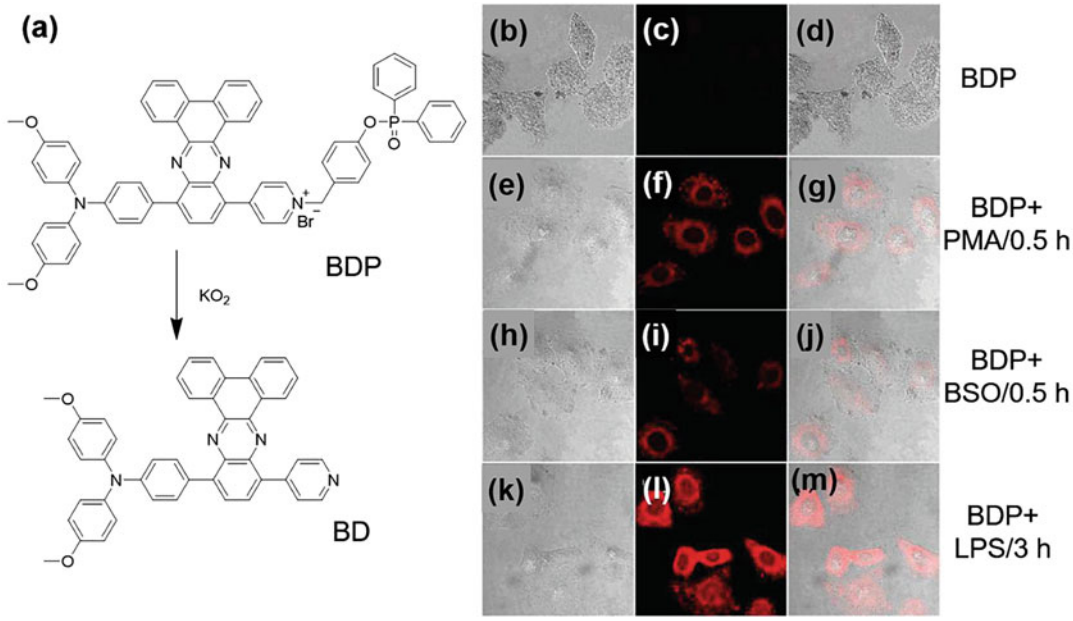

Fig. 19 (**a**) Proposed transformation process from BDP to BD by KO_2. (**b**–**m**) Confocal microscopy images of HepG2 cells with different treatments. (**b**–**d**) HepG2 cells treated with BDP for1 h at 37.4 °C. (**e**–**m**) HepG2 cells treated with BDP, followed by treatment of (**e**–**g**) PMA for 30 min, (**h**–**j**) BSO for 30 min, and (**k**–**m**) LPS for 3 h. Reprinted with permission from Ref. [36]. Copyright © 2013, American Chemical Society

cell apoptosis and inflammation, the ROS level in cells is also increased. *L*-buthionine sulfoximine (BSO) and lipopolysaccharide (LPS) can induce cell apoptosis and inflammation, respectively. After treatment with BSO for 30 min or LPS for 3 h, BDP stained HepG2 cells show bright emission, indicative of their higher superoxide concentration than normal cells. These results demonstrate the feasibility of employing BDP as a sensitive superoxide probe both in vitro and in vivo. BDP is expected to provide insight into the superoxide involved biological processes and find useful applications in screening of drugs that regulate cell through apoptosis or inflammation.

6.2 Imaging of Mercury Ion

Mercury ion (Hg^{2+}) is a heavy metal and is toxic to all the living creatures. Environmental Hg^{2+} can pass through the food chain and accumulate in human beings. Hg^{2+} tends to accumulate in human central nervous system, leading to serious consequences, including language and hearing impairment and contraction of visual field with paralysis, limbs deformity, difficulty in swallowing (dysphagia), and even death in severe cases. It is thus of crucial importance to develop simple and sensitive approach for detection of Hg^{2+} both in the environment and in human.

Tang et al. recently develop a probe, *p*-TPE-RNS, for Hg^{2+} detection, which operates through a dark through-bond energy transfer (DTBET) mechanism [37]. *p*-TPE-RNS contains a TPE unit and rhodamine in a spirolactam form. Rhodamine in the spirolactam form is not emissive due to the absence of large conjugation, which preclude the energy transfer between TPE and rhodamine. Thus, only blue emission from TPE can be observed from the aggregates of *p*-TPE-RNS. The presence of Hg^{2+} transforms the spirolactam form of rhodamine to positively charged form of rhodamine, (*p*-TPE-RNO) (Fig. 20a). This transformation both solubilizes *p*-TPE-RNO and enables the DTBET from TPE to rhodamine. Thus, the red fluorescence from rhodamine can be observed through exciting TPE and the concentration of Hg^{2+} can be determined by calculating the fluorescence ratio of red to blue (I_{595}/I_{485}). As the transformation from *p*-TPE-RNS to *p*-TPE-RNO very much depends on the presence of Hg^{2+}, the detection is highly selective (Fig. 20b) and no other metal ion can activate the transformation. Thanks to the well-separated emission peaks of TPE and rhodamine with a large emission wavelength difference of up to 115 nm, low detection limit of 0.3 ppm was achieved. Besides, *p*-TPE-RNS can enter cells and demonstrate good biocompatibility. More importantly, the Hg^{2+} promoted transformation from *p*-TPE-RNS to *p*-TPE-RNO remains feasible in living cells, which enables the imaging of Hg^{2+} in living cells (Fig. 20c–f). Without Hg^{2+}, *p*-TPE-RNS stained cells emit mostly blue light, which is transformed to red fluorescence in the presence of Hg^{2+}. This study provides a new design strategy for the development of sensors with high performance, which could be a powerful tool for the tracking and exploration of various biological and physiological processes.

6.3 Imaging of Glutathione (GSH)

Cellular thiols are closely related to many biological processes, such as antioxidant defense, cell signaling, and cell proliferation. Among all the thiols, glutathione (GSH) is the most abundant, whose abnormal levels are associated with many diseases, including Alzheimer's disease, liver damage, and cancer. Besides, GSH levels in cancer cells also affect the effectiveness of chemotherapy. Detection of intracellular thiol levels is thus of high importance.

Taking advantage of the AIE process, lots of sensing applications can be developed by employing AIEgens. One widely utilized strategy is the solubility change of the AIEgens. The core part of most AIEgens, such as TPE and HPS, is hydrophobic and attachment of hydrophilic moieties to these cores will increase their water solubility, making them non-emissive in biological conditions (off state). In the presence of target analysts, the hydrophilic moieties will be cleaved, releasing the hydrophobic cores. These hydrophobic cores will agglomerate to form

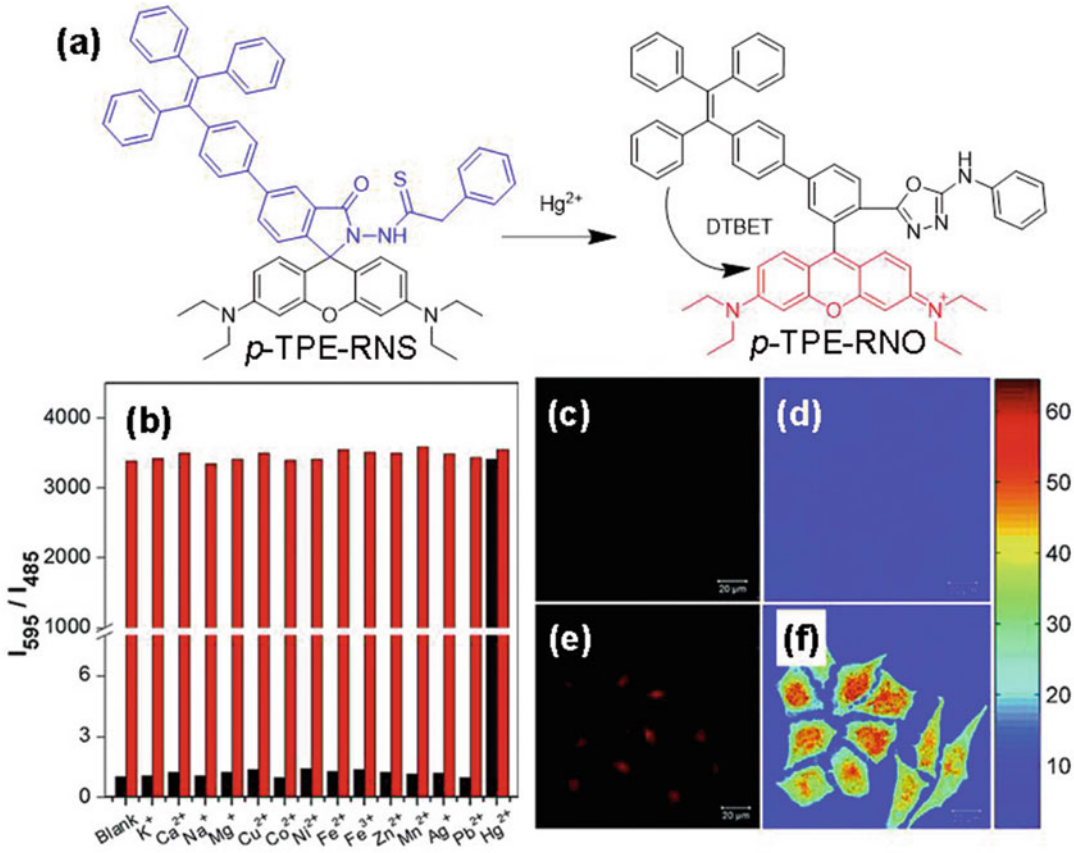

Fig. 20 (**a**) Schematic illustration of the sensing mechanism of Hg^{2+} with *p*-TPE-RNS. (**b**) Selectivity of *p*-TPE-RNS towards Hg^{2+} over other metal ions. (**c**–**f**) Confocal microscopy images of HeLa cells stained with 20 μM of *p*-TPE–RNS for 40 min in the absence (**c**, **d**) and presence (**e**–**f**) of 2 μM Hg^{2+} for 30 min. (**c**, **e**) Red channel images: 550–650 nm; (**d**, **f**) ratio images of red/blue

particles and their emission will be turned on (Fig. 21a).

Taking advantage of this strategy, TPE-ss-D5-cRGD is designed and synthesized (Fig. 21b) [38]. TPE-ss-D5-cRGD bears targeted cyclic arginine–glycine–aspartic acid (cRGD) peptide, a highly water soluble peptide with five aspartic acids, a TPE fluorogen, and a thiol-specific cleavable disulfide linker. Benefiting from the aspartic acid moieties, TPE-ss-D5-cRGD is soluble in aqueous solutions and is thus non-fluorescent. GSH can break the disulfide bond, release the TPE fluorogen, and turn on its emission. The detection limit of this method in bulk solution is determined to be 1 μM. The cRGD peptide functionality of TPE-ss-D5-cRGD endows it with the specificity towards integrin $\alpha_v\beta_3$-expressing cells. As shown in Fig. 21c–h, U87-MG cells, which are integrin $\alpha_v\beta_3$ positive, can be stained, while integrin $\alpha_v\beta_3$ negative MCF-7 cells remain unstained. The derivatives of TPE-ss-D5-cRGD without cRGD or disulfide group cannot stain both U87-MG and MCF-7, due to the absence of cleavage site and targeting group, respectively.

Tang et al. report another probe TPE-DCV for GSH detection [39]. TPE-DCV contains dicyanovinyl (DCV) group, which can react with thiol group through thiol-ene click reaction (Fig. 22a). This reaction breaks the conjugation between TPE and dicyano group and changes the fluorescence of TPE-DCV from red to blue. Interestingly, the reaction is highly selective towards

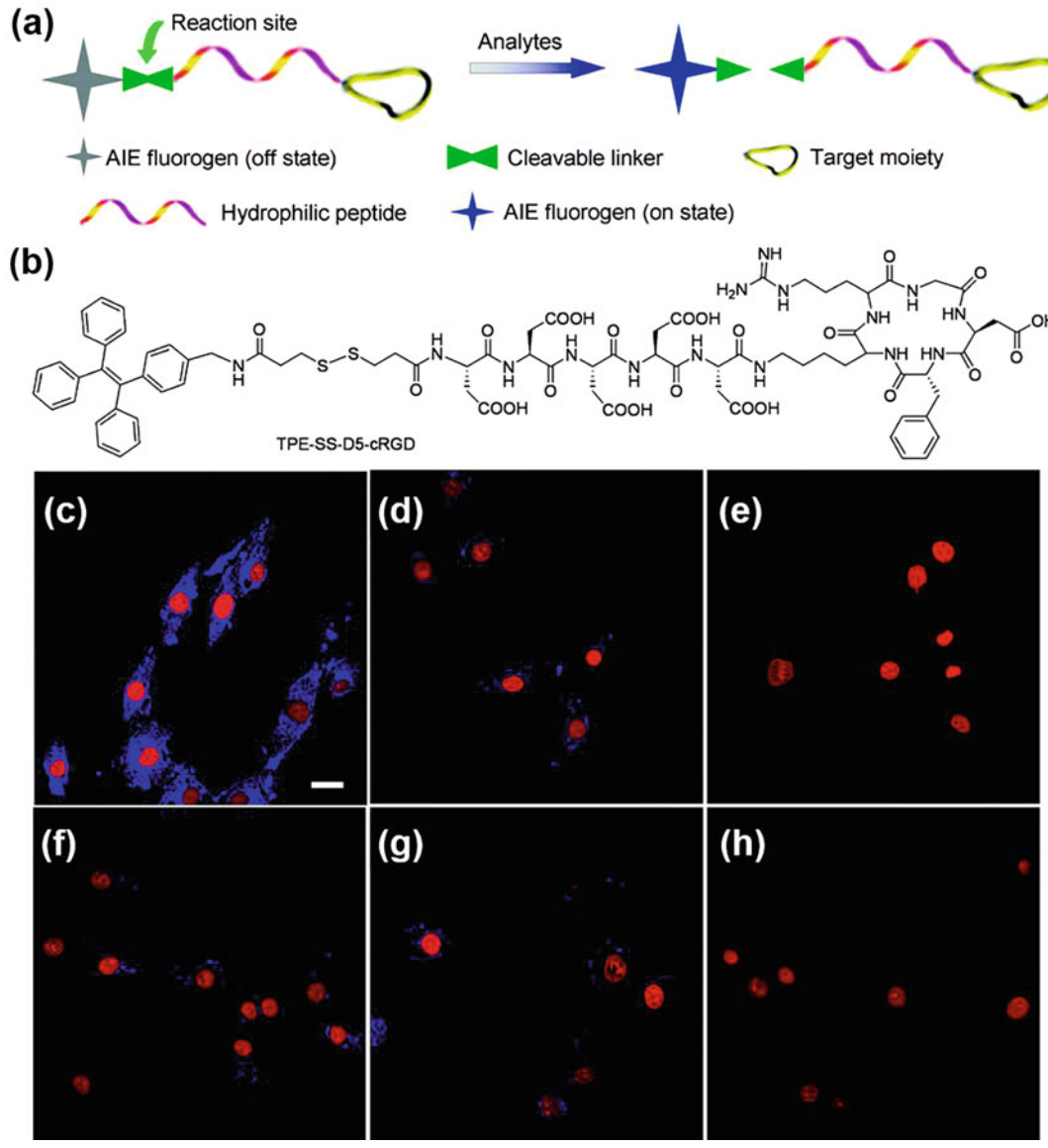

Fig. 21 (**a**) General design strategy of AIE probes. (**b**) Molecular structure of TPE-ss-D5-cRGD. (**c**–**h**) Confocal microscopy images of (**c**–**e**) U87-MG and (**f**–**h**) MCF-7 cells after incubation with (c and f) TPE-ss-D5-cRGD, (**d**, **g**) derivative of TPE-ss-D5-cRGD without cRGD group, and (**e**, **h**) derivative of TPE-ss-D5-cRGD without disulfide. The nuclei were stained with propidium iodide. All images share the same scale bar (20 μm). Reprinted with permission from Ref. [38]. Copyright © 2014, Royal Society of Chemistry

GSH over amino acids, including cysteine and homocysteine (Fig. 22b), and thus the GSH concentration can be determined by tracking the increase in emission intensity at 520 nm. In the GSH concentration range of 200–500 μM, the plot of fluorescence increment (I/I_0) at 520 nm as a function of GSH concentration is in a linear regression with a correlation coefficient of 0.985. TPE-DCV is cell permeable and stains the cytoplasmic region but not the nucleic parts (Fig. 22c). When the cells are pretreated with *N*-ethylmaleimide (NEM, 20 mM), a trapping reagent of thiol species, for 0.5 h, the signals from the cytoplasmic regions are decreased in

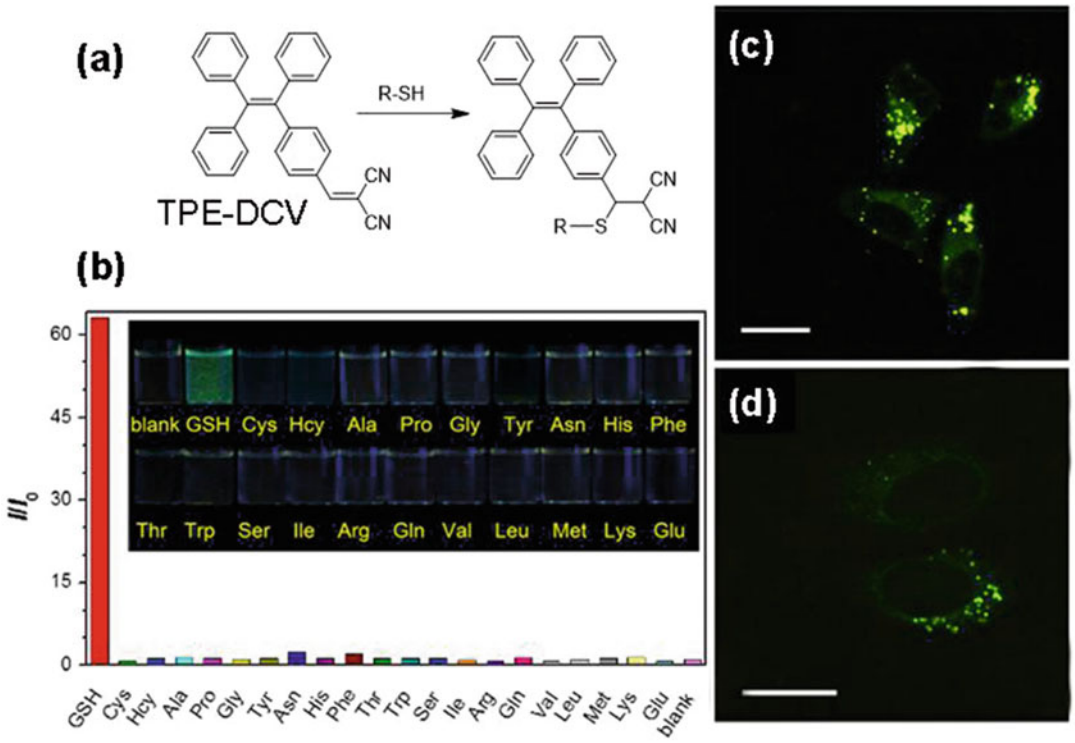

Fig. 22 (**a**) Illustration of thiol-ene "click" reaction between TPE-DCV and thiols. (**b**) Selective detection of GSH over amino acids in water/ethanol mixture with a water fraction of 68%. (**c**, **d**) Confocal images of living HeLa cells incubated with TPE-DCV for 0.5 h (**c**) without and (**d**) with NEM treatment

both green and yellow channels (Fig. 22d). Since NEM can react and thus consume partial thiols, less amount of thiol is available for TPE-DCV to react. This result in turn implies the occurrence of the thiol-ene click reaction between TPE-DCV and the intracellular thiols-mainly GSH.

6.4 Imaging of Enzyme Activity

Alkaline Phosphatase (ALP)

ALP is a hydrolase, which catalyzes the dephosphorylation process of phosphate monoesters to produce phosphate salts and the associated alcohols, phenols, sugars, etc. The catalytic activity of ALP can be regarded as a biomarker for disease diagnosis and abnormally high level of ALP in serum is indicative of diseases, such as breast cancer, prostate cancer, liver dysfunction, intestinal disease, bone disease, and diabetes.

Tang et al. report an AIE probe, HCAP (Fig. 23a), for ALP detection. HCAP contains the HCA fluorophore and phosphate group [40]. The presence of phosphate breaks the ESIPT process of HCA, which endows HCAP with greenish yellow emission. ALP can hydrolyze the phosphate group and transform HCAP to HCA and recover the red ESIPT and AIE emission of HCA (Fig. 23b). Due to the high specificity and efficiency of the ALP catalyzed dephosphorylation reaction and the high brightness of HCAP, ALP concentration can be quantified in a linear ratiometric fluorescence response, which enables in vitro quantification of ALP activity in a range of 0−150 mU/mL with a detection limit of 0.15 mU/mL. HCAP can enter cells and sense the ALP activity of living cells. Without HCAP, the cells are non-emissive (Fig. 23c). After staining with HCAP, orange fluorescence is observed, which

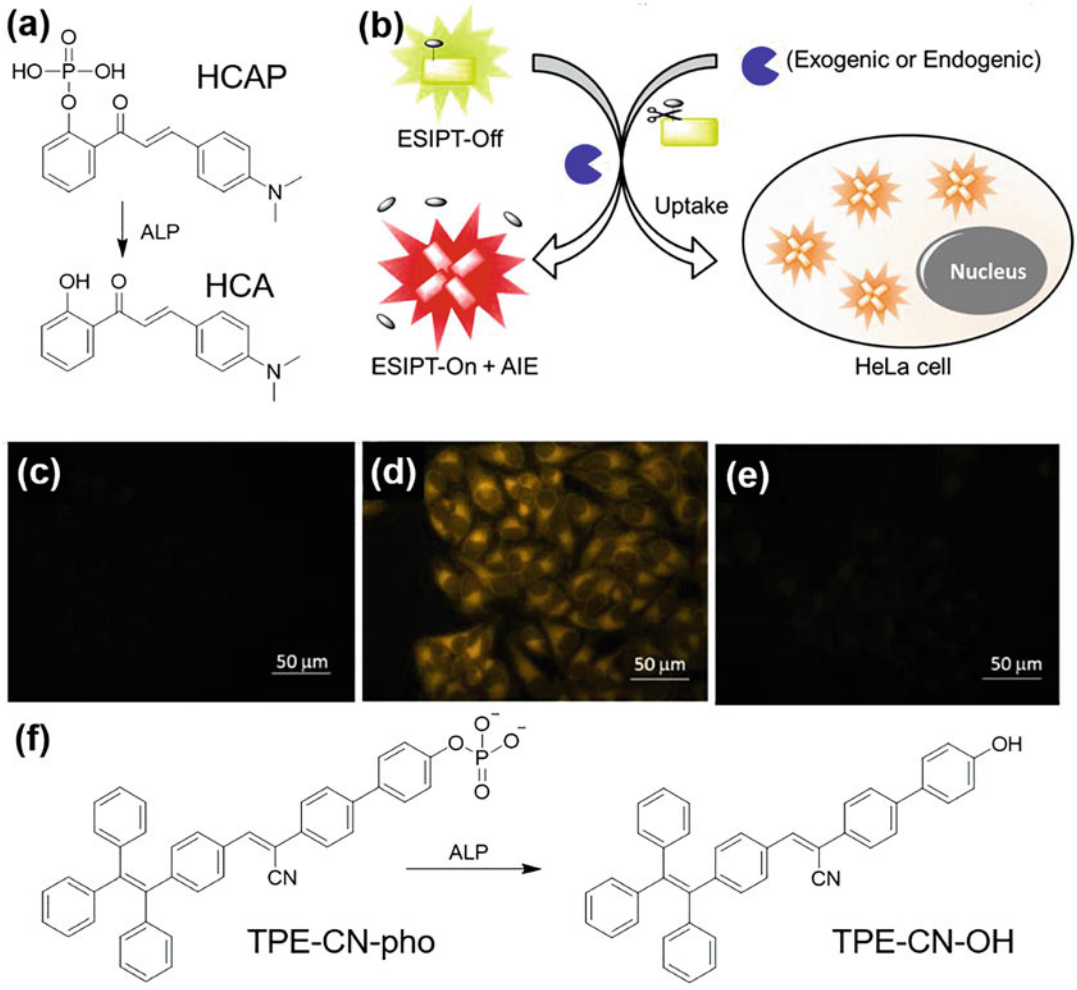

Fig. 23 (**a**) Transformation of HCAP to HCA in the presence of ALP. (**b**) Illustration of the in vitro and in vivo detection of ALP. (**c**–**e**) Fluorescence images of HeLa cells with (**c**) no HCAP, (**d**) HCAP (10 μM), and (**e**) HCAP (10 μM) and levamisole (5 mM). (**f**) Transformation of TPE-CN-pho to TPE-CN-OH in the presence of ALP. Reprinted with permission from Ref. [40]. Copyright © 2019 WILEY-VCH Verlag GmbH & Co. KGaA, Weinheim

is blue-shifted compared with the detection in solutions. Levamisole is an inhibitor of ALP. Pretreating cells with levamisole inhibit the activity of ALP and no orange emission can be observed. Close inspection of the process reveals that HCAP is not cell permeable. The secreted ALP from HeLa cells can dephosphorylate HCAP to HCA, which can enter cells and endow cell with orange fluorescence.

By employing similar strategy, Zeng and Wu et al. report another probe, TPE-CN-pho, for ALP detection (Fig. 23f) [41]. TPE-CN-pho is a typical AIEgen. Interaction with ALP can cleave the phosphate group and lead to TPE-CN-OH. Without the phosphate, TPE-CN-OH has poor water solubility and tends to form aggregated in solution, which turns on its emission and enables the detection of ALP in a fluorescence turn-on manner. Besides, TPE-CN-pho is also successfully applied to imaging intracellular activity, which enables its promising applications in biological researches.

Esterase

Lysosomes are responsible for digesting unwanted materials in the cytoplasm, acting as

the waste disposal system of cell. Determining enzyme activity in lysosome is thus of great importance, which provides information on whether the lysosome is functioning well. Malfunction of these lysosomal enzymes may lead to serious consequences. For example, the deficiency of lysosomal esterase will result in Wolman disease with a series of symptoms, including diarrhea, swelling of the abdomen, enlargement of the liver, and failure to gain weight.

Recently, an AIEgen (AIE-Lyso-1; Fig. 24a) is applied to sensing of lysosomal esterase [42]. AIE-Lyso-1 is designed to contain esterase reactive acetoxyl groups and lysosome-targeting morpholines. The acetoxyl group blocks the excited state intramolecular proton transfer

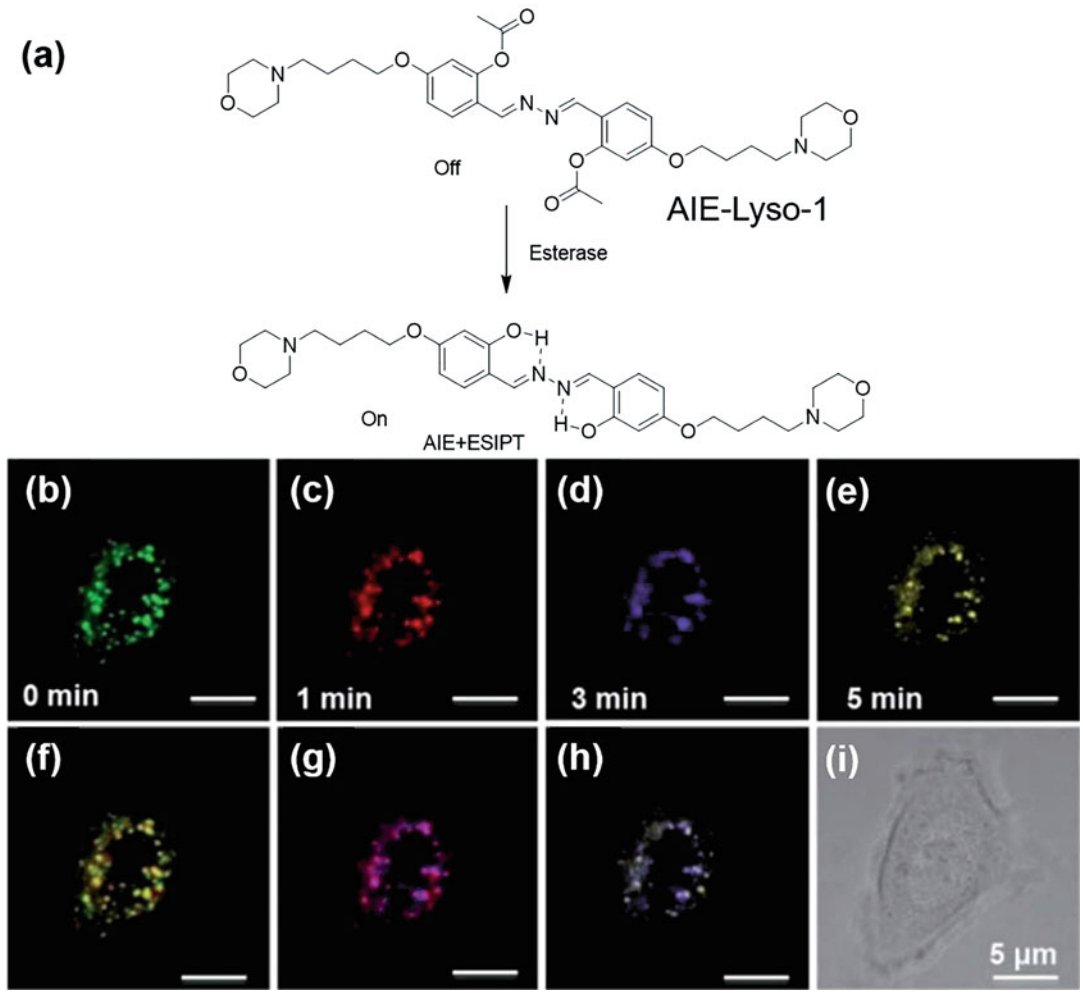

Fig. 24 (**a**) Molecular structure and working principle of AIE-Lyso-1. (**b**–**i**) Real-time monitoring of the movement of lysosome. Confocal images of an MCF-7 cell stained with 1.0 μM of AIE-Lyso-1 and stimulated using 3 μM of chloroquine. Different pseudocolors are used to illustrate the fluorescence images at different stimulation times of (**b**) 0, (**c**) 1, (**d**) 3, and (**e**) 5 min. (**f**–**h**) Merging images at two different times: (**f**) 0 and 1 min, (**g**) 1 and 3 min, (**h**) 3 and 5 min, and (**i**) bright-field image. Scale bar: 5 μm. Reprinted with permission from Ref. [42]. Copyright © 2014 Royal Society of Chemistry

(ESIPT) process of the chromophore, thus AIE-Lyso-1 is almost non-emissive. Cleavage of the ester group by esterase recovers the ESIPT emission and results in fluorescence enhancement, which enables the fluorescence turn-on detection of lysosomal esterase activity. To test the feasibility of the method, detection of esterase activity is firstly conducted in solution. Good linearity is achieved in the esterase concentration range of 0.10–0.50 U mL^{-1} and the detection limit is determined to be 2.4×10^{-3} U mL^{-1}. Guided by the morpholine group, AIE-Lyso-1 selectively accumulates in the lysosome of cell. Its emission is turned on gradually and reaches the maximum at 8 min. Due to the low background emission of AIE-Lyso-1, the lysosomal esterase activity can be followed in real time. Additionally, AIE-Lyso-1 enjoys the advantage of high photostability, which enables continuous tracking of lysosome movement. To demonstrate this feasibility, cells are stimulated by chloroquine to drive the lysosome movement. As shown in Fig. 24b–h, fluorescence images are collected at different time points of chloroquine treatment and assigned with different colors. Even slight movement of lysosomes can be traced by AIE-Lyso-1 in the merged images by tracking the change of different colors.

Caspase

Caspase-3 is a key mediator of cell apoptosis and has been regarded as an attractive target for monitoring apoptosis. Real-time tracking of cell apoptosis, which is a programmed cell death process in multicellular organisms, is of crucial importance for uncovering the detailed biological process, early diagnosis of therapeutic efficiency, and designing of effective drugs.

Taking advantage of the fluorescence light-up property of AIEgens, a caspase probe (DEVDK-TPE) is prepared by conjugating TPE moiety with Asp-Glu-Val-Asp (DEVD) peptide, which is substrate for Caspase (Fig. 25a) [43]. In the presence of Caspase, the DEVD chain is cleaved effectively, releasing the hydrophobic TPE unit. These hydrophobic TPE units show poor solubility in aqueous solution and tend to form aggregates. Aggregation of the TPE moieties activates the RIM process and hence turns on their emission. As shown in Fig. 25b–i, the emission of DEVDK-TPE is switched on in apoptotic cell and cell apoptosis process can be monitored in real time. Normal cells or those treated with caspase inhibitor cannot activate the emission of DEVDK-TPE. These results confirm the success of apoptotic imaging in target cells. Through molecular engineering, cRGD moiety is further introduced to the probe to selectively detect the apoptosis process of cells expressing integrin $\alpha_v\beta_3$.

7 Imaging of Biological Processes

7.1 Imaging of Apoptosis

As previously mentioned, apoptosis is a very important biological process. Apoptosis level is of critical importance in regulating cell growth and its dysregulation may result in cancers or neurodegenerative diseases, thus apoptosis should be precisely controlled. So far, several approaches have been developed to monitor apoptosis process, such as laddering of DNA fragmentation, caspase activation, and externalization of phosphatidylserine (PS). Among all these methods, externalization of PS has emerged as an attractive indicator for apoptosis detection as it is more straightforward and occurs prior to DNA fragmentation and plasma membrane permeabilization. During apoptosis, cell membrane depolarizes and exposes PS to the surface of plasma membrane. By examination of the presence of PS in plasma membrane, early apoptosis can be detected.

Tang et al. constructed an AIE probe for detection of apoptosis process [44]. By attaching zinc dipicolylamine (ZnDPA) complexes, which recognize PS, to TPE, TPE-Zn_2BDPA (Fig. 26a) is obtained. TPE-Zn_2BDPA recognizes the PS on plasma membrane of cells undergoing early apoptosis and light up the plasma membrane. As PS externalization takes place in the early stage of apoptosis, TPE-Zn_2BDPA is capable of detecting the early apoptotic cells. As shown in Fig. 26b–c,

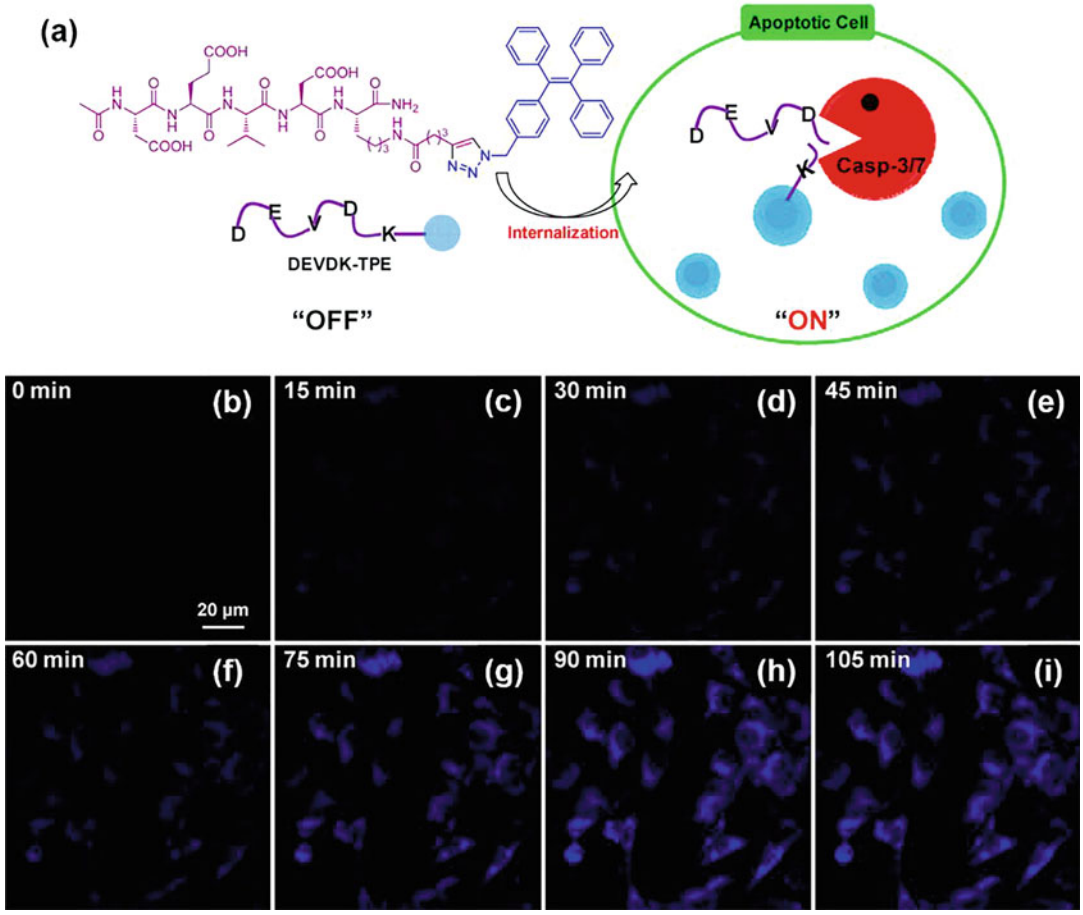

Fig. 25 (**a**) Design principle of the apoptosis probe. (**b–i**) Real-time fluorescence images showing the cell apoptotic process of MCF-7 cells with DEVED-TPE at room temperature. Staurosporine (1 μM) was used to induce cell apoptosis. All images have the same scale bar (20 μm). Reprinted with permission from Ref. [43]. Copyright © 2012, American Chemical Society

HeLa cells are induced to early apoptosis stage by treatment with 300 μM H_2O_2 and were then costained with TPE-Zn_2BDPA and propidium iodide (PI), which accumulates in and lights up the nucleus of late apoptotic or dead cells. No fluorescence can be observed from the PI channel and blue fluorescence of TPE-Zn_2BDPA emerges from the membrane of cells, indicative of the early apoptotic stage of these cells. By pretreating cells with high H_2O_2 concentration of 2000 μM, fluorescence from both PI and TPE-Zn_2BDPA channels can be observed, suggesting that the cell membrane is permeable and these cells are in late apoptotic stage. Due to the compromised plasma membrane of late apoptotic cells, more TPE-Zn_2BDPA molecules enter the cells, and brighter emission from TPE-Zn_2BDPA can be observed.

Liu et al. report another probe AIE-ZnDPA for apoptosis detection (Fig. 26h) [45]. AIE-ZnDPA also bears DPA group and can selectively stain apoptotic cells with externalized PS. Staurosporine is employed to induce cell apoptosis, and early and late stages of apoptosis can be clearly discerned (Fig. 26i–n): early apoptotic cells show circular emission from plasma membrane, while in late apoptotic cells fluorescence comes from the cytosol and nucleus. Due to the AIE characteristics of AIE-ZnDPA and its good water solubility, AIE-ZnDPA emits faintly in aqueous solution.

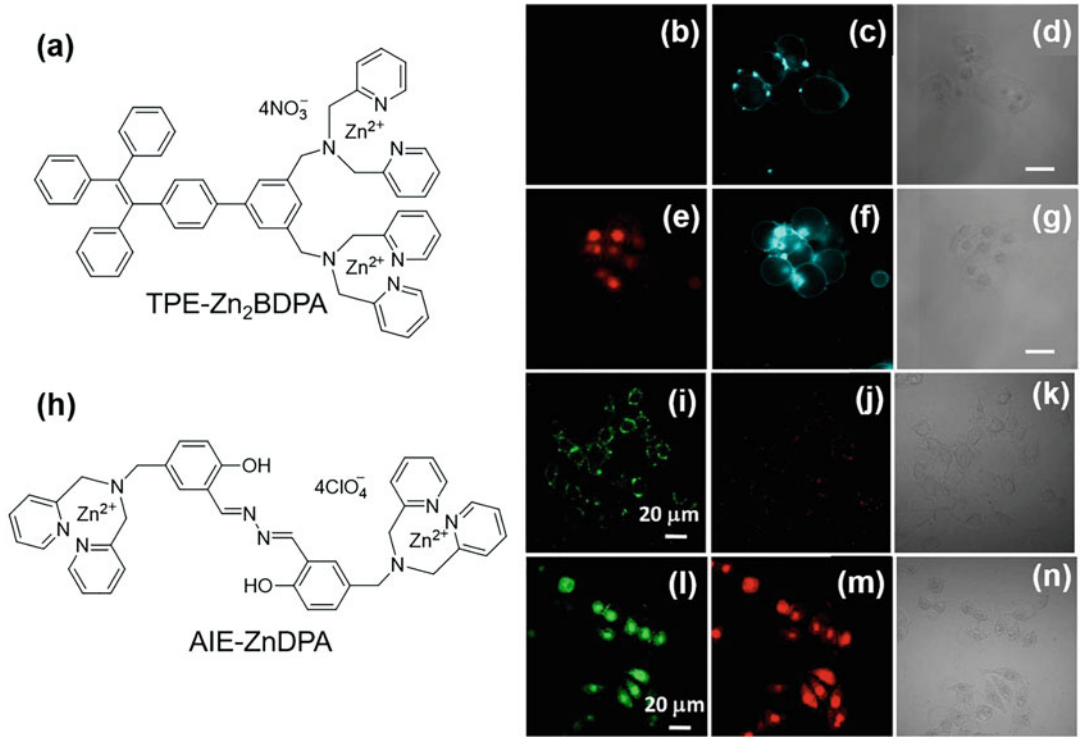

Fig. 26 (**a**, **h**) Molecular structures of TPE-Zn_2BDPA and AIE-ZnDPA, respectively. (**b**–**g**) (**b**–**c**, **e**–**f**) Confocal microscopy and (**d**, **g**) bright-field images of (**b**–**d**) early apoptotic HeLa cells induced by H_2O_2 (300 μM) and (**e**–**g**) late apoptotic HeLa cells induced by H_2O_2 (2000 μM), followed by costaining with (**b**, **e**) propidium iodide (PI) and (**c**, **f**) TPE-Zn_2BDPA. (**i**–**n**) (**i**–**j**, **l**–**m**) Confocal microscopy and (**k**, **n**) bright-field images of (**i**–**k**) early stage and (**l**–**n**) late stage apoptotic HeLa cells induced by (**i**–**k**) 1 μM and (**l**–**n**) 2 μM staurosporine, respectively, followed by costaining with AIE-ZnDPA and PI. All images share the same scale bar of 20 μm. Reprinted with permission from Ref. [44]. Copyright © 2016 Royal Society of Chemistry. Reprinted with permission from Ref. [45]. Copyright © 2015, American Chemical Society

Upon binding to the PS of apoptotic cells, bright fluorescence can be observed. The low background emission of AIE-ZnDPA enables the real-time monitoring of apoptosis process. This provides a more direct and easy way for investigating apoptosis and may provide insight into the apoptosis process, which is not available with previous probes.

7.2 Imaging of Mitophagy

Autophagy is an important biological process, through which cell degrades dysfunctional or damaged cell components and replenishes cell nutrition to support metabolism. Mitochondri on is a main target for autophagy, as the production of ATP in mitochondria involves many highly reactive species, which can easily lead to damage of cell components. Thus, the mitochondrial autophagy is termed as mitophagy. During mitophagy, autolysosome is produced, which digests the dysfunctional mitochondria. In order to visualize the mitophagy process, photostable mitochondrial probe with high mitochondrial affinity is required, which ensures the long-term visualization of mitochondria.

Tang et al. develop a mitochondrial probe, TPE-Py-NCS (Fig. 27a), which contains isothiocyanate functionality (NSC) [46]. The NSC group may react with the amine group in mitochondria and ensures the targeting of TPE-Py-NCS. Besides, TPE-Py-NCS enjoys good photostability during cell imaging, which enables long-term

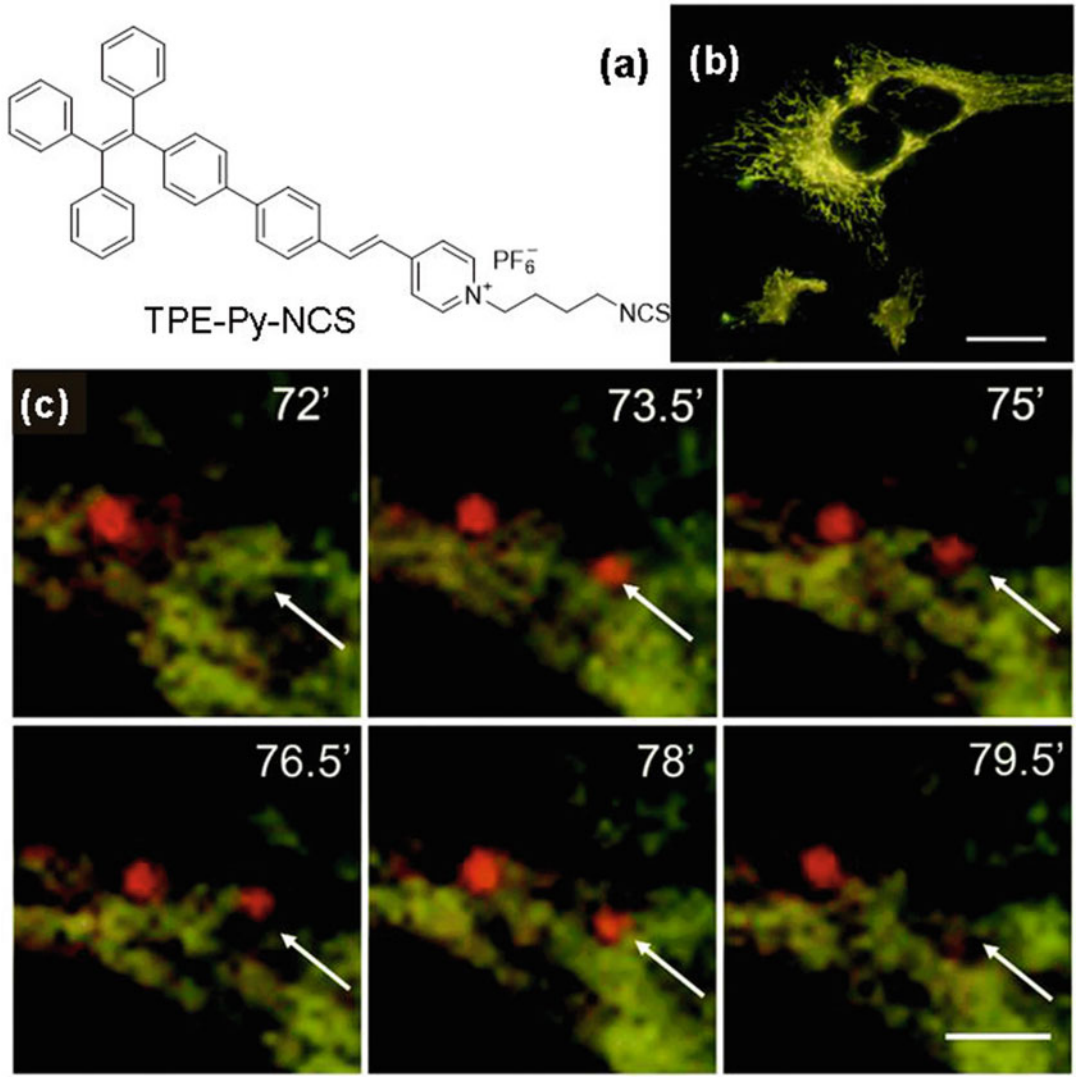

Fig. 27 (**a**) Molecular structure of TPE-Py-NCS. (**b**) Imaging of the mitochondria of HeLa cell with TPE-Py-NCS. Scale bar: 20 μm. (**c**) Confocal images of HeLa cells stained with TPE-Py-NCS (5 μM, yellow) and LysoTracker Red DND-99 (150 nM, red) in the presence of rapamycin (50 mg mL^{-1}) at different time points. Scale bar: 2 μm. Reprinted with permission from Ref. [46]. Copyright © 2015 Royal Society of Chemistry

monitoring of the associated biological processes. Due to the positively charged pyridium group, TPE-Py-NCS selectively stains the mitochondria of HeLa cells with high brightness and contrast (Fig. 27b). To monitor the mitophagy process, HeLa cells are costained with TPE-Py-NCS and LysoTracker Red DND-99, which target mitochondria and lysosome, respectively. Afterwards, the cells are treated with rapamycin, a well-known drug for inducing autophagy, and imaged with confocal microscope at selected time points. From 0 to 72 mins, no obvious change is observed (Fig. 27c). After 73.5 min of rapamycin addition, a new red fluorescent dot appears, overlapping with mitochondria. The newly formed red dot disappears after 79.5 min of rapamycin treatment. The newly formed red dot is autophagosome, which initiates the autophagy process in mitochondria. After digesting the mitochondria, the autophagosome

disappears. Besides, the fluorescence from mitochondrial regions that overlap with red dot became dimmer, while other regions remain unchanged. The results clearly demonstrate that the mitochondria are digested and the whole mitophagy process can be monitored.

7.3 Imaging of Mitosis

Mitosis describes the cell division process, through which chromosomes in the nucleus are evenly distributed between two cells and two daughter cells with identical generic materials produced. Mitosis is the foundation for growth and repair in the body. Generally, mitosis is divided into several stages, and each stage exhibits characteristics in morphology and chromosome alignments, reflecting the different behavior of chromosome in mitosis.

Tang et al. developed a probe, TTAPE-Me (Fig. 28a) for detection and imaging of DNA [47]. In the presence of DNA and RNA, the fluorescence intensity of TTAPE-Me increases accordingly. Besides, TTAPE-Me can also visualize nucleic acid in gel. The detection limit of TTAPE-Me in DNA gel electrophoresis is determined to be as low as 0.25 μg per lane. Afterwards, plant cells are stained with TTAPE-Me. Onion (*Allium cepa*) root tip is employed to perform the experiment. As shown in Fig. 28b–g, cell in different phases of mitotic cell division can be clearly visualized by tracking the fluorescence from TTAPE-Me. In interphase, the nucleus membrane is intact and the chromosome is still in the form of chromatin. For the cells in prophase, the nuclear membrane is disappeared and chromosomes are freed into the surrounding cytoplasm. When the cells enter metaphase, the chromosomes are aligned along the metaphase plate. During anaphase, the sister chromatids are dragged towards the opposite poles of the cells by the polar fiber. The picture shown in Fig. 28f presents the cell in the early anaphase. At telophase, the chromosomes are cordoned off into distinct new nuclei in the emerging daughter cells and nuclear envelopes of these nuclei form. Due to the high affinity of TTAPE-Me to DNA, TTAPE-Me lights up the chromosomes and nucleus with high efficiency. By counterstaining

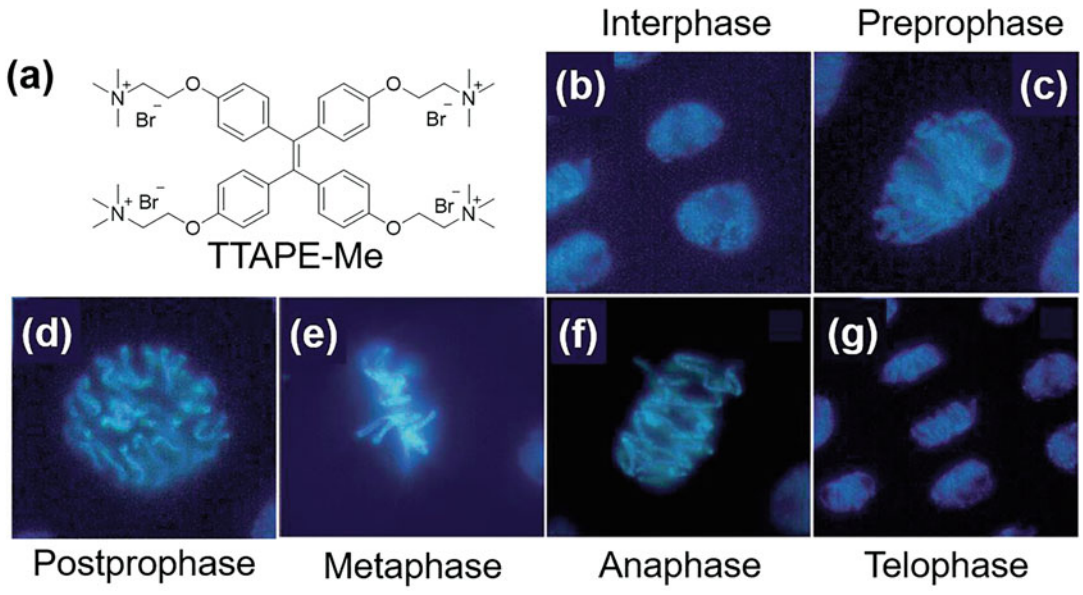

Fig. 28 (**a**) Molecular structure of TTAPE-Me. (**b**–**g**) Fluorescence images of cells from onion root tips at different stages of the cell cycle stained by TTAPE-Me. Reprinted with permission from Ref. [47]. Copyright © 2013 WILEY-VCH Verlag GmbH & Co. KGaA, Weinheim

with other probes, the method is expected to become more useful for multicolor fluorescence imaging, and visualize more details during the mitosis process.

7.4 Imaging of Stem Cell Differentiation

Cell differentiation is the foundation for a single-celled zygote to develop into a multicellular adult organism. Through cell differentiation, generic cell can develop into a specific type of cell in response to specific triggers from the body or the cell itself. Stem cells are a kind of undifferentiated cells with pluripotency, that is, they can differentiate into specialized cells. The pluripotency of stem cells enables them to be employed in regenerative therapies and has drawn tremendous attention. As more investigation on stem cell based therapy are reported, it becomes increasingly important to comprehend how stem cell contributes to tissue regeneration and what is the ultimate fate of these stem cells.

Ding et al. report an AIEgen-based method for tracking the activity of stem cell during therapies [48]. TPETPAFN (Fig. 29a), a typical AIEgen is employed to fabricate AIE dots with Tat surface functionalities, which demonstrates bright and stable emission. These AIE dots exhibit long-term retention in adipose-derived stem cells (ADSC). After 5 days culturing, the AIE dots stained ADSCs are 6.2 and 4.8 folds brighter than that of Qtracker® 655 and PKH26 stained ones, respectively (Fig. 29b–d). Besides, staining ADSCs with AIE dots does not influence the pluripotency of ADSCs and their ability to transform into chondrogenic, adipogenic, and osteogenic cell lines is not affected. The AIE dots do not exert impact on the secretome, with similar expression levels of monocyte chemoattractant protein-1 (MCP-1), interleukin-6 (IL-6), angiopoietin-1 (Ang-1), basic fibroblast growth factor (bFGF), and vascular endothelial growth

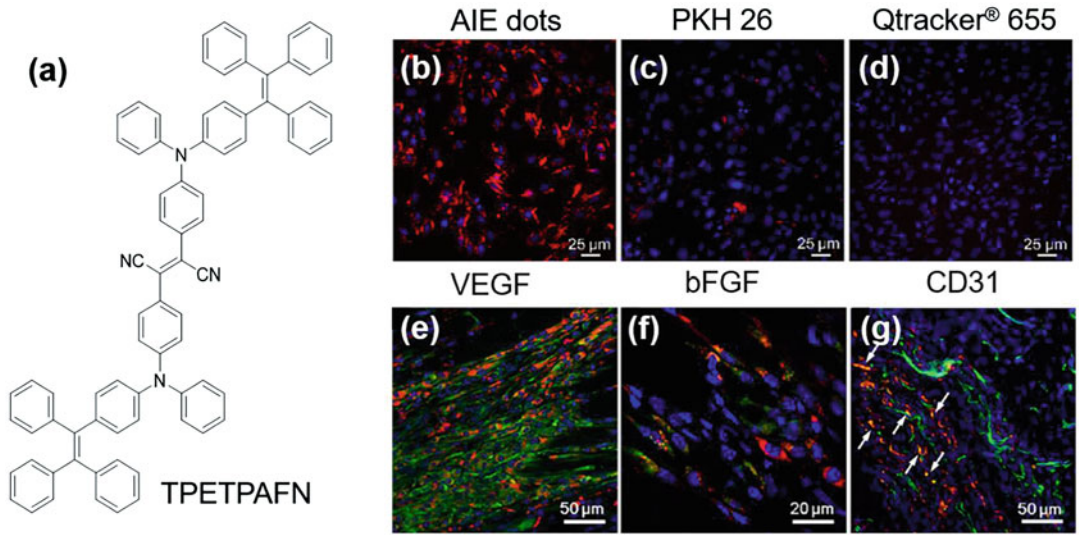

Fig. 29 (**a**) Molecular structure of TPETPAFN. (**b**–**d**) Confocal microscopy images of ADSCs labeled with (**b**) AIE dots, (**c**) PKH26, and (**d**) Qtracker® 655, followed by culturing for 5 days. (**e**, **f**) Confocal microscopy images of ischemic hind limb slices from mice after administration of AIE dot-ADSC-M for 14 days. The slices were immunostained against (**e**) VEGF and (**f**) bFGF, respectively. (**g**) Representative CD31-staining confocal microscopy image ischemic of hind limb slices from mice treated with AIE dot-ADSC-M for 42 days. Reprinted with permission from Ref. [48]. Copyright © 2014, American Chemical Society

factor a (VEGFa). Close investigation on the mice after transplantation of AIE dot-labeled ADSC-containing matrigels for 14 days reveals that ADSC contributes to regeneration by secreting angiogenic factors in the ischemic tissue.

It is also found that most AIE dot-labeled ADSCs (red fluorescence) are distributed near or close to the CD31-positive blood vessels (green fluorescence, Fig. 29g), indicating the induction of therapeutic angiogenesis via the cells. More importantly, as shown in Fig. 7c, several AIE dot-labeled cells are located in the blood vessels and participate in blood vessel formation through forming vascular structures. These results clearly illustrate that the AIE dots are able to track and visualize the regenerative capacity of ADSCs in a long-term manner.

8 Conclusions and Perspectives

Since the first report in 2001, AIEgens are finding increasing applications in biological researches. In this chapter, we select some representative examples and focus on introducing their applications in cell imaging and sensing. These AIEgens demonstrate favorable properties of excellent photostability, good biocompatibility, and high sensitivity and selectivity, making them suitable candidates for visualizing subcellular structures [49], long-term cell tracking [50–52], sensing of cellular microenvironment [53–62], and monitoring of biological processes [63–65]. Besides the application regimes mentioned in this chapter, lots of applications are made in other areas, such as super-resolved imaging [66–70], multimodality imaging [71–73], multiphoton imaging [74–78], and photodynamic therapy [79–86]. Due to the length limit, we cannot include all these applications in this book chapter. Interested readers can refer to other reviews and books for more information on the research frontier of the biological applications of AIEgens [9, 87–92].

As the investigations on biological applications of AIEgens proceed, more research endeavor should be devoted to the following areas: (1) New sensing mechanism: Currently, most sensing applications are based on solubility changes, cleavage of blocker, and confinement of phenyl rotations. A few new sensing mechanism is arising, such as DTBET and photo-oxidative dehydrogenation. We believe more interesting discoveries will be made in this area. (2) Sensing of more critical biological targets: By enriching the targets, AIEgens are expected to contribute to more biological researches. (3) Advanced imaging techniques: As the imaging technology advances, it places more requirements on fluorescent probes. Specialized probes for specific advanced imaging applications will be developed. (4) Elucidation of more biological processes: Previous successful examples have demonstrated the advantages of AIEgens in monitoring biological process. With these desirable attributes, AIEgens may help to provide insight into more biological processes.

References

1. Hong Y, Lam JWY, Tang BZ (2011) Aggregation-induced emission. Chem Soc Rev 40:5361–5388
2. Saigusa H, Lim EC (1995) Excited-state dynamics of aromatic clusters: correlation between exciton interactions and excimer formation dynamics. J Phys Chem 99:15738–15747
3. Wang J, Zhao Y, Dou C, Sun H, Xu P, Ye K et al (2007) Alkyl and dendron substituted quinacridones: synthesis, structures, and luminescent properties. J Phys Chem B 111:5082–5089
4. Hecht S, Fréchet JMJ (2001) Dendritic encapsulation of function: applying nature's site isolation principle from biomimetics to materials science. Angew Chem Int Ed 40:74–91
5. Nguyen BT, Gautrot JE, Ji C, Brunner PL, Nguyen MT, Zhu XX (2006) Enhancing the photoluminescence intensity of conjugated polycationic polymers by using quantum dots as antiaggregation reagents. Langmuir 22:4799–4803
6. Chen L, Xu S, McBranc D, Whitten D (2000) Tuning the properties of conjugated polyelectrolytes through surfactant complexation. J Am Chem Soc 122:9302–9303
7. Luo J, Xie Z, Lam JWY, Cheng L, Chen H, Qiu C et al (2001) Aggregation-induced emission of 1-methyl-1,2,3,4,5-pentaphenylsilole. Chem Commun 1740–1741
8. Hong Y, Lam JWY, Tang BZ (2009) Aggregation-induced emission: phenomenon, mechanism and applications. Chem Commun 29:4332–4353

9. Mei J, Hong Y, Lam JWY, Qin A, Tang Y, Tang BZ (2014) Aggregation-induced emission: the whole is more brilliant than the parts. Adv Mater 26:5429–5479
10. Zhu C, Kwok RTK, Lam JWY, Tang BZ (2018) Aggregation-induced emission: a trailblazing journey to the field of biomedicine. ACS Appl Bio Mater 1:1768–1786
11. Wang H, Zhao E, Lam JWY, Tang BZ (2015) AIE luminogens: emission brightened by aggregation. Mater Today 18:365–377
12. Leung CWT, Hong Y, Chen S, Zhao E, Lam JWY, Tang BZ (2013) A photostable AIE luminogen for specific mitochondrial imaging and tracking. J Am Chem Soc 135:62–65
13. Zhao N, Li M, Yan Y, Lam JWY, Zhang YL, Zhao YS et al (2013) A tetraphenylethene-substituted pyridinium salt with multiple functionalities: synthesis, stimuli-responsive emission, optical waveguide and specific mitochondrion imaging. J Mater Chem C 1:4640–4646
14. Chen WD, Zhang DW, Gong WT, Lin Y, Ning GL (2013) Aggregation-induced emission of a novel conjugated phosphonium salt and its application in mitochondrial imaging. Spectrochim Acta A Mol Biomol Spectrosc 110:471–473
15. Zhao N, Chen S, Hong Y, Tang BZ (2015) A red emitting mitochondria-targeted AIE probe as an indicator for membrane potential and mouse sperm activity. Chem Commun 51:13599–13602
16. Gui C, Zhao E, Kwok RTK, Leung ACS, Lam JWY, Jiang M et al (2017) AIE-active theranostic system: selective staining and killing of cancer cells. Chem Sci 8:1822–1830
17. Gu X, Zhao E, Zhao T, Kang M, Gui C, Lam JWY et al (2016) A mitochondrion-specific photoactivatable fluorescence turn-on AIE-based bioprobe for localization super-resolution microscope. Adv Mater 28:5064–5071
18. Gu X, Zhao E, Lam JWY, Peng Q, Xie Y, Zhang Y et al (2015) Mitochondrion-specific live-cell bioprobe operated in a fluorescence turn-on manner and a well-designed photoactivatable mechanism. Adv Mater 27:7093–7100
19. Xu X, Yan S, Zhou Y, Huang R, Chen Y, Wang J et al (2014) A novel aggregation-induced emission fluorescent probe for nucleic acid detection and its applications in cell imaging. Bioorg Med Chem Lett 24:1654–1656
20. Zhao Y, Yu CYY, Kwok RTK, Chen Y, Chen S, Lam JWY et al (2015) Photostable AIE fluorogens for accurate and sensitive detection of S-phase DNA synthesis and cell proliferation. J Mater Chem B 3:4993–4996
21. Ouyang J, Zang Q, Chen W, Wang L, Li S, Liu RY et al (2016) Bright and photostable fluorescent probe with aggregation-induced emission characteristics for specific lysosome imaging and tracking. Talanta 159:255–261
22. Wu J, Li Y, Tan C, Wang X, Zhang Y, Song J et al (2018) Aggregation-induced near-infrared emitting platinum(ii) terpyridyl complex: cellular characterisation and lysosome-specific localisation. Chem Commun 54:11144–11147
23. Wang E, Zhao E, Hong Y, Lam JWY, Tang BZ (2014) A highly selective AIE fluorogen for lipid droplet imaging in live cells and green algae. J Mater Chem B 2:2013–2019
24. Wang Z, Gui C, Zhao E, Wang J, Li X, Qin A et al (2016) Specific fluorescence probes for lipid droplets based on simple AIEgens. ACS Appl Mater Interfaces 8:10193–10200
25. Gao M, Su H, Li S, Lin Y, Ling X, Qin A et al (2017) An easily accessible aggregation-induced emission probe for lipid droplet-specific imaging and movement tracking. Chem Commun 53:921–924
26. He D, Zhuang Z, Wang X, Li J, Li J, Wu W et al (2019) Assembly of 1 *H*-isoindole derivatives by selective carbon–nitrogen triple bond activation: access to aggregation-induced emission fluorophores for lipid droplet imaging. Chem Sci 10:7076–7081
27. Gao M, Su H, Lin Y, Ling X, Li S, Qin A et al (2017) Photoactivatable aggregation-induced emission probes for lipid droplets-specific live cell imaging. Chem Sci 8:1763–1768
28. Li Y, Wu Y, Chang J, Chen M, Liu R, Li F (2013) A bioprobe based on aggregation induced emission (AIE) for cell membrane tracking. Chem Commun 49:11335–11337
29. Zhang W, Huang Y, Chen Y, Zhao E, Hong Y, Chen S et al (2019) Amphiphilic tetraphenylethene-based pyridinium salt for selective cell-membrane imaging and room-light-induced special reactive oxygen species generation. ACS Appl Mater Interfaces 11:10567–10577
30. Shi H, Liu J, Geng J, Tang BZ, Liu B (2012) Specific detection of integrin $\alpha_v\beta_3$ by light-up bioprobe with aggregation-induced emission characteristics. J Am Chem Soc 134:9569–9572
31. Yu Y, Feng C, Hong Y, Liu J, Chen S, Ng KM et al (2011) Cytophilic fluorescent bioprobes for long-term cell tracking. Adv Mater 23:3298–3302
32. Wang Z, Chen S, Lam JWY, Qin W, Kwok RTK, Xie N et al (2013) Long-term fluorescent cellular tracing by the aggregates of AIE bioconjugates. J Am Chem Soc 135:8238–8245
33. Feng G, Tay CY, Chui QX, Liu R, Tomczak N, Liu J et al (2014) Ultrabright organic dots with aggregation-induced emission characteristics for cell tracking. Biomaterials 35:8669–8677
34. Chen S, Hong Y, Liu Y, Liu J, Leung CWT, Li M et al (2013) Full-range intracellular pH sensing by an aggregation-induced emission-active two-channel ratiometric fluorogen. J Am Chem Soc 135:4926–4929
35. Chen S, Hong Y, Zeng Y, Sun Q, Liu Y, Zhao E et al (2015) Mapping live cell viscosity with an

aggregation-induced emission fluorogen by means of two-photon fluorescence lifetime imaging. Chem Eur J 21:4315–4320
36. Yang J, Liu X, Wang H, Tan H, Xie X, Zhang X et al (2018) A turn-on near-infrared fluorescence probe with aggregation-induced emission based on dibenzo [*a,c*] phenazine for detection of superoxide anions and its application in cell imaging. Analyst 143:1242–1249
37. Chen Y, Zhang W, Cai Y, Kwok RTK, Hu Y, Lam JWY et al (2017) AIEgens for dark through-bond energy transfer: design, synthesis, theoretical study and application in ratiometric Hg^{2+} sensing. Chem Sci 8:2047–2055
38. Yuan Y, Kwok RTK, Feng G, Liang J, Geng J, Tang BZ et al (2014) Rational design of fluorescent light-up probes based on an AIE luminogen for targeted intracellular thiol imaging. Chem Commun 50:295–297
39. Lou X, Hong Y, Chen S, Leung CWT, Zhao N, Situ B et al (2014) A selective glutathione probe based on AIE Fluorogen and its application in enzymatic activity assay. Sci Rep 4:4272
40. Song Z, Kwok RTK, Zhao E, He Z, Hong Y, Lam JWY et al (2014) A ratiometric fluorescent probe based on ESIPT and AIE processes for alkaline phosphatase activity assay and visualization in living cells. ACS Appl Mater Interfaces 6:17245–17254
41. Lin M, Huang J, Zeng F, Wu S (2019) A fluorescent probe with aggregation-induced emission for detecting alkaline phosphatase and cell imaging. Chem Asian J 14:802–808
42. Gao M, Hu Q, Feng G, Tang BZ, Liu B (2014) A fluorescent light-up probe with "AIE + ESIPT" characteristics for specific detection of lysosomal esterase. J Mater Chem B 2:3438–3442
43. Shi H, Kwok RTK, Liu J, Xing B, Tang BZ, Liu B (2012) Real-time monitoring of cell apoptosis and drug screening using fluorescent light-up probe with aggregation-induced emission characteristics. J Am Chem Soc 134:17972–17981
44. Leung ACS, Zhao E, Kwok RTK, Lam JWY, Leung CWT, Deng H et al (2016) An AIE-based bioprobe for differentiating the early and late stages of apoptosis mediated by H_2O_2. J Mater Chem B 4:5510–5514
45. Hu Q, Gao M, Feng G, Chen X, Liu B (2015) A cell apoptosis probe based on fluorogen with aggregation induced emission characteristics. ACS Appl Mater Interfaces 7:4875–4882
46. Zhang W, Kwok RTK, Chen Y, Chen S, Zhao E, Yu CYY et al (2015) Real-time monitoring of the mitophagy process by a photostable fluorescent mitochondrion-specific bioprobe with AIE characteristics. Chem Commun 51:9022–9025
47. Hong Y, Chen S, Leung CWT, Lam JWY, Tang BZ (2013) Water-soluble tetraphenylethene derivatives as fluorescent "light-up" probes for nucleic acid detection and their applications in cell imaging. Chem Asian J 8:1806–1812
48. Ding D, Mao D, Li K, Wang X, Qin W, Liu R et al (2014) Precise and long-term tracking of adipose-derived stem cells and their regenerative capacity via superb bright and stable organic nanodots. ACS Nano 8:12620–12631
49. Chen Y, Qiao L, Yu B, Li G, Liu C, Ji L et al (2013) Mitochondria-specific phosphorescent imaging and tracking in living cells with an AIPE-active iridium (III) complex. Chem Commun 49:11095–11097
50. Li K, Zhu Z, Cai P, Liu R, Tomczak N, Ding D et al (2013) Organic dots with aggregation-induced emission (AIE dots) characteristics for dual-color cell tracing. Chem Mater 25:4181–4187
51. Li K, Qin W, Ding D, Tomczak N, Geng J, Liu R et al (2013) Photostable fluorescent organic dots with aggregation-induced emission (AIE dots) for noninvasive long-term cell tracing. Sci Rep 3:1150
52. Qin W, Li K, Feng G, Li M, Yang Z, Liu B et al (2014) Bright and photostable organic fluorescent dots with aggregation-induced emission characteristics for noninvasive long-term cell imaging. Adv Funct Mater 24:635–643
53. Yu C, Huang Z, Gu W, Wu Q, Hao E, Xiao Y et al (2019) A novel family of AIE-active *meso*-2-ketopyrrolyl BODIPYs: bright solid-state red fluorescence, morphological properties and application as viscosimeters in live cells. Mater Chem Front 3:1823–1832
54. Koenig M, Storti B, Bizzarri R, Guldi DM, Brancato G, Bottari G (2016) A fluorescent molecular rotor showing vapochromism, aggregation-induced emission, and environmental sensing in living cells. J Mater Chem C 4:3018–3027
55. Chen W, Gao C, Liu X, Liu F, Wang F, Tang LJ et al (2018) Engineering organelle-specific molecular viscosimeters using aggregation-induced emission luminogens for live cell imaging. Anal Chem 90:8736–8741
56. Song Z, Mao D, Sung SHP, Kwok RTK, Lam JWY, Kong D et al (2016) Activatable fluorescent nanoprobe with aggregation-induced emission characteristics for selective in vivo imaging of elevated peroxynitrite generation. Adv Mater 28:7249–7256
57. Wen X, Wang Q, Fan Z (2018) An active fluorescent probe based on aggregation-induced emission for intracellular bioimaging of Zn^{2+} and tracking of interactions with single-stranded DNA. Anal Chim Acta 1013:79–86
58. Yan L, Kong Z, Shen W, Du W, Zhou Y, Qi Z (2016) An aggregation-induced emission (AIE) ratiometric fluorescent cysteine probe with an exceptionally large blue shift. RSC Adv 6:5636–5640
59. Wang M, Gu X, Zhang G, Zhang D, Zhu D (2009) Convenient and continuous fluorometric assay method for acetylcholinesterase and inhibitor screening based on the aggregation-induced emission. Anal Chem 81:4444–4449

60. Hong Y, Wang H, Xue M, Zhang P, Liu W, Chen S et al (2019) Rational design of ratiometric and lysosome-targetable AIE dots for imaging endogenous HClO in live cells. Mater Chem Front 3:203–208
61. He X, Wang X, Zhang L, Fang G, Liu J, Wang S (2018) Sensing and intracellular imaging of Zn^{2+} based on affinity peptide using an aggregation induced emission fluorescence "switch-on" probe. Sensors Actuators B Chem 271:289–299
62. Ma H, Yang M, Zhang S, Yin P, Wang T, Yang Y et al (2019) Two aggregation-induced emission (AIE)-active reaction-type probes: for real-time detecting and imaging of superoxide anions. Analyst 144:536–542
63. Ding D, Liang J, Shi H, Kwok RTK, Gao M, Feng G et al (2014) Light-up bioprobe with aggregation-induced emission characteristics for real-time apoptosis imaging in target cancer cells. J Mater Chem B 2:231–238
64. Gao M, Chen J, Lin G, Li S, Wang L, Qin A et al (2016) Long-term tracking of the osteogenic differentiation of mouse BMSCs by aggregation-induced emission nanoparticles. ACS Appl Mater Interfaces 8:17878–17884
65. Ni JS, Zhang P, Jiang T, Chen Y, Su H, Wang D et al (2018) Red/NIR-emissive benzo[*d*]imidazole-cored AIEgens: facile molecular design for wavelength extending and in vivo tumor metabolic imaging. Adv Mater 30:1805220
66. Li C, Gong WL, Hu Z, Aldred MP, Zhang GF, Chen T et al (2013) Photoswitchable aggregation-induced emission of a dithienylethene-tetraphenylethene conjugate for optical memory and super-resolution imaging. RSC Adv 3:8967–8972
67. Lo CYW, Chen S, Creed SJ, Kang M, Zhao N, Tang BZ et al (2016) Novel super-resolution capable mitochondrial probe, MitoRed AIE, enables assessment of real-time molecular mitochondrial dynamics. Sci Rep 6:30855
68. Li D, Qin W, Xu B, Qian J, Tang BZ (2017) AIE nanoparticles with high stimulated emission depletion efficiency and photobleaching resistance for long-term super-resolution bioimaging. Adv Mater 29:1703643
69. Fang X, Chen X, Li R, Liu Z, Chen H, Sun Z et al (2017) Multicolor photo-crosslinkable AIEgens toward compact Nanodots for subcellular imaging and STED nanoscopy. Small 13:1702128
70. Yu J, Sun X, Cai F, Zhu Z, Qin A, Qian J et al (2015) Low photobleaching and high emission depletion efficiency: the potential of AIE luminogen as fluorescent probe for STED microscopy. Opt Lett 40:2313–2316
71. Li K, Ding D, Prashant C, Qin W, Yang CT, Tang BZ et al (2013) Gadolinium-functionalized aggregation-induced emission dots as dual-modality probes for cancer metastasis study. Adv Healthc Mater 2:1600–1605
72. Chen Y, Li M, Hong Y, Lam JWY, Zheng Q, Tang BZ (2014) Dual-modal MRI contrast agent with aggregation-induced emission characteristic for liver specific imaging with long circulation lifetime. ACS Appl Mater Interfaces 6:10783–10791
73. Zhang J, Li C, Zhang X, Huo S, Jin S, An FF et al (2015) In vivo tumor-targeted dual-modal fluorescence/CT imaging using a nanoprobe co-loaded with an aggregation-induced emission dye and gold nanoparticles. Biomaterials 42:103–111
74. Alifu N, Dong X, Li D, Sun X, Zebibula A, Zhang D et al (2017) Aggregation-induced emission nanoparticles as photosensitizer for two-photon photodynamic therapy. Mater Chem Front 1:1746–1753
75. Gao Y, Qu Y, Jiang T, Zhang H, He N, Li B et al (2014) Alkyl-triphenylamine end-capped triazines with AIE and large two-photon absorption cross-sections for bioimaging. J Mater Chem C 2:6353–6361
76. Geng J, Li K, Ding D, Zhang X, Qin W, Liu J et al (2012) Lipid-PEG-folate encapsulated nanoparticles with aggregation induced emission characteristics: cellular uptake mechanism and two-photon fluorescence imaging. Small 8:3655–3663
77. Ye Q, Chen S, Zhu D, Lu X, Lu Q (2015) Preparation of aggregation-induced emission dots for long-term two-photon cell imaging. J Mater Chem B 3:3091–3097
78. Liu P, Li S, Jin Y, Qian L, Gao N, Yao SQ et al (2015) Red-emitting DPSB-based conjugated polymer nanoparticles with high two-photon brightness for cell membrane imaging. ACS Appl Mater Interfaces 7:6754–6763
79. Hu F, Xu S, Liu B (2018) Photosensitizers with aggregation-induced emission: materials and biomedical applications. Adv Mater 30:1801350
80. Zhao E, Chen Y, Wang H, Chen S, Lam JWY, Leung CWT et al (2015) Light-enhanced bacterial killing and wash-free imaging based on AIE fluorogen. ACS Appl Mater Interfaces 7:7180–7188
81. Chang CC, Hsieh MC, Lin JC, Chang TC (2012) Selective photodynamic therapy based on aggregation-induced emission enhancement of fluorescent organic nanoparticles. Biomaterials 33:897–906
82. Yuan Y, Feng G, Qin W, Tang BZ, Liu B (2014) Targeted and image-guided photodynamic cancer therapy based on organic nanoparticles with aggregation-induced emission characteristics. Chem Commun 50:8757–8760
83. Zhao E, Deng H, Chen S, Hong Y, Leung CWT, Lam JWY et al (2014) A dual functional AEE fluorogen as a mitochondrial-specific bioprobe and an effective photosensitizer for photodynamic therapy. Chem Commun 50:14451–14454
84. Zhang T, Li Y, Zheng Z, Ye R, Zhang Y, Kwok RTK et al (2019) In situ monitoring apoptosis process by a self-reporting photosensitizer. J Am Chem Soc 141:5612–5616
85. Hu Q, Gao M, Feng G, Liu B (2014) Mitochondria-targeted cancer therapy using a light-up probe with aggregation-induced-emission characteristics. Angew Chem Int Ed 53:14225–14229

86. Yuan Y, Zhang CJ, Gao M, Zhang R, Tang BZ, Liu B (2015) Specific light-up bioprobe with aggregation-induced emission and activatable photoactivity for the targeted and image-guided photodynamic ablation of cancer cells. Angew Chem Int Ed 54:1780–1786
87. Ding D, Li K, Liu B, Tang BZ (2013) Bioprobes based on AIE fluorogens. Acc Chem Res 46:2441–2453
88. Kwok RTK, Leung CWT, Lam JWY, Tang BZ (2015) Biosensing by luminogens with aggregation-induced emission characteristics. Chem Soc Rev 44:4228–4238
89. Mei J, Leung NLC, Kwok RTK, Lam JWY, Tang BZ (2015) Aggregation-induced emission: together we shine, united we soar! Chem Rev 115:11718–11940
90. Gao H, Zhao X, Chen S (2018) AIEgen-based fluorescent nanomaterials: fabrication and biological applications. Molecules 23:419
91. Gu X, Kwok RTK, Lam JWY, Tang BZ (2017) AIEgens for biological process monitoring and disease theranostics. Biomaterials 146:115–135
92. He Z, Ke C, Tang BZ (2018) Journey of aggregation-induced emission research. ACS Omega 3:3267–3277

Luminescent Coordination Compounds for Cell Imaging

Mingdang Li, Feiyang Li, Shujuan Liu, and Qiang Zhao

1 Introduction

Cell imaging plays a significant role in both fundamental research and clinical application. Visualization of the cell has been widely used to study cell structure and function, track the morphological changes, explore the biological roles of organelles, and reveal the mechanisms of the interaction between morphologic information and chemical stimulation. Furthermore, chemotherapy interventions and further understanding of physiological and pathophysiological processes can be guided by the visualization of cellular and subcellular morphology [1, 2]. To date, numerous materials such as organic dyes [3, 4], nanoparticles [5–7], quantum dots [8–10], fluorescent proteins [11, 12], and coordination compounds [13–15] have been explored for cell and organelle imaging. Among them, as a promising luminescent dye, coordination compounds can provide high brightness and signal-to-noise ratio with minimal background interference for cellular and subcellular imaging, which is difficult to be achieved at the cellular level by general fluorophores [16, 17]. Besides, the photobleaching in long-term observation can be avoided by the remarkable photostability of coordination compounds. Moreover, coordination compounds for cell imaging have made considerable progress so far, and a large amount of novel dyes are emerging [18–22]. Coordination compounds are typically synthesized in a flexible and modular method, and the functionalized organic ligands are bound to the metal center in a fixed manner, making it easier to produce analogues to improve its photophysical and photochemical properties for cell imaging [23–27].

Over the past several decades, the application of luminescent coordination compounds for cell imaging has witnessed tremendous growth, especially for the utilization of luminescent metal complexes [28–31]. Recently, numerous luminescent transition metal complexes have been designed for cell imaging. Compared with the general fluorophores, unique and complicated photochemical and photophysical properties are achieved by the presence of metal ions in complexes, such as Au(I), Ag(I), Pt(II), Cu(I), Zn (II), Ru(II), and Ir(III) [32–39]. As aforementioned, luminescent complexes contain organic ligands bound to the metal center in a precise three-dimensional arrangement. The fascinating and adjustable properties of the complex are induced by the appropriate metal ions and flexible ligands, potentially allowing fine-control of the functions of the complex for complicated imaging demands. The properties of metal complexes in cell imaging are highly advantageous compared

M. Li · F. Li · S. Liu · Q. Zhao (✉)
Key Laboratory for Organic Electronics and Information Displays & Jiangsu Key Laboratory for Biosensors, Institute of Advanced Materials (IAM), Nanjing University of Posts and Telecommunications (NUPT), Nanjing, P. R. China
e-mail: iamqzhao@njupt.edu.cn

F.-G. Wu (ed.), *Fluorescent Materials for Cell Imaging*, https://doi.org/10.1007/978-981-15-5062-1_9

to the general fluorophores in the following aspects [40]. Firstly, high luminance can meet the needs of the cell and subcellular fraction imaging. Secondly, they display wide excitation and emission tunability. Thirdly, most of the luminescent complexes are stable toward long-term irradiation. Fourthly, they exhibit large Stokes shifts, allowing the lower energy emission to be easily distinguished from the excitation and preventing self-quenching. Finally, they can show long-lived phosphorescence, such as for Ir(III) complexes, which can eliminate interference from short-lifetime autofluorescence in biological samples through time-resolved luminescence technique. Although the emission wavelength of transition metal complexes can be easily tuned, the near-infrared (NIR) emission is still a big challenge, limiting the in vivo real-time optical imaging. Recently, many groups have designed NIR emissive lanthanide (Ln(III)) complexes to facilitate NIR imaging, which can further improve the imaging quality by reducing scattering, minimizing absorption, and neglecting autofluorescence [41–43]. Meanwhile, an evolution of bioimaging may be caused by the large extinction coefficient and high penetration depth [44–46].

In recent years, the ligand design, optical property, luminescent mechanism of photofunctional metal complexes, and their applications in bioimaging have been summarized in various highly informative reviews and books [47–51]. Considering the rapid development of the research area, in this chapter, a comprehensive overview of the recent applications of luminescent metal complexes in cell imaging is provided; meanwhile, the prospect of such a kind of fascinating luminescent compounds in clinical application is also discussed.

2 Luminescent Coordination Compounds

As mentioned above, metal complexes possess several advantageous features that make them capable as attractive imaging agents. Furthermore, due to the complicated excited states and easily modified ligands, the richer optical properties and more functionalities than most of organic fluorophores could be provided by metal complexes. Consequently, new opportunities are brought about by metal complexes for the development of cell image techniques, as well as biosensing systems and phototherapy. In this chapter, we focus on transition metal complexes and Ln(III) complexes that have been widely and successfully utilized as imaging agents for cell imaging applications.

2.1 Luminescent Transition Metal Complexes

Due to the excellent properties such as high quantum yield and photostability, wide modulation of the emission wavelength, and long phosphorescence lifetime, transition metal complexes are promising candidates as bioimaging agents. Besides, transition metal complexes can display the excellent performances such as rich excited states, including metal-to-ligand charge-transfer (MLCT), ligand-to-metal charge-transfer (LMCT), intraligand charge-transfer (ILCT), ligand-to-ligand charge-transfer (LLCT), metal-centered (MC) excited states, ligand-to-metal–metal charge-transfer (LMMCT), metal–metal-to-ligand charge-transfer (MMLCT), and metal-to-ligand–ligand charge-transfer (MLLCT) states [28, 40]. These excited states are mainly determined by the type of metal center and the structures and triplet-state energy levels of the ligands. Furthermore, the intramolecular and intermolecular interactions and the ambient environment also have significant influence on the excited states of transition metal complexes, making them show diverse photophysical and photochemical properties under physiological conditions. The complicated excited state properties of transition metal complexes have attracted increasing interest in bioimaging and biosensing.

2.2 Luminescent Transition Metal Complexes for Bioimaging

Currently, a great number of luminescent metal complexes have been applied to visualize live cells and explore cellular processes by laser-scanning confocal microscopy [52–54]. Typically, the complexes of Pt(II), Au(I), Ru(II), and Ir(III) were popular in bioimaging and biosensing, and have made significant progress.

2.2.1 Transition Metal Complexes for Intensity-Based Luminescent Cell Imaging and Sensing

Pt(II) Complexes for Intensity-Based Luminescent Cell Imaging and Sensing

Pt(II) complexes were well-known class of luminescent coordination compounds with promising applications in bioimaging and biosensing [55–57]. In recent years, Pt(II) complexes were initially proposed as alternative agents to organic fluorophores for staining cells, and it was now apparent that their outstanding photophysical properties can make them available for broad areas of biological science [58, 59]. In the field of cell imaging, Pt(II) complexes have been developed as novel staining agents. Pt(II) complexes and derivatives are indispensable in the application of cell imaging by laser-scanning confocal microscopy. For example, Zhou et al. designed and synthesized three Pt(II) complexes with bidentate ligands (Pt-dfppy (*Pt1*), Pt-ppy (*Pt2*), and Pt-bt (*Pt3*)) for applying in living cell imaging and protein staining [60]. These complexes have almost no cytotoxicity toward HeLa cell lines, and are mainly distributed in the cytoplasm. In addition, the quite low limits of detection (below 50 ng) in protein staining of the designed Pt(II) complexes provide great commercial opportunities. However, the poor water solubility is one of the prime challenges in using Pt(II) complexes as bioimaging agent. For this purpose, Jana et al. designed a highly water-soluble Pt(II) complex ([Pt(ppy)(en)]Cl, *Pt4*) for bioimaging applications [61]. The imaging results showed that *Pt4* can easily penetrate the cell membrane in cancer cells and normal cells, and showed a much higher uptake in cancerous cells. Lately, Dragonetti et al. reported three new neutral terdentate Pt(II) complexes bearing cyclometalated di(2-pyridyl)-benzene substituted with ethylene glycol moieties of various lengths, as luminescent cell imaging agents [62]. The chemical structures of these three Pt(II) complexes (PtL^1Cl (*Pt5*), PtL^1NCS (*Pt6*), and PtL^2Cl (*Pt7*)) were shown in Chart. 1. As expected, the designed Pt(II) complexes exhibited high cell permeability and low cytotoxicity, with an internalization kinetics that relied on the influence of both the ethylene glycol chain length and the ancillary ligand. The introduction of oligo-ethylene glycol chains on the designed Pt(II) complexes was used to improve the solubility and biocompatibility. All three complexes displayed bright green-yellow emission under excitation at 300 nm, and the ancillary ligand had little impact on the emission wavelengths (λ_{em} = 542, 540, and 546 nm for *Pt5*, *Pt6*, and *Pt7*, respectively). The rigidity of the tridentate cyclometalated ligand effectively reduced the molecular distortions of the excited states, and the strong ligand field of tridentate chelate increased the energy of the metal centered (MC) d-d excited states, contributing to long excited-state lifetime as 12.4, 11.8 and 12.1 μs for *Pt5*, *Pt6*, and *Pt7*, respectively. The cell imaging properties of the designed three Pt(II) complexes were analyzed by using the luminescence confocal images. HeLa cells can be rapidly stained (within 10 min) by each of the three compounds (Fig. 1), and the emission profile obtained from living cells was in accordance with the emission spectra measured in dilute dichloromethane (CH_2Cl_2) (Fig. 1), confirming the similar nature of the emitting excited state for the two compared conditions. Furthermore, z-stack experiments and co-localization experiments (Fig. 2) confirmed that the designed Pt(II) complexes can cross the nuclear membrane and localize in the nuclear region which depends on their molecular structure or hydrophobic/hydrophilic nature. Furthermore, with intrinsic photophysical characteristics that are highly

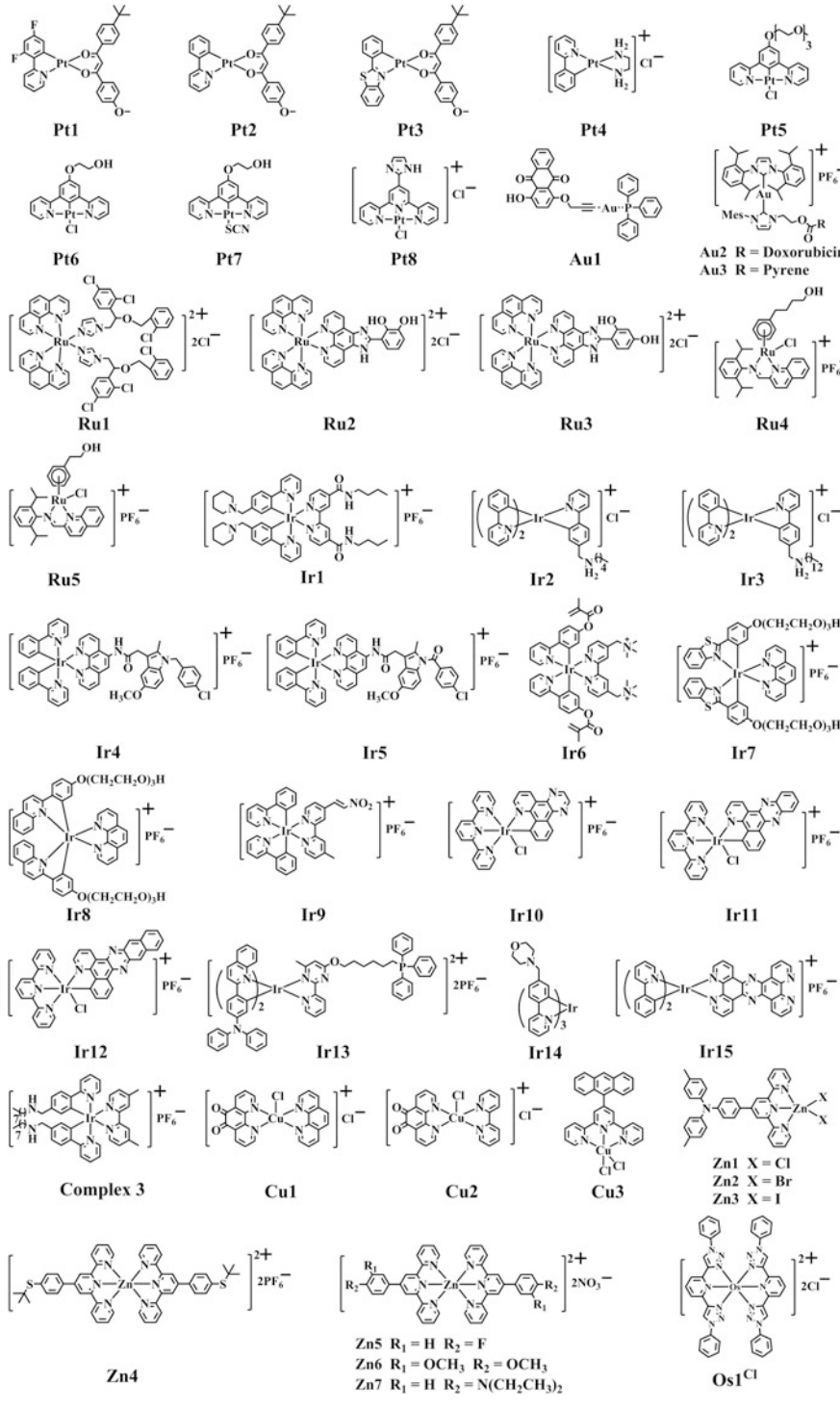

Chart 1 Chemical structures of transition metal complexes for bioimaging

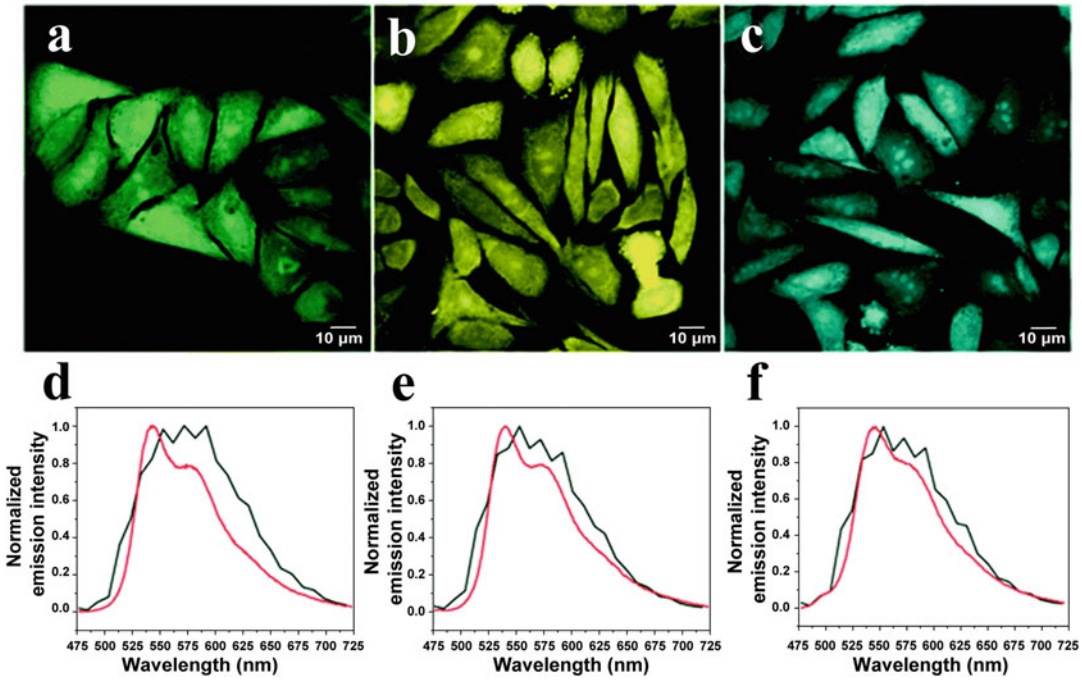

Fig. 1 Images of the internalization of three different platinum complexes at 50 μM into HeLa cells with <1% DMSO/PBS as the incubating medium. (**a**) *Pt5*, (**b**) *Pt6*, and (**c**) *Pt7*. The emission spectra recorded from different cellular regions ($\lambda_{ex} = 405$ nm, black lines) and in dilute CH_2Cl_2 ($\lambda_{ex} = 300$ nm, red lines) are displayed for (**d**) *Pt5*, (**e**) *Pt6*, and (**f**) *Pt7*. (Reprinted with permission from Ref. [62]. Copyright © 2015 Royal Society of Chemistry)

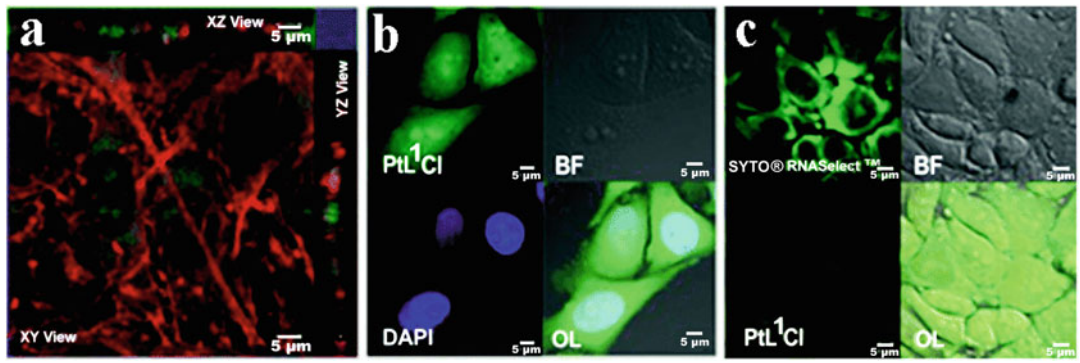

Fig. 2 Images of the distribution of *Pt5* (50 μM in less than 1% DMSO containing PBS) inside HeLa cells and co-localization experiments showing the presence of compound *Pt5* inside the cell nucleus, nucleoli, and cytoplasmic parts of the cell. (**a**) Orthogonal views of the image showing *Pt5* signals (green) coming from the cytoplasmic and nuclear regions of the cells. The cells are stained with Phalloidin Alexa Fluor® 647 (red). (**b**) *Pt5*, bright-field (BF) image of HeLa cells, DAPI staining of the nucleus, and overlay (OL) of the three panels. (**c**) SYTO® RNASelect™ green stains the RNA inside cells including nucleoli; BF image, *Pt5*, and overlay of the three panels. DAPI and *Pt5* were excited at 405 nm, while SYTO® RNASelect™ and Phalloidin Alexa Fluor® 647 were excited at 488 and 633 nm, respectively. (Reprinted with permission from Ref. [62]. Copyright © 2015 Royal Society of Chemistry)

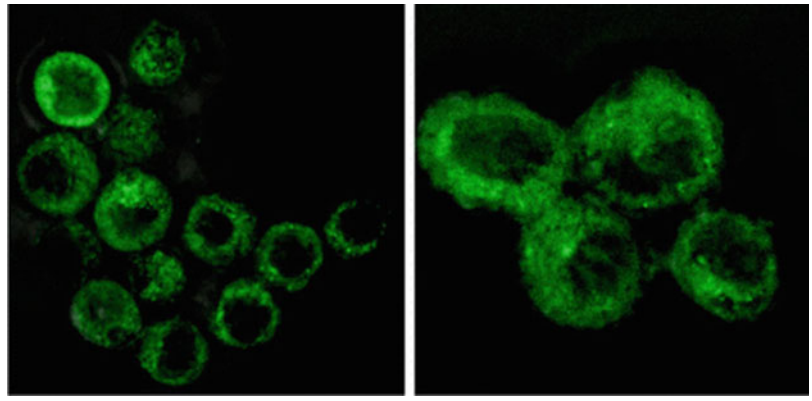

Fig. 3 Images of human breast adenocarcinoma (MCF-7) cells incubated with *Au1* (100 μg mL^{-1}, 4 °C, 30 min). Excited at 405 nm, acquired 530–580 nm. (Reprinted with permission from Ref. [66]. Copyright © 2012 American Chemical Society)

sensitive to the microenvironment, the pincer Pt (II) complexes have been developed as a promising agent for cancer phototherapy. Huang et al. successfully synthesized a series of green-light-activated Pt(II) Schiff base complexes containing tetradentate salicylaldimine chelating ligands for confocal cellular imaging [63]. The designed complexes mostly localized in the cytoplasm of cancer cells and exhibited significant photocytotoxicity, while remaining non-toxic in the dark, indicating that these photoactive Pt (II) complexes have potential for photodynamic anticancer therapy as new theranostic and therapeutic agents. This shows that the luminescent Pt (II) complexes provide additional options to meet the challenges for further progress of bioimaging, biosensing, and phototherapy.

Au(I) Complexes for Intensity-Based Luminescent Cell Imaging and Sensing

Au(I) complexes are confirmed to possess stable luminescence properties, which are suitable for bioimaging applications [64–67]. To date, a series of Au(I) complexes were designed and synthesized as potential cell imaging agents. For example, Coogan et al. reported a series of Au (I) triphenylphosphine complexes for luminescence and cell imaging studies [66]. All of the Au(I) complexes displayed room-temperature anthraquinone-based visible luminescence and applicable cytotoxicity, which allowed their successful application as cell imaging agents with good uptake (>80%). As shown in Fig. 3, the cells were successful stained by the Au (I) complex (L^2-Au-PPh_3, *Au1*) with an apparently healthy cell morphology and the luminescence originated from the cytoplasm with little or no nuclear localization. Recently, N-heterocyclic carbene (NHC) based Au(I) complexes have attracted growing interest due to their excellent luminescent and biological properties. Some excellent studies put forward the NHC-based Au(I) complexes have practical potentials on bioimaging applications. Poyatos et al. designed and synthesized three pyrene-based tetraalkynyl Au(I) complexes [68]. Among them, an Au (I) complex bearing aromatic NHC was found to be highly emissive in dichloromethane solution with quantum yields exceeding 90%. Besides, confocal microscopy images of healthy cheek cells confirmed that the complex can rapidly stain the cells. Berners-Price et al. synthesized a new series of luminescent dinuclear Au(I)-NHC complexes for live cell imaging applications [69]. Of particular interest was the *cis-3*.2Br, which was used to map the distribution of the complex inside live tumor cells without any additional fluorescent tag, giving valuable insight into the subcellular distribution for this class of compounds. However, the mechanisms of the cellular uptake and intracellular distribution of Au(I) complexes is still lacked now, and thus continued researches are needed for further

understanding of Au(I) complexes based biological applications.

Ru(II) Complexes for Intensity-Based Luminescent Cell Imaging and Sensing

Ru(II) complexes exhibited significantly advantageous photophysical properties for biological imaging applications. In recent years, these complexes have expanded to diverse applications such as cell imaging agents and promising candidates for phototherapy [70–73]. Lately, Renfrew et al. reported a new Ru(II) complex (*Ru1*) for live cell imaging and selective release of the imidazole-based drug econazole [74]. The *Ru1* was highly stable in the dark, but the green-light irradiation induced release of one of the econazole ligands, which led to a turn-off luminescence response and up to a 34-fold increase in cytotoxicity toward tumor cells. Tsui et al. synthesized a novel luminescent Ru(II)-cyanide complex with NHC-based C^N^C pincer ligand for live cell imaging of endocytosis [75]. It showed extremely low cytotoxicity to both MCF-7 cell and human retinal pigmented epithelium (RPE) cell in a wide range of concentration (0.1–500 μM), and can be applied for the luminescent endocytosis imaging in these cells. Wang et al. designed and synthesized two isomeric Ru (II) complexes, $[Ru\text{-}m\text{-}OH]^{2+}$ (*Ru2*) and $[Ru\text{-}o\text{-}OH]^{2+}$ (*Ru3*) with two hydroxyl substituents at different positions of ligands for cell imaging [76]. Both of the two complexes can be clearly visualized in live cell by confocal microscopy. Interestingly, the cellular uptake efficiency of *Ru3* was much better than that of *Ru2* (Fig. 4), and can activate mitochondrial apoptosis pathway by upgrading the expression of Bax and downgrading the level of Bcl-2. Remarkably, *Ru3* showed great selectivity between cancer cells (BEL-7402) and human normal cell (HBMEC) (IC_{50} = 11.8 μM to BEL-7402 cells; $IC_{50} > 100$ μM to HBMEC), and exhibited higher toxicity toward BEL-7402 cells than *Ru2*, which showed that the designed isomeric Ru (II) complexes have great prospect for anticancer as medicine.

Ir(III) Complexes for Intensity-Based Luminescent Cell Imaging and Sensing

Ir(III) complexes are one of the most widely studied and developed in the family of luminescent transition metal complexes for various bioimaging applications [77–79]. Typically, Ir (III) complexes consist of a trivalent iridium ion center bound to two cyclometalated ligands and one auxiliary ligand. The chemical properties of

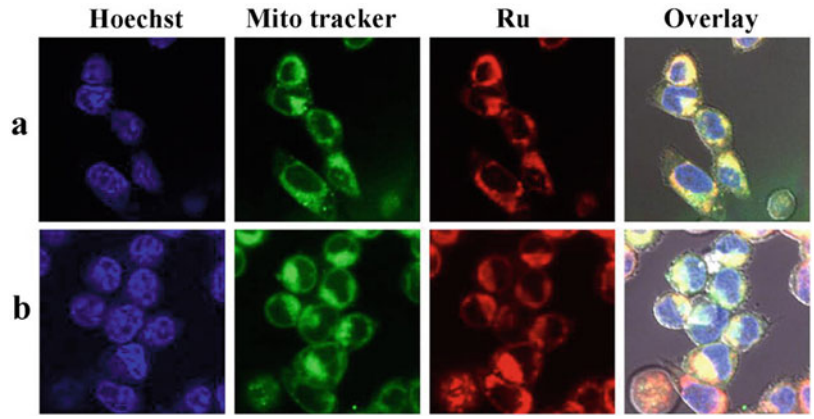

Fig. 4 The confocal images of BEL-7402 cells treated with 15 μM *Ru2* (**a**) or *Ru3* (**b**) (λ_{ex} = 488 nm, λ_{em} = 600 ± 50 nm, red) for 6 h, the nucleus stained with Hoechst 33258 (λ_{ex} = 405 nm, λ_{em} = 450 ± 30 nm, blue) and mitochondria stained with MitoTracker Green (λ_{ex} = 458 nm, λ_{em} = 520 ± 30 nm, green). (Reprinted with permission from Ref. [76]. Copyright © 2017 Elsevier B.V)

this family of complexes can be easily tuned by chemical variations of the coordinated ligands, and this brings high versatility for bioimaging applications. In the last decade, Ir(III) complexes have received extensive investigation for applications in cell imaging. In recent years, Zhao et al. have designed and synthesized different types of Ir(III) complexes, and successfully applied them in various bioimaging applications, particularly in biosensing and cellular imaging [80–84]. For example, they designed and synthesized a series of Ir(III) complexes containing aminomethyl substituted phenylpyridine ligands for intracellular oxygen sensing in both of hypoxia, normoxia and hyperoxia ranges. The designed Ir(III) complexes incorporated with aminomethyl substituted phenylpyridine ligands were expected to achieve the dual-phosphorescence properties and the spectral profile response toward oxygen level. The limited internal conversion between triplet metal/ligand-to-ligand charge-transfer (^{3}CT) and intraligand (^{3}IL) excited states leads to dual phosphorescence from two different excited states upon excitation at a single wavelength. Structural manipulation of the Ir(III) complexes can effectively tune the dual-phosphorescence properties and the spectral response toward both hyperoxia and hypoxia. Interestingly, one of the tertiary-amine-substituted Ir(III) complex (*Ir1*) exhibited dual phosphorescence in aqueous buffer solution under ambient air, showing the orange phosphorescence color. *Ir1* exhibited naked-eye distinguishable green, orange, and red emission in aqueous buffer solution under hypoxia, normoxia, and hyperoxia, respectively. Furthermore, they demonstrated that the ratiometric spectral response of *Ir1* toward oxygen was owing to the different quenching efficiency of the two above-mentioned excited states. Remarkably, this complex was successfully used for imaging different oxygen level (including hypoxia, normoxia, and hyperoxia) in living cells. As shown in Fig. 5, *Ir1* was distributed in cytoplasm of HeLa, HepG2, and 3T3 cells. The green and red phosphorescence became predominant

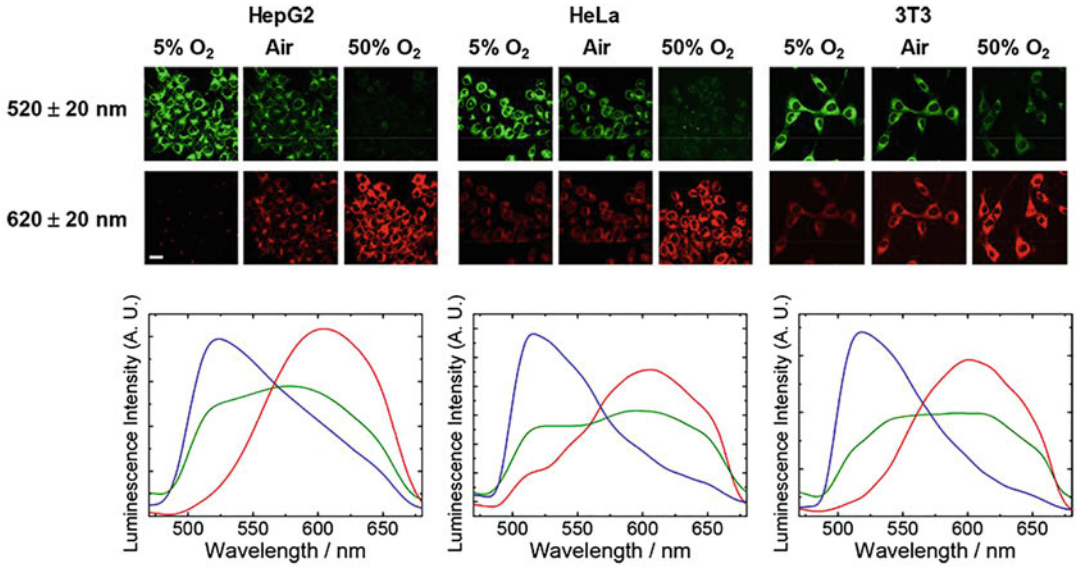

Fig. 5 Laser-scanning luminescence microscopy images and intracellular phosphorescence spectra of HepG2, HeLa, and 3T3 cells incubated with *Ir1* (5 μM, 2 h, 37 °C) cultured under 5% (blue), 21% (green), and 50% (red) oxygen conditions. Scale bar: 30 μm. (Reprinted with permission from Ref. [84]. Copyright © 2018 American Chemical Society)

when the cells were cultured under low (5%) and high (50%) oxygen conditions, respectively. The sensitive spectral response toward both intracellular hypoxia and hyperoxia was achieved by the use of *Ir1* at the first time. In addition, Pal et al. reported the synthesis and investigation of properties of two aminoalkyl tris-cyclometalated luminescent Ir(III) complexes *(Ir2* and *Ir3*) as cell imaging agents [85]. These complexes were highly emissive with long lifetimes even in aerated aqueous solutions. The designed Ir(III) complexes were successfully taken up by living cells and remained emissive with lifetimes in the microsecond domain, which provided new possibility to develop more imaging agents based on their core structure. Remarkably, the cyclometalated ligands of Ir(III) complexes are easy to be modified by organic groups or compounds, providing a broader application prospect in bioimaging and biosensing. Tan et al. reported two novel luminescent Ir(III) complexes (*Ir4* and *Ir5*) containing indomethacin analogue functionalized N^N ligands as imaging agents for COX-2 in cancer cells [86]. Both of the two Ir(III) complexes possessed excellent photophysical characteristics and high stability in living cells. Compared with *Ir5*, *Ir4* displayed higher solubility and lower cytotoxicity, which indicated that *Ir4* can be developed to monitor COX-2 in living cells and potentially to diagnose cancer. Hou et al. designed and synthesized a novel cyclometalated Ir(III) complex (*Ir6*) with good water solubility for specifically detecting hypochlorite (ClO^-) via incorporating a methacrylate group into cyclometalated ligands, which was performed as a specific response site toward ClO^- through an oxidation process [87]. In aqueous buffer solution, the emission of *Ir6* (615 nm) was significantly quenched upon addition of ClO^- with a low detection limit of 0.41 μM and a rapid response rate (<30 s). Furthermore, bioimaging of ClO^- was successfully performed by the designed *Ir6* in living human liver hepatocellular carcinoma (HepG2) cells, which provided a potential application in luminescent biosensing. Li et al. designed and synthesized two triethylene glycol-modified Ir(III) complexes (*Ir7* and *Ir8*) for imaging of living HeLa cell and *Schistosoma japonicum* [88]. As shown in Fig. 6a, b, both of *Ir7* and *Ir8* have good membrane permeability for staining living HeLa cells. As shown in Fig. 6c, d, *Ir7* and *Ir8* have remarkable luminescence labeling effect on living *Schistosoma japonicum*. Besides, bright-field images of *Schistosoma japonicum* displayed an intact skin surface structure and good survival, indicating that the designed *Ir7* and *Ir8* have excellent biocompatibility and low injury to *Schistosoma japonicum*. At present, many groups now emphasize on the research and development of Ir(III) complexes in biological applications, owing to their advantageous photophysical properties such as high brightness and photobleaching resistance, large Stokes shifts, and long emission lifetime. Therefore, Ir(III) complexes are emerged as promising alternative candidates to organic dyes for bioimaging and biosensing.

Cheap Transition Metal Complexes for Intensity-Based Luminescent Cell Imaging and Sensing

Typically, Cu(II) and Zn(II) complexes have been widely utilized as a promising candidates in various cell imaging applications [89–91]. Torkzadeh-Mahani et al. synthesized two water-soluble Cu(II) complexes (*Cu1* and *Cu2*) for live cancer cells imaging [38]. Yoon et al. designed and synthesized a novel water-soluble Cu(II) naphthalimide complex, and it was successfully applied for the imaging of exogenous and endogenous NO and HNO in living cells [92]. Mayilmurugan et al. reported an anthracenyl appended terpyridine Cu(II) complex ($Cu(L)Cl_2$, *Cu3*) as highly selective "turn-on" fluorescence imaging probe for cysteine (Cys) [93]. The selectively visualization of exogenously added Cys in HeLa cells (Fig. 7), HepG2 cells, and (human embryonic kidney 293) HEK293 cells was achieved under identical conditions at pH 7.4. Recently, Chao et al. reported low-cost terpyridine-Zn(II) complexes for selective nanomolar pyrophosphate detection in living cells, which provided a powerful tool for pyrophosphate related studies such as cell imaging and diagnosis [94]. Zhang et al. synthesized and characterized three terpyridine-based Zn

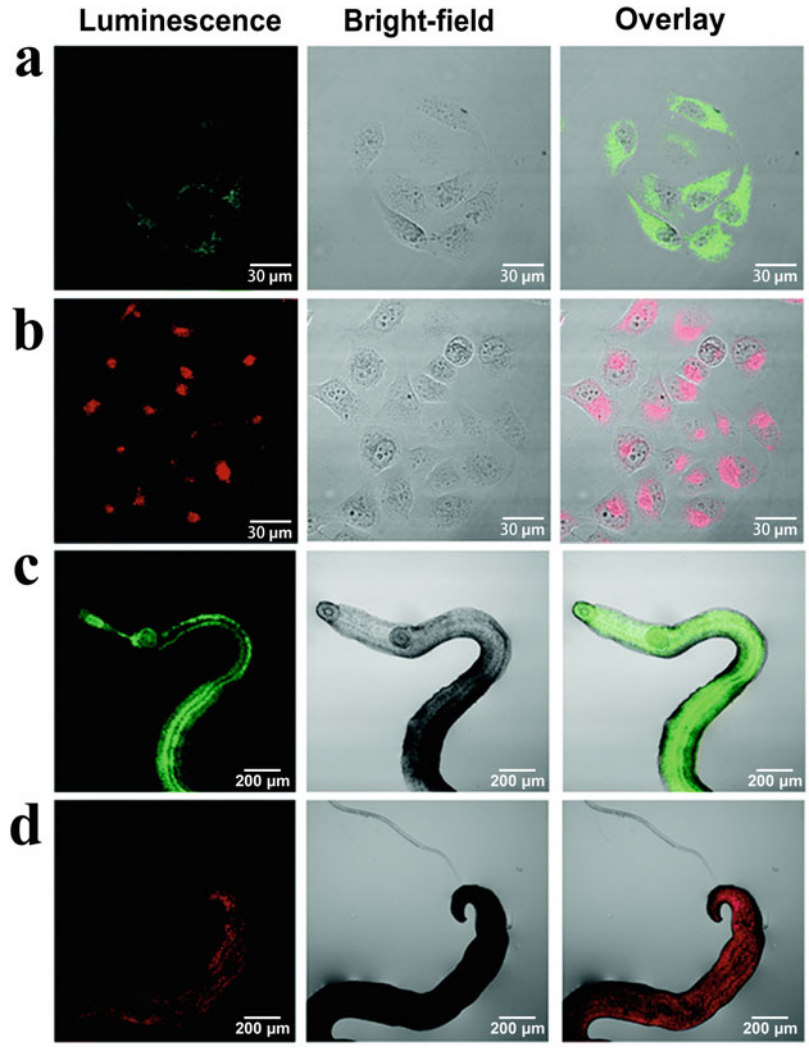

Fig. 6 The luminescence, bright-field, and overlay images of HeLa cells incubated with 5 μM *Ir7* (**a**) and *Ir8* (**b**) in PBS (pH 7) for 20 min, $\lambda_{ex} = 405$ nm, $\lambda_{em} = 560 \pm 50$ nm. Confocal luminescence, bright-field, and overlay images of living *Schistosoma japonicum* treated with 5 μM *Ir7* (**c**) and *Ir8* (**d**) in PBS (pH 7) for 15 min, $\lambda_{ex} = 405$ nm, $\lambda_{em} = 560 \pm 50$ nm. (Reprinted with permission from Ref. [88]. Copyright © 2017 Royal Society of Chemistry)

(II) complexes (*Zn1*, *Zn2*, and *Zn3*) for bioimaging application [95]. Biological tests confirmed that all the Zn(II) complexes possessed low cytotoxicity, good membrane permeability, and excellent photostability, and displayed a strong fluorescence in the cytoplasm of living HeLa cells (Fig. 8). In 2017, Tang et al. summarized the principles and trends including the design, functionality, and reactivity of Zn (II) complexes detailedly [91]. The bioimaging applications of various luminescent Zn (II) complexes as biological probes have been well reviewed, and have pointed further desirable research in biological imaging. Interestingly, the utilization of Zn(II) complexes in two-photon fluorescence microscopy (TPM) has attracted increasing attentions and has made great progress in bioimaging and biosensing in recent years [96–98]. In TPM, a fluorophore was excited by two long wavelength photons simultaneously, and the photon with low energy can effectively reduce the total photodamage to living cells [99]. Furthermore, the increased penetration depth can make meaningful sense for the visualization of living tissues [100, 101]. In 2008, a two-photon metal complex as bioimaging agent was reported for the first time by Williams [56]. Afterwards, the TPM bioimaging by utilizing metal complexes as

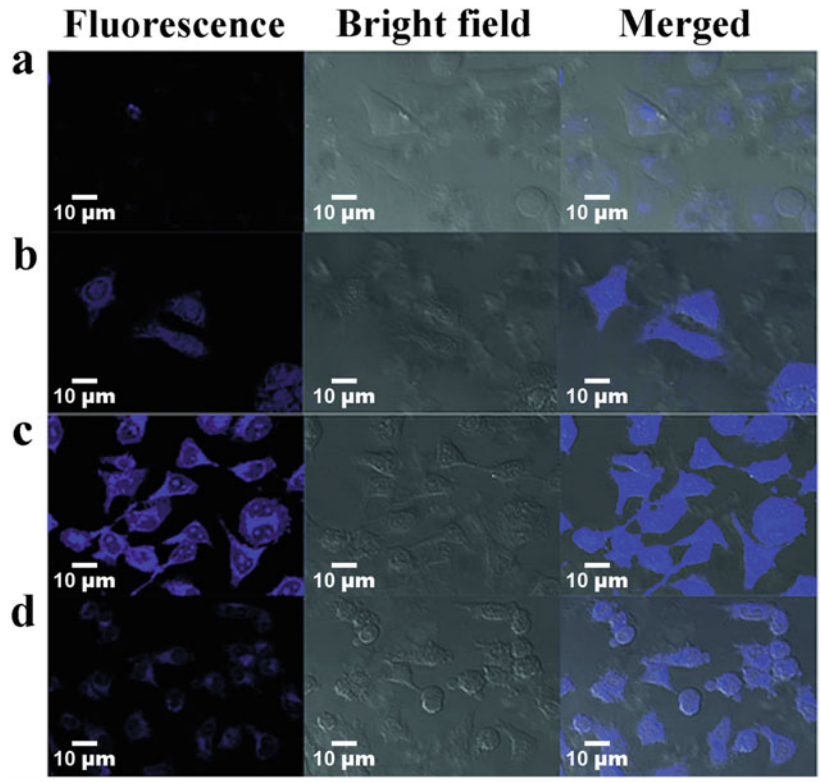

Fig. 7 Confocal fluorescence and bright-field images of HeLa cells: Cells in the absence of *Cu3* (**a**); Cells incubated with *Cu3* (5 μM) for 30 min without treatment of Cys (**b**); Cells pretreated with 100 μM Cys and incubated with *Cu3* (5 μM) for 30 min (**c**); Cells pretreated with 200 μM N-ethylmaleimide and incubated with *Cu3* (5 μM) for 30 min (**d**). (Reprinted with permission from Ref. [93]. Copyright © 2017 Wiley-VCH Verlag GmbH & Co. KGaA, Weinheim)

luminescent probes was kept trying and has progressed rapidly in recent years. However, the balance between synthetic costs, biocompatibility, and photophysical properties of metal complexes is still a challenge in bioimaging applications. Particularly, Zn(II) complexes generally possess lower toxicity and lower molecular weight than heavy metal complexes (such as Pt (II)-, Ru(II)-, Au(I)-, and Ir(III) complexes), and their high luminescence and electron dense cores make them suitable as imaging agents for TPM [102–105]. Wu et al. synthesized a novel D-A type terpyridine-based carbazole Zn(II) complex for bioimaging application [106]. TPM images confirmed that the cytoplasm of living HepG2 cells was successfully stained with the designed Zn(II) complex. Then, they further reported a series of Zn(II) terpyridine complexes with enhanced two-photon-excited fluorescence for in vitro and in vivo bioimaging [107]. Among them, the synthesized $[L_1\text{-Zn-}L_1][PF_6]_2$ (*Zn4*) was evaluated as bioimaging probe for HepG2 cells in vitro imaging. Furthermore, in vivo imaging of intestinal system of zebrafish larva was achieved by TPM. Tian et al. successfully synthesized a two-photon absorption water-soluble Zn(II) terpyridine complex for bioimaging [96]. Long time irradiation (150 s continued irradiation by 820 nm excitation light) indicated that the designed Zn(II) complex displayed good photostability in live cells. Last year, they further designed three Zn (II) terpyridine-based nitrate complexes (*Zn5*, *Zn6*, and *Zn7*) as two-photon fluorescent probe for identifying live/apoptotic cells at subcellular level by TPM [97]. Importantly, *Zn7* was successfully applied as an indicator for cell mortality at subcellular level, which laid a valuable foundation for further design and application of this type Zn(II) complexes.

With the excellent advantages of TPM, a great number of two-photon absorption transition metal

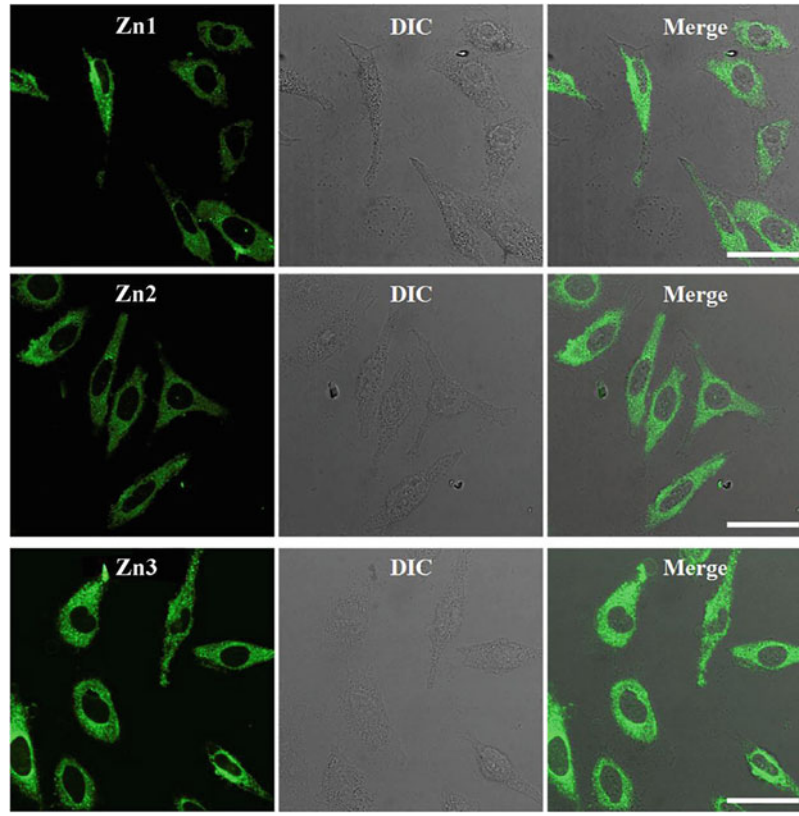

Fig. 8 Confocal imaging of HeLa cells treated with *Zn1*, *Zn2*, and *Zn3* for 0.5 h. The scale bars present 20 mm. (Reprinted with permission from Ref. [95]. Copyright © 2019 Elsevier B.V)

complexes have been studied for cell imaging applications, such as Pt(II)-, Ru(II)-, and Ir(III) complexes, and have progressed rapidly [108–110]. As one of the most advanced imaging technique, TPM has made significant sense in bioimaging and biosensing, and maintained continuous research.

2.2.2 Transition Metal Complexes for Time-Resolved Luminescent Cell Imaging and Sensing

Time-resolved photoluminescence techniques include time-gated luminescence microscopy (TGLM) and photoluminescence lifetime imaging microscopy (PLIM). In TGLM, luminophores were excited by a pulsed light source, and the detector was maintained in the off-state until short-lived signals fade completely [111]. Therefore, only long-lived signals were collected and clearly distinguished from short-lived unwanted interference in time domain (Fig. 9). In contrast, all photons were collected for calculation of lifetimes in PLIM measurement, and the desired signals can be easily distinguished from short-lived autofluorescence and light scattering based on their different decay rates [112–114]. Both TGLM and PLIM are used to obtain high quality images with minimized autofluorescence interference and high signal-to-noise ratio.

In recent years, the significant long emissive lifetime has sparked the investigation of Ir(III) complexes from traditional confocal imaging to time-resolved photoluminescence imaging techniques, which is a highly useful way to eliminate short-lived interference from autofluorescence [115–117]. Additionally, the lifetime is independent of concentration variation and the excitation laser power, and the luminophores that absorb or emit at similar

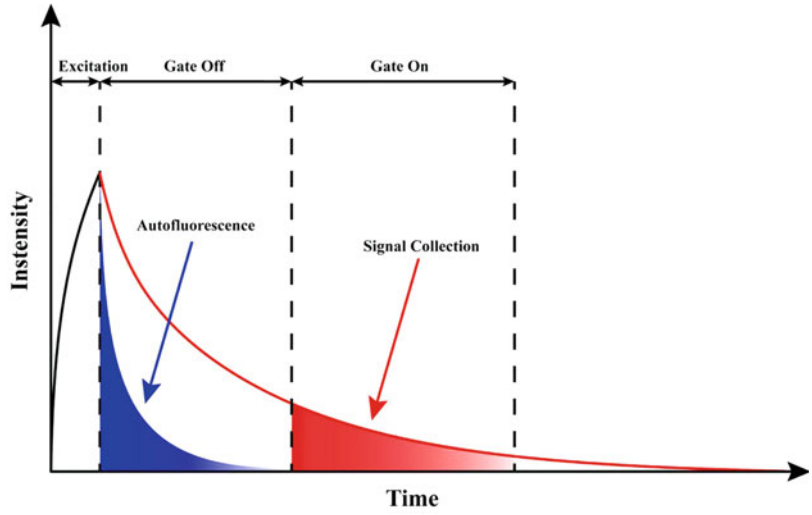

Fig. 9 Principle of TGLM technique to suppress autofluorescence

wavelengths can be distinguished based on their different emission lifetimes. Thus the utilization of Ir(III) complexes for bioimaging via time-resolved imaging techniques has attracted increasingly attentions. Recently, Zhao et al. have reported a series of excellent Ir(III) complexes for time-resolved luminescent cell imaging and sensing [118–122]. For example, they synthesized a mesoporous silica-coated core-shell UCNPs covalently attached with complex Ir (core-shell UCNPs@mSiO_2-Ir) as probe for monitoring oxygen level by time-resolved luminescent imaging technology [123]. As shown in Fig. 10, the lifetime of oxygen sensitive long-lived Ir(III) complex reduced from 4.0 to 0.8 μs when the environment changed from hypoxia into normoxia, which was clearly visualized by PLIM, allowing the monitoring of oxygen level. Besides, short-lived autofluorescence was already filtered via TGLM to enhance signal-to-noise ratio. Furthermore, they reported a phosphorescent peroxynitrite nanoprobe (MSN-ONOO) by immobilizing two long-lived phosphorescent Ir(III) complexes for exogenous and endogenous peroxynitrite detection in living cells via ratiometric photoluminescence imaging [124]. The designed probe has successfully achieved in vivo peroxynitrite sensing in living zebrafish and mouse with diminished autofluorescence interference and high signal-to-noise ratio by time-resolved photoluminescence imaging. In addition, Zhang et al. reported an activatable Ir(III) complex probe ([Ir$(ppy)_2$(NTY-bpy)](PF_6), *Ir9*) for phosphorescence/time-gated luminescence detection of Cys in vitro and in vivo [125]. The designed *Ir9* exhibited good biocompatibility, cell membrane permeability, and mitochondria-targeting ability, and achieved visualizations and flow cytometry analysis of mitochondrial Cys levels and Cys-mediated redox activities of live cells. Wong et al. designed and synthesized two Ir(III) complexes bearing methylthio group for detecting periodate in aqueous buffer and in living cells [126]. Meanwhile, these long emission lifetime of Ir(III) complexes can be applied to detect periodate in the presence of organic dyes by TGLM. Nowadays, long-lived emissive Ir(III) complexes have attracted fast-growing interest as suitable agents for time-resolved photoluminescence imaging, and have received widespread and continuous attention in bioimaging and biosensing.

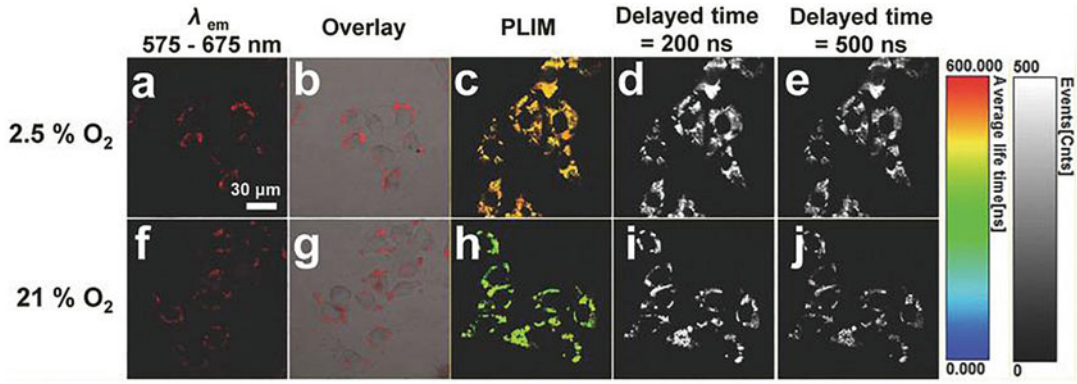

Fig. 10 (**a**, **b**, **f**, **g**) Confocal luminescent images, (**c**, **h**) PLIM images, and (**d**, **e**, **i**, **j**) TGLI images (delayed time = 200 or 500 ns) of living HeLa cells incubated with core-shell UCNPs@mSiO_2-Ir (200 μg/mL) at 37 °C for 2 h and then incubated at 37 °C and under 2.5% and 21% O_2 for another 1 h by 405 nm excitation. All the images share the same scale bar of 30 μm. Images were taken at 25 °C. (Reprinted with permission from Ref. [123]. Copyright © 2015 Wiley-VCH Verlag GmbH & Co. KGaA, Weinheim)

2.2.3 Transition Metal Complexes for Organelle-Targeting Luminescent Cell Imaging and Sensing

Organelle-targeting bioimaging is essential for understanding biological functions, specifically detecting chemical molecules, and studying effective cancer therapeutics [127, 128]. Transition metal complexes have emerged as a suitable agent for organelle-targeting bioimaging applications, which have attracted increasing attention in recent years [129–132]. In 2017, Chao et al. summarized organelle-targeting regulating strategies, characteristics of organelle-targeting metal complexes, and their bio-applications, and also outlined the existing opportunities and challenges for designing new generation of organelle-targeting metal complexes [133]. Herein, we focus on the latest organelle-targeting transition metal complexes and their bioimaging and biosensing applications. Figure 11 shows the distribution and morphology of main cellular organelles, including the cytomembrane, lysosome, mitochondrion, Golgi apparatus, endoplasmic reticulum (ER), and nucleus.

Luminescent Transition Metal Complexes for Endoplasmic Reticulum Staining

Lim et al. reported a series of ER-targeted Ir(III) complexes as photodynamic therapy (PDT) agents [134]. Co-localization with ER tracker dyes confirmed that the Ir(III) complexes were primarily localized in ER. The designed Ir(III) complexes exhibited two-photon absorption, followed by reactive oxygen species (ROS) generation, which triggered the death of cancer cells. Recently, Chao et al. reported three ER-targeted Ir(III) complexes (*Ir10–Ir12*) as PDT photosensitizers [135]. As shown in Fig. 12, all of these Ir (III) complexes can specifically accumulate in ER. Among them, *Ir11* displayed the best photocytotoxicity index (PI) value and co-localization extent with ER. Besides, *Ir11* with extended conjugation area in the main ligand can effectively improve their singlet oxygen quantum yield and cytotoxicity, which introduce cell apoptosis after PDT therapeutics (405 nm, 6 J/cm^2). Furthermore, they confirmed that intracellular singlet oxygen generated by *Ir11* can cause ER stress and efflux of Ca^{2+} from ER, which further increased cellular damage. Thus, *Ir11* has promising potential as an ER-targeted PDT photosensitizer candidate.

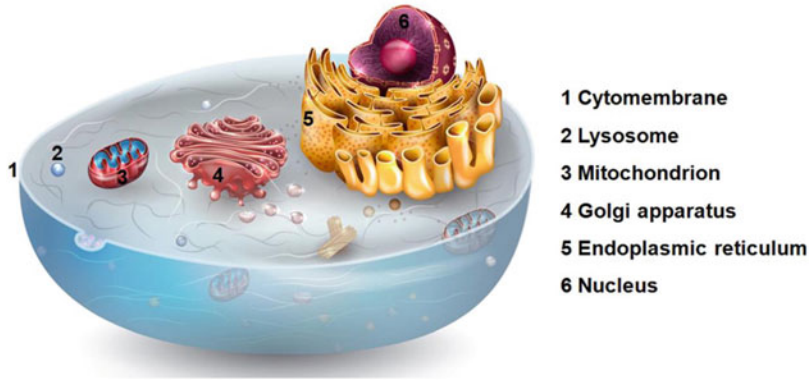

Fig. 11 Schematic illustration of organelles (cytomembrane, lysosome, mitochondrion, Golgi apparatus, endoplasmic reticulum, and nucleus) in a cell. (Reprinted with permission from Ref. [133]. Copyright © 2017 Elsevier B.V)

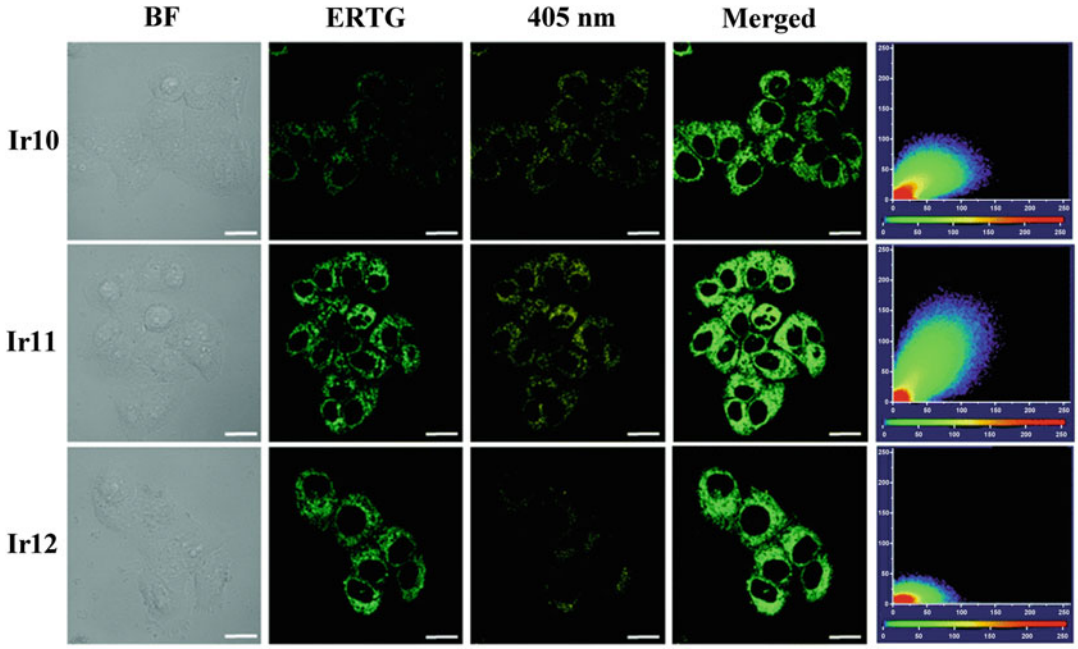

Fig. 12 Confocal co-localization imaging of living human lung cancer (A549) cells incubated with 1 μM of *Ir10–Ir12* (λ_{ex} = 405 nm, λ_{em} = 520–570 nm) in DMEM with 10% FBS (PH = 7.4, 0.1% DMSO) for 1 h at 37 °C followed by the incubation of 0.2 μM of ERTG (λ_{ex} = 488 nm, λ_{em} = 512–520 nm). Inset scale bars: 20 μm. (Reprinted with permission from Ref. [135]. Copyright © 2019 Royal Society of Chemistry)

Luminescent Transition Metal Complexes for Cell Membrane Staining

Generally, the complexes incorporated with long carbon chains can enhance the affinity with cell membrane, owing to the lipophilic–lipophilic interaction with the bilayer cell membrane. Patra et al. reported a series of Ir(III) complexes bearing imidazole-based ligands with different alkyl chain length for cell imaging and anticancer applications [136]. As expected, the Ir(III)

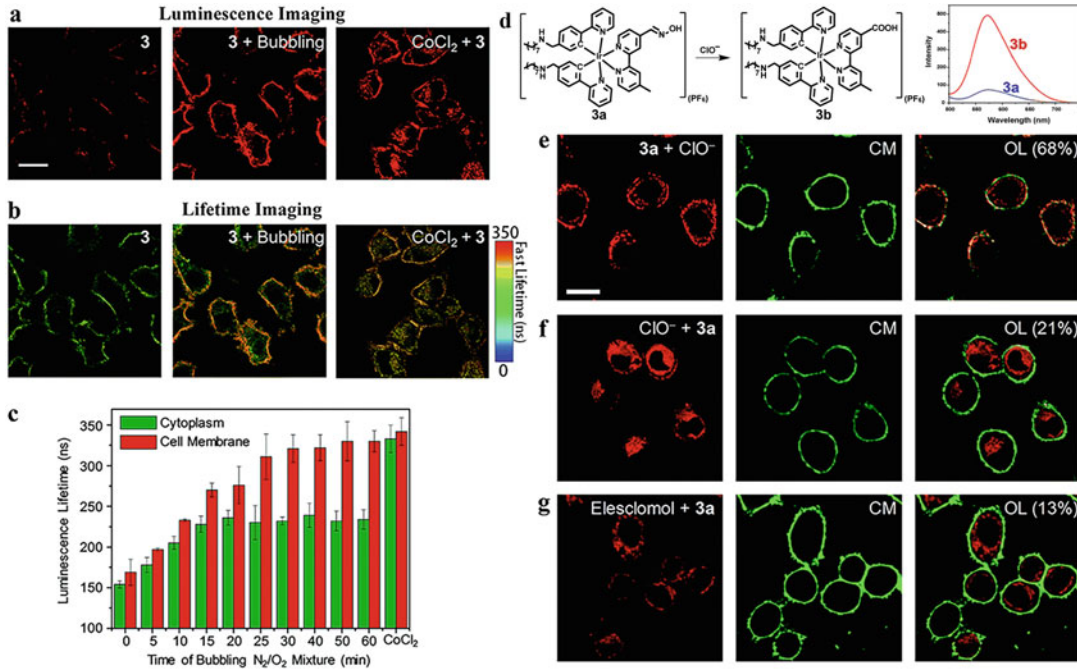

Fig. 13 (**a**) Laser-scanning luminescence confocal microscopy and (**b**) photoluminescence lifetime imaging microscopy images of living HeLa cells incubated with complex *3* (5 μM, 20 min, 37 °C) before and after bubbling a gas mixture of 5% O_2 and 95% N_2 into the culture medium for 60 min and the cells pretreated with $CoCl_2$ (100 μM, 2 h, 37 °C) and incubated with complex *3* (5 μM, 20 min, 37 °C). Scale bar: 20 μm. (**c**) Bar chart showing the luminescence lifetime values in the cytoplasm (green) and the cell membrane (red) of the HeLa cells incubated with complex 3 (5 μM, 20 min, 37 °C) during the bubbling gas mixture and after $CoCl_2$ pretreatment. The error bars represent the standard deviations of ten lifetime values randomly obtained from independent cells. (**d**) Chemical structure of complex *3a* and the structural and spectral (in CH_3OH) responses toward hypochlorite. (**e**) Images of living HeLa cells incubated with complex *3a* (5 μM, 20 min, 37 °C) followed by treatment with NaClO (25 μM, 20 min, 37 °C) and costaining with CellMask (CM). (**f**) Images of living HeLa cells preincubated with NaClO (25 μM, 20 min, 37 °C), washed with PBS three times, incubated with complex *3a* (5 μM, 20 min, 37 °C) and costained with CellMask. (**g**) Laser-scanning luminescence confocal microscopy images of living HeLa cells treated with elesclomol (125 nM, 2 h, 37 °C) followed by incubation with complex *3a* (5 μM, 20 min, 37 °C) and costaining with CellMask. OL: overlaid images. Percentage values: co-localization coefficients. Scale bar: 20 μm. (Reprinted with permission from Ref. [137]. Copyright © 2018 Royal Society of Chemistry)

complexes with long alkyl chain mainly accumulated near the cell membrane of cells and displayed a clear image of the cell membrane. In contrast, the Ir(III) complexes with short alkyl chain were distributed in cytoplasm of cells. Interestingly, the Ir(III) complexes with shorter alkyl chain showed higher anticancer activity compared to the Ir(III) complexes with longer alkyl chain against MCF-7 cells. Therefore, the anticancer activity and cell imaging property of these complexes can be mediated by the length of alkyl chain. Zhao et al. designed and synthesized a series of Ir(III) complexes that stain both the cytoplasm and the cell membrane for sensing and distinguishing between exogenous and endogenous analytes [137]. The hypoxia and hypochlorite were used as two examples of target analytes. As shown in Fig. 13a, b, complex *3* was located in both the cytoplasm and the cell membrane with similar lifetimes of about 154 ns and 169 ns in living HeLa cells. The exogenous hypoxia gave rise to luminescence enhancement and lifetime elongation in both the cytoplasm and the cell membrane (Fig. 13), and more significant luminescence response was found in the cell membrane than that in the cytoplasm. In $CoCl_2$

introduced endogenous hypoxia, the lifetime of complex *3* was elongated to about 333 and 342 ns in the cytoplasm and the cell membrane, respectively. Thus, the exogenous and endogenous hypoxia can be easily distinguished by PLIM images. Furthermore, they designed complex *3a* to distinguish exogenous and endogenous hypochlorite in HeLa cells. Exogenous hypochlorite gave rise to luminescence turn-on in the cell membrane (Fig. 13), due to the oxidation of complex *3a*. Besides, the cytoplasm with internalized hypochlorite displayed less intense luminescence than cell membrane. Toward the elesclomol triggered endogenous hypochlorite production, the cells exhibited bright luminescence in the perinuclear region, but became non-emissive in cell membrane. These differences can be successfully applied for sensing and distinguishing exogenous and endogenous hypochlorite in cells.

Luminescent Transition Metal Complexes for Mitochondrion Staining

Triphenylphosphonium (TPP) cation mediated complexes can specifically accumulate in mitochondria because of the electrostatic attraction between positively charged TPP with negatively charged mitochondrial matrix [138, 139]. Guo et al. reported a series of TPP-based Pt(II) complexes, which successfully achieved mitochondria staining [140]. Zhao et al. designed and synthesized a TPP-based Ir (III) complex (*Ir13*) for specifically staining the mitochondria [141]. After treated with *Ir13*, HeLa cells displayed a slower respiration rate, which brought about a higher intracellular oxygen level under hypoxia. As a result, *Ir13* showed an excellent PDT effect under hypoxia conditions, which provided a practicable potential of mitochondria-targeted PDT in hypoxic tumor cells. Furthermore, the complexes with intrinsic cationic lipophilicity can target mitochondria without any modification. Sessler et al. reported a series of hydroxyl-functionalized heteroleptic bis-NHC Au (I) complexes and studied its applications using cell proliferation assays and luminescent microscopic imaging of human cancer cell lines [142]. The designed Au(I) complexes can conjugate to various amines via carbamate bond formation to enhance cell membrane permeability, and meanwhile their basic pharmacological properties and structure–activity relationship features have been investigated. Among them, bis-NHC Au(I) *7* (*Au2*) and *10* (*Au3*), which contains inherently fluorescent doxorubicin and pyrene motifs, were used as probes in vitro. Mitochondrial localization of *Au2* and *Au3* in A549 cells was well confirmed by co-localization with the mitochondrial probe Mitotracker Red (Fig. 14). The luminescent imaging of the mitochondria can be achieved at the concentrations of *Au2* as low as 500 nM, but not observed for *Au3* due to its weak absorption at 405 nm excitation wavelength. Furthermore, doxorubicin (DOX) was found to be redirected to the mitochondria when incorporated within *Au2* (Fig. 15). This discovery may be expected to eliminate or reduce the nuclear effects linked with cardiotoxicity, indicating its promising biological potential. Elliott et al. reported a triazole-based Os(II) complex ($Os(btzpy)_2]Cl_2$, $Os1^{Cl}$) for targeting mitochondria, and studied its potential application for PDT [143]. As shown in Fig. 16, $Os1^{Cl}$ was accumulated in the mitochondria of both the HeLa cells and human bone osteosarcoma epithelial (U2OS) cells after 4 h incubation, and the clear phosphorescence can be seen at concentrations as low as 1 μM. Co-localization with the mitochondrial stain MitoView 633 confirmed the well mitochondria targeting of $Os1^{Cl}$, and the Pearson's correlation coefficients were 0.85 and 0.7 for HeLa cells and U2OS cells, respectively. The $Os1^{Cl}$ was emissive in both of aerated aqueous solution and acetonitrile with an emission maximum at 589 nm and 599 nm, respectively. Furthermore, MTT and clonogenic assays demonstrated that $Os1^{Cl}$ was non-toxic in dark condition. The yield of singlet oxygen generation of $Os1^{Cl}$ was 57% in air-equilibrated acetonitrile toward 355 nm irradiation. Therefore, the mitochondria localization, non-toxicity in the dark, and high singlet oxygen yield indicated that the $Os1^{Cl}$ can be utilized as a promising photosensitizer for PDT applications.

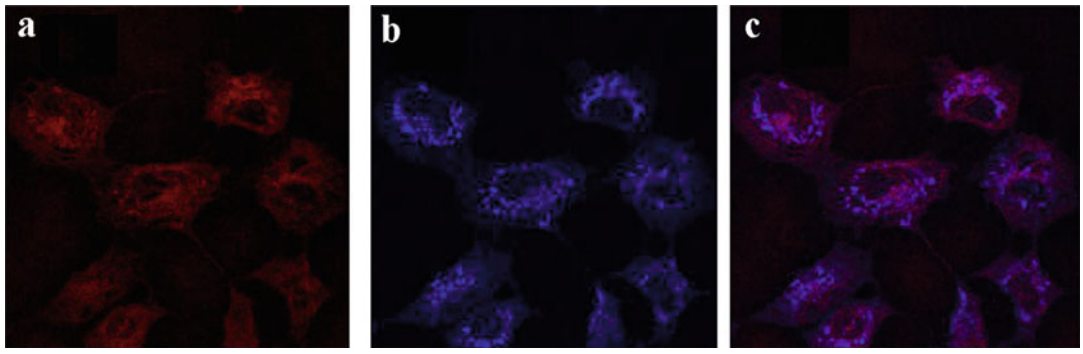

Fig. 14 Confocal microscopy images of A549 cell line treated with *Au3* for 7 h. (**a**) Mitotracker Red channel (excited at 588 nm). (**b**) *Au3* (excited at 405 nm). (**c**) Merged image. The overlap indicates that *Au3* localizes to the mitochondria. (Reprinted with permission from Ref. [142]. Copyright © 2019 Royal Society of Chemistry)

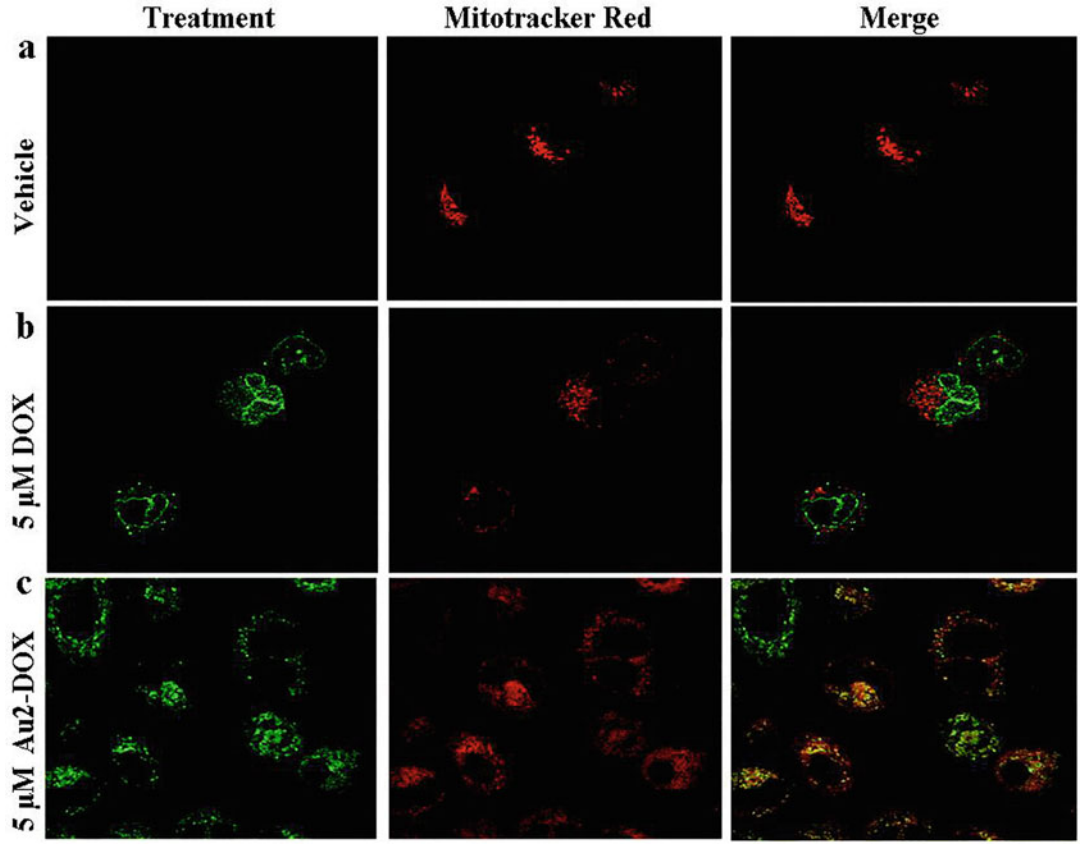

Fig. 15 Confocal microscopy images of A549 cells post-treatment with (**a**) vehicle only, (**b**) 5 μM DOX, and (**c**) 5 μM *Au2-DOX* for 6 h. (Reprinted with permission from Ref. [142]. Copyright © 2019 Royal Society of Chemistry)

Importantly, they proposed that the absorption wavelengths of $Os1^{Cl}$ should be optimized to a low energy region to further improve the theranostic performance.

Luminescent Transition Metal Complexes for Lysosome Staining

Currently, incorporation of morpholine moiety in transition metal complexes is the most common

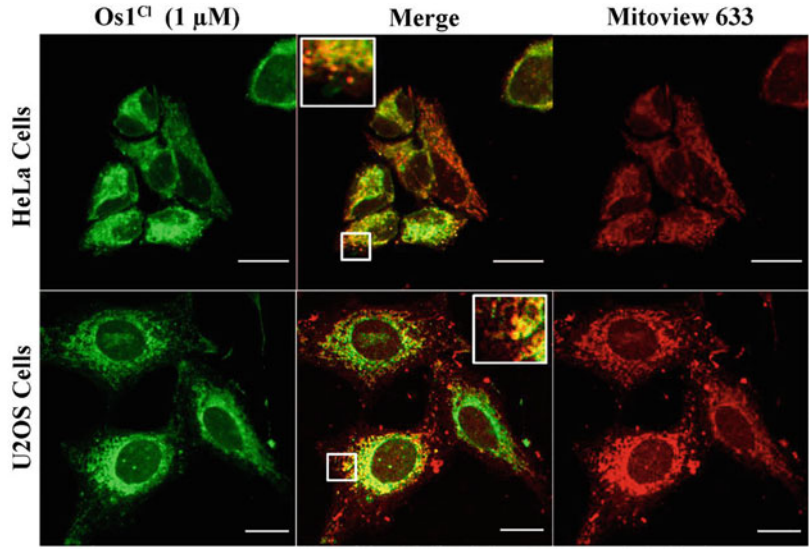

Fig. 16 Confocal images of complex $Os1^{Cl}$ (green) following 4 h incubation in HeLa and U2OS cells co-localized with MitoView 633 (red) with central overlaid image, scale bars 20 μm. (Reprinted with permission from Ref. [143]. Copyright © 1996–2019 MDPI)

way to target lysosome [144]. For example, Chao et al. designed and synthesized a water-soluble Ir (III) complex (*Ir14*) attached with a morpholine moiety for lysosome imaging [145]. With excellent two-photon properties, *Ir14* was utilized to illuminate the lysosomes in living cells and 3D tumor spheroids. Besides, *Ir14* can accumulate in lysosomes more than 4 days, which indicated that it can achieve long-term monitoring of lysosomes during cell migration and apoptosis. Furthermore, transition metal complexes can target lysosomes by the endocytic pathway. Jansson et al. reported a series of novel Zn(II)-thiosemicarbazone complexes for direct lysosomal targeting [146]. Remarkably, they further confirmed that their activity can be mediated by transmetallation with copper ions and lysosomal membrane permeabilization. Liu et al. designed and synthesized a series of Ru(II) complexes to selectively target tumor cells [147]. They confirmed all the complexes displayed cytotoxicity ($IC_{50} < 100$ μM) against both HeLa cells and A549 cells. Besides, all five complexes exhibited lower cytotoxicity toward normal cells over cancer cells. More importantly, they found that *Ru4* and *Ru5* displayed high cytotoxic selectivity with almost seven times more activity toward cancer cells. The results may indicate that the introduction of the quinolyl group can improve the antiproliferative activity and the selectivity for cancer cells. Furthermore, *Ru5* showed high cellular uptake efficiency than others, and thus was selected for further investigation. As shown in Fig. 17a, *Ru5* was located in the lysosome in A549 cells with high Pearson's co-localization coefficient (0.81–0.93) and showed no different organelle-targeting behavior after 6 h incubation. The A549 cells were stained with *Ru5* and acridine orange (AO) to test the lysosomal integrity. As shown in Fig. 17b, with the increase of *Ru5*, the red fluorescence intensity decreased, indicating the destruction of lysosomes integrity. The *Ru5* stained lysosomes may trigger the generation of intracellular ROS, enhance the lysosomal permeability, and then induce cell apoptosis.

Luminescent Transition Metal Complexes for Nucleus Staining

Recently, Kiran et al. reported new Pt (II) complexes containing imidazolyl terpyridine (*Pt8*) as a DNA staining agent to visualize the nuclear DNA without addition of any external fluorophore in dead cells [148]. Mei et al. reported a novel Ru(II) complex coordinated with 6-chloro-5-hydroxylpyrido[3,2-a]phenazine

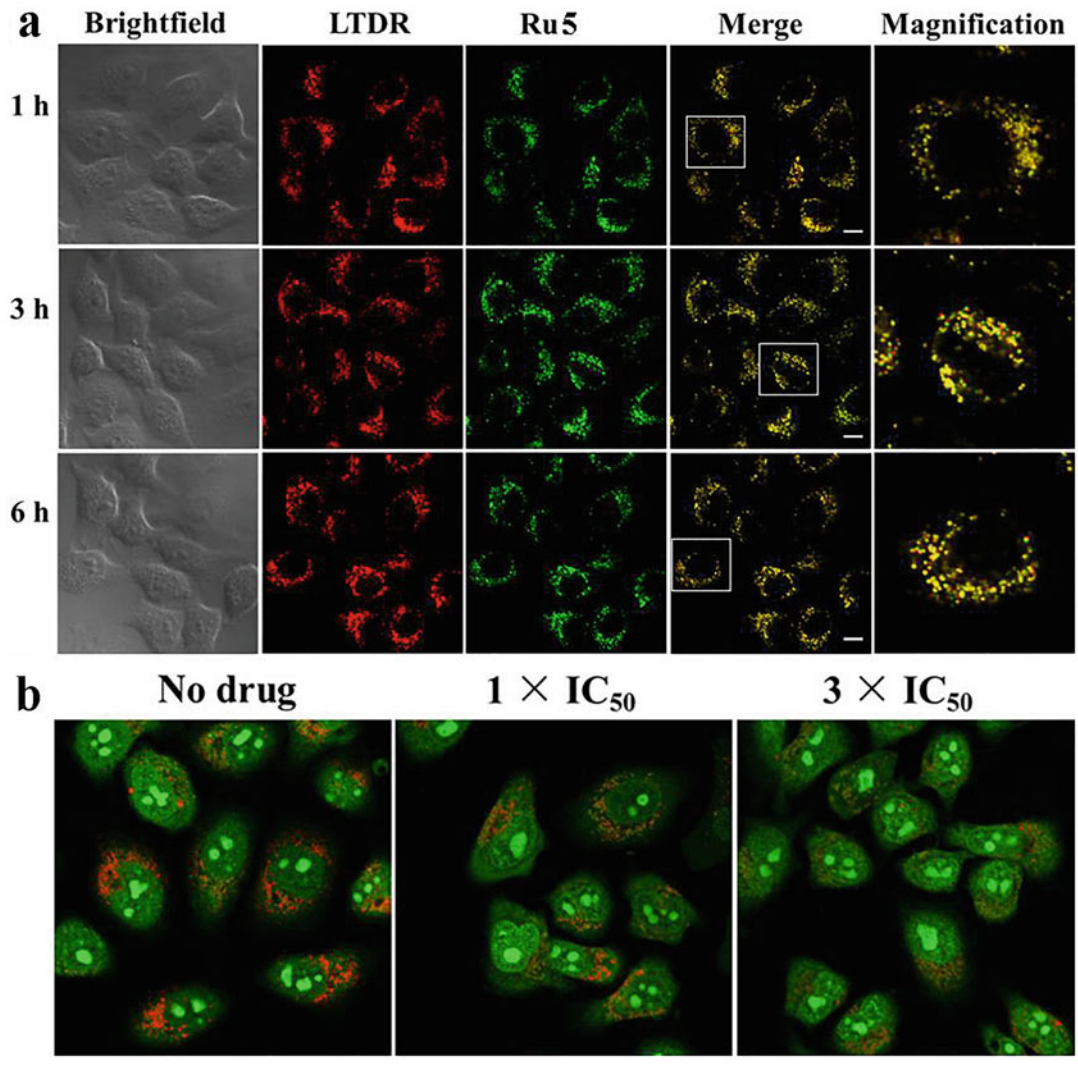

Fig. 17 (**a**) Determination of intercellular localization of *Ru5* in A549 cells by confocal microscopy. The A549 cells were labeled with LysoTracker Deep Red (LTDR) and then exposed to *Ru5* (5 μM) for various periods of time. Lysosomes and Ru complex were visualized by red and green fluorescence, respectively. The Ru complex was excited at 488 nm, and the emission was collected at 550 ± 30 nm. LTDR was excited at 594 nm, and the emission was collected at 630 ± 30 nm. Scale bar: 10 μm. (**b**) Observation of lysosomal disruption in A549 cells caused by *Ru5* with Acridine orange (5 μM) staining. (Reprinted with permission from Ref. [147]. Copyright © 2018 American Chemical Society)

(CQM), $(Ru(L)_2(CQM)]ClO_4$, L = 1,10-phenanthroline) for imaging nuclei of living cells [149]. As expected, the designed Ru (II) complex exhibited low toxicity and mainly accumulated in the nuclei of HepG2 cells, which provided a new choice for nucleus staining. Zhao et al. synthesized a multifunctional phosphorescent Ir(III) complex (*Ir15*) for specific nucleus staining and applied it for monitoring intranuclear oxygen level [150]. The nucleus targeting capability was achieved by utilizing a DNA intercalator as auxiliary ligand on the designed Ir(III) complex. In live HepG2 cells, *Ir15* was well co-localized with Hoechst 33342 with high overlap coefficient (89.6%), which demonstrated the specific nucleus targeting capability of *Ir15*

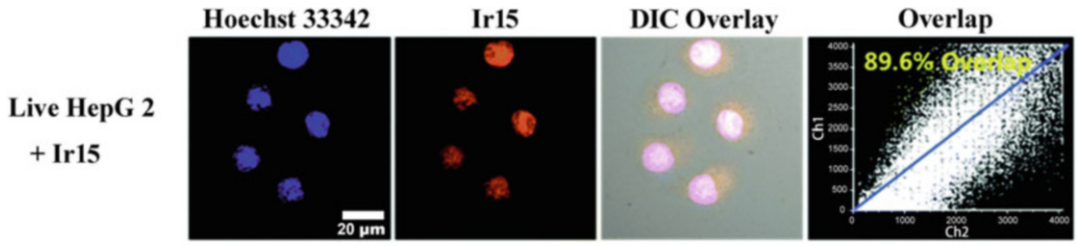

Fig. 18 The cell imaging of live HepG2 cells incubated with *Ir15* for 1 h at 37 °C and then further incubated with Hoechst 33342 for 10 min. The concentrations of *Ir15* and Hoechst 33342 in incubation solution were 10 μM and 10 μg/mL, respectively. Excitation wavelength was 405 nm. The scale bars were 20 μm. (Reprinted with permission from Ref. [150]. Copyright © 2015 Royal Society of Chemistry)

(Fig. 18). Furthermore, *Ir15* was successfully used to monitor the oxygen level in nuclei via PLIM imaging, indicated that it has promising potential for intranuclear hypoxia detection.

Accurately tracking organelles by imaging agents plays a significant role in bioimaging, biosensing, and therapeutic applications. Organelle-targeting transition metal complexes can help to image organelle morphological changes, understand the biological roles, detect the chemical molecules, and extend the potential therapeutic pathways, which have made great progress over the past decades. The functionality and cellular distribution of transition metal complexes are tunable via structural modification of the ligands, accelerating the development of cell imaging applications continuously.

2.3 Near-Infrared Luminescent Lanthanide Complexes for Bioimaging

In recent years, complexes based on trivalent lanthanide ions (Ln(III) complexes) represent remarkable potential for bioimaging and biosensing [151–153]. The luminescence from lanthanide ions originates from 4f-4f transitions, interconfigurational $4f^{n} \rightarrow 4f^{n}5d^{1}$ transitions, LMCT, and MLCT [154, 155]. The emission of lanthanide ions generated from the forbidden f-f transition covers from UV to NIR regions [156, 157]. However, the forbidden f-f transition also leads to low molar extinction coefficient and the difficult direct excitation [158]. Excitingly, these problems can be resolved by introducing high absorptive antenna ligands to promote the transfer of the absorbed energy into the lanthanide ions [159, 160]. Furthermore, the photochemical and photophysical properties of Ln(III) complexes can be tuned by structural modification of the ligands, which provides potential capabilities for their applications in cell imaging field [161–163]. Undoubtedly, the emission wavelength is one of the most important photophysical properties of the luminescent metal complexes. In the field of bioimaging, the NIR emissive complexes are of great importance and have attracted increasing attentions in the last years. Compared with relatively short-wavelength emissive luminophores, the NIR emissive complexes can effectively increase the penetration depth, reduce the cell damage, eliminate autofluorescence, and resist photobleaching, which are beneficial to improve the imaging quality and signal-to-noise ratio [164]. As a promising NIR emissive luminophores, Ln(III) complexes will stimulate the development of NIR bioimaging and biosensing [165–167]. Herein, we will introduce the latest NIR Ln(III) complexes for in vitro and in vivo bioimaging and biosensing.

2.3.1 Near-Infrared Luminescent Lanthanide Complexes for Cell Imaging and Sensing

NIR Ln(III) complexes are currently arousing wide attentions for in vitro and in vivo bioimaging applications [168, 169]. Cell imaging performed in NIR range can minimize tissue absorption, autofluorescence, and photon scattering, providing a higher signal-to-noise ratio and imaging resolution. Combined with the advanced imaging techniques, various NIR Ln(III) complexes have been designed to achieve the NIR cell imaging in recent years, such as Nd (III)-, Sm(III)-, and Yb(III) complexes. Maury et al. successfully synthesized novel pyclen based Eu(III)- and Sm(III) complexes for imaging of living cells via TPM [170]. Eliseeva et al. designed and synthesized highly photostable and biocompatible NIR emissive Zn(II)/Nd(III) and Zn(II)/Yb(III) metallacrowns for necrotic cell imaging [171]. Besides, they further reported the applications of similar Zn(II)/Ln(III) metallacrowns for combined in vitro cell fixation and counter staining. Zhang et al. reported a series of biocompatible Yb(III) complexes (*Yb1–Yb5c*) for NIR living cell imaging [172]. Upon excitation at either the visible or red region, the designed Yb(III) complexes displayed high NIR luminescence (quantum yields up to 23% and 13% in DMSO and water, respectively) and excellent photostability. As shown in Fig. 19, strong and specific intracellular Yb(III) luminescence was observed in NIR confocal fluorescence images of living cells. Besides, the luminescence lifetime of these Yb(III) complexes was prolonged up to 249 μs, and the intracellular lifetime distribution was ranged from 100 to 200 μs, allowing elimination of cell autofluorescence and high signal-to-noise ratios in time-resolved fluorescence lifetime imaging.

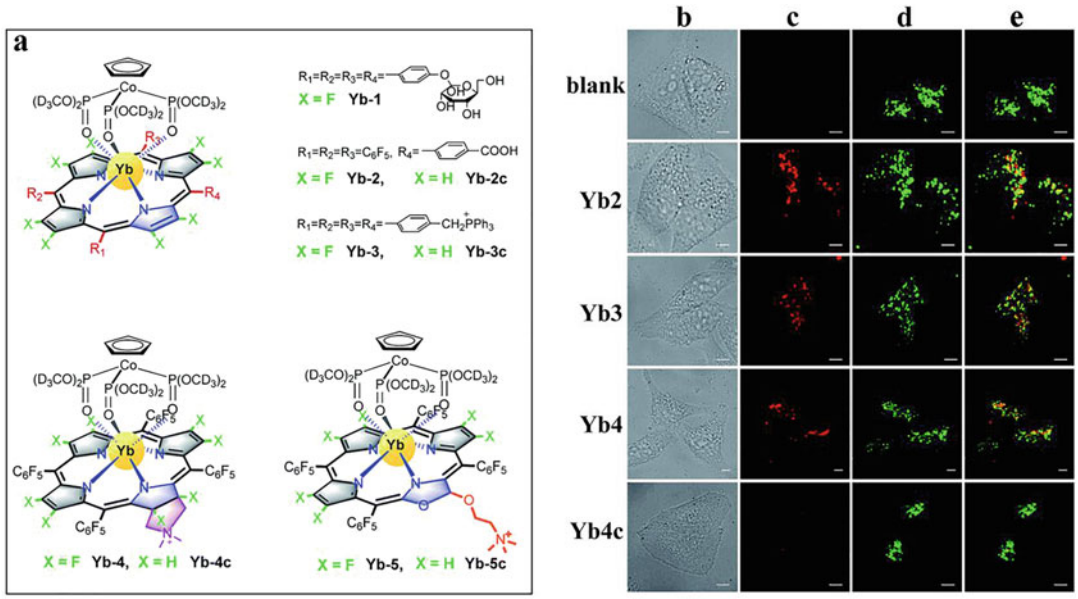

Fig. 19 (**a**) Chemical structures of Yb(III) complexes (*Yb1–Yb5c*). NIR confocal images performed on HeLa cells incubated with 10 μM of the corresponding Yb(III) complexes for 12 h followed by 30 min incubation with 75 nM LysoTracker Green. (**b**) Bright field; (**c**) NIR signal arising from Yb(III) in channel 1 (λ_{ex}, 408 nm; λ_{em}, 935/170 nm bandpass); (**d**) visible signal arising from LysoTracker Green in channel 2 (λ_{ex}, 470 nm; λ_{em}, 530/43 nm bandpass); (**e**) merged b and c showing colocalization ($P = 0.75$ for *Yb2*, 0.78 for *Yb3*, 0.67 for *Yb4*, 0.29 for *Yb4c*). Scale bar: 10 μm. (Reprinted with permission from Ref. [172]. Copyright © 2018 Royal Society of Chemistry)

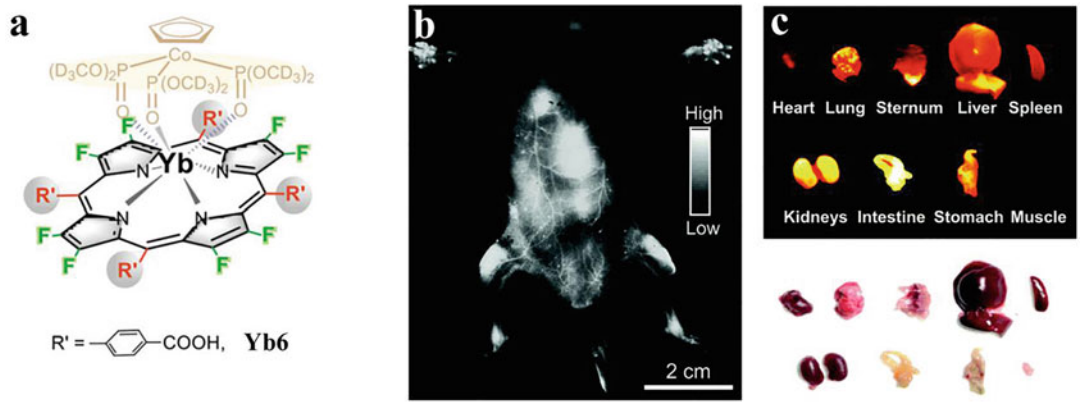

Fig. 20 (**a**) Chemical structure of *Yb6*. (**b**) Whole body NIR-II fluorescence images of *Yb6* (150 μL, 3 mg/mL) after 5 min intravenous injection into C57BL/6 mice (λ_{ex}, 520 nm; λ_{em}, 1000 nm longpass filter; 3000 ms exposure; color bar ranges from 5000 to 40,000, $n = 3$ per group). (**c**) ex vivo biodistribution studies at 12 h after the injection of *Yb6*. (Reprinted with permission from Ref. [178]. Copyright © 2019 the Partner Organisations)

2.3.2 Near-Infrared Luminescent Lanthanide Complexes for In Vivo Bioimaging

In recent years, the applications of Ln(III) complexes have been extended from in vitro to in vivo level, and have a promising future in in vivo biological applications [173–176]. Zeng et al. reported a Nd(III)-diethylene triamine pentaacetate acid (DTPA) complex as NIR II-emitting probe for in vivo bioimaging and tiny tumor detection [177]. The designed Nd(III) complex processes NIR II emission at 1330 nm and high photostability. Taking the advantage of bright NIR emission and good biocompatibility, this complex was successfully utilized to in vivo imaging of mouse kidney and optical-guided tiny tumor (down to 3 mm) detection. Recently, Cheng and Zhang et al. designed three water-soluble Yb(III) complexes for in vivo whole body bioimaging [178]. Among them, *Yb6*, which combined with the large extinction coefficient of the carboxylate modified porphyrin ligand, displayed high in vivo luminescence, and achieves high-resolution vasculature imaging in small animals. As shown in Fig. 20a, after tail vein injection, the vasculature and whole body of C57BL/6 mice were clearly visualized in the NIR-II window. By the utilization of 1000 nm longpass filter, the surrounding background signals including scattering, tissue absorption, and autofluorescence were eliminated. After 12 h post-injection, ex vivo biodistribution study demonstrated that *Yb6* mainly accumulated in kidneys and intestines, and only a small fraction of signal was detected in the liver and no signal was observed in muscles as shown in Fig. 20b. The results indicate that the clearance routes of the *Yb6* complexes are through both hepatobiliary and renal systems, which provide a promising pathway to research the in vivo metabolism mechanism. Finally, they propose that the tumor targeting NIR Ln(III) complexes are highly desirable in the field of in vivo biology. Consequently, developing novel NIR Ln(III) complexes with high emission intensity, relatively increased molar extinction coefficient, and tumor targeting ability via the design and optimization of ligands will make significant progress in in vivo bioimaging and biosensing.

3 Conclusions and Outlook

In this chapter, we have comprehensively reviewed the recent applications of luminescent transition metal complexes and NIR emissive lanthanide complexes in cell imaging. These complexes exhibit excellent photophysical and photochemical properties and good cell uptake behavior, allowing them to be utilized in cellular

and subcellular imaging. Meanwhile, the recent applications of these complexes in two-photon bioimaging, time-resolved bioimaging, and in vivo bioimaging have been overviewed. Nowadays, the application of coordination compounds as cell imaging agents is still a developing research field. This fast-growing research field is attracting increasing attention in recent years.

For the further research to improve the cell imaging and sensing performance of the coordination compounds, the following challenges should be considered. Firstly, the rapid cellular uptake of coordination compounds is still a challenge. Further efforts should be made for optimizing the conjugated moiety, molecular size, and water solubility of the coordination compounds. Secondly, the mechanisms of cellular uptake and the intracellular distribution of coordination compounds are still lacked, which urgently need to be addressed. Thirdly, the excitation and emission wavelength of coordination compounds in the deep red or NIR range is required in in vivo bioimaging. Fourthly, long-term imaging is required in clinical application, and the coordination compounds with excellent photostability and low toxicity should be further developed. Finally, in order to further improve the imaging quality, the coordination compounds should be ingeniously designed to meet the demands of modern imaging techniques, such as stimulated emission depletion microscopy. We expect that the combination of fast-growing luminescent coordination compounds with advanced imaging techniques will lead to significant improvements in bioimaging and biosensing.

References

1. Hong G, Antaris AL, Dai H (2017) Near-infrared fluorophores for biomedical imaging. Nat Biomed Eng 1:0010
2. Naumova AV, Modo M, Moore A, Murry CE, Frank JA (2014) Clinical imaging in regenerative medicine. Nat Biotechnol 32:804–818
3. Wysocki LM, Lavis LD (2011) Advances in the chemistry of small molecule fluorescent probes. Curr Opin Chem Biol 15:752–759
4. Sarkar AR, Kang DE, Kim HM, Cho BR (2014) Two-photon fluorescent probes for metal ions in live tissues. Inorg Chem 53:1794–1803
5. Lewis DJ, Pikramenou Z (2014) Lanthanide-coated gold nanoparticles for biomedical applications. Coordin Chem Rev 273:213–225
6. Xu H, Li Q, Wang L, He Y, Shi J, Tang B, Fan C (2014) Nanoscale optical probes for cellular imaging. Chem Soc Rev 43:2650–2661
7. Chen M, He X, Wang K, He D, Yang X, Shi H (2014) Inorganic fluorescent nanoprobes for cellular and subcellular imaging. TrAC Trend Anal Chem 58:120–129
8. Chen H, Lin L, Li H, Lin JM (2014) Quantum dots-enhanced chemiluminescence: mechanism and application. Coordin Chem Rev 263:86–100
9. Kairdolf BA, Smith AM, Stokes TH, Wang MD, Young AN, Nie S (2013) Semiconductor quantum dots for bioimaging and biodiagnostic applications. Annu Rev Anal Chem 6:143–162
10. Jing L, Ding K, Kershaw SV, Kempson IM, Rogach AL, Gao M (2014) Magnetically engineered semiconductor quantum dots as multimodal imaging probes. Adv Mater 26:6367–6386
11. Alford SC, Ding Y, Simmen T, Campbell RE (2012) Dimerization-dependent green and yellow fluorescent proteins. ACS Synth Biol 1:569–575
12. Wang Y, Shyy JYJ, Chien S (2008) Fluorescence proteins, live-cell imaging, and mechanobiology: seeing is believing. Annu Rev Biomed Eng 10:1–38
13. Vellaisamy K, Li G, Wang W, Leung CH, Ma DL (2018) A long-lived peptide-conjugated iridium(III) complex as a luminescent probe and inhibitor of the cell migration mediator, formyl peptide receptor 2. Chem Sci 9:8171–8177
14. Mauro M, Aliprandi A, Septiadi D, Kehr NS, De Cola L (2014) When self-assembly meets biology: luminescent platinum complexes for imaging applications. Chem Soc Rev 43:4144–4166
15. You Y, Cho S, Nam W (2014) Cyclometalated iridium(III) complexes for phosphorescence sensing of biological metal ions. Inorg Chem 53:1804–1815
16. Liu S, Xu A, Chen Z, Ma Y, Yang H, Shi Z, Zhao Q (2016) Phosphorescent ion-paired iridium(III) complex for ratiometric and time-resolved luminescence imaging of intracellular biothiols. Opt Express 24:28247–28255
17. Liu Z, He W, Guo Z (2013) Metal coordination in photoluminescent sensing. Chem Soc Rev 42:1568–1600
18. Tang J, Yin HY, Zhang JL (2018) A luminescent aluminium salen complex allows for monitoring dynamic vesicle trafficking from the Golgi apparatus to lysosomes in living cells. Chem Sci 9:1931–1939
19. Zhao Q, Yu M, Shi L, Liu S, Li C, Shi M, Zhou Z, Huang C, Li F (2010) Cationic iridium(III) complexes with tunable emission color as phosphorescent dyes for live cell imaging. Organometallics 29:1085–1091

20. Coogan MP, Fernández-Moreira V (2014) Progress with, and prospects for, metal complexes in cell imaging. Chem Commun 50:384–399
21. Thorp-Greenwood FL, Balasingham RG, Coogan MP (2012) Organometallic complexes of transition metals in luminescent cell imaging applications. J Organomet Chem 714:12–21
22. Butler SJ, Lamarque L, Pal R, Parker D (2014) EuroTracker dyes: highly emissive europium complexes as alternative organelle stains for live cell imaging. Chem Sci 5:1750–1756
23. Ma DL, Wang M, Liu C, Miao X, Kang TS, Leung CH (2016) Metal complexes for the detection of disease-related protein biomarkers. Coordin Chem Rev 324:90–105
24. Zhao Q, Li F, Huang C (2010) Phosphorescent chemosensors based on heavy-metal complexes. Chem Soc Rev 39:3007–3030
25. Wong KMC, Yam VWW (2011) Self-assembly of luminescent alkynylplatinum(II) terpyridyl complexes: modulation of photophysical properties through aggregation behavior. Acc Chem Res 44:424–434
26. Zhu L, Tang X, Yu Q, Lv W, Yan H, Zhao Q, Huang W (2015) Tuning the optical properties of 2-thienylpyridyl iridium complexes through carboranes and anions. Chem Eur J 21:4721–4730
27. Shi C, Sun H, Tang X, Lv W, Yan H, Zhao Q, Wang J, Huang W (2013) Variable photophysical properties of phosphorescent iridium(III) complexes triggered by *closo*- and *nido*-carborane substitution. Angew Chem Int Ed 52:13434–13438
28. Ma DL, He HZ, Leung KH, Chan DSH, Leung CH (2013) Bioactive luminescent transition-metal complexes for biomedical applications. Angew Chem Int Ed 52:7666–7682
29. Baggaley E, Weinstein JA, Williams JAG (2012) Lighting the way to see inside the live cell with luminescent transition metal complexes. Coordin Chem Rev 256:1762–1785
30. Banerjee S, Chakravarty AR (2015) Metal complexes of curcumin for cellular imaging, targeting, and photoinduced anticancer activity. Acc Chem Res 48:2075–2083
31. Yeung MCL, Yam VWW (2014) Molecular design of novel classes of luminescent transition metal complexes and their use in sensing, biolabeling, and cell imaging. In: Lo KKW (ed) Luminescent and photoactive transition metal complexes as biomolecular probes and cellular reagents. Springer, Heidelberg, pp 109–129
32. Ma DL, Ma VPY, Chan DSH, Leung KH, He HZ, Leung CH (2012) Recent advances in luminescent heavy metal complexes for sensing. Coordin Chem Rev 256:3087–3113
33. Fernández-Moreira V, Thorp-Greenwood FL, Coogan MP (2010) Application of d^6 transition metal complexes in fluorescence cell imaging. Chem Commun 46:186–202
34. Gómez-Suárez A, Nelson DJ, Thompson DG, Cordes DB, Graham D, Slawin AM, Nolan SP (2013) Synthesis, characterization and luminescence studies of gold(I)–NHC amide complexes. Beilstein J Org Chem 9:2216–2223
35. Ma Y, Liu S, Yang H, Wu Y, Yang C, Liu X, Zhao Q, Wu H, Liang J, Li F (2011) Water-soluble phosphorescent iridium(III) complexes as multicolor probes for imaging of homocysteine and cysteine in living cells. J Mater Chem 21:18974–18982
36. Neugebauer U, Pellegrin Y, Devocelle M, Forster RJ, Signac W, Moran N, Keyes TE (2008) Ruthenium polypyridyl peptide conjugates: membrane permeable probes for cellular imaging. Chem Commun 5307–5309
37. Chen M, Lei Z, Feng W, Li C, Wang QM, Li F (2013) A phosphorescent silver(I)–gold(I) cluster complex that specifically lights up the nucleolus of living cells with FLIM imaging. Biomaterials 34:4284–4295
38. Anjomshoa M, Torkzadeh-Mahani M (2015) In vitro DNA and BSA-binding, cell imaging and anticancer activity against human carcinoma cell lines of mixed ligand copper(II) complexes. Spectrochim Acta A 150:390–402
39. Alizadeh R, Yousuf I, Afzal M, Srivastav S, Srikrishna S, Arjmand F (2015) Enantiomeric fluoro-substituted benzothiazole Schiff base-valine Cu(II)/Zn(II) complexes as chemotherapeutic agents: DNA binding profile, cleavage activity, MTT assay and cell imaging studies. J Photochem Photobiol B Biol 143:61–73
40. Zhao Q, Huang C, Li F (2011) Phosphorescent heavy-metal complexes for bioimaging. Chem Soc Rev 40:2508–2524
41. Bünzli JCG (2014) Luminescence bioimaging with lanthanide complexes. In: de Bettencourt-Dias A (ed) Luminescence of lanthanide ions in coordination compounds and nanomaterials. Wiley, Hoboken, pp 125–196
42. Liu P, Mu X, Zhang XD, Ming D (2020) The near-infrared-II fluorophores and advanced microscopy technologies development and application in bioimaging. Bioconjug Chem 31:260–275
43. Cai Y, Wei Z, Song C, Tang C, Han W, Dong X (2019) Optical nano-agents in the second near-infrared window for biomedical applications. Chem Soc Rev 48:22–37
44. Amoroso AJ, Pope SJA (2015) Using lanthanide ions in molecular bioimaging. Chem Soc Rev 44:4723–4742
45. He S, Song J, Qu J, Cheng Z (2018) Crucial breakthrough of second near-infrared biological window fluorophores: design and synthesis toward multimodal imaging and theranostics. Chem Soc Rev 47:4258–4278
46. Li J, Pu K (2019) Development of organic semiconducting materials for deep-tissue optical imaging,

phototherapy and photoactivation. Chem Soc Rev 48:38–71
47. Thorp-Greenwood FL (2012) An introduction to organometallic complexes in fluorescence cell imaging: current applications and future prospects. Organometallics 31:5686–5692
48. Papkovsky DB (2010) Live cell imaging: methods and protocols. Springer, Munich
49. Long NJ, Wong WT, Immergut EH (2015) The chemistry of molecular imaging. Wiley Online Library
50. Yu M, Zhao Q, Shi L, Li F, Zhou Z, Yang H, Yi T, Huang C (2008) Cationic iridium(III) complexes for phosphorescence staining in the cytoplasm of living cells. Chem Commun 2115–2117
51. Zhang KY, Lo KKW (2014) Metal complexes for cell and organism imaging. In: Gasser G (ed) Inorganic chemical biology: principles, techniques and applications: principles, techniques and applications. Wiley, Chichester
52. Dilworth JR, Pascu SI, Waghorn PA, Vullo D, Bayly SR, Christlieb M, Sun X, Supuran CT (2015) Synthesis of sulfonamide conjugates of Cu(II), Ga(III), In (III), Re(V) and Zn(II) complexes: carbonic anhydrase inhibition studies and cellular imaging investigations. Dalton Trans 44:4859–4873
53. Omar SAE, Scattergood PA, McKenzie LK, Jones C, Patmore NJ, Meijer AJHM, Weinstein JA, Rice CR, Bryant HE, Elliott PIP (2018) Photophysical and cellular imaging studies of brightly luminescent osmium(II) pyridyltriazole complexes. Inorg Chem 57:13201–13212
54. Lo KKW, Li SPY (2014) Utilization of the photophysical and photochemical properties of phosphorescent transition metal complexes in the development of photofunctional cellular sensors, imaging reagents, and cytotoxic agents. RSC Adv 4:10560–10585
55. Wu P, Wong ELM, Ma DL, Tong GSM, Ng KM, Che CM (2009) Cyclometalated platinum (II) complexes as highly sensitive luminescent switch-on probes for practical application in protein staining and cell imaging. Chem Eur J 15:3652–3656
56. Botchway SW, Charnley M, Haycock JW, Parker AW, Rochester DL, Weinstein JA, Williams JAG (2008) Time-resolved and two-photon emission imaging microscopy of live cells with inert platinum complexes. Proc Natl Acad Sci U S A 105:16071–16076
57. Xiao XS, Kwong WL, Guan X, Yang C, Lu W, Che CM (2013) Platinum(II) and gold(III) allenylidene complexes: phosphorescence, self-assembled nanostructures and cytotoxicity. Chem Eur J 19:9457–9462
58. Septiadi D, Aliprandi A, Mauro M, De Cola L (2014) Bio-imaging with neutral luminescent Pt (II) complexes showing metal···metal interactions. RSC Adv 4:25709–25718
59. Mou X, Wu Y, Liu S, Shi M, Liu X, Wang C, Sun S, Zhao Q, Zhou X, Huang W (2011) Phosphorescent platinum(II) complexes containing different β-diketonate ligands: synthesis, tunable excited-state properties, and their application in bioimaging. J Mater Chem 21:13951–13962
60. Zhou Y, Jia J, Cai L, Huang Y (2018) Protein staining agents from low toxic platinum(II) complexes with bidentate ligands. Dalton Trans 47:693–699
61. Pasha SS, Das P, Rath NP, Bandyopadhyay D, Jana NR, Laskar IR (2016) Water soluble luminescent cyclometalated platinum(II) complex—a suitable probe for bio-imaging applications. Inorg Chem Commun 67:107–111
62. Colombo A, Fiorini F, Septiadi D, Dragonetti C, Nisic F, Valore A, Roberto D, Mauro M, De Cola L (2015) Neutral N^C^N terdentate luminescent Pt (II) complexes: their synthesis, photophysical properties, and bio-imaging applications. Dalton Trans 44:8478–8487
63. Banerjee S, Capper MS, Clarkson GJ, Huang H, Sadler PJ (2019) Dual-action platinum(II) Schiff base complexes: photocytotoxicity and cellular imaging. Polyhedron 172:157–166
64. Langdon-Jones EE, Pope SJA (2014) Recent developments in gold(I) coordination chemistry: luminescence properties and bioimaging opportunities. Chem Commun 50:10343–10354
65. Fernández-Moreira V, Marzo I, Gimeno MC (2014) Luminescent Re(I) and Re(I)/Au(I) complexes as cooperative partners in cell imaging and cancer therapy. Chem Sci 5:4434–4446
66. Balasingham RG, Williams CF, Mottram HJ, Coogan MP, Pope SJA (2012) Gold(I) complexes derived from alkynyloxy-substituted anthraquinones: syntheses, luminescence, preliminary cytotoxicity, and cell imaging studies. Organometallics 31:5835–5843
67. Luo Z, Yuan X, Yu Y, Zhang Q, Leong DT, Lee JY, Xie J (2012) From aggregation-induced emission of Au(I)–thiolate complexes to ultrabright Au(0)@Au (I)–thiolate core–shell nanoclusters. J Am Chem Soc 134:16662–16670
68. Gutiérrez-Blanco A, Fernández-Moreira V, Gimeno MC, Peris E, Poyatos M (2018) Tetra-Au(I) complexes bearing a pyrene tetraalkynyl connector behave as fluorescence torches. Organometallics 37:1795–1800
69. Wedlock LE, Barnard PJ, Filipovska A, Skelton BW, Berners-Price SJ, Baker MV (2016) Dinuclear Au (I) N-heterocyclic carbene complexes derived from unsymmetrical azolium cyclophane salts: potential probes for live cell imaging applications. Dalton Trans 45:12221–12236
70. Tang TSM, Yip AMH, Zhang KY, Liu HW, Wu PL, Li KF, Cheah KW, Lo KKW (2015) Bioorthogonal labeling, bioimaging, and photocytotoxicity studies of phosphorescent ruthenium(II) polypyridine

dibenzocyclooctyne complexes. Chem Eur J 21:10729–10740
71. Ru J, Tang X, Ju Z, Zhang G, Dou W, Mi X, Wang C, Liu W (2015) Exploitation and application of a highly sensitive Ru(II) complex-based phosphorescent chemodosimeter for Hg^{2+} in aqueous solutions and living cells. ACS Appl Mater Interfaces 7:4247–4256
72. Poynton FE, Bright SA, Blasco S, Williams DC, Kelly JM, Gunnlaugsson T (2017) The development of ruthenium(II) polypyridyl complexes and conjugates for in vitro cellular and in vivo applications. Chem Soc Rev 46:7706–7756
73. Svensson FR, Abrahamsson M, Strömberg N, Ewing AG, Lincoln P (2011) Ruthenium(II) complex enantiomers as cellular probes for diastereomeric interactions in confocal and fluorescence lifetime imaging microscopy. J Phys Chem Lett 2:397–401
74. Karaoun N, Renfrew AK (2015) A luminescent ruthenium(II) complex for light-triggered drug release and live cell imaging. Chem Commun 51:14038–14041
75. Tsui WK, Chung LH, Wong MMK, Tsang WH, Lo HS, Liu Y, Leung CH, Ma DL, Chiu SK, Wong CY (2015) Luminescent ruthenium(II) complex bearing bipyridine and N-heterocyclic carbene-based C^N^C pincer ligand for live-cell imaging of endocytosis. Sci Rep 5:9070
76. Zhang P, Huang W, Wang Y, Li H, Liang C, He C, Wang H, Zhang Q (2018) Isomeric ruthenium (II) complexes for cancer therapy and cellular imaging. Inorg Chim Acta 469:593–599
77. Yang H, Li L, Wan L, Zhou Z, Yang S (2010) Synthesis of water soluble PEG-functionalized iridium complex via click chemistry and application for cellular bioimaging. Inorg Chem Commun 13:1387–1390
78. Han D, Qian M, Gao H, Wang B, Qi H, Zhang C (2019) A "switch-on" photoluminescent and electrochemiluminescent multisignal probe for hypochlorite via a cyclometalated iridium complex. Anal Chim Acta 1074:98–107
79. Wang W, Dong ZZ, Yang C, Li G, Tse YC, Leung CH, Ma DL (2017) An iridium(III) complex-based chemosensor for the detection of thiourea in living cells. Sens Actuators B Chem 251:374–379
80. Wu Y, Jing H, Dong Z, Zhao Q, Wu H, Li F (2011) Ratiometric phosphorescence imaging of Hg(II) in living cells based on a neutral iridium(III) complex. Inorg Chem 50:7412–7420
81. Liu S, Qiao W, Cao G, Chen Y, Ma Y, Huang Y, Liu X, Xu W, Zhao Q, Huang W (2013) Smart poly (*N*-isopropylacrylamide) containing iridium(III) complexes as water-soluble phosphorescent probe for sensing and bioimaging of homocysteine and cysteine. Macromol Rapid Commun 34:81–86
82. Sun H, Yang L, Yang H, Liu S, Xu W, Liu X, Tu Z, Su H, Zhao Q, Huang W (2013) Heteronuclear phosphorescent iridium(III) complexes with tunable photophysical and excited-state properties by chelating BF_2 moiety for application in bioimaging. RSC Adv 3:8766–8776
83. Feng Z, Tao P, Zou L, Gao P, Liu Y, Liu X, Wang H, Liu S, Dong Q, Li J (2017) Hyperbranched phosphorescent conjugated polymer dots with iridium(III) complex as the core for hypoxia imaging and photodynamic therapy. ACS Appl Mater Interfaces 9:28319–28330
84. Zhang KY, Gao P, Sun G, Zhang T, Li X, Liu S, Zhao Q, Lo KKW, Huang W (2018) Dual-phosphorescent iridium(III) complexes extending oxygen sensing from hypoxia to hyperoxia. J Am Chem Soc 140:7827–7834
85. Sansee A, Meksawangwong S, Chainok K, Franz KJ, Gál M, Pålsson LO, Puniyan W, Traiphol R, Pal R, Kielar F (2016) Novel aminoalkyl tris-cyclometalated iridium complexes as cellular stains. Dalton Trans 45:17420–17430
86. Liu C, Yang C, Lu L, Wang W, Tan W, Leung CH, Ma DL (2017) Luminescent iridium(III) complexes as COX-2-specific imaging agents in cancer cells. Chem Commun 53:2822–2825
87. Lu Z, Shangguan M, Jiang X, Xu P, Hou L, Wang T (2019) A water-soluble cyclometalated iridium(III) complex with fluorescent sensing capability for hypochlorite. Dyes Pigments 171:107715
88. Wu Y, Zeng G, Lvyue N, Wu W, Jiang T, Wu R, Guo W, Li X, Fan X (2017) Triethylene glycol-modified iridium(III) complexes for fluorescence imaging of *Schistosoma japonicum*. J Mater Chem B 5:4973–4980
89. Wang H, Wu Z, Li S, Hu K, Tang G (2017) Synthesis and evaluation of a radiolabeled bis-zinc(II)-cyclen complex as a potential probe for in vivo imaging of cell death. Apoptosis 22:585–595
90. Priyanga S, Khamrang T, Velusamy M, Karthi S, Ashokkumar B, Mayilmurugan R (2019) Coordination geometry-induced optical imaging of L-cysteine in cancer cells using imidazopyridine-based copper (II) complexes. Dalton Trans 48:1489–1503
91. Tang J, Yin HY, Zhang JL (2017) Luminescent zinc complexes as bioprobes for imaging molecular events in live cells. In: Inorganic and organometallic transition metal complexes with biological molecules and living cells. Elsevier, pp 1–53
92. Sun X, Kim G, Xu Y, Yoon J, James TD (2016) A water-soluble copper(II) complex for the selective fluorescence detection of nitric oxide/nitroxyl and imaging in living cells. ChemPlusChem 81:30–34
93. Maheshwaran D, Nagendraraj T, Manimaran P, Ashokkumar B, Kumar M, Mayilmurugan R (2017) A highly selective and efficient copper (II)-"turn-on" fluorescence imaging probe for L-cysteine. Eur J Inorg Chem 2017:1007–1016
94. Chao D, Ni S (2016) Nanomolar pyrophosphate detection and nucleus staining in living cells with simple terpyridine–Zn(II) complexes. Sci Rep 6:26477

95. Wang H, Cai F, Feng D, Zhou L, Li D, Wei Y, Feng Z, Zhang J, He J, Wu Y (2019) Synthesis, crystal structure, photophysical property and bioimaging application of a series of Zn (II) terpyridine complexes. J Mol Struct 1194:157–162
96. Tian X, Zhang Q, Zhang M, Uvdal K, Wang Q, Chen J, Du W, Huang B, Wu J, Tian Y (2017) Probe for simultaneous membrane and nucleus labeling in living cells and in vivo bioimaging using a two-photon absorption water-soluble Zn (II) terpyridine complex with a reduced π-conjugation system. Chem Sci 8:142–149
97. Liu D, Zhang M, Du W, Hu L, Li F, Tian X, Wang A, Zhang Q, Zhang Z, Wu J (2018) A series of Zn (II) terpyridine-based nitrate complexes as two-photon fluorescent probe for identifying apoptotic and living cells via subcellular immigration. Inorg Chem 57:7676–7683
98. Hu JY, Wu ZY, Chai K, Yang ZS, Meng YS, Ning Y, Zhang J, Zhang JL (2017) β-Fluorinated porpholactones and metal complexes: synthesis, characterization and some spectroscopic studies. Inorg Chem Front 4:1539–1545
99. Squirrell JM, Wokosin DL, White JG, Bavister BD (1999) Long-term two-photon fluorescence imaging of mammalian embryos without compromising viability. Nat Biotechnol 17:763–767
100. Chen Y, Guan R, Zhang C, Huang J, Ji L, Chao H (2016) Two-photon luminescent metal complexes for bioimaging and cancer phototherapy. Coordin Chem Rev 310:16–40
101. Lozano-Torres B, Galiana I, Rovira M, Garrido E, Chaib S, Bernardos A, Muñoz-Espín D, Serrano M, Martínez-Máñez R, Sancenón F (2017) An OFF-ON two-photon fluorescent probe for tracking cell senescence in vivo. J Am Chem Soc 139:8808–8811
102. Gao Y, Wu J, Li Y, Sun P, Zhou H, Yang J, Zhang S, Jin B, Tian Y (2009) A sulfur-terminal Zn (II) complex and its two-photon microscopy biological imaging application. J Am Chem Soc 131:5208–5213
103. Chen Y, Bai Y, Han Z, He W, Guo Z (2015) Photoluminescence imaging of Zn^{2+} in living systems. Chem Soc Rev 44:4517–4546
104. Tang J, Cai YB, Jing J, Zhang JL (2015) Unravelling the correlation between metal induced aggregation and cellular uptake/subcellular localization of Znsalen: an overlooked rule for design of luminescent metal probes. Chem Sci 6:2389–2397
105. Jing J, Chen JJ, Hai Y, Zhan J, Xu P, Zhang JL (2012) Rational design of ZnSalen as a single and two photon activatable fluorophore in living cells. Chem Sci 3:3315–3320
106. Kong C, Peng M, Shen H, Wang Y, Zhang Q, Wang H, Zhang J, Zhou H, Yang J, Wu J, Tian Y (2015) A novel D-A type terpyridine-based carbazole Zn(II) complex with enhanced two-photon absorption and its bioimaging application. Dyes Pigments 120:328–334
107. Zhang Q, Tian X, Hu Z, Brommesson C, Wu J, Zhou H, Li S, Yang J, Sun Z, Tian Y (2015) A series of Zn(II) terpyridine complexes with enhanced two-photon-excited fluorescence for in vitro and in vivo bioimaging. J Mater Chem B 3:7213–7221
108. Zhang P, Huang H, Chen Y, Wang J, Ji L, Chao H (2015) Ruthenium(II) anthraquinone complexes as two-photon luminescent probes for cycling hypoxia imaging in vivo. Biomaterials 53:522–531
109. Baggaley E, Sazanovich IV, Williams JAG, Haycock JW, Botchway SW, Weinstein JA (2014) Two-photon phosphorescence lifetime imaging of cells and tissues using a long-lived cyclometallated $N_{pyridyl}$^C_{phenyl}^$N_{pyridyl}$ Pt(II) complex. RSC Adv 4:35003–35008
110. Baggaley E, Gill MR, Green NH, Turton D, Sazanovich IV, Botchway SW, Smythe C, Haycock JW, Weinstein JA, Thomas JA (2014) Dinuclear ruthenium(II) complexes as two-photon, time-resolved emission microscopy probes for cellular DNA. Angew Chem Int Ed 53:3367–3371
111. Zwier JM, Hildebrandt N (2017) Time-gated FRET detection for multiplexed biosensing. In: Geddes CD (ed) Reviews in fluorescence 2016. Springer, Cham, pp 17–43
112. Zhang KY, Yu Q, Wei H, Liu S, Zhao Q, Huang W (2018) Long-lived emissive probes for time-resolved photoluminescence bioimaging and biosensing. Chem Rev 118:1770–1839
113. Ebrecht R, Paul CD, Wouters FS (2014) Fluorescence lifetime imaging microscopy in the medical sciences. Protoplasma 251:293–305
114. Bastiaens PIH, Squire A (1999) Fluorescence lifetime imaging microscopy: spatial resolution of biochemical processes in the cell. Trends Cell Biol 9:48–52
115. Jiang J, Zhang C, Lin W, Liu Y, Liu S, Xu Y, Zhao Q, Huang W (2015) Long-lived phosphorescent iridium(III) complexes conjugated with cationic polyfluorenes for heparin sensing and cellular imaging. Macromol Rapid Commun 36:640–646
116. Murphy L, Congreve A, Pålsson LO, Williams JAG (2010) The time domain in co-stained cell imaging: time-resolved emission imaging microscopy using a protonatable luminescent iridium complex. Chem Commun 46:8743–8745
117. Shi H, Sun H, Yang H, Liu S, Jenkins G, Feng W, Li F, Zhao Q, Liu B, Huang W (2013) Cationic polyfluorenes with phosphorescent iridium(III) complexes for time-resolved luminescent biosensing and fluorescence lifetime imaging. Adv Funct Mater 23:3268–3276
118. Tang Y, Yang HR, Sun HB, Liu SJ, Wang JX, Zhao Q, Liu XM, Xu WJ, Li SB, Huang W (2013) Rational design of an "OFF-ON" phosphorescent chemodosimeter based on an iridium(III) complex and its application for time-resolved luminescent

detection and bioimaging of cysteine and homocysteine. Chem Eur J 19:1311–1319
119. Xu W, Zhao X, Lv W, Yang H, Liu S, Liang H, Tu Z, Xu H, Qiao W, Zhao Q (2014) Rational design of phosphorescent chemodosimeter for reaction-based one- and two-photon and time-resolved luminescent imaging of biothiols in living cells. Adv Healthc Mater 3:658–669
120. Ma Y, Liang H, Zeng Y, Yang H, Ho CL, Xu W, Zhao Q, Huang W, Wong WY (2016) Phosphorescent soft salt for ratiometric and lifetime imaging of intracellular pH variations. Chem Sci 7:3338–3346
121. Zhao Q, Liu Y, Cao Y, Lv W, Yu Q, Liu S, Liu X, Shi M, Huang W (2015) Rational design of nanoparticles with efficient lanthanide luminescence sensitized by iridium(III) complex for time-gated luminescence bioimaging. Adv Opt Mater 3:233–240
122. Yu Q, Huang T, Li Y, Wei H, Liu S, Huang W, Du J, Zhao Q (2017) Rational design of a luminescent nanoprobe for hypoxia imaging in vivo via ratiometric and photoluminescence lifetime imaging microscopy. Chem Commun 53:4144–4147
123. Lv W, Yang T, Yu Q, Zhao Q, Zhang KY, Liang H, Liu S, Li F, Huang W (2015) A phosphorescent iridium(III) complex-modified nanoprobe for hypoxia bioimaging via time-resolved luminescence microscopy. Adv Sci 2:1500107
124. Chen Z, Yan P, Zou L, Zhao M, Jiang J, Liu S, Zhang KY, Huang W, Zhao Q (2018) Using ultrafast responsive phosphorescent nanoprobe to visualize elevated peroxynitrite in vitro and in vivo via ratiometric and time-resolved photoluminescence imaging. Adv Healthc Mater 7:1800309
125. Du Z, Zhang R, Song B, Zhang W, Wang YL, Liu J, Liu C, Xu ZP, Yuan J (2019) Iridium(III) complex-based activatable probe for phosphorescent/time-gated luminescent sensing and imaging of cysteine in mitochondria of live cells and animals. Chem Eur J 25:1498–1506
126. Wang W, Lu L, Wu KJ, Liu J, Leung CH, Wong CY, Ma DL (2019) Long-lived iridium(III) complexes as luminescent probes for the detection of periodate in living cells. Sens Actuators B Chem 288:392–398
127. Zhang DY, Zheng Y, Zhang H, He L, Tan CP, Sun JH, Zhang W, Peng X, Zhan Q, Ji LN, Mao ZW (2017) Ruthenium complex-modified carbon nanodots for lysosome-targeted one- and two-photon imaging and photodynamic therapy. Nanoscale 9:18966–18976
128. Shum J, Leung PKK, Lo KKW (2019) Luminescent ruthenium(II) polypyridine complexes for a wide variety of biomolecular and cellular applications. Inorg Chem 58:2231–2247
129. Zhang KY, Liu HW, Tang MC, Choi AWT, Zhu N, Wei XG, Lau KC, Lo KKW (2015) Dual-emissive cyclometalated iridium(III) polypyridine complexes as ratiometric biological probes and organelle-selective bioimaging reagents. Inorg Chem 54:6582–6593
130. Zhang Q, Lu X, Wang H, Tian X, Wang A, Zhou H, Wu J, Tian Y (2018) A benzoic acid terpyridine-based cyclometalated iridium(III) complex as a two-photon fluorescence probe for imaging nuclear histidine. Chem Commun 54:3771–3774
131. Chakrabortty S, Agrawalla BK, Stumper A, Vegi NM, Fischer S, Reichardt C, Kögler M, Dietzek B, Feuring-Buske M, Buske C (2017) Mitochondria targeted protein-ruthenium photosensitizer for efficient photodynamic applications. J Am Chem Soc 139:2512–2519
132. Li J, Tian Z, Zhang S, Xu Z, Mao X, Zhou Y, Liu Z (2019) Organometallic ruthenium and iridium phosphorus complexes: synthesis, cellular imaging, organelle targeting and anticancer applications. Appl Organomet Chem 33:e4685
133. Qiu K, Chen Y, Rees TW, Ji L, Chao H (2019) Organelle-targeting metal complexes: from molecular design to bio-applications. Coordin Chem Rev 378:66–86
134. Nam JS, Kang MG, Kang J, Park SY, Lee SJC, Kim HT, Seo JK, Kwon OH, Lim MH, Rhee HW, Kwon TH (2016) Endoplasmic reticulum-localized iridium (III) complexes as efficient photodynamic therapy agents via protein modifications. J Am Chem Soc 138:10968–10977
135. Yuan B, Liu J, Guan R, Jin C, Ji L, Chao H (2019) Endoplasmic reticulum targeted cyclometalated iridium(III) complexes as efficient photodynamic therapy photosensitizers. Dalton Trans 48:6408–6415
136. Laha P, De U, Chandra F, Dehury N, Khullar S, Kim HS, Patra S (2018) Alkyl chain-modified cyclometalated iridium complexes as tunable anticancer and imaging agents. Dalton Trans 47:15873–15881
137. Zhang KY, Zhang T, Wei H, Wu Q, Liu S, Zhao Q, Huang W (2018) Phosphorescent iridium(III) complexes capable of imaging and distinguishing between exogenous and endogenous analytes in living cells. Chem Sci 9:7236–7240
138. Liu X, Hao H, Ge X, He X, Liu Y, Wang Y, Wang H, Shao M, Jing Z, Tian L, Liu Z (2019) Triphenylamine-appended cyclometallated iridium (III) complexes: preparation, photophysical properties and application in biology/luminescence imaging. J Inorg Biochem 199:110757
139. Zielonka J, Joseph J, Sikora A, Hardy M, Ouari O, Vasquez-Vivar J, Cheng G, Lopez M, Kalyanaraman B (2017) Mitochondria-targeted triphenylphosphonium-based compounds: syntheses, mechanisms of action, and therapeutic and diagnostic applications. Chem Rev 117:10043–10120
140. Zhu Z, Wang Z, Zhang C, Wang Y, Zhang H, Gan Z, Guo Z, Wang X (2019) Mitochondrion-targeted platinum complexes suppressing lung cancer through multiple pathways involving energy metabolism. Chem Sci 10:3089–3095
141. Lv W, Zhang Z, Zhang KY, Yang H, Liu S, Xu A, Guo S, Zhao Q, Huang W (2016) A mitochondria-

targeted photosensitizer showing improved photodynamic therapy effects under hypoxia. Angew Chem Int Ed 55:9947–9951
142. Sen S, Li Y, Lynch V, Arumugam K, Sessler JL, Arambula JF (2019) Expanding the biological utility of bis-NHC gold(I) complexes through post synthetic carbamate conjugation. Chem Commun 55:10627–10630
143. Omar SAE, Scattergood PA, McKenzie LK, Bryant HE, Weinstein JA, Elliott PIP (2016) Towards water soluble mitochondria-targeting theranostic osmium (II) triazole-based complexes. Molecules 21:1382
144. Galindo F, Burguete MI, Vigara L, Luis SV, Kabir N, Gavrilovic J, Russell DA (2005) Synthetic macrocyclic peptidomimetics as tunable pH probes for the fluorescence imaging of acidic organelles in live cells. Angew Chem Int Ed 44:6504–6508
145. Qiu K, Huang H, Liu B, Liu Y, Huang Z, Chen Y, Ji L, Chao H (2016) Long-term lysosomes tracking with a water-soluble two-photon phosphorescent iridium(III) complex. ACS Appl Mater Interfaces 8:12702–12710
146. Stacy AE, Palanimuthu D, Bernhardt PV, Kalinowski DS, Jansson PJ, Richardson DR (2016) Zinc(II)–thiosemicarbazone complexes are localized to the lysosomal compartment where they transmetallate with copper ions to induce cytotoxicity. J Med Chem 59:4965–4984
147. Tian Z, Li J, Zhang S, Xu Z, Yang Y, Kong D, Zhang H, Ge X, Zhang J, Liu Z (2018) Lysosome-targeted chemotherapeutics: half-sandwich ruthenium(II) complexes that are selectively toxic to cancer cells. Inorg Chem 57:10498–10502
148. Manikandamathavan VM, Duraipandy N, Kiran MS, Vaidyanathan VG, Nair BU (2015) A new platinum (II) complex for bioimaging applications. RSC Adv 5:24877–24885
149. Ding Y, Wu Q, Zheng K, An L, Hu X, Mei W (2015) Imaging of the nuclei of living tumor cells by novel ruthenium(II) complexes coordinated with 6-chloro-5-hydroxylpyrido[3,2-*a*]phenazine. RSC Adv 5:63330–63337
150. Liu S, Liang H, Zhang KY, Zhao Q, Zhou X, Xu W, Huang W (2015) A multifunctional phosphorescent iridium(III) complex for specific nucleus staining and hypoxia monitoring. Chem Commun 51:7943–7946
151. Selvin PR (2002) Principles and biophysical applications of lanthanide-based probes. Annu Rev Biophys Biomol Struct 31:275–302
152. Eliseeva SV, Bünzli JCG (2010) Lanthanide luminescence for functional materials and bio-sciences. Chem Soc Rev 39:189–227
153. Montgomery CP, Murray BS, New EJ, Pal R, Parker D (2009) Cell-penetrating metal complex optical probes: targeted and responsive systems based on lanthanide luminescence. Acc Chem Res 42:925–937
154. Dasari S, Singh S, Sivakumar S, Patra AK (2016) Dual-sensitized luminescent europium(III) and terbium(III) complexes as bioimaging and light-responsive therapeutic agents. Chem Eur J 22:17387–17396
155. Bünzli JCG (2010) Lanthanide luminescence for biomedical analyses and imaging. Chem Rev 110:2729–2755
156. Wei C, Ma L, Wei H, Liu Z, Bian Z, Huang C (2018) Advances in luminescent lanthanide complexes and applications. Sci China Technol Sci 61:1265–1285
157. Hasegawa Y, Kitagawa Y, Nakanishi T (2018) Effective photosensitized, electrosensitized, and mechanosensitized luminescence of lanthanide complexes. NPG Asia Mater 10:52–70
158. Bünzli JCG (2016) Lanthanide light for biology and medical diagnosis. J Lumin 170:866–878
159. Bünzli JCG, Eliseeva SV (2010) Lanthanide NIR luminescence for telecommunications, bioanalyses and solar energy conversion. J Rare Earth 28:824–842
160. Moore EG, Samuel APS, Raymond KN (2009) From antenna to assay: lessons learned in lanthanide luminescence. Acc Chem Res 42:542–552
161. Ning Y, Liu YW, Meng YS, Zhang JL (2018) Design of near-infrared luminescent lanthanide complexes sensitive to environmental stimulus through rationally tuning the secondary coordination sphere. Inorg Chem 57:1332–1341
162. Pershagen E, Borbas KE (2014) Designing reactivity-based responsive lanthanide probes for multicolor detection in biological systems. Coordin Chem Rev 273:30–46
163. Sy M, Nonat A, Hildebrandt N, Charbonnière LJ (2016) Lanthanide-based luminescence biolabelling. Chem Commun 52:5080–5095
164. Liu Q, Feng W, Li F (2014) Water-soluble lanthanide upconversion nanophosphors: synthesis and bioimaging applications in vivo. Coordin Chem Rev 273:100–110
165. Liu C, Lu S, Yang L, Chen P, Bai P, Wang Q (2017) An NIR neodymium-tag for quantifying targeted biomarker and counting its host circulating tumor cells. Anal Chem 89:9239–9246
166. Ning Y, Cheng S, Wang JX, Liu YW, Feng W, Li F, Zhang JL (2019) Fluorescence lifetime imaging of upper gastrointestinal pH in vivo with a lanthanide based near-infrared τ probe. Chem Sci 10:4227–4235
167. Cieslikiewicz-Bouet M, Eliseeva SV, Aucagne V, Delmas AF, Gillaizeau I, Petoud S (2019) Near-infrared emitting lanthanide(III) complexes as prototypes of optical imaging agents with peptide targeting ability: a methodological approach. RSC Adv 9:1747–1751
168. Bradberry SJ, Savyasachi AJ, Martinez-Calvo M, Gunnlaugsson T (2014) Development of responsive visibly and NIR luminescent and supramolecular coordination self-assemblies using lanthanide ion directed synthesis. Coordin Chem Rev 273:226–241

169. Buenzli JCG (2015) On the design of highly luminescent lanthanide complexes. Coordin Chem Rev 293:19–47
170. Hamon N, Galland M, Le Fur M, Roux A, Duperray A, Grichine A, Andraud C, Le Guennic B, Beyler M, Maury O, Tripier R (2018) Combining a pyclen framework with conjugated antenna for the design of europium and samarium luminescent bioprobes. Chem Commun 54:6173–6176
171. Martinić I, Eliseeva SV, Nguyen TN, Pecoraro VL, Petoud S (2017) Near-infrared optical imaging of necrotic cells by photostable lanthanide-based metallacrowns. J Am Chem Soc 139:8388–8391
172. Ning Y, Tang J, Liu YW, Jing J, Sun Y, Zhang JL (2018) Highly luminescent, biocompatible ytterbium (III) complexes as near-infrared fluorophores for living cell imaging. Chem Sci 9:3742–3753
173. Alcala MA, Shade CM, Uh H, Kwan SY, Bischof M, Thompson ZP, Gogick KA, Meier AR, Strein TG, Bartlett DL (2011) Preferential accumulation within tumors and in vivo imaging by functionalized luminescent dendrimer lanthanide complexes. Biomaterials 32:9343–9352
174. Mani T, Tircso G, Togao O, Zhao P, Soesbe TC, Takahashi M, Sherry AD (2009) Modulation of water exchange in Eu(III) DOTA-tetraamide complexes: considerations for in vivo imaging of PARACEST agents. Contrast Media Mol I 4:183–191
175. Ma H, Song B, Wang Y, Cong D, Jiang Y, Yuan J (2017) Dual-emissive nanoarchitecture of lanthanide-complex-modified silica particles for in vivo ratiometric time-gated luminescence imaging of hypochlorous acid. Chem Sci 8:150–159
176. Song B, Ye Z, Yang Y, Ma H, Zheng X, Jin D, Yuan J (2015) Background-free in-vivo imaging of vitamin C using time-gateable responsive probe. Sci Rep 5:14194
177. Li Y, Li X, Xue Z, Jiang M, Zeng S, Hao J (2018) Second near-infrared emissive lanthanide complex for fast renal-clearable in vivo optical bioimaging and tiny tumor detection. Biomaterials 169:35–44
178. Ning Y, Chen S, Chen H, Wang JX, He S, Liu YW, Cheng Z, Zhang JL (2019) A proof-of-concept application of water-soluble ytterbium(III) molecular probes in in vivo NIR-II whole body bioimaging. Inorg Chem Front 6:1962–1967